VOLUME 77 MAY 24, 1973 NUMBER 11

JPCHAx

THE JOURNAL OF PHYSICAL CHEMISTRY

PUBLISHED BIWEEKLY BY THE AMERICAN CHEMICAL SOCIETY

THE JOURNAL OF

PHYSICAL CHEMISTRY

BRYCE CRAWFORD, Jr., *Editor*
STEPHEN PRAGER, *Associate Editor*
ROBERT W. CARR, Jr., FREDERIC A. VAN-CATLEDGE, *Assistant Editors*

EDITORIAL BOARD: A. O. ALLEN (1970–1974), C. A. ANGELL (1973–1977), J. R. BOLTON (1971–1975), F. S. DAINTON (1972–1976), M. FIXMAN (1970–1974), H. S. FRANK (1970–1974), R. R. HENTZ (1972–1976), J. R. HUIZENGA (1969–1973), W. J. KAUZMANN (1969–1973), R. L. KAY (1972–1976), W. R. KRIGBAUM (1969–1973), W. J. MOORE (1969–1973), R. M. NOYES (1973–1977), J. A. POPLE (1971–1975), B. S. RABINOVITCH (1971–1975), H. REISS (1970–1974), S. A. RICE (1969–1975), F. S. ROWLAND (1973–1977), R. L. SCOTT (1973–1977), W. A. ZISMAN (1972–1976)

AMERICAN CHEMICAL SOCIETY, *1155 Sixteenth St., N.W., Washington, D. C. 20036*

Books and Journals Division

JOHN K CRUM *Director*
RUTH REYNARD *Assistant to the Director*

CHARLES R. BERTSCH *Head, Editorial Processing Department*
D. H. MICHAEL BOWEN *Head, Journals Department*
BACIL GUILEY *Head, Graphics and Production Department*
SELDON W. TERRANT *Head, Research and Development Department*

©Copyright, 1973, by the American Chemical Society. Published biweekly by the American Chemical Society at 20th and Northampton Sts., Easton, Pa. 18042. Second-class postage paid at Washington, D. C., and at additional mailing offices.

All manuscripts should be sent to *The Journal of Physical Chemistry*, Department of Chemistry, University of Minnesota, Minneapolis, Minn. 55455.

Additions and Corrections are published once yearly in the final issue. See Volume 76, Number 26 for the proper form.

Extensive or unusual alterations in an article after it has been set in type are made at the author's expense, and it is understood that by requesting such alterations the author agrees to defray the cost thereof.

The American Chemical Society and the Editor of *The Journal of Physical Chemistry* assume no responsibility for the statements and opinions advanced by contributors.

Correspondence regarding accepted copy, proofs, and reprints should be directed to Editorial Processing Department, American Chemical Society, 20th and Northampton Sts., Easton, Pa. 18042. Head: CHARLES R. BERTSCH. Assistant Editor: EDWARD A. BORGER. Editorial Assistant: JOSEPH E. YURVATI.

Advertising Office: Centcom, Ltd., 142 East Avenue, Norwalk, Conn. 06851.

Business and Subscription Information

Send all new and renewal subscriptions *with payment* to: Office of the Controller, 1155 16th Street, N.W., Washington, D. C. 20036. Subscriptions should be renewed promptly to avoid a break in your series. All correspondence and telephone calls regarding changes of address, claims for missing issues, subscription service, the status of records, and accounts should be directed to Manager, Membership and Subscription Services, American Chemical Society, P.O. Box 3337, Columbus, Ohio 43210. Telephone (614) 421-7230.

On changes of address, include both old and new addresses with ZIP code numbers, accompanied by mailing label from a recent issue. Allow four weeks for change to become effective.

Claims for missing numbers will not be allowed (1) if loss was due to failure of notice of change in address to be received before the date specified, (2) if received more than sixty days from date of issue plus time normally required for postal delivery of journal and claim, or (3) if the reason for the claim is "issue missing from files."

Subscription rates (1973): members of the American Chemical Society, $20.00 for 1 year; to nonmembers, $60.00 for 1 year. Those interested in becoming members should write to the Admissions Department, American Chemical Society, 1155 Sixteenth St., N.W., Washington, D. C. 20036. Postage to Canada and countries in the Pan-American Union, $5.00; all other countries, $6.00. Single copies for current year: $3.00. Rates for back issues from Volume 56 to date are available from the Special Issues Sales Department, 1155 Sixteenth St., N.W., Washington, D. C. 20036.

Subscriptions to this and the other ACS periodical publications are available on microfilm. Supplementary material not printed in this journal is now available in microfiche form on a current subscription basis. For information on microfilm or microfiche subscriptions, write Special Issues Sales Department at the address above.

Notice to Authors last printed in the issue of November 23, 1972

THE JOURNAL OF

PHYSICAL CHEMISTRY

Volume 77, Number 11 May 24, 1973

JPCHAx 77(11) 1319–1474 (1973)

1A
ห้องสมุด ... วิทยาศาสตร์
24 ต.ค. 2518

COMMUNICATIONS TO THE EDITOR

AUTHOR INDEX

In papers with more than one author the name of the author to whom inquiries about the paper should be addressed is marked with an asterisk in the by-line.

ANNOUNCEMENT

On the last two pages of this issue you will find reproduced the table of contents of the April 1973 issue of the *Journal of Chemical and Engineering Data.*

THE JOURNAL OF
PHYSICAL CHEMISTRY

Registered in U. S. Patent Office © *Copyright, 1973, by the American Chemical Society*

VOLUME 77, NUMBER 11 MAY 24, 1973

Moderation of Photochemically Produced Hot Deuterium Atoms[1a]

Richard A. Fass* and Deen L. Wong[1b]

Department of Chemistry, Pomona College, Claremont, California 91711 *(Received December 18, 1972)*

Publication costs assisted by the Research Corporation

The relative moderating efficiencies of various gases for hot deuterium atoms produced by photodissociation of DBr have been determined. For deuterium atoms produced initially at 2–3 eV the moderators, in order of increasing efficiency, are Xe, Ar, Ne, CO_2, D_2, CD_4, and He. The results provide direct experimental evidence for an inelastic moderation mechanism with the polyatomic moderators, and are consistent with a "soft" interaction potential between D and He. The difficulty of achieving a completely "thermal" D atom population by this method is noted and discussed.

Introduction

The ultraviolet photolysis of hydrogen halides has been used for many years to produce hydrogen atoms with nonthermal energy distributions (*i.e.*, "hot" hydrogen atoms).[2,3] The reactions of these atoms with molecular hydrogen,[4,5] with hydrocarbons,[6,7] and with hydrogen halides and halogens[2,8-12] have been widely studied. One of the details of these studies which remains problematic is the mechanism by which some of these hot atoms are cooled to thermal energies after they escape hot chemical reaction. The object of this study is to obtain some information about this mechanism by measuring the relative moderating efficiencies of a series of gases which are chemically inert to hot or thermal deuterium atoms.

In a previous paper[11] it has been shown that the ratio of the rate constant of the reaction $D + Br_2 \rightarrow DBr + Br$ to that of $D + DBr \rightarrow D_2 + Br$ can be determined by measuring the quantum yield of Br_2 decomposition from photolysis of DBr in $DBr-Br_2$ mixtures. This ratio was shown[11] to be 58 for thermal D atoms at 25° and 6.7 for D atoms produced at ~2 eV in unmoderated systems. The energy dependence of this ratio can therefore be used to study the effect of various moderators, since a more efficient moderator will give a rate constant ratio closer to the thermal value compared to an equal concentration of a less efficient moderator. This paper discusses the determination of relative moderating efficiencies in $DBr-Br_2$ systems photolyzed at 2139 and 1850 Å in the presence of the moderators He, D_2, Ne, CD_4, Ar, CO_2, and Xe.

The possible energy-loss mechanisms to be considered are (a) elastic hard-sphere collisions, (b) elastic collisions involving a "soft" interaction potential, and (c) inelastic collisions in which energy is absorbed by internal degrees of freedom of the moderator. (In the special case of D_2 moderating hot D atoms we also have the possibility of the exchange reaction $D + D_2 \rightarrow D_2 + D$ which is chemically indistinguishable from nonreactive collisions in these systems.) Some consideration has been given[8-11,13] to these alternate mechanisms, but the conclusions have been tentative and sometimes contradictory. There is, on the other hand, a substantial amount of information about the efficiencies of various moderators for hot nuclear recoil tritium atoms produced at energies well above the chemically reactive region.[14-16] Some comparisons of

(1) (a) This research has been supported in part by a Cottrell College Science Grant from Research Corporation. (b) NSF Undergraduate Research Participant, summers 1971 and 1972.
(2) H. A. Schwarz, R. R. Williams, Jr., and W. H. Hamill, *J. Amer. Chem. Soc.*, **74**, 6007 (1952).
(3) R. M. Martin and J. E. Willard, *J. Chem. Phys.*, **40**, 3007 (1964).
(4) A. Kuppermann and J. M. White, *J. Chem. Phys.*, **44**, 4352 (1966).
(5) D. Seewald and R. Wolfgang, *J. Chem. Phys.*, **46**, 1207 (1967).
(6) R. G. Gann, W. M. Ollison, and J. Dubrin, *J. Amer. Chem. Soc.*, **92**, 450 (1970).
(7) J. E. Nicholas, F. Bay-akceken, and R. D. Fink, *J. Phys. Chem.*, **75**, 841 (1971).
(8) R. D. Penzhorn and B. deB. Darwent, *J. Phys. Chem.*, **72**, 1639 (1968).
(9) R. A. Fass, *J. Phys. Chem.*, **74**, 984 (1970).
(10) G. O. Wood and J. M. White, *J. Chem. Phys.*, **52**, 2613 (1970).
(11) R. A. Fass, J. W. Hoover, and L. M. Simpson, *J. Phys. Chem.*, **76**, 2801 (1972).
(12) J. M. White and H. Y. Su, *J. Chem. Phys.*, **57**, 2344 (1972).
(13) R. E. Tomalesky and J. E. Sturm, *J. Chem. Soc., Faraday Trans. 2*, **68**, 1241 (1972).

the photochemical with the nuclear recoil results will be made.

The photodissociation of hydrogen halides,[8,9,11,17-19] H_2S,[20] and C_2H_5SH[21] have also been used as convenient sources of hydrogen atoms for studies of the thermal reactions of hydrogen atoms with various molecules. In these studies it is necessary to use a large amount of inert moderator in order to be sure that all of the atoms are thermalized before they undergo chemical reaction. There has been some disagreement in the literature[11] about the amount of moderator required to effectively thermalize all of the photochemically produced hot atoms. A further object of the present work was, therefore, to obtain more information about the moderator/reactant ratios needed to produce a thermal population of hydrogen or deuterium atoms in these systems.

Experimental Section

DBr was purchased from International Chemical and Nuclear Corp. (isotopic purity 99 atom %). It was stored in a Pyrex flask on a mercury-free vacuum line, and showed no appreciable decomposition over a period of several months. Br_2 was Matheson Coleman and Bell ACS Reagent grade and was stored in an evacuated Pyrex tube. Air Reduction Co. research grade CO_2, International Chemical and Nuclear Corp. CD_4 (99 atom %), Matheson ultrahigh purity grade He, Matheson D_2 (CP grade, 99.5 atom %), Ne, Ar, and Xe were used as received. All of these chemicals were stored behind Teflon stopcocks.

The experimental details of cell filling, photolysis, and spectrophotometric measurement of the rate of Br_2 production have been given previously.[11] The method of analysis used (see below) did not require actinometry, but it did require constant absorbed light intensity throughout a run for each moderator. The Zn (2139 Å) and Hg (1850 Å) lamps were run continuously during each run to minimize the possibility of intensity variations, and the measurements at different $[Br_2]/[DBr]$ ratios were made in random order to minimize the effect of any gradual changes of intensity that might occur. The relatively small changes in the intercepts obtained from the linear plots for consecutive runs made with the same lamps and geometry suggested that variation of lamp intensity during a run was not a serious problem.

The slight curvature exhibited in some of the plots of the rate of Br_2 production *vs.* $[Br_2]/[DBr]$ indicated that the slopes and intercepts determined from linear least-squares analysis might be a function of the range of $[Br_2]/[DBr]$ used. To minimize this effect for purposes of comparison of different moderators, the range was maintained constant at $0 < [Br_2]/[DBr] < 0.07$. Runs were conducted for each moderator at an initial [DBr]/[moderator] ratio of 20 Torr/200 Torr at 2139 Å. For two moderators (Ne and CD_4) an additional run at 1850 Å was made. For CO_2 and D_2 runs were also made with initial [DBr]/[moderator] of 20 Torr/1400 Torr. These choices of reactant and moderator concentrations were dictated by a desire to obtain maximum precision in measurements of the rate of Br_2 production while the ratios of concentrations of Br_2 to DBr and of (Br_2 + DBr) to moderator were kept nearly constant.

Mechanism and Analysis of Data

The mechanism for the photodissociation of DBr in the presence of Br_2 and inert moderator has been described.[11]

$$DBr \rightarrow D^* + Br\ (^2P_{3/2}) \quad (1)$$

$$D^* + DBr \rightarrow D_2 + Br \quad (2^*)$$

$$D^* + Br_2 \rightarrow DBr + Br \quad (3^*)$$

$$D^* + M \rightarrow D \quad (4)$$

$$D + DBr \rightarrow D_2 + Br \quad (2)$$

$$D + Br_2 \rightarrow DBr + Br \quad (3)$$

$$2Br + M' \rightarrow Br_2 + M' \quad (5)$$

When DBr is photolyzed with the Zn resonance lamp, the translational energy of the D* atom formed in (1) is ~2.0 eV for the 2139-Å line and ~2.3 eV for the 2026-Å line emitted by the same source. Photolysis of DBr at 1850 Å produces a ~2.8-eV D atom.

The hot deuterium atoms reacting in (2*) and (3*) have energies between the initial D* energy and thermal energies. Thermalization is accomplished by collisions with added inert moderator [M in (4)]. When the D* atom energy becomes less than the threshold energy of (2) it is regarded as a thermal atom (D). The threshold energy is probably in the neighborhood of 1-2 kcal mol^{-1} which is well into the thermal Maxwell-Boltzmann distribution at 25°. This fact makes the distinction between D* and D somewhat ambiguous, a point which is discussed later. For our purposes thermal atoms will be defined as those atoms which give a ratio k_3/k_2 equal to the ratio for a thermal population of D atoms.

In general, M should be interpreted as including DBr and Br_2 which might also undergo nonreactive, moderating collisions with D* atoms. The analogous moderation processes have been shown to be significant in HCl-Cl_2 systems.[10] For reasons discussed in an earlier paper[11] we can assume that in the DBr-Br_2 systems moderation by inert moderators is much more significant than that by DBr or Br_2.

The usual steady-state considerations based on the above mechanism lead to the following differential rate equation

$$\frac{1}{\phi_{Br_2}} = \frac{I_a}{d[Br_2]/dt} = \frac{1 + \frac{k_4[M]}{k_2^*[DBr]} + \frac{k_3^*[Br_2]}{k_2^*[DBr]}}{1 + \frac{k_4[M]}{k_2^*[DBr]} + \frac{k_3[Br_2]}{k_2[DBr]}}\left[1 + \frac{k_3[Br_2]}{k_2[DBr]}\right] \quad (I)$$

where I_a is the rate of absorption of photons by DBr, and ϕ_{Br_2} is the quantum yield of Br_2 production. The rate constant k_4 is an averaged parameter representing many collisions of moderator with D atoms over a wide energy range.

Two limits of eq I are of particular interest. When no

(14) (a) J. W. Root and F. S. Rowland, *J. Chem. Phys.*, **38**, 2030 (1963); (b) *ibid.*, **46**, 4299 (1967).
(15) P. J. Estrup, *J. Chem. Phys.*, **41**, 164 (1964).
(16) D. Seewald and R. Wolfgang, *J. Chem. Phys.*, **47**, 143 (1967).
(17) R. D. Penzhorn and H. L. Sandoval, *J. Phys. Chem.*, **74**, 2065 (1970).
(18) R. J. Letelier, H. L. Sandoval, and R. D. Penzhorn, *J. Phys. Chem.*, **75**, 835 (1971).
(19) R. D. Penzhorn and B. deB. Darwent, *J. Chem. Phys.*, **55**, 1508 (1971).
(20) G. R. Woolley and R. J. Cvetanovic, *J. Chem. Phys.*, **50**, 4697 (1969).
(21) R. B. Steer and A. R. Knight, *Can. J. Chem.*, **47**, 1335 (1969).

inert moderator is added and mixtures of DBr and Br_2 are photolyzed we obtain the limiting equation

$$\frac{1}{\phi_{Br_2}} = 1 + \frac{k_3^*[Br_2]}{k_2^*[DBr]} \quad (II)$$

Plots of $1/\phi_{Br_2}$ *vs.* $[Br_2]/[DBr]$ are linear, and the slope yields a value[11] of $k_3^*/k_2^* = 6.7 \pm 0.13$ from DBr photolysis at 2139 Å. Using a slightly different method, White and Su[12] obtain $k_3^*/k_2^* = 5.07 \pm 0.12$ from DBr photolysis at 1850 Å.

When enough inert moderator is added to effectively thermalize all of the D* atoms before they react with DBr or Br_2 eq I reduces to

$$\frac{1}{\phi_{Br_2}} = 1 + \frac{k_3[Br_2]}{k_2[DBr]} \quad (III)$$

Plots of $1/\phi_{Br_2}$ *vs.* $[Br_2]/[DBr]$ are linear, and the slope yields a value[11] of $k_3/k_2 = 58.0 \pm 1.7$ at 25°.

In the presence of moderator concentrations intermediate between the limits of (II) and (III) two methods of analysis can be used based on two different assumptions. One assumption[9,11] is that these systems are characterized by an average value of k_3'/k_2' which lies somewhere between k_3/k_2 and k_3^*/k_2^* so that the following can be used

$$\frac{1}{\phi_{Br_2}} = 1 + \frac{k_3'[Br_2]}{k_2'[DBr]} \quad (IV)$$

if we plot $1/\phi_{Br_2}$ *vs.* $[Br_2]/[DBr]$ and obtain a straight line, this implies that k_3'/k_2' is constant over the range of $[Br_2]/[DBr]$ studied, which in turn implies that the energy distribution of deuterium atoms is constant over this range. The results below indicate that this condition is only approximately satisfied over a small range of $[Br_2]/[DBr]$, and that eq IV leads to a pronounced curvature in plots of $1/\phi_{Br_2}$ *vs.* $[Br_2]/[DBr]$ for some systems. Nevertheless, this procedure is useful for comparing one moderator with another over small but identical ranges of $[Br_2]/[DBr]$.

In this paper, we have used eq IV in a slightly modified form

$$\frac{1}{R_{Br_2}} = \frac{1}{d[Br_2]/dt} = \left[\frac{1}{I_a}\right] + \left[\frac{1}{I_a}\right]\frac{k_3'[Br_2]}{k_2'[DBr]} \quad (IVa)$$

If I_a is constant for each series of measurements, the ratio of slope to intercept of plots of $1/R_{Br_2}$ *vs.* $[Br_2]/[DBr]$ will yield k_3'/k_2'. In practice, $1/R_{Br_2}$ has been measured in (arbitrary) units of [min/(absorbance change at 4150 Å)] $\times 10^{-2}$.

The alternative assumption is that the energy distribution of deuterium atoms may change with $[Br_2]/[DBr]$, but that those deuterium atoms which react while hot do so with the same k_3^*/k_2^* at all $[Br_2]/[DBr]$. The very small energy dependence of k_3^*/k_2^*[11,12] lends some support to this assumption. The analysis is then based on eq I after making the additional assumption that

$$\frac{k_3^*[Br_2]}{k_2^*[DBr]} \ll 1 + \frac{k_M[M]}{k_2^*[DBr]} \quad (V)$$

The left-hand side of this inequality is never greater than $(6.7) \times (0.07) = 0.47$. The ratio $[M]/[DBr]$ is at least 10/1 in this work. Wood and White[10] found $k_M/k_2^* \approx 1$ for CO_2 moderator in analogous DCl-Cl_2 systems, and if k_M/k_2^* is anywhere in this region in the DBr-Br_2 systems the right-hand side of the inequality is about 11. If this assumption about k_M/k_2^* is not valid, nonlinearity should be detected in the plots described below.

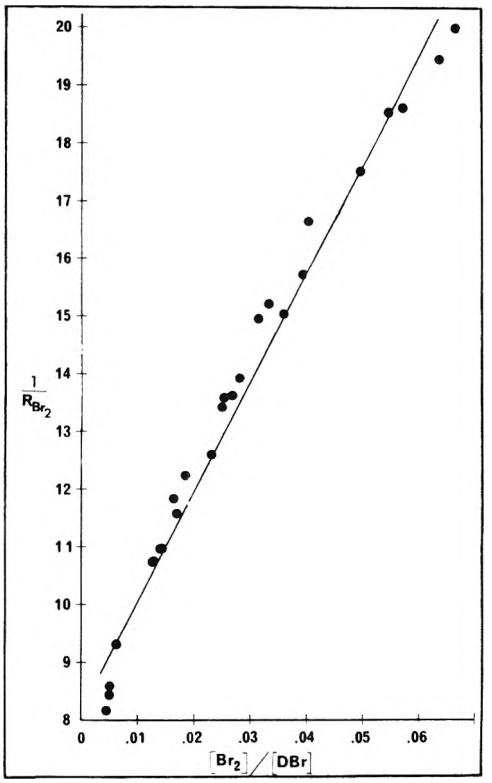

Figure 1. $1/R_{Br_2}$ *vs.* $[Br_2]/[DBr]$ for a mixture containing 20 Torr of DBr and 200 Torr of Ar photolyzed at 2139 Å (see eq IVa). Units for the ordinate are arbitrary, and are inversely proportional to the rate of Br_2 production. Results of a least-squares analysis are given in Table I.

Equation I can be rearranged, using the simplifying assumption (V), to give

$$Y_{Br_2} = R_{Br_2}\left[1 + \frac{k_3[Br_2]}{k_2[DBr]}\right] = I_a + \frac{I_a\left(\frac{k_3}{k_2}\right)}{1 + \frac{k_M[M]}{k_2^*[DBr]}}\left(\frac{[Br_2]}{[DBr]}\right) \quad (VI)$$

Since $k_3/k_2 = 58$ at 25°[11] and I_a is kept constant, a plot of the left-hand side of (VI) *vs.* $[Br_2]/[DBr]$ should be linear if our assumptions are valid. Fortunately the results prove to be quite insensitive to the value of k_3/k_2 used in this calculation. The ratio of slope to intercept of this line then contains only one unknown, k_M/k_2^*, which can be calculated from the data.

The data have been analyzed according to both eq IVa and VI. Although the qualitative conclusions of this work are the same either way, it should be noted that eq IVa is in better agreement with the data for highly moderated systems (*i.e.*, most of the deuterium atoms thermalized before they react) while eq VI gives better linear plots for less moderated systems (*i.e.*, most of the deuterium atoms react while hot).

Results

All experiments were analyzed according to eq IVa and VI. An example of this analysis is given for the system consisting of 20 Torr of DBr, 200 Torr of argon, and

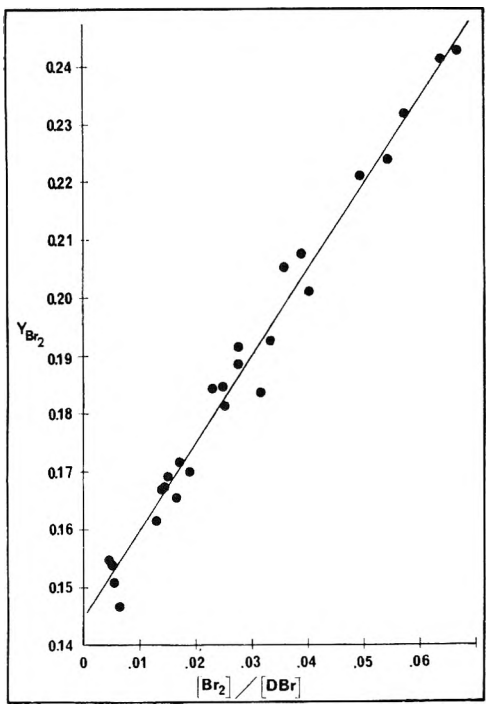

Figure 2. Y_{Br_2} *vs.* $[Br_2]/[DBr]$ for the same data as Figure 1. See eq VI and the results of the least-squares analysis in Table I: $Y_{Br_2} = R_{Br_2}[1 + (k_3[Br_2]/k_2[DBr])]$.

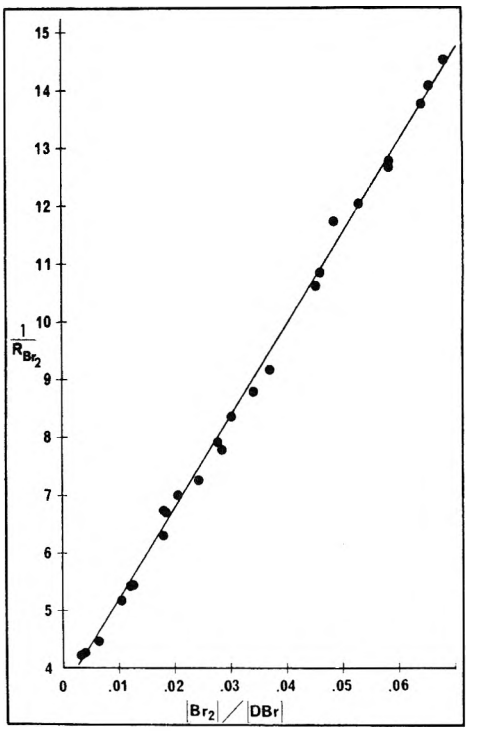

Figure 3. $1/R_{Br_2}$ *vs.* $[Br_2]/[DBr]$ for a mixture containing 20 Torr of DBr and 200 Torr of He photolyzed at 2139 Å.

$[Br_2]/[DBr]$ ratios up to 0.07. The results plotted according to eq IVa are shown in Figure 1. Although the data can be fitted reasonably well to a straight line ($k_3'/k_2' = 22.6 \pm 0.8$) there is a noticeable curvature in the data suggesting that the dependence of R_{Br_2} on $[Br_2]/[DBr]$ is more complex. The same data are plotted according to eq VI in Figure 2. The linearity is significantly improved, and the plot yields a value of $k_M/k_2^* = 0.46 \pm 0.02$.

(The uncertainties used throughout this paper are standard deviations, unless otherwise indicated, and least-squares analysis has been used on all of the linear plots.)

A contrasting situation is the system consisting of 20 Torr of DBr, 200 Torr of He, and $[Br_2]/[DBr]$ ratios up to 0.07. When the data are plotted according to eq IVa the result is a straight line (see Figure 3) with no detectable curvature. The value of k_3'/k_2' obtained from a least-squares analysis is 44.7 ± 1.0. The analysis based on eq VI (not shown) gives a good linear relationship with $k_M/k_2^* = 1.79 \pm 0.26$.

Table I summarizes the results of linear plots in all of the systems studied. In no case was the curvature more pronounced than that shown in Figure 1. Since the range of $[Br_2]/[DBr]$ was the same in all cases (0–0.07), a comparison could be made between different moderators despite this curvature. The fact that both methods of analysis give identical rank orders of moderator efficiency is added support for the assumptions of the data analysis. In the discussion that follows, the ratio k_M/k_2^* will be used most of the time since it is most directly related to the quantity of interest, *i.e.*, the efficiency of reaction 4.

Discussion

An analysis of the results of these measurements is complicated by the inability to precisely define the difference between a hot and thermal deuterium atom. Ordinarily, the dividing line between hot and thermal is defined as the threshold energy of the hot reaction being studied. In the present studies, the activation energy of reaction 2 is known[22] to be ~0.9 kcal mol^{-1} higher than that of (3), but the activation energy of (3) is itself not known. It is generally considered to be equal to or less than 1 kcal mol^{-1}, so the activation energy of (2) is between 0 and 2 kcal mol^{-1}. This is well within the energy distribution of a thermal population of deuterium atoms at 25°, so the distinction between "hot" and "thermal" deuterium atoms is ambiguous.

The low threshold energies of the reactions involved in these systems are important to this study for two reasons. First, the ratio k_3^*/k_2^* is apt to be very highly energy dependent near the threshold energy, so this ratio will be a very sensitive measure of the approach of the energy distribution to thermal equilibrium when moderators are added. Secondly, the overlapping energy regions loosely defined as hot and thermal make it impossible to arrive at quantitative conclusions about moderating collisions as has been done[14,16] for recoil tritium atoms abstracting hydrogen atoms from hydrocarbons. The best we can do is come to some qualitative conclusions based on the assumption that a higher value of k_3'/k_2' or a higher value of k_M/k_2^* represent better moderation than lower values.

Moderation by Monatomic Gases. The inert gases He, Ne, Ar, and Xe can moderate deuterium atoms by elastic collisions only since the first electronic states of these atoms are too high in energy to be excited by collisions with 2-eV D atoms. There is considerable evidence and theoretical justification[14-16] for the fact that collisions with He (and, to a much lesser extent, with Ne) are characterized by a "soft" interaction potential rather than a

(22) A. F. Trotman-Dickenson and G. S. Milne, *Nat. Stand. Ref. Data Sec., Nat. Bur. Stand.*, **No. 9** (1967).

TABLE I: Least-Squares Results for Photolyses of Mixtures of 20 Torr of DBr with Moderator at $[Br_2]/[DBr]$ from 0 → 0.07

Moderator	[M]/[DBr]	λ, Å	No. of points	$1/R_{Br_2}$ vs. $[Br_2]/[DBr]$ (eq IVa) Slope	Intercept	k_3'/k_2'	Y_{Br_2} vs. $[Br_2]/[DBr]$ (eq VI) Slope	Intercept	k_M/k_2^*
Xe	10/1	2139	25	111.6 ± 4.4	7.72 ± 0.19	14.5 ± 0.7	2.541 ± 0.083	0.160 ± 0.004	0.26 ± 0.01
Ar	10/1	2139	26	187.5 ± 5.5	8.28 ± 0.18	22.6 ± 0.8	1.501 ± 0.043	0.145 ± 0.001	0.46 ± 0.02
Ne	10/1	2139	20	134.3 ± 6.0	5.60 ± 0.22	24.0 ± 1.4	2.212 ± 0.117	0.210 ± 0.004	0.47 ± 0.03
Ne	10/1	1850	20	151.6 ± 5.3	6.92 ± 0.21	21.9 ± 1.0	1.830 ± 0.087	0.175 ± 0.004	0.46 ± 0.03
CO_2	10/1	2139	22	214.3 ± 6.5	7.30 ± 0.22	29.4 ± 1.3	1.230 ± 0.075	0.156 ± 0.002	0.59 ± 0.04
CO_2	20/1	2139	22	230.6 ± 7.5	7.26 ± 0.32	31.8 ± 1.7	0.821 ± 0.071	0.164 ± 0.003	0.53 ± 0.05
CO_2	70/1	2139	19	173.9 ± 3.4	4.16 ± 0.13	41.8 ± 1.5	0.761 ± 0.112	0.264 ± 0.004	0.27 ± 0.04
D_2	10/1	2139	20	175.9 ± 3.8	4.82 ± 0.15	36.5 ± 1.4	1.015 ± 0.076	0.235 ± 0.003	1.24 ± 0.11
D_2	70/1	2139	20	233.0 ± 4.8	4.44 ± 0.18	52.5 ± 2.4	0.228 ± 0.105	0.232 ± 0.004	0.83 ± 0.39
CD_4	10/1	2139	20	136.6 ± 5.0	3.67 ± 0.22	37.3 ± 2.6	1.240 ± 0.183	0.306 ± 0.008	1.33 ± 0.21
CD_4	10/1	1850	20	199.7 ± 7.4	6.65 ± 0.28	30.0 ± 1.7	1.138 ± 0.096	0.177 ± 0.004	0.80 ± 0.08
He	10/1	2139	25	159.3 ± 1.8	3.56 ± 0.07	44.7 ± 1.0	0.915 ± 0.127	0.298 ± 0.005	1.79 ± 0.26

hard-sphere potential, leading to a smaller average fractional energy loss per collision than predicted by the hard-sphere model (*i.e.*, less efficient moderation). It is generally assumed[10,13,16,23] that moderation by Ar and Xe is elastic and hard sphere. Although this is not strictly correct,[24] the effect of soft interactions does become less for higher mass moderators.

The ratios of $k_M/k_2^* = K$ obtained in this work for these gases, referenced to Ar, are $K_{He}/K_{Ar} = 3.89$, $K_{Ne}/K_{Ar} = 1.03$, and $K_{Xe}/K_{Ar} = 0.57$. These numbers can be compared with the corresponding ratios of hard-sphere α values, α being the average logarithmic energy loss parameter used in the kinetic theory of hot reactions.[15,16] α, which is related to the moderation efficiency, is given by

$$\alpha = [\ln (E_{initial}/E_{final})]_{av} = 1 - \frac{(M-m)^2}{2Mm} \ln \left|\frac{M+m}{M-m}\right|$$

for hard spheres, which gives $\alpha_{He}/\alpha_{Ar} = 7.50$, $\alpha_{Ne}/\alpha_{Ar} = 1.93$, and $\alpha_{Xe}/\alpha_{Ar} = 0.31$. Considering the possibility of soft potentials between D* and the moderators, one can calculate[25] $\alpha_{He}/\alpha_{Ar} = 4.93$, $\alpha_{Ne}/\alpha_{Ar} = 1.83$, and $\alpha_{Xe}/\alpha_{Ar} = 0.33$. Although there is no direct correspondence between α and k_M/k_2^*, it can be seen that the k_M/k_2^* ratios predict relative moderating efficiencies which are closer to the values calculated for soft potentials than those for hard-sphere potentials. These data are, therefore, consistent with the moderation effects in recoil tritium systems, in which the evidence of soft interactions with He and Ne is convincing.[14,16]

Moderation by Polyatomic Gases. A comparison of k_M/k_2^* for a polyatomic molecule with k_M/k_2^* for a monatomic gas of the same approximate mass can provide evidence regarding inelastic collisions with the polyatomic moderator. For example, $(k_M/k_2^*)_{Ar} = 0.46$ while $(k_M/k_2^*)_{CO_2} = 0.59$, indicating that CO_2 is a more efficient moderator than Ar; they would have equal moderation efficiencies if all collisions were hard sphere and elastic. Unless the D-Ar potential is substantially softer than the D-CO_2 potential, this suggests that inelastic processes are involved in moderation by CO_2, contrary to the conclusions of Penzhorn and Darwent,[8] and in agreement with the conclusions of Wood and White[10] and Tomalesky and Sturm.[13] Similarly, $(k_M/k_2^*)_{Ne} = 0.47$ while $(k_M/k_2^*)_{CD_4} = 1.33$ indicating that the four C-D bonds in CD_4 offer a very effective source of inelastic energy loss for D* atoms.

It should be pointed out that although the chemical inertness of CO_2 to hot hydrogen or deuterium atoms is often assumed in these studies[8-11] it has been shown that there is a small amount of hot reaction[13] of H* with CO_2; it is not enough to affect the conclusions of this work.

The data also show $(k_M/k_2^*)_{He} = 1.79$ while $(k_M/k_2^*)_{D_2} = 1.24$. Since we expect that the collisions with He will be less effective than if they were hard-sphere collisions (*i.e.*, collisions with He are elastic but soft), these results suggest that moderation by D_2 is characterized by soft elastic collisions.[26] One additional mechanism of moderation which is certain to be significant for D_2 is the chemically undetectable exchange reaction

$$D^* + D_2 \rightarrow D_2 + D^* \qquad (6)$$

White[27] has shown that the D atom produced in (6) is not a thermal D atom, but carries off some of the translational energy originally coming from D*. It cannot be said with certainty whether reaction 6 will be more or less efficient than elastic hard-sphere collisions for slowing down hot deuterium atoms, and this complicates any attempt to explain the results with D_2 moderator.

Additional evidence regarding inelastic collisions is supplied by the wavelength dependence of k_M/k_2^* for Ne and CD_4 moderators. The data of Table I show no significant wavelength effect for Ne. The additional energy given to the D* atoms at 1850 Å (2.8 eV compared to 2.0 eV) results in very few additional collisions so that the energy distribution of D atoms that react with DBr or Br_2 is not appreciably changed by increasing the initial energy. The average fractional energy loss of a D* atom suffering an elastic hard-sphere collision with Ne is $\sim 1/6$, so that the difference between initial D* energy in 1850-Å photolysis and the initial D* energy in 2139-Å photolysis is lost in only approximately one collision. For elastic hard-sphere collisions approximately 16 total collisions are required to moderate a 2-eV D atom all the way to 0.1 eV, so the additional energy makes very little difference (approximately one collision out of 16) in the moderating efficiency.

CD_4, on the other hand, shows a very marked wave-

(23) D. M. Chapin and M. D. Kostin, *J. Chem. Phys.*, **48**, 3067 (1968).
(24) C. Rebick and J. Dubrin, *J. Chem. Phys.*, **53**, 2079 (1970).
(25) M. Baer and S. Amiel, *J. Chem. Phys.*, **53**, 407 (1970).
(26) R. G. Gann and J. Dubrin, *J. Phys. Chem.*, **76**, 1321 (1972).
(27) J. M. White, *Chem. Phys. Lett.*, **4**, 441 (1969).

length dependence of k_M/k_2^*, with values of 1.33 and 0.80 at 2139 and 1850 Å, respectively. The energy distribution of D atoms has been shifted to higher energies at 1850 Å compared to 2139 Å; the results indicate that the 2.0–2.8-eV energy range adds a significant number of hot collisions to the average lifetime of a hot deuterium atom. This must be because significantly fewer than 16 collisions are required for CD_4 to moderate a 2-eV D atom to 0.1 eV, so that the average number of collisions between 2.8 and 2.0 eV is a significant fraction of the total required to moderate. CD_4 is therefore more efficient than a hard sphere of equal mass from ~2 to 0.1 eV. Again our conclusion is that CD_4 moderates by inelastic collisions.

Production of Thermal D Atoms. It was also the object of this work to investigate the use of inert moderators in photolytic hydrogen halide systems in order to study the reactions of thermal H or D atoms. Several previous studies[8,9,11,17-19] have utilized this technique, and there has been some disagreement[9,11] about the amount of moderator required to produce a thermal population of H and D atoms. We have compared the ratios k_3'/k_2' for CO_2 and D_2, when [M]/[DBr] = 70. The results, shown in Table I, are $k_3'/k_2' = 41.8$ for CO_2 and $k_3'/k_2' = 52.5$ for D_2. Previously,[11] with [D_2]/[DBr] ratios in the range 80–150, we obtained $k_3'/k_2' = 58$, a value which we have taken as k_3/k_2, the ratio for thermal deuterium atoms. It is clear, therefore, that in the presence of a 70:1 ratio of [M]/[DBr] neither CO_2 nor D_2 produce a completely thermal population of D atoms.

The effect of [M]/[DBr] on k_3'/k_2' for CO_2 is shown in Table I. When [M]/[DBr] = 10:1, 20:1, and 70:1, $k_3'/k_2' = 29.4$, 31.8, and 41.8, respectively. The corresponding values of k_M/k_2^* are 0.59, 0.53, and 0.27. The fact that k_M/k_2^* decreases with increasing [M]/[DBr] indicates that the average moderating efficiency decreases as the system approaches an equilibrium thermal D atom distribution. A similar effect can be seen with D_2, where $k_M/k_2^* = 1.24$ and 0.68 for [D_2]/[DBr] = 10:1 and 70:1, respectively. A plausible explanation for this is that as the D* atom energy approaches the average thermal energy of moderator molecules, there are many collisions in which a thermal moderator molecule *increases* the energy of a colliding D* atom. This makes complete thermalization extremely difficult, and qualitatively explains the appearance of apparent plateaus[8,9,11] in plots of k_3'/k_2' *vs.* [M]/[HX] where X is Br or I. Such plateaus have been taken as an indication of complete thermalization, but they could also be due to a greatly decreased efficiency of moderation at energies near the threshold, resulting in the illusion that moderation has been completed.

The DBr–Br_2 system should be extremely sensitive to small deviations from the equilibrium thermal energy distribution of deuterium atoms, because of the low threshold energies of the D atom reactions. It is entirely possible that in a different system with higher threshold energies all of the hot atoms might be "thermalized" with much less moderator. Thermalization in these systems does not necessarily imply achievement of an equilibrium thermal distribution, but rather it implies the lowering of the D* atom energy to below some threshold energy. It is possible that this is the case in some of the systems previously studied using CO_2 moderator. Care must be exercised, however, when rate parameters obtained in this way are compared with equilibrium thermal kinetic data. The only certain tests of thermalization would be comparison of the results with those obtained with a substantially more efficient moderator or with the results obtained by a conventional thermal kinetic method.

On the Gas-Phase Recombination of Chlorine Atoms

R. P. Widman and B. A. DeGraff*[1]

Department of Chemistry, University of Virginia, Charlottesville, Virginia 22901 and Department of Chemistry, Madison College, Harrisonburg, Virginia 22801 *(Received April 26, 1972)*

Publication costs assisted by Madison College

The recombination of chlorine atoms in the presence of various chaperons has been studied over the range 195–373°K using kinetic spectroscopy. The rate coefficients obtained, in M^{-2} sec^{-1} units and expressed as $k_M = A \exp(E/RT)$ or $\log k_M = B + C \log T$, were $k_{He} = 1.4_7 \times 10^9 \exp(260 \pm 10/RT)$ or $\log k_{He} = 10.55 \pm 0.12 - (0.48 \pm 0.009) \log T$; $k_{Ne} = 1.2_6 \times 10^9 \exp(660 \pm 20/RT)$ or $\log k_{Ne} = 12.74 \pm 0.26 - (1.27 \pm 0.02) \log T$; $k_{Ar} = 2.5 \times 10^8 \exp(1800 \pm 50/RT)$ or $\log k_{Ar} = 18.62 \pm 0.60 - (3.59 \pm 0.05) \log T$; $k_{N_2} = 5.8 \times 10^8 \exp(1600 \pm 140/RT)$ or $\log k_{N_2} = 15.61 \pm 0.65 - (2.32 \pm 0.02) \log T$; $k_{SF_6} = 2.4 \times 10^9 \exp(970 \pm 100/RT)$ or $\log k_{SF_6} = 13.72 \pm 0.76 - (1.47 \pm 0.02) \log T$; $k_{CF_4} = 1.6_2 \times 10^9 \exp(1200 \pm 200/RT)$ or $\log k_{CF_4} = 14.43 \pm 1.36 - (1.77 \pm 0.04) \log T$; $k_{CO_2} = 1.5_6 \times 10^9 \exp(1500 \pm 200/RT)$ or $\log k_{CO_2} = 15.75 \pm 0.60 - (2.22 \pm 0.018) \log T$. Where comparison values are available they are in good agreement with the results of this investigation. The values reported here are compared with the available data for iodine and bromine atom recombination.

Introduction

The mechanism of atomic recombination in the presence of a third body is a fundamental process in chemical kinetics and continues to be the subject of numerous experimental and theoretical investigations. Experimentally, the recombination rates of bromine[2] and iodine[3] atoms have been extensively studied over a wide temperature range for many chaperons. However, there exist only limited data, especially at temperatures below 1000°K, on the gas-phase recombination of chlorine atoms. Because of the low extinction coefficients for chlorine, a formidable experimental problem is encountered in using the chlorine absorption to monitor the progress of the reaction. As a result, the presently available data from shock wave studies[4-7] and flow system experiments[8-10] were obtained using other detection means. Also, the high chemical reactivity of chlorine atoms sharply limits the available chaperons.

One of the most interesting results of the iodine and bromine studies is the wide range of efficiencies shown by the various third bodies in promoting recombination. Further, the efficiency of a chaperon can be correlated with the temperature dependence of k_M, the recombination rate constant for the particular third body. Since chlorine atoms have the highest electron affinity of the halogen atoms, it is of interest to see if the recombination rate constants span a range similar to that observed for bromine and iodine and further to see if the same efficiency-temperature dependence relationship exists. To these ends we have determined the termolecular recombination rate constants and their temperature dependence for chlorine atoms in the presence of various chaperons of differing molecular complexity. This was done using the techniques of kinetic spectroscopy and utilizing the absorption of molecular chlorine to monitor the recombination.

Experimental Section

The reaction cell consisted of a length of Pyrex pipe (approximately 76 cm long with a 12.7-cm diameter) fitted with aluminum end plates. Multiple passes of the monitoring light through the cell were effected by use of three mirrors in a modified White cell configuration.[11,12] For this study, four traversals were used giving an effective light path of 2.8 m. Two flash lamps of 22-mm quartz pass longitudinally through the cell about 3 cm above and below the observed portion of the reaction zone. A piece of polished aluminum was curled to fit inside the reaction vessel and served as a reflector. Energy for the flash lamps was provided by two 14-μF capacitors charged to about 10 kV. With the flash tubes filled with a xenon–nitrogen mixture, the discharge time to 1% intensity was about 80 μsec. A 100-W Osram mercury arc powered by two 12-V batteries served as the monitoring source. The wavelength used for this study, 365 nm, was isolated with a Spex 0.75-meter spectrometer fitted with a polychromator attachment. Since considerable amplification of the photomultiplier output was necessary to obtain useful signals, baseline stability was a problem. The evaluation of the rate constants proved to be quite sensitive to baseline fluctuations and hence the baseline was monitored by a second photomultiplier set outside the chlorine absorption region. The relationship between the baseline as monitored by the two detectors was established by comparing scope trace photographs obtained on flashing the empty cell. The correlation between the two detectors was quite reproducible. Thus, the inverted output from the baseline monitor was added to the output from the photomultiplier

(1) Present address: Madison College, Harrisonburg, Va. 22801.
(2) (a) B. A. DeGraff and K. J. Lang, *J. Phys. Chem.*, **74**, 4181 (1970), and references therein; (b) J. K. K. Ip and George Burns, *J. Chem. Phys.*, **51**, 3414 (1969), and references therein.
(3) J. A. Blake and George Burns, *J. Chem. Phys.*, **56**, 3155 (1972), and references therein.
(4) R. W. Diesen and J. Felmlee, *J. Chem. Phys.*, **39**, 2115 (1963).
(5) T. A. Jacobs and R. R. Giedt, *J. Chem. Phys.*, **39**, 749 (1963).
(6) R. A. Carbetta and H. B. Palmer, *J. Chem. Phys.*, **46**, 1333 (1967).
(7) M. van Thiel, D. J. Seery, and D. Britton, *J. Phys. Chem.*, **69**, 834 (1965).
(8) E. Hutton and M. Wright, *Trans. Faraday Soc.*, **61**, 78 (1965).
(9) L. W. Bader and E. A. Ogryslo, *Nature (London)*, **201**, 491 (1964).
(10) M. A. A. Clyne and D. H. Stedman, *Trans. Faraday Soc.*, **64**, 2698 (1968).
(11) J. U. White, *J. Opt. Soc. Amer.*, **32**, 285 (1942).
(12) R. V. Fitzsimmons and E. J. Bair, *J. Chem. Phys.*, **40**, 451 (1964).

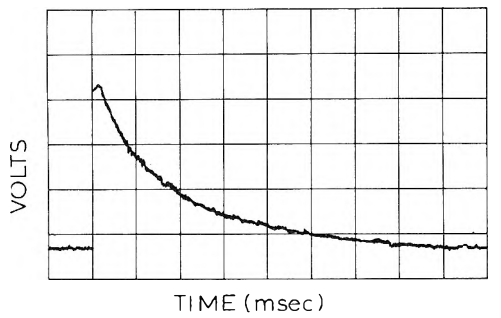

Figure 1. Oscilloscope trace for the recombination of Cl atoms in Ne: P_{Cl_2} = 0.91 Torr; P_{Ne} = 290.0 Torr; T = 327.2°; scale factors: 0.01 V/division; 5 m sec/division.

monitoring the Cl_2 absorption. This technique gave a reproducible empty and filled cell baseline and the data scatter was reduced to *ca.* ±5% random about the least-squares line. The rate of appearance of Cl_2 after the flash was followed by displaying the photomultiplier output for λ 365 nm on a Tektronix 547 oscilloscope. Photographs of the oscilloscope traces were measured with precision calipers and the deflection converted to Cl concentration. A typical oscilloscope trace is shown in Figure 1.

A conventional glass vacuum line was used to fill the reaction cell. To load the cell, chlorine was expanded from a storage bulb into a 5-l. mixing bulb and the pressure measured with a sulfuric acid manometer. The mixing bulb was then filled with chaperon gas to a pressure of about 1 atm. The gases were mixed by mechanical stirring for ~30 min, and then expanded into the reaction cell. The total pressure in the reaction cell was measured with a Wallace-Tiernan absolute pressure gauge. As all the volumes involved were calibrated, the partial pressure of chlorine in the reaction cell could be readily calculated. The mixtures obeyed Beer's Law and for 23°, ϵ 24 M^{-1} cm^{-1} at 365 nm, in good agreement with the data of Gibson and Bayliss.[13] After the correlation between the manometric and photometric values for the chlorine pressure was established, the photometric method was used to determine the Cl_2 pressure in the cell.

The cell was surmounted in a Styrofoam box and the cell itself was wrapped with asbestos tape over which was wound nichrome heating wire. Temperatures above room temperature were obtained by adjusting the current through the coils until the desired temperature was reached and remained constant over a 2-hr period. The mixture was flashed several times during the 2-hr equilibration period to assure thermal equilibrium between the cell walls and the gas mixture. A calibrated iron–constantan thermocouple was used to monitor the cell wall temperature. Measurements at −78° were performed by packing the Styrofoam box with Dry Ice and allowing at least 4-hr for equilibration.

The chaperon gases used in this study did not react chemically with either Cl_2 or Cl and did not undergo direct photolysis. The concentration of chlorine in the cell was checked both before and after a set of experiments to determine if any permanent chemical change had occurred. For the data reported here this change was never greater than the photometric error in measuring the Cl_2 concentration (*i.e.*, ~1%). All gases used were of reagent grade and were used without further purification. Stopcocks which came in contact with chlorine or its mixtures were greased with either Dow Corning silicone grease or 3-M Kel-F stopcock grease.

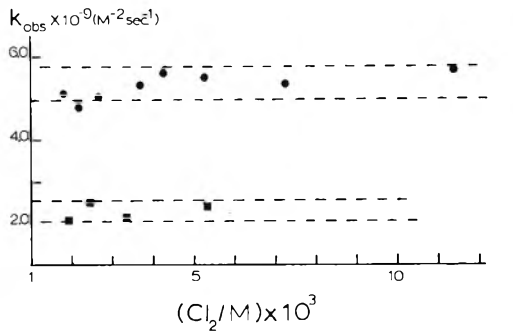

Figure 2. Plot of k_{obsd} *vs.* (Cl_2/M) for M = He, ■; M = Ar, ●. The dashed lines define our estimated error limits for the average value of k_{obsd}.

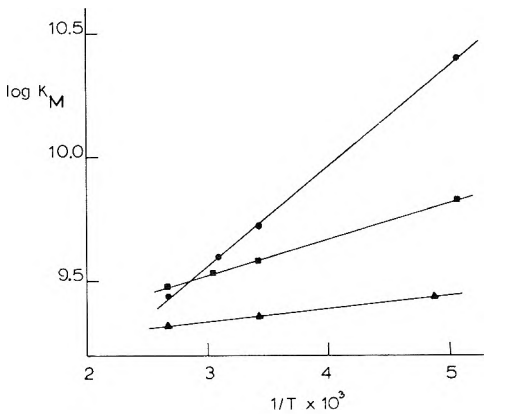

Figure 3. Arrhenius plots of $k_{obsd} \simeq k_M$ for M = He, ▲; M = Ne, ■; and M = Ar, ●.

Results

For this study flash energies centered around 1500 J which resulted in *ca.* 10% initial dissociation of the chlorine. Further, $P_{Cl_2} \simeq 1.0$ Torr and $2 \times 10^{-3} \leq X_{Cl_2} \leq 1C \times 10^{-3}$ with most experiments done at $X_{Cl_2} = 4 \times 10^{-3}$.[14] If the average wavelength absorbed by the chlorine is taken as λ(max), we calculate that under the worst conditions the maximum temperature rise expected at the completion of the recombination was 10° and that the usual rise lay in the range of 3–5° for most of our experiments. To minimize any possible error due to thermal effects, the data points were taken only over the first two half-lives of the reaction.

The data obtained in this study were treated according to the following rate expression

$$\frac{-d[Cl]}{dt} = 2k_{obsd}(M,T)[Cl]^2[M] \qquad (1)$$

where $k_{obsd} = k_M + [Cl_2]/[M]k_{Cl_2}$. The contribution from atomic chlorine was neglected. The observed rate constant, k_{obsd}, was obtained through a least-squares fit of the data to the integrated form of eq 1. To assess the contribution of the second term to k_{obsd} under our conditions, a series of experiments was performed in which the Cl_2–M ratio was varied over a five- to tenfold range. The chaperons chosen for these experiments were helium and argon since the k_M for these gases was expected to be among the smallest observed and hence any contribution from the

(13) G. E. Gibson and N. S. Bayliss, *Phys. Rev.*, **44**, 188 (1933). The temperature dependence of ϵ at this wavelength is within experimental error for the temperature range used.
(14) $X_{Cl_2} = P_{Cl_2}/(P_{Cl_2} + P_M) \simeq P_{Cl_2}/P_M$.

TABLE I: Rate Constants for Chlorine Atom Recombination

Chaperon	No. of expt	T, °C	$k_M \times 10^{-9}$, M^{-2} sec^{-1}	$k_M = A \exp(E/RT)$; $\log k_M = B + C \log T$, M^{-2} sec^{-1}
He	10	−68	2.77 ± 0.26	$k_{He} = 1.4_7 \times 10^9 \exp(260 \pm 10/RT)$;
	20	20	2.28 ± 0.13	$\log k_{He} = 10.55 \pm 0.12 - (0.48 \pm 0.009) \log T$
	8	100	2.09 ± 0.15	
Ne	9	−78	6.85 ± 0.45	$k_{Ne} = 1.2_6 \times 10^9 \exp(660 \pm 20/RT)$;
	8	20	3.78 ± 0.37	$\log k_{Ne} = 12.74 \pm 0.26 - (1.27 \pm 0.02) \log T$
	11	54	3.45 ± 0.15	
	11	100	3.06 ± 0.30	
Ar	9	−78	25.3 ± 2.5	$k_{Ar} = 2.5_0 \times 10^8 \exp(1800 \pm 50/RT)$;
	40	20	5.32 ± 0.33	$\log k_{Ar} = 18.62 \pm 0.60 - (3.59 \pm 0.05) \log T$
	7	50	4.02 ± 0.20	
	6	100	2.79 ± 0.18	
N_2	8	20	8.08 ± 0.81	$k_{N_2} = 5.8_0 \times 10^8 \exp(1600 \pm 140/RT)$;
	9	50	6.09 ± 0.29	$\log k_{N_2} = 15.61 \pm 0.65 - (2.32 \pm 0.02) \log T$
	8	100	4.60 ± 0.46	
SF_6	10	20	12.0 ± 1.2	$k_{SF_6} = 2.4_0 \times 10^9 \exp(970 \pm 100/RT)$;
	9	52	11.0 ± 0.4	$\log k_{SF_6} = 13.72 \pm 0.76 - (1.47 \pm 0.02) \log T$
	7	100	8.48 ± 0.80	
CF_4	8	20	12.3 ± 1.2	$k_{CF_4} = 1.6_2 \times 10^9 \exp(1200 \pm 200/RT)$;
	8	50	9.19 ± 0.49	$\log k_{CF_4} = 14.43 \pm 1.36 - (1.77 \pm 0.04) \log T$
	9	100	7.93 ± 0.69	
CO_2	9	20	18.8 ± 1.6	$k_{CO_2} = 1.5_6 \times 10^9 \exp(1500 \pm 200/RT)$;
	9	50	15.7 ± 0.5	$\log k_{CO_2} = 15.75 \pm 0.60 - (2.22 \pm 0.018) \log T$
	4	70	12.7 ± 0.9	
	9	100	11.2 ± 0.9	

k_{Cl_2} term would be more readily detected. The plots of k_{obsd} *vs.* $[Cl_2]/[M]$ for M = He and Ar, Figure 2, indicate that for all our experiments the contribution of Cl_2 to the recombination was within experimental error. Thus, the approximation that $k_{obsd} = k_M$ is valid for our experiments.

Table I presents a summary of our experimental results. The rate constants are cast in both an Arrhenius form and as $\log k_M = B + C \log T$. The error limits shown in Table I represent the standard deviation of the appropriate least-squares line and should be taken as a measure of the precision of the data. However, due to the difficult nature of the experiments (*e.g.*, such problems as thermostating a 14-l. cell at −78°) the accuracy is likely less by about a factor of 2. Arrhenius plots of $\log k_M$ *vs.* $1/T$ for M = He, Ne, and Ar are shown in Figure 3. Similar plots were obtained for all chaperons studied.

Discussion

The rate constant for $Cl(^2P_{3/2})$ recombination with argon as the chaperon has recently been obtained using a low-pressure flow system.[10] The value of $k_{Ar} = 2.0 \times 10^8 \exp(1800 \pm 700/RT)$ M^{-2} sec^{-1} reported in that study is in good agreement with the present results as is the value for k_{Ar} reported in ref 9 and the reinterpretation[10] of the data from ref 8. The only other chaperon for which a rate constant has been reported and with which we can compare our results is that for helium, $k_{He} \simeq 3 \times 10^9$ M^{-2} sec^{-1} at 25°,[9] which is in satisfactory agreement with our value. That the contribution to k_{obsd} from the k_{Cl_2} term in (1) is negligible for the $[Cl_2]/[M]$ ratios used in this study is consistent with the reported $k_{Cl_2} = 20 \pm 3 \times 10^9$ M^{-2} sec^{-1} at 25°.[10] Referring to Table II, it appears that Cl_2 is the least efficient of the halogens as a chaperon.

Porter,[15a] in his classic studies on iodine atom recombination, observed a distinct correlation between the efficiency of a chaperon and the temperature dependence of k_M as expressed in the form $k = A \exp(E/RT)$. A similar relationship is found for bromine atoms.[2a] To rationalize and correlate these and other experimentally observed trends in atom recombination data, two recombination mechanisms have been used as the basis for several formal approaches to the calculation of k_M. The "bound complex" (BC) mechanism[15,16] can be represented as

$$Cl + M \rightleftharpoons MCl^* \quad k_1, k_{-1}$$

$$MCl^* + M \rightleftharpoons MCl + M \quad k_2, k_{-2}$$

$$MCl + Cl \longrightarrow Cl_2 + M \quad k_3$$

where $E(MCl^*) \geq 0$ and $E(MCl) < 0$ while the energy transfer (ET) approach[17-19] can be represented as

$$Cl + Cl \rightleftharpoons Cl_2^* \quad k_4, k_{-4}$$

$$Cl_2^* + M \longrightarrow Cl_2 + M \quad k_5$$

Also, Keck and coworkers have developed a classical phase-space theory which includes contributions from both mechanisms.[20]

There has been considerable discussion as to the relative contribution of the BC and ET mechanisms. Simple calculations by Johnston[21] and more detailed work by Clarke and Burns[22,23] suggest that for I atom and Br atom recombination in the room temperature region, the BC mechanism is dominant for all but the lightest chap-

(15) (a) G. Porter, *Discuss. Faraday Soc.*, **33**, 198 (1962); (b) D. L. Bunker and N. Davidson, *J. Amer. Chem. Soc.*, **80**, 5085 (1958).
(16) S. K. Kim, *J. Chem. Phys.*, **46**, 123 (1967).
(17) E. Rabinowitch, *Trans. Faraday Soc.*, **33**, 283 (1937).
(18) D. L. Bunker, *J. Chem. Phys.*, **32**, 1001 (1960).
(19) S. W. Benson and T. Fueno, *J. Chem. Phys.*, **36**, 1597 (1962).
(20) V. H. Shui, J. P. Appleton, and J. C. Keck, *J. Chem. Phys.*, **53**, 2547 (1970), and references therein.
(21) H. S. Johnston, "Gas-Phase Reaction Rate Theory," Ronald Press, New York, N. Y., 1966.
(22) A. G. Clarke and G. Burns, *J. Chem. Phys.*, **55**, 4717 (1971).
(23) A. G. Clarke and G. Burns, *J. Chem. Phys.*, **56**, 4636 (1972).

TABLE II: Room Temperature (20°) Rate Constants and E/R Values for Halogen Atom Recombination

Chaperon	Cl_2			Br_2			I_2		
	$k_M \times 10^{-9}$, M^{-2} sec^{-1}	E/R,[i] °K	k_M/k_{Ar}[i]	$k_M \times 10^{-9}$, M^{-2} sec^{-1}	E/R, °K	k_M/k_{Ar}	$k_M \times 10^{-9}$, M^{-2} sec^{-1}	E/R, °K	k_M/k_{Ar}
He	2.3	131	0.44	1.2[b]	438[c]	0.54	1.5[e]	201[e]	0.52
Ne	3.8	331	0.72	1.5[b]	494[b]	0.68	1.9[f]	755[g]	0.65
Ar	5.3	904	1.0	2.2[b]	703[c]	1.0	2.9[e]	554[e]	1.0
N_2	8.1	803	1.5	3.3[b]	755[c]	1.5	4.5[f]		1.6
SF_6	12.0	487	2.3	8.1[b]	906[b]	3.7			
				10.1[d]	1045[d]				
CF_4	12.3	602	2.3	10.2[d]	1169[d]				
CO_2	18.8	753	3.5	7.8[c]		3.5	13.4[e]	880[e]	4.6
X_2 (halogen)	20[a]	803	3.8	44[b]	1060[c]	20	1600[h]	2215[h]	550

[a] Reference 10. [b] Reference 1. [c] Reference 2. [d] Reference 25. [e] Reference 26. [f] Reference 27. [g] Reference 28. [h] Reference 15. [i] This work.

erons. However, recent work by Pack, Snow, and Smith[24] suggests that the ET mechanism dominates for H atom recombination in He, Ar, and H_2 except at very low temperatures.

A comparison of the room temperature k_M values shown in Table II[25-28] indicates that k_M for Cl atom recombination is somewhat greater than for I atoms and about twice the corresponding value for Br atoms. The singular exception is the case of the halogen itself acting as a chaperon. The recombination in this case would, according to the BC model, take place *via* an X_3 intermediate. While Cl_3 has been observed in low-temperature infrared experiments,[29] direct measurements of the bond energies for I_3, Br_3, and Cl_3 are not available. However, the kinetic data would indicate that $I_3 > Br_3 \simeq Cl_3$.

The formulations of k_M which are based on the BC mechanism and also the phase-space approach of Keck, which includes both mechanisms, suggest that when the atom-chaperon interaction is large with respect to RT, the temperature dependence of k_M is approximately exponential. Thus, it is instructive to compare the observed temperature dependence of k_M, expressed in exponential form, for the three halogen atoms for which data is available (see Table II).

Interestingly, the correspondence between the efficiency of a chaperon and the E/R value which is observed for I atom (see extensive data of ref 15a) and Br atom recombination is not well defined for the Cl atom case with the chaperons used here. In the simpler[16] formulations based on the BC mechanism E/R is interpreted as a measure of the atom-chaperon potential well. In recent work, Burns[30] using a modified BC approach and Keck[31] using the phase-space approach have used the atom-chaperon potential well as the adjustable parameter in order to fit the available Cl atom experimental data. Interestingly Keck found that the best fit to the available chlorine atom data in excess argon was obtained with a Cl-A well depth of 900°. This may be compared with the value of 904°K from this work using the very simple Arrhenius formulation. However, this is likely just fortuitious.

Finally, the lack of a simple correlation between the efficiency of the chaperon and the temperature dependence of k_M as expressed in exponential form may be due to the fact that the simplifying assumptions required to obtain an Arrhenius expression are not valid under our conditions. Further, while an Arrhenius formulation of k_M may be used to fit the data, a simple correlation between the argument of the exponent and the depth of the Cl-chaperon potential well as suggested for I and Br atom recombination is not valid. Indeed, recent scattering experiments[32] suggest that even when the BC mechanism represents the major pathway for recombination, the relationship between the experimental temperature dependence of k_M and the atom-chaperon potential well may not be as straightforward as the simpler formulations based on the BC mechanism suggest.

(24) R. T. Pack, R. L. Snow, and W. D. Smith, *J. Chem. Phys.*, **56**, 926 (1972).
(25) S. K. Chang, A. G. Clarke, and G. Burns, *J. Chem. Phys.*, **54**, 1835 (1971).
(26) G. Porter and J. A. Smith, *Proc. Roy. Soc., Ser. A*, **261**, 28 (1961).
(27) K. E. Russell and J. Simons, *Proc. Roy. Soc., Ser. A*, **217**, 271 (1953).
(28) G. Porter, Z. G. Szabo, and M. G. Townsend, *Proc. Royal Soc., Ser. A*, **270**, 493 (1962).
(29) L. Y. Nelson and G. C. Pimentel, *Inorg. Chem.*, 7, 1695 (1968).
(30) G. Burns and R. J. Browne, *J. Chem. Phys.*, **53**, 3318 (1970).
(31) V. H. Shui, J. P. Appleton, and J. C. Keck, *Symp.* (Int.) Combust., [*Proc.*], *12th, 1968*, 21 (1969).
(32) M. J. Cardillo, M. S. Chou, and E. F. Greene, Abstracts of the 163rd National Meeting of the American Chemical Society, Boston, Mass., paper 77, Physical Division, Apr 1972.

Reaction of Cyanogen and Hydrogen behind Reflected Shock Waves[1]

J. M. Brupbacher and R. D. Kern*

Department of Chemistry, Louisiana State University in New Orleans, New Orleans, Louisiana 70122
(Received September 29, 1972)

Publication costs assisted by the National Science Foundation

The metathetical reaction, $C_2N_2 + H_2 \rightleftarrows 2HCN$, has been studied by shocking equimolar amounts of the reactants in the presence of an inert gas diluent over the temperature range 1850–2650°K. A complementary shock tube facility was utilized to obtain the data from the reflected shock zone by recording the infrared emission of HCN and the time-resolved mass spectra at m/e 27 (HCN) and 52 (C_2N_2). The total density variation was 1.8–4.4 × 10^{-6} mol/cm^3. Observation times were typically 500 μsec during which period an equilibrium condition was established for the higher temperature experiments. The growth of the mole fraction of HCN, f_{HCN}, was found to be a nonlinear function of time and to depend upon the inert gas concentration, [M]. The data from the two independent techniques of infrared emission and mass spectrometry were fitted to the bimolecular rate expression that includes the back reaction, $\ln \{[(K-4)f_{HCN} - (K+2K^{1/2})]/[(K-4)f_{HCN} - (K-2K^{1/2})]\} = 4k_1[C_2N_2]_0[M]^{0.75}K^{-1/2}t^2 + \ln [(K+2K^{1/2})/(K-2K^{1/2})]$, where the forward rate constant is given by $k_1 = 10^{25.35\pm0.21} \exp(-61{,}610 \pm 2070/RT)$ cm^3 mol^{-1} sec^{-2} [M]$^{-0.75}$. These results rule out the direct bimolecular reaction. This complex reaction is discussed in terms of an atomic mechanism and a mechanism involving vibrationally excited species. Experiments on an equimolar mixture of cyanogen and deuterium revealed a lowering of the preexponential factor in reasonable agreement with that predicted from the square root of the inverse ratio of reduced masses.

Introduction

Reactions of hydrogen with various halogens and their reverse decompositions have played an important role in the development of chemical kinetics. The most notable of these reactions is that of hydrogen with iodine which was first investigated by Bodenstein.[2] This reaction was most recently demonstrated by Sullivan to occur by an atomic pathway after having been for some 70 years the classic example of a reaction proceeding *via* a four-center transition state.[3]

One interesting feature of this reaction is that in applying the symmetry rules proposed by Pearson for predicting possible reaction mechanisms, it is found that the direct molecular channel is symmetry forbidden.[4,5] The same prediction holds for all of the halogen–hydrogen reactions. An examination of the coefficients of the atomic orbitals which contribute to the highest occupied molecular orbital (HOMO) of cyanogen discloses that it is antibonding while the lowest unfilled[6] molecular orbital (LUMO) is bonding.[7] Both the transfer of electron density from HOMO of cyanogen (π_g*) to the LUMO of hydrogen (σ_u*) or from HOMO of hydrogen (σ_g) to LUMO of cyanogen (π_u) occur with positive orbital overlap. Hence, when the entire molecular orbitals are considered with respect to positive overlap, the forward reaction appears to be symmetry allowed. It also follows that the same prediction holds for the reverse reaction. However, this argument is incomplete since the bonds made and broken during the course of reaction have been ignored.[8]

A previous investigation of the reaction of cyanogen and hydrogen was performed in a silica vessel[9] over the temperature range 550–675° and was reported to fit reasonably well with the expression developed by Bodenstein and Lind for the H_2–Br_2 system.[10] The reaction was found to take place in an essentially homogeneous manner with an activation energy of 72 kcal/mol. The decomposition of cyanogen has been extensively investigated in shock tubes.[11-14] Kinetic data are not available for the decomposition of hydrogen cyanide.

The purpose of this work is to study this metathetical reaction under truly homogeneous conditions at elevated temperatures and to test for the existence of the direct bimolecular reaction mechanism. Furthermore, the discussion of the role of cyanogen as a possible intermediate in the HCN + D_2 exchange[15] was limited due to the lack of data on the reaction of cyanogen and hydrogen in the temperature region 2000–3000°K. The extent and nature

(1) (a) Support of this work by the National Science Foundation under Grants No. GP-23137 and GP-33949 X is gratefully acknowledged. (b) Paper presented in part at 163rd National Meeting of the American Chemical Society, Boston, Mass., April 1972.
(2) M. Bodenstein, *Z. Phys. Chem.*, **13**, 56 (1894); **22**, 1 (1897); **29**, 295 (1899).
(3) J. H. Sullivan, *J. Chem. Phys.*, **46**, 73 (1967).
(4) R. G. Pearson, *Chem. Eng. News*, **48**, 66 (1970).
(5) R. G. Pearson, *Accounts Chem. Res.*, **4**, 152 (1971).
(6) W. L. Smith, *J. Chem. Educ.*, **49**, 654 (1972).
(7) A. D. McLean and M. Yoshimine, "Tables of Linear Molecule Wave Functions," International Business Machines Corporation, San Jose, Calif., 1967.
(8) We are grateful to Professor Roald Hoffman for sending us a correlation diagram which shows a crossing of electronic levels when the carbon–carbon σ bond of cyanogen and the H_2 bond are included. This more complete analysis reveals that the direct bimolecular pathway is forbidden.
(9) N. C. Robertson and R. N. Pease, *J. Amer. Chem. Soc.*, **64**, 1880 (1942).
(10) M. Bodenstein and S. C. Lind, *Z. Phys. Chem.*, **57**, 168 (1907).
(11) K. T. Knight and J. P. Rink, *J. Chem. Phys.*, **35**, 199 (1961).
(12) W. Tsang, S. H. Bauer, and M. Coperthwaite, *J. Chem. Phys.*, **36**, 1768 (1962).
(13) M. W. Slack and E. S. Fishburne, *J. Chem. Phys.*, **52**, 5830 (1970).
(14) M. W. Slack and E. S. Fishburne, *J. Chem. Phys.*, **54**, 1652 (1971).
(15) J. M. Brupbacher and R. D. Kern, *J. Phys. Chem.*, **76**, 285 (1972).

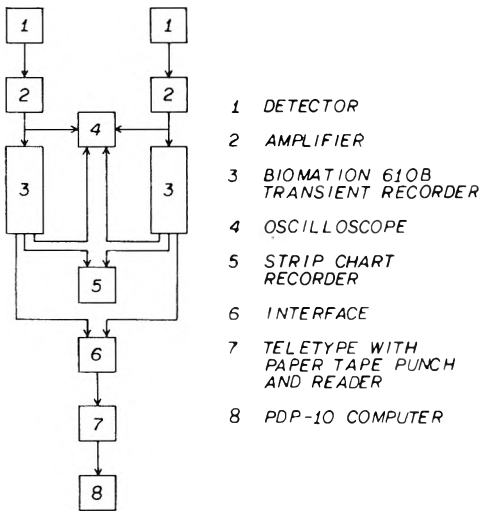

Figure 1. Schematic of infrared emission analog to digital conversion system.

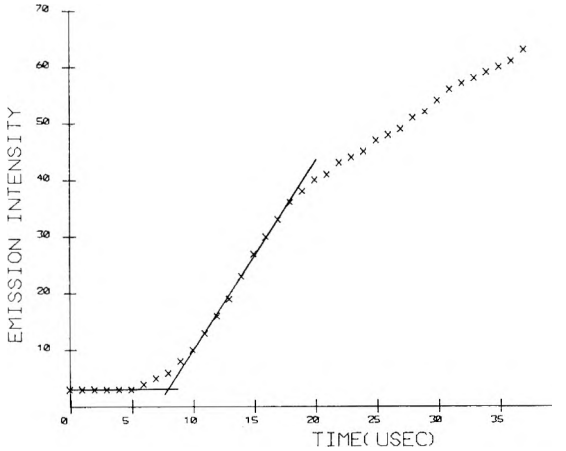

Figure 2. Plot of signal at 5.05 μ *vs.* time to determine shock arrival at observation station.

of isotopic effects are examined with data collected from an equimolar mixture of cyanogen and deuterium.

Experimental Section

The complementary shock tube facility upon which all data were obtained has been described previously.[16] The TOF shock tube system remains to a large extent unchanged. However, the ir system has been significantly improved in the data reduction phase of operation. Two Biomation 610B transient recorders have been acquired which utilize a very high-speed six-bit analog to digital converter to digitize the amplified ir profiles. These recorders accept full-scale signals from 50 mV to 50 V with a frequency response of dc to 2.5 MHz. Sampling rates are available from 0.1 μsec to 50 msec for 256 words. The digitized output of the Biomation units is then fed *via* a Pivan Data Systems Model B103 interface to a 33ASR Teletype equipped with an acoustic coupler, paper tape punch, and reader. A permanent paper tape record is made for each experiment. The output for each trace from the interface is formatted in a 10 × 25 array of two-digit numbers followed by a line of five numbers and a terminating colon. Each number corresponds to the relative emission intensity on a scale of 1 to 63 where 63 represents the full-scale voltage setting. The Biomation units can also output a smoothed form of the ir signals on an oscilloscope or strip chart recorder for visual analysis or a permanent paper record, respectively. The additional equipment does not interfere with the previous method of oscilloscope analog analysis if it is desired. The ir profiles can now be analyzed in minutes as compared to several hours by earlier techniques. Figure 1 shows a diagram of the analog to digital conversion system. The remaining portion of the ir shock tube facility has been reported.[16]

The experiments were performed using Matheson cyanogen (98.5%) which was distilled several times keeping only the middle fraction in each distillation. Liquid Carbonic cylinder hydrogen (99.99%) was used without further purification as was the Matheson CP deuterium (99.5%). Calibration experiments on the ir system consisted of doubly distilled hydrogen cyanide which had been prepared for an earlier study.[15] The diluent gas for the TOF experiments was a mixture of Matheson Research Grade 99% Ne–1% Ar. For the ir experiments Liquid Carbonic argon (99.99%) was used as the diluent.

Vacuums during mixture preparation were typically 1×10^{-6} Torr and outgassing rates were less than 0.5 μ/min. The partial pressures of all gases were measured with Wallace-Tiernan differential pressure gauges 0–10 and 0–400 in water. The gases were stored in 5-l. bulbs and analyzed using the TOF mass spectrometer. The mixtures were found not to contain any contaminant in a concentration greater than background. The O_2 level was less than 25 ppm as compared to a standard O_2 mixture. Mixtures were allowed to stand at least 24 hr before shocking.

In the TOF experiments, mole fractions of HCN and C_2N_2 were obtained from careful measurement of the peak heights corresponding to m/e 27 (HCN) and 52 (C_2N_2). For each experiment mass spectra were recorded at 20-μsec intervals on Polaroid 10,000 speed film. Due to the unequal ionization cross sections of C_2N_2 and HCN, an equimolar mixture was analyzed at room temperature in order to establish a sensitivity factor. A value of 1.054 was obtained using an ionization voltage of 35 eV for the equimolar ratio C_2N_2/HCN. It was also noted that this value did not change appreciably over the range 25–45 eV. A small contribution to m/e 27 resulted from isotopic contributions from the CN cracking peak. A value of 0.062 for CN (27)/CN (26) was determined by performing several shock experiments with a mixture of 2% C_2N_2 in diluent gas at 35 eV. The effective HCN peak height in the metathetical reaction experiments then resulted from the difference between the measured value at m/e 27 and 0.062 times the measured value of m/e 26. This value was used in conjunction with the peak height at m/e 52 divided by 1.054 to obtain the mole fraction of product at any time. Corrections of this type were not necessary for those experiments in which deuterium was used instead of hydrogen. Peaks at m/e 28 (DCN), 40 (Ar), and 52 (C_2N_2) were measured and used directly to calculate the mole fraction of DCN as a function of time. Argon served as an internal standard for the ion source pressure. In the TOF experiments mixtures were analyzed for O_2 within 20 sec of shocking. Experiments were not performed on any mixture which had an oxygen content greater than 25 ppm.

(16) R. D. Kern, Jr., and G. G. Nika, *J. Phys. Chem.*, **75**, 171 (1971).

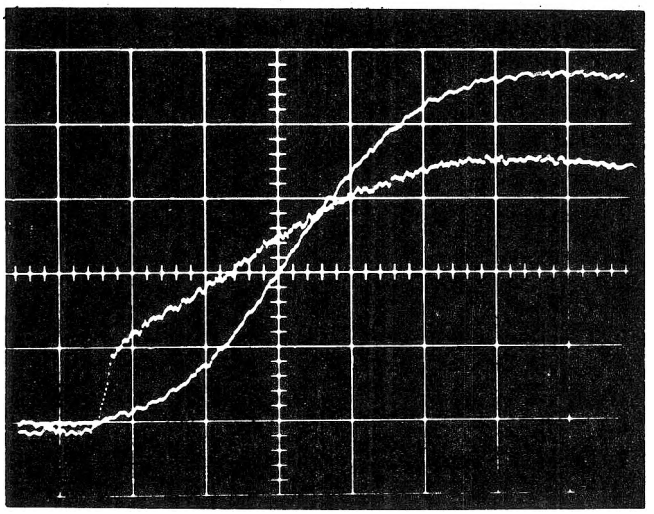

Figure 3. Polaroid record of ir experiment: lower trace at left-hand side is emission from HCN at 3.0 μ; upper trace is emission from C_2N_2 at 5.05 μ.

A narrow-band Infrared Industries interference filter with center wavelength at 3.0 μ was selected to monitor the emission from the production of HCN. A suitable filter could not be found for cyanogen which would permit meaningful kinetic analysis. However, a second filter at 5.05 μ was chosen to observe the emission from the C≡N stretch of both C_2N_2 and HCN. Measurements of this emission were taken at 0.2-μsec intervals for all ir experiments. The emission at 5.05 μ was plotted as a function of time and the rising portion was extrapolated to the base line. This resulted in an accurate determination of the time of shock wave arrival at the slits. One of these plots is displayed in Figure 2. Measurements at the 3.0-μ filter were taken at 1-, 2-, or 5-μsec intervals depending upon the reaction rate. No attempt was made to study the C_2N_2–D_2 system on the ir shock tube because of complicated emission at 3.8 μ where DCN emits. The slit width for both filters was kept constant at 0.5 mm.

The possibility of emission from CN radicals in these experiments is discounted by the work of Slack and Fishburne who studied the decomposition of C_2N_2[14] by recording CN emission. The lowest temperature included in their report, 2750°K, was limited by weak emission and exceeds the upper extent of the range investigated herein, 2650°K. Calibration experiments described in the next section confirm the stability of the species HCN and C_2N_2 with regard to pyrolysis within the observation period and temperature range of this work.

The temperature for each experiment was determined as mentioned in an earlier work.[15] Hydrogen was used as the driver gas for all experiments. All calculations were accomplished with the aid of a DEC PDP-10 computer. Plotting of experimental results was carried out by a Complot Model DP3 plotter.

Results

Reacting experiments on the ir system were performed on equimolar C_2N_2–H_2 mixtures. A Polaroid record of the emission time history for one of these runs is shown in Figure 3. The trace shows clearly the nonlinear growth of product and the establishment of an equilibrium value in the 500 μsec of reaction time. Calibration runs were carried out on equimolar HCN–H_2 mixtures of the same concentration as the reacting experiments. From these experiments a plot of log of the steady calibration intensity as a function of temperature was constructed. The mole fraction of HCN, f_{HCN}, at any time was calculated using the relationship

$$f_{HCN} = \frac{HCN_t}{2HCN_c} \tag{1}$$

where HCN_t is the reacting HCN signal height at some time t and HCN_c is the signal obtained from the calibration plot at that temperature.

Several experiments were performed on a 2% C_2N_2 in argon mixture. The Polaroid record of one of these runs at 5.05 μ is depicted in Figure 4. These photographs display the achievement of vibrational equilibrium for C_2N_2 at shock temperatures and pressures similar to those recorded for the metathesis experiments. An approximate value for vibrational equilibration of C_2N_2 was found to be 130 μsec at 2500°K.

Experiments on the TOF shock tube facility were carried out with equimolar mixtures of C_2N_2 and H_2 at 5 Torr starting pressure. For reasons which will become apparent in the Discussion section, a number of experiments were performed on the TOF in which D_2 was used instead of H_2. The mole fraction of product, f_p, at any time is given by

$$f_p = \frac{h_p}{\frac{2}{1.054}h_{C_2N_2} + h_p} \tag{2}$$

where $h_{C_2N_2}$ is the observed peak height of C_2N_2 and h_p is the corrected peak of HCN if H_2 is used. For those experiments where D_2 is a reactant, f_p and h_p are the mole fractions of DCN and the peak heights attributed to DCN, respectively.

The calculated mole fractions for both the ir and TOF experiments were fit to the second-order rate equation that includes the back reaction

$$\ln\left[\frac{(K-4)f_p - (K+2\sqrt{K})}{(K-4)f_p - (K-2\sqrt{K})}\right] = 4k'K^{-1/2}t^z + \ln\left[\frac{(K+2\sqrt{K})}{(K-2\sqrt{K})}\right] \tag{3}$$

where f_p is the mole fraction of product, z is the time power for product formation, and K is the equilibrium constant of the reaction. Equilibrium constants were obtained from a van't Hoff plot which was prepared using thermodynamic data from JANAF.[17] The kinetic parameter k' is given by the expression

$$k' = k_1[R]_0[M]^y \tag{4}$$

where k_1 is the rate constant for the forward reaction and y is the order with respect to the total density. The symbol $[R]_0$ refers to the initial concentration of either reactant. Equation 3 may be recognized in its standard form by setting $z = 1$ and $y = 0$.

As a consequence of the exothermicity of reaction ($\Delta H°_{2000\,K} = -12$ kcal/mol), the reflected shock zone was heated approximately 40°K for a 2% equimolar mixture. To minimize the effects of this heating on the reaction

(17) "JANAF Thermochemical Tables," The Dow Chemical Co., Midland, Mich., 1971.

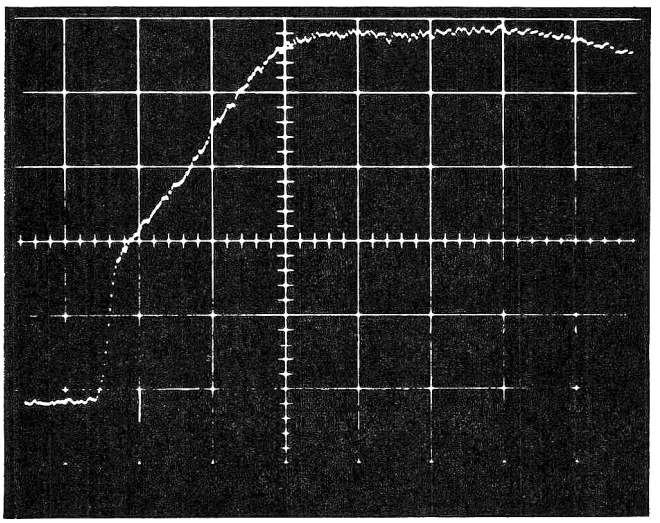

Figure 4. Experimental record showing ir emission from C_2N_2 at 5.05 μ; 2% C_2N_2 in argon at 2500°K.

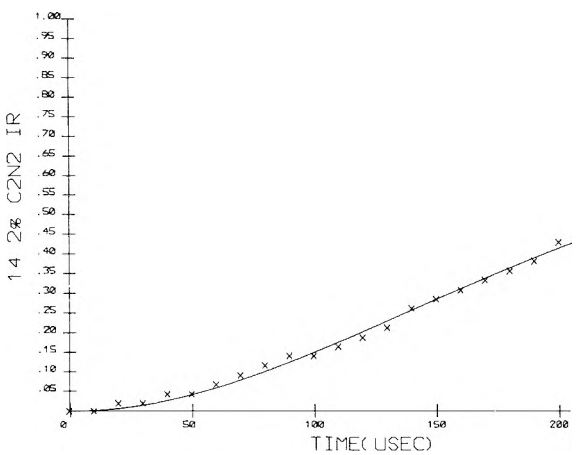

Figure 5. Reaction profile for HCN generated from an ir experiment at 2123°K and fit to a quadratic time dependence; every fifth point is plotted.

rate, only those mole fractions less than 50% of the equilibrium amount were used in the profile calculation. The equilibrium mole fraction of product was determined with the following equation

$$f_p = \frac{K^{1/2}}{K^{1/2} + 2} \tag{5}$$

The values calculated from eq 5 ranged from 0.91 at 1800°K to 0.86 at 2500°K and agreed satisfactorily with the experimental value obtained from both the ir and TOF facilities. Thus, the validity of sampling a low enthalpy change reaction from the reflected shock zone is supported by equilibrium constants obtained from tables of thermodynamic data. This is not the first demonstration of such agreement.[15,16]

Plots of the log of the left-hand side of eq 3 *vs.* the log of reaction time displayed slopes of $z = 2$ for those mole fractions less than the limit described in the preceding paragraph. For all experimental profiles of which Figure 5 is but one example, the data could be adequately fit with a quadratic time power. The value of k' for each experiment was determined by variation of k' until a minimum

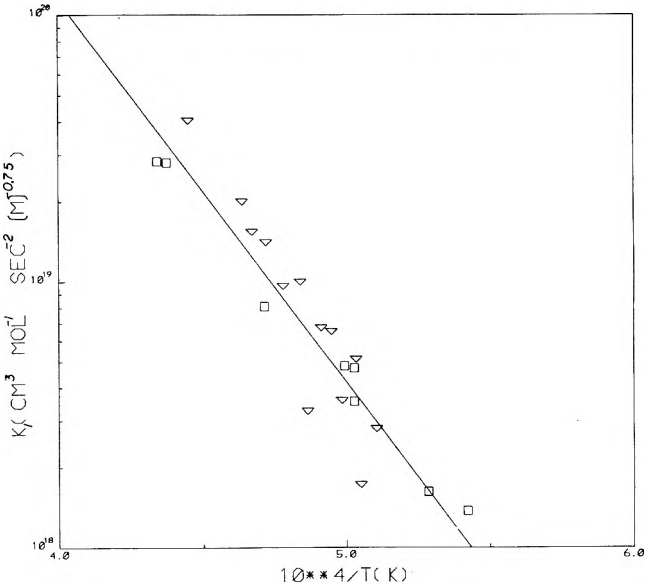

Figure 6. Arrhenius plot for data in Table I; ▽, mixture A; and □, mixture B.

standard deviation was obtained by the method of least squares between the experimental mole fractions and those generated using eq 3. The resulting best fit line and the experimental mole fractions were drawn with the aid of a digital plotter as shown in Figure 5.

The order with respect to reactants was confirmed by shocking a 1% C_2N_2–1% H_2 and a 2% C_2N_2–2% H_2 mixture on the TOF at an initial pressure of 5 Torr. Arrhenius plots of ln k' *vs.* T^{-1} were constructed for these mixtures. The resulting parallel lines differ by a factor of two. Thus, doubling the initial concentration of reactants had the effect of doubling the value of the kinetic parameter k' within the experimental error associated with k'. This indicated that the reaction was second order with respect to the reactants.

The total density dependence was determined by performing experiments on the ir shock tube system on a 2% C_2N_2–2% H_2 mixture at both 5 and 10 Torr initial pressure. Several runs were accomplished on a 1% C_2N_2–1% H_2 mixture at 10 Torr. The value of y was arrived at by variation of y until a minimum standard deviation was obtained in an Arrhenius plot of the data with the rate constants on a total density basis. Using a value of 2 for z, a value of 0.75 was found for y. The total density rate constants for the ir experiments are given in Table I and the Arrhenius plot in Figure 6. The least-squares treatment yielded values of log A = 25.29 ± 0.23 and E^* = 61.02 ± 2.29 kcal/mol. The units of A and [M] are consistently $cm^3\ mol^{-1}\ sec^{-2}\ (M)^{-0.75}$ and $mol\ cm^{-3}$, respectively.

Using values of 0.75 and 2 for y and z, the TOF rate constants were likewise converted to a total density basis and fit to the Arrhenius equation. Least-squares treatment of this data gave values of log A = 25.80 ± 0.57 and E^* = 65.72 ± 5.38 kcal/mol. The TOF rate constants are given in Table II and the Arrhenius plot in Figure 7.

The ir and TOF experiments agree within one standard deviation. Combination of the data followed by least-squares treatment to the Arrhenius equation gave values of log A = 25.35 ± 0.21 and E^* = 61.60 ± 2.07 kcal/mol. The Arrhenius plot for the combined data is displayed in Figure 8.

TABLE I: Rate Constants for the C_2N_2–H_2 Reaction from Ir Experiments

Mixture	T, °K	$\rho \times 10^6$, mol cm^{-3}	$k_1 \times 10^{-18}$, cm^3 mol^{-1} sec^{-2} (M)$^{-0.75}$
Argon diluent			
A. 2% C_2N_2–2% H_2	1944	1.95	3.94
P_1 = 5 Torr	2041	1.99	3.75
	2075	2.03	7.10
	2123	2.03	8.18
	2175	2.05	10.5
	2212	2.09	24.5
	2224	2.07	15.5
	2279	2.09	25.1
	2586	2.19	194
	2668	2.22	286
B. 2% C_2N_2–2% H_2	1838	3.85	1.18
P_1 = 10 Torr	1891	3.87	2.14
	1989	3.96	2.91
	2037	4.00	4.24
	2082	4.06	11.4
	2097	4.04	9.16
	2101	4.04	6.90
	2120	4.06	13.2
	2128	4.08	13.2
	2143	4.12	15.9
	2237	4.15	14.6

TABLE II: Rate Constants for the C_2N_2–H_2 Reaction from TOF Experiments

Mixture	T, °K	$\rho \times 10^6$, mol cm^{-3}	$k_1 \times 10^{-18}$, cm^3 mol^{-1} sec^{-2} (M)$^{-0.75}$
Ne–1% Ar diluent			
A. 2% C_2N_2–2% H_2	1962	1.95	2.77
P_1 = 5 Torr	1963	1.98	1.70
	1990	1.96	5.06
	2009	1.98	3.53
	2024	2.00	6.44
	2039	2.02	6.66
	2059	1.97	3.22
	2069	2.03	9.89
	2095	2.04	9.53
	2122	2.04	13.9
	2144	2.09	15.2
	2160	2.07	19.8
	2251	2.10	39.8
B. 1% C_2N_2–1% H_2	1844	1.79	1.35
P_1 = 5 Torr	1892	1.81	1.59
	1989	1.89	3.48
	1989	1.85	4.65
	2003	1.85	4.73
	2121	1.93	7.95
	2285	1.97	27.4
	2303	1.98	27.8

A series of experiments were performed on the TOF using a 2% C_2N_2–2% D_2 mixture at 5 Torr. These experiments were treated in a manner similar to that of the C_2N_2–H_2 system. The results of these experiments compared to the C_2N_2–H_2 Arrhenius dashed line are shown in Figure 9. These experiments show a marked decrease in the values of k_1 by a factor of about 0.6 when D_2 is used in place of H_2. Least-squares treatment of this data gave values of log A = 25.11 ± 0.33 and E^* = 61.48 ± 3.27 kcal/mol. Table III gives the rate data obtained for the C_2N_2–D_2 system.

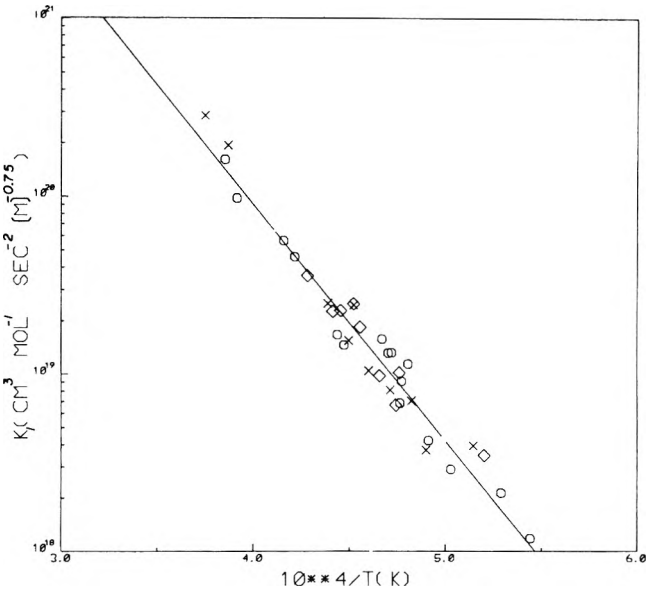

Figure 7. Arrhenius plot for data in Table II: ×, mixture A; O, mixture B; and ◊, mixture C.

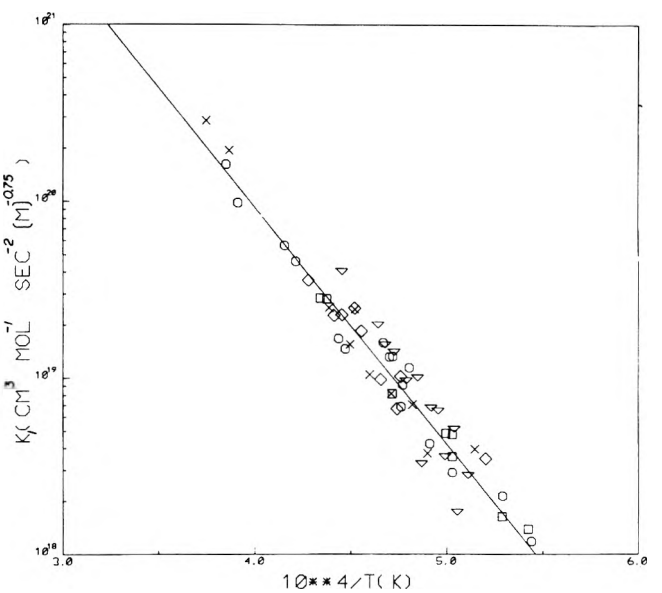

Figure 8. Combined Arrhenius plot for data in Tables I and II.

A few experiments were performed on the TOF on a 2% C_2N_2–2% H_2 mixture in which the TOF was adjusted for high mass analysis (m/e 40 → m/e 100). In the 500 μsec of reaction time no species could be observed other than C_2N_2.

Discussion

The results obtained on the complementary shock tube facility for the C_2N_2–H_2 reaction indicate that the mechanism is complex. Both the quadratic time dependence for product formation and the order dependence on the total density argue effectively against the direct four-center mechanism which predicts a linear time dependence and zero order with respect to inert gas.

TABLE III: Rate Constants for the C_2N_2–D_2 Reaction from TOF Experiments

Mixture	T, °K	$\rho \times 10^6$, mol cm^{-3}	$k_1 \times 10^{-18}$, cm^3 mol^{-1} sec^{-2} (M)$^{-0.75}$
Ne–1% Ar diluent			
2% C_2N_2–2% D_2	1857	1.93	0.751
P_1 = 5 Torr	1984	1.95	2.18
	2062	1.99	3.25
	2109	2.01	6.78
	2213	2.08	12.6
	2383	2.10	18.7
	2393	2.12	33.1
	2469	2.14	50.7
	2482	2.13	58.2

An atomic mechanism may contain the following steps.

$$H_2 + M \xrightarrow{k_{d_1}} 2H + M \quad \text{(a)}$$

$$C_2N_2 + M \xrightarrow{k_{d_2}} 2CN + M \quad \text{(b)}$$

$$CN + H_2 \xrightarrow{k_{a_1}} HCN + H \quad \text{(c)}$$

$$H + C_2N_2 \xrightarrow{k_{a_2}} HCN + CN \quad \text{(d)}$$

Invoking the condition of low conversions and neglecting the back reactions, allows the following relations.

$$\frac{d[HCN]}{dt} = k_{a_2}[H][C_2N_2]_0 + k_{a_1}[CN][H_2]_0 \quad (6)$$

$$[H]_t = 2k_{d_1}[H_2]_0[M]^y t \quad (7)$$

$$[CN]_t = 2k_{d_2}[C_2N_2]_0[M]^{y'} t \quad (8)$$

Equation 7 has been shown to be applicable under the reaction conditions herein[18] and a similar argument may be made for eq 8.[14] Substitution of eq 7 and 8 into 6 followed by integration yields

$$[HCN]_t = (k_{a_2}k_{d_1}[M]^y + k_{a_1}k_{d_2}[M]^{y'})[C_2N_2]_0[H_2]_0 t^2 \quad (9)$$

The relative importance of the terms in parentheses in eq 9 may be estimated with regard to their activation energies. For reactions b and c, the sum is (69[14] + 7[19]) kcal/mol whereas for reactions a and d the minimum value of the sum (96[20] + ≥10[17]) is 106 kcal/mol. Equation 9 may then be approximated by

$$[HCN]_t = k_{a_1}k_{d_2}[C_2N_2]_0[H_2]_0[M]^{y'} t^2 \quad (10)$$

The value of y' may be less than 1 if reaction b is taking place in the fall-off region.

The metathesis of C_2N_2 and H_2 may also occur *via* a vibrational energy chain mechanism (VEC). For the temperature interval spanned in this study, a reaction mechanism is written employing the following sequence

$$H_2 + M \rightleftharpoons H_2^{\upsilon} + M \text{ (fast)} \quad \text{(e)}$$

$$C_2N_2 + M \xrightarrow{k_{\upsilon_2}} C_2N_2^{\upsilon} + M \text{ (slow)} \quad \text{(f)}$$

$$C_2N_2^{\upsilon} + H_2 \xrightarrow{k_m} 2HCN^{\upsilon} \quad \text{(g)}$$

$$HCN^{\upsilon} + C_2N_2 \longrightarrow C_2N_2^{\upsilon} + HCN \quad \text{(h)}$$

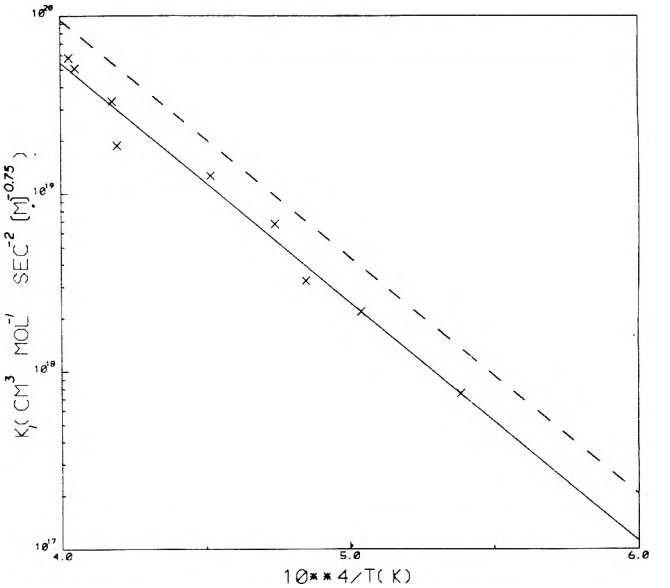

Figure 9. Arrhenius plot of the data in Table III; ×, solid line. Dashed line taken from Figure 8.

where υ implies one or more quanta of vibrational energy. If the time required for C_2N_2 to achieve vibrational equilibration is long compared to the metathesis reaction time, the following equation is applicable

$$[C_2N_2]^{\upsilon} = k_{\upsilon_2}[C_2N_2]_0[M]^y t \quad (11)$$

The rate of formation of product, neglecting the back reaction, is given by

$$\frac{d[HCN]}{dt} = 2k_m[C_2N_2]^{\upsilon}[H_2]_0 \quad (12)$$

Substitution of eq 11 into 12 followed by integration yields

$$[HCN]_t = k_m k_{\upsilon_2}[C_2N_2]_0[H_2]_0[M]^y t^2 \quad (13)$$

A vibrational excitation mechanism (VEX) may also be written for this reaction system. VEX would predict a rate expression of the form

$$[HCN]_t = k[C_2N_2]_0^x[H_2]_0^{x'}[M]^y t^{z=f(t)} \quad (14)$$

The reader may fill in the individual steps for this mechanism by referring to an earlier work by Bauer.[21] It is sufficient here to say that in this mechanism C_2N_2 and H_2 undergo a set of elementary excitation steps whereby they reach their critical vibrational levels. The rate of reaction is controlled by the population of molecules in these critical levels; for instance, H_2 in υ = 3 is the threshold level for the $H_2 + D_2$ exchange according to VEX.

A theoretical treatment of the $C_2N_2 + H_2$ system would require solution of a large set of coupled differential equations with many unknowns. For the simpler $H_2 + D_2$ reaction, these equations have been solved with the result that the value of z changes from 1.2 to 3 without an induction period.[22]

It has been suggested that the reaction of C_2N_2 with D_2 to form DCN would be faster than C_2N_2 with H_2 if VEX

(18) R. D. Kern, Jr., and G. G. Nika, *J. Phys. Chem.*, **75**, 2545 (1971).
(19) P. Hartel and M. Polanyi, *J. Chem. Phys.*, **11**, 97 (1930).
(20) A. L. Myerson and W. S. Watt, *J. Chem. Phys.*, **49**, 425 (1968).
(21) S. H. Bauer and E. Ossa, *J. Chem. Phys.*, **45**, 434 (1966).
(22) S. H. Bauer, D. M. Lederman, E. L. Resler, Jr., and E. R. Fisher, *Int. J. Chem. Kinet.*, in press.

were the dominant mechanism.[23] This prediction is related to the observation reported in the single-pulse shock tube study of the $H_2 + D_2$ exchange that the rate depended more strongly on the concentration of D_2 than on H_2.[21,24] In the temperature range 1050–1200°K, the rate of D_2 with C_2N_2 was found to be faster than that of H_2 with C_2N_2 although the rate decreased with increasing temperature.[23]

According to VEC, the important species is $C_2N_2^v$ and not H_2^v or D_2^v. Consequently, there should be a decrease in the rate constant as expected from the normal isotope effect when D_2 rather than H_2 is reacting with C_2N_2. The magnitude of the isotope effect, A_{D_2}/A_{H_2}, calculated from collision theory, is listed below for both atomic and VEC mechanisms.

$$H_2,\ D_2 + CN \longrightarrow HCN,\ DCN + H,\ D \quad 0.73 \quad (15)$$

$$H,\ D + C_2N_2 \longrightarrow HCN,\ DCN + CN \quad 0.715 \quad (16)$$

$$H_2,\ D_2 + C_2N_2^v \longrightarrow 2HCN,\ DCN \quad 0.72 \quad (17)$$

The experimental ratio (k_{D_2}/k_{H_2}) is about 0.6 which agrees with either the atomic or VEC mechanism within experimental error.

The quadratic time dependence and the order with respect to reactants and total density are facts which can be rationalized in terms of an atomic or vibrational energy chain mechanism. The experimental activation energy of 62 kcal/mol is less than the 76 kcal/mol predicted by eq 10. This discrepancy plus the lack of any direct evidence for the presence of radicals argues somewhat against the atomic route. The observation of an appreciable vibrational equilibration time for C_2N_2 compared to the metathesis reaction time lends support to VEC. However, the activation energy predicted by eq 13 is not known and it is possible that it is high.

A more definite statement may be made with regard to the role of cyanogen in the HCN + D_2 exchange.[15] The proposal involved the following steps.

$$2HCN \longrightarrow C_2N_2 + H_2 \quad (i)$$

$$C_2N_2 + D_2 \longrightarrow 2DCN \quad (j)$$

This work has demonstrated that the rate of reaction j is much slower than the exchange process and therefore cyanogen is not an important intermediate in the exchange sequence.

The evidence is conclusive with respect to the complex nature of this metathetical reaction. The direct bimolecular combination of the reactants with the formation of a four-center transition state does not occur to any appreciable extent and provides another example of a "simple" chemical reaction that avoids the four-center pathway.

Acknowledgments. The authors would like to thank Mr. Tim Dupuy for his assistance with data reduction, Mr. Darryl Olivier who helped maintain the equipment, and Professors Robert Flurry and Peter Politzer for fruitful discussions. We appreciate very much a critical review of the manuscript by Professor S. H. Bauer.

(23) D. K. Lewis, Thesis, Cornell University, 1970; University Manuscripts, Ann Arbor, Mich
(24) D. K. Lewis, private communication.

A Mass-Spectrometric Study of the Reaction of Trifluoromethyl Radicals with Nitric Oxide[1]

Hiok-Seng Tan and F. W. Lampe*

Whitmore Laboratory Department of Chemistry, The Pennsylvania State University, University Park, Pennsylvania 16802
(Received December 18, 1972)

Publication costs assisted by The U. S. Atomic Energy Commission and The Petroleum Research Fund

Trifluoromethyl radicals, formed by the photolysis of hexafluoroazomethane, react with nitric oxide by successive addition to yield trifluoronitrosomethane and perfluorotrimethylhydroxylamine. Trifluoronitrosomethane is the sole product until the nitric oxide concentration has been reduced to very low levels, at which time the addition reaction to form perfluorotrimethylhydroxylamine can occur. After the trifluoronitrosomethane has been depleted the trifluoromethyl radicals can react with hexafluoroazomethane to yield perfluorotetramethylhydrazine and with each other to yield hexafluoroethane. Kinetic analysis of the data subsequent to depletion of nitric oxide permits evaluation of a lower limit to the specific reaction rate for the addition of trifluoromethyl radicals to trifluoronitrosomethane. The value found is $k_8 \geq 9.7 \pm 0.7 \times 10^{-14}$ cm^3 molecule^{-1} sec^{-1} at 56°.

The photolysis of hexafluoroazomethane in the visible and near-ultraviolet regions of the spectrum has been well studied[2-7] and often used[8-12] as a convenient source of trifluoromethyl radicals at near room temperature. The products of the photolysis are nitrogen, hexafluoroethane, perfluorotetramethylhydrazine, and perfluorohexamethyl-

tetrazine and it is generally accepted[2-7] that these arise from the mechanism

$$CF_3N_2CF_3 + h\nu \longrightarrow 2CF_3\cdot + N_2 \quad (1)$$

$$CF_3\cdot + CF_3N_2CF_3 \longrightarrow (CF_3)_2\dot{N}\dot{N}CF_3 \quad (2)$$

$$CF_3\cdot + CF_3\cdot \longrightarrow C_2F_6 \quad (3)$$

$$CF_3 + (CF_3)_2\dot{N}\dot{N}CF_3 \longrightarrow (CF_3)_2NN(CF_3)_2 \quad (4)$$

$$(CF_3)_2\dot{N}\dot{N}CF_3 + (CF_3)_2\dot{N}\dot{N}CF_3 \longrightarrow (CF_3)_2NN(CF_3)N(CF_3)N(CF_3)_2 \quad (5)$$

If nitric oxide is added to a system in which trifluoromethyl radicals are present the trifluoromethyl radicals will be scavenged by nitric oxide, *via* (6),[12-18] to form tri-

$$CF_3 + NO \longrightarrow CF_3NO \quad (6)$$

fluoronitrosomethane, a stable blue gas that can be isolated.[19,20] The scavenging reaction, (6), is very efficient, the rate constant having been shown[21] to be at least 10^{-13} cm^3 $molecule^{-1}$ sec^{-1}, and it will, therefore, be the essentially exclusive fate of trifluoromethyl radicals until the nitric oxide concentration has been reduced to very low levels. Trifluoronitrosomethane, the product of (6), will also scavenge trifluoromethyl radicals by successive addition of the radicals to form perfluorotrimethylhydroxylamine,[22-26] as shown by (7) and (8). Indeed, the photolysis of

$$CF_3\cdot + CF_3NO \longrightarrow (CF_3)_2NO\cdot \quad (7)$$

$$CF_3 + (CF_3)_2NO\cdot \longrightarrow (CF_3)_2NOCF_3 \quad (8)$$

2:1 mixtures of trifluoroiodomethane and trifluoronitrosomethane has been used to prepare perfluorotrimethylhydroxylamine in 90% yield.[25] Reactions 7 and 8 are thus similar to reactions occurring when small amounts of nitric oxide are added to systems in which hydrogen atoms,[27] methyl radicals,[28] and ethyl radicals[29] are present.

Since its discovery and isolation by Blackley and Reinhard,[30] the nitroxide radical produced in (7) has been well studied.[25,31-35] It abstracts hydrogen atoms from alkanes[33] and adds to olefins[32,33] in a reaction predominating over hydrogen atom abstraction[33] from olefins. It reacts very rapidly with free radicals, as would be expected, since it is itself a free radical. Therefore, since activation energies for addition to olefins are 7-10 kcal/mol[32] and addition appears to predominate over hydrogen abstraction, one may conclude that in the presence of trifluoromethyl radicals (7) will be followed rapidly by (8) to yield the perfluorotrimethylhydroxylamine.

This paper describes a mass-spectrometric study of the photolysis of hexafluoroazomethane in the presence of up to 10% of nitric oxide.

Experimental Section

Trifluoromethyl radicals were generated by the photolysis of hexafluoroazomethane in the presence of up to 10% of nitric oxide. The reactions were carried out in a photolysis cell containing a pinhole leak leading directly into the ionization chamber of a somewhat-modified Bendix Model 14-101 time-of-flight mass spectrometer. The photolysis cell was 8.35 cm in length with a diameter of 2.10 cm and was connected *via* 3-mm stainless steel and 6-mm Pyrex tubing to a large reservoir (5-12 l.) containing the reactants, hexafluoroazomethane and nitric oxide. The apparatus and general techniques have been fully described in previous publications from this laboratory.[27-30,36]

An Osram HBO-100 high-pressure mercury arc was used as a light source. The spectral emission of this lamp and the wavelength dependence of the hexafluoroazomethane absorption coefficient[6] are such that the average effective photolytic wavelength was about 3660 Å. The lamp was operated at 5.2 A using a power supply obtained from George W. Gates Co. (Model P109); with this power supply the lamp current could be reproduced to within ±2%.

Hexafluoroazomethane was purchased from Merck Sharpe and Dohme, Ltd. It contained 1-2% of trifluoroiodomethane which was not removed by repeated freeze-pump-thaw cycles in liquid nitrogen. However, the long wavelength limit of its absorption[37] nearly coincides with the short wavelength cut-off of the lamp emission, so that photolysis of the trifluoroiodomethane is undoubtedly negligible. Nitric oxide having a stated minimum purity of 98.5% was purchased from the Matheson Co. It was purified by first freezing onto silica gel at liquid nitrogen temperature and then allowing a slow temperature increase of the condensed gas to occur. The initial and final

(1) United States Atomic Energy Commission Document No. COO-3416-7.
(2) J. R. Dacey and D. M. Young, *J. Chem. Phys.*, **23**, 1302 (1955).
(3) G. O. Pritchard, H. O. Pritchard, and A. F. Trotman-Dickenson, *Chem. Ind.*, 564 (1955).
(4) G. O. Pritchard, H. O. Pritchard, H. I. Schiff, and A. F. Trotman-Dickenson, *Trans. Faraday Soc.*, **52**, 849 (1956).
(5) J. R. Dacey, R. F. Mann, and G. O. Pritchard, *Can. J. Chem.*, **43**, 3215 (1965).
(6) E-Chung Wu and O. K. Rice, *J. Phys. Chem.*, **72**, 542 (1968).
(7) S-L. Chong and S. Toby, *J. Phys. Chem.*, **74**, 2801 (1970).
(8) L. Herk, M. Feld, and M. Szwarc, *J. Amer. Chem. Soc.*, **83**, 2998 (1961).
(9) A. P. Stefani, L. Herk, and M. Szwarc, *J. Amer. Chem. Soc.*, **83**, 4732 (1961).
(10) V. A. Ginsburg, E. S. Vlasova, N. M. Vasil'eva, N. S. Mirzabekova, S. P. Makarov, A. I. Shchekotikhin, and A. Ya. Yakubovich, *Dokl. Akad. Nauk SSSR*, **149**, 97 (1963).
(11) W. G. Alcock and E. Whittle, *Trans. Faraday Soc.*, **62**, 664 (1966).
(12) O. Dobis, J. M. Pearson, and M. Szwarc, *J. Amer. Chem. Soc.*, **90**, 278 (1968).
(13) R. N. Haszeldine, *J. Chem. Soc.*, 2075 (1953).
(14) J. Banus, *J. Chem. Soc.*, 3755 (1953).
(15) J. Jander and R. N. Haszeldine, *Naturwissenschaften*, **40**, 579 (1953).
(16) J. Jander and R. N. Haszeldine, *J. Chem. Soc.*, 912 (1954).
(17) D. A. Barr and R. N. Haszeldine, *J. Chem. Soc.*, 1881 (1955).
(18) J. Heicklen, *J. Phys. Chem.*, **70**, 112 (1966).
(19) O. Ruff and M. Giese, *Berichte*, **69**, 600 (1936).
(20) O. Ruff and M. Giese, *Berichte*, **69**, 684 (1936).
(21) S. W. Charles as quoted by B. G. Tucker and E. Whittle, *Trans. Faraday Soc.*, **61**, 490 (1965).
(22) A. Ya. Yakubovich, S. P. Makarov, V. A. Ginsburg, N. F. Privezentseva, and L. L. Martynova, *Dokl. Akad. Nauk SSSR*, **141**, 125 (1961).
(23) J. Mason, *J. Chem. Soc.*, 4537 (1963).
(24) A. H. Dinwoodie and R. N. Haszeldine, *J. Chem. Soc.*, 1681 (1965).
(25) R. E. Banks, R. N. Haszeldine, and M. J. Stevenson, *J. Chem. Soc. C*, 901 (1966).
(26) R. N. Haszeldine and A. E. Tipping, *J. Chem. Soc. C*, 1236 (1966).
(27) F. C. Kohout and F. W. Lampe, *J. Chem. Phys.*, **46**, 4075 (1967).
(28) A. Maschke, B. S. Shapiro, and F. W. Lampe, *J. Amer. Chem. Soc.*, **86**, 1929 (1964).
(29) H-S. Tan and F. W. Lampe, *J. Phys. Chem.*, **76**, 3303 (1972).
(30) W. D. Blackley and R. R. Reinhard, *J. Amer. Chem. Soc.*, **87**, 802 (1965).
(31) S. P. Makarov, A. F. Videiko, V. A. Tobolin, and M. Englin, *Zh. Obshch. Khim.*, **37**, 1528 (1967).
(32) A. V. Melnikova, M. K. Baranaev, and S. P. Makarov, *Zh. Obshch. Khim.*, **40**, 382 (1970).
(33) R. N. Haszeldine, R. E. Banks, and B. Justin, *J. Chem. Soc. C*, 2777 (1971).
(34) R. N. Haszeldine, R. E. Banks, and T. Myerscough, *J. Chem. Soc. C*, 1951 (1971).
(35) D. P. Babb and J. M. Shreeve, *Intra-Sci. Chem. Rep.*, 55 (1971).
(36) E. Kamaratos and F. W. Lampe, *J. Phys. Chem.*, **74**, 2267 (1970).
(37) J. G. Calvert and J. N. Pitts, "Photochemistry," Wiley, New York, N. Y., 1966, p 527.

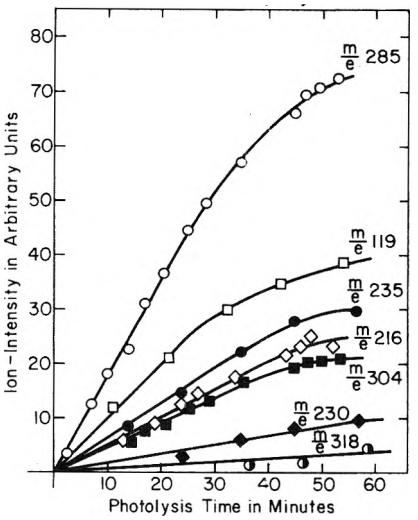

Figure 1. Dependence of ion intensities on time of photolysis of pure hexafluoroazomethane at 11.4 Torr: O, m/e 285; □, m/e 119; ●, m/e 235; ◊, m/e 216; ■, m/e 304; ♦, m/e 230; ◑, m/e 318.

10% of the gas distilling from the silica gel were discarded and the entire procedure repeated.

All photolyses were carried out at a temperature of 56 ± 3°.

Results and Discussion

1. Photolysis of Pure Hexafluoroazomethane. When 11.4 Torr of pure hexafluoroazomethane is photolyzed at 56° one clearly observes, as may be seen in Figure 1, a simultaneous growth in the intensities of ions having m/e values of 119, 216, 230, 235, 285, 304, and 318. The relative intensities of these ions are independent of photolysis time, indicating that they arise from electron impact ionization of a common molecule or of different molecules produced in simultaneous reactions. Mass spectrometric and stoichiometric considerations, within the framework of the known products of the photolysis,[2-7] lead to the following conclusions concerning the identification of these ions: (1) m/e 119 is $C_2F_5^+$ arising from electron impact ionization and dissociation of C_2F_6; (2) m/e 304 is $(CF_3)_2NN(CF_3)_2^+$, the parent ion of perfluorotetramethylhydrazine, while m/e 285, 235, and 216 are, respectively, $(CF_3)_2NN(CF_3)CF_2^+$, $(CF_3)_2NN(CF_3)^+$, and $(CF_3)_2NN{=}CF_2^+$, all fragment ions produced from perfluorotetramethylhydrazine; (3) m/e 318 and 230 are observed only at very low intensities and we conclude that they are $(CF_3)_2NN(CF_3)NCF_3^+$ and $CF_3NN(CF_3)N{=}CF_2^+$, respectively, which are expected fragment ions of perfluorohexamethyltetrazine. The most predominant ion in the mass spectra of all the product molecules of the photolysis is expected to be CF_3^+ at m/e 69.[26,38] However, this ion is also the most predominant one in the mass spectrum of the reactant hexafluoroazomethane[39] and so the contributions of the products to the intensity at m/e 69 are completely obscured. The very low intensities of the ions at m/e 230 and 318 are in accord with previous observations that under our conditions perfluorotetramethylhydrazine is found in much greater abundance than is the perfluorohexamethyltetrazine.[2,4] The mass spectrometric results are thus in general accord with the accepted mechanism depicted by eq 1-5.

In Figure 2 is shown the ion intensities of m/e 119, 285, and 166 as a function of time in the initial stages of the photolysis. The ion at m/e 166 arises from the hexafluoroazomethane; the dependence of intensity on time indicates that only about 5% of the reactant was consumed over the time of the experiment.

Assuming the mechanism 1-5 to be operative, the trifluoromethyl radicals to be at all times at steady-state concentration, and the amount of perfluorohexamethyltetrazine to be negligible leads to the result shown by

$$\phi I_0 \alpha [CF_3N_2CF_3]_0 = \beta_{119}\left(\frac{di_{119}}{dt}\right)_0 + \beta_{285}\left(\frac{di_{285}}{dt}\right)_0 \quad (9)$$

where ϕ is the quantum yield of (1); I_0 is the light flux incident on the photolysis cell; α is the effective absorption coefficient of hexafluoroazomethane; $i_{m/e}$ is the ion intensity at the m/e indicated; and the mass spectrometric calibration constants are defined by $\beta_{119}i_{119} = [C_2F_6]$ and $\beta_{285}i_{285} = [(CF_3)_2NN(CF_3)_2]$. The subscript zero on the derivatives and on the concentration of hexafluoroazomethane indicates initial rates and initial concentration.

The quantity $(\phi I_0 \alpha)$ was found to be 3.41 ± 0.3 × 10^{-5} sec^{-1} from replicate measurements of the initial rates of nitric oxide consumption when ~1% of nitric oxide was added to the photolysis cell. This calibration procedure is valid because the intensity-concentration proportionality constant for m/e 30 from nitric oxide can be measured directly and in the initial stages of the reaction trifluoronitrosomethane is the sole product. The proportionality constant β_{119} can also be determined directly using C_2F_6, and, therefore, the data of Figure 2 may be treated by (9) to yield the proportionality constant β_{285} that relates ion intensity to concentration of perfluorotetramethylhydrazine.

In terms of the mechanism 1-5 we may write for the photolysis of pure hexafluoroazomethane

$$\left(\frac{d[C_2F_6]}{dt}\right)_0 = \beta_{119}\left(\frac{di_{119}}{dt}\right)_0 = k_3[CF_3]^2 \quad (10)$$

$$\left(\frac{d[(CF_3)_2N_2(CF_3)_2]}{dt}\right)_0 = \beta_{285}\left(\frac{di_{285}}{dt}\right)_0 = k_2[CF_3][CF_3N_2CF_3]_0 \quad (11)$$

where in (11) the term $k_2[CF_3][CF_3N_2CF_3]_0$ is equated to $k_4[CF_3][(CF_3)_2N_2CF_3]$ because of our assumptions of a steady state for $[CF_3]$ and a negligible rate of formation of perfluorohexamethyltetrazine. The steady-state concentration, $[CF_3]$, may be eliminated from (10) and (11) to yield (12), which permits calculation of the ratio $(k_2/k_3^{1/2})$ from data such as shown in Figure 2. Thus, we have from three replicate experiments at 56°, of which a typical one is shown in Figure 2

$$\frac{k_2}{k_3^{1/2}} = \frac{1}{[CF_3N_2CF_3]_0}\frac{\beta_{285}\left(\frac{di_{285}}{dt}\right)_0}{\beta_{119}^{1/2}\left(\frac{di_{119}}{dt}\right)_0^{1/2}} = 2.7 \pm 0.3 \times 10^{-11}\ \frac{cm^{3/2}}{molecule^{-1/2}\ sec^{-1}} \quad (12)$$

The value of $k_2/k_3^{1/2}$ shown in (12) is in satisfactory agreement with that of 1.8 ± 0.6 × 10^{-11} $cm^{3/2}$ mole-

(38) S. S. Dubov and A. M. Khokhlova, *Zh. Obshch. Khim.*, **34**, 586 (1964).
(39) P. B. Ayscough, *J. Chem. Phys.*, **24**, 944 (1956).

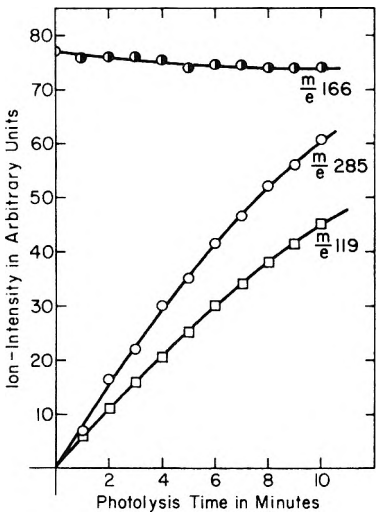

Figure 2. Intensity–time dependence of ions from C_2F_6 and $(CF_3)_2N_2(CF_3)_2$ in initial stages of photolysis: O, m/e 285; □, m/e 119; ◑, m/e 166 (from $CF_3N_2CF_3$).

cule$^{-1/2}$ sec^{-1}, reported by Pritchard, Pritchard, Schiff, and Trotman-Dickenson.[4] This agreement confirms the general validity of our experimental method. Combining the value of $(k_2/k_3^{1/2})$ from (12) with that of $k_3 = 3.88 \times 10^{-11}$ cm^3 molecule^{-1} sec^{-1} reported by Ayscough[39] leads to the result $k_2 = 1.7 \pm 0.2 \times 10^{-16}$ cm^3 molecule^{-1} sec^{-1}.

2. *Photolysis of Hexafluoroazomethane–Nitric Oxide Mixtures.* When mixtures of hexafluoroazomethane and nitric oxide (1–10 mol %) were photolyzed, the only product formed in the initial stages was CF_3NO, as indicated by the rapid increase with time of the peak height at m/e 99 (CF_3NO^+). As shown in Figure 3, which refers to photolysis of 12 Torr of a mixture containing 10% nitric oxide, the intensity of CF_3NO^+ increases to a maximum at a photolysis time of about 20 min. At about the same time as the maximum in [CF_3NO], there is observed a simultaneous formation of ions with m/e values of 237, 218, 168, 149, and 130, of which only m/e 237, 218, and 130 are shown in Figure 3. The absence of a time dependence of the relative intensities of m/e 130 and 218, as shown in the inset of Figure 3, suggests that these ions arise from electron impact on a common molecule. Due to the very low peak heights of m/e 237, 168, and 149, the intensities of these ions were not used in quantitative calculations; however, on the basis of the simultaneous increase in intensities at m/e 237, 218, 168, 149, and 130, there is little doubt that they all arise from the expected[22-26,31] product $(CF_3)_2NOCF_3$ (mol wt = 237 amu). The ions in the mass spectrum are then taken to be $(CF_3)_2NOCF_3^+$ (m/e 237), $(CF_3)_2NOCF_2^+$ (m/e 218), $(CF_3)_2NO^+$ (m/e 168), $(CF_3)(CF_2)NO^+$ (m/e 149), and $(CF_3)(CF)NO^+$ (m/e 130), respectively, although not much significance should be attached to the actual structures written for the fragment ions. It is concluded, therefore, that the common precursor to the above set of ions is perfluorotrimethylhydroxylamine, and that at low concentrations of nitric oxide the kinetic behavior of trifluoromethyl radicals is analogous to that of methyl[28] and ethyl radicals.[29] These conclusions and facts upon which they are based are in accord with previous studies[22-26,31] of the thermal and photochemical reactions of trifluoronitrosomethane. We

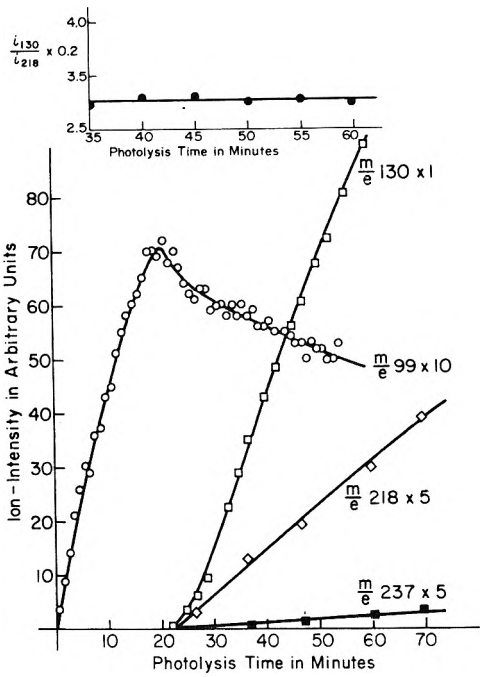

Figure 3. Dependence of ion intensities of product ions in photolysis of $CF_3N_2CF_3$ (90%)–NO (10%) mixture at 12.2 Torr: O, m/e 99 × 10; □, m/e 130 × 1; ◊, m/e 218 × 5; ■, m/e 237 × 5.

have assumed in the above that contributions of the perfluorodimethylnitroxide radical to the observed mass spectra are negligible. Although stable, this radical is expected to react sufficiently fast with the trifluoromethyl radicals[30-35] *via* (8) to keep its stationary concentration below our mass-spectrometric detection level.

The dependence of the intensity of m/e 30 (NO^+) on photolysis time for two different electron energies is shown in Figure 4. At an ionizing energy of 75 eV the intensity of m/e 30 parallels that of m/e 99 (CF_3NO^+), shown in Figure 3, in that a maximum at ~20 min is observed. However, for a nominal ionizing energy of 16 eV, at which NO^+ arises essentially exclusively from electron impact on nitric oxide, the intensity of m/e 30 decreases to a steady-state minimum at ~20 min. Since no product other than trifluoronitrosomethane (Figure 3) is observed prior to the maximum in the intensity of m/e 99 (CF_3NO^+), we may write for this time interval the material balance

$$[NO]_0 = [NO] + [CF_3NO] \qquad (13)$$

where $[NO]_0$ is the initial concentration of nitric oxide. It is thus apparent from Figure 4 that trifluoronitrosomethane contributes an intense m/e 30 peak upon impact of 75-eV electrons. The minimum in the intensity of m/e 30 at 16 eV indicates that the nitric oxide concentration has been so reduced, that at this time, and subsequent to it, nitric oxide contributes only negligibly to the intensity of m/e 30. Thus, we conclude that at the maximum in m/e 99 (CF_3NO^+), shown in Figure 3, the intensity of m/e 30 (NO^+) observed at 75 eV, and shown in Figure 4, is due entirely to formation of NO^+ by electron impact on trifluoronitrosomethane. For 75-eV electrons, then, we interpret the maxima in m/e 30 and 99 to signify the time at which depletion of nitric oxide *via* (6) is essentially complete.

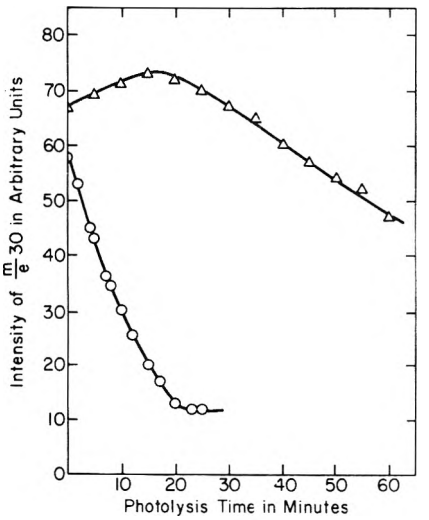

Figure 4. Dependence of intensity of m/e 30 (NO^+) at 75 and 16 eV. Ionizing energy on time of photolysis of $CF_3N_2CF_3$ (90%)–NO (10%) at 12.2 Torr: Δ, i_{30} × 0.1 at 75 eV; O, i_{30} × 2.5 at 16 eV.

When 10 Torr of hexafluoroazomethane was photolyzed in the presence of a much lower concentration of nitric oxide, namely, 0.96%, $[CF_3NO]$, the corresponding intensities of m/e 30 (NO^+) and 99 (CF_3NO^+) attain maxima at about 2 min of photolysis time. The intensity at m/e 99 (CF_3NO^+) is, however, too weak at this low concentration of nitric oxide for use in quantitative calculations. Hence, as shown in Figure 5, the maximum in $[CF_3NO]$ and subsequent decrease of $[CF_3NO]$ due to formation of perfluorotrimethylhydroxylamine *via* (7) and (8) and to leakage into the mass spectrometer are manifested (for 75-eV ionizing energy) by the maximum and subsequent decrease in the intensity of m/e 30 (NO^+).

As in the experiments with 10% of nitric oxide, it can be seen from Figure 5 that at the time of occurrence of the maximum in $[CF_3NO]$ (and in i_{30}), $[(CF_3)_2NOCF_3]$, as reflected by the intensity of m/e 130, increases rapidly, reaching a broad maximum after about 8 min of photolysis. Near the beginning of this broad maximum in $[(CF_3)_2NOCF_3]$ there is observed an onset of ions at m/e 304, 285, 235, 216, 119, and 114, of which only those at m/e 304 and 119 are shown in Figure 5. The ions at m/e 304, 285, 235, 216, and 114 arise from electron impact on perfluorotetramethylhydrazine, while the ion at m/e 119 is from hexafluoroethane, as described in the previous section.

It is interesting to note in Figure 5 that after the maximum in the intensity of m/e 130, the intensity of m/e 30 shows a small but real increase. This observation suggests that, as the reaction proceeds, products are being formed which upon electron impact yield significant amounts of NO^+. A careful search of the mass spectrum subsequent to the maximum in $[(CF_3)_2NOCF_3]$ has not revealed the nature of these products. However, Haszeldine and Tipping[26] have reported that both the compounds I and II yield significant amounts of NO^+ on electron impact. We believe that in our system II is much more likely to be formed than I because it can arise simply by association of the radical product of (2) with nitric oxide, the latter being present in the latter stages of the reaction at a steady-state concentration that is about 10% of it's initial value. The actual consumption of nitric oxide in this experiment may be seen in Figure 6, where the intensity of

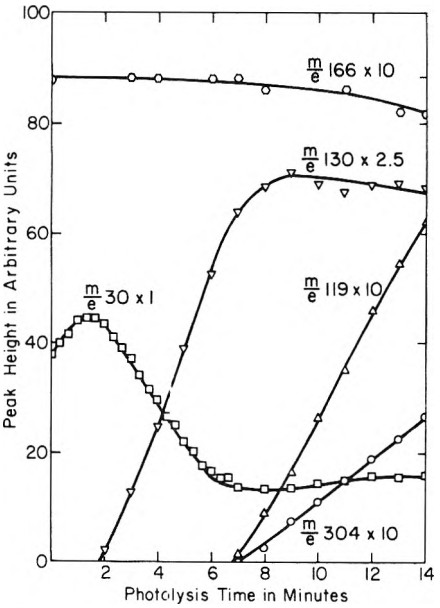

Figure 5. Time dependence of ion intensities in photolysis of $CF_3N_2CF_3$ (99%)–NO (1%) mixture at 10.4 Torr: O, m/e 304 × 10; Δ, m/e 119 × 10; ∇ m/e 130 × 2.5; □, m/e 30 × 1; ○, m/e 166 × 10.

m/e 30 at 16-eV ionizing energy is plotted as a function of time.

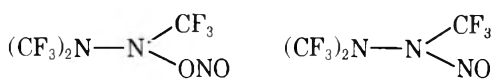

I II

The absence of an ion at m/e 198 indicates that within experimental error no dimerization of trifluoronitrosomethane occurs. This is in contrast to the mass-spectrometric observations with nitrosomethane[40] and nitrosoethane[29] but is in agreement with previous work on trifluoronitrosomethane.[13-17] The rearranged "dimer," $(CF_3)_2NONO$, is known to be formed by the successive addition of a trifluoromethyl radical and a nitric oxide molecule to trifluoronitrosomethane;[26] however, under our conditions of low concentrations of nitric oxide such a sequence is very improbable.

As may be seen in Figure 5, the concentration of hexafluoroazomethane does not vary much during the photolysis. It is interesting to note, however, that, as shown by the time dependence of i_{166}, an increased conversion rate of the hexafluoroazomethane occurs simultaneously with the onset of formation of perfluorotetramethylhydrazine (m/e 304). This clearly shows the increased consumption rate of hexafluoroazomethane that begins when the [NO] and $[CF_3NO]$ have been reduced to such low values that (2) can occur.

All these observations discussed above confirm clearly that the reaction mechanism is shown by eq 1–8. In addition, we suggest that our results support the minor occurrence of

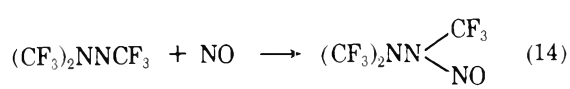

(14)

3. Rate Constant for Addition of Trifluoromethyl Radical to Trifluoronitrosomethane. Assuming that under our

(40) F. A. Thomassy and F. W. Lampe, *J. Phys. Chem.*, **74**, 1188 (1970).

ห้องสมุด

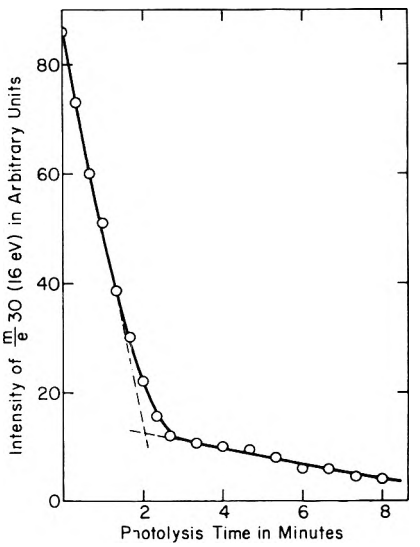

Figure 6. Depletion of NO in photolysis of 10.4 Torr of $CF_3N_2CF_3$ (99%)–NO (1%) mixture.

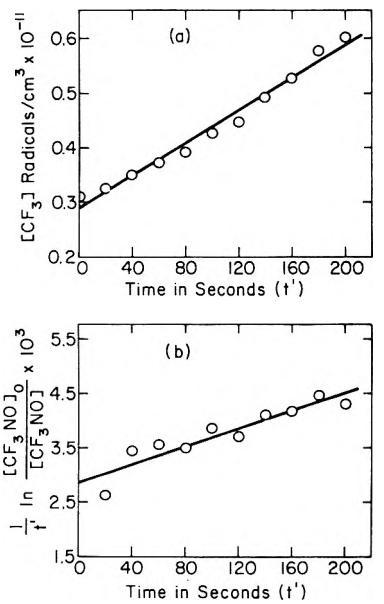

Figure 7. (a) Stationary concentration of CF_3 radicals as a function of photolysis time after consumption of NO. (b) Kinetic description of CF_3NO depletion after consumption of NO.

conditions the radical-combination reaction, (8), is very rapid, the rate-determining step for the formation of perfluorotrimethylhydroxylamine is (7). The specific reaction rate of (7) may be evaluated by kinetic analysis of the photolyzing mixture at reaction times after the maximum in $[CF_3NO]$; that is, after essentially complete depletion of nitric oxide, provided it may be assumed that the produced perfluorotrimethylhydroxylamine does not contribute a mass peak at m/e 30 and provided we may take [NO] = 0. With 16-eV electron impact, the mass peak at m/e 30 decreases rapidly to about 10% of its initial intensity at about the time $[CF_3NO]$ reaches a maximum, as shown in Figure 6. Subsequent to this maximum, the decrease in intensity of the peak at m/e 30 with 75-eV ionizing energy is so steady that with little doubt the $(CF_3)_2NOCF_3$ molecule does not contribute significantly to m/e 30. As shown in Figure 6, [NO] is reduced from 0.96% to less than 0.096% in 2 min of photolysis. The subsequent decrease of $[CF_3NO]$ and the increase of $[(CF_3)_2NOCF_3]$ indicate that [NO] becomes so small by 2 min that the reactions of trifluoromethyl radicals can no longer be inhibited and thus for this system [NO] has effectively become zero.

The rate of depletion of $[CF_3NO]$, after the maximum, is then described by

$$d[CF_3NO]/dt = k_7[CF_3NO][CF_3] + \lambda[CF_3NO] \quad (15)$$

where λ is the first-order leak-rate constant through the pinhole of the photolysis cell. The steady-state concentration of trifluoromethyl radicals is given by

$$[CF_3] = \frac{\sqrt{(k_7[CF_3NO] + k_2[CF_3N_2CF_3])^2 + 4\phi I_0 \alpha k_3[CF_3N_2CF_3]}}{2k_3} - \frac{(k_7[CF_3NO] + k_2[CF_3N_2CF_3])}{2k_3} \quad (16)$$

The relationship between $[CF_3NO]$ and the ion intensity at m/e 30, after the maximum in $[CF_3NO]$, is described by

$$[CF_3NO] = \beta_{30} i_{30} \quad (17)$$

where β_{30} is a proportionality constant and i_{30} is the ion intensity at m/e 30 for 75-eV ionizing energy.

As described in the preceding sections, the values of k_2 and $\phi I_0 \alpha$ are known and k_3 has been reported in the literature.[39] Then with an initial guess that k_7 is the same as for the corresponding reaction in the nitrosoethane system,[29] the steady-state $[CF_3]$ can be computed from (16) as a function of $[CF_3NO]$, and hence as a function of time, using (17) and the experimental data of the ion intensity at m/e 30 with 75-eV ionizing energy, as shown in Figure 4. When this is done, it is found that over an appreciable range of time, beginning about 40 sec past the $[CF_3NO]$ maximum, the computed steady-state $[CF_3]$ is an approximately linear function of time. Hence, we can write for this time range

$$[CF_3] = a + bt' \quad (18)$$

where t' is the reaction time less some convenient time t_0, ($t' = t - t_0$), and a and b are empirical constants determined by a plot of $[CF_3]$ *vs.* t' as shown in Figure 7a. Substituting (18) into (15) and integrating leads to

$$\frac{1}{t'} \ln \frac{[CF_3NO]_0}{[CF_3NO]} = ka + \lambda + \frac{k_7 b}{2} t' \quad (19)$$

where $[CF_3NO]_0$ is the trifluoronitrosomethane concentration at t_0. In a manner completely analogous to that described previously for the nitrosoethane case,[29] a plot of the left-hand side of (19) *vs.* t' should be linear with a slope of $k_7 b/2$ and an intercept of $(ka + \lambda)$. Such a plot for an initial pressure of nitric oxide of 0.1 Torr is shown in Figure 7b. Using the first values of a and b as determined by computation of $[CF_3]$ from (16) a first-improved k_7 can be computed. Then, with the improved k_7, the process can be repeated until successive iterations give no significant change in k_7. The linearity of the plot according to (19), shown in Figure 7b, attests to the validity and internal consistency of the method. The average value obtained from two replicate experiments at 56° is $k_7 = 9.7 \pm 0.7 \times 10^{-14}$ cm^3 molecule^{-1} sec^{-1}. As discussed in the determination of the specific rate of the corresponding ni-

trosoethane reaction,[29] k_7 determined by this procedure is actually a lower limit.

The lower limit found for k_7 indicates that (7) is a very fast reaction and that therefore trifluoronitrosomethane is an effective scavenger for trifluoromethyl radicals. The scavenging sequence in the trifluoromethyl radical–nitric oxide system is clearly seen in Figures 5 and 6. Thus, the behavior of m/e 30 and 130 with time shows that (6) occurs exclusively until the nitric oxide has been so depleted and the trifluoronitrosomethane so abundant that (7) replaces (6) as the exclusive fate of the trifluoromethyl radicals. The onset of m/e 119 and 304 at about 7 min when the trifluoronitrosomethane has been consumed shows that only after this time can the uninhibited photochemical decomposition mechanism *via* eq 2–5 take place. The almost complete inhibition of reactions 2–5 by (7) indicates that trifluoronitrosomethane is a more effective scavenger for trifluoromethyl radicals than is nitrosomethane for methyl radicals[28] or nitrosoethane for ethyl radicals.[29]

Acknowledgment. This work was supported in part by the United States Atomic Energy Commission under Contract No. AT(11-1)-3416 and in part by the Petroleum Research Fund, administered by the American Chemical Society. We also thank the National Science Foundation for providing funds to assist in the original purchase of the time-of-flight mass spectrometer.

Reaction of Excited Oxygen Atoms with Nitrous Oxide. Rate Constants for Reaction of Ozone with Nitric Oxide and with Nitrogen Dioxide[1]

J. A. Ghormley, R. L. Ellsworth,[2] and C. J. Hochanadel*

Chemistry Division, Oak Ridge National Laboratory, Oak Ridge, Tennessee 37830 *(Received December 15, 1972)*

Publication costs assisted by the U. S. Atomic Energy Commission

The ratio of rate constants for reaction of $O(^1D)$ with O_2 and with N_2O was found to be 0.31 ± 0.01, and assuming the absolute value for reaction with O_2 to be 3.6×10^{10} M^{-1} sec^{-1}, this gives 1.20×10^{11} M^{-1} sec^{-1} for reaction of $O(^1D)$ with N_2O. This reaction proceeds predominantly by two paths giving either (a) $N_2 + O_2$ or (b) 2NO. We found the ratio a/b to be 0.70 ± 0.02. The rate constant for reaction of O_3 with NO was $8.5 \pm 0.1 \times 10^6$ M^{-1} sec^{-1} at 298°K, and for reaction of O_3 with NO_2 the rate constant was $4.7 \pm 0.3 \times 10^4$ M^{-1} sec^{-1} at 298°K. The $O(^1D)$ were produced by flash photolysis of O_3 at low concentration in an atmosphere of $O_2 + N_2O$, and the rates of reaction of O_3 with NO and with NO_2, both produced *in situ*, were measured by means of kinetic spectrophotometry.

Introduction

Reactions of electronically excited oxygen atoms, particularly the $O(^1D)$ which possesses 1.96-eV excess energy over the ground state $O(^3P)$, are of considerable interest in atmospheric chemistry, radiation chemistry, and other branches of chemical kinetics. We are particularly interested in the role played by $O(^1D)$ in O_3 formation in the radiolysis of O_2, especially in the presence of other gases. Ground state O atoms are known to react slowly with molecules such as H_2, H_2O, NH_3, CH_4, N_2O, etc.,[3,4] whereas reaction with $O(^1D)$ is often close to the diffusion-controlled rate. The reaction with $O(^1D)$ may be deactivation as with O_2,[5] N_2,[6] and CO_2,[7] or chemical reaction as with the above list of molecules.[8] The $O(^1D)$ can be produced by photolysis at suitable wavelength of any of several oxygen-containing molecules such as O_2 itself, O_3, CO_2, NO_2, N_2O, etc.

In this paper we report results of a study of the reaction of $O(^1D)$ with N_2O. The $O(^1D)$ atoms were produced by the flash photolysis of O_3 at low concentration ($\sim 10^{-6}$–10^{-5} M) in mixtures of O_2 and N_2O at a total pressure of 1 atm ($\sim 4 \times 10^{-2}$ M). Under these conditions the system is relatively simple, and allows evaluation of the rate constants of several important reactions. Following the initial decomposition of O_3 by the flash, we observe, by means of kinetic spectrophotometry, three distinct processes leading to a net loss of O_3. The fastest occurs with a half-time of ~10 μsec, the next ~10 msec, and the longest ~5 sec. We also observe the formation of NO_2 on the 10-msec time scale, and its decay on the 5-sec time scale.

The principal reactions in the sequence observed are the following

$$O_3 \xrightarrow{h\nu} O(^1D) + O_2(^1\Delta) \qquad (1)$$

(1) Research sponsored by the U. S. Atomic Energy Commission under contract with the Union Carbide Corp.
(2) Student trainee under the Great Lakes College Association program from the College of Wooster, Wooster, Ohio 44691.
(3) W. D. McGrath and J. J. McGarvey, *Planet. Space Sci.*, **15**, 427 (1967).
(4) K. Schofield, *Planet. Space Sci.*, **15**, 643 (1967).
(5) J. F. Noxon, *J. Chem. Phys.*, **52**, 1852 (1970).
(6) M. Loewenstein, *J. Chem. Phys.*, **54**, 2282 (1971).
(7) L. F. Loucks and R. J. Cvetanovic, *J. Chem. Phys.*, **57**, 1682 (1972).
(8) G. Paraskevopoulos and R. J. Cvetanovic, *J. Amer. Chem. Soc.*, **91**, 7572 (1969).

$$O(^1D) + O_2 \rightarrow O(^3P) + O_2(O_2(^1\Sigma) \text{ and } O_2(v > 0)) \quad (2)$$

$$O(^3P) + O_2 + M \rightarrow O_3 + M \quad (3)$$

$$O(^1D) + N_2O \rightarrow N_2 + O_2 \quad (4a)$$

$$\rightarrow 2NO \quad (4b)$$

$$NO + O_3 \rightarrow NO_2 + O_2 \quad (5)$$

$$NO_2 + O_3 \rightarrow NO_3 + O_2 \quad (6)$$

$$NO_2 + NO_3 + M \rightarrow N_2O_3 + M \quad (7)$$

Ozone is dissociated by the flash predominantly into $O(^1D)$ and $O_2(^1\Delta)$. In an atmosphere of O_2 the quantum yield for permanent loss of O_3 is nearly zero, indicating that the O_3 is re-formed by reactions 2 and 3.[9] (The excited O_2 molecules are either deactivated by O_2 or react with O_3 to form O atoms which rapidly re-form O_3.)

In the presence of N_2O, reaction 4 (4a + 4b) results in a net loss of O_3. From measurements of the loss of O_3 *vs.* $[O_2]/[N_2O]$ we evaluated the ratio of rate constants k_2/k_4. Young, *et al.*,[10] found this ratio to be 0.222, but their absolute value for $k_2 = 2.4 \times 10^{10}\ M^{-1}\ \text{sec}^{-1}$ differs from Noxon's[5] more recent value of $3.6 \times 10^{10}\ M^{-1}\ \text{sec}^{-1}$. Scott and Cvetanovic[11] found this ratio to be 0.359 ± 0.006.

Reaction 4 is known to occur predominantly by the two paths 4a and 4b. The more recent values for the ratio k_{4a}/k_{4b} are 0.83 ± 0.06 by Heicklen, *et al.*,[12] and 1.01 ± 0.06 by Scott, *et al.*[13] Heicklen, *et al.*, found a lower value for this ratio (0.65) for translationally energetic $O(^1D)$ atoms. The NO produced in 4b reacts with O_3 according to reaction 5 with a half-time ~10 msec. From the amount of O_3 lost in this reaction and the amount lost in reaction 4, we evaluated k_{4a}/k_{4b}. We also evaluated the rate constant k_5 by measuring both the decay of O_3 and the formation of NO_2. Johnston and Crosby,[14] using a stopped-flow technique with measurement by absorption spectroscopy, obtained a value $k_5 = 0.8 \times 10^9 \exp(-2500/RT)\ M^{-1}\ \text{sec}^{-1}$ ($1.21 \times 10^7\ M^{-1}\ \text{sec}^{-1}$ at 298°K). More recently Thrush, *et al.*,[15] obtained nearly the same value, $k_5 = 9.2 \times 10^6\ M^{-1}\ \text{sec}^{-1}$ at 298°K, by following the kinetics of chemiluminescence. Other values differing from these are listed in the review of Schofield.[4]

The NO_2 produced in reaction 5 then reacts with O_3 according to reaction 6 with a half-time ~5 sec. The rate constant for this reaction was evaluated by measuring the decay of both the O_3 and the NO_2. Johnston and Yost[16] evaluated $k_6 = 5.9 \times 10^9 \exp(-7000/RT)\ M^{-1}\ \text{sec}^{-1}$ ($4.9 \pm 0.1 \times 10^4\ M^{-1}\ \text{sec}^{-1}$ at 298°K). Ford, *et al.*,[17] reported $2 \times 10^4\ M^{-1}\ \text{sec}^{-1}$ for this rate constant and $3 \times 10^7\ M^{-1}\ \text{sec}^{-1}$ for k_5 at 302°K.

Experimental Section

Most of the features of the flash system have been described.[18] It consists of a high-pressure mercury–xenon analytical lamp (Hanovia 901 B-II), a 25 cm × 1 cm i.d. jacketed flow-through Suprasil cell, a McPherson Model 216 monochromator, an EMI 9558 photomultiplier, and a Tektronix Model 556 oscilloscope. Two 1-cm i.d. photolysis lamps, with an 8-mm diameter silica rod in the center of each,[19] are located 1.5 cm from the cell inside a MgO-coated reflector that was purged continually with breathing air. The Suprasil lamps contained Xe at 15 Torr, and the discharge at 1 μF and 24 kV gave a flash of ~3-μsec duration at half-peak height.

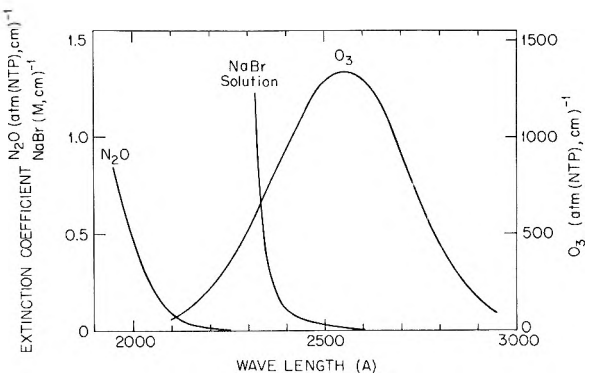

Figure 1. Absorption spectra of gaseous O_3 and N_2O, and the NaBr filter solution. In the O_3 spectrum the fine structure variations, which amount to <4% of the continuum at the peak, have been averaged out.

The jacketed cell provided a 2-mm annulus that was filled with a filter solution of deoxygenated 2 *M* NaBr. As shown in Figure 1, this filter cuts off at ~2300 Å thereby preventing photolysis of N_2O (and O_2), while allowing adequate absorption by O_3 for production of $O(^1D)$. The filter solution was replaced periodically in order to avoid the strong absorption by Br_3^- (ϵ(2700 Å) = 38,000 $M^{-1}\ \text{cm}^{-1}$) which could have been produced by photolysis of NaBr solution containing O_2. Frequent checks were made using the loss of O_3 in the O_2–O_3–N_2O system as actinometer.

The long wavelength edge of the absorption spectrum of N_2O shown in Figure 1 was measured on a Model 15 Cary spectrophotometer and agrees with that published by Zelikoff, *et al.*[20]

Ozone measurements were made with the mercury line at 2650 Å taking $\epsilon = 2540\ M^{-1}\ \text{cm}^{-1}$,[21,22] NO_2 absorbs in a broad band centered at ~4000 Å, with considerable superimposed structure. The NO_2 was measured using the mercury line at 4050 Å. We used the extinction coefficient of Hall and Blacet,[23] however, we determined the exact position of the 4050-Å line (width ~5 Å) on their spectrum by calibration on a Model 15 Cary spectrophotometer. The value from their plot at 4050 Å was taken to be $9.9 \times 10^{-3}\ \text{mm}^{-1}\ \text{cm}^{-1}$ at 25°, corresponding to a molar extinction coefficient of $184\ M^{-1}\ \text{cm}^{-1}$. The relative ex-

(9) I. T. N. Jones and R. P. Wayne, *J. Chem. Phys.*, **51**, 3617 (1969); *Proc. Roy. Soc., Ser. A*, **319**, 273 (1970).
(10) R. A. Young, G. Black, and T. G. Slanger, *J. Chem. Phys.*, **49**, 4758 (1968).
(11) P. M. Scott and R. J. Cvetanovic, *J. Chem. Phys.*, **54**, 1440 (1971).
(12) R. Simonaitis, R. I. Greenberg, and J. Heicklen, *Int. J. Chem. Kinet.*, **4**, 497 (1972). References to earlier papers are given therein.
(13) P. M. Scott, K. F. Preston, R. J. Anderson, and L. M. Quick, *Can. J. Chem.*, **49**, 1808 (1971).
(14) H. S. Johnston and H. J. Crosby, *J. Chem. Phys.*, **22**, 689 (1954).
(15) P. N. Clough and B. A. Thrush, *Chem. Commun.*, **783**, 915 (1966); M. A. A. Clyne, B. A. Thrush, and R. P. Wayne, *Trans. Faraday Soc.*, **60**, 359 (1964).
(16) H. S. Johnston and D. M. Yost, *J. Chem. Phys.*, **17**, 386 (1949).
(17) H. W. Ford, G. J. Doyle, and N. Endow, *J. Chem. Phys.*, **26**, 1336 (1957).
(18) C. J. Hochanadel, J. A. Ghormley, and J. W. Boyle, *J. Chem. Phys.*, **48**, 2416 (1968).
(19) C. J. Hochanadel, J. A. Ghormley, J. W. Boyle, and J. F. Riley, *Rev. Sci. Instrum.*, **39**, 1144 (1968).
(20) M. Zelikoff, K. Watanabe, and E. C. Y. Inn, *J. Chem. Phys.*, **21**, 1643 (1953).
(21) E. C. Y. Inn and Y. Tanaka, *J. Opt. Soc. Amer.*, **43**, 870 (1953).
(22) W. B. DeMore and O. Raper, *J. Phys. Chem.*, **68**, 412 (1964).
(23) T. C. Hall, Jr., and F. E. Blacet, *J. Chem. Phys.*, **20**, 1745 (1952).

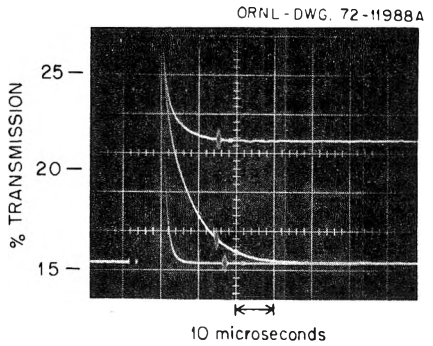

Figure 2. Typical oscillograms showing the decomposition and re-formation of O_3 in the flash photolysis of O_3 (1.3×10^{-5} *M*) in O_2 at 1 atm (4×10^{-2} *M*) (center trace), and the re-formation of only part of the O_3 in a mixture of $O_2 + N_2O$ in the ratio $[O_2]/[N_2O] = 1.18$ (upper trace). The O_3 absorption was measured at 2650 Å. The lower trace is a measure of scattered light from the photolytic flash with the analytical light off.

tinction coefficients for O_3 and NO_2 were shown to be consistent by comparison of the amounts of O_3 lost and NO_2 formed in reaction 5.

For measurements on the short time scale (microseconds), the gas sample flowed continuously through the cell. For measurements on the milliseconds and seconds time scales the flow was stopped just before the flash. In order to minimize photolysis of O_3 by the analytical lamp during measurements of O_3, the light intensity was reduced with neutral filters to ~5% for measurements on the milliseconds time scale, and to ~0.5% for measurements on the seconds time scale. With no filters, photolysis by the analytical lamp occurred with $t_{1/2} \simeq 6$ sec. For measurements of NO_2 at 4050 Å a Corning C.S. 0-52 filter (cut off ~3600 Å) was placed ahead of the cell.

The N_2O (Matheson 98%) was used without purification. Chromotographic analysis indicated only 0.03% N_2 and 0.01% O_2. Mixtures with $[O_2]/[N_2O]$ ratios ranging from 0.3 to 57 were prepared using calibrated flow meters. The O_3 was prepared by photolysis of the O_2 flowing through a Suprasil cell in the form of a trap, surrounded by a Hanovia SC-2537 helical low-pressure mercury lamp. The concentration of O_3 in the O_2 was controlled by adjusting the voltage on the lamp and/or the position of a mask surrounding the photolysis cell. This method of preparing the O_3 provided a very constant concentration in the flowing mixture. The range of O_3 concentrations studied was from 0.5×10^{-6} to 20×10^{-6} *M*.

Results and Discussion

Relative Rates of Reaction of $O(^1D)$ with N_2O and O_2. On flashing O_3 at low concentration (10^{-6}-10^{-5} *M*) in an atmosphere of O_2 (4×10^{-2} *M*), the O_3 dissociated by the flash is essentially all re-formed ($t_{1/2} \simeq 6$ μsec) as shown in Figure 2 (center trace). With N_2O added to the system, only part of the O_3 is re-formed, as shown by the upper trace. Also, the recovery time with N_2O added is somewhat faster since N_2O is two to three times more efficient than O_2 as third body in reaction 3.[24,25] The net loss of O_3 increased as the proportion of N_2O increased. This is attributed to the competition of N_2O with O_2 for $O(^1D)$ according to reactions 4 and 2. The kinetic equation, derived on the assumption that this is the only competition that determines the net loss of O_3, indicates that a plot of $[O_3]/\Delta[O_3]$ *vs.* $[O_2]/[N_2O]$ should be a straight line with

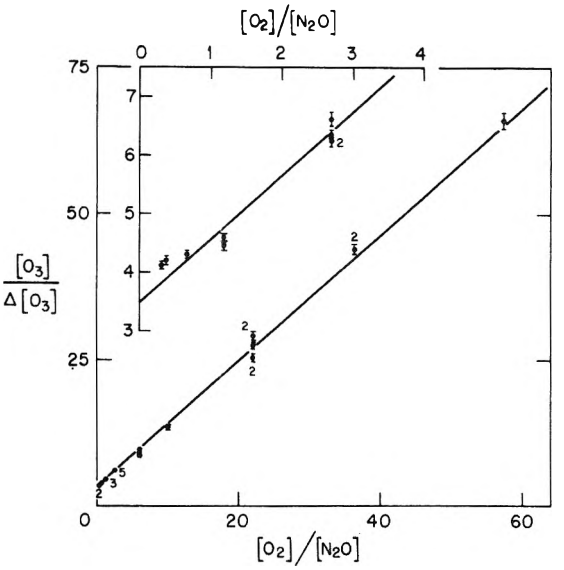

Figure 3. Reciprocal plot showing the loss of O_3 resulting from the competition of N_2O with O_2 for reaction with $O(^1D)$. The inset shows the points near the origin plotted on an enlarged scale. The small numbers indicate the number of data points. The initial O_3 concentration was 9.5×10^{-6} *M*.

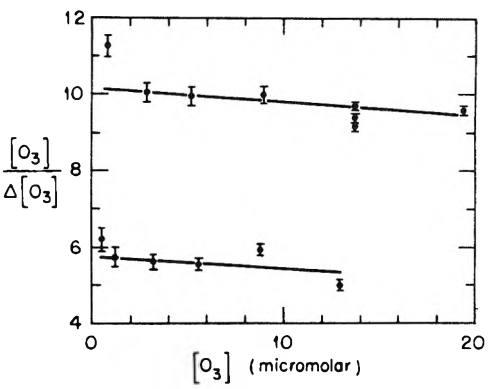

Figure 4. Plot showing only a small dependence of $[O_3]/\Delta[O_3]$ on ozone concentration. The ratio of concentrations $[O_2]/[N_2O]$ is 5.09 for the upper line and 1.18 for the lower line.

the ratio, slope/intercept = k_2/k_4. A plot of our results for concentration ratios ranging from 0.3 to 57 is given in Figure 3. The line, derived from a least-squares fit using Lietzke's[26] generalized least-squares program, gives a ratio, slope/intercept = $k_2/k_4 = 0.31 \pm 0.01$, compared with reported values 0.222[10] and 0.359.[11] Assuming Noxon's[5] value for $k_2 = 3.6 \times 10^{10}$ M^{-1} sec^{-1}, the value for $k_4 = 1.20 \times 10^{11}$ M^{-1} sec^{-1} at 25°. This is a relatively simple system for measuring this competition. The reciprocal plot is based on the assumption that there is no dependence on O_3 concentration. Figure 4 shows there is little or no dependence (<10%) on O_3 concentration over the range studied from 0.5×10^{-6} to 20×10^{-6} *M*, for two ratios of concentrations, $[O_2]/[N_2O] = 1.18$ and 5.09. On the basis of known rate constants, at the concentration employed in our experiments, very little dependence on O_3 concentration is expected. In the competition for $O(^1D)$, even though reaction 8 is fast, the concentration ratios

(24) F. Kaufman and J. R. Kelso, *J. Chem. Phys.*, **46**, 4541 (1967).
(25) M. C. Sauer, Jr., *J. Phys. Chem.*, **71**, 3311 (1967).
(26) M. H. Lietzke, ORNL-3259 (1962).

TABLE I: Ratio of Rate Constants k_{4a}/k_{4b}[a]

Expt	OD_0	OD_4	OD_5	$(OD_0 - OD_4)$	$\frac{1}{2}(OD_4 - OD_5)$	Col 5 − Col 6	k_{4a}/k_{4b}
1	0.6180	0.4802	0.3143	0.1378	0.0830	0.0548	0.661
2	0.6198	0.4776	0.3160	0.1422	0.0808	0.0614	0.760
3	0.6198	0.4815	0.3178	0.1383	0.0818	0.0565	0.692
4	0.8268	0.6556	0.4522	0.1712	0.1017	0.0695	0.683
5	0.8268	0.6596	0.4634	0.1672	0.0981	0.0691	0.705
6	0.6073	0.4881	0.3487	0.1192	0.0697	0.0495	0.710
7	0.5528	0.4401	0.3098	0.1127	0.0656	0.0471	0.718

[a] The OD are optical densities of O_3 measured at 2650 Å. OD_0 is the initial OD; OD_4 is the OD after completion of the fast reaction 4; OD_5 is the OD after completion of reaction 5; k_{4a}/k_{4b} is the ratio of the value in column 7 to that in column 6. The ratio of concentration $[O_2]/[N_2O]$ was 1.18 for all of these experiments.

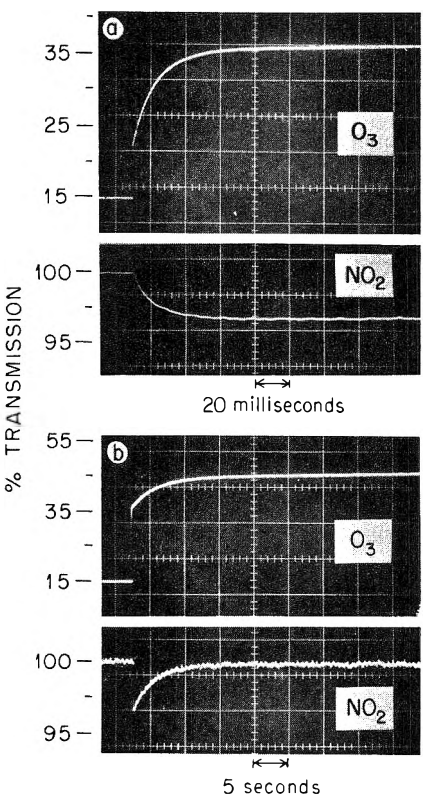

Figure 5. Typical oscillograms showing (a) the loss of O_3 and formation of NO_2 due to reaction of O_3 with NO (reaction 5), and (b) the loss of O_3 and NO_2 due to reaction 6. The instantaneous loss of O_3 in 5a corresponds to the rapid loss shown in Figure 2 due to reaction 4, and the instantaneous loss of O_3 in 5b corresponds to the sum of losses in reactions 4 and 5.

$$O(^1D) + O_3 \rightarrow 2O_2 \quad (8a)$$

$$O(^1D) + O_3 \rightarrow 2O(^3P) + O_2 \quad (8b)$$

$$(k_8 = 1.5 \text{ to } 4 \times 10^{11}\ M^{-1}\ \text{sec}^{-1})^{27,28}$$

are such that less than 0.5% of the $O(^1D)$ react with O_3. This is confirmed by the fact that in the $O_2 + O_3$ system with no N_2O present, essentially all of the O_3 destroyed by the flash is re-formed. In the competition for $O(^3P)$, reaction with O_3 is too slow ($k = 4.6 \times 10^6\ M^{-1}\ \text{sec}^{-1}$)[29] to be important. Also, the third-order combination of O atoms ($k \sim 1 \times 10^9\ M^{-2}\ \text{sec}^{-1}$)[4,30] is not important. The reaction of NO with $O(^3P)$ is fast, and could be followed

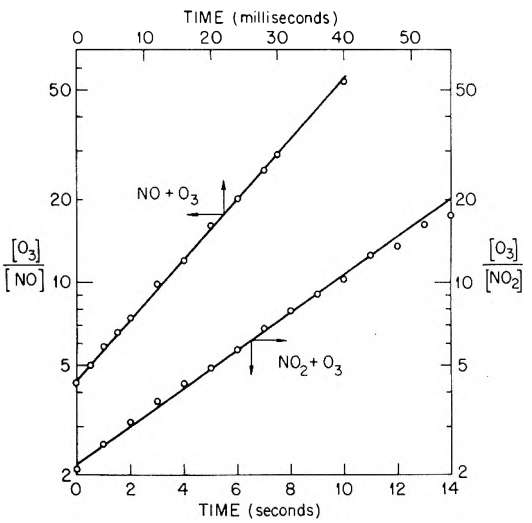

Figure 6. Typical second-order semilog plots of $[O_3]/[NO]$ *vs.* time, and $[O_3]/[NO_2]$ *vs.* time, corresponding to the reactions of O_3 with NO and NO_2, respectively.

by the fast reaction of NO_2 with $O(^3P)$

$$O(^3P) + NO + O_2 \rightarrow NO_2 + O_2\ (k = 2.2 \times 10^{10}\ M^{-2}\ \text{sec}^{-1})^4 \quad (9)$$

$$O(^3P) + NO_2 \rightarrow NO + O_2\ (k = 4 \times 10^9\ M^{-1}\ \text{sec}^{-1})^4 \quad (10)$$

the net result being the combination of O atoms to form O_2. However, again because of concentration ratios, reaction 9 amounts to less than 1% of reaction 3.

Ratio of Rate Constants, k_{4a}/k_{4b}. It is known that the reaction of N_2O with $O(^1D)$ goes predominantly by two pathways, 4a and 4b. The NO produced in reaction 4b is expected to react with O_3 according to 5, and from the reported[14,15] rate constant of $\sim 1 \times 10^7\ M^{-1}\ \text{sec}^{-1}$, we would expect an additional loss of O_3 on a millisecond time scale for our conditions. We observed this additional slow loss of O_3 as shown by the upper trace in Figure 5a. (The instantaneous loss of O_3 is also indicated. This loss occurs in ~ 20 μsec, after which the O_3 concentration remains essentially constant for ~ 100 μsec, as shown pre-

(27) R. Gilpin, H. I. Schiff, and K. H. Welge, *J. Chem. Phys.*, **55**, 1087 (1971).
(28) C. S. Goldman, R. I. Greenberg, and J. Heicklen, *Int. J. Chem. Kinet.*, **3**, 501 (1971).
(29) J. L. McCrumb and F. Kaufman, *J. Chem. Phys.*, **57**, 1270 (1972).
(30) J. E. Morgan and H. I. Schiff, *J. Chem. Phys.*, **38**, 1495 (1963).

viously in Figure 2.) The lower curve in Figure 5a shows the build-up of NO_2 on the same time scale. For each $O(^1D)$ reacting with N_2O according to 4b, two additional O_3 molecules are lost by reaction 5. Therefore, from the amount of O_3 lost (or NO_2 formed) in the slow reaction (twice 4b), the ratio of rate constants k_{4a}/k_{4b} was evaluated. Seven measurements, listed in Table I, gave an average value $k_{4a}/k_{4b} = 0.70 \pm 0.02$, compared with reported values of 0.83 ± 0.06[12] and 1.01 ± 0.06.[13]

Rate Constant for the Reaction of O_3 with NO. A typical second-order plot of $[O_3]/[NO]$ on a log scale *vs.* time, based on measurements of O_3 and NO_2 as in Figure 5a, is shown as the upper line in Figure 6. The second-order rate constant, given by $k_5 = 2.303 \text{ slope}/[O_3]_0 - [NO]_0$, was $8.5 \pm 0.1 \times 10^6 M^{-1} \text{ sec}^{-1}$ at 298°K, based on five sets of measurements. This agrees closely with the value of Thrush, *et al.*,[15] ($9.2 \times 10^6 M^{-1} \text{ sec}^{-1}$), and reasonably close to that of Johnston and Crosby[14] ($1.21 \times 10^7 M^{-1} \text{ sec}^{-1}$).

Rate Constant for the Reaction of O_3 with NO_2. The reaction of O_3 with NO is complete in <0.1 sec, after which the slow reaction of O_3 with the NO_2 produced takes place as shown in Figure 5B. The instantaneous loss of O_3 in Figure 5b corresponds to the total loss of O_3 in Figure 5a. The overall reaction corresponds to the equation[31]

$$2NO_2 + O_3 \rightarrow N_2O_5 + O_2$$

and was shown[16] to occur in two steps

$$NO_2 + O_3 \rightarrow NO_3 + O_2 \quad (6)$$

$$NO_2 + NO_3 + M \rightarrow N_2O_5 + M \quad (7)$$

the first of which is rate determining. The reaction follows second-order kinetics as shown by the plot of $[O_3]/[NO_2]$ on a log scale *vs.* time in Figure 6. Concentrations of O_3 and NO_2 were obtained either from oscillograms as shown in Figure 5b, or from recorder charts using a Sargent Model MR recorder. The second-order rate constant, defined by the rate equation $d[O_3]/dt = k_6[NO_2][O_3] = \frac{1}{2}d[NO_2]/dt$, is obtained from the slope of the line using the equation $k_6 = 2.303 \text{ slope}/[O_3]_0 - [NO_2]_0$. The average value of k_6 at 298°K, based on three sets of measurements, was $4.7 \pm 0.3 \times 10^4 M^{-1} \text{ sec}^{-1}$, in close agreement with the old value of Johnston and Yost[16] ($4.9 \pm 0.1 \times 10^4$).

(31) O. R. Wulf, F. Daniels, and S. Karrer, *J. Amer. Chem. Soc.*, **44**, 2398 (1922).

The Role of Singlet and Triplet States in Aromatic Substitution Reactions. II. Fluorescence Quenching of Anisole and *p*-Hydroquinone by Acids

George F. Vesley* and Barry D. Olafson

Department of Chemistry, University of North Dakota, Grand Forks, North Dakota 58201 *(Received December 7, 1971)*

Fluorescence quenching data using various acids and solvents for anisole and *p*-hydroquinone are presented. The quenching rate shows a large dependence on the acid used, (CF_3CO_2H > HCl) indicating participation of the anion or undissociated acid. The quantum yield for exchange in THF is measured as 0.008 and complications in this reaction are indicated.

Introduction

In a previous report[1] we have shown that if a singlet state is responsible for photochemical hydrogen–deuterium exchange in aromatic systems, a correlation should exist between fluorescence quenching data and quantum yield data. If the reaction can be explained by the simple mechanism shown below, application of Stern–Volmer kinetics yield eq 8 and 9. The data presented for the exchange on *p*-hydroquinone in DCl–D_2O solutions showed the value of $k_f\tau$ obtained from the fluorescence quenching experiments was two orders of magnitude smaller than that obtained from the quantum yield measurements. Arguments were presented which showed a σ complex between the deuterium ion and the *p*-hydroquinone was formed in a vibrational level of the ground state, and not in an excited state, thereby preventing the reversibility of reaction 5. On the basis of the data presented, the singlet state was eliminated as an intermediate for exchange, and the triplet state of *p*-hydroquinone was proposed as the intermediate responsible for the H–D exchange.

$$Ar \xrightarrow{h\nu} {}^1Ar \quad (1)$$

$${}^1Ar \xrightarrow{k_{ds}} Ar \quad (2)$$

$${}^1Ar \xrightarrow{k_{isc}} {}^3Ar \quad (3)$$

$${}^1Ar \xrightarrow{k_f} Ar + h\nu \quad (4)$$

$${}^1Ar + D^+ \xrightarrow{k_r} (ArD)^+ \quad (5)$$

$$(ArD)^+ \xrightarrow{k_1} Ar + D^+ \quad (6)$$

(1) G. F. Vesley, *J. Phys. Chem.*, **75**, 1775 (1971).

TABLE I: Fluorescence Quenching Constants

Compound[a]	Solvent	Acid	$k_q\tau$, M^{-1}	k_q, M^{-1} sec^{-1} [b]
Anisole	THF[c]	TFA[d]	1.8	2.17×10^8
Anisole	Ethyl ether	TFA	0.43	5.2×10^7
Anisole	95% ethanol	TFA	5.6	6.7×10^8
Anisole	40% water–60% ethanol	TFA	5.6	6.7×10^8
Anisole	95% ethanol	Acetic acid	0.033	4×10^6
Anisole	95% ethanol	NaTFA[e]	No quenching	
Anisole	95% ethanol	HCl	0.025	3×10^6
p-Hydroquinone	Ethyl ether	TFA	2.2	1.05×10^9
p-Hydroquinone	Water	TFA	2.05	9.8×10^8
p-Hydroquinone	Ethyl ether	Acetic acid	0.43	2.05×10^8
p-Hydroquinone	Deuterium oxide	DCl	0.059[f]	2.80×10^7

[a] [anisole] = 10^{-2} *M*; [*p*-hydroquinone] = 3×10^{-3} *M*. [b] τ = 8.3 nsec for anisole[9] and 2.1 sec for *p*-hydroquinone.[1] [c] THF = tetrahydrofuran. [d] TFA = trifluoroacetic acic. [e] NaTFA = sodium trifluoroacetate. [f] Reference 1.

$$(\mathrm{ArD})^+ \xrightarrow{k_2} \mathrm{Ar} + \mathrm{H}^+ \tag{7}$$

$$\frac{1}{\phi_{ex}} = \frac{k_1 + k_2}{k_2}\left[1 + \frac{1}{k_r\tau[\mathrm{D}^+]}\right] \tag{8}$$

$$\phi_{fo}/\phi_f = 1 + k_r\tau[\mathrm{D}^+] \tag{9}$$

In contrast to our results, Havinga and Kronenberg[2] have studied the photochemical exchange of anisole using trifluoroacetic acid (TFA) in tetrahydrofuran (THF). In their experiments they have measured the quantum yield for hydrogen deuterium exchange and have explained their data using a singlet intermediate. The fact that both singlet and triplet states can lead to exchange is reasonable if in some cases the singlet lifetime is long so that fluorescence quenching can compete with radiative decay. This was not the case with *p*-hydroquinone. In this paper we wish to report fluorescence quenching data to help determine the mechanism of these exchange processes.

Experimental Section

Materials. Acetic acid (Fisher Chemical Co.), deuterium chloride in D_2O (Merck Sharp and Dome) 99% D, hydrochloric acid (Fisher Chemical Co.), and sodium trifluoroacetate (Pierce Chemical Co.) were used as received. The trifluoroacetic acid (Pierce Chemical Co.) and anisole (Fisher Chemical Co.) were distilled before use. *p*-Hydroquinone (Aldrich Chemical Co.) was recrystallized twice from benzene–alcohol mixtures. The ethyl ether (Mallinckrodt Chemical Works AR) and tetrahydrofuran (Fisher Chemical Co.) were treated with ozone and lithium aluminum hydride, and distilled under vacuum.[3,4]

The purity of the solvents was determined by uv analysis of N_2 purged solutions. The THF used for quantum yield experiments showed no uv absorptions above 245.0 nm. The THF used for the fluorescence studies reported in Table I shows greater than 99% transmission at 290 nm. In some preliminary runs a small impurity emission centered around 340 nm was observed. The intensity of this impurity emission was depended upon the intensity of absorption above 250 nm. It runs where the THF absorbed 2–3% of the light at 290 nm, it was very hard to observe the anisole emission. In these runs the Stern–Volmer constant varied, being as low as 0–5 M^{-1}.

Fluorescence Experiments. The fluorescence experiments were performed in 1-cm^2 quartz cells using an Aminco Bowman spectrophotofluorometer, λ_x 290 nm. The solutions were purged with N_2 before the spectra were run. Corrections were made for light not absorbed by the anisole.

Quantum Yields. The quantum yield solutions were degassed in 13-mm diameter quartz tubes which had a constriction to facilitate sealing and 14/35 joint for connection to the vacuum system. Five freeze–thaw cycles, the last two using a diffusion pump, were used. The quantum yield was measured using a Hanovia low-pressure 253.7-nm mercury resonance lamp in a merry-go-round[5] with a cation X–cobalt sulfate filter. The actinometry was done using a modified ferrioxalate method.[6,7] The deuterium analysis was done on a Du Pont MS 491 mass spectrometer. Conversions of ~1% were obtained.

Results and Discussion

We have measured the Stern–Volmer quenching constant, $k_q\tau$, for anisole and *p*-hydroquinone using trifluoroacetic acid, hydrochloric acid, and acetic acid in various solvents. The important points of the data, presented in Table I, are the slight increase in k_q with increasing solvent polarity with a given acid, and the dependence of k_q on the acid used. It is quite evident that the quenching process is significantly less efficient when DCl or HCl is used. All plots using trifluoroacetic acid and acetic acid were linear when concentrations of less than 3.3 *M* acid were used. Above 3.3 *M* the plots curve upward. The HCl plots curved upward above 2 *M*.[1] It would appear that two mechanisms are competing at these high concentrations, one of which is possibly static quenching.[8] The data presented in Table I[9] were taken from the linear portion of the curve below 3 *M*.

(2) E. Havinga and M. E. Kronenberg, *Pure Appl. Chem.*, **16**, 137 (1968), and references therein.
(3) V. I. Stenberg, R. D. Olson, C. T. Wang, and N. Kulevsky, *J. Org. Chem.*, **32**, 3227 (1967).
(4) E. S. Proskauer, J. A. Riddick, and E. E. Toops, Jr., "Technique of Organic Chemistry," Vol. III, 2nd ed, A. Weissberger, Ed., Interscience, New York, N. Y., 1965, p 366.
(5) G. F. Vesley, *Mol. Photochem.*, **3**, 193 (1971).
(6) G. F. Vesley and G. S. Hammond, *J. Amer. Chem. Soc.*, submitted for publication.
(7) C. G. Hatchard and C. A. Parker, *Proc. Roy. Soc., Ser. A*, **235**, 518 (1956).
(8) A. Weller, *Progr. React. Kinet.*, **1**, 189 (1961); J. L. Kropp and M. Burton, *J. Chem. Phys.*, **37**, 1742 (1962); P. J. Wagner, *J. Amer. Chem. Soc.*, **89**, 5715 (1967).
(9) L. Berlman, "Handbook of Fluorescence Spectra of Aromatic Molecules," Academic Press, New York, N. Y., 1965, p 65.

If we compare our fluorescence quenching data with the quantum yield data reported by Havinga,[2,10] a correlation was not obtained. This prompted us to reinvestigate the H-D exchange quantum yields in THF. At a TFA concentration of 1 *M*, we obtained a quantum yield for exchange of 0.008. This is considerably less than previously reported. Lodder and Havinga have recently reported that their original quantum yields are in error.[11]

If we assume the only decay processes available to the anisole singlet state are fluorescence (ϕ_f = 0.29)[9] and intersystem crossing we can calculate rate constants of 8.5 × 10^7 and 3.5 × 10^7 sec^{-1}, respectively, for these processes. It is evident that the rate of quenching of the singlet state by the acid is competitive with fluorescence and intersystem crossing at 1 *M* acid. At this concentration, approximately 60% of the singlets would be quenched and the intersystem crossing quantum yield would be reduced to 0.26. On the basis of these rate constants it would appear that the exchange could arise from both singlet and triplet states of anisole. Assuming that a triplet and singlet intermediate can lead to the exchange product, the maximum quantum yield for exchange *via* the triplet component would be 0.13 and 0.32 *via* the singlet state. The predicted value is obviously higher than the measured quantum yield.

There are several reasons for the observed quantum yield being less than the maximum value. Previous workers have explained the low exchanged quantum yield by proposing an acid-catalyzed non-radiative deactivation of the excited state,[2,10,12] however, the formation of a π complex does not appear to increase the modes of non-radiative decay sufficiently to accommodate the loss of ~100 kcal of energy. Other alternatives must be considered. Bryce-Smith[13] has reported the photochemical addition of trifluoroacetic acid to benzene. Since the efficiency of the addition reaction of TFA to the hydrocarbon has not been measured, the quantum yield for exchange cannot be adjusted for this competing reaction. The product of this addition, *p*-methoxy-α,α,α-trifluoroacetophenone, could serve as a quencher of the triplet component of the exchange and absorb light in competition with the anisole to reduce the amount of exchange *via* the singlet component. Mass spectral evidence for an adduct was observed in the deuterium analysis. Lodder and Havinga[11] have recently isolated an adduct between anisole and TFA.

Another possibility is complication due to the THF solvent. At 1 *M* trifluoroacetic acid and 10^{-2} *M* anisole, the acid absorbs about 25% of the 253.7-nm radiation. Our quantum yield was corrected for this competitive absorption, however, we cannot compensate for quenching due to impurities in the solvent.

It can be concluded that both singlet and triplet states are available for the exchange process. To show the contribution of each state to the overall exchange process, the quantum yields in the presence of quenchers and sensitizers are required. These experiments would be difficult to perform due to the absorption properties of anisole, its high triplet energy, and the strong acid conditions of the reaction. We therefore feel that these experiments would be more meaningful using a different system in which the possibility of impurity quenching (THF) and competitive absorption by the TFA are eliminated. However we do trust the quenching data in the other solvents and it is evident that the quenching is not a function of the availability of H^+. The anion of the acid appears to be involved, however, it is not a quencher itself. This presents several new mechanistic possibilities which are outlined in Scheme I. We are justified in using undissociated TFA since its pK_a is 0.3.[14] Experiments to determine the extent of these processes are underway.

Scheme I

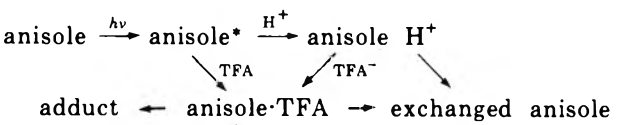

Acknowledgment. The discussion of Dr. Virgil I. Stenberg, the technical assistance of Mr. R. Elkins, and the use of the University of North Dakota Biochemistry Department's Aminco Bowman spectrofluorometer are gratefully acknowledged. One of us, G. F. V., wishes to thank the University of North Dakota for a Hill Research Professorship (1972). This work was supported by a University of North Dakota Faculty Research Grant and a Research Corporation Grant. The MS 491 was purchased with the assistance of a NSF Departmental Equipment Grant No. GP-28407.

(10) D. A. DeBie, Ph.D. Thesis, University of Leiden, The Netherlands, 1966.
(11) G. Lodder and E. Havinga, *Tetrahedron*, **28**, 5583 (1972).
(12) M. G. Kuzmin, V. L. Ivanov, and Yu. Yu. Kulis, *High Energy Chem., (USSR)*, **2**, 229 (1968).
(13) D. Bryce-Smith, G. B. Cox, and A. Gilbert, *Chem. Commun.*, 914 (1971).
(14) J. B. Hendrickson, D. J Cram, and G. S. Hammond, "Organic Chemistry," 3rd ed, McGraw-Hill, New York, N. Y., 1970, p 320.

Rapid Evaluation of Dielectric Relaxation Parameters from Time-Domain Reflection Data

G. A. Brehm and W. H. Stockmayer*

Department of Chemistry, Dartmouth College, Hanover, New Hampshire 03755 *(Received January 8, 1973)*

Publication costs assisted by the National Science Foundation

A rapid approximate method is presented for obtaining the Davidson-Cole dielectric response parameters from time-domain reflection measurements. The method is restricted to systems of moderate polarity and negligible dc conductivity.

Time-domain reflectometry (TDR) has excited current interest[1-4] as a convenient method for the study of relatively fast dielectric relaxation, corresponding roughly to the interval 10^7-10^{11} Hz in the frequency domain. Because of the quadratic relation between dielectric constant and refractive index, a calculation of the dielectric correlation function[5] from the observed time dependence of the reflection coefficient is not simple, even for Debye dielectrics.[2] A method of obtaining the dielectric response function in the general case has been described by Suggett, Loeb, and coworkers.[3,4] who perform a Fourier inversion of the reflection curve by applying a sampling of theorem of Shannon[6] as adapted by Samulon.[7] The computation is lengthy, inviting expensive data-acquisition equipment, and requires measurements of fairly high precision.

For many purposes, it is quite sufficient to express the relaxation behavior of a dielectric material in terms of just two parameters, typically an average response time and a breadth parameter; the familiar Cole-Cole[8] and Davidson-Cole[9] functions are two examples of this level of treatment. Recently van Gemert and deGraan[10,11] have presented sample calculations of reflection curves for Cole-Cole and Davidson-Cole dielectrics, and in particular have stressed the limitations imposed by high dc conductivity. However, their results also do not lend themselves to easy evaluation of TDR measurements. In the present paper we offer a simple approximate method for obtaining two dielectric relaxation parameters, essentially those of the Davidson-Cole function, from TDR data for systems of moderate polarity and negligible dc conductivity.

In the frequency domain the reflection coefficient $\rho^*(\omega)$ is related to the complex dielectric constant $\epsilon^*(\omega)$ as follows

$$\epsilon^*(\omega) = [1 - \rho^*(\omega)]^2/[1 + \rho^*(\omega)]^2 \qquad (1)$$

Clearly, if the dependence of ϵ^* on frequency *exactly* obeyed a Davidson-Cole function the reflection coefficient could not do so; however, for moderate values of the ratio of static to high-frequency dielectric constants, $\epsilon_0/\epsilon_\infty$, the reflection coefficient could still be well approximated by a Davidson-Cole function, of course with adjusted parameters. This remark is the basis of our method.

Observing also that the Davidson-Cole function is essentially empirical (though not without theoretical sense), we therefore write

$$\rho^*(\omega) = \rho_\infty + (\rho_0 - \rho_\infty)(1 + i\omega\tau)^{-\alpha} \qquad (2)$$

in which ρ_0 and ρ_∞ are clearly the values of the reflection coefficient at zero and infinite frequency, respectively. We then assert that the dielectric constant can be approximately written as

$$\epsilon^*(\omega) \cong \epsilon_\infty + (\epsilon_0 - \epsilon_\infty)(1 + i\omega\tau_0)^{-\beta} \qquad (3)$$

and that the parameters τ_0 and β of the latter expression can be related to those, τ and α, of the former through eq 1. Our procedure for doing this was the following. For various values of ρ_0, ρ_∞, and α, the complex dielectric constant was evaluated as a function of $\omega\tau$ by means of eq 1 and 2, and Cole-Cole plots were constructed. The two characteristic features of $\epsilon^*(\omega)$ were taken to be the frequency ω_m (in units of τ^{-1}) for which the loss factor has its maximum value ϵ_m'', and the reduced magnitude $\epsilon_m''/(\epsilon_0 - \epsilon_\infty)$ of this maximum. These are related for Davidson-Cole dielectrics to the parameters τ_0 and β by the expressions[12]

$$\omega_m\tau_0 = \tan\phi_m \qquad \phi_m = \pi/(2 + 2\beta) \qquad (4a)$$

$$\epsilon_m''/(\epsilon_0 - \epsilon_\infty) = (\cos\phi_m)^\beta \sin\beta\phi_m \qquad (4b)$$

Thus for each set of values of ϵ_0, ϵ_∞, τ, and α we can find related values of the Davidson-Cole parameters τ_0 and β.

By starting with eq 2, we have ensured a simple transformation to the time domain. Thus, the time variation of the voltage step reflected from the surface of the dielectric is

$$\rho(t) = \rho_\infty + (\rho_0 - \rho_\infty)(t/\tau)^\alpha\gamma^*(\alpha, t/\tau)$$

in which

$$\gamma^*(\alpha, t/\tau) = (t/\tau)^{-\alpha}\int_0^{t/\tau} y^{\alpha-1}e^{-y}\,dy/\Gamma(\alpha) \qquad (5)$$

is the incomplete γ function.[13] By means of eq 5 we can

(1) H. Fellner-Feldegg, *J. Phys. Chem.*, **73**, 616 (1969).
(2) H. Fellner-Feldegg and E. F. Barnett, *J. Phys. Chem.*, **74**, 1962 (1970).
(3) A. Suggett, P. A. Mackness, M. J. Tait, H. W. Loeb, and G. M. Young, *Nature (London)*, **228**, 456 (1970).
(4) H. W. Loeb, G. M. Young, P. A. Quickenden and A. Suggett, *Ber der Bunsenges. Phys. Chem.*, **75**, 1155 (1971).
(5) G. Williams, *Chem. Rev.*, **72**, 55 (1972).
(6) C. Shannon, *Proc. IRE*, **37**, 10 (1949).
(7) H. A. Samulon, *Proc. IRE*, **39**, 175 (1951).
(8) K. S. Cole and R. H. Cole, *J. Chem. Phys.*, **9**, 341 (1949).
(9) D. W. Davidson and R. H. Cole, *J. Chem. Phys.*, **18**, 1417 (1951).
(10) M. J. C. van Gemert, *J. Phys. Chem.*, **75**, 1323 (1971).
(11) M. J. C. van Gemert and J. G. deGraan, *Appl. Sci. Res.*, **26**, 1 (1972).
(12) N. G. McCrum, B. E. Read, and G. Williams, "Anelastic and Dielectric Effects in Polymeric Solids," Wiley, New York, N. Y., 1967.
(13) M. Abramowitz and J. A. Stegun, "Handbook of Mathematical Functions," Dover Publications, New York, N. Y., 1968.

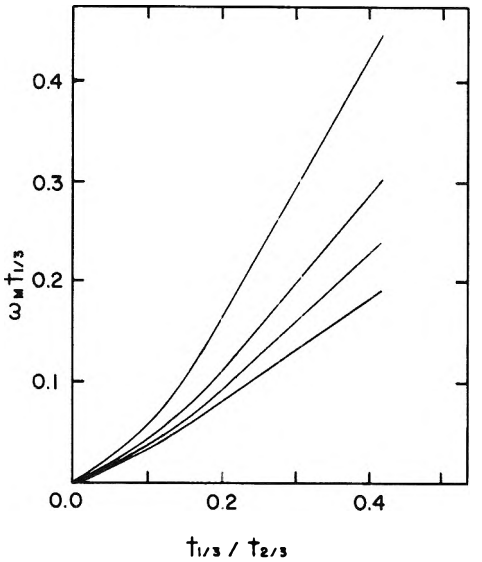

Figure 1. Curves for the determination of the frequency of maximum dielectric loss factor, ω_m, from time-domain reflection measurements. From top to bottom, the curves correspond to the following values of the ratio $\epsilon_0/\epsilon_\infty$: 1, 2, 3, and 4.

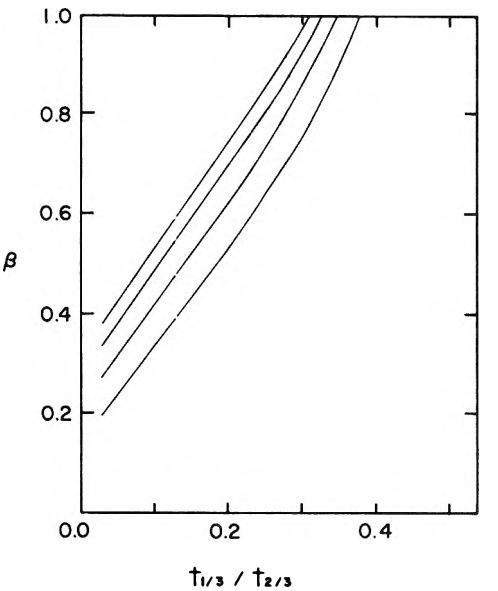

Figure 2. Curves for the determination of the breadth parameter β from time-domain reflection measurements. From top to bottom, the curves correspond to the following values of the ratio $\epsilon_0/\epsilon_\infty$: 4, 3, 2, and 1.

calculate reflection curves for various chosen values of the parameters and then attempt to characterize these by their appropriate principal features In addition to the initial and final reflection coefficients ρ_∞ and ρ_0, we choose to designate the times $t_{1/3}$ and $t_{2/3}$ at which $\rho(t)$ has fallen one-third and two-thirds, respectively, of the way from its initial to its final value.

The practical results of the calculations outlined above are shown in Figures 1 and 2. We have preferred to replace the time constant τ_0 of eq 3 by the circular frequency of maximum loss, ω_m, as given by eq 4b. Thus, for various values of the dielectric constant ratio $\epsilon_0/\epsilon_\infty$, we plot the dimensionless quantities $\omega_m t_{1/3}$ and β against the ratio $t_{1/3}/t_{2/3}$. From these graphs, therefore, it is possible directly to obtain ω_m and β from a measured reflection curve in the time domain. Although in principle both ρ_0 and ρ_∞ (and thence ϵ_0 and ϵ_∞) can be read from such curves, in practice it is usually advisable to get ϵ_0 by separate low-frequency bridge measurements. A time-marker system[4] aids in obtaining reproducible values of ρ_∞.

We have used Figures 1 and 2 routinely for rapid evaluation of the reflection curves from numerous polymer solutions, finding the method quite adequate for the precision of our measurements. It is not intended as a replacement for more precise methods.[4]

Acknowledgments. This investigation was supported in part by a National Institutes of Health Fellowship (No. FO1 GM43303-03) to G. A. B. from the General Medical Sciences division, and in part by the National Science Foundation under Grant No. GP-30343X. The authors thank Dr. F. I. Mopsik of the National Bureau of Standards for valuable criticisms and suggestions.

Picosecond Pulse Radiolysis. IV. Yield of the Solvated Electron at 30 Picoseconds

R. K. Wolff, M. J. Bronskill, J. E. Aldrich, and J. W. Hunt*

Ontario Cancer Institute and Department of Medical Biophysics, University of Toronto, Toronto M4X 1K9, Ontario, Canada
(Received January 27, 1972)

Publication costs assisted by the Ontario Cancer Institute and the University of Toronto

The "spur" diffusion model has long been the basis for the interpretation of the radiation chemistry of aqueous solutions. Two aspects of this model have been studied using picosecond pulse radiolysis: $G(e_{aq}^-)$ at 30 psec, and the rate of decay of e_{aq}^- from 30 to 350 psec in the absence of scavengers. Two independent methods, one absolute and one relative to $G(e_{aq}^-)$ at 0.1 μsec, have established $G(e_{aq}^-) = 4.0 \pm 0.2$ at 30 psec. In pure water the decay of e_{aq}^- is less than 5% between 30 and 350 psec. These results disagree to the details of the theoretical predictions of the spur diffusion model. Additional experiments have determined $G(e_{sol}^-)$ at 30 psec in simple alcohols to be much lower than $G(e_{aq}^-)$ at 30 psec. It appears likely that an accurate model of the early events in the radiolysis of polar solvents must take into account the fate of the initial ion pair, *i.e.*, H_2O^+ and e^-, in water.

Introduction

Previous papers in this series[1-3] have described experiments to determine the physical and chemical properties of the solvated electron (e_{sol}^-) in various solvents during the time interval from 20 to 350 psec after a very short pulse of ionizing radiation. Many aspects of the stroboscopic pulse radiolysis (SPR) technique used to perform these experiments have also been described.[4-6] On this very early time scale the solvated electron has been found to exhibit physical and chemical properties virtually identical with the same properties measured on a microsecond time scale. Moreover, the formation process of the solvated electron at room temperature is complete within at least 10 psec in all solvents we have studied.[1]

For the past 20 years the spur diffusion model[7,8] has constituted the theoretical basis for understanding the radiation chemistry of aqueous solutions. The reactive species produced by the ionizing radiation (usually assumed to be OH, e_{aq}^-, H, and H_{aq}^+) are believed to be distributed nonhomogeneously in the solution. Local regions of high concentrations of these species are known as spurs. The subsequent fate of these species is described in terms of their reactions with each other in the spur, their diffusion from the spur into the bulk of the solution, and their reactions with solute molecules in the solution. Pulse radiolysis studies in the past decade have been invaluable in determining the bimolecular reaction rates of these species (particularly e_{aq}^- and OH) with many solutes,[9] and their yields[10] at microsecond times. Thus the remaining unmeasured parameters in the spur diffusion model are the initial yield and distribution of these species. Reasonable estimates of these parameters have been made, usually from nonkinetic measurements of hydrogen yields in the presence of added solutes, and the spur diffusion model has proven quite satisfactory in explaining such measurements.

The observation "window" of the SPR system from 30 to 350 psec is ideally suited to study early processes in radiation chemistry. This paper describes the measurement of $G(e_{aq}^-)$ at 30 psec and the derivation of the yields of e_{sol}^- in several alcohols by comparison with the yield of e_{aq}^-.

Method

The SPR system allows observation of optically absorbing transients in the time interval between fine structure electron pulses from the University of Toronto Linear Accelerator (spacing between fine structure pulses is 350 psec). Knowledge of some of the more intricate aspects of the SPR system is necessary for a complete understanding of these experiments. These details are described in previous papers on this system[1-6] and are assumed to be understood in the following discussion.

The types of e_{sol}^- absorption signal which can be measured using the picosecond pulse radiolysis system are shown in Figure 1. The average absorption per fine structure pulse, S, is measured as the peak height of the trace (Figure 1a and 1b, see also ref 3). Traces such as Figure 1a are obtained in high concentrations of scavenger (typically ~ 1 M) where the lifetime of e_{sol}^- is much less than 350 psec. Figure 1b is typical of solutions where the lifetime of e_{sol}^- is ~ 1 nsec. The average absorption per fine structure pulse can also be obtained in the absence of scavengers where the lifetime of e_{sol}^- is much greater than 1 nsec. This type of trace is shown in Figure 1c where the step height, h, can be related to the average absorption per fine structure pulse. In this case the sum of the absorption signals from all fine structure pulses in the macropulse (in the absence of signal decay) is measured as

(1) M. J. Bronskill, R. K. Wolff, and J. W. Hunt, *J. Chem. Phys.*, **53**, 4201 (1970).
(2) R. K. Wolff, M. J. Bronskill, and J. W. Hunt, *J. Chem. Phys.*, **53**, 4211 (1970).
(3) J. E. Aldrich, M. J. Bronskill, R. K. Wolff, and J. W. Hunt, *J. Chem. Phys.*, **55**, 530 (1971).
(4) M. J. Bronskill, W. B. Taylor, R. K. Wolff, and J. W. Hunt, *Rev. Sci. Instrum.*, **41**, 333 (1970).
(5) M. J. Bronskill, R. K. Wolff, and J. W. Hunt, *J. Phys. Chem.*, **73**, 1175 (1969).
(6) J. E. Aldrich, P. Foldvary, J. W. Hunt, W. B. Taylor, and R. K. Wolff, *Rev. Sci. Instrum.*, **43**, 991 (1972).
(7) A. Kuppermann in "Radiation Research," G. Silini, Ed., North-Holland Publishing Co., Amsterdam, 1967.
(8) H. A. Schwarz, *J. Chem. Phys.*, **73**, 1928 (1969), and personal communication.
(9) M. Anbar and P. Neta, *Int. J. Appl. Radiat. Isotopes*, **18**, 493 (1967).
(10) E. M. Fielden and E. J. Hart, *Radiat. Res.*, **32**, 564 (1967).

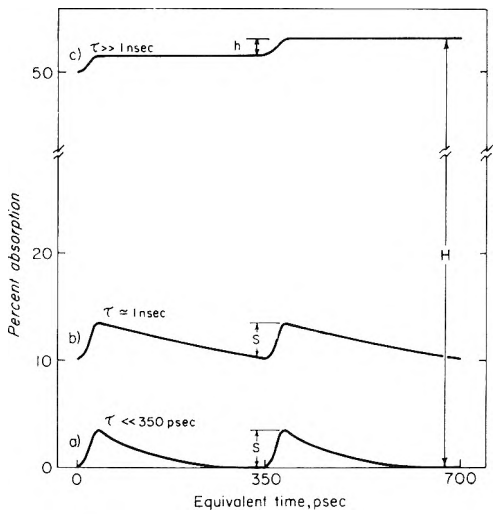

Figure 1. Various types of e_{sol}^- absorption signal detected with the SPR system. τ is the lifetime of e_{sol}^- in the solution being studied: (a) $\tau \ll 350$ psec; the peak height, S, is a measure of e_{sol}^- yield; (b) $\tau \sim 1$ nsec; the peak height, S, is still a measure of e_{sol}^- yield, although the trace does not return to the baseline; (c) $\tau \gg 1$ nsec; the step height, h, and the height, H, of the trace above the baseline are measures of e_{sol}^- yield.

H, the height of the trace baseline above the zero absorption level. Comparison of the signals S, h, and H provides an internal monitor of the accuracy of the detection system because h and H can be calculated from S, provided the shape of the macropulse is known. The absorption signals S, h, and H should all indicate the same yield of e_{sol}^-.

Two types of experiment were performed to measure $G(e_{aq}^-)$ at 30 psec. One experiment determined the ratio, R, of the absorption signal of e_{aq}^- at 30 psec to the absorption signal at 0.1 μsec under identical experimental conditions. Thus the yield of e_{aq}^- at 30 psec equals the yield at 0.1 μsec multiplied by R. A concurrent experiment was done to measure the yield of e_{aq}^- using Perspex HX dosimetry.[11] The G value necessary to give the observed absorption signal at 30 psec could than be calculated. These experiments give two independent measurements of $G(e_{aq}^-)$ at 30 psec. In both types of experiment the three absorption signals S, h, and H were obtained as an internal monitor of the accuracy of the SPR system.

Experimental Section

The complete SPR system has been described in detail previously.[1-6] For this set of experiments the specific parameters of the Toronto Linear Accelerator electron beam were as follows: energy $\simeq$ 41 MeV; peak current $\simeq$ 1.2 A; pulse width $\simeq$ 6 or 15 nsec at half maximum; beam focused to $\sim$5 mm diameter at the front face of the 2 cm path length sample cell.

For most of these experiments on R196 photomultiplier tube (Hamamatsu TV Co.) was used in a five-stage configuration with a cathode-to-collecting dynode potential of $\sim$1600 V. A silicon photodiode (United Detector Technology, PIN-10) coupled to a fast linear amplifier gave identical results. The subsequent electronics consisted of an integrator, stretcher, and sample/hold circuits.[4,6] These circuits were linear to within 5% over the range of light levels used in these experiments.[6] Signal processing was carried out with a small on-line computer (Digital Equipment Corporation, PDP-8) and permanent records of the resultant signals were obtained on an X-Y recorder.

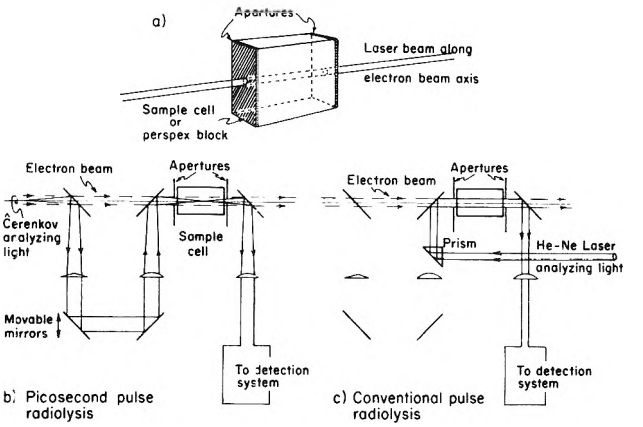

Figure 2. Experimental arrangement for measurement of $G(e_{aq}^-)$ at 30 psec: (a) alignment of light apertures on sample cell or Perspex block; (b) picosecond pulse radiolysis to give S, h, and H; (c) conventional pulse radiolysis using a He-Ne laser to measure $G\epsilon$ at 0.1 μsec.

The optical system was optimized for the red region of the visible spectrum by alignment with a He-Ne laser (Optics Technology Inc., Model 171, 0.3 mW at 633 nm). The same laser was used as an analyzing light source for the conventional pulse radiolysis experiments. Stray uv light was prevented from passing through the monochromator by a 460-nm sharp cutoff filter.

1. Absolute Measurement of $G(e_{aq}^-)$. The analyzing Cerenkov light beam was constrained to travel through two circular 3-mm apertures at the front and rear of the sample cell. The position of these apertures was determined by a laser beam aligned to coincide with the axis of the electron beam, as shown in Figure 2a. The absorption signals (S, h, and H) due to e_{aq}^- were measured at 30 psec in the presence and absence of scavenger (1.0 M H_{aq}^+, in the form of $HClO_4$ (BDH Ltd)). The sample cell was then replaced with a block of Perspex HX[11] consisting of six 3-mm slices of Perspex with small spacers between slices to give the block a density approximating that of the sample solution. A series of these blocks was irradiated with different numbers of linac macropulses and the average dose per linac macropulse was subsequently determined by measuring the change in Perspex absorbance at 305 nm. This change in absorbance was measured through the same 3-mm apertures 4 days after irradiation using a Zeiss spectrophotometer and normal procedures for Perspex dosimetry.[12]

2. $G(e_{aq}^-)$ at 30 psec and 0.1 μsec. This experiment was designed to compare the absorption signal of e_{aq}^- at 30 psec with the absorption signal obtained at 0.1 μsec by conventional pulse radiolysis techniques. The absorption signal at 30 psec was obtained both with and without added scavengers, using the same 3-mm light apertures described above (Figure 2b). A He-Ne laser was then arranged to pass through the same apertures (the sample cell being untouched) and the absorption signal at 633 nm was measured using the laser as the analyzing light for a conventional pulse radiolysis experiment (Figure 2c). Thus the ratio, R, of the two absorption signals at the same wavelength could be used to obtain the yield of e_{aq}^- at 30 psec with respect to the yield of 0.1 μsec, assuming the dose per linac pulse to be constant for the duration of the experiment.

(11) A special type of Perspex developed by I.C.I. (Great Britain) for dosimetry can be obtained from the Wantage Research Laboratory (AERE), Wantage, Berks, England.
(12) R. J. Berry and C. H. Marshall, *Phys. Med. Biol.*, **14**, 585 (1969).

3. Pulse Shape. The shape of the linac pulse was measured by monitoring the Cerenkov light produced at 633 nm by the electron beam in the sample cell. The R196 photomultiplier was connected by 50 cm of RG-58A/U coaxial cable and matched to the 50-Ω input impedance of a sampling unit (Tektronix 556 oscilloscope with 1S1 plug-in). The overall risetime of this system was less than 2 nsec. Better resolution of the macropulse shape was obtained using a planar phototube (ITT, Model F4014) in a matched holder designed at the Argonne National Laboratory. With a bias of 1500 V, this device has a risetime less than 120 psec.[13] Using the 1S1 sampling plug-in, the measured system risetime was less than 500 psec.

4. Experimental Sequence. The determination of $G(e_{aq}^-)$ outlined above requires the execution of several different types of experiment and the subsequent comparison of the results of these experiments. Obviously under these conditions the long-term stability of the linear accelerator beam becomes extremely important. In order to prevent changes in electron beam position or intensity from influencing the outcome of these experiments, the experimental sequence was designed to repeat some experiments to check the linac parameters. The sequence of experiments was as follows: (a) measurement of the shape of the linac pulse; (b) picosecond pulse radiolysis to determine the absorbance at 633 nm of e_{aq}^- in the presence of 1.0 *M* $HClO_4$ (*S* in Figure 1) and in the absence of scavengers (*H* and *h* in Figure 1); (c) conventional pulse radiolysis using the He–Ne laser to determine the absorbance at 633 nm of e_{aq}^- at the end of the linac pulse (*i.e.*, at about 10^{-7} sec); (d) Perspex dosimetry; (e) repeat b.

It must be emphasized that this sequence of experiments was performed without touching the sample cell, apertures, or optical alignment of the SPR system from step a through step c. The sample cell was removed during the Perspex dosimetry, although the laser alignment beam was untouched, and the sample cell was then reinserted for step e, centering the 3-mm apertures in the alignment beam.

Results

1. Absolute Measurement of $G(e_{aq}^-)$. The results of the Perspex dosimetry experiment are shown in Figure 3 where the change in absorbance at 305 nm is plotted as a function of the number of linac pulses. The slope of the least-squares line fitted to the points of Figure 3 is 2.47×10^{-3} absorbance units/linac pulse. The depth–dose distribution, also obtained from the Perspex slices, is shown in Figure 4. The points plotted in Figure 3 are the average dose along the length of the cell, represented by the dotted line in Figure 4. In these experiments the electron beam is tightly focused in order to obtain the maximum dose; thus, the decrease in dose along the axis of the sample cell is caused by scattering of the electron beam.

Our particular batch of Perspex was calibrated against the conventional Fricke dosimeter[14] under full build-up conditions in a Gamma cell (AECL). $G(Fe^{3+}\beta b)$ was taken as 15.6/100 eV, and the calibration factor was determined to be 1.27 Mrads/absorbance unit at 305 nm for ^{60}Co γ-rays. The factor for high-energy electrons was corrected to 1.41 Mrads/absorbance unit.[12] Thus the slope of Figure 3 corresponds to a dose of 3.47 krads per linac pulse.

The shape of the linac macropulse (nominally ~6 nsec) is shown in Figure 5. The number and relative magnitude of the fine structure pulses were determined from this

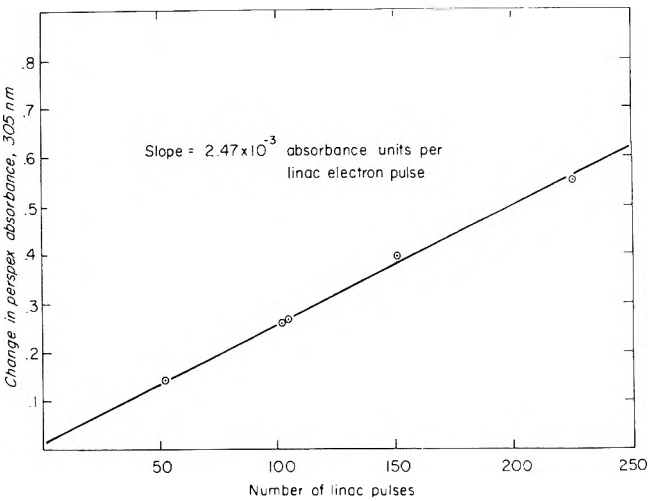

Figure 3. Change in Perspex HX absorbance at 305 nm as a function of number of linac electron pulses delivered. The slope of the least-squares line fitted to the points is 2.47×10^{-3} absorbance units per linac pulse. The small positive intercept represents linac dark current.

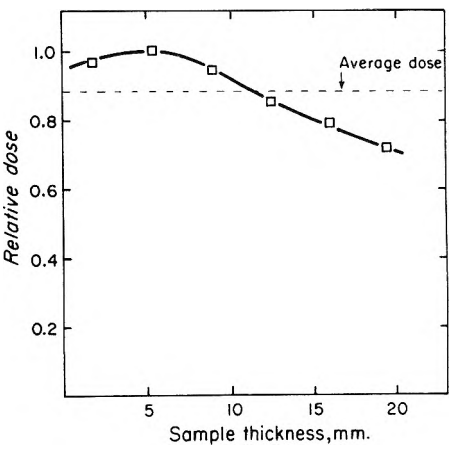

Figure 4. Depth–dose distribution obtained from the Perspex dosimetry.

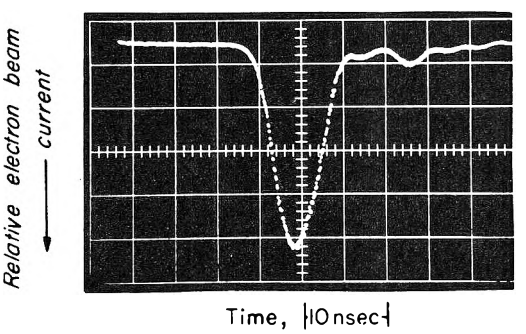

Figure 5. Shape of the linac pulse obtained with the R196 photomultiplier and sampling scope. The small satellite pulse is real and was included in the calculations.

shape. This measured distribution of fine structure pulses is also a dose distribution because total dose is obtained from Perspex dosimetry. In a separate experiment it was determined that the 2-nsec risetime of the photomultiplier detection system spreads this pulse slightly. The half-width observed with the planar phototube was 5.2 nsec,

(13) J. W. Hunt, R. K. Wolff, M. J. Bronskill, C. D. Jonah, E. J. Hart, and M. S. Matheson, *J. Phys. Chem.*, 77, 425 (1973).
(14) H. Fricke and E. J. Hart in "Radiation Dosimetry," Vol. 2, R. H. Attix and W. C. Roesch, Ed., Academic Press, New York, N. Y., 1966.

TABLE I: Experimental Sequence

Experiment	Measurement	Value
(a) Pulse shape	Pulse shape	See Figure 5
(b) Picosecond pulse radiolysis	Peak height, S, step height, h, and absorption level, H (see Figure 1)	S = 3.49%[a] h = 3.70% H = 42.0%
(c) Conventional pulse radiolysis	Absorbance at ~100 nsec after linac pulse	Absorbance = 0.284 (3.55 krads)[b]
(d) Perspex dosimetry	Dose per linac pulse	3.47 krads per linac pulse
(e) Picosecond pulse radiolysis	S, h, and H	S = 3.78% h = 3.80% H = 43.5%

[a] S is corrected by a factor of 1.22 to account for peak height decay due to the short lifetime of e_{aq}^- in 1.0 M $HClO_4$.[3] [b] This absorbance is equivalent to a dose of 3.55 krads using $G(e_{aq}^-) = 2.7$ at 100 nsec.

while the half-width observed with the photomultiplier was 5.7 nsec. A correction factor of 0.91 was applied to the pulse shape measured with the photomultiplier (Table II, experiment 1). Both detection systems gave the same half-width for a nominally 15-nsec pulse.

The pulse shape information was used in a computer program to simulate the signals observed in our experiments. This program (described in Appendix I) calculated the absorption for each analyzing Cerenkov light flash corresponding to the known distribution of fine structure pulses and summed all such absorptions to give the total calculated absorption signal. The only variables left in this calculation were the initial G value and the decay rate of e_{aq}^-. Such decay rates have, however, already been measured[1,3] leaving the initial G value as the only undetermined parameter in the calculation. This G value was then varied for a best fit to the observed absorption signal. In the case of the S absorption signal, a decay rate characteristic of 1 M $HClO_4$ was used, *i.e.*, 1.2×10^{10} sec^{-1}.[1] The decay rate for the H signal (*i.e.*, e_{aq}^- in pure water) was chosen to agree with the measurements of Buxton[15] and Hunt, *et al.*[13] The empirical spur decay of e_{aq}^- fits a first-order rate of 10^8 sec^{-1} until the "steady-state" G value of 2.7 is reached, *i.e.*, $G(e_{aq}^-)(t) = 2.7 + 1.3 \exp(-10^8 t)$. In practice, the calculated H signal was found to be insensitive to both pulse shape and decay rate. In fact, almost any pulse shape with the same total dose gave the same value of H for a given G value.

The measured values of S, h, and H obtained are presented in the proper sequence in Table I. The value of 3.47 krads/pulse from the Perspex dosimetry was used in the computation to determine the G value necessary at 30 psec to produce these values. From the average value of S, the G value at 30 psec was calculated to be 4.1; from the average value of h, $G(e_{aq}^-) = 4.2$ at 30 psec; similarly, from the average value of H, $G(e_{aq}^-)$ at 30 psec is 3.9. These calculations assume a value $\epsilon_{633\,nm} = 1.44 \times 10^4$ M^{-1} cm^{-1} for e_{aq}^-.[10]

2. $G(e_{aq}^-)$ at 30 psec and 0.1 μsec. The conventional pulse radiolysis absorption signal at 633 nm for e_{aq}^- was measured at 100 nsec. The result is given in Table Ic, an absorbance of 0.284.

The average values for S, h, and H from Table I b and e were again used in the computer program to obtain $G(e_{aq}^-)$ at 30 psec. In this case, however, the starting point was the observed absorbance at 100 nsec, corresponding to the known G value for e_{aq}^- at microsecond times of 2.7.[13] This determination is thus independent of absolute dose and $\epsilon_{633\,nm}$ for e_{aq}^-, and assumes only that $\epsilon_{633\,nm}$ is constant from 30 psec to 100 nsec. This calculation yielded $G(e_{aq}^-) = 3.8$ at 30 psec using the average value of H, $G(e_{aq}^-) = 4.0$ using the average value of S, and $G(e_{aq}^-) = 4.1$ using the average value of h.

TABLE II: $G(e_{aq}^-)$ Values[a] Calculated from S, h, H, and Dose Determination

Experiment	1	2	3
Pulse width, nsec	6	6	15
Shape determination	R196 PM (corrected)	Planar phototube	R196 PM
S	4.0, 4.1	4.0	3.9
h	4.1, 4.2	4.2	4.2
H	3.8, 3.9	4.0	3.8
Dose determination	e_{aq}^- and Perspex	Perspex	Perspex

[a] Each G value is an average of the yield obtained before and after the dosimetry. The variation was never more than 10%.

3. Dosimetry and Reproducibility. The overall stability of the linac parameters during this experimental sequence was confirmed by the agreement of the measurements in Table I, b and e. Moreover, the validity of the Perspex dosimetry was reinforced by the agreement of parts c and d. The absorbance observed at 100 nsec was equivalent to a single pulse dose of 3.55 krads (assuming $G(e_{aq}^-) = 2.7$) while the average dose per pulse measured with Perspex was 3.47 krads. This agreement confirms that the dose per pulse is constant for single pulses and pulses delivered at the normal SPR system 60-Hz rate. (This result was also determined by direct pulse amplitude observations.)

In this particular experiment (Table II, experiment 1) the pulse width was corrected by a factor of 0.91 as described earlier. To ensure the validity of this procedure, the experiment was repeated using the planar phototube to determine pulse shape (Table II, experiment 2). In this case the conventional pulse radiolysis determination of e_{aq}^- absorbance at 100 nsec was omitted. The result previously described (and two other experiments) had already shown that the Perspex dosimetry and e_{aq}^- absorbance consistently agreed within ±5%. The results of this experiment (Table II, experiment 2) confirmed the previous result.

A third experiment was also performed using the 15-nsec macropulse to minimize any chance of error in determining pulse shape and to demonstrate that the results obtained were independent of pulse width. These results are given in Table II, experiment 3, and corroborate experiments 1 and 2.

4. Rate of Decay of e_{sol}^- in the Absence of Scavengers. The actual signals observed in pure H_2O and pure ethanol (*i.e.*, in the absence of scavengers) are shown in Figure 6a and 6b, respectively. Small signal "steps" are clearly visible on a relatively flat absorption level (*cf.* Figure 1c). The flatness of the signal between steps is a measure of the rate of decay of e_{sol}^-.

Obtaining this type of signal is difficult in practice. The signal steps (h) are superimposed on such a high absorp-

(15) G. V. Buxton, *Proc. Roy. Soc., Ser. A*, **328**, 9 (1972).

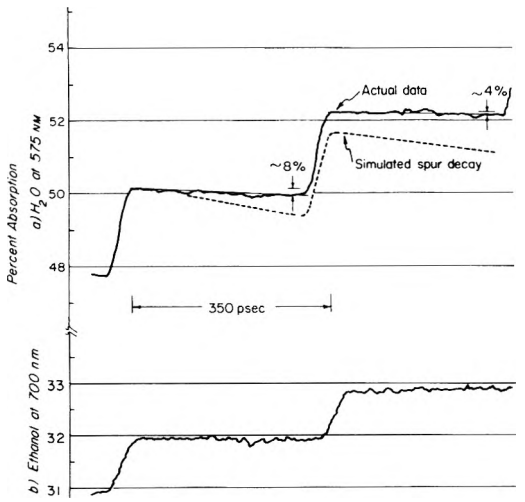

Figure 6. Absorption signals of e_{sol}^- obtained in pure solvents. (a) Absorption signal of e_{aq}^- at 575 nm in pure H_2O. There is very little decay over 350 psec. This decay is measured as 8% *of the step height* for the first step and 4% for the second. The dashed curve indicates the result expected from a simulated spur decay.[8] (b) Absorption signal of e_{sol}^- at 700 nm in pure ethanol. Again there is little decay over 350 psec.

tion level (H) that noise becomes a severe problem. The best signals which we have obtained to date are shown in Figure 6. The upper trace is the absorption at 575 nm of e_{sol}^- in water; the lower trace is the absorption at 700 nm of e_{sol}^- in ethanol. The amount of decay over 350 psec is about 8% *of the step height* for the first e_{aq}^- absorption step, and about 4% for the second step. The computer-calculated, simulated spur decay[8] in Figure 6a would predict much more decay than is observed. In fact, an analysis of 25 decay traces of e_{aq}^- in pure H_2O from 10 separate experiments showed that the average decay was 2% of the step height with an average deviation of ±4% about this value.

5. $G(e_{sol}^-)$ in Alcohols at 30 psec. In previous experiments[1] and subsequently we have measured the ratio $G\epsilon(e_{sol}^-)/G\epsilon(e_{aq}^-)$ for a range of alcohols, both from the initial peak heights of solutions containing 0.1 M perchloric acid, and also from the step heights in pure solution as shown in Figure 6. Both methods give similar results and we report here the averages from both methods. Our determination of the absolute value of $G(e_{aq}^-)$ at 30 psec permits $G(e_{sol}^-)$ values for alcohols to be calculated (see Table III). There is still some uncertainty, however, in the values of the extinction coefficients of the solvated electron in alcohols. Consequently, the absorbance ratios and extinction coefficients used in the calculations are also given in Table III.

TABLE III: $G(e_{sol}^-)$ at 30 psec

Solvent	Ratio of absorbances at 575 nm	ϵ_{575}, M^{-1} cm^{-1}	$G(e_{sol}^-)$
H_2O	1.0	1.04×10^4 [a]	4.0 ± 0.2
Methanol	0.60	1.55×10^4 [b]	1.6 ± 0.2
Ethanol	0.47	1.2×10^4 [b]	1.6 ± 0.2
1-Propanol	0.38	0.84×10^4 [b]	1.8 ± 0.2
2-Propanol	0.31	0.84×10^4 [b]	1.5 ± 0.2

[a] Reference 10. [b] M. C. Sauer, S. Arai and L. M. Dorfman, *J. Chem. Phys.*, **42**, 708 (1965).

Discussion

Based on the results of all these experiments we conclude that $G(e_{aq}^-)$ at 30 psec is 4.0 ± 0.2.[16-18] The uncertainty in this result is influenced by a number of factors. The absolute determination of $G(e_{aq}^-)$ involved Perspex dosimetry which can be related to the absorbance measured at the end of the pulse. This simple comparison (using $\epsilon_{633\,nm} = 1.44 \times 10^4$) gives the result that $G(e_{aq}^-)$ at 0.1 μsec is 2.64 (*cf.* 2.7[10]). This close agreement made it possible to omit e_{aq}^- dosimetry in experiments 2 and 3, Table II. However, the linac parameters used in these experiments (~40-MeV electron beam energy and 3.47 krads absorbed dose per 6-nsec pulse) yield an instantaneous dose rate of $\sim 6 \times 10^{11}$ rads/sec. Most Perspex calibration experiments have been done at energies and dose rates considerably below these values. Thus we assign an error of ±10% to the absolute determination of $G(e_{aq}^-)$ at 30 psec.

The comparative determination of $G(e_{aq}^-)$ assumes only that $\epsilon_{633\,nm}$ for e_{aq}^- remains constant from 30 psec to 0.1 μsec. This assumption seems valid, particularly in view of the evidence of Figure 6. Other possible sources of error have been carefully considered. Nonlinearities in our electronic signal-processing circuits would affect H much more than S. The excellent agreement we consistently obtain between H, h, and S indicates that error due to electronic nonlinearity is small (see Table II and Appendix I).

Inadequate resolution of macropulse shape could increase the ratio of S to the absorption signal observed at 0.1 μsec. The absorption signal H is insensitive, however, to pulse shape and the agreement of S and H (particularly for both 6- and 15-nsec pulses) indicates that our pulse shape resolution is sufficient. Dark current (*i.e.*, linac beam current outside the 6-nsec beam pulse) could also affect our measurements by increasing the absorbance observed at 0.1 μsec while leaving S and H virtually unchanged. Perspex dosimetry showed that this dark current was less than 1% of the main pulse intensity. We estimate, then, that the maximum error in the comparative experiment is ±10%. Although the possible error on any one determination is ±10%, three different measures of the G value are made in each experiment and three separate experiments have been done, all in close agreement. Thus, the G value for the solvated electron in water at 30 psec is assigned the value 4.0 ± 0.2.

Figure 7 shows the theoretical time dependence (solid curve) for the yield of e_{aq}^- during the time interval from 10^{-12} to 10^{-6} sec in the absence of added scavenger molecules.[8] The initial G value for e_{aq}^- is estimated to be 4.8.[8] By 10^{-7} sec this yield is reduced to about 2.7 representing those aqueous electrons which escape the spur diffuse into the bulk of the solution. The decay over the time interval

(16) The value of 4.0 ± 0.2 reported in this paper represents a considerable change from our original reported value of 3.3 ± 0.3.[17] The earlier value was in error for two basic reasons. (1) There were small deviations from linearity in the electronic systems used which were only discovered and corrected later: (a) the photomultiplier–dynode chain combination used for the original μsec e_{aq}^- absorbance determination was nonlinear; and (b) the SPR system photomultiplier saturated slightly for large signals. (2) The decay kinetics of e_{aq}^- over the first few nseconds were not determined and it had been assumed in the original calculations that there was no decay of e_{aq}^- over the 15-nsec pulse used at that time. These two errors caused us to interpret the agreement of S and H signals for $G(e_{aq}^-) = 3.3$ as confirmation of SPR system linearity. The inconsistency of this result was clearly demonstrated by the work of Jonah, Matheson, and Hart[13,18] which defined the decay kinetics of e_{aq}^- over the critical time region from 0.5 to 10 nsec.

(17) J. W. Hunt, M. J. Bronskill, and R. K. Wolff, *Proc. Int. Cong. Radiat. Res., 4th, 1972*, in press.

(18) C. D. Jonah, M. S. Matheson, and E. J. Hart, manuscript in preparation.

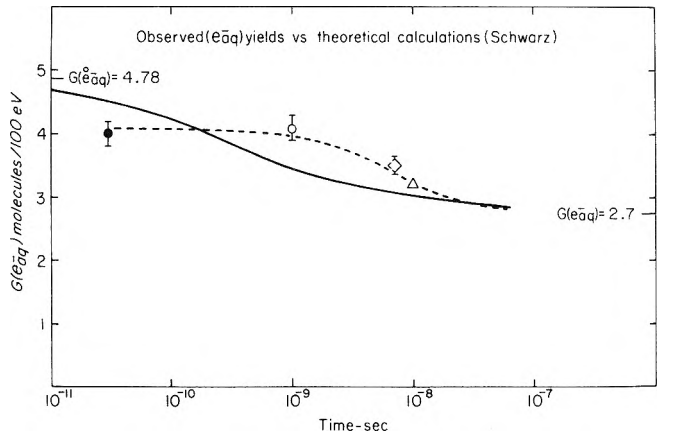

Figure 7. Yield of e_{aq}^- as a function of time. The solid line is based on the theoretical calculations of Schwarz.[8] The dashed line is the empirical fit[13] to the experimental observations: □, this work; ○, ref 18; ◇, ref 15; △, ref 19.

from 10^{-11} to 10^{-9} sec is due to the bimolecular reaction of e_{aq}^- with other species in the spur. The most important aspects of this theoretical curve are the initial yield of e_{aq}^- and the drastic decrease in this yield due to bimolecular reactions in the spur.[7,8] The dotted curve is drawn to agree with results from joint experiments conducted by this laboratory and Argonne National Laboratory.[13] The G value at 30 psec is 4.0 and then the e_{aq}^- yield decreases exponentially with a τ_{37} of 10^{-8} sec to a yield of 2.7. Buxton[15] has also observed this decay of e_{aq}^-. His measured yield after 7.5 nsec and that of Thomas and Bensasson[19] estimated to be at 10 nsec are shown in Figure 7 and these points are within experimental error of the dashed curve, calculated according to $G(e_{aq}^-)_t = 2.7 + 1.3\exp(-10^8 t)$.

These yield data are in excellent agreement with the kinetic 30–350 psec traces of e_{aq}^- in pure H_2O shown in Figure 6. There is effectively no change in yield between the 30-psec measurements in our laboratory and the <1- to 10-nsec Argonne observations.[13,18] This behavior is confirmed by the observation that almost no decay of e_{aq}^- is observed over the 30–350-psec interval although the amount of decay observed depends on macropulse shape and length. This point is critical in understanding the information presented in Figure 6. The observed decay of Figure 6 (roughly 6% of the step height) is *not* the decay of a single population of solvated electrons created by a single fine structure pulse. The decay we measure is an *average* decay for solvated electrons of different ages created by different fine-structure pulses; the average is, of course, over all fine structure pulses in the macropulse.[20] Thus the dashed line in Figure 6 is the theoretical spur decay (Figure 7, solid curve) averaged by computer over the fine structure pulse distribution used to obtain the absorption trace of Figure 6a.

It must be noted that this averaging aspect of the SPR system makes it impossible to rule out the possibility that we are observing a "slow" formation of e_{aq}^- over ~1 nsec superimposed on the theoretical spur decay.[7,8] For a variety of reasons we consider this possibility highly unlikely.

These results are obviously a serious contradiction to the parameters of the spur-diffusion model. This finding is not surprising, however, in view of recent evidence that there is a highly reactive, scavengeable precursor to e_{aq}^- [3,21,22] which is not considered in the spur-diffusion model. It appears that an accurate theoretical treatment of the radiation chemistry of aqueous solutions must start with the initial products of the ionizing event

$$H_2O \rightarrow H_2O^+ + e^-$$

Both H_2O^+ and e^- should be treated as scavengeable species, although present experimental results do not clearly define the nature of these species. Both the dry hole–dry electron treatments of Hamill[21,22] and the quantum mechanical tunnelling theories[23] seem consistent with the experimental facts. Other factors which must be considered at picosecond times include time dependent rate constants,[24] geminate electrostatic recombination,[25] and the charge-pair exciton of Weiss.[26]

Acknowledgments. The work described in this paper was assisted by the cooperation of C. D. Jonah, E. J. Hart, and M. S. Matheson in determining the yield and rate of decay of e_{aq}^- in early times. The help of T. L. Penner, L. Gilles, K. Y. Lam, H. B. Michaels, and P. C. Shragge in performing many lengthy experiments is also acknowledged. E. W. Horrigan and the staff of the Linac Laboratory of the University of Toronto provided excellent electron beam parameters and the SPR equipment was maintained by P. Nielsch. This work was supported by the Medical Research Council of Canada and the National Cancer Institute of Canada.

(19) J. K. Thomas and R. V. Bensasson, *J. Chem. Phys.*, **46**, 4147 (1967).
(20) Appendix I, a simplified discussion of our signal derivation using the macropulse shape, and a listing of the computer program actually used in these calculations will appear following these pages in the microfilm edition of this volume of the journal. Single copies may be obtained from the Business Operations Office, Books and Journals Division, American Chemical Society, 1155 Sixteenth St., N.W., Washington, D. C. 20036. Remit check or money order for $3.00 for photocopy or $2.00 for microfiche, referring to code number JPC-73-1350.
(21) W. H. Hamill, *J. Phys. Chem.*, **73**, 1341 (1969).
(22) T. Sawai and W. H. Hamill, *J. Chem. Phys.*, **52**, 3843 (1970).
(23) J. R. Miller, *J. Chem. Phys.*, **56**, 5173 (1972).
(24) H. A. Schwarz, *J. Chem. Phys.*, **55**, 3647 (1971).
(25) G. R. Freeman, *Advan. Chem. Ser.*, **No. 82**, 339 (1968).
(26) J. J. Weiss, *Nature (London)*, **215**, 150 (1967).

A Liquid Chromatographic Study of the Radiolysis of Aqueous Solutions of *p*-Bromophenol[1]

Kishan Bhatia and Robert H. Schuler*

Radiation Research Laboratories, Center for Special Studies and Department of Chemistry, Mellon Institute of Science, Carnegie-Mellon University, Pittsburgh, Pennsylvania 15213 *(Received November 27, 1972)*

Publication costs assisted by Carnegie-Mellon University

The potentialities of using liquid chromatographic methods to examine radiation chemical effects in aqueous systems has been explored using the radiolysis of *p*-bromophenol as a test system. It is shown that one can readily follow both the consumption of the starting material and the formation of products with sufficient accuracy that detailed measurements of the dependence of the reaction on various kinetic parameters are possible. Hydrated electrons are found to react quantitatively with *p*-bromophenol to produce *p*-hydroxyphenyl radicals. In the absence of a scavenger for these radicals they add to the parent molecule to produce 2-bromo-5,4′-dihydroxybiphenyl and 5-bromo-2,4′-dihydroxybiphenyl with the initial yields at millimolar solute concentrations being estimated as 1.3 and 1.0, respectively. A very pronounced dose dependence in the formation of these products is, however, observed as a result of very rapid tertiary reactions of the *p*-hydroxyphenyl radical which result in the production of terphenyls. Addition of a suitable source of hydrogen to the system results in the conversion of *p*-hydroxyphenyl radical to phenol. The yield of phenol at a *p*-bromophenol concentration of 5×10^{-4} *M* and high concentrations of isopropyl alcohol is 2.8. Measurements of the dependence of the phenol yield on the concentration of added alcohol indicate that abstraction of H from the alcohol is 2.4 times slower than the addition to *p*-bromophenol. By comparison with the known rate for the addition reaction a rate constant of 3×10^{7} M^{-1} sec^{-1} for the abstraction process is obtained. The experiments described in this paper were carried out on solutions containing solutes in the concentration range 10^{-4}–10^{-2} *M* and products were measured in the region of 10^{-6}–10^{-4} *M*. In appropriate systems measurements can be carried out on components present at concentrations as low as 10^{-8} *M*. The availability of rapid ultrasensitive analytical methods of the type used here obviously makes possible many types of studies which heretofore could be carried out only with difficulty or not at all.

The recent development of very sensitive high-speed liquid chromatographic methods[2] has opened many possibilities for studying product formation in the radiolysis of dilute aqueous solutions of organic compounds. In liquid chromatography component separation is, in many cases, comparable to that attained in gas chromatographic analysis and detectors are now available which, in instances where the material being examined has an appropriately high extinction coefficient, reduce the sensitivity levels to below the micromolar level so that product formation can be studied at exceedingly low dose levels. We have undertaken an investigation of product formation in the radiolysis of *p*-bromophenol solutions in order to examine some of the potentialities of the liquid chromatographic approach. An aromatic system was chosen because all aromatic products will have relatively high extinction coefficients at the 254-nm wavelength of a convenient commercially available optical detector. *p*-Bromophenol has previously been the subject of a number of steady-state investigations which show that e_{aq}^- reacts to form Br^- quantitatively.[3,4] Presumably *p*-hydroxyphenyl radical is

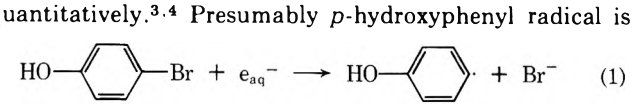

(1)

produced as a complementary intermediate but measurements of its yield have not, as yet, been made. Pulse radiolysis investigations have shown that this radical reacts extremely rapidly with the parent compound.[5] Classical elution and thin-layer chromatographic methods have been applied to characterize certain of the products from both the radiolysis and photolysis as substituted biphenyls[6,7] but no detailed quantitative study of product formation has been undertaken. The results of our study are presented here in some detail in order to demonstrate the excellent promise of the application of liquid chromatographic methods to kinetic investigations on aqueous systems. These studies, of course, provide further information on the radiolysis of *p*-bromophenol solutions. The reaction of e_{aq}^- with *p*-bromophenol is shown to be an excellent source of the *p*-hydroxyphenyl radical for studies of the reaction kinetics of this latter species.

Experimental Section

An high-speed liquid chromatographic apparatus assembled in our laboratory, which is suitable for analysis of dilute aqueous solutions, is described in detail elsewhere.[8] The principal components are a Model 709 Laboratory Data Control solvent delivery system (Milton Roy con-

(1) Supported in part by the U. S. Atomic Energy Commission.
(2) "Modern Practice of Liquid Chromatography," J. J. Kirkland, Ed., Wiley, New York, N. Y., 1971.
(3) F. A. Peter and P. Neta, *J. Phys. Chem.*, **76**, 630 (1972).
(4) M. Anbar, Z. B. Alfassi, and H. Bregman-Reisler, *J. Amer. Chem. Soc.*, **89**, 1263 (1967).
(5) B. Cercek and M. Kongshaug, *J. Phys. Chem.*, **74**, 4319 (1970).
(6) (a) M. Namiki, T. Komiya, S. Kawakishi, and H. Aoki, *Chem. Commun.*, 311 (1970); (b) T. Komiya, S. Kawakishi, H. Aoki, and M. Namiki, *Agr. Biol. Chem.*, **34**, 349 (1970); (c) *ibid.*, **35**, 1558 (1971).
(7) H. I. Joschek and S. I. Miller, *J. Amer. Chem. Soc.*, **88**, 3269 (1966).

trolled volume minipump equipped with a pulse dampener), dual chromatographic columns for analysis and reference streams, and a Model 1205 Laboratory Data Control uv monitor. This monitor has a volume of 8 μl and a path length of 10 mm. Samples were introduced onto the column through a Teflon sealed valve using an injection loop of 0.19 ml.

The output of the uv monitor corresponds to a signal of 10 mV for an optical absorbance of 0.02. Using an RC filter with a time constant of 10 sec in the output of the uv monitor we have found it possible to spread an absorbance of 0.002 full scale (*i.e.*, 1 mV output) on a 10-in. recorder with, under optimum conditions, a short-term noise level of ~0.1 in. (0.01 mV). This noise corresponds to an absorbance of 2×10^{-5} and the long-term drift on a well-conditioned column is comparable. For a compound with an extinction coefficient of 10^4 M^{-1} cm^{-1} the potentially available sensitivity is, therefore, $\sim 2 \times 10^{-9}$ M provided the peak width can be maintained comparable to the injection volume. For a product with a radiation chemical yield (G) of 3 molecules/100 eV, a product concentration at this level corresponds to a dose of ~1 rad (6.24×10^{13} eV/g) so it is seen that for products which have appropriately high extinction coefficients the system can, indeed, be made very sensitive. In the present work the sensitivities are appreciably less (phenol and *p*-bromophenol, for example, have extinction coefficients of about 520 and 350 M^{-1} cm^{-1} at 254 nm although the extinction coefficients at the maxima of 270 and 280 nm are larger by a factor of ~3). We have not attempted to push the present studies to any ultimate level.

The chromatographic columns used in this work consisted of a 0.5–2 m length of ⅛-in. No. 316 stainless steel tubing (2.1 mm i.d.). Most studies were carried out with columns packed with Corasil/C_{18}, a packing material supplied by Waters Associates which consists of 37–50 μ superficially porous silicous particles with octadecyl groups permanently bonded to the surface. These columns were found to be particularly useful for analyzing the substituted biphenyls and terphenyls. In some of the later studies, where consumption of *p*-bromophenol was to be measured, Du Pont Strong Anion Exchange Chromatographic Packing was used to separate the various radiation-produced products from the *p*-bromophenol. This material permits regulation of retention time by adjustment of pH and ionic strength. Over the short term, column stability is sufficiently good that peak height is a good measure of concentration for a given component provided one does not exceed column capacity and artificially broaden the peak. In fact, over moderate changes, peak height is in many ways a better measure of concentration in that it tends to be invariant with flow rate whereas peak area is, of course, inversely dependent on the flow. Most of the results obtained here were from comparison of peak heights with reference samples run under identical chromatographic conditions, usually on the same day. Intercomparison under different chromatographic conditions can, of course, be done only in terms of peak area. All chromatographic data were collected under isothermal conditions using distilled water, aqueous methanol, or an appropriately buffered aqueous solution as eluent.

Certain of the peaks were collected as they came off the column and examined with a Cary 14 spectrophotometer. A semimicro cell with a 10-mm path length was used and permitted the examination of 0.6 ml of solution.

Reference compounds and other chemicals were used as received from various suppliers. The compounds used were *p*-bromophenol and hydroquinone (Eastman Organic Chemical), resorcinol, catechol and methanol (Baker Analyzed Reagent), 4-bromoresorcinol (Aldrich), isopropyl alcohol (Fisher Certified Grade), ethylene (Philips Research Grade), nitrogen (Union Carbide High Purity Grade), and nitrous oxide (Matheson). Buffers were solutions of KH_2PO_4 (Baker Analyzed Reagent) adjusted to a pH of 7.0 with KOH (Baker Analyzed Reagent). Water was triply distilled.

Irradiations were carried out in ^{60}Co γ-ray sources at absorbed dose rates of 6.16×10^{16} or 8.60×10^{17} eV g^{-1} min^{-1}. Most of these studies involved absorbed doses in the range of 6×10^{16}–1×10^{19} eV g^{-1}. Solutions of *p*-bromophenol were purged of oxygen by bubbling with either nitrogen, ethylene, or nitrous oxide at atmospheric pressure prior to irradiation. Irradiated samples were introduced into the liquid chromatograph approximately 1 min after completion of the irradiation.

Results and Discussion

Resolution of Products. In the present study separation of phenol, the dihydroxybenzenes, the parent *p*-bromophenol, and phenolic biphenyls and terphenyls is of principal interest. All of these compounds are well separated on the nonpolar column described in the Experimental Section. The relative retention times of benzene, phenol, and a number of their derivatives are tabulated in ref 8. The monocyclic compounds had well-defined Gaussian shape peaks with peak widths from 1 to 4 times the sample size of 0.19 ml. Under the chromatographic conditions used to examine the monocyclic phenols the higher molecular weight products produced from *p*-bromophenol eluted at very long times and had very wide band widths. Higher molecular weight products appeared as well-defined peaks and were resolved from *p*-bromophenol and other monocyclic aromatic compounds by eluting at ~1 ml/min with 25–40% methanol at a somewhat elevated temperature. Under these conditions the lower molecular weight products were only partly resolved. In general it was not found practical to attempt to analyze for all products in a single chromatogram. Rather, attention was focused on a group of products which eluted in a particular region and conditions adjusted to optimize their resolution.

Consumption of p-Bromophenol. In a given series of experiments peak heights are, in general, reproducible to ~1% so that it is readily possible to determine the yield for the consumption of a particular component with reasonable accuracy in the region of ~20% conversion. Chromatographic separation of the reactant from the products, of course, avoids interference from the latter's absorption which is a problem in the conventional spectrophotometric approach. We can cite, for example, the results of an experiment with 1.4×10^{-4} M *p*-bromophenol (N_2O saturated) irradiated with a dose of 4×10^{18} eV/g. The chromatographic experiment showed that the *p*-bromophenol concentration was reduced to 39% of its initial value. Other products which eluted in the same region had an integrated absorption about equal to that of the remaining *p*-bromophenol. The uv absorption spectrum of the irradiated sample showed, however, a considerable absorption at all wavelengths below 350 nm (*p*-bromophenol which

(8) K. Bhatia, *Anal. Chem.*, in press.

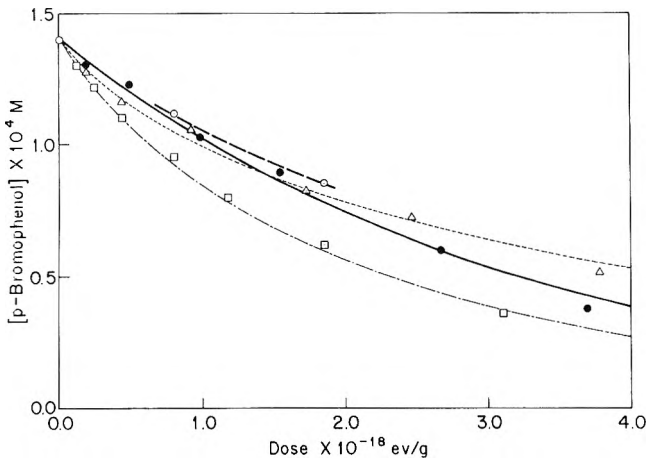

Figure 1. Consumption of *p*-bromophenol in phosphate buffer at pH 7: □, nitrogen purged; △, saturated with N_2O; ●, saturated with C_2H_4; and ○ containing 10^{-2} *M* isopropyl alcohol and purged with N_2. Curves are calculated by numerical integration of eq I as described in the text.

has a strong maximum at 280 nm does not absorb appreciably above 300 nm) and an increase over the original solution by a factor of 4 at the wavelength of the detector. One obviously cannot obtain significant quantitative analytical data solely from the spectrophotometric results.

Typical reactant consumption curves are given in Figure 1 for 1.4×10^{-4} *M* solutions of *p*-bromophenol buffered to pH 7 with 10^{-3} *M* phosphate and saturated with N_2, N_2O, or C_2H_4. The slopes determined in the region of ~25% consumption correspond to radiation chemical yields for loss of *p*-bromophenol of 2.2, 3.0, and 3.7 molecules/100 eV respectively for the C_2H_4, N_2O, and N_2 saturated solutions. There is, however, considerable curvature to the plots and it is obvious that these values represent only very rough lower limits to initial yields. Examination of the highly irradiated solutions under a variety of column conditions shows that there is no interference with the *p*-bromophenol determinations from impurities and/or other products. We are, of course, primarily interested in determining the initial yields for purposes of comparing them with the yields of radicals produced from the water. The problem of determining these yields from the observed data becomes one of properly taking into account the effect of buildup of product as the reaction progresses.

A simple solution to the above problem is obtained for the case where the rate constant for reaction of the intermediate with the product (k_p) is equal to that for reaction with the initial reactant. In this case it is easily shown that one expects an exponential decrease with dose in the concentration of the reactant.[9] The initial slope is given by $[S]_0 \ln 2/D_{1/2}$ where $D_{1/2}$ is the dose for 50% reaction as determined from a semilogarithmic plot of the data and $[S]_0$ is the original concentration of the solute of interest. In the actual experiment a qualitative indication as to whether the product is more or less reactive than the reactant is obtained from the sign of the curvature of such logarithmic plots. A logarithmic plot of the data on C_2H_4 saturated solutions (the data of Figure 1) shows only a slight negative curvature at the highest doses and gives a $D_{1/2}$ of 2.3×10^{18} eV/g. This value corresponds to an initial radiation chemical yield of 2.6. Logarithmic plots of the other data show marked positive curvature and the initial yields can only be estimated to be greater than 4.1 and 3.3 for the N_2 and N_2O saturated solutions.

If it is assumed that the concentration of reactive product is equal to the loss in concentration of reactant and that the relative rate constants for the competing reactions are describable by a single ratio k_p/k_1 the differential equation describing the change in *p*-bromophenol concentration ([BrPhOH]) with dose is

$$-\frac{d[BrPhOH]}{dD} = \frac{10G_i}{N} \frac{1}{1 + \dfrac{k_p([BrPhOH]_0 - [BrPhOH])}{k_1[BrPhOH]}} \quad (I)$$

In eq I $10G_i/N$ is the change of concentration per unit dose at zero dose, D is the dose in eV/g, and G_i is the initial radiation chemical yield in molecules per 100 eV absorbed energy, and N Avogadro's number (the factor 10 is introduced to convert eV/g to units of 100 eV/l.). Integration of this equation does not give an expression of the form $[BrPhOH] = f(D)$[10] and numerical integration methods are indicated. We have conveniently carried out such integrations on a Hewlett-Packard calculator-plotter using a Runge-Kutta routine. Equation I is obviously an over simplification in that it does not take into account tertiary and higher order reactions or the buildup of product which is not produced from the reactant being investigated. It is, however, a reasonable approximation and is useful in attempting to obtain information on the initial yields. In an approach such as used here two parameters are important: the initial slope and the ratio of the rate constants. One finds that the corrections to the yields at low conversions are not unduly sensitive to the rate constant ratio so that one can proceed by successive approximations after first adjusting this ratio to fit the curvature at high conversions. Curves obtained in this way are given in Figure 1. The initial slopes correspond to radiation chemical yields of 2.65, 4.2, and 5.3 for the C_2H_4, N_2O, and N_2 saturated solutions. The first of these values is quite well known since the semilogarithmic plots show k_p/k_1 to be slightly less than 1 (0.95 was used in calculating the curve). The other two values are somewhat problematical since, in order to fit the data, they require values for k_p/k_1 which seem excessively high (respectively, 4.0 and 2.0).

The simplest case to discuss is that for solutions saturated with C_2H_4 [0.0043 *M*]. The ethylene serves both to remove the H atoms and OH radicals and also prevent secondary reactions of the *p*-hydroxyphenyl radical so that the *p*-bromophenol should be consumed principally by the reactions of the hydrated electrons (the rate constant for this reaction is 6×10^9 M^{-1} sec^{-1}).[3,4] At a *p*-bromophenol concentration of 1.4×10^{-4} *M* the yield for attack on the solute by hydrated electrons is expected to be 2.62 by comparison with the yields observed in the case of CH_3Cl solutions[11] and with other measurements at low solute concentrations (2.63 ± 0.07; see ref 11). The initial yield observed here agrees extremely well. Since bromide ion is

(9) E. N. Weber and R. H. Schuler, *J. Amer. Chem. Soc.*, **74**, 4415 (1972).

(10) Equation I can be integrated to give an integral of the form $D = f(BrPhOH)$. Methods similar to those used by D. Perner and R. H. Schuler (*J. Phys. Chem.*, **70**, 2224 (1966)) in treating the radiolysis of HI solutions can be used to construct a plot of $[BrPhOH] = f(D)$. However, with currently available computational tools it is much more convenient to carry out integrations of kinetic expressions such as I by numerical methods such as those used by I. Mani and R. J. Hanrahan (*J. Phys. Chem.*, **70**, 2233 (1966)) in treating the HI problem.

(11) T. I. Balkas, J. H. Fendler, and R. H. Schuler, *J. Phys. Chem.*, **74**, 4497 (1970).

produced with an identical yield[3] it is clear that hydrated electrons react with *p*-bromophenol essentially entirely according to reaction 1. One set of experiments was performed with unbuffered solutions 10^{-3} *M* in *p*-bromophenol and saturated with ethylene. The results were comparable to those of Figure 1 and the initial yield found to be 2.8. A slightly higher yield (~3.0) is expected since ~20% of the H atoms and OH radicals will escape scavenging by the ethylene but the difference is within the errors involved in interpreting the data.

Two experiments were done on isopropyl alcohol containing solutions and the results are also given in Figure 1. In this case the principal products which can interfere with the initial reaction are phenol (see below), acetone, and hydrogen peroxide. The rate constant for the reaction of e_{aq}^- with phenol is low and the principal problem is the buildup of acetone and hydrogen peroxide both of which have rate constants for reaction with e_{aq}^- a factor ~2 greater than that for *p*-bromophenol.[12] Taking into account the relative yields of these products the effective rate constant ratio to be used in eq 1 is 1.74. The dashed curve in Figure 1 was calculated based on this ratio and an initial yield of 2.65 and constitutes an *a priori* prediction of the dependence of *p*-bromophenol concentration on dose for this case. The agreement is seen to be excellent. These results show that in dilute solution *p*-bromophenol does not react to any significant extent with isopropyl alcohol radicals either by addition or by an electron transfer process.

The yield of 4.2 for consumption of *p*-bromophenol from N_2O saturated solutions is considerably less than the yield expected if all the H atoms ($G(H) = 0.6$) and OH radicals ($G(OH) = 6.0$) react irreversibly with the *p*-bromophenol. The rate constant for OH attack on *p*-bromophenol is very high ($7 \times 10^9\ M^{-1}\ sec^{-1}$)[12] so that one can rule out the competitive reaction of OH with radiation produced product as the principal source of the curvature exhibited in Figure 1. Since OH adds to the aromatic ring to form hydroxycyclohexadienyl type radicals (at least initially) the low initial yields observed would seem to require secondary processes that somehow reverse the loss of *p*-bromophenol which results from the addition process.

There are, of course, four different types of addition sites in this molecule. Addition at the bromine position undoubtedly results in loss of Br^- *via* a dehydrohalogenation process.

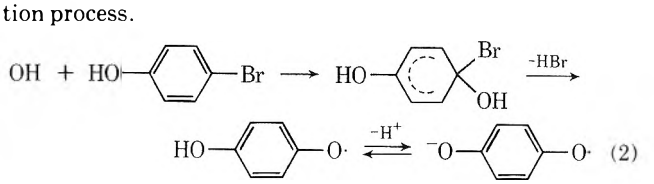

(2)

In situ esr experiments,[13] in fact, show that benzosemiquinone radical anion is produced from OH attack in this system. The experiments of Peter and Neta,[3] where a Br^- yield of 3.5 was observed in the absence of OH scavenger, indicate that about 20% of the OH radicals result in Br^- formation and this would seem to be a reasonable contribution for reaction 2. Such reaction must, of course, result in the irreversible destruction of *p*-bromophenol. Attack of OH at the other positions can lead to the formation of the *p*-bromophenoxyl radical *via* loss of water from the addition product. A first-order decay of the dihydroxycyclohexadienyl intermediate with a period of ~100 μsec has been observed in pulse radiolysis experiments on *p*-bromophenol and has been identified with loss of water.[14] Such a process follows quite reasonably if addition occurs at the OH position. Addition of OH at the other positions

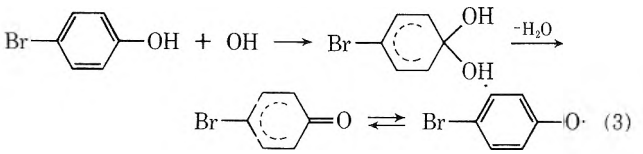

(3)

can, however, also lead to the same radical *via* ionization of the original phenolic group followed by charge transfer to the added OH group and subsequent loss of OH^-. It seems likely that the *p*-bromophenoxyl radical produced from these reactions is readily reduced to *p*-bromophenol by reaction with other radiation produced product. If so, the loss of *p*-bromophenol resulting from OH attack obviously need not be quantitative. The high curvature of the data for N_2O solutions in Figure 1 can be readily explained by a rapidly increasing importance of these reduction reactions as the irradiation progresses. A complete quantitative treatment of this system requires detailed and as yet unavailable information on the relative importance of the different reactions. Except for the small contribution of reaction 2, the reactions of OH with the aromatic ring do not directly involve the presence of Br on the ring. The complications involving the reactions of OH in phenolic systems can be better studied by examining phenol itself and will not be discussed here further in any detail.

The N_2 purged system shows complications similar to those in the N_2O system. Since, as we will show below, the *p*-hydroxyphenyl radical produced in reaction 1 reacts rapidly with a second molecule of *p*-bromophenol we expect the initial yield for reactant consumption to be $2G(e_{aq}^-)$ plus the contributions from the reaction of H and OH. The latter can be estimated as approximately one-half the yield from the N_2O saturated system or 2.1. A total initial yield of ~8 is therefore expected whereas the experimental value is considerably lower (only 5.3). In this case product buildup rapidly interferes with the secondary reaction of the *p*-hydroxyphenyl radical with *p*-bromophenol and the initial slope of data such as those given in Figure 1 can easily be severely underestimated. It is seen that for both the N_2 and N_2O saturated cases the secondary chemical reactions are sufficiently complicated that when the loss of the reactant is being examined it is difficult to draw detailed quantitative conclusions at the conversion levels required to make significant observations.

Production of p-Hydroxyphenyl Radical. From the above it would appear that reaction 1 should be an excellent source of the *p*-hydroxyphenyl radical. Reaction of this radical with any source of hydrogen present in the system is expected to produce phenol. In the irradiation of

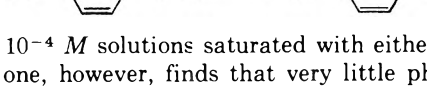

(4)

4.7×10^{-4} *M* solutions saturated with either N_2, N_2O, or C_2H_4 one, however, finds that very little phenol (PhOH) is produced at dose levels sufficient to consume only a small fraction (<5%) of the *p*-bromophenol ($G(PhOH) < 0.05$). Neither the hydrated electron nor OH radical ap-

(12) M. Anbar and P. Neta, *Int. J. Appl. Rad. Isotopes*, **18**, 493 (1967).
(13) Experiments of the type described by K. Eiben and R. W. Fessenden, *J. Phys. Chem.*, **75**, 1186 (1971).
(14) E. J. Land and M. Ebert, *Trans. Faraday Soc.*, **63**, 1181 (1967).

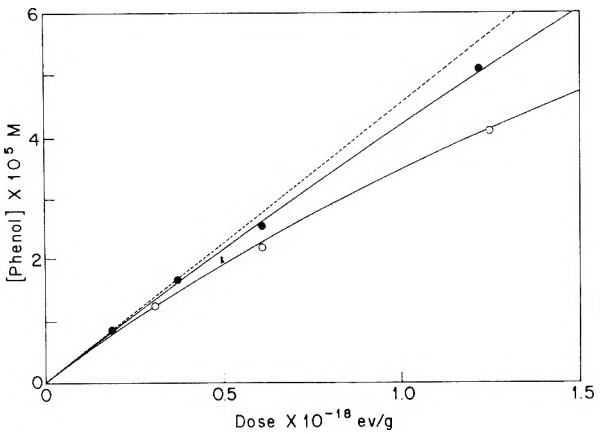

Figure 2. Production of phenol from 1.4 (O) and 4.7 (●) × 10^{-4} *M* pH 7 solutions of *p*-bromophenol containing a 300-fold higher concentration of isopropyl alcohol. Curves are calculated by integration of the right-hand side of eq I using kinetic parameters identical with those used to compute the curves of Figure 1. The dashed line corresponds to an initial yield of 2.75 for phenol production.

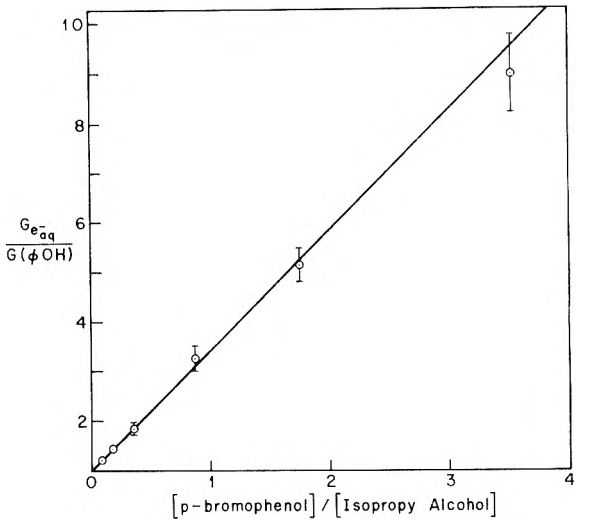

Figure 3. Competitive plot for the production of phenol from solutions containing added isopropyl alcohol (see eq II). The vertical bars represent error limits of ±0.3 × 10^{-6} *M* in the measurement of the phenol concentration. A ratio of 2.4 for the rate constants for addition of *p*-hydroxyphenyl to *p*-bromophenol and abstraction from the alcohol was calculated from the slope of the linear relationship.

pears to be a direct source of phenol. In the case of N_2 purged systems some phenol is produced at higher doses but is attributable to reaction of the *p*-hydroxyphenyl radical with radiation produced product. Irradiation of isopropyl alcohol containing solutions shows a large yield of phenol which presumably results from reaction 4. Competitive studies described below show that an alcohol concentration of ~300 times that of *p*-bromophenol is sufficient to scavenge ~99% of the initial radicals. Yield-dose plots for phenol production from isopropyl alcohol containing solutions are given in Figure 2. The data obtained at 1.4 × 10^{-4} *M* *p*-bromophenol (and isopropyl alcohol 0.04 *M*) exhibit a slight dependence of yield on dose which is related to the curvature of the plot in Figure 1. Taking d[PhOH]/d*D* = −d[BrPhOH]/d*D* one can carry out a numerical integration of the right-hand side of eq I to obtain the dose dependence of the phenol concentration. The lower curve of Figure 2 is calculated with parameters identical with those used in Figure 1 and the agreement is seen to be excellent, *i.e.*, in this system the *p*-bromophenol consumed appears entirely as phenol. At a *p*-bromophenol concentration of 4.7 × 10^{-4} *M* (and the isopropyl alcohol concentration increased proportionately to 0.13 *M*) the buildup of product interferes less at a given dose and an almost linear yield-dose plot is observed. One can estimate by trial integrations that for this solution irradiated to a dose of 1.2 × 10^{18} eV/g the observed yield should be 9.5% low as the result of the interfering secondary reactions. Correcting the yield observed by this factor one obtains an initial slope which corresponds to a phenol production yield of 2.75. The correction for the secondary reactions is small and believed to be known to within the overall experimental error of the measurement which is estimated to be ~2%. The upper solid curve is calculated from an integration of eq I on the basis of this initial yield. If we apply a 1% correction for inefficiency of scavenging by isopropyl alcohol the *p*-hydroxyphenyl radical yield resulting from electron attack on 5 × 10^{-4} *M* *p*-bromophenol can be given as 2.78 ± 0.05. This value is slightly higher than that of 2.68 expected at this concentration from the generalizations from the methyl chloride study.[11]

The variation in yield observed over the factor of 3 change in *p*-bromophenol concentration is expected to be only 0.06 units.[11] The experimentally observed increase (0.10) is certainly small although the uncertainties in the determination of the initial yields, particularly at the lower concentration, introduce errors in the difference of the magnitude of the expected effect. Similar experiments at significantly higher *p*-bromophenol concentrations are precluded by the inordinately high concentrations of alcohol required to completely scavenge the *p*-hydroxyphenyl radicals.

Competitive Scavenging of the p-Hydroxyphenyl Radical. In the absence of a hydrogen source the *p*-hydroxyphenyl radical is rapidly removed from the system by addition to *p*-bromophenol and ultimately produces products other than phenol. The competition between reac-

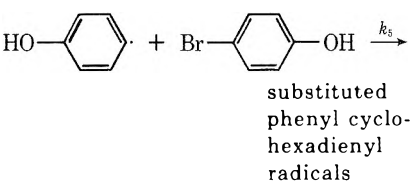

(5)

tions 4 and 5 can be readily carried out by determining the dependence of the yield for phenol production on the relative concentration of the hydrogen donor. This competition is described by

$$\frac{G(e_{aq}^-)}{G(\mathrm{PhOH})} = 1 + \frac{k_5}{k_4}\frac{[\mathrm{BrPhOH}]}{[\mathrm{RH}]} \qquad \text{(II)}$$

where the yield of hydrated electrons is identified with the limiting yield at infinite scavenger concentration, *i.e.*, 2.8. Data for competition between isopropyl alcohol and *p*-bromophenol (the latter at 4.7 × 10^{-4} *M*) are given in Figure 3. The rate constant ratio k_5/k_4 determined from the slope of the linear dependence given in this figure is 2.4 ± 0.2. Cercek and Kongshaug[5] have measured the absolute rate constant for the addition reaction to be 7 × 10^7 M^{-1} sec^{-1}. From this value the absolute rate constant for the abstraction of hydrogen from isopropyl alcohol by *p*-hydroxyphenyl radical is calculated to be 3 × 10^7 M^{-1}

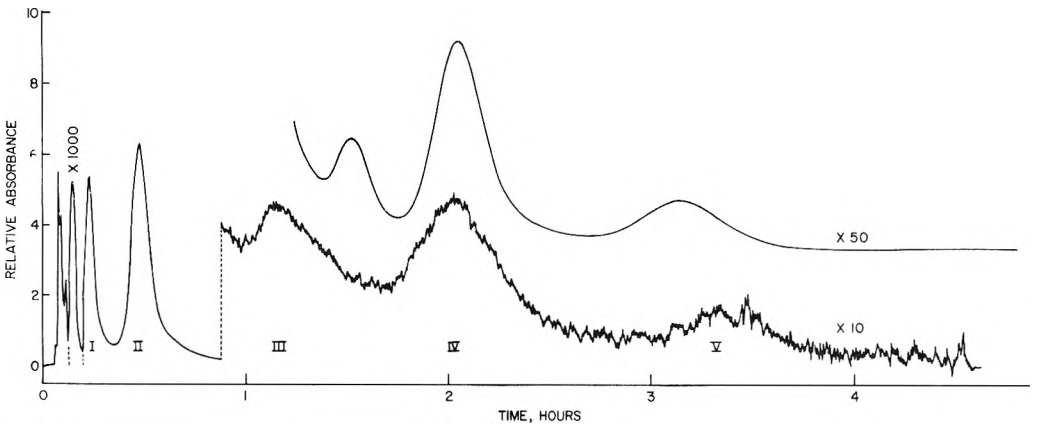

Figure 4. Chromatographic analysis of the substituted biphenyl and terphenyl products: lower trace from a solution of 10^{-2} *M* *p*-bromophenol (nitrogen purged) irradiated to a dose of 5×10^{19} eV/g; upper trace from a solution 5×10^{-2} *M* irradiated to a dose of 10^{20} eV/g. The eluents used were 25 and 40% methanol in water. Chromatograms were recorded at an attenuation of 200 unless indicated otherwise. The *p*-bromophenol peak was recorded at X1000 and the peaks to the left of this are phenol and other low molecular weight products. Peaks identified as I and II are identifiable with the substituted biphenyls similarly labeled in the text. Peaks III, IV, and V are assignable as substituted terphenyls with the structure of IV being given in the text. The noise level in the lower recording is about ten times poorer than that obtained under optimum conditions.

sec^{-1}. These high reaction rates make it impractical to directly examine for *p*-hydroxyphenyl radical by steady-state esr methods since the observation time ($\sim 10^{-4}$ sec) in such experiments would require experiments to be carried out at concentrations below 10^{-4} *M*.

Other Low Molecular Weight Products. Two components in addition to phenol are observed at elution times shorter than that of *p*-bromophenol. The first, which is not significantly separated from the solvent peak, is attributable to quinone and/or hydroquinone.[8] Under the chromatographic conditions used, hydroquinone is partially oxidized to quinone and cannot be quantitatively determined. The upper limit for the formation of hydroquinone is estimated as 0.4 and that for quinone as 0.1. Peter and Neta's results on bromide production indicate that the yield for debromination of *p*-bromophenol by OH radicals is ~0.5. The second component has an elution volume ~90% of that of *p*-bromophenol and was not resolved from the starting material sufficiently well and hence quantitative measurements were not possible. The peak is very probably a mixture of 4-bromoresorcinol and 4-bromocatechol. The retention time was, in fact, shown to be comparable to that of 4-bromoresorcinol. Other products are either produced in low yield or have very low extinction coefficients.

Identification of the Addition Products. The substituted phenylcyclohexadienyl radicals produced in reaction 5 will, in part, disproportionate or be oxidized by other means to form the corresponding substituted biphenyls. Only addition at the 2 or 3 position, however, can result simply in the formation of a derivative of biphenyl so that only two such derivatives are expected, *i.e.*

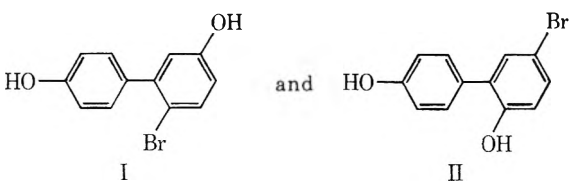

I II

Both I and II have been isolated in previous experiments and identified by comparison of the nmr spectra of their methyl ethers with authentic samples.[6a,b] These compounds have very large extinction coefficients (>5 × 10^3

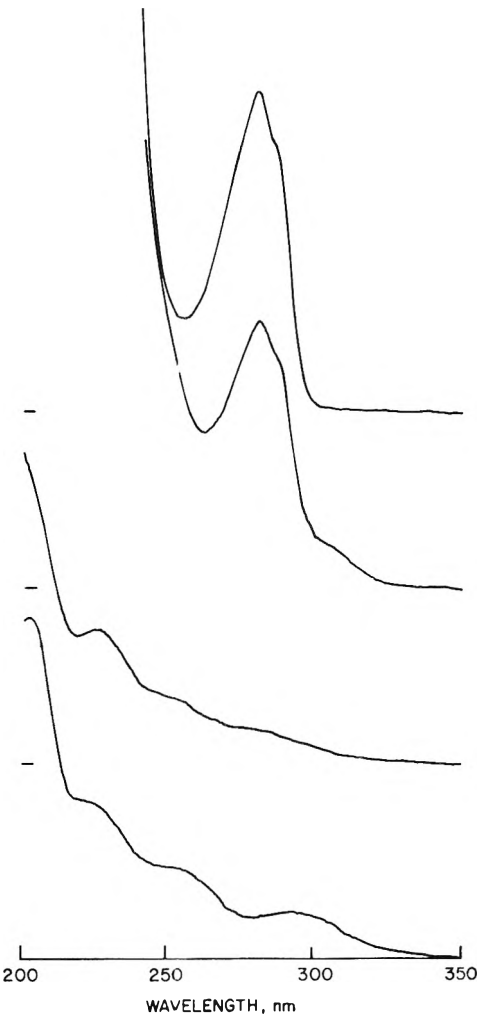

Figure 5. Absorption spectra of (from top to bottom) *p*-bromophenol, the *p*-bromophenol fraction recovered from the irradiated sample, and central cuts from Peaks I and II of Figure 4. The spectra are displaced upward by an absorbance of 0.4 indicated by the tick marks on the left. The *p*-bromophenol from the irradiated sample was taken as a broad cut and shows the presence of a component which absorbs below 320 nm. Peaks I and II are seen to be free of any significant contribution from *p*-bromophenol.

TABLE I: Spectral Data on Chromatographic Peaks I, II, and IV

λ_{max}, nm		Extinction coefficients, M^{-1} cm^{-1}	
Present work	ref 6[a]	Present work	ref 6[a]
Peak I. 2-Bromo-5,4′-dihydroxybiphenyl			
230	230	12,200	11,400
253	252	(5,800)[b]	5,800
284	284	2,200	2,300
Peak II. 5-Bromo-2,4′-dihydroxybiphenyl			
203		54,000	
223	224	25,500	22,400
254	259	(14,800)[b]	14,800
295	295	7,600	7,000
Peak IV. 5-Bromo-2,4′,4″-trihydroxy-*m*-terphenyl[c]			
232	223	27,000	29,500
253	256	(28,000)[b]	28,000
298	295	11,600	12,800

[a] Values reported by Namiki, *et al.*, (ref 6) for authentic methyl ether derivatives of I, 2-bromo-5,4′-dihydroxbiphenyl; II, 5-bromo-2,4′-dihydroxybiphenyl; and IV, 5-bromo-2,4′,4″-trihydroxy-*m*-terphenyl. It has been shown in ref 6b that the parent compound and its methyl ether have essentially the same absorption spectrum. [b] Assumed, other extinction coefficients normalized to these values. [c] The three other isomers of this terphenyl reported in ref 6 have extinction coefficients of 34,000, 13,200, and 11,200 M^{-1} cm^{-1} at 254 nm.

M^{-1} cm^{-1}) at 254 nm and it is expected that they should be readily observable in an appropriate chromatographic experiment. As is illustrated in Figure 4 we find for a 10^{-2} M solution of *p*-bromophenol irradiated to a dose of 5×10^{19} eV/g two large peaks (labeled I and II) with retention volumes ~1.6 and 3.2 times that of the *p*-bromophenol. Samples of 0.6 ml taken at the center of each of these peaks were examined spectrophotometrically. Comparison of the absorption spectra given in Figure 5 with the data reported by Komiya, *et al.*,[6b] (see Table I) allows identification of peaks I and II as 2-bromo-5,4′-dihydroxybiphenyl and 5-bromo-2,4′-dihydroxybiphenyl, respectively. Saturation of the solution with N_2O reduces the intensity of peaks I and II by an amount equal to the fractional scavenging of e_{aq}^- by the N_2O. A comparison at 10^{-3} M *p*-bromophenol of N_2 and N_2O saturated solution ([N_2O] = 0.02 M) showed that >95% of peak II was essentially eliminated by the competitive reaction of e_{aq}^- with the N_2O. These products do not appear to be (nor are they expected to be) produced by the reactions of OH. No other products from OH reaction with retention volumes greater than that of *p*-bromophenol were detected in these experiments.

Three additional peaks labeled III, IV, and V also appear in the chromatogram at longer retention times. At the dose levels employed in the experiments illustrated in Figure 4 tertiary reactions involving the substituted biphenyls are important (see below) and it seems likely that these peaks all represent substituted terphenyls produced in such tertiary reactions. Eight derivatives of terphenyl are possible products of the reaction of *p*-hydroxyphenyl radical with I and II. The absorption spectra of the methyl ethers of four have been reported by Namiki, *et al.*[6a,c] Using the 0–0.1 A scale expansion slide wire of the Cary 14 spectrophotometer we were able to obtain the spectrum of peak IV in Figure 4 from the 0.05 M sample irradiated to a dose of 10^{20} eV/g. The data are reported in Table I. As is evident from Table I, peak IV is assignable to 5-bromo-2,4′,4″-trihydroxy-*m*-terphenyl (IV). Product IV would be produced by addition at the 3′ position of II. We have not attempted to identify the other peaks. It is pointed out that the initial addition reaction (reaction II) produces a cyclohexadienyl radical which is not capable of further direct reaction with *p*-bromophenol. As a result the terphenyl products must be produced by tertiary reactions rather than by a chain of addition events in which the product radical simply adds to another *p*-bromophenol. These terphenyls are, therefore, a trivial result of the buildup of product and have nothing to do with the initial reactions in the *p*-bromophenol system.

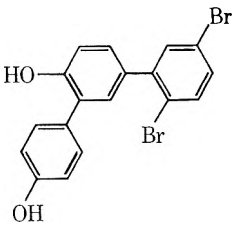

IV

Dose Dependence for the Formation of Substituted Biphenyls. The buildup of 5-bromo-2,4′-dihydroxybiphenyl (peak II) with dose is illustrated in Figure 6 for three concentrations of *p*-bromophenol. At the highest concentration the production of this biphenyl is essentially linear with dose and the slope should represent the initial yield. Although we did not have a reference sample available the sensitivity of the detector could be estimated from the extinction coefficients given by Namiki, *et al.*[6a] In taking the chromatogram of Figure 4 the entire peak (9.14 ml) was collected and found from the spectrophotometric measurement to contain 1.2×10^{-7} M 5-bromo-2,4′-dihydroxybiphenyl. The concentration in chromatographic sample (0.189 ml) was 48.5 times greater. This measurement allowed the chromatographic sensitivity to be determined as 2.7×10^{-7} M/unit peak height (unit peak height = absorbance of 0.0002). The initial slope for the formation of this product was then determined in the region of 10^{18} eV/g for the solution 0.05 M in *p*-bromophenol. The slope corresponds to G(5-bromo-2,4′-dihydroxybiphenyl) = 1.6. Such a yield represents 47% of the hydrated electrons which should be scavenged by the *p*-bromophenol at this concentration ($G(e_{aq}^-)$ = 3.4 at k[S] = 3×10^8 sec^{-1}).[11] The accuracy here is primarily limited by the available information on the extinction coefficient which is estimated to be good only to ~20%.

The yield of 2-bromo-5,4′-dihydroxybiphenyl can be estimated from the above by comparing the relative areas of peaks I and II. The ratio of the heights of peaks I and II does not depend on dose in any obvious way so that it is believed proper to make a comparison at the relatively high dose of Figure 4. Correcting the relative peak areas of 0.35:1 for the relative extinction coefficients at 254 mμ of 0.39:1 (Table I) one finds that the yield of I is 0.79 that of II. From this ratio G(2-bromo-5,4′-dihydroxybiphenyl) is 1.3. In the initial stages compounds I and II account for essentially all (*i.e.*, 85 ± 20%) of the *p*-hydroxyphenyl radicals produced in reaction 1 so that addition must occur predominantly at the positions ortho and meta to the hydroxyl group of *p*-bromophenol. The cyclohexadienyl type radicals produced in reaction 5 (or products formed from them) ultimately must be almost quantitatively oxidized in the subsequent reactions. It was pointed out earlier that in the absence of scavenger the *p*-bromo-

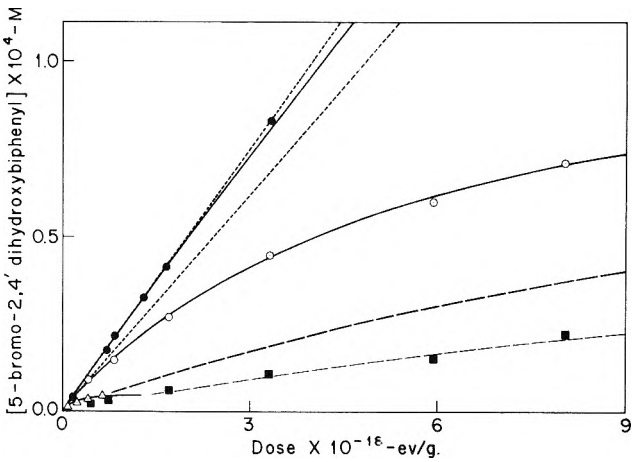

Figure 6. Production of 5-bromo-2,4′-dihydroxybiphenyl in nitrogen purged solutions as a function of dose. Initial *p*-bromophenol concentrations were (●) 4.7 × 10^{-2}, (○) 2 × 10^{-3}, and (△) 10^{-4} *M*. Data (■) for solutions containing 2.5 × 10^{-3} *M* *p*-bromophenol and 1.2 × 10^{-2} *M* isopropyl alcohol are also given. The solid curves were calculated by integration of eq III. The initial slopes (given by the dashed lines) correspond to yields, respectively, of 1.6 and 1.3 at the highest and the lower two *p*-bromophenol concentrations. The heavy dashed line corresponds to the yields predicted for the alcohol containing solutions. The experimentally observed yields are lower indicating that in the alcohol containing system the intermediate radicals are less efficiently oxidized by the secondary reactions than in the alcohol free system.

phenoxyl radical resulting from OH attack appears to be reduced to a considerable extent back to *p*-bromophenol. The high yield of substituted biphenyls noted here appears to result from a complementary oxidation of the phenyl cyclohexadienyl radicals formed in reaction 5. The similarity in the yields of I and II indicates very little selectivity in the addition reaction (reaction II).

A comparison of the relative areas of peaks IV and II in the lower curve of Figure 4, together with the appropriate extinction coefficients (Table I), shows that peak IV corresponds to a yield of ~5% of that of II. The extinction coefficients at 254 nm of the other substituted terphenyls expected to be formed are about the same or lower than that of IV (lower by a factor of ~3 in certain instances; see footnote c in Table I) so it is possible that the smaller peaks in the chromatogram actually correspond to comparable amounts of product. Since IV is the end product of only one out of ten possible reaction paths it is reasonable to estimate the total amount of terphenyl product to be 20–30% of II. At the dose involved this particular experiment, however, only ~20% of the *p*-bromophenol has been consumed. Since the relative concentrations of biphenyl product is low relative to *p*-bromophenol a high yield of terphenyl product implies that the *p*-hydroxyphenyl radical reacts considerably more rapidly with I and II than with *p*-bromophenol itself. This tentative conclusion appears to be substantiated by the kinetic treatment of the dose dependence given below.

The data of Figure 6 show that at concentrations of *p*-bromophenol in the region of millimolar and less, the rate of formation of product II decreases with dose in the region of 10^{18} eV/g and higher. At such high doses the *p*-hydroxyphenyl radical can react with any of the products including the biphenyls, the molecular H_2O_2, and the products of the OH reactions. The yield of *p*-hydroxyphenyl radical will itself decrease because of reactions of e_{aq}^- with radiation produced product as has been illustrated in Figure 2. A complete kinetic treatment of this complex situation is obviously very difficult and requires a considerable amount of data not yet available. Since it appears that *p*-hydroxyphenyl radical reacts considerably more rapidly with the biphenyl derivatives than with *p*-bromophenol we will treat the dose dependence as a consequence of the simple competition between reaction 5 and 6. If we assume that the fraction of reaction 5 that results in the formation of II is f_{II} and that the rate constants for the removal of both I and II by reaction 6 are identical then

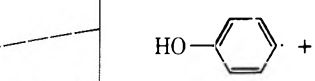

(6)

$$\frac{d[Br(PhOH)_2]_{II}}{dD} = \frac{10G(HOPh\cdot)}{N} f_{II}\left[1 - \frac{k_6[Br(PhOH)_2]_{II}}{f_{II}k_5[BrPhOH]}\right] \Bigg/ \left[1 + \frac{k_6[Br(PhOH)_2]_{II}}{f_{II}k_5[BrPhOH]}\right] \quad \text{(III)}$$

In eq III $G(HOPh\cdot)$ is the yield of *p*-hydroxyphenyl radicals which, from the above results, should be approximated by

$$G(HOPh\cdot) = G(e_{aq})^- \frac{1}{1 + \dfrac{k_p([BrPhOH]_0 - [BrPhOH])}{k_1[BrPhOH]}} \quad \text{(IV)}$$

The quantity $(10G(HOPh\cdot)_0/N)f_{II}$ can be determined from the initial slope in the absence of added solute (see above) and the ratio of rate constants k_6/k_5 by appropriately fitting the dose dependence. The solid curves in Figure 6 were obtained by numerical integrations of eq III, for three concentrations of *p*-bromophenol. A relatively high rate constant for reaction 6 (~3 × 10^8 M^{-1} sec^{-1}) is indicated by the pronounced curvature of the results at 2 × 10^{-3} *M* and is in accord with a high yield for formation of terphenyl products in secondary processes as noted above.

While the treatment given here greatly oversimplifies the actual situation it does show that competition with radiation produced product should not be important at high concentrations of *p*-bromophenol (>10^{-2} *M* for doses ~10^{18} eV/g). For the experiments at 2 × 10^{-3} *M* *p*-bromophenol the measurements at even the lowest doses used here are slightly affected by product buildup. Approximate, but reasonably accurate, corrections for the dose dependence can be estimated from the calculations. By applying these corrections to the measured yields the initial slope is found to be ~20% lower than that at 5 × 10^{-2} *M*. An effect of this magnitude is expected from the concentration dependence for scavenging electrons from within the spurs.[11] For experiments at 10^{-4} *M* the dose dependence is so severe that no reasonable estimates of the initial yield can be obtained from the experimental measurements.

Effect of Scavengers on the Biphenyl Products. Addition of a solute that reacts with *p*-hydroxyphenyl radical such as isopropyl alcohol causes a pronounced decrease in

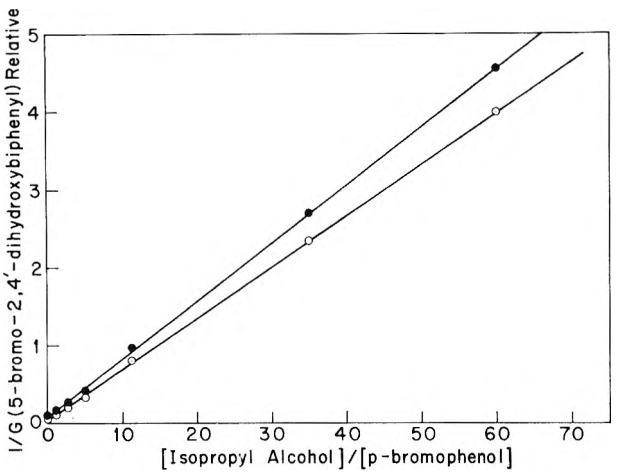

Figure 7. Competitive plot of the dependence of the yield of 5-bromo-2,4′-dihydroxybiphenyl on the ratio of the concentrations of isopropyl alcohol and *p*-bromophenol (see eq VI) ●, observed at a dose of 9×10^{18} eV/g; O, from calculated initial yields. The ratio of k_4/k_5 calculated from the slope–intercept ratio of the lower plot is 1.3. Although the dependence on [RH]/[BrPhOH] seems to follow simple competitive kinetics the rate constant ratio appears to be anomalously high because of changes in the radical termination process.

the formation of the biphenyl products. For example, the yield of 5-bromo-2,4′-dihydroxybiphenyl from a solution 2×10^{-3} *M* in *p*-bromophenol and 0.1 *M* isopropyl alcohol is only 2% of that in the absence of the alcohol. Appropriate modification of eq III to take into account the competitive effect of reaction 4 gives

$$\frac{d[Br(PhOH)_2]_{II}}{dD} = \frac{10G(HOPh\cdot)}{N} f_{II}\left[1 - \frac{k_6[Br(PhOH)_2]_{II}}{f_{II}k_5[BrPhOH]}\right] \Bigg/ \left[1 + \frac{k_4[RH]}{k_5[BrPhOH]} + \frac{k_6[Br(OH)_2]_{II}}{f_{II}k_5[BrPhOH]}\right] \quad (V)$$

The competition can be expressed in terms of the initial yields as

$$G_i[Br(PhOH)_2]_{II} = G(e_{aq}^-)f_{II} \frac{1}{1 + \frac{k_4[RH]}{k_5[BrPhOH]}} \quad (VI)$$

where k_5 is the rate constant for reaction of the *p*-hydroxyphenyl radical with the *p*-bromophenol. It would appear that, in principle, the rate constant ratio k_4/k_5 should be determinable from measurements of the slopes and intercepts of plots of $1/G_i[Br(PhOH)_2]_{II}$ *vs.* [RH]/[BrPhOH]. For a number of reasons it is attractive to attempt to measure the relative rate constants for the reaction of *p*-hydroxyphenyl radical with various solutes based on their effect in reducing the formation of the substituted biphenyls. In contrast to the measurements of phenol production, competitive experiments can be carried out at relatively high scavenger concentrations since one can quantitatively measure small concentrations of the substituted biphenyls. One can also examine substances such as ethylene which give no easily measurable product. Only measurements of the relative yields in the presence and absence of a scavenger are required for the determination of k_4/k_5 from eq VI so that knowledge of the extinction coefficients or the absolute calibration of the apparatus is not involved.

Competitive experiments were carried out with isopropyl alcohol and the results are given in Figure 7. With correction of the experimentally observed data (the solid circles) to zero dose by factors determined from appropriate trial integrations of eq V, the open circles of Figure 7 were obtained. From the slope and intercept an apparent value of 1.3 was obtained for k_4/k_5. This value is considerably higher than that of 0.42 given above from measurements on phenol production. The discrepancy is far outside the errors involved in the interpretation of the data in terms of the initial slopes. On reflection it is obvious that the difficulty lies in the importance of the term f_{II} in eq VI. Basically the efficiency for the oxidation of the phenyl cyclohexadienyl radicals produced in reaction 5 is dependent on the nature of the radical termination process. Addition of the alcohol results in the replacement of the easily reduced *p*-bromophenoxyl radicals (see above) by isopropyl alcohol radicals. This change apparently causes a decrease in the efficiency of the disproportionation or other oxidation processes that result in the production of compounds I and II from the radicals. This effect is also seen in Figure 6 where the heavy dashed curve gives the dose dependence for the formation of II in a system containing isopropyl alcohol which is predicted from the parameters determined in the alcohol free system and the value of k_4/k_5 determined from the phenol production measurements. The experimentally observed yields are considerably lower and can be accounted for if f_{II} is reduced to 0.30 (the light dashed curve). Further experiments are in order to examine the effects of changes in the termination processes on f_{II} since if this can be elucidated the approach outlined here should provide ready access to a large amount of comparative rate information on the reactions of aromatic radicals.

Electron Paramagnetic Resonance Evidence for the Formation of SO_3^- by the Oxidation of SO_2^- on MgO

Y. Ben Taarit[1] and J. H. Lunsford*

Department of Chemistry, Texas A & M University, College Station, Texas 77843 *(Received December 15, 1972)*

Publication costs assisted by the Environmental Protection Agency

Molecular oxygen reacts with a high concentration of SO_2^- ions on MgO forming stable SO_3^- radicals. The epr spectra of $^{33}SO_3^-$ is characterized by $g = 2.0034 \pm 0.0003$ with $a_{\parallel} = 147 \pm 2$ G and $a_{\perp} = 102 \pm 2$ G. The sp hybridization on the sulfur atom indicates an OSO bond angle of 112°. At 25° the ion appears to librate in a plane which includes the symmetry axis.

Introduction

Reactions involving the SO_2^- ion on surfaces have been studied in an effort to determine the importance of this species in the catalytic oxidation and reduction of SO_2. In the present work the reaction between adsorbed SO_2^- ions and molecular oxygen to form SO_3^- on MgO has been investigated.

Che,[2] as well as Kazanskii and coworkers,[3] has detected by means of electron paramagnetic resonance (epr) spectroscopy the formation of SO_2^- on TiO_2, but no evidence is given for subsequent reactions leading to SO_3^-. To the contrary, it was reported that SO_2^- reacted with O_2 over TiO_2, forming O_2^- plus diamagnetic ions.[3] The SO_2^- ion has now been observed on a number of other reducing surfaces.[4,5]

Sulfur dioxide reacts with MgO at room temperature to form sulfite and sulfinato complexes, as indicated by their infrared spectra.[6] At elevated temperatures the infrared evidence suggests that the sulfite ions react with molecular oxygen to form bidentate sulfato complexes in addition to strongly held SO_3.[6] If trapped electrons are available at the surface of the MgO, SO_2 also reacts to form the stable SO_2^- ion.[4] The epr spectra of SO_2^- enriched with sulfur-33 and oxygen-17 have been used to demonstrate that the binding forces between this ion and the surface are purely electrostatic. Provided the concentration of the SO_2^- ion is sufficiently high, it will readily react with molecular oxygen to form SO_3^-.

The epr spectrum of SO_3^- has been well characterized by Chantry and coworkers.[7] In their studies the ion was formed upon γ-irradiation of a number of salts such as sodium dithionate, which has an unusually long S–S bond. From the ^{33}S hyperfine structure it was possible to compare SO_3^- with the isoelectronic ions PO_3^{2-} and ClO_3^-. More recently Lind and Kewley[8] also observed the spectrum of SO_3^- upon γ-irradiation of taurine. This natural amino acid in its zwitterion form (H_3N^+–CH_2–$CH_2SO_3^-$) undergoes homolysis of the C–S bond, thus generating the SO_3^- ion.

Experimental Section

The magnesium oxide pellets were prepared in the manner as previously reported.[4] The samples were degassed for 2 hr at 350° and for 1 hr at either 450 or 850°. The final pressure in the vacuum system was 10^{-5} Torr. Trapped electrons at the surface, known as S centers, were formed by uv irradiation (2537 Å) of the MgO which was in an atmosphere of pure hydrogen. The S centers were subsequently allowed to react with purified N_2O or SO_2 producing O^- or SO_2^- on the surface.[4,9] Alternately, the activated MgO was irradiated at room temperature for 72 hr in the presence of N_2O which yielded adsorbed O_3^- as well as excess O_2 and N_2.[10,11]

Sulfur-33 enriched SO_2 was prepared by reacting ~3 mg of sulfur containing 25% ^{33}S with an excess of pure O_2 at 450° for 1 hr. The SO_2 was purified by the conventional freeze–pump technique prior to each adsorption step.

The epr spectra were recorded at X band either at room temperature or at 77°K using a Model E-6S Varian spectrometer. The g values were determined relative to a phosphorous-doped silicon standard with $g = 1.9987$.

Results

Upon addition of excess molecular oxygen to adsorbed SO_2^- it was observed that the spectrum of SO_2^- decreased and a nearly isotropic line with $g = 2.0034 \pm 0.0003$ was formed. Evidence will subsequently be given for the assignment of the new spectrum to the SO_3^- ion. The formation of SO_3^- was not reversible, *i.e.*, the original SO_2^- signal could not be restored by evacuating the sample at room temperature for over 4 hr. It should be noted, however, that some SO_2^- remained unreacted as indicated by the g_{yy} component which could still be detected, though it was greatly reduced in amplitude.

The rate and extent of the reaction increased with an increased concentration of the initial SO_2^- ion. The SO_3^- ion could be generated from SO_2^- produced from S centers; however, the reaction was more extensive if SO_2 was

(1) On leave from Institut de Recherches sur la Catalyse, C.N.R.S., Villeurbanne, France.
(2) M. Che, Thesis, University of Lyon, 1968.
(3) A. I. Mashchenko, G. P. Pariiskii, and V. B. Kazanskii, *Kinet. Katal.*, **9**, 151 (1968).
(4) R. A. Schoonheydt and J. H. Lunsford, *J. Phys. Chem.*, **76**, 323 (1972).
(5) V. M. Vorotyntsev, V. A. Shvets, and V. B. Kazanskii, *Kinet. Katal.*, **12**, 1249 (1971).
(6) A. J. Goodsel, M. J. D. Low, and N. Takezawa, *Environ. Sci. Tech.*, **6**, 268 (1972); R. A. Schoonheydt and J. H. Lunsford, *J. Catal.*, **26**, 261 (1972).
(7) G. W. Chantry, A. Horsfield, J. R. Morton, J. R. Rowlands, and D. H. Whiffen, *Mol. Phys.*, **5**, 233 (1962).
(8) G. Lind and R. Kewley, *Can. J. Chem.*, **50**, 43 (1972).
(9) N.-B. Wong and J. H. Lunsford, *J. Chem. Phys.*, **55**, 3008 (1971).
(10) N.-B. Wong and J. H. Lunsford, *J. Chem. Phys.*, **56**, 2665 (1972); Y. Ben Taarit and J. H. Lunsford, *Proc. Int. Congr. Catal.*, *5th*, *1972* (1972).
(11) R. J. Cvetanović, *J. Chem. Phys.*, 23, 1203, 1208, 1375 (1955).

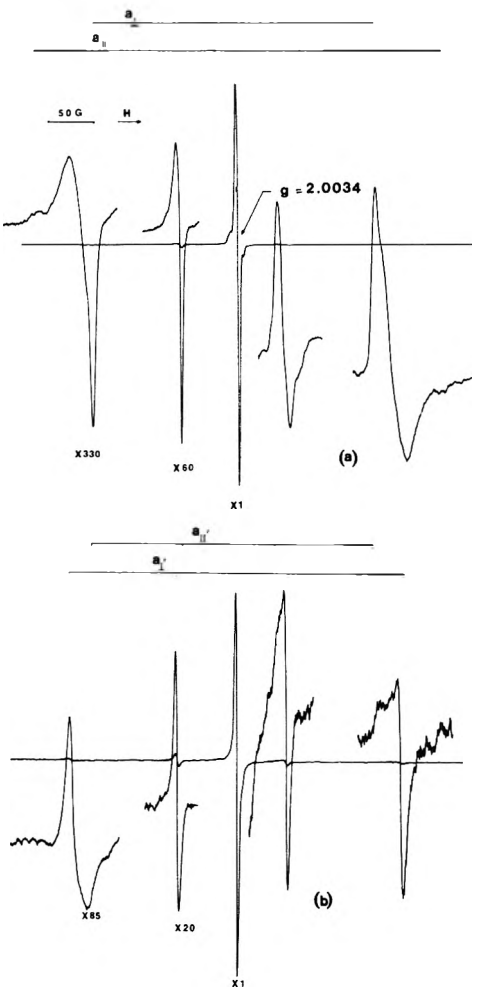

Figure 1. Epr spectrum of SO_3^- on MgO: (a) recorded at 77°K, (b) recorded at 25°.

first allowed to react with the ozonide ion to form a much higher SO_2^- concentration. Upon addition of SO_2, the symmetric line at $g = 2.0034$ appeared directly. In the latter case no additional O_2 was needed since it is photochemically produced from N_2O.[11] When excess oxygen formed during the uv irradiation of N_2O was removed prior to adsorption of SO_2, only SO_2^- was observed and no oxidation occurred unless O_2 was added back to the system.

The oxidation of SO_2^- to SO_3^- was difficult on samples degassed at 850°. This may be related to a decrease in the concentration of one type of SO_2^- ion,[4] or to a decrease in the concentration of certain diamagnetic ions[6] as will be discussed in a subsequent section.

By using SO_2 enriched to 25% in $^{33}S(I = 3/2)$ four distinct hyperfine lines were observed. These lines in addition to the ^{32}S spectrum are depicted in Figures 1a and 1b. As noted by other investigators[7,8] the outer lines are shifted about 3 G downfield and the inner lines about 8 G downfield with respect to the $^{32}SO_3^-$ line. This shift in the hyperfine components is predicted by second-order terms in the spin Hamiltonian. The shape of the hyperfine spectra varied significantly with changes in the sample temperature. The spectrum of Figure 1a was recorded with the sample at 77°K, whereas the spectrum of Figure 1b was recorded with the sample at room temperature. In both cases it was relatively easy to saturate the spin system with microwave power. From the shape of the hyperfine lines of Figure 1 the values of $a_{\parallel}$ and $a_{\perp}$ were determined. The principal values of the hyperfine tensors are given in Table I.

TABLE I: Epr Parameters for SO_3^-

	g	$a_{\parallel}$, G	$a_{\perp}$, G
SO_3^- on MgO (77°K)	2.0034 ± 0.0003	147 ± 2	102 ± 2
SO_3^- on MgO (25°)	2.0034 ± 0.0003	102 ± 2	121 ± 2
SO_3^- in $K_2CH_2(SO_3)_2$[a]	2.0036 ± 0.0007	153 ± 1	112 ± 1
SO_3^- in taurine[b]	2.0035 ± 0.0004	135 ± 4	99 ± 4

[a] Reference 7. [b] Reference 8.

Under conditions of high modulation amplitude and gain it was even possible to detect the hyperfine structure from SO_3^- containing natural sulfur, which has only 0.74% sulfur-33. This means that the presence of this ion may be confirmed without resorting to the use of enriched SO_2.

It is perhaps worthwhile to mention that O^- did not react with SO_2 to form SO_3^-. This result was rather surprising in view of the observations that O^- reacts with O_2 forming O_3^-,[10] with CO forming CO_2^-,[12] with C_2H_4 forming $C_2H_4O^-$,[12] and with CO_2 forming CO_3^-.[13] In this experiment O^- was first produced from N_2O and SO_2 was then condensed above the sample which was at 77°K. The sample was allowed to warm progressively to higher temperatures and the resulting spectra indicated that O^- reacted with SO_2 forming SO_2^-. The same electron transfer step was detected upon treating SO_2 with adsorbed O_2^-.

Discussion

g Tensor. According to a Walsh diagram[7] for AB_3 type molecules, SO_3^- with 25 valence electrons should be pyramidal with C_{3v} symmetry. The filling of the $^2A_1$ ground state should be according to the sequence[14]

$$\ldots (1e)^4(5a_1)^2(2e)^4(3e)^4(1a_2)^2(6a_1)^1$$

The g tensor should reflect the axial symmetry of the anion. The g shifts for the perpendicular direction would be due to the excitation from the $^2A_1$ ground state to the ^2E state, either as

$$\ldots (1e)^4(5a_1)^2(2e)^3(3e)^4(1a_2)^2(6a_1)^2$$

or as

$$\ldots (1e)^4(5a_1)^2(2e)^4(3e)^3(1a_2)^2(6a_1)^2$$

For the parallel direction g shifts would be due to excitation from the ground state to the $^2A_2$ state

$$\ldots (1e)^4(5a_1)^2(2e)^4(3e)^4(1a_2)^1(6a_1)^2$$

In terms of energy the $6a_1$ orbital lies well separated from the 2e, 3e, and $1a_2$ orbitals; hence, only a small departure of the principal g values from the free electron value is expected. One would predict that $g_{\parallel}$ and $g_{\perp}$ would be slightly greater than 2.0023, which is consistent with the observed value of 2.0034.

Hyperfine Tensor. The hyperfine structure of Figure 1a is in good agreement with that reported for the SO_3^- ion,

(12) C. Naccache, *Chem. Phys. Lett.*, **3**, 323 (1971).
(13) A. J. Tench, T. Lawson, and J. F. J. Kibblewhite, *J. Chem. Soc., Faraday Trans. 1*, **68**, 1169 (1972).
(14) K. P. Dinse and K. Möbius, *Z. Naturforsch. A*, **23**, 695 (1968).

TABLE II: Comparison of Hyperfine Couplings, Spin Densities, and Bond Angles for SO_3^- in Different Environments

	SO_3^- on MgO	SO_3^- in $K_2CH_2(SO_3)_2$	SO_3^- in taurine
Isotropic coupling, A_{iso}, G	117	126	111
Anisotropic coupling, 2β, G	30	27	24
Spin density			
3s	0.12	0.13	0.11
3p	0.51	0.46	0.41
OSO angle, degree	112	111	111

thus confirming the identification of the ion on magnesium oxide. The tensor has nearly cylindrical symmetry, which is expected for the pyramidal SO_3^- ion. The direction of the unique axis is normal to the plane formed by the three oxygen atoms.

The hyperfine tensor may be resolved into its isotropic part, A_{iso}, and anisotropic part, 2β, in the usual manner. Upon assuming that the d orbital contribution to the wave function was negligible, the s and p character of the unpaired electron localized on the sulfur were calculated. Here, values of A_{iso} = 970 G for a pure 3s orbital of ^{33}S and 2β = 59 G for a pure 3p orbital were used.[7,14] Results for SO_3^- in different environments are given in Table I.

The OSO bond angle for this ion was calculated from the equation[15]

$$\phi = \cos^{-1}\left[\frac{1.5}{2\lambda^2 + 3} - \frac{1}{2}\right] \quad (1)$$

where λ^2 is the ratio of the p to s character of the unpaired electron on the sulfur. This leads to a calculated bond angle of 112°, which is very similar to that reported by Chantry, *et al.*[7] Obviously the crystalline environment does not greatly distort the SO_3^- ion.

The spectrum of SO_3^- in Figure 1b is unique to MgO. It appears to suggest that $a_\perp > a_{||}$, which yields a value for the 3p character of only 0.27. This drastic reduction in the 3p character is unlikely in view of the consistent parameters noted in Table II for SO_3^- in quite different environments. A more plausible explanation of the spectrum observed at room temperature is evident if one assumes motion in a plane which includes the threefold symmetry axis. A libration such as depicted in Figure 2, would have the effect of averaging $a_{||}$ and one $a_\perp$ component giving $a_\perp'$. The other $a_\perp$ component would become $a_{||}'$. The numerical values of $a_\perp'$ and $a_{||}'$ given in Table I are in agreement with this model. Such motion could easily occur on edges of the MgO crystallites which are approximately 100 Å on a side.[16] Similar motion for S_3^- on MgO was detected even at 77°K.[17]

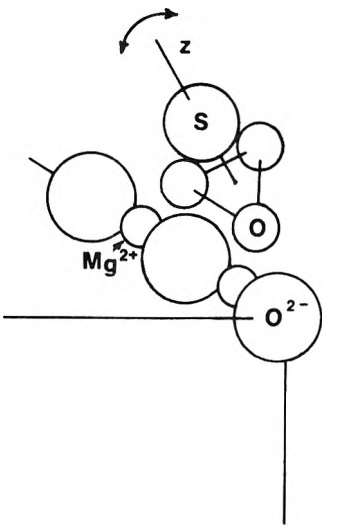

Figure 2. Schematic representation of SO_3^- motion on the edge of a MgO crystallite.

Reaction Mechanism. The epr results reported here clearly establish that SO_2^- may be oxidized to SO_3^- with molecular oxygen. Furthermore, the ease and extent of oxidation depend on the concentration of SO_2^- ions. This concentration effect may be interpreted in terms of a concerted process involving an intermediate such as $SO_2^-\cdots O\text{-}O\cdots SO_2^-$, although the line width of the epr spectrum indicates that the paramagnetic ions are separated from one another by a distance greater than 5 Å. It is more reasonable to assume that an intermediate such as $SO_2^-\cdots O\text{-}O\cdots SO_3^{2-}$ is formed, which then results in SO_3^- and a diamagnetic SO_4^{2-} ion. Experiments currently in progress on other types of surfaces may help to resolve this mechanistic problem.

Acknowledgment. The authors acknowledge the contributions of Dr. Robert Schoonheydt during the early part of this study. This investigation was supported by research Grant No. 801136, Air Pollution Control Office, Environmental Protection Agency.

(15) P. W. Atkins and M. C. R. Symons, "The Structure of Inorganic Radicals," Elsevier, New York, N. Y., 1967.
(16) P. J. Anderson and R. F. Horlock, *Trans. Faraday Soc.*, **58**, 1993 (1962); R. F. Horlock, P. L. Morgan, and P. J. Anderson, *ibid.*, **59**, 721 (1963).
(17) J. H. Lunsford and D. P. Johnson, *J. Chem. Phys.*, **58**, 2079 (1973).

Substituent Effects on Electron Spin Resonance Parameters of Benzyl Radicals[1]

P. Neta and Robert H. Schuler*

Radiation Research Laboratories, Center for Special Studies and Department of Chemistry, Mellon Institute of Science, Carnegie-Mellon University, Pittsburgh, Pennsylvania 15213 *(Received January 9, 1973)*

Publication costs assisted by Carnegie-Mellon University and the U. S. Atomic Energy Commission

The esr spectra of benzyl radicals substituted on the ring by CO_2^-, O^-, SO_3^-, CH_3O, CH_3, CH_3CO, CN, F, or Cl have been observed during the radiolysis of aqueous solutions of the appropriate derivatives of toluene at pH 13.7. All of these radicals show esr parameters very similar to those of benzyl radical. The extremes of the values for the CH_2 hyperfine constants are 14.91 and 16.43 G for the para O^- and F derivatives (16.34 G for benzyl) with most values, however, being in excess of 15.64 G. Effects of substitution on the hyperfine constants of the ring protons are extremely small. The smallness of the effects of substitution on the hyperfine constants shows that these various groups cause only a very limited perturbation of the electron spin distribution in the aromatic system. While the accuracy of the measurements is considerably greater than the small differences noted, it was not possible to derive any significant correlation with available substituent constants nor with theoretical calculations of the effects of substitution on spin distribution.

Introduction

Substituent effects on the electron spin resonance parameters of aromatic radicals have been recently reviewed by Janzen.[2] Correlations have been found between the substituent Hammett σ values and the hyperfine constants of a series of substituted aromatic semidiones, nitro anions, nitroxides, and certain other nitrogen-centered radicals. The spin probes in all of these radicals have electronic properties which strongly influence the electron spin distribution. Since it seemed that substituted benzyl radicals would simulate more closely the molecules themselves, we have measured the hyperfine constants for various substituted benzyl radicals for the purpose of attempting a correlation with the substituent σ values. These benzyl radicals have considerably shorter lifetimes than the radicals summarized by Janzen and can be studied only by continuously producing them during the course of the esr observations. We have chosen the *in situ* radiolysis method developed by Eiben and Fessenden[3] for this purpose.

Benzyl radicals can be produced in irradiated aqueous solutions by the reaction of O^- with substituted toluenes at high pH, as has been recently demonstrated.[4] Although OH radicals add to an aromatic ring much more rapidly than they abstract hydrogen from an aliphatic side chain, the situation is reversed when OH is converted into O^- (pK = 11.9).[5] At pH >13 the main reaction in irradiated solutions of substituted toluenes involves abstraction of H from the methyl group to produce the corresponding benzyl radicals.

Experimental Section

Most of the organic compounds used were of the purest grade available from Aldrich and from Eastman. Toluene was a Matheson Coleman and Bell Spectrograde reagent and *p*-xylene was Research Grade from Phillips. Saturated or 0.01 M solutions were prepared in doubly distilled water containing 0.5 M Baker Analyzed KOH. The solutions were also saturated with N_2O in order to convert e_{aq}^- to O^-. They were irradiated by 2.8-MeV electrons while flowing through a silica cell located within the esr cavity. The details of these experiments are similar to those previously described.[3]

Results and Discussion

The spectra of the radicals reported in Table I were uncomplicated by the presence of other radicals.[6] The spectral patterns consist of from 27 lines (for benzyl substituted with CO_2^-, O^-, and SO_3^- at the para position) to 108 lines (for the para derivatives containing CH_3 groups). The signal-to-noise ratio for the least intense spectra was ~2:1, with greater intensities being observed for radicals with less complex patterns and for those bearing negative charges which decrease the radical decay rates. The line widths were ~0.1 G. The parameters calculated from the spectra are summarized in Table I.

The present results for benzyl are in very good agreement with the hyperfine constants reported by Dixon and Norman[7] and by Fischer.[8] Except for *p*-carboxybenzyl none of the other radicals have been previously observed by esr.

It is seen in Table I that substitution of an aromatic position produces no large effect on either the CH_2 proton hyperfine constant or that of any of the ring protons. The largest changes are observed for the radicals *p*-$\dot{C}H_2C_6H_4O^-$ and *p*-$\dot{C}H_2C_6H_4COCH_3$. In these cases the CH_2 coupling constants are only ~10% less than that for benzyl. In all other cases the CH_2 coupling constants range between 15.64 (*p*-$\dot{C}H_2C_6H_4CN$) and 16.43 G (*p*-

(1) Supported in part by the U.S. Atomic Energy Commission.
(2) E. G. Janzen, *Accounts Chem. Res.*, **2**, 279 (1969).
(3) K. Eiben and R. W. Fessenden, *J. Phys. Chem.*, **75**, 1186 (1971).
(4) P. Neta, M. Z. Hoffman, and M. Simic, *J. Phys. Chem.*, **76**, 847 (1972).
(5) J. Rabani and M. S. Matheson, *J. Phys. Chem.*, **70**, 761 (1966).
(6) In the case of *p*-nitrotoluene the spectrum of *p*-nitrobenzyl radical was not observed because it was masked by an intense spectrum of the nitrotoluene anion radical.
(7) W. T. Dixon and R. O. C. Norman, *J. Chem. Soc.*, 4857 (1964).
(8) H. Fischer, *Z. Naturforsch. A*, **20**, 488 (1965).

TABLE I: Esr Parameters of Substituted Benzyl Radicals[a]

Radical	*g* factor	$a_{CH_2}^H$	a_o^H	a_m^H	a_p^H	Other hyperfine constants
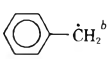	2.00260	16.34 (2)	5.13 (2)	1.77 (2)	6.17	
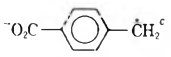	2.00273	15.76 (2)	5.07 (2)	1.77 (2)		
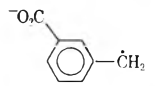	2.00258	16.40 (2)	5.13; 5.13	1.75	6.10	
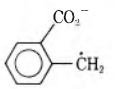	2.00266	16.23; 16.07	5.07	1.77; 1.82	6.14	
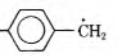	2.00293	14.91 (2)	4.63 (2)	1.10 (2)		
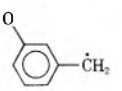	2.00253	16.26 (2)	5.06; 4.77	1.69	5.92	
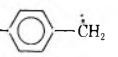	2.00254	16.10 (2)	5.13 (2)	1.78 (2)		
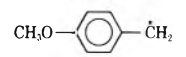	2.00273	15.93 (2)	5.06 (2)	1.58 (2)		0.63 (CH_3)
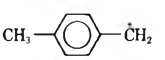	2.00257	16.07 (2)	5.13 (2)	1.75 (2)		6.70 (CH_3)
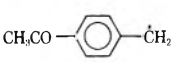	2.00292	15.25 (2)	4.90 (2)	1.75 (2)		0.54 (CH_3)
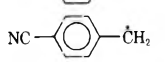	2.00258	15.64 (2)	5.06 (2)	1.81 (2)		0.92 (N)
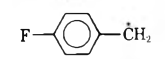	2.00283	16.43 (2)	5.26 (2)	1.74 (2)		14.04 (F)
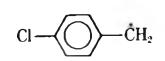	2.00315	16.08 (2)	5.22 (2)	1.83 (2)		0.50 (Cl) 0.54

[a] Produced in irradiated aqueous alkaline solutions, saturated with N_2O, by the reaction of O^- radicals with the substituted toluenes. The *g* factors were determined by comparison with the signal from the silica cell and are accurate to ±0.00003. The hyperfine constants are given in gauss and are accurate to ±0.03 G. The number of protons displaying the splitting is given in parentheses if other than one. [b] Hyperfine constants of 16.4, 5.1, 1.6, and 6.3 G respectively for the CH_2, ortho, meta, and para protons were reported by Dixon and Norman (ref 7) and values of 16.40, 5.17, 1.77, and 6.19 G by Fischer (ref 8). [c] From ref 4.

$\dot{C}H_2C_6H_4F$). The coupling constants for the ortho protons vary only from 5.06 to 5.26 G and those for the meta protons from 1.58 to 1.83 G. Although most radicals involved substitution at the para position, the effect on the para proton hyperfine constants in the three ortho- or meta-substituted radicals was similarly very small (5.92 to 6.10 G as compared to 6.17 for the para proton in benzyl).

The present results can be contrasted with differences as large as a factor of 2 observed for the nitrogen coupling constants in substituted nitrobenzene radical anions and similar differences found for the methyl protons in substituted phenylpropanesemidiones.[2] Hehre, Radom, and Pople[9] have recently calculated the distributions of electron spin density in a number of substituted benzenes. They find, in general, that in all cases substitution produces changes of less than 10% in the spin density on the ring carbon atoms. Substituents such as CH_3, F, COOH, or CN affect the distribution only at the level of ~4% or less. From this work one expects only small effects of substitution on the relative values of hyperfine constants of the ring protons of the benzyl radicals since these protons provide a direct probe of the spin density distribution. We find here that, in fact, neither the absolute values of the hyperfine constants of the ring protons nor those of the CH_2 protons, which provide a direct measure of the spin density on the side group, change appreciably. It is seen that substitution has an effect on the benzylic spin system of the magnitude calculated by Hehre, *et al.*, for the simple aromatic molecules. There is, however, no quantitative agreement between the predicted effects on spin density and the changes in esr parameters reported here. The very large effects noted above for the nitrobenzene anions and the semidiones[2] are undoubtedly due to the fact that the spin density distribution in the π system is affected appreciably by the spin probe itself so that the effects of substitution are magnified considerably.

One can also compare the present results with the relatively large effects of substitution observed in some aliphatic radicals. Fischer[10] has, for example, interpreted the changes produced by CO_2H or CN substitution as resulting, respectively, from 7 and 15% withdrawal of electron spin density from adjacent radical sites. In recent work from these laboratories effects of the order of 30% were found to be produced by CN, CO_2H, or CO_2^- substitution in the allylic radicals derived by H atom addition to the furan system.[11] However, CO_2^- substitution in allyl itself is found to have little effect.[4]

(9) W. J. Hehre, L. Radom, and J. A. Pople, *J. Amer. Chem. Soc.*, **94**, 1496 (1972).
(10) H. Fischer, *Z. Naturforsch. A*, **19**, 866 (1964).

We have attempted to obtain a correlation of the esr parameters with the substituent constants for the various groups but find no obvious correlation within the small but accurately known differences between the data given in Table I. We can, however, make a few remarks on the details of a number of the individual comparisons. First of all it is seen that the *p*-methylbenzyl radical has hyperfine constants almost identical with those for benzyl. The 6.70-G constant for the CH_3 protons provides a measure of the spin density at the para position. A comparison with benzyl can be obtained by multiplying the observed value by the ratio of the α and β proton hyperfine constants of the isopropyl radical (22.1 and 24.7 G).[12] This gives an equivalent coupling constant of 6.00 G which can be compared with the 6.17-G constant of benzyl. A similar calculation in the case of the cyano derivative based on the 3.51-G nitrogen splitting observed in the CH_2CN radical[13] would indicate a nitrogen coupling of 1.03 G. The drop in the proton hyperfine constants shows that a small amount of spin density is lost from the ring to the CN group but it is seen that, in fact, a ~10% decrease in the nitrogen splitting from that expected is observed.

The para fluoro derivative shows a very small increase in the proton hyperfine constants. If we use the a^H to a^F ratio of 3.97 to 8.41 G observed[14] for the nitrobenzene anion and its fluoro derivative, one expects a fluorine hyperfine constant in the p-$FC_6H_4\dot{C}H_2$ radical of 13.1 G which agrees quite well with the observed value of 14.04 G. A comparison of this latter value to the 6.17 G in the benzyl radical indicates that an α fluorine atom in a planar radical should have a hyperfine constant of ~50 G. This value is somewhat lower than the 64 G observed[15] for the CH_2F radical which is, however, slightly nonplanar as indicated by the ^{13}C hyperfine constant.

The three isomeric carboxybenzyl radicals can be compared internally and with benzyl itself. It is seen that in the ortho and meta derivatives the parameters are essentially identical with those of benzyl. The para isomer, however, shows lower hyperfine constants and a higher g factor indicating a small shift of spin density onto the carboxyl group. Substitution of CO_2^- on the side chain of benzyl radical produces a somewhat larger effect in that it reduces all of the coupling constants by ~10% (a_α^H = 15.04, a_o^H = 4.67, a_m^H = 1.58, a_p^H = 5.51 G, g = 2.00298).[4] The difference between the two isomeric $^-OC_6H_4\dot{C}H_2$ radicals is very much more pronounced. Substitution at the meta position has essentially no effect on the benzylic system. Substitution at the para position, however, causes a very large decrease in all of the hyperfine constants and a marked increase in the g factor. Both changes indicate pronounced transfer of the electron to the oxygen end of the molecule.

In summary, the effects noted here are disappointingly small and do not appear to be able to provide a measure of the substituent effects. They do, however, accurately reflect the fact that substitution causes only small changes in the spin distribution. It is obvious from this that even small changes in spin distribution can have relatively large effects on the reaction rates and ionization equilibria used to measure the substituent constants.

(11) R. H. Schuler, G. P. Laroff, and R. W. Fessenden, *J. Phys. Chem.*, **77**, 456 (1973).
(12) R. W. Fessenden and R. H. Schuler, *J. Chem. Phys.*, **39**, 2147 (1963).
(13) R. Livingston and H. Zeldes, *J. Magn. Resonance*, **1**, 169 (1969).
(14) A. H. Maki and D. H. Geske, *J. Amer. Chem. Soc.*, **83**, 1852 (1961).
(15) R. W. Fessenden and R. H. Schuler, *J. Chem. Phys.*, **43**, 2704 (1965).

Spectroscopy and Chemistry of Aprotic Nd^{3+} Laser Liquids[1]

C. Brecher* and K. W. French

Waltham Research Center, GTE Laboratories Incorporated, Waltham, Massachusetts 02154 *(Received January 2, 1973)*

Publication costs assisted by GTE Laboratories

Measurements have been made on various aspects of the spectroscopy of the $SeOCl_2$ and $POCl_3$ aprotic Nd^{3+} laser liquids, with emphasis on the latter. Unusual features in the chemical behavior are described and some apparent inconsistencies resolved. The formation of complex PO_2Cl_2–Lewis acid groups is deemed to be a major factor in the solubilizing of the Nd^{3+} ion in $POCl_3$ solution. A consistent and coherent model is proposed to explain the observations.

Introduction

One of the major advances in the liquid laser field has been the development of aprotic hosts for the Nd^{3+} ion. This ion, which is the basis for the most widely used class of crystalline and glass lasers, had never before been usable in the liquid state because of its high susceptibility to nonradiative deexcitation. The importance of high-energy vibrations in this quenching process, and the mechanism

(1) This research was partially supported by the Advanced Research Projects Agency of the Department of Defense and was monitored by the Office of Naval Research under Contract No. N00014-68-C-0110.

of the interaction, were elucidated by Heller,[2a] whose work led to the first successful utilization of an inorganic aprotic liquid, $SeOCl_2$, as a laser host medium.[2b] Subsequent work[3-6] yielded more practical systems involving the much less toxic and corrosive $POCl_3$ liquid, now the mainstay of present liquid laser research. Many individual aspects of these laser media have been studied in relation to laser applications.[7-15] There have, however, been many unanswered questions regarding the details of their chemical and spectroscopic behavior. It is the purpose of this paper to gather the pertinent observations in these areas in order to construct a coherent and consistent, if not necessarily unique, picture of the behavior of the Nd^{3+} ions in such liquid media.

Experimental Section

Chemical. Although the procedures for preparation of the solutions involved in this work have been described elsewhere,[6,8,15,16] they are sufficiently important to the subsequent discussion to be summarized here. The $SeOCl_2$–$SnCl_4$–Nd^{3+} solution is prepared by dissolving (with heating) pure anhydrous Nd_2O_3 in an anhydrous 5:1 (by volume) mixture of $SeOCl_2$ and $SnCl_4$. The mixture is then distilled under reduced pressure (40 mm) until a boiling point of about 90° (pure $SeOCl_2$) is reached and about one-third of the total solution has been removed to eliminate the last traces of protic contamination. The solution is then reconstituted to the desired Nd^{3+} concentration and acidity by addition of appropriate quantities of pure $SeOCl_2$ and $SnCl_4$. Similar procedures are followed if $NdCl_3$ rather than Nd_2O_3 is used.

The $POCl_3$–$SnCl_4$–Nd^{3+} solution was prepared in a similar manner, with the following important exception. Water, in the molar ratio of 1:10, is added to the $POCl_3$–$SnCl_4$ mixture to enable dissolution of the Nd_2O_3 or $NdCl_3$, for reasons to be discussed later. The deliberately introduced protic contamination is then removed by boiling off (at atmospheric pressure, final temperature 116°) a sufficient fraction of the total liquid volume. The solution is reconstituted to the desired concentrations by addition of the appropriate pure liquids. The $POCl_3$–$ZrCl_4$–Nd^{3+} liquid, in contrast, utilizes the pure anhydrous trifluoroacetate salt of Nd^{3+} rather than the oxide or chloride, since the presence of water causes precipitation of the zirconium. The $Nd(CF_3COO)_3$ can be prepared by crystallization from a solution of Nd_2O_3 in aqueous trifluoroacetic acid, followed by complete removal of the water by heat and vacuum. This salt dissolves directly in the $POCl_3$–$ZrCl_4$ mixture, which is then boiled to remove traces of protic contamination and reconstituted as before. Other pertinent points are mentioned in the subsequent text.

Spectroscopic. Emission measurements were made on the Nd^{3+} solutions at both liquid N_2 and room temperatures, with spot checks at various intermediate temperatures. All three liquid systems passed continuously from liquid to glassy state, with no crystallization or spectral discontinuities (except for occasional problems at low acidity). The systems are excited by a Hanovia 538C-1 xenon arc lamp through Corning 3-69 and 4-97 filters, and the emissions measured with a Jarrell-Ash 0.5-m Ebert monochromator and an ITT FW 118 photomultiplier. Some absorption measurements, particularly at low temperatures were made with the same apparatus but with a tungsten ribbon filament lamp replacing the xenon arc lamp. Room temperature absorptions were also made with a Cary-14 spectrophotometer. Decay time measurements were made with a helical xenon flashlamp surrounding the sample, with the emission detected axially. Some of the pertinent spectra are shown in Figures 1-5 and values listed in Table I; further discussion follows.

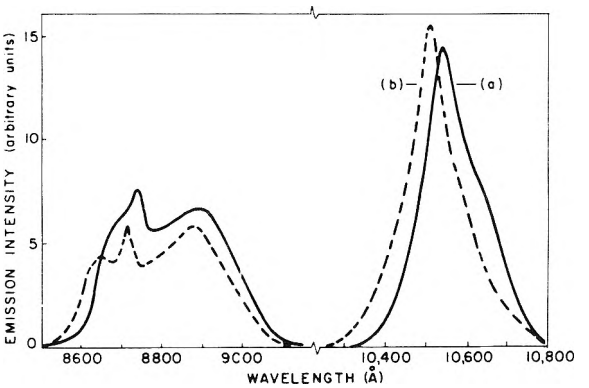

Figure 1. Emission spectrum of 0.3 *M* Nd^{3+} solutions at 300°K: (a) $SeOCl_2$; (b) $POCl_3$. Stoichiometric concentration of $SnCl_4$. Spectrum with $ZrCl_4$ not measurably different.

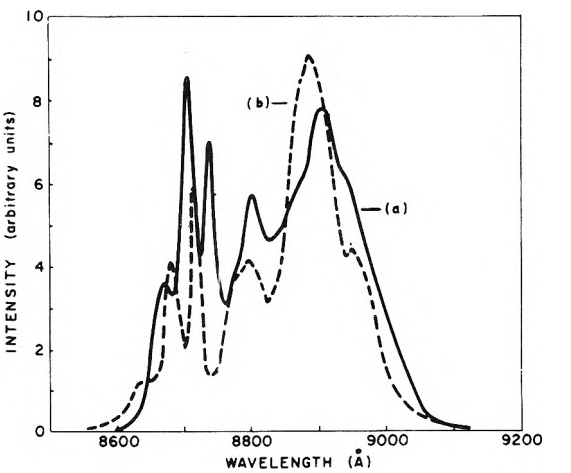

Figure 2. Emission spectrum of 0.3 *M* Nd^{3+} solutions at 100°K: (a) $SeOCl_2$; (b) $POCl_3$. Stoichiometric concentration of $SnCl_4$. Spectrum with $ZrCl_4$ differs in relative intensity of components (see Figure 4).

(2) (a) A Heller, *J. Amer. Chem. Soc.*, **88**, 2058 (1966); (b) A. Heller, *Appl. Phys. Lett.*, **9**, 106 (1966); A. Lempicki and A. Heller, *ibid.*, **9**, 198 (1966).
(3) V. P. Belan, V. V. Grigoryants, and M. E. Zhabotinski, IEEE Conference on Laser Engineering and Applications, Washington, D. C., 1967.
(4) N. Blumenthal, C. B. Ellis, and D. Grafstein, *J. Chem. Phys.*, **48**, 5726 (1968).
(5) E. J. Schmitschek, *J. Appl. Phys.*, **39**, 6120 (1968).
(6) C. Brecher and K. W. French, *J. Phys. Chem.*, **73**, 1785 (1969).
(7) D. Kato and K. Shimoda, *Jap. J. Appl. Phys.*, **7**, 548 (1968).
(8) A. Heller, *J. Amer. Chem. Soc.*, **90**, 3711 (1968); *J. Mol. Spectrosc.*, **28**, 101 (1968); *ibid.*, **28**, 208 (1968).
(9) H. Samelson, A. Heller and C. Brecher, *J. Opt. Soc. Amer.*, **58**, 1054 (1968).
(10) H. Samelson, A. Lempicki, and V. A. Brophy, *IEEE J. Quantum Electron.*, **4**, 849 (1968); *J. Appl. Phys.*, **39**, 4029 (1968).
(11) H. Samelson and A. Lempicki, *J. Appl. Phys.*, **39**, 6115 (1968).
(12) C. LeSergent, M. Michon, S. Rousseau, F. Collier, H. Dubost, and G. Raoult, *C. R. Acad. Sci., Ser. B*, **268** 1501 (1969).
(13) H. Samelson, R. Kocher, T. Waszak, and S. Kellner, *J. Appl. Phys.*, **41**, 2459 (1970).
(14) H. Weichselgartner and J. Perchermeier, *Z. Naturforsch. A*, **25**, 1244 (1970).
(15) C. Brecher, K. W. French, W. Watson, and D. Miller, *J. Appl. Phys.*, **41**, 4578 (1970).
(16) A. Heller, K. W. French, and P. O. Haugsjaa, *J. Chem. Phys.*, **56**, 2368 (1972).

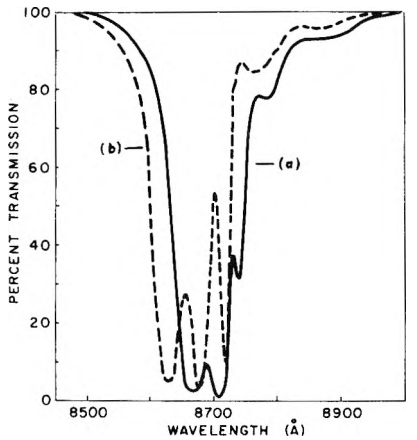

Figure 3. Absorption spectrum of 0.3 *M* Nd^{3+} solutions at 100°K: (a) $SeOCl_2$; (b) $POCl_3$. Stoichiometric concentration of $SnCl_4$.

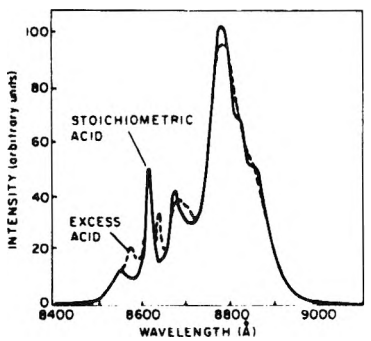

Figure 4. Emission spectrum of 0.3 *M* Nd^{3+} solutions in $POCl_3$–$ZrCl_4$ solutions at different Lewis acid concentration (at 100°K).

TABLE I: Components of the $^4F_{3/2}$–$^4I_{9/2}$ Transition of Nd^{3+} (0.3 *M*) in $SeOCl_2$ and $POCl_3$

$SeOCl_2$			$POCl_3$	
Wavelength, Å	Energy, cm^{-1}	Assignment[a]	Wavelength, Å	Energy, cm^{-1}
8668	11,537	b-1	8628	11,590
8705	11,488	a-1	8679	11,522
8738	11,444	b-2	8718	11,471
8778	11,393	a-2	8768	11,405
		b-3		
8801	11,362	a-3	8805	11,357
8865	11,280	b-4		
8905	11,230	a-4	8889	11,250
8950	11,173	b-5	8960	11,162
~8990	11,123	a-5		

[a] Components of the $^4I_{9/2}$ level are numbered consecutively from the ground state (1); for the $^4F_{3/2}$ level, a denotes the lower component and b the higher. These assignments yield the following values (cm^{-1}) for the energies of levels 1, 2, 3, 4, 5, a and b, respectively; In $SeOCl_2$: 0, 94, 125, 245, 352, 11,487, 11,537; in $POCl_3$: 0, 118, 165, 272, 428, 11,522, 11,589. See ref 6.

Discussion

Spectroscopy. One of the sensitive optical probes is the behavior of the fluorescence decay time. The influence of the acidity is shown in Figures 6 and 7, which reveal two distinct effects. When the concentration of Lewis acid is below stoichiometric with respect to the Nd^{3+}, the fluorescence decay time and emission intensity are strong

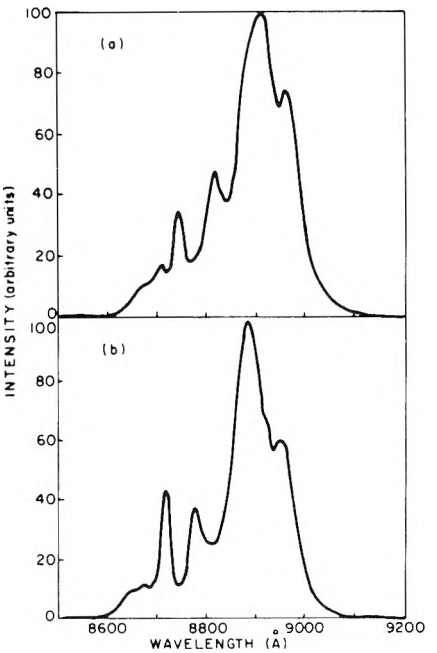

Figure 5. Emission spectrum of Nd^{3+} in two aprotic hosts (at 100°K): (a) in crystalline $Nd_2(ZrCl_6)_3 \cdot 12POCl_3$; (b) in $POCl_3$ solution at stoichiometric $ZrCl_4$ concentration.

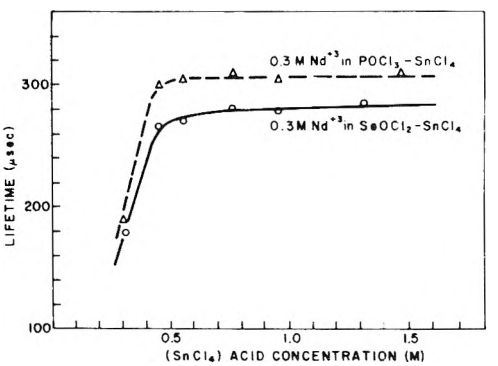

Figure 6. Fluorescence decay time of 0.3 *M* Nd^{3+} in $SeOCl_2$–$SnCl_4$ and $POCl_3$–$SnCl_4$ as function of Lewis acid concentration (at 300°K).

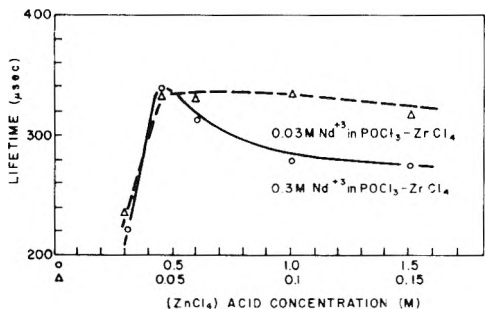

Figure 7. Fluorescence decay time of Nd^{3+} in $POCl_3$–$ZrCl_4$ as function of Lewis acid concentration (at 300°K).

functions of acid concentration, dropping sharply as the acidity is reduced. This is true both at room temperature and at liquid N_2 temperature, in all systems studied, and in the total absence of measurable protic contamination. This behavior is accompanied by marked decrease in the chemical stability of the solutions, with precipitation occurring more and more readily. Only in the $SeOCl_2$ sys-

tems could solutions be prepared at zero acid concentration, and even they eventually precipitated out. This would indicate that the coordination sphere which solubilizes and protects the Nd^{3+} ion is becoming less and less effective, allowing external influences (Nd–Nd or Nd–solvent interactions) first to quench the fluorescence, and finally to cause the Nd to precipitate out of solution. This point will be considered later.

On the other side of stoichiometry, however, the systems behave quite differently. With $SnCl_4$ as the acid in both $POCl_3$ and $SeOCl_2$, the decay time remains essentially constant as the acidity increases to even three or four times stoichiometric. With $ZrCl_4$ in $POCl_3$ (it is insoluble in $SeOCl_2$), however, the decay time has a rather well-defined maximum, dropping significantly as the acid concentration is increased. Furthermore, as the acid concentration is increased new emission peaks appear in the fluorescence spectrum (particularly at liquid N_2 temperatures (Figure 4)), becoming continuously more intense up to the solubility limit of $ZrCl_4$. It is apparent that the $ZrCl_4$ is altering the coordination structure surrounding the Nd^{3+} ion; indeed it is likely that a Zr-containing anion is entering into the coordination structure, since the mere increase in acidity should have produced the same effect with $SnCl_4$ (which has the same shape and size). A supporting, if circumstantial, point is the remarkable structural similarity (Figure 5) in the spectra of Nd^{3+} in stoichiometric $POCl_3$–$ZrCl_4$ solutions and in the $Nd_2(ZrCl_6)_3 \cdot 12POCl_3$ salt (see Chemistry discussion). It should also be noted, as shown in Figure 7, that at a 1:10 dilution with pure $POCl_3$, the decay time drop-off for the same stoichiometry ratios is considerably slower; indeed, the effect seems to be proportional to the actual excess over stoichiometry, rather than the ratio, as would be expected for a new species in equilibrium with the old one.[17]

The decay time is also affected by the concentration of the Nd^{3+} ion itself. This arises from two characteristics of the energy level structure. First, most of the emission from the $^4F_{3/2}$ metastable state arises from transitions to either the $^4I_{9/2}$ or the $^4I_{11/2}$ lower states. The latter transition is the laser transition; the former, on the other hand, is the resonance transition to the ground state, and with increasing concentration considerable self-absorption will occur. Such self-absorption has the result of decreasing the apparent radiative probability for emission through the $^4F_{3/2}$–$^4I_{9/2}$ transition, thus effectively increasing the lifetime of the $^4F_{3/2}$ state in optically thick samples. Such behavior is observed in the $SeOCl_2$–$SnCl_4$ and $POCl_3$–$SnCl_4$ systems;[10] indeed, as seen in Figure 8, the lifetime increases by as much as 30% from its low-concentration value.

There is, however, also a second effect which arises from the fact that the energy gap between the $^4F_{3/2}$ emitting state and the $^4I_{15/2}$ state, the highest of the ^4I "ground" multiplet, is essentially the same as the energy of the $^4I_{15/2}$ state above ground. Thus when an unexcited Nd^{3+} ion is in close proximity to one excited to the $^4F_{3/2}$ state, transfer of energy between them can take place, leaving both in the $^4I_{15/2}$ state, from which they rapidly decay nonradiatively to ground. This sort of mechanism can provide a sufficiently competitive path for deexcitation to markedly reduce the lifetime of the $^4F_{3/2}$ state, and give rise to the concentration quenching observed with Nd^{3+} in many crystalline and glassy hosts.[18] Such behavior is also observed in the $POCl_3$–$ZrCl_4$ medium,

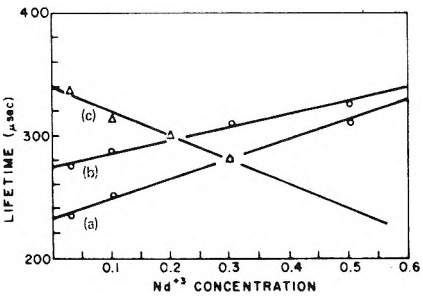

Figure 8. Fluorescence decay time of Nd^{3+} aprotic solutions at stoichiometric acidity as function of Nd^{3+} concentration (at 300°K): (a) $SeOCl_2$–$SnCl_4$; (b) $POCl_3$–$SnCl_4$; (c) $POCl_3$–$ZrCl_4$.

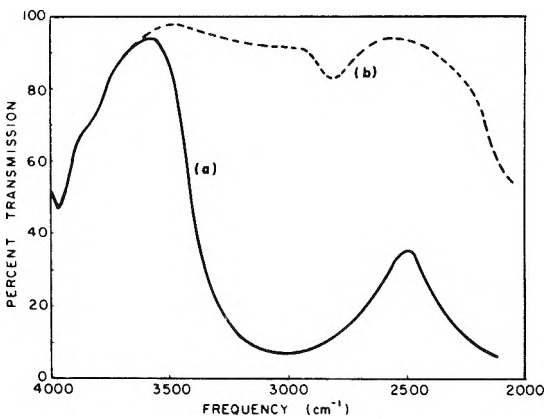

Figure 9. Infrared absorption spectrum of 0.3 *M* Nd^{3+} in $SeOCl_2$: (a) contaminated with H_2O (about 10^{-5} *M*); (b) anhydrous.

where the decay time decreased with increasing Nd^{3+} concentration even in the face of the lifetime lengthening effect of the self-absorption, which is still taking place. Since, as we have seen, the coordination in the $POCl_3$–$ZrCl_4$ liquid is such as to allow excess $ZrCl_4$ to alter it, it is not surprising that excess Nd^{3+} should do the same. This will be discussed subsequently.

The remaining important influence on the lifetime to be discussed here is that of protic contamination. It is now well established that the effectiveness of O–H and other hydrogen-containing groups in deexciting Nd^{3+}, or other ions, arises from the relatively high energy of vibrations involving the proton; so that with Nd^{3+}, only two O–H vibrational quanta are needed to bridge the gap between the $^4F_{3/2}$ and $^4I_{15/2}$ states. It is as a consequence of this mechanism that the aprotic liquid media were developed for Nd^{3+} liquid lasers. Generally, great care must be taken in the preparation of such solutions to avoid even small amounts of protic contamination, which, even at the level of 10^{-4}–10^{-5} *M*, can be readily detected both by infrared (Figures 9 and 10) and by the sharp decrease in lifetime (as much as 30–50%). Indeed, exposure of the

(17) (Nd^{3+}, solvated (I)) + $ZrCl_4 \rightleftarrows$ (Nd^{3+}–$ZrCl_4$, solvated complex (II))

$$K_{eq} = [\text{species II}]/[\text{species I}][ZrCl_4]$$

or, if

$$\rho = [\text{species II}]/[\text{species I}]$$

then

$$\rho = K_{eq}[ZrCl_4]$$

(18) See, for example, G. E. Peterson and P. M. Bridenbaugh, *J. Opt. Soc. Amer.*, **54**, 644 (1964); K. Hauptmanova, J. Pantoflicek, and K. Patek, *Phys. Status Solidi*, **9**, 525 (1965); C. K. Asawa and M. Robinson, *Phys. Rev.*, **141**, 257 (1966); other references cited.

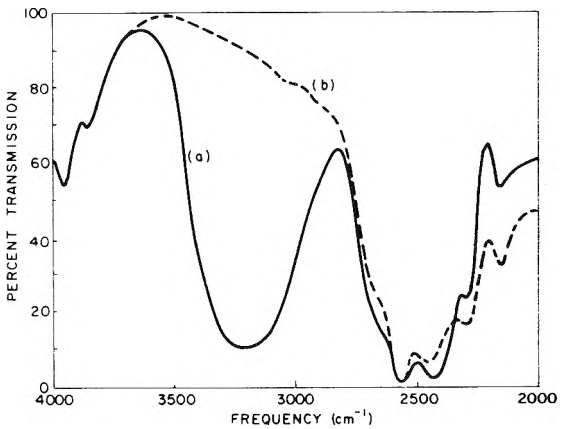

Figure 10. Infrared absorption spectrum of 0.3 *M* Nd^{3+} in $POCl_3$: (a) contaminated with H_2O (about 10^{-5} *M*); (b) anhydrous.

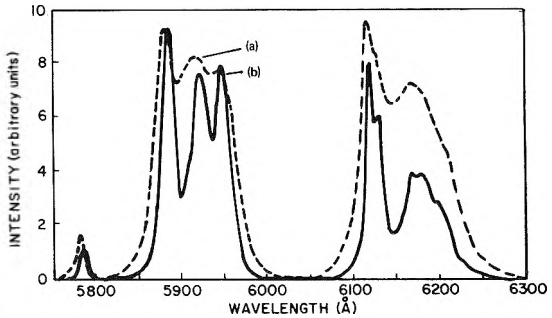

Figure 11. Emission spectrum of 0.3 *M* Eu^{3+} in $POCl_3$–$ZrCl_4$ solutions: (a) at 300°K; (b) at 100°K.

TABLE II: Emissions from Eu^{3+} (0.3 *M*) in $POCl_3$–$ZrCl_4$ Solution at 100°K

Wavelength, Å	Assignment	Energy of underlined state, cm^{-1}
5788	$^5D_0$–$^7F_0$	17,277
5884		282
5920	$^5D_0$–$^7F_1$	385
5945		456
6116		926
6127		956
6166	$^5D_0$–$^7F_2$	1,059
6182		1,101
6201		1,151

$SeOCl_2$–$SnCl_4$ and $POCl_3$–$SnCl_4$ to the open air for even a short time enables sufficient water to be absorbed to have a markedly deleterious effect on the lifetime. In contrast to this, however, the $POCl_3$–$ZrCl_4$ medium is remarkably insensitive to protic contamination. Short exposures to atmospheric moisture seem to have almost no measurable effect on the lifetime. Dropwise addition of water does have the expected effect, drastically decreasing the lifetime and the emission intensity; however (unlike the other two media), over a period of hours the solution restores itself with the lifetime and intensity regaining their original levels. This is accompanied by the slow precipitation from the solution of the white powder of $ZrOCl_2$ (or its hydrate), and the virtual disappearance of the previously intense O–H infrared absorption. The contaminated solution, if carefully filtered, becomes as good a laser solution as before.

As an explanation for the unusual behavior of the $POCl_3$–$ZrCl_4$ solutions, we observe that Zr has a much greater affinity for oxygen than has Sn.[19] For example, if water is added to pure $SnCl_4$ liquid, the crystalline $SnCl_4 \cdot nH_2O$ hydrate forms; if the same is done to $ZrCl_4$, a strong reaction takes place, with the liberation of HCl gas and formation of $ZrOCl_2$, which dissolves in water. The ability of other oxygen-containing acids, such as acetic, to displace chlorine from $ZrCl_4$, forming $ZrCl_2(OR)_2$, has been well established.[19] Thus, the following model is proposed for the behavior of aqueous contamination. The addition of water to the solution forms the protic acid

$$H_2O + SeOCl_2 \rightarrow H_2SeO_2Cl_2 \quad (1a)$$

$$H_2O + POCl_3 \rightarrow HPO_2Cl_2 + HCl \quad (1b)$$

Unless removed by boiling (with evolution of HCl), the protic acid remains in solution as a contaminant, and $SnCl_4$ has no measurable effect on its presence. With $ZrCl_4$, however, we can get further reaction

$$ZrCl_4 + HPO_2Cl_2 \rightarrow ZrCl_3(PO_2Cl_2) + HCl \quad (2a)$$

$$ZrCl_4 + 2HPO_2Cl_2 \rightarrow Zr(OH)_2Cl_2 + POCl_3 \quad (2b)$$

effectively removing the protic contamination. In eq 2a, the $ZrCl_3(PO_2Cl_2)$ in solution may then slowly rearrange to regenerate one molecule of $POCl_3$ and one of $ZrOCl_2$, which is insoluble in $POCl_3$ and precipitates out.

At this point, nothing has been said of the symmetry and structure of the coordination sphere surrounding the Nd^{3+} ion. In earlier work on Eu^{3+} liquid laser solutions,[20] it was shown that eightfold coordination around the central metal ion is almost universal in strongly bonded rare-earth compounds like chelates, with the few exceptions leading toward higher (nine- or tenfold) rather than lower coordination. It would seem quite unlikely that Nd^{3+}, with the same chemical bonding behavior and even a slightly larger ionic radius, would be satisfied with lower coordination.

Detailed information on the symmetry and stability of the various coordination structures could be unequivocally obtained because of certain unique spectroscopic properties of the Eu^{3+} ion, and it was hoped to glean similar information about the aprotic Nd^{3+} laser solutions by studying equivalent solutions made with Eu^{3+}. This hope was dashed by the highly structured spectra of the resulting solutions (Figure 11; see also ref 8c). In many cases, particularly under strongly acid conditions, more than one $^5D_0$–$^7F_0$ transition was observed, a unique positive indication of more than one coordination species. Whenever a clearly defined single $^5D_0$–$^7F_0$ transition was found (generally at stoichiometric acidity), the $^5D_0$–$^7F_1$ and $^5D_0$–$^7F_2$ transition regions showed three and five components, respectively, the maximum possible splitting.[21] This was true at both room temperature and liquid nitrogen temperatures, although of course the components were much better resolved in the latter case (Table II). Indeed, the

(19) P. Pascal, "Nouveau Traite de Chimie Mineral," Masson et Cie, Paris, 1963.

(20) H. Samelson, C. Brecher, and A. Lempicki, *J. Mol. Spectrosc.*, **19**, 349 (1966); other references cited therein.

(21) Emissions from the $^5D_1$ state to the $^7F_5$ and $^7F_6$ states, respectively, can also fall in these regions. Such emissions are generally much less intense (the observed emissions from the $^5D_1$ state to the $^7F_0$, $^7F_1$, and $^7F_2$ states are two orders of magnitude weaker), and are neglected here.

TABLE III: Analytical Results on Various Nd^{3+} Precipitates from $POCl_3$ Solutions

Material	% composition					
	Nd	Cl	O	P	Zr	
Precipitate 3 (measured)	7.9	63.0	4.6	14.9	9.6	(by difference)
$Nd_2(ZrCl_6)_3 \cdot 12POCl_3$ or $Nd_2(ZrCl_4(PO_2Cl_2)_2)_3 \cdot 6PCl_5$ (theory)	9.5	63.0	6.3	12.2	9.0	
Precipitate 2 (measured)	15.1	59.4	7.8	19.5		
$NdCl_3 \cdot 5POCl_3$ (theory)	14.2	62.7	7.9	15.2		
$NdCl_2(PO_2Cl_2) \cdot 4POCl_3$ (theory)	15.0	58.9	10.0	16.1		
Schimitschek precipitate[a] (measured)	24.2	43.8	15.0	17.0		
$Nd(PO_2Cl_2)_3$ (theory)	26.4	39.0	17.6	17.0		

[a] Reference 28.

spectrum is reminiscent of those obtained from tris bidentate chelates of europium in polar solvents.[22] While an analogy between two such different systems is tenuous at best (see Appendix), this would imply that the coordination needs of rare earths in $POCl_3$ are satisfied in a similar manner; that is, with six equivalent oxygens (three bidentate groups) and two or three other (solvent) molecules. In any event, no single coordination species having a symmetry higher than C_2 is compatible with the spectrum and, while it is not unlikely that there are actually more than one symmetry species in solution, the single $^5D_0$–$^7F_0$ transition would indicate that, in the primary coordination sphere, the differences are largely matters of geometric arrangement.

Similar evidence of low symmetry and/or possible multiple species is obtained from the Nd^{3+} spectra (Figures 2 and 3). Here at least eight clearly defined components can be found in the $^4F_{3/2}$–$^4I_{9/2}$ (resonance) transition region in all three types of solution, indicating a complete splitting of both upper and lower states (ten possible energies). While this does not agree with a nearly octahedral symmetry inferred by Kato from the laser behavior[23] and Tb^{3+} spectra,[24] it is completely consistent with various studies in the Soviet Union,[25] and appears unequivocal.

The effect of acidity on the Nd^{3+} spectrum is shown in Figure 4. In all three cases, when the Lewis acid concentration is below stoichiometric there is no measurable distortion of the spectrum from the normal (stoichiometric) situation shown in Figures 1–4, indicating no significant emission from more than one species. The intensity of the emission, however, does decrease sharply, in line with the decrease in measured decay time. The $SeOCl_2$–$SnCl_4$ and $POCl_3$–$SnCl_4$ media also show no significant spectroscopic effect above stoichiometric acidity; in $POCl_3$–$ZrCl_4$, however, at least four new components do appear, exceeding the maximum of ten allowed for a single species. This supports the multiple species hypothesis inferred from the lifetime measurements, but gives no information about its nature. For further insight, we must consider other aspects of the chemistry of these solutions.

Chemistry. Although all three types of aprotic solutions were prepared with similar starting materials (a Nd^{3+} salt, a strong Lewis acid, and the aprotic solvent), there are considerable differences in the product solutions. The chemistry of the $SeOCl_2$ system has been discussed elsewhere,[8] and appears straightforward. This solvent is highly polar (dielectric constant ~46), and can thus readily dissolve ionic salts. The Nd^{3+} goes into solution, solvated by a shell of $SeOCl_2$ molecules (akin to hydration in aqueous solutions), to which it is bonded through the oxygen,[26] and which interchange readily with other solvent molecules. The Nd^{3+} chloride can even dissolve in hot $SeOCl_2$ without any Lewis acid, producing a clear solution but with considerably reduced fluorescence intensity and short ($\approx$100 μsec) decay time. The cooled solution is not stable, and precipitates out in a matter of days, somewhat akin to the slow precipitation of $FeCl_{3-x}(OH)_x$ from an aqueous unbuffered solution of ferric chloride. With Lewis acid ($SnCl_4$) at stoichiometric or higher concentrations, the solution is completely stable and suitable for laser use.

Phosphorus oxychloride behaves rather differently. Its dielectric constant in only 14, and hence it will not readily dissolve most ionic salts. Thus, Nd_2O_3 will not dissolve under completely anhydrous conditions, and the addition of water is needed for the reaction to proceed. When this reaction is performed slowly, at moderate Nd^{3+} concentrations (say 0.01 *M*), with reactants cooled in an ice bath, the intermediate product (a granular light blue precipitate, denoted ppt 1) can be held for some time. If the temperature of the solution is allowed to rise, the precipitate dissolves forming a clear solution, followed by a new precipitate (ppt 2) some seconds later. The new precipitate does not dissolve, except upon addition of sufficient Lewis acid.

Similar observations are made in the third case. Here, at moderate Nd^{3+} concentrations, the $Nd(CF_3COO)_3$ can be observed to dissolve completely to form a clear blue solution, only to be followed a few seconds later by formation of a precipitate (ppt 2), which itself is soluble only on addition of Lewis acid ($ZrCl_4$). Addition of PCl_5 to the resulting stable solution causes yet another precipitate (ppt 3) to form. Analyses of these precipitates (except ppt 1, which was not stable), thoroughly dried by flowing nitrogen gas at room temperature, but not heated or pumped to drive off bound solvent of crystallization, is given in Table III.

The following mechanism is proposed to explain the dissolution of Nd^{3+} salts in $POCl_3$. First, the addition of water (or the use of the trifluoroacetate salt) forms the dichlorophosphate

$$3H_2O + 6POCl_3 + Nd_2O_3 \rightarrow 2Nd(PO_2Cl_2)_3 + 6HCl\uparrow \quad (3a)$$

(22) C. Brecher, H. Samelson, and A. Lempicki, *J. Chem. Phys.*, **42**, 1081 (1968).
(23) D. Kato, *J. Phys. Soc. Jap.*, to be submitted for publication.
(24) D. Kato and K. Shimoda, *Jap. J. Appl. Phys.*, 9, 581 (1970).
(25) M. N. Tolstoi, E. L. Lyubimov, and I. M. Batyaev, *Opt. Spectrosc.*, **28**, 389 (722) (1970); other references cited therein.
(26) I. Lindqvist, "Inorganic Adduct Molecules of Oxo-Compounds," Springer-Verlag, Berlin, 1963.

$$3H_2O + 3POCl_3 + NdCl_3 \rightarrow Nd(PO_2Cl_2)_3 + 6HCl\uparrow \quad (3b)$$

$$Nd(CF_3COO)_3 + 3POCl_3 \rightarrow Nd(PO_2Cl_2)_3 + 3CF_3COCl\uparrow \quad (3c)$$

The by-products go off as gases, leaving the dichlorophosphate in solution. This material, crystallized by cooling, is identified as ppt 1. However, in solution this compound is unstable in the presence of $POCl_3$,[27] reacting further and being converted to the pyrophosphoryl chloride

$$Nd(PO_2Cl_2)_3 + 3POCl_3 \rightarrow NdCl_3 + 3P_2O_3Cl_4 \quad (4)$$

The $NdCl_3$ precipitates out of solution, carrying with it approximately five molecules of $POCl_3$ as solvent of crystallization, as confirmed in Table III (ppt 2). This material differs from that obtained by Schimitschek and Trias,[28] who identified a similar precipitate as the dichlorophosphate $Nd(PO_2Cl_2)_3$. However, they isolated and dried the precipitate differently, as will be seen.

Since addition of Lewis acid causes the precipitate to dissolve, the final step (as in $SeOCl_2$) might be written as

$$2NdCl_3 + 3SnCl_4 \rightarrow Nd_2(SnCl_6)_3 \quad (5a)$$

$$2NdCl_3 + 3ZrCl_4 \rightarrow Nd_2(ZrCl_6)_3 \quad (5b)$$

in which the Lewis acid simply lowers the Cl^- concentration in the solution sufficiently to shift the equilibrium from the precipitated chloride to the solubilized $Nd^{3+}\cdot nPOCl_3$ ion. This, however, does not answer a number of specific observations on the chemical behavior:

(1) Neither this precipitate ($NdCl_3\cdot 5POCl_3$), nor pure $NdCl_3$, will dissolve in pure $POCl_3$ to which adequate Lewis acid ($ZrCl_4$ or $SnCl_4$) has been added but do dissolve if water is also added. (Except that too much water will cause $ZrOCl_2$ to precipitate.)

(2) They also dissolve when Lewis acid is added to the clear liquid from which the material originally precipitated, or to the clear liquid prepared by reaction of $POCl_3$ with the requisite amounts of water or sodium trifluoroacetate.

(3) The addition of sufficient water will cause the precipitate (or the pure chloride) to dissolve even without and Lewis acid.

(4) A precipitate prepared in the same manner, but baked out under vacuum to remove *all* solvent of crystallization (Schimitschek), does dissolve in pure $POCl_3$–$ZrCl_4$.

(5) Completely stable solutions prepared in the standard manner are caused to precipitate by addition of PCl_5 (forming ppt 3).

The behavior of Lewis acids in $POCl_3$ is complicated. The low dielectric constant is much less favorable for the formation of $POCl_2^+$ and Cl^- species than for the corresponding ions ($SeOCl^+$ and Cl^-) in $SeOCl_2$ and is even less favorable for the doubly negative $SnCl_6^{2-}$ and $ZrCl_6^{2-}$ ion. This is borne out by the low conductivity ($\sim 10^{-5}$ ohm/cm) of $POCl_3$–$ZrCl_4$ solutions. Indeed research on $POCl_3$-containing systems by many investigators[29] indicates that the validity of extending to it the ionic model appropriate to $SeOCl_2$ is extremely questionable. On the other hand, it is known that both Sn and Zr chlorides readily satisfy their coordination needs in $POCl_3$ by direct addition of two solvent molecules, forming $MCl_4\cdot 2POCl_3$, and compounds of this form have been isolated. Furthermore, as stated earlier, suitable oxygen donors (water, acetic acid, etc.) will readily displace chlorine from Zr (but not from Sn), forming stable compounds of the form $ZnCl_2(OR)_2$ (or $ZrOCl_2$ with water). We therefore propose that the important factor in the dissolution of Nd^{3+} in $POCl_3$ is the stabilization of the $PO_2Cl_2^-$ ionic species, and hence the reversal of eq 4. The Lewis acid would accomplish this, not by forming $ZrCl_6^{2-}$ or $SnCl_6^{2-}$ ions, but by direct bonding with the $PO_2Cl_2^-$ ion itself. Thus in item 1, the precipitate or the $NdCl_3$ will not dissolve in pure $POCl_3$ even with sufficient Lewis acid, because not enough $P_2O_3Cl_4$ is present to be converted back into $PO_2Cl_2^-$ (reverse of eq 4). If, however, enough is generated even by other means (item 2) dissolution will occur. Item 3 is merely item 2 carried to extreme, in which enough $P_2O_3Cl_4$ is formed to push the equilibrium in eq 4 sufficiently to the left. Item 4 is merely the result of the same leftward push of eq 4, this time by the complete removal of $POCl_3$ by heat and vacuum, followed by dissolution in pure $POCl_3$–$ZrCl_4$. And finally, item 5 is a result of the destruction of the solubilizing species by PCl_5

$$P_2O_3Cl_4 + PCl_5 \rightarrow 3POCl_3 \quad (6a)$$

$$PO_2Cl_2^- + PCl_5 \rightarrow 2POCl_3 + Cl^- \quad (6b)$$

This leads to the following picture of the Nd^{3+} ion in $POCl_3$. With $SnCl_4$ as the Lewis acid, species of the type $SnCl_4\cdot 2POCl_3$ are present with the two oxygens donating electrons into vacant 5d orbitals of the tin and completing its octahedral coordination. The $PO_2Cl_2^-$ ion, being a stronger electron donor, displaces the $POCl_3$, forming species like $SnCl_4(PO_2Cl_2)^-$. Exchange of the $PO_2Cl_2^-$ ions would readily take place among the $SnCl_4$ molecules and between them and the Nd^{3+} ion. The primary coordination sphere of the Nd^{3+} would be occupied by these $POCl_3$ and $PO_2Cl_2^-$ groups and the $SnCl_4$ molecules associated with them, producing a number of possible coordination species. The most probable ones, because of the low dielectric constant, would bear no net charge, and would have the general composition

$$Nd(PO_2Cl_2\cdot SnCl_4)_{3-n}(SnCl_5\cdot POCl_3)_n \quad (n = 0, 1, 2)$$

where the relative proportions would be determined by the concentration of Lewis acid and by the equilibrium constants between the respective species. The remaining coordination needs for both Nd and Sn would be filled by $POCl_3$ groups, leaving only oxygen in the primary coordination sphere of the neodymium ion. The overall size of the coordination entity would necessarily be considerably larger than in $SeOCl_2$; this is supported by the rather large Rayleigh wing scattering observed in such solutions.[30] A small but nonnegligible concentration of charged species, of the same general structure but with a neutral $POCl_3$ group replacing one or more of the chlorines or the larger negatively charged groups, must also be present, as indicated by the electrical conductivity; indeed studies of the electroluminescence in similar solutions[16] lead to essentially the same chemical model.

With $ZrCl_4$ as the Lewis acid, the picture is different only in the strength of the metal–oxygen association; here the stronger Zr–O bond (involving the 4d orbitals rather

(27) J. R. Van Wazer, "Phosphorus and Its Compounds," Interscience, New York, N. Y., 1961.
(28) E. J. Schimitschek and J. A. Trias, *Inorg. Nucl. Chem. Lett.*, 6, 761 (1970); see also E. J. Schimitschek, J. A. Trias, and C. Y. Liang, *Spectrochim. Acta, Part A*, **27**, 2141 (1971).
(29) V. Gutmann, "The Chemistry of Non-Aqueous Solvents," J. J. Lagowski, Ed., Academic Press, New York, N. Y., 1966.
(30) R. Pappalardo and A. Lempicki, *J. Appl. Phys.*, **43**, 1699 (1972).

than the much higher energy 5d's as in Sn), and the ability to form neutral $ZrCl_2(PO_2Cl_2)_2$ species, would lead to more stable Nd^{3+} coordination structures and probably ring formation of the type

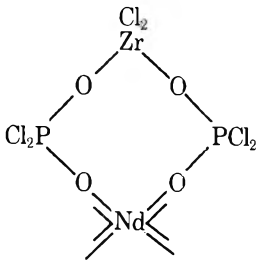

which is known to take place in other systems.[31]

This picture of the solvation of Nd^{3+} in $POCl_3$, while speculative and far from proven, has the virtue of explaining all our various experimental observations as well as those of others. It also provides a rationale for the differences in the behavior of Nd^{3+} in $POCl_3$ with the two Lewis acids. The more stable ring formations in the $POCl_3$–$ZrCl_4$ solution would be more effective in shielding in the Nd^{3+} ion from interaction with contaminants. The sharp increase in viscosity when both Nd^{3+} and Lewis acid are present in the solution, as against either one separately, is explained by the relatively large size of the agglomerations. The fact that excess $ZrCl_4$ alters the lifetime and spectrum of Nd^{3+} (see Figures 4 and 8) while $SnCl_4$ does not, arises from the ability of the $ZrCl_4$ to become directly bonded into the Nd^{3-} complex species. And finally, since at higher Nd^{3+} concentrations the -OPO-Zr-OPO groups should form bridges between different Nd^{3+} ions as readily as they form rings with only one Nd^{3+} ion, the observed concentration quenching is a straightforward result of the model. In conclusion, therefore, the foregoing picture reveals both the fundamental similarities and the disparities in detail characteristic of the most widely used Nd^{3+} aprotic liquid laser solutions, and we feel that we have derived a consistent and coherent model for their chemical and spectroscopic behavior.

Acknowledgments. The authors are indebted to H. Samelson and A. Heller for many helpful discussions on various aspects of this work.

Appendix

Spectroscopic Characteristics of Eu^{3+} Tris Chelates in Polar Solvents. The emission spectra of europium chelates were subject to intense study a number of years ago.[20] Considerable information was generated because of two particularly useful spectroscopic characteristics. First, the $^5D_0$–$^7F_0$ transition cannot be split by the coordination field, so that the observation of more than one component is a positive indication of more than one coordination structure. Secondly, the small number of components possible in the $^5D_0$–$^7F_1$ and $^5D_0$–$^7F_2$ transitions (three and five, respectively) and the great sensitivity of the latter to the symmetry of the coordination structure makes it possible to distinguish between structures having the same coordination number. It was further ascertained that for rare earths, a coordination number of less than eight is a rarity, and that tris and bis chelates will fill their unsatisfied coordination needs by associating with polar solvent molecules, either in solution or as molecules of solution in the solid. This tendency results in a low molecular symmetry and consequently a highly structured spectrum with full splitting of the known transitions.

Nevertheless, and despite differences in detail, the various europium tris chelates had many qualitative features in common, particularly in contrast to the tetrakis chelates. The $^5D_0$–$^7F_0$ transition falls between 5796 and 5800 Å, as against over 5800 Å for the tetrakis and below 5796 Å for others. The intensity of this transition is within an order of magnitude of the $^5D_0$–$^7F_2$, and some 1.5 orders of magnitude stronger than for the tetrakis. The intensity of the $^5D_0$–$^7F_1$ transition is nearly the same as that of the $^5D_0$–$^7F_2$, instead of almost 1 order of magnitude weaker. The existence of a $^5D_0$–$^7F_1$ component in the 5870–5900-Å region is characteristic of these chelates, since those for tetrakis chelates are higher. And finally, the existence of strong $^5D_0$–$^7F_2$ components in the 6160–6220 Å region is similarly characteristic of the tris species.

The large number of components makes determination of the actual symmetry difficult. The fact that there are two chemically distinct types of oxygen coordinated to the europium, to be distributed among eight (or nine) positions results in not only a low symmetry, but also the possibility of many geometric arrangements, each with its own selection rules and its own contribution to the spectrum. Since these species are virtually indistinguishable chemically, the $^5D_0$–$^7F_0$ transition will be essentially unaffected.

(31) See, for example, J. Danielsen and S. E. Rasmussen, *Acta Chem. Scand.*, **17**, 1971 (1963); H. Grunze, K. H. Jost, and G. U. Wolf, *Z. Anorg. Allg. Chem.*, **365**, 294 (1969).

Relaxation of $[Cr(H_2O)_6]^{3+}$ and $[Mn(H_2O)_6]^{2+}$ in Polyacrylonitrile in the Glassy and Rubber-Like States Studied by Electron Spin Resonance

S. Reich,* S. Raziel, and I. Michaeli

Polymer Department, The Weizmann Institute of Science, Rehovot, Israel *(Received November 10, 1972)*

Publication costs assisted by The Weizmann Institute of Science

X-Band and Q-band esr line widths and intensities of $[Cr(H_2O)_6]^{3+}$ and $[Mn(H_2O)_6]^{2+}$ in acrylonitrile and polyacrylonitrile were measured as functions of the concentrations of $Zn(ClO_4)_2 \cdot 6H_2O$ or $Li(ClO_4)$ added to the monomer and polymer systems. The line width of $[Cr(H_2O)_6]^{3+}$ incorporated in the polymer was studied as a function of temperature and concentration both in the glassy and rubber-like states. The zero-field splitting parameter was evaluated for $[Cr(H_2O)_6]^{3+}$ and for $[Mn(H_2O)_6]^{2+}$ in the polymeric system both above and below the glass transition temperature. It is shown that the electronic relaxation in the polymeric matrix is due to modulation of the zero-field splitting interaction, probably *via* rotational tumbling of the $[Cr(H_2O)_6]^{3+}$ ion. A correlation time of $\sim 2 \times 10^{-11}$ sec at 300°K for the hydrated chromium ion is found both in the glassy and the rubber-like states. In view of the short correlation time scale found and the possibility that ligand exchange mechanisms may operate in the rubber-like state, the similarities of the polymeric system to true liquid solutions are discussed. Evidence from esr and magnetic susceptibility measurements for strong Cr–Cr interaction in the glassy state at low temperature is presented.

Introduction

The purpose of this work is to study the dynamics of small ions embedded in an amorphous polymeric matrix, by the esr technique, both in the glassy and the rubber-like states. The system chosen is polyacrylonitrile (PAN) in which Mn^{2+} or Cr^{3+} are embedded. Three aspects of the dynamic behavior of the embedded ions are discussed: the dynamic ligand exchange, correlation times of tumbling, and Cr–Cr interactions. The interest in such systems stems from the fact that solid polymer media such as polyacrylonitrile may provide an environment in which the motion of small ions is less restricted than in more compact solids such as low molecular weight glasses. A considerable number of esr studies have been performed in the latter systems.[1,2] As a rule, those glasses served for magnetic dilution while maintaining the paramagnetic ions in a solid matrix.[3] The esr spectra observed differed markedly from those found in the corresponding liquid solutions of paramagnetic ions, since the motional signal averaging found in liquids is quenched in the glassy state. Such quenching is observed, for example, in rapidly cooled solutions of small ions in alcohols which form glasses at low temperature. It will be shown that the dynamic characteristics of $[Cr(H_2O)_6]^{3+}$ and $[Mn(H_2O)_6]^{2+}$ in PAN, as derived from esr spectra, are closely similar to those found in the corresponding liquid monomer solutions. We find that the ligand exchange mechanisms assumed for the liquid state may very well operate in the rubber-like state.

Rotational tumbling times found in the PAN glasses are of the order of 10^{-11} to 10^{-12} sec at room temperature. This surprisingly short time scale, characteristic of liquids, suggests that in the case of the above polymeric systems, the macroscopic viscosity is not a suitable parameter to be used in the evaluation of tumbling times, according to the Debye theory.[4] The tumbling times of the embedded ions are, evidently, not affected by some of the relaxation mechanisms involved in the macroscopic viscosity. In fact, the short tumbling times found suggest that the "local environment" of the ions embedded within the solid polymer matrix is similar to that of a low molecular weight solution. An important question now arises whether the transition of the polymer from the rubber-like to the glassy state would involve changes in this "local environment." It is shown in this paper that the tumbling times are scarcely affected by the glass transition. Thus, the solution like "local environment" of the ion within the amorphous polymer is also maintained at low temperature, in the glassy state. Such amorphous polymer systems, therefore, make it possible to study the dynamic properties of ions in a solution-like environment over a rather wide range of temperatures usually not accessible to measurement in true liquid solutions.

Experimental Section

A. Materials and Preparation. Solutions of $Cr(ClO_4)_3 \cdot 6H_2O$, $Mn(ClO_4)_2 \cdot 6H_2O$, $Zn(ClO_4)_2 \cdot 6H_2O$, and $Li(ClO_4)$ in distilled acrylonitrile (AN) were prepared using the G. Frederick Smith Chemical Co. analytical salts and BDH monomer.

Bulk polymerization of these solutions was performed at 54° in glass tubes of 3-mm diameter and 20–30-cm length, according to a method developed by Oplatka, Konigsbuch, and Shavit.[5] The latter method was found to work also for very high salt concentrations, in the case of hydrated perchlorates. For example, polymerization was obtained in a solution containing 0.3 mol of $Zn(ClO_4) \cdot 6H_2O$/mol of AN. In all cases described below, a trans-

(1) J. Wong and C. A. Angell, *Appl. Spectrosc. Rev.*, **4**, 200 (1971).
(2) D. Loveridge and S. Parke, *Phys. Chem. Glasses*, **12**, 19 (1971).
(3) R. Neiman and D. Kivelson, *J. Chem. Phys.*, **35**, 156 (1961).
(4) P. Debye, "Polar Molecules," Chapter V, Dover Publications, New York, N. Y., 1929.
(5) A. Oplatka, M. Konigsbuch, and N. Shavit, *J. Polym. Sci., Part C*, **16**, 2795 (1967).

parent homogeneous amorphous solid was obtained in the form of rods 3 mm in diameter and 4–10 cm in length.

B. Glass Transition Measurements. A Perkin-Elmer dilatometer (MS-1 thermomechanical analyzer) was used to measure the glass transition (T_g). The instrument was operated in the penetration mode at a heating rate of 10°/min. The sensitivity of the instrument is 4×10^{-5} in./in. on a 10-mV recorder. The samples used for the T_g measurement were 3 mm in diameter and 5 mm in length.

C. Esr Measurements. The esr spectra were taken on a Varian E-3 X-band spectrometer and, for Q-band measurements, on a Varian E-12 spectrometer. For solid samples, g was determined relative to external DPPH. Variable temperature measurements were performed both in the X and Q bands using the Varian E-257 unit. The temperature was measured to ±1° with a thermocouple placed in the cavity next to the small solid sample. The relative intensity was measured only at X band, at room temperature, and corrections have been made for the geometry of the samples (filling factor). For liquids, the sample holder was the standard flat solution cell. To get comparable intensity measurements for series of solutions, care was taken to keep the cell in a fixed position in the cavity.

D. Magnetic Susceptibility Measurements. A motor-driven vibrating sample magnetometer (vsm) of the type described by Flanders and Doyle[6] was used to measure the magnetic susceptibility in the temperature range 77–300°K. The sensitivity of the instrument was 10^{-4} emu.

Results and Discussion

A. Rheological Properties of PAN Containing Different Amounts of Hydrated Perchlorates. It was shown previously[7] that the glass transition temperature T_g for polyacrylonitrile is a decreasing function of the $Fe(ClO_4)_2 \cdot 6H_2O$ concentration in the polymer matrix. The present measurements show that this dependence holds also for $Zn(ClO_4)_2 \cdot 6H_2O$ and $Cr(ClO_4)_3 \cdot 6H_2O$ (as well as for many other hydrated perchlorates in PAN). This is demonstrated in Table I where T_g is given for increasing concentrations of $Zn(ClO_4)_3 \cdot 6H_2O$. Samples 4 and 5 exhibit rubber-like behavior at room temperature; all samples become hard glasses when cooled below their glass transition temperature and remain transparent and optically homogeneous.

B. Esr Spectra. I. Effect of Added Diamagnetic Salts. Esr spectra at X-band frequency of solutions of $Cr(ClO_4)_3 \cdot 6H_2O$ and of $Mn(ClO_4)_2 \cdot 6H_2O$ in acrylonitrile have been observed, as well as the spectra of the corresponding polymers at the same salt concentrations. Comparison of the esr signals in solution and in the solid polymer brings to light the following features.

Cr^{3+} in solution in AN, at room temperature, at a concentration of 1.99×10^{-3} mol of $Cr(ClO_4)_3 \cdot 6H_2O$/mol of AN, gives a single Lorentzian line of width (measured from peak to peak on the derivative line) ΔH = 139 G. The Cr^{3+} in PAN, at the same conditions of concentration and temperature, exhibits a single-line spectrum. The latter is slightly asymmetric; the width ΔH = 225 G.

Mn^{2+} in AN solution at room temperature, at a concentration of 1.83×10^{-4} mol of $Mn(ClO_4)_2 \cdot 6H_2O$/mol of AN shows the six typical hyperfine components, $m_I = -5/2, -3/2, -1/2, 1/2, 3/2, 5/2$. The hyperfine constant $\langle A \rangle$ is 91.5 G and the width of line $m_I = 1/2$ (fourth line) is ΔH = 32.5 G. The PAN having the same Mn^{2+} concentration also exhibits the six hyperfine component spectrum. The latter, however, is broadened and highly distorted, with forbidden transition lines also appearing at room temperature. The hyperfine constant $\langle A \rangle$ = 92 G, and ΔH of the fourth line is 65 G.

When increasing amounts of diamagnetic salt, $Li(ClO_4)$ or $Zn(ClO_4)_2 \cdot 6H_2O$, are added to a given $Cr(ClO_4)_3 \cdot 6H_2O$ solution in AN, one observes a decrease in the intensity of the Cr^{3+} esr signal. Similar results are obtained in the case of the Mn^{2+} solution upon addition of $Zn(ClO_4)_2 \cdot 6H_2O$. The intensity is evaluated by $\Delta H^2 \times h$, when ΔH is the width and h is the height of the derivative line, from peak to peak. The same type of behavior is also observed when the diamagnetic salt is added to the corresponding polymer systems. The results both for the solutions and for the polymers are shown in Figure 1 (for Mn^{2+} in the presence of $Zn(ClO_4)_2 \cdot 6H_2O$) and in Figure 2a and b (for Cr^{3+} in the presence of $Zn(ClO_4)_2 \cdot 6H_2O$ and $Li(ClO_4)$). In the above figures the normalized signal intensity is plotted *vs.* diamagnetic salt concentration. As can be seen in Figure 2, the effects of Zn and Li salts are similar on a molar basis.

It is worth noticing that in all cases addition of the diamagnetic salt produces a decrease in the intensity without affecting the line width. In the case of both Cr^{3+} and Mn^{2+}, the esr line shape is governed by zero-field splitting (zfs). The decrease in intensity upon addition of diamagnetic salt is analogous to that found by Luz, *et al.*, in Mn^{2+} complexes in methanol[8] and Fe^{3+} in aqueous solutions.[9] They suggest a mechanism of ligand exchange which produces asymmetric species with a zfs large enough to make the esr spectrum too broad to be detectable. Therefore, the total paramagnetic signal is reduced in intensity. In our case, the same interpretation could hold for the monomer solutions. This interpretation should, however, be applied with caution when dealing with the corresponding polymer systems. The similar behavior of both the monomer and polymer systems seen in Figures 1 and 2 should not necessarily lead to the conclusion that a dynamic ligand exchange mechanism takes place also in the case of the polymer system. The effect of the added diamagnetic salt would evidently be the same if the distribution of the paramagnetic ions between symmetric and asymmetric complexing states would be frozen in, with no dynamic exchange taking place in the system. It is reasonable to expect that in the rubber-like state, dynamic ligand exchange processes may occur, while in the glassy state, the distribution of the complexing states may be frozen in. Supporting evidence for the existence of translational freedom in the rubber-like state could be obtained from leaching experiments with water; the salt components were found to migrate from the polymer matrix into the external aqueous phase.

According to Figures 1 and 2, the decrease in the relative intensity, due to the diamagnetic salt added, is more pronounced in the polymer system than in the corresponding monomer solution. It will be noticed that the concentrations in Figure 2 are given in moles of salt per mole of monomer unit. Comparison of the data on the basis of volume concentrations would give a smaller discrepancy between the monomer and polymer systems, but could not fully account for the existing discrepancy. The

(6) P. J. Flanders and W. D. Doyle, *Rev. Sci. Instrum.*, **33**, 691 (1962).
(7) S. Reich and I. Michaeli, *J. Chem. Phys.*, **56**, 2350 (1972).
(8) H. Levanon and Z. Luz, *J. Chem. Phys.*, **49**, 2031 (1968).
(9) H. Levanon, G. Stein, and Z. Luz, *J. Chem. Phys.*, **53**, 876 (1970).

TABLE I

No.	$Cr(ClO_4)_3 \cdot 6H_2O$, mol/mol of AN	$Zn(ClO_4)_2 \cdot 6H_2O$, mol/mol of AN	T at maximum X band, °K	T_g, °K	ΔT at Q band, °K	Data at 330°K: ΔH_X, G	ΔH_Q, G	$\Delta \times 10^3$, cm^{-1}	$\tau \times 10^{12}$, sec
1	5.55×10^{-3}	0	305	335	250–340	213.5	80.0	95.6	4.98
2	5.55×10^{-3}	4.43×10^{-3}	330	...	260–305	237.0	75.0	95.2	5.92
3	5.55×10^{-3}	6.2×10^{-2}	305	...	240–288	206.0	71.5	91.4	5.40
4	5.55×10^{-3}	9.77×10^{-2}	300	263	245–267	...	...	...	...
5	5.55×10^{-3}	2.15×10^{-1}	303	250	240–270	201.0	66.0	88.8	5.70

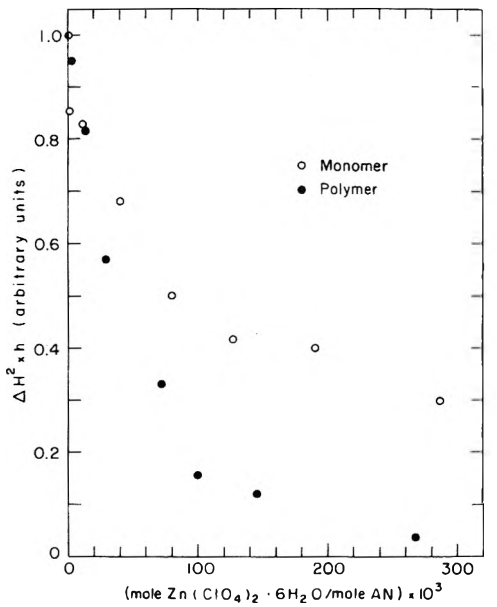

Figure 1. Normalized Mn^{2+} esr signal intensity as a function of $Zn(ClO_4)_2 \cdot 6H_2O$ concentration; mol of $Mn(ClO_4)_2 \cdot 6H_2O$/mol of AN = 1.83×10^{-4}.

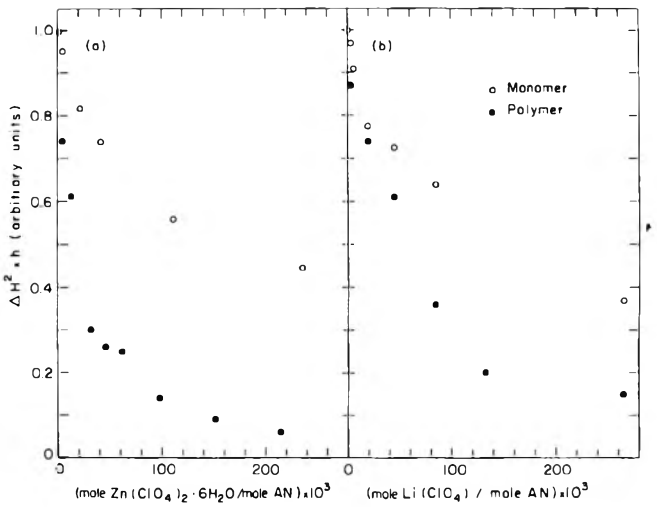

Figure 2. (a) Normalized Cr^{3+} esr signal intensity as a function of $Zn(ClO_4)_2 \cdot 6H_2O$ concentration; mol of $Cr(ClO_4)_3 \cdot 6H_2O$/mol of AN = 5.55×10^{-3}. (b) Normalized Cr^{3+} esr signal intensity as a function of $Li(ClO_4)$ concentration; mol of $Cr(ClO_4)_3 \cdot 6H_2O$/mol of AN = 1.99×10^{-3}.

nature of the species responsible for the esr signal both in the monomer and polymer systems is assumed to be the hydrated paramagnetic ion. The strong complexing tendency of water especially to Cr^{3+} is well known.[10] We find that the only way to introduce a large number of water molecules into the monomer solution or into the solid polymer is to increase the salt concentration of the system. In fact, the maximum amount of water that can be added to the monomer solution is linear in the concentration of the paramagnetic ions; the increase in water solubility is found to be 16 mol of water per mole of hydrated chromium perchlorate, and 8 mol of water per mole of the hydrated manganese perchlorate.

A number of nmr spectra were also taken for the polymer system. As could be expected from the above considerations, the water signal could not be detected in PAN containing Cr^{3+} or Mn^{2+} (as well as Co^{2+} or Ni^{2+}), while in the case of $Zn(ClO_4)_2 \cdot 6H_2O$ the water signal could be clearly seen (Figure 3). This may serve as additional evidence to the strong interaction of water with the paramagnetic ion.

This hydrated symmetric complex exchanges ligands to form asymmetric species. The nature of the latter is unknown, but the resulting effect on the esr spectrum is strongly dependent on the perchlorate concentration. This means that in spite of the very low complexing tendency of ClO_4^- ion, it takes part in the ligand arrangement at the rather high perchlorate concentrations used.

II. Temperature Studies. (1) Cr^{3+} in PAN. We would like to have an estimate of the rotational tumbling time or some other correlation time characterizing the dynamics of the paramagnetic complex within the solid matrix. In the case of Cr^{3+} in fluid solution, the dominant relaxation mechanism was assumed to arise from the coupling of the zfs of the spin multiplet with the random tumbling of the molecules in the system.[11] The correlation time is affected by the intensive parameters of the system, such as temperature or viscosity. We performed a systematic study of the esr line shape as a function of temperature in PAN at a fixed low concentration of $Cr(ClO_4)_3 \cdot 6H_2O$ and varying concentrations of $Zn(ClO_4)_2 \cdot 6H_2O$. This was done both at X-band and Q-band frequencies ($\omega_X = 0.58 \times 10^{11}$ radians/sec, $\omega_Q = 2.2 \times 10^{11}$ radians/sec). A typical spectrum at X-band of a solid polymer sample containing 5.55×10^{-3} mol of $Cr(ClO_4)_3 \cdot 6H_2O$/mol of AN and 2.15×10^{-1} mol of $Zn(ClO_4)_2 \cdot 6H_2O$/mol of AN (at two temperatures, 133 and 353°K) is presented in Figure 4. It should be noticed that the esr line is asymmetric at low temperature, while this asymmetry vanishes upon heating. The variation of the line width as a function of reciprocal temperature for different concentrations of $Zn(ClO_4)_2 \cdot 6H_2O$ is presented in Figures 5a and b.

At the X-band frequency the following features are observed. (a) The line width passes through a maximum for all samples at about 300°K. Line width variation with

(10) J. P. Hunt and R. A. Plane, *J. Amer. Chem. Soc.*, **76**, 5960 (1954).
(11) A. Carrington and G. R. Luckhurst, *Mol. Phys.*, **8**, 125 (1964).

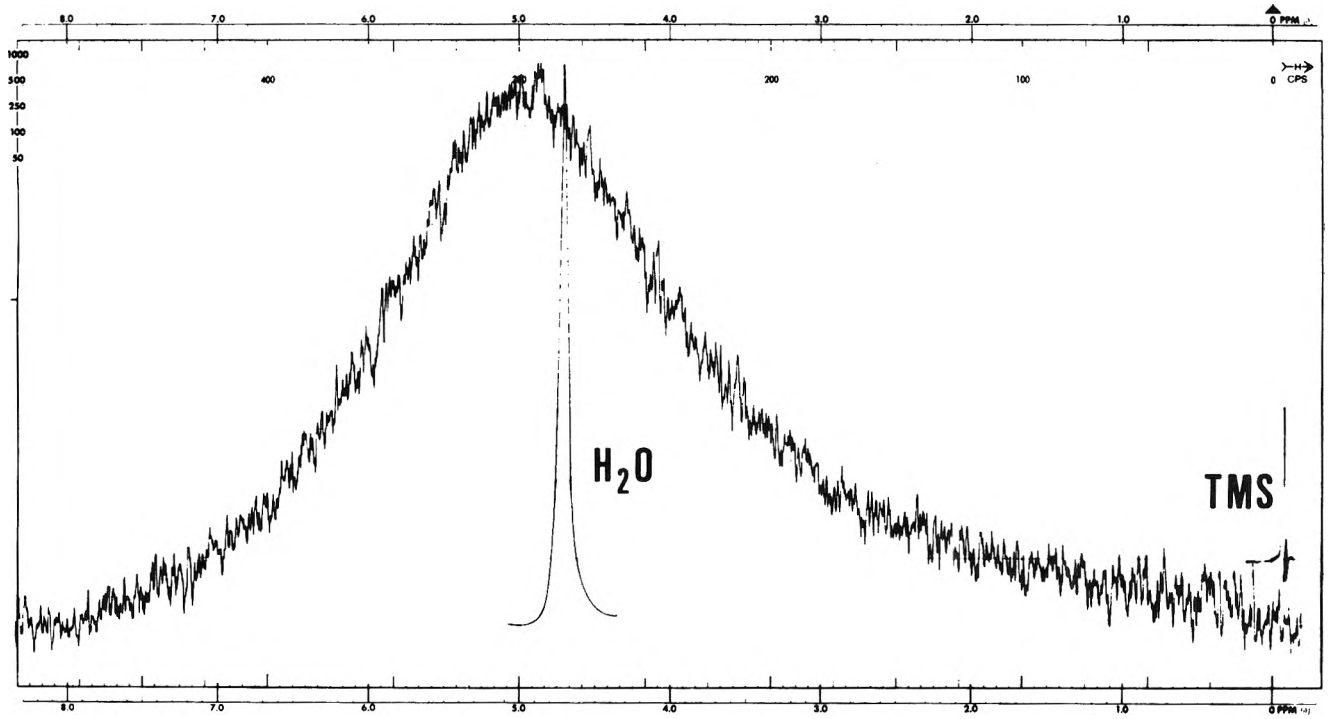

Figure 3. Nmr spectrum of $Zn(ClO_4)_2 \cdot 6H_2O$ in PAN; mol of $Zn(ClO_4)_2 \cdot 6H_2O$/mol of AN = 2.26×10^{-1}.

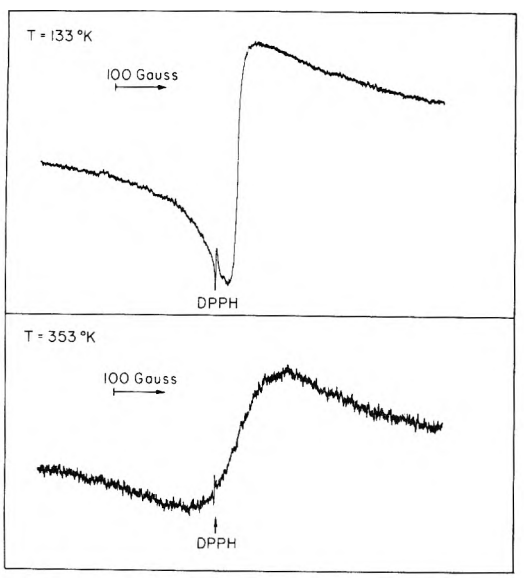

Figure 4. Esr signal of $Cr(ClO_4)_3 \cdot 6H_2O$ in a sample of PAN containing $Zn(ClO_4)_2 \cdot 6H_2O$, at 133°K and at 353°K; mol of $Cr(ClO_4)_3 \cdot 6H_2O$/mol of AN = 5.55×10^{-3}; mol of $Zn(ClO_4)_2 \cdot 6H_2O$/mol of AN = 2.15×10^{-1}.

composition at this temperature is small. (b) As temperature decreases, a sharp line narrowing is observed. This narrowing is more drastic at higher concentration of $Zn(ClO_4)_2 \cdot 6H_2O$.

At the Q band frequency we observe the following. (a) The Q-band line is narrower than the X-band line, at corresponding temperature and composition. (b) The overall trend in the variation of the line width with temperature and composition is analogous to that observed at X-band frequency. However, a shoulder appears at temperatures around the glass transition temperatures of the given compositions (see Table I, column ΔT). (c) Up to the experimental limit of 370°K, at Q-band frequency, ΔH increases but no maximum is observed. This experimental temperature limit is dictated both by instrumentation and by the thermal properties of the materials (partial pyrolysis and decomposition at high temperatures).

The electronic relaxation of solvated $Cr^{3+}(d^3)$ $S = 3/2$ is believed to be governed by modulation of the quadratic zero field splitting (zfs) interaction.

$$\mathcal{H}_{zfs} = D[S_z^2 - S(S+1)/3] + E(S_x^2 - S_y^2)$$

where D and E are the quadratic zfs parameters. The time-dependent modulation in solutions of the solvated chromium ion probably arises from rotational Brownian tumbling or from temporary deviations from spherical symmetry of the solvation shell around the paramagnetic ion, due to collisions with solvent molecules.[12] In the case of Cr^{3+} ion, the esr spectrum is composed of two Lorentzian lines arising from the transitions ($+1/2 \rightarrow -1/2$) and ($3/2 \rightarrow 1/2$, $-1/2 \rightarrow -3/2$) which have a common center of gravity. The half-width for those transitions is given by the following equations[11]

$$\frac{1}{T_{2(1/2,\,-1/2)}} = \frac{6}{5}\Delta^2[\tau/(1+\omega^2\tau^2) + \tau/(1+4\omega^2\tau^2)] \quad (1)$$

$$\frac{1}{T_{2\substack{(-1/2,\,-3/2)\\(3/2,\,1/2)}}} = \frac{6}{5}\Delta^2[\tau + \tau/(1+\omega^2\tau^2)] \quad (2)$$

where Δ^2 is the trace of the square zfs tensor (in the case of axial field $E = 0$, and $\Delta^2 = 2/3D^2$), τ is the correlation time for modulation of the zfs, and ω is the Larmor frequency of the electron. $1/T_2$ is related to the measured peak to peak width ΔH by

$$1/T_2 = (\sqrt{3}/2)\Delta H$$

It is apparent from the above equations that for high values of τ, line 2 is smeared out, and only line 1 is ob-

(12) H. Levanon, S. Charbinsky, and Z. Luz, *J. Chem. Phys.*, **53**, 3056 (1970).

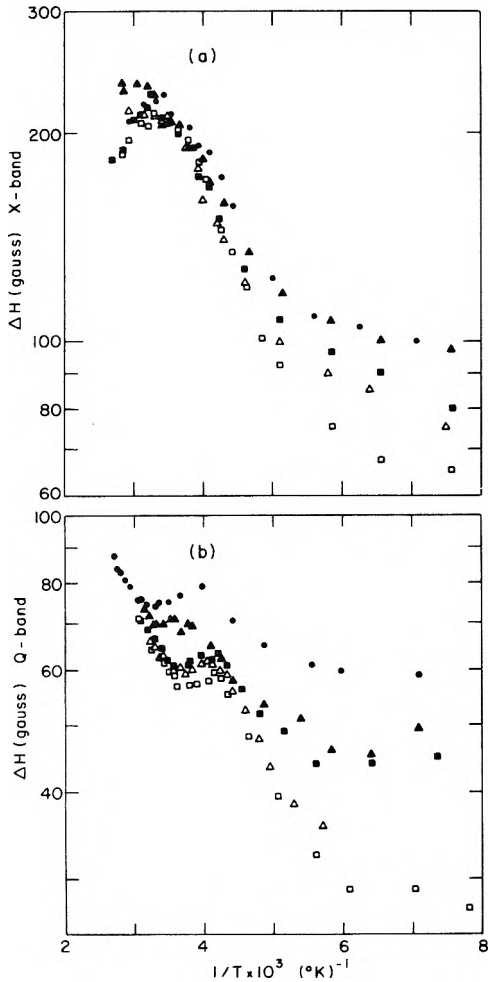

Figure 5. (a) Esr line width at X band of Cr^{3+} signal as a function of reciprocal temperature in PAN containing varying concentrations of $Zn(ClO_4)_2 \cdot 6H_2O$; mol of $Cr(ClO_4)_3 \cdot 6H_2O$/mol of AN = 5.55 × 10^{-3}. Concentrations (mol of $Zn(ClO_4)_2 \cdot 6H_2O$/mol of AN): ●, 0; ▲, 4.43 × 10^{-3}; ■, 6.2 × 10^{-2}; △, 9.77 × 10^{-2}; □, 2.15 × 10^{-1}. (b) Same at Q band.

served. Line 1 should pass through a maximum at $\omega\tau \simeq 1$. Experimentally, we observe a maximum in ΔH *vs.* $1/T$ at X-band frequency. At this maximum, we find $\tau \simeq 1.7 \times 10^{-11}$ sec. In the vicinity of $\omega\tau \simeq 1$ the line width is strongly dependent on ω. At Q-band frequency the maximum is expected at a lower value of τ, because $\omega_Q/\omega_X \simeq 4$, *i.e.*, at a higher temperature, since the trend of the variation of τ is that of the reciprocal of temperature. We suggest that this maximum was not reached because it should occur at a temperature that is higher than our experimental limit. It is of interest to note the similarity between our experimental results (Figure 5a,b) and the theoretically expected behavior of ΔH *vs.* τ as shown in ref 12, Figure 5 top. This similarity is apparent both in the trend of variation of ΔH *vs.* $1/T$ and in the sharp decrease in ΔH when going from X-band to Q-band. For $\omega\tau < 1$, in the vicinity of the maximum, that is for the quite narrow range of temperatures to the left of the X-band maximum, we use the approach presented in ref 12 to calculate τ and Δ from the ratio of the line width measured at two frequencies, $\Delta H_X/\Delta H_Q$. In this range $\tau\Delta < 1$, and the theory is valid. In Table I, Δ and τ are calculated for all the samples at a temperature of 330°K. As can be seen, the polymer system is characterized by surprisingly short

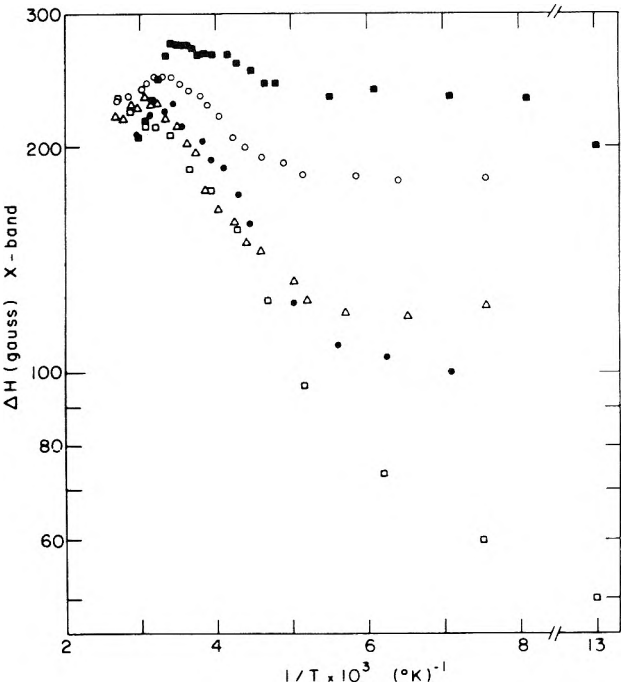

Figure 6. Esr line width at X band of Cr^{3+} signal in PAN as a function of reciprocal temperature at various Cr^{3+} concentration (mol of $Cr(ClO_4)_2 \cdot 6H_2O$/mol of AN): □, 2.22 × 10^{-3}; ●, 5.57 × 10^{-3}; △, 1.48 × 10^{-2}; ○, 2.96 × 10^{-2}; □, 4.45 × 10^{-2}.

correlation times, of the order of 10^{-11} to 10^{-12} sec. The calculated values of τ and Δ and the measured line width of the Cr^{3+} ion signal are of the same order of magnitude as those measured in solutions.[12] Therefore we are inclined to suggest that though we deal with a solid system the behavior of the solvated chromium ion incorporated in the polymer matrix is that found in its solutions.

At lower temperatures, to the right of the maximum in Figure 5a, that is for $\omega\tau > 1$, we observe a sharp decrease in ΔH *vs.* T^{-1}. A similar behavior was observed by Burlamacchi[13] in solutions of Mn^{2+} and Fe^{3+} in various solvents. Such a decrease is indeed predicted by the above theory. It should be realized, however, that in this range $\tau\Delta$ approaches unity. The application of the theory is therefore doubtful, and a mechanism other than the modulation of the zfs parameter may take over at lower temperatures.

As pointed out previously, the line width at low temperature decreases with increasing concentration of the diamagnetic salt. This effect may be due to Cr–Cr interaction. The tendency of Cr^{3+} ions in solid solutions and glasses to form pairs is well known,[14,15] and the above observation can be explained as a magnetic dilution caused by the addition of the diamagnetic salt. To test the Cr–Cr interaction, we performed a study of ΔH *vs.* $1/T$ in PAN containing varying concentrations of $Cr(ClO_4)_3 \cdot 6H_2O$. The results are presented in Figure 6. Indeed, a broadening of the esr signal is observed with increasing Cr^{3+} concentration. This behavior is prominent at low temperature and is in line with the temperature effect seen in Figure 5a. The existence of Cr–Cr pairs should manifest itself in magnetic susceptibility measurements, since the effective molar magnetic moment (μ_m) should decrease with pair

(13) L. Burlamacchi, *J. Chem. Phys.*, **55**, 1205 (1971).
(14) D. E. O'Reilly and D. S. MacIver, *J. Phys. Chem.*, **66**, 276 (1962).
(15) R. J. Londry, J. T. Fournier, and C. G. Young, *J. Chem. Phys.*, **46**, 1285 (1967).

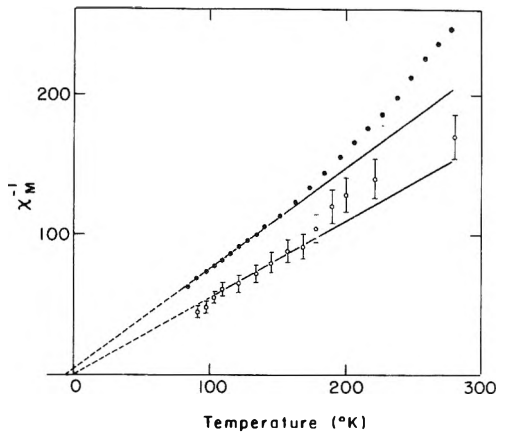

Figure 7. Reciprocal molar susceptibility as a function of temperature (mol of $Cr(ClO_4)_3 \cdot 6H_2O$/mol of AN): ●, 4.44 × 10^{-2}; O, = 5.55 × 10^{-3}.

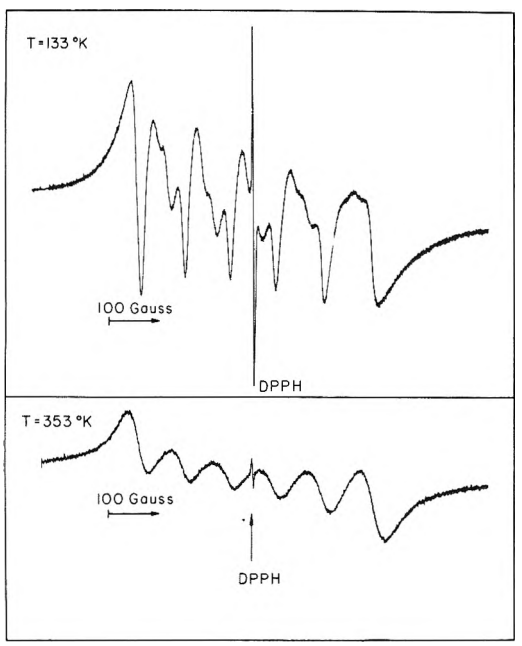

Figure 8. Esr signal of $Mn(ClO_4)_2 \cdot 6H_2O$ in a sample of PAN containing $Zn(ClO_4)_2 \cdot 6H_2O$ at 133 and 353°K; mol of $Mn(ClO_4)_2 \cdot 6H_2O$/mol of AN = 1.83 × 10^{-4}; mol of $Zn(ClO_4)_2 \cdot 6H_2O$/mol of AN = 1.42 × 10^{-1}.

formation. This is indeed confirmed experimentally (Figure 7). At low temperature the magnetic susceptibility approaches the Curie–Weiss behavior, and the value of μ_m is derived from the slope of reciprocal susceptibility *vs.* temperature. We find for the "low concentration" case (5.55 × 10^{-3} mol of Cr^{3+}/mol of AN), μ_m = 3.83 ± 0.18, and for the high concentration, (4.44 × 10^{-2} mol of Cr^{3+}/mol of AN), μ_m = 3.36 ± 0.02.[16] The extrapolated Weiss constant is 0 ± 3°K for the "low concentration" and −6 ± 2°K for "high concentration." The lower value of μ_m for higher salt concentrations and the deviation from linearity at high temperature indicate the existence of a Cr–Cr interaction. It should also be pointed out that in all experiments presented in Figure 6, Cr^{3+} to water ratio is kept constant; thus variation of line width with composition at a constant temperature would strongly suggest a homogeneous solid solution phase for the system rather than a microphase separated system.

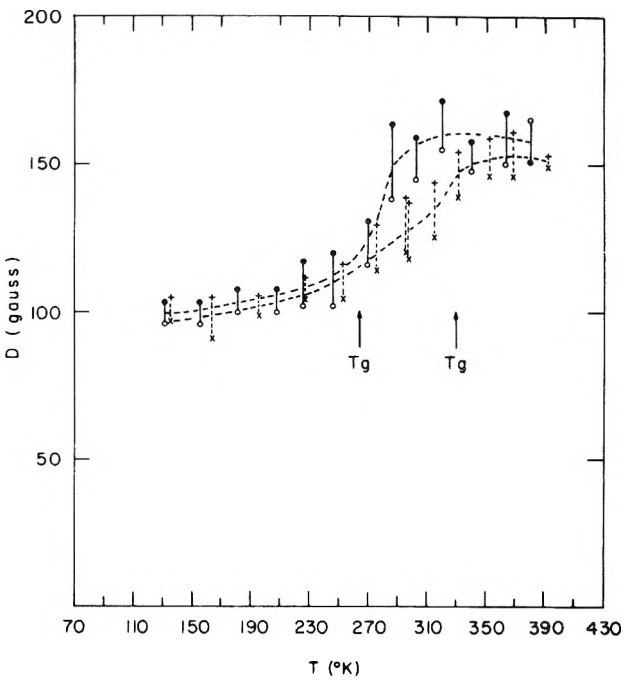

Figure 9. Variation of *D* parameter with temperature for $Mn(ClO_4)_2 \cdot 6H_2O$; mol of $Mn(ClO_4)_2 \cdot 6H_2O$/mol of AN = 1.83 × 10^{-4}. (1) Mol of $Zn(ClO_4)_2 \cdot 6H_2O$/mol of AN = 1.42 × 10^{-1}: ●, *D* calculated from $I_{5/2}/I_{3/2}$; O, *D* calculated from $I_{5/2}/I_{1/2}$, T_g = 265°K. (2) Mol of $Zn(ClO_4)_2 \cdot 6H_2O$/mol of AN = 1.73 × 10^{-2}: +, *D* calculated from $I_{5/2}/I_{3/2}$; ×, *D* calculated from $I_{5/2}/I_{1/2}$; T_g = 330°K.

(2) Mn^{2+} in PAN. The variation of esr line shape with temperature was measured in PAN containing $Mn(ClO_4)_2 \cdot 6H_2O$ and varying concentrations of $Zn(ClO_4)_2 \cdot 6H_2O$. A typical spectrum at 133°K and at 353°K for a system containing 1.83 × 10^{-4} mol of Mn^{2+}/mol of AN and 1.42 × 10^{-1} mol of Zn^{2+}/mol of AN is presented in Figure 8. At low temperature the spectrum is highly asymmetric and consists of a hyperfine sextet, with forbidden transitions showing up between each pair of the sextet. At high temperature the hyperfine components broaden and the forbidden transitions disappear. The hyperfine splitting is $\langle A \rangle$ = 92 G. This value of $\langle A \rangle$ is rather typical of an octahedrally coordinated manganous ion.[17]

Due to the high complexity of the observed Mn^{2+} spectra we could not derive the zfs parameters by a method similar to that used for Cr^{3+} in PAN. We followed therefore a method developed by Allen[18] which allows the derivation of zfs parameters for Mn^{2+} incorporated in glassy media from the relative intensities of the esr hyperfine components; zfs values are calculated both from the ratio $I_{5/2}/I_{1/2}$ and from $I_{5/2}/I_{3/2}$ for the case of an axial zero field splitting term *D* in the spin Hamiltonian.[19] Figure 9 presents *D* as a function of temperature for PAN containing 1.83 × 10^{-4} mol of $Mn(ClO_4)_2 \cdot 6H_2O$/mol of AN, at two concentrations of incorporated $Zn(ClO_4)_2 \cdot 6H_2O$.

In both cases *D* increases with temperature, following an S-shaped curve. Measured values of the glass transition temperature for these systems are indicated in the

(16) The theoretical μ_m calculated according to the formula $\mu_m = [n(n+2)]^{1/2}$ where *n* is the number of unpaired electrons is μ_m = 3.87.
(17) S. I. Chan, B. M. Fung, and H. Lütje, *J. Chem. Phys.*, **47**, 2121 (1967).
(18) B. T. Allen, *J. Chem. Phys.*, **43**, 3820 (1965).
(19) In the case of $[Cr(H_2O)_6]^{3+}$ axial symmetry was not assumed.

figure. They roughly coincide with the inflection points of the curves. A similar result was found by Allen[18] in the case of Mn^{2+} in glassy methanol.

Conclusions

$[Cr(H_2O)_6]^{3+}$ and $[Mn(H_2O)_6]^{2+}$ ions embedded in a polymeric matrix of PAN behave in many respects like true liquid solutions. This is manifested both in the ligand exchange mechanism and in the surprisingly short correlation times $\sim 2 \times 10^{-11}$ sec at room temperature. The mechanism for the modulation of the zfs is probably due to rotational tumbling of $[Cr(H_2O)_6]^{3+}$ and $[Mn(H_2O)_6]^{2+}$ ions in the polymeric matrix. The esr method of studying the dynamics of these ions observes only the effects of the very close vicinity of the paramagnetic species, and to a first approximation does not reflect the macroscopic rheological properties of the systems. The Debye formula which correlates the viscosity η to the tumbling time τ_c is

$$\eta = \tau_c 3kT/4\pi a^3$$

where a is the radius of the hydrated complex ($a \simeq 3$ Å for $[Cr(H_2O)_6]^{3+}$). Its application in our system leads to a viscosity of 6×10^{-3} P. This is many orders of magnitude smaller than the macroscopic value in glasses or rubber-like systems, and reflects the "local viscosity." Also, the glass transition, which is accompanied by a drastic change in the macroscopic viscoelastic parameters, is only weakly reflected in the esr line shape.

There is strong evidence for Cr–Cr interactions in the polymeric matrix. Such interactions probably lead to the formation of Cr pairs, a phenomenon that was previously found in solid solutions. The interaction is concentration dependent and may be the main factor that determines the esr line width at low temperature.

The fact that the esr line shape of $[Cr(H_2O)_6]^{3+}$ in PAN is concentration dependent when the Cr^{3+} to water ratio is kept constant points to the conclusion that we deal with a true solid solution and not with a microphase separated system. In conclusion we would like to suggest that PAN is a good matrix for the study of esr spectra of small ions in a solution-like environment over a wide temperature range.

Acknowledgment. We wish to thank Mrs. T. Robinson for very careful and tedious work in preparing the samples and for many helpful suggestions.

Raman Spectra of Zirconium(IV) Fluoride Complex Ions in Fluoride Melts and Polycrystalline Solids

L. M. Toth,* A. S. Quist, and G. E. Boyd

Oak Ridge National Laboratory, Oak Ridge, Tennessee 37830 *(Received January 15, 1973)*

Publication costs assisted by the Oak Ridge National Laboratory

Raman spectrum measurements were performed with molten LiF–NaF–ZrF_4 mixtures at 650° in an investigation of the coordination chemistry of zirconium(IV) in alkali metal fluoride melts. The spectra of several $M_xZr_yF_{4y+x}$ polycrystalline compounds were also examined to assess the utility of using crystalline spectra as a means of identifying species present in molten fluoride solution. Octahedral coordination for Zr(IV) in a 31–36–33 mol % LiF–NaF–ZrF_4 melt was established by comparing its Raman spectrum with that of crystalline Li_2ZrF_6 where X-ray diffraction measurements have shown the presence of unbridged ZrF_6^{2-} ions. The occurrence of eight-, seven-, and five-coordinated zirconium in molten fluoride was inferred from frequency shifts accompanying changes in "free" fluoride ion concentration caused by varying the mole per cent ZrF_4.

Introduction

The occurrence of a variety of discrete complex ions formed by magnesium and by cadmium in alkali metal halide melts has been inferred from recent measurements of the Raman and infrared spectra of these systems.[1] The relative concentrations of the complex ions and the equilibria between them has been shown to depend on the amount of alkali metal halide present. Studies of equilibria in fluoride melts between species of differing coordination number using vibrational spectroscopy have not been reported, however.

Several different alkali metal fluorozirconate complexes are known in the crystalline compounds $M_xZr_yF_{4y+x}$. Octahedral, six coordination occurs in Cs_2ZrF_6,[2] Rb_2ZrF_6,[2] and Li_2ZrF_6.[3] Seven coordination is found in $(NH_4)_3ZrF_7$,[4] and Na_3ZrF_7;[5] and eight coordination is ob-

(1) (a) V. A. Maroni, E. J. Hathaway, and E. J. Cairns, *J. Phys. Chem.*, 75, 155 (1971); (b) J. H. R. Clarke, P. J. Hartley, and Y. Kuroda, *J. Phys. Chem.*, **76**, 1831 (1972).
(2) V. H. Bode and G. Teufer, *Z. Anorg. Chem.*, **283**, 18 (1956).
(3) R. Hoppe and W. Dahne, *Naturwissenschaften*, **47**, 397 (1960).
(4) H. J. Hurst and J. C. Taylor, *Acta Crystallogr., Sect. B*, **26**, 417 (1970).

served in K_2ZrF_6,[6] $Na_7Zr_6F_{31}$,[7] and ZrF_4.[8] All of these coordination numbers are found in $Rb_5Zr_4F_{21}$,[9] which contains four crystallographically independent ions. Aqueous and molten salt solution measurements have proved to be less definitive for the identification of zirconium complexes. Only ZrF_6^{2-} ions were reported to exist in aqueous solutions as a result of Raman,[10] nmr,[11] and other techniques, whereas infrared studies[12] on molten LiF-KF-ZrF_4 and NaF-KF-ZrF_4 indicated a band near 480 cm^{-1} possibly from a single zirconium complex. Evaluation of surface tension measurements with LiF-KF-ZrF_4 and LiF-NaF-ZrF_4 melts at several temperatures indicated the presence of ZrF_7^{3-} in both salt mixtures with some ZrF_5^- ion also reported in the latter.[13a] However, interpretation of these measurements in terms of complex ion formation has been questioned.[13b]

Despite the uncertainties cast on previous experiments with molten fluorides, the X-ray crystal data and experience with other halide melts suggest that an equilibrium between several coordination species of zirconium could exist. Because the interaction of Zr^{4+} with the solvent to form complex ions is effective in reducing the concentration of available fluoride ions in solution, the coordination number of the zirconium complexes determines the extent of the effect. Molten mixtures of LiF-BeF_2 have found application in the molten salt reactor experiment, MSRE, where ZrF_4 is added as a scavenger for oxide impurity. This, therefore, is the practical importance of understanding coordination behavior of zirconium in fluoride melts.

A method frequently employed in the past for establishing the existence of a complex ion in a molten salt has been to compare melt spectra with those of crystalline compounds where presumably the same species exists. Unfortunately, this method is often subject to important limitations, especially when the species possess more than five atoms, or are of low symmetry. In these cases there are many bands in the crystal and melt which often cannot be matched, and there are frequency shifts which cannot be explained. Complications of this type are found with zirconium(IV) fluorides where coordination numbers greater than six are common in the crystalline state and are expected also in molten fluoride mixtures. However, the frequency of the symmetric stretching vibration may be used to distinguish between complexes which differ only in coordination number. The limitations of this method are examined in this paper by comparing the Raman spectra of several zirconium fluorides. The method is then used within its recognized limitations to examine the coordination chemistry of Zr(IV) in the molten LiF-NaF-ZrF_4 system.

Experimental Section

The advantages of windowless cells for laser Raman spectroscopy of melts which are corrosive toward the usual optical window materials have been described.[14,15] These cells were contained in a furnace[16] which was positioned in the sample chamber of a Jarrell-Ash 25-300 Raman spectrometer; 4880-Å radiation from an argon ion laser (Coherent Radiation Laboratories Model 52B) was used to excite the spectra. The scattered light collection system and sample handling techniques have been described.[14-16]

Polycrystalline fluorozirconate compounds were prepared by mixing stoichiometric amounts of alkali metal fluoride salt with ZrF_4 and melting in a platinum crucible using a simple resistance furnace. Since zirconium melts hydrolyze readily when exposed to the atmosphere, the above procedure was performed in a helium-filled glove box of <1 ppm of H_2O and O_2 content. It was possible to melt, stir, and quench the samples with the formation of only a minimum amount (<1 mol %) of oxide. Using this technique, it was also possible to fill Raman cells prior to sealing in quartz ampoules. A great improvement in the quality of the spectra was obtained by performing the cell loadings within the glove box.

The melts studied were prepared from Harshaw LiF and NaF crystal fragments which had been purified by HF-H_2 sparging to remove oxide impurities. The ZrF_4 was in the form of single crystal fragments with <50 ppm of oxide content prepared from triply sublimed reagent grade material.

The melt composition was dictated by the volatility of the ZrF_4. Melts containing more than 25 mol % ZrF_4 had volatile components at temperatures greater than 600°[17] which reacted with the silica capsule enclosing the Raman windowless cell and ultimately contaminated the melt with oxide. To minimize the problem of etching, a combination of two alkali metal fluorides was used to give a mixture melting at less than 550° for *ca.* 40 mol % ZrF_4 concentrations. The ternary system, LiF-NaF-ZrF_4, with a LiF-NaF mole ratio of 0.465/0.535 had the lowest melting points and was used.[18] Even with the low (550°) melting point of the 40 mol % ZrF_4 solution, there was only a period of 1 hr during which spectra could be taken before the silica capsule was attacked. This complication precluded the study of higher ZrF_4 concentrations or measurements in other alkali metal fluoride systems which melted at considerably higher temperatures.

Results and Discussion

Crystalline Spectra. The Raman spectra of several crystalline alkali metal fluoride-zirconium tetrafluoride compounds with known crystal structures were examined to determine under what conditions the frequency position of the symmetric stretching vibration could be useful for identifying species present in melts. Initially, it was anticipated that the frequency of the symmetric stretching vibration could be measured for several crystalline compounds of different coordination number and then used to identify the coordination number of species present in melts. The crystalline systems did not prove to be so generally useful, as will be illustrated by the spectra of Li_2ZrF_6, Na_3ZrF_7, and K_2ZrF_6 of Figure 1.

The compound Li_2ZrF_6 contains free ZrF_6^{2-} ions where the fluoride ions are octahedrally coordinated to zirconi-

(5) L. A. Harris, *Acta Crystallogr.*, **12**, 172 (1959).
(6) H. Bode and G. Teufer, *Acta Crystallogr.*, **9**, 929 (1956).
(7) J. H. Burns, R. D. Ellison, and H. A. Levy, *Acta. Crystallogr., Sect. B*, **24**, 230 (1968).
(8) R. D. Burband and F. N. Bensey, Jr., Oak Ridge Gaseous Diffusion Plant Report No. K-1280, Oct 31, 1956.
(9) G. Brunton, *Acta Crystallogr., Sect. B*, **27**, 1944 (1971).
(10) W. P. Griffith and T. D. Wickens, *J. Chem. Soc. A*, 675 (1967).
(11) P. A. W. Dean and D. F. Evans, *J. Chem. Soc. A*, 698 (1967).
(12) K. J. Wilmshurst, *J. Chem. Phys.*, **39**, 2545 (1963).
(13) (a) G. W. Mellors and S. Senderoff, *J. Electrochem. Soc.*, **111**, 1355 (1964); (b) M. A. Bredig, *J. Electrochem. Soc.*, **112**, 665 (1965).
(14) A. S. Quist, J. B. Bates, and G. E. Boyd, *J. Chem. Phys.*, **54**, 4896 (1971).
(15) A. S. Quist, *Appl. Spectrosc.*, **25**, 80 (1971).
(16) A. S. Quist, *Appl. Spectrosc.*, **25**, 82 (1971).
(17) K. A. Sense, M. J. Snyder, and R. B. Filbert, Jr., *J. Phys. Chem.*, **58**, 995 (1954).
(18) E. M. Levin, C. R. Robbins, and H. F. McMurdie, "Phase Diagrams for Ceramists," American Chemical Society, Washington, D.C., 1964, p 438.

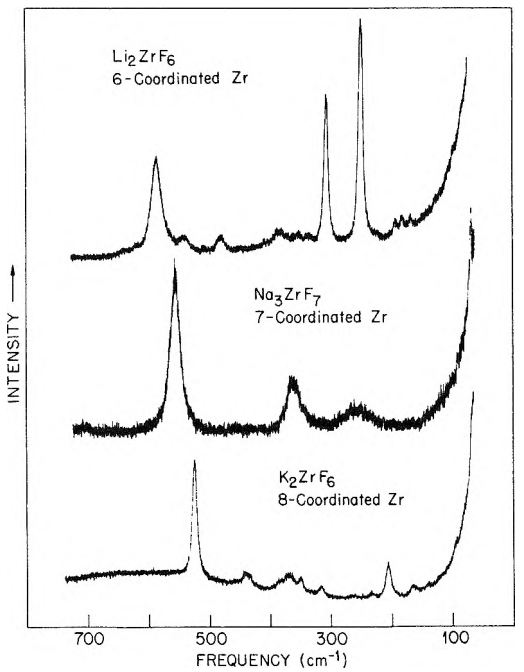

Figure 1. Raman spectra of polycrystalline Li_2ZrF_6, Na_3ZrF_7, and K_2ZrF_6 at 25°.

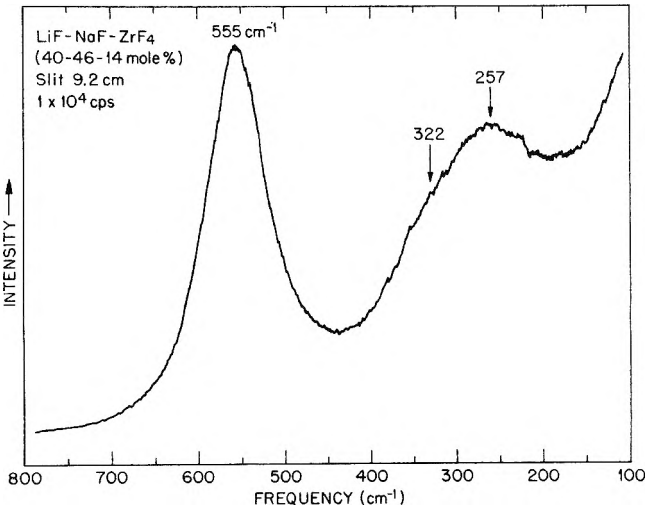

Figure 2. Raman spectrum of molten LiF–NaF–ZrF_4 (40–46–14 mol %) at 650°.

um. A complete assignment of the spectrum could be made[19] because the crystal structure and the resulting infrared and Raman spectra are particularly simple. The band at 585 cm^{-1} was assigned to the symmetric stretching mode of ZrF_6^{2-} while the two strong bands at 251 and 303 cm^{-1} were assigned to the T_{2g} mode of the octahedral ZrF_6^{2-} molecular group which splits into two components because the zirconium atom is on a site of lower symmetry. The spectrum of the ZrF_6^{2-} ion in Cs_2ZrF_6 also was measured and found to be similar to that of Li_2ZrF_6. (The spectrum of the cesium salt is not shown here.) Its symmetric stretching vibration was at 577 cm^{-1} and the splitting of the T_{2g} mode was reduced. However, there is little overall effect on the spectrum of ZrF_6^{2-} caused by changing the alkali metal cation. In addition, increasing the temperature to 570° produced a decrease in the symmetric stretching vibration of only *ca.* 7 cm^{-1}. This latter observation, of course, gives a basis for the comparison of crystal and melt spectra.

The spectrum of the ZrF_7^{3-} ion in crystalline Na_3ZrF_7 (Figure 1) has a band at 556 cm^{-1} assigned to the symmetric stretch. Although the ZrF_7^{3-} species is present in the crystal as a free complex ion, it is distorted to the extent[20] that it cannot be described by a simple geometry such as a pentagonal bipyramid which is expected to exhibit two instead of one polarized band in the region of 550 cm^{-1}. Assignments of the bands in the spectrum from such a disordered structure are, therefore, subject to much uncertainty and an unambiguous explanation for the shift of the 556-cm^{-1} band (relative to that of the 585-cm^{-1} band in Li_2ZrF_6) is impossible.

The spectrum of eight-coordinated K_2ZrF_6 (Figure 1) shows a strong band at 525 ± 1 cm^{-1} attributed to the symmetric stretching mode. The ZrF_8^{4-} complex in this case is not a free ion because fluoride ions bridge neighboring Zr^{4+} ions. The frequency difference between the 525-cm^{-1} band and that of 586 cm^{-1} for Li_2ZrF_6 has been attributed entirely to the effect of bridging.[21] However, in view of the coordination number increase and bridging, it is impossible to explain the position of the 525-cm^{-1} band as due solely to either one of these two possibilities.

Another example of a ZrF_8^{4-} bridged complex ion is found in crystalline $Na_7Zr_6F_{31}$. The Raman spectrum exhibits a strong band at 548 cm^{-1} which is assigned to the symmetric stretch. This frequency value when compared with 525 cm^{-1} for eight-coordinated zirconium in crystalline K_2ZrF_6 clearly shows that when bridging of the fluorides in the crystal occurs the frequencies of the vibrational modes cannot be predicted accurately.

Other crystalline fluorozirconates such as $Rb_5Zr_4F_{21}$ and β-Li_3ZrF_7 were examined in this study. All structures involved fluoride ion bridging between neighboring zirconium atoms. The occurrence of bridging should produce a decrease in the symmetric stretching vibration based on the premise that the formation of bridged species causes a decrease in the bond order of the individual bonds and thus a decrease in their force constants. There are exceptions,[22] however, when bridging has little (and sometimes apparently opposite) effects in crystalline systems, and it must be concluded in these instances that more complicated potential interactions are occurring than are implied by a generalized valence force field. Although it is common practice to utilize crystalline spectra in discussions of coordination chemistry in liquid systems, when bridged complex ions are present in the solid too many interfering effects occur to permit their spectra to be used as a reliable guide. Therefore, only the spectrum of octahedrally coordinated ZrF_6^{2-} from Li_2ZrF_6 or Cs_2ZrF_6 will be useful in the melt study.

Melt Spectra. The Raman spectrum of molten LiF–NaF–ZrF_4 (40–46–14 mol %) at 650° (Figure 2) exhibits a strong polarized band at 555 cm^{-1} and a broad depolarized band at 257 cm^{-1} with a shoulder at *ca.* 322 cm^{-1}. A large excess of alkali metal fluoride was present in this melt to minimize fluoride ion bridging between zirconium-containing complex ions. Therefore, the spectrum is presumed to arise from a free ZrF_x^{4-x} species.

The frequency of the strong polarized band remains constant as the ZrF_4 content of the melt is increased from

(19) L. M. Toth and J. B. Bates, results to be published.
(20) W. H. Zachariasen, *Acta Crystallogr.*, **1**, 265 (1948).
(21) A. P. Lane and D. W. A. Sharp, *J. Chem. Soc. A*, 2942 (1969).
(22) J. H. R. Clarke, P. J. Hartley, and Y. Kuroda, *J. Phys. Chem.*, **76**, 1831 (1972).

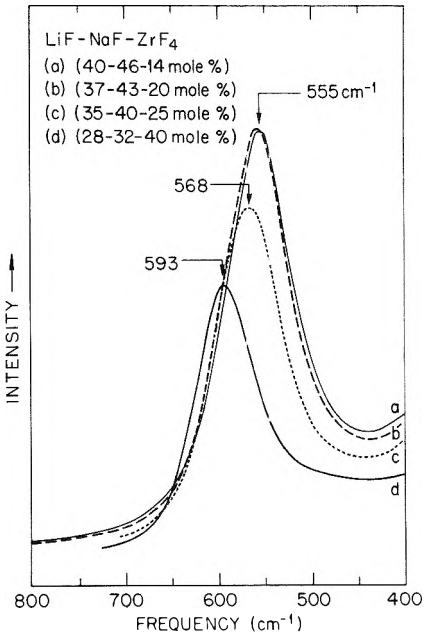

Figure 3. Band profiles of 500–600-cm^{-1} region in the Raman spectrum of LiF–NaF–ZrF_4 melts with respective concentrations (a) 40–46–14 mol %, 650°; (b) 37–43–20 mol %, 650°; (c) 35–40–25 mol %, 650°; (d) 28–32–40 mol %, 550°.

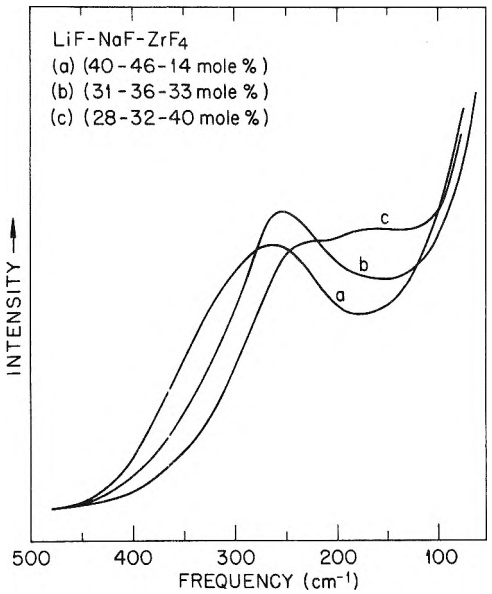

Figure 4. Band profiles of 100–500-cm^{-1} region in the Raman spectrum of LiF–NaF–ZrF_4 melts with respective concentrations (a) 40–46–14 mol %, 650°; (b) 31–36–33 mol %, 550°; (c) 28–32–40 mol %, 550°.

14 to 20 mol %, but, for further additions, the frequency increases with the amount of ZrF_4 added. The values in Table I and the band envelopes (Figure 3) depict this trend. No significance should be associated with the decrease in the band intensities shown in the figure, because this apparent change is merely a function of slightly different instrument parameters employed and also reflects the difficulty in maintaining optical alignment with the molten fluoride solutions in the windowless cell.[23]

There was very little change in the band widths at half-height, w, as a function of melt composition. A slight increase in w from 75 to 80 cm^{-1} was observed in going from 14 to 29 mol % ZrF_4 which decreased to 75 cm^{-1} for 33 mol % ZrF_4. Because the error associated with the measurement of the band width approaches 5 cm^{-1}, it must be concluded that $\Delta w \leq 5$ cm^{-1}.

The frequency shift in the bands observed in depolarized region of the spectrum accompanies the frequency increase in the polarized band. A broad band at 257 cm^{-1} with a shoulder at *ca.* 322 cm^{-1} was found with the 14 mol % ZrF_4 solution. But this shoulder disappears as the ZrF_4 concentration is increased. At high ZrF_4 concentrations, *viz.*, 40 mol %, an additional band at 165 cm^{-1} was found. Figure 4 illustrates the trend for three pertinent concentrations of ZrF_4, the two extremes and an intermediate case, 33 mol % ZrF_4, where only the 250 cm^{-1} band is present.

The spectrum of a melt at 500° containing 33 mol % ZrF_4 (Figure 5) is remarkably similar to the spectrum of crystalline ZrF_6^{2-} in Li_2ZrF_6 when it is recognized that the two bands at 251 and 303 cm^{-1} in the crystal arising from the T_{2g} mode should collapse into one for the melt. Note that this latter band was found at 250 cm^{-1}. Because of the close similarity between the spectrum of crystalline Li_2ZrF_6 (Figure 1) and the melt spectrum (Figure 5), the coordination number for zirconium(IV) in the 33 mol % melt is identified as six.

The shift in the melt spectra from that of ZrF_6^{2-} (*cf.* Figures 3 and 4) when the fluoride ion concentration

TABLE I: Measured Raman Frequencies (cm^{-1}) for LiF–NaF–ZrF_4 Melts at a Constant LiF–NaF Ratio = 0.465/0.535[a]

Mol % ZrF_4					
14	20	25	29	33	40
					165
257	258	255	250	250	230
322 sh	322 sh				
555 p	554 p	568 p	573 p	577 p	593 p

[a] Melt temperature was 650° for 14–29 mol % zirconium compositions and 550° for 33 and 40 mol % compositions; p = polarized, sh = shoulder.

changes is interpreted in the following manner. Providing that the species in solution are not linked by bridging F^- ions, an increase in the F^- concentration should then only increase the coordination number of these species. This, of course, presumes that the additional F^- can be accommodated by the central metal cation. When alkali metal fluorides are added to a melt causing a decrease in the ZrF_4 concentration from 33 to 20 mol %, the symmetric stretching vibration shifts progressively from 577 to 555 cm^{-1} (*cf.* Table I). Because the addition of more alkali metal fluoride, moving the melt composition to 14 mol % ZrF_4, produces no further change, the melt stoichiometry where the shift ceases suggests that the higher coordination number is eight.

Increasing the ZrF_4 concentration from 33 to 40 mol % shifts the polarized band to higher frequencies (*cf.* Table I) and causes the appearance of a band at 165 cm^{-1} as well. In accordance with the explanation given in the preceding paragraphs, this trend is interpreted as the appearance of coordination numbers less than six.

If network formation through fluoride bridging were to occur in these melts, a decrease in the frequency of the symmetric stretching vibration should have occurred

(23) The spectra were measured under many conditions to ensure that the trends presented here were not artifacts.

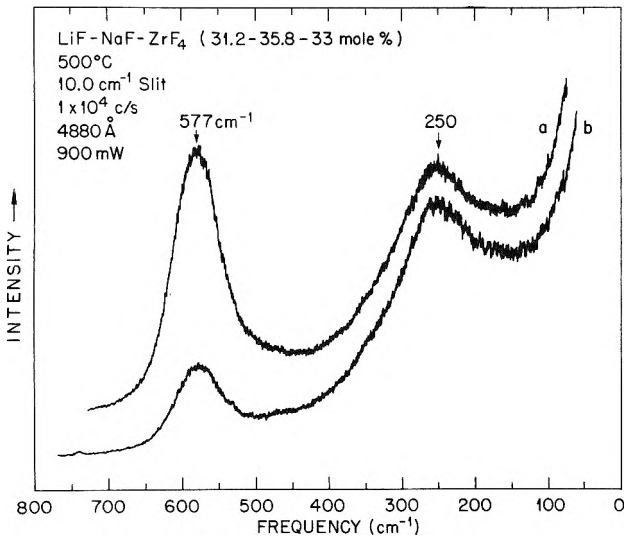

Figure 5. Raman spectrum of LiF-NaF-ZrF_4 (31-36-33 mol %) incident beam at (a) perpendicular and (b) parallel polarization.

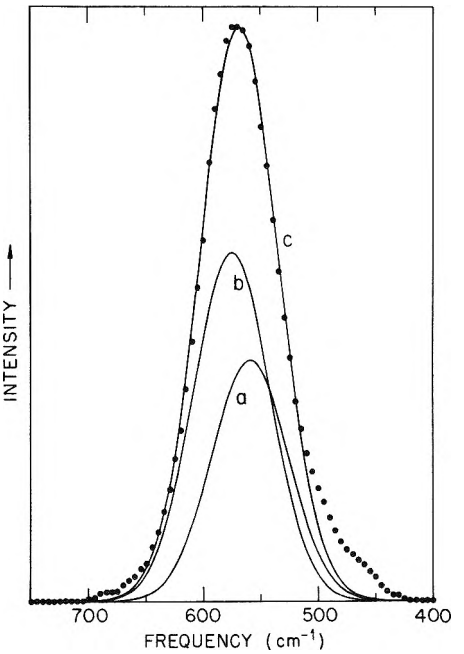

Figure 6. Gaussian resolution of 568-cm^{-1} Raman band of LiF-NaF-ZrF_4 (33-38-29 mol %) into two components: (a) first component at 560 cm^{-1}, w = 79 cm^{-1}; (b) second component at 575 cm^{-1}, w = 79 cm^{-1}; (c) composite at 568 cm^{-1}, w = 80 cm^{-1}.

when the ZrF_4 concentration was increased based on the premise of a decrease in bond order. In the case of such large complex ions as are found here, this decrease in the bond order might not be great enough in the melt to produce a measurable shift in the band frequency. Nevertheless, the experimental measurements (Table I) show that the frequency of the symmetric stretch increases with ZrF_4 content in the range from 14 to 40 mol % suggesting that no fluoride ion bridging is present in these melts.

It is noteworthy that the band width of the symmetric stretching vibration showed no appreciable change in going from 14 to 40 mol % ZrF_4. If the 14 mol % composition is identified with a single coordination species in solution, it is expected that the half-width should increase as additional coordination numbers entered. However, if the symmetric stretching modes for several species (*e.g.*, six-, seven-, and eight-coordination) lie close together and the widths at half-height are much greater than this separation, a gradual shift in an equilibrium distribution involving these species would cause the composite spectrum of their individual stretching modes to shift gradually in position with little change in the half-width. Figure 6 illustrates this for the strong polarized band of the 29 mol % ZrF_4 melt. The composite band (indicated by the data points) was resolved into two gaussian components by an iterative non-linear least-squares procedure.[24] The half-width for the composite spectrum at 568 cm^{-1} is 80 cm^{-1}; and for the two components at 560 and 575 cm^{-1}, it is 79 cm^{-1}. Furthermore, the frequencies of the components match those for the eight- and six-coordinated species (*cf.* 555 and 577 cm^{-1} attributed to these in the preceding paragraphs). If it is assumed that a ZrF_7^{3-} species is present with a symmetric stretching mode between those of the six- and eight-coordinated species, *i.e.*, (555 + 577)/2 = 566 cm^{-1}, a smoother fit can be obtained.

We, therefore, propose that an equilibrium distribution of several ZrF_x^{4-x} coordination species (where x = 8, 7, 6, and possibly 5 or 4) exists in molten fluoride solutions which is dependent on the fluoride ion concentrations

$$ZrF_x^{4-x} \rightleftharpoons ZrF_{x-1}^{5-x} + F^-$$

Direct evidence for the six coordinate zirconium is found by comparison with crystalline Li_2ZrF_6 whereas the eight-coordinated species is deduced from the melt stoichiometry. The existence of ZrF_8^{4-} and ZrF_7^{3-} is also suggested by analogy with the coordination chemistry of dilute UF_4 in LiF-BeF_2 solutions[25] where similar equilibria have been measured.

Acknowledgment. The authors wish to thank J. B. Bates for many helpful suggestions relating to this work.

(24) R. E. Biggers, J. T. Bell, E. C. Long, and O. W. Russ, ORNL-3834 (1971).
(25) L. M. Toth, *J. Phys. Chem.*, **75**, 631 (1971).

Microwave Absorption and Potential Barrier for Orientation. Methyl Chloride Adsorbed on Sodium Chloride and Potassium Chloride

Tsvia Ron and M. Folman*

Department of Chemistry, Technion—Israel Institute of Technology, Haifa, Israel *(Received August 15, 1972)*

Microwave adsorption of CH_3Cl adsorbed on finely powdered NaCl and KCl has been investigated in the 3000-MHz region. From T tan δ *vs.* temperature dependence, the relaxation time and the free energy of activation for orientation were calculated. The energy of interaction of the molecule with the solid adsorbents was computed for different adsorption sites and orientation of the adsorbate and as a function of angle of rotation. The computed values of heat of adsorption and potential barrier for orientation were compared with the experimental one.

Introduction

In a previous paper[1] a model for quantitative treatment of microwave absorption of SO_2 adsorbed on face-centered cubic NaCl and KCl crystals was described together with experimental results. The present work is concerned with another polar molecule, namely, CH_3Cl, adsorbed on the same two substrates.

This molecule was chosen due to its high dipole moment and suitability for the mentioned purpose. Adsorption isotherms and dielectric absorptions of the adsorbate were measured at microwave frequencies; experimental values for isosteric heats of adsorption and free energy of activation for rotation of the adsorbate molecule were obtained. These values were also calculated theoretically using a model and by means of a procedure described previously.[1,2] The adsorption potential was calculated as a function of the orientation of the adsorbate molecule. It was found, for both adsorbents, that the molecule is adsorbed on the cation with the Cl atom pointing to the surface and its axis of symmetry makes an angle of 70° with the normal to the surface. A potential barrier exists with a maximum at the normal to the adsorbents surface, and the molecule exerts a processional movement around this barrier. The molecule has to overcome another, much higher potential barrier in order to rotate into a position in which the CH_3 group will be closer to the surface. Since the height of the second barrier is of the order 5 kcal/mol, the probability of an end over rotation is very small indeed. The free energy of activation for overcoming the first barrier was calculated from the difference between the values of the adsorption potentials for the orientations corresponding to 0 and 70° with respect to the normal.

The calculated heats of adsorption and ΔF^* fit quite well to the experimental values when the parameters used in calculations of these functions lie within the range of values accepted in the literature.

Experimental Section

The measurements were performed by employing a microwave system operating at 3000 MHz. The system has already[1] been described in detail. The apparatus was based on a sensitive heterodyne beat method in which the solid adsorbent is placed inside a resonance cavity of a transmission type operating in the TH_{01} mode. The cavity was connected to a conventional vacuum system. Measurements were performed in the range 165–227°K by means of a thermostat bath controlled within 0.5°K.

For a cavity, partially filled, the loss factor, tan δ, is given by

$$\tan \delta = K\left(\frac{1}{Q_1} - \frac{1}{Q_2}\right) = \frac{K}{Q_2}(10^{\Delta/20} - 1) \qquad (1)$$

where Q_1 and Q_2 are the quality factors of the filled cavity after and before adsorption, respectively. Δ is the difference in readings of a precision attenuator connected in series with the cavity, and adjusted to maintain the transmitted power at constant level. K is a factor which allows for the fact that the cavity is only partially filled and is given by[3]

$$K = \frac{\left(\frac{a}{b}\right)^2 + F^2\left(\frac{\epsilon_1}{\epsilon_0} - 1\right)}{\frac{\epsilon_1}{\epsilon_0}F^2\left[1 + \frac{J_1^2(\beta_1 b)}{J_0^2(\beta_1 b)}\right]} \qquad (2)$$

where a is the cavity radius, b the radius of the adsorbent sample, and ϵ_1 and ϵ_0 are the dielectric permittivities of the sample and the free space, respectively. J_1 and J_0 are Bessel functions of the first order, $\beta_1 = \beta_0(\epsilon_1/\epsilon_0)^{1/2} = 2\pi/\lambda_0(\epsilon_1/\epsilon_0)^{1/2}$, λ_0 is the free space wavelength, and F is defined by

$$F \equiv [Y_0(\beta_0 a)J_0(\beta_0 b) - Y_0(\beta_0 b)J_0(\beta_0 a)](\beta_0 \pi a/2) \qquad (3)$$

where Y_0 is the second-order Bessel function. The ratio ϵ_1/ϵ_0 is a complicated function of a and b. Provided, however, that the sample radius and the ratio ϵ_1/ϵ_0 to be determined are not too large, the following explicit expression may be used[3]

$$\frac{\epsilon_1}{\epsilon_0} = 1 + \frac{\left(\frac{a}{b}\right)\frac{J_0(\beta_0 b)}{J_1(\beta_0 b)}}{F\left[1 + \frac{(\beta_0 b)^2}{8} + \frac{(\beta_0 b)^2 a J_0(\beta_0 a)}{8 \quad b J_1(\beta_0 b)}\right]} \qquad (4)$$

The validity of the described procedure was checked previously[1] and was found satisfactory. In the microwave region it is difficult to work within a wide range of frequencies since a narrow frequency band can only be covered by a single system. Instead, it is possible to work at one frequency and at different temperatures and to obtain relax-

(1) Ts. Ron and M. Folman, *J. Phys. Chem.*, 75, 2602 (1971).
(2) I. Lubezky and M. Folmar, *Trans. Faraday Soc.*, 67, 222 (1971).
(3) H. Horner, T. A. Taylor, R. Dunsmuir, J. Lamb, and W. Jackson, *J. Inst. Elec. Eng.*, 95, 53 (1946).

ation times from plots of $T \tan \delta$ against temperature. If it is assumed that the adsorbent-adsorbate system may be treated as a dilute solution, the Debye equation for solutions may be applied to obtain the relaxation time of the adsorbate, and $T \tan \delta$ is expressed by

$$T \tan \delta = \frac{(\epsilon + 2)^2}{\epsilon} \frac{4\pi\mu^2 cN}{27k} \frac{\omega\tau}{1 + \omega^2\tau^2} \quad (5)$$

where ϵ is the dielectric constant of the solution, c is the concentration in mol/ml, ω is the frequency of the system, and τ is the relaxation time, given by the absolute reaction rate theory as

$$\tau = \frac{h}{kT} \exp(\Delta F^*/RT) \quad (6)$$

where ΔF^* is the free energy of activation.

Materials and Sample Preparation

The preparation of NaCl and KCl adsorbents was described previously.[1] The sample weights used for the measurements were 23.9 and 28.3 g for NaCl and KCl, respectively. The specific surfaces areas obtained by the BET method, using Argon as adsorbate, were approximately 1.7 m^2/g for the two salts.

CH_3Cl of spectroscopic grade was supplied by Matheson and Co. It was further purified by bulb-to-bulb distillation and multiple freezing.

Results and Discussion

The adsorption isotherms of CH_3Cl on NaCl and KCl are shown in Figures 1 and 2. From these, isosteric heats of adsorption were calculated. The q^{st} were practically constant for the range of surface coverages measured and equal to 5.9 and 5.6 kcal/mol for CH_3Cl adsorbed on NaCl and KCl, respectively.

The tan δ values as a function of surface coverage at different temperatures are shown in Figures 3–5. Plots of $T \tan \delta$ against temperature at constant surface coverages are given in Figures 6 and 7. Figure 6 shows that CH_3Cl adsorbed on NaCl has two absorption regions with maxima at 174 and 158°K. It may be easily shown that the curve of $T \tan \delta$ as a function of T will reach a maximum at the point where $\omega\tau = 1$. Since ω is known, the relaxation time τ was obtained for the two temperatures as 5.3×10^{-11} sec. From eq 3 ΔF^*, the free energy of activation, was calculated as 1.8 and 1.6 kcal/mol for the two maxima.

Figure 7 shows the existence of one maximum only, at 158°K, for CH_3Cl adsorbed on KCl. From that, ΔF^* was calculated as 1.6 kcal/mol.

Adsorption Potentials and Activation Energies for Reorientation

The procedure for calculating the adsorption potential has already been described.[1] The model which served as a basis for calculations was that of a linear dipole with a single axis of rotation similar to the previous one. The difference between the two cases is due to the fact that the center of mass and the geometrical center of CH_3Cl are separated by a distance of about 0.5 Å.

The overall potential was taken as the sum of five potentials

$$\Phi = \Phi_D + \Phi_I + \Phi_Q + \Phi_E + \Phi_R \quad (7)$$

Explicit expressions for Φ_D, Φ_I, Φ_Q, Φ_E, and Φ_R were given previously.[1] Since all the parameters used in the calculation of dispersion Φ_D, induction Φ_I, quadrupole Φ_Q, and repulsion potentials Φ_R are related to the center of mass, this was chosen as the center of interaction for these four potentials. The geometrical center served as the center of interaction for the calculation of electric dipole potential Φ_E.

The adsorption potential was calculated (employing a fast computer) as a function of the distance of the mass center of CH_3Cl molecule from the surface, and the orien-

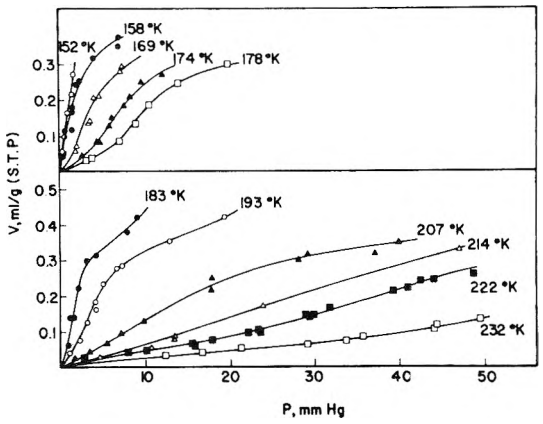

Figure 1. Adsorption isotherms of CH_3Cl on NaCl.

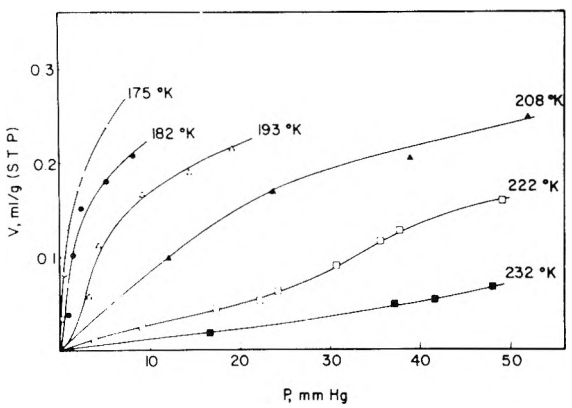

Figure 2. Adsorption isotherms of CH_3Cl on KCl.

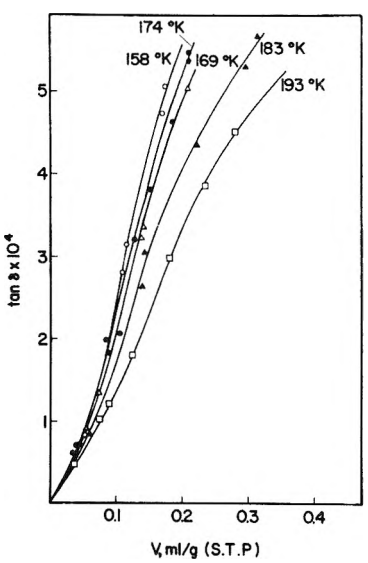

Figure 3. Plots of tan δ *vs.* volume of CH_3Cl adsorbed on NaCl at 3000 MHz.

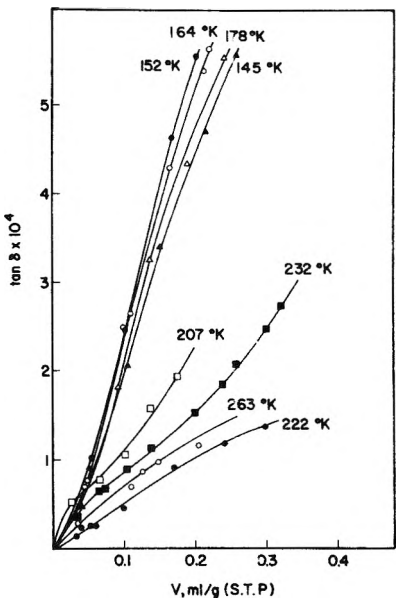

Figure 4. Plots of tan δ *vs.* volume of CH_3Cl adsorbed on NaCl at 3000 MHz.

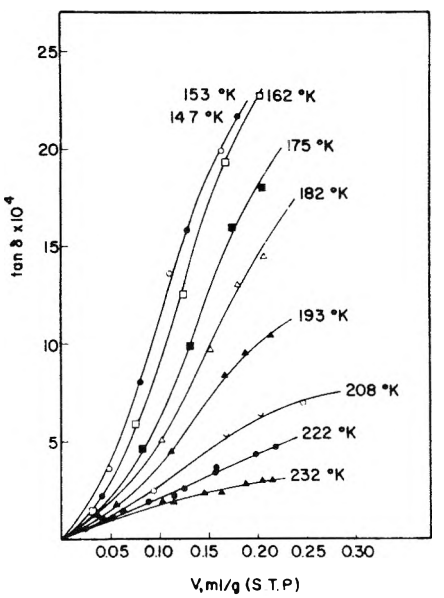

Figure 5. Plots of tan δ *vs.* volume of CH_3Cl adsorbed on KCl at 3000 MHz.

tation of the molecular axis. This distance was expressed in terms of the lattice parameter, a, and was given as $\rho = r/a$ where r is the distance of the adsorbate molecule from the surface. Adsorption potentials for CH_3Cl adsorbed on the two adsorbents were calculated for several sites, of which Na^+ and K^+ cations were found to be the most energetic ones. Therefore final results are given for these sites only, and plots obtained are shown in Figures 8 and 9 for three orientations of CH_3Cl above the Na^+ and K^+ cations. In these orientations the adsorption potential has extremal values, as shown in Figures 10 and 11. The angle α, given in the figures, is the angle between the molecular axis of CH_3Cl and the normal to the surface. At $\alpha = 0°$ the adsorbed molecule is in a normal position with the Cl atom pointing to the surface.

The calculated potential depends on the choice of the plane in which the molecule rotates. Separate calculations were carried out for rotation in different planes perpendic-

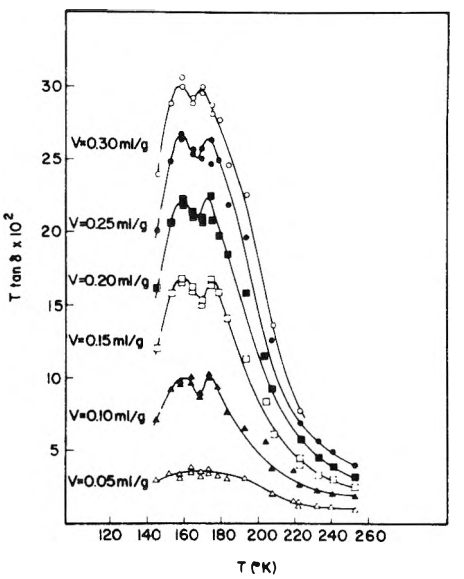

Figure 6. *T* tan δ *vs.* temperature plots at 3000 MHz for CH_3Cl adsorbed on NaCl at constant coverages.

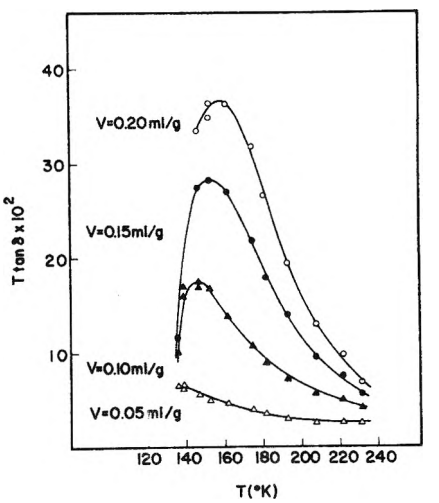

Figure 7. *T* tan δ *vs.* temperature plots at 3000 MHz for CH_3Cl adsorbed on KCl at constant coverages.

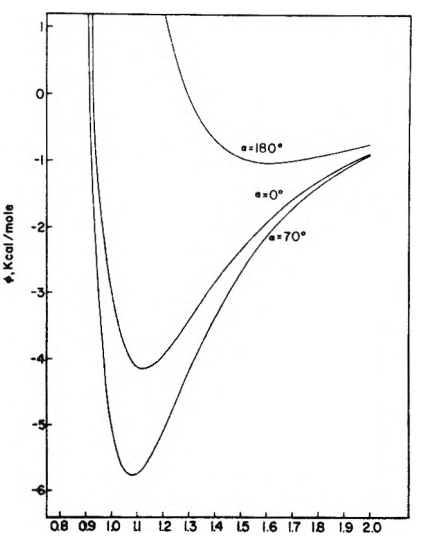

Figure 8. Adsorption potential curves of CH_3Cl on (100) plane of NaCl in different orientations.

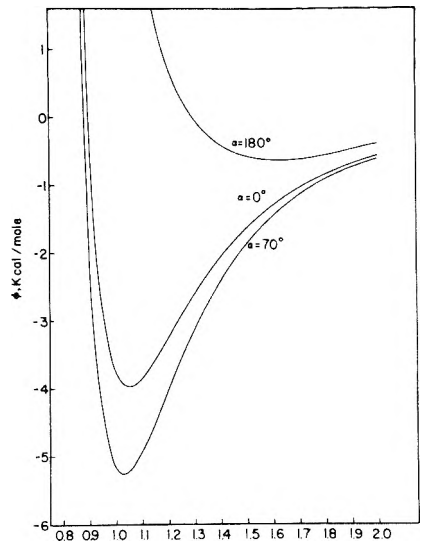

Figure 9. Adsorption potential curves of CH_3Cl on (100) plane of KCl in different orientations.

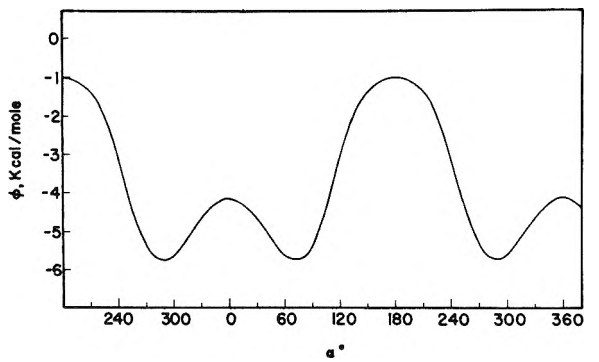

Figure 10. Adsorption potential of CH_3Cl adsorbed on Na^+ ion as a function of the angle of rotation.

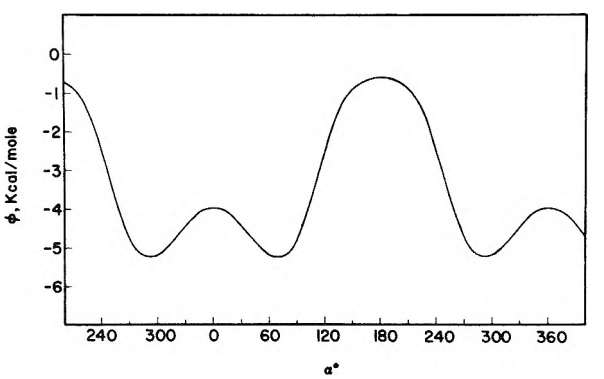

Figure 11. Adsorption potential of CH_3Cl adsorbed on K^+ ion as a function of the angle of rotation.

ular to the surface. One calculation was done for rotation in $x = 0$ or $y = 0$ plane. The other calculations for rotation in planes making different angles with the previous one, in steps of 5°.

The rotation in the different planes considered leads to similar potential barriers and to a minimum at $\alpha = 70°$. The maximum difference in the heights of the potential barriers is about 30 cal. This implies that the molecule exerts a processional type of movement about the normal to the surface and encounters only a small barrier to this precession. In polar coordinates this movement would be described by a constant height and differing azimuthal angles. During this precession the dipole exerts at the same time an oscillatory motion around the $\alpha = 70°$ orientation and occasionally jumps over the barrier at $\alpha = 0°$. This reorientation is connected with a nonresonant or dielectric absorption.

As mentioned above the minimum in the potential was obtained (see Figures 10 and 11) at $\alpha = 70°$. This minimum potential is related to the measured heat of adsorption by

$$q^{st} = -\Delta H = -(\Phi_{min} + (1/2)Nh\nu) + RT \qquad (8)$$

where ν is the vibration frequency of the adsorbate normal to the surface and is given by $(1/2\pi)(f/m)^{1/2}$, where f is the force constant and m is the mass of the CH_3Cl molecule. The force constant was derived using the assumption of a parabolic shaped potential near the minimum. For CH_3Cl adsorbed on both salts, two maxima exist in Φ *vs.* α curves (Figures 10 and 11). The maximum for 180° is much higher than that for $\alpha = 0°$, therefore, the probability of passing through $\alpha = 180°$ orientation is negligible, due to the height of this barrier.

In our previous work[1,2] the theory of Fröhlich in its extended form[4] was adapted successfully to describe dielectric relaxation in the adsorbed state. According to this theory, there exist several equilibrium positions separated by potential barriers for dipoles in a polar solid. When an external field is applied, the system becomes polarized. The relaxation time of this process is defined by a kinetic expression

$$\frac{1}{\tau} = K = A \exp\left(-\frac{\Delta E}{RT}\right) \qquad (9)$$

where ΔE is the height of the potential barrier separating two equilibrium positions, τ is the relaxation time, and K is the rate constant for the process. This equation is analogous to eq 6 of the reaction rate theory.

The two minima in the adsorption potential curve for the present case are identical, whereas in the case previously described (SO_2 on NaCl and KCl) the minima were different; therefore the extended Fröhlich theory was used.

The ΔF^* for orientation is given by

$$\Delta F^* = \Delta H^* - T\Delta S^* = \Phi_{min}{}^0 - \Phi_{min}{}^{70} + (1/2)h(\nu^0 - \nu^{70}) - T\Delta S^* \qquad (10)$$

where ΔS^* is the entropy of activation and $\Phi_{min}{}^0$ and $\Phi_{min}{}^{70}$ are the minimum values of the adsorption potential as calculated for orientations corresponding to $\alpha = 0°$ and 70°. ΔS^* was calculated by assuming that only the vibration normal to the surface contributes to the change in entropy.

It was found that the distance of the adsorbate molecule from the surface at the potential minimum varies with α from $r = 3.0$ to 4.5 Å for the case of NaCl adsorbent, and from $r = 3.2$ to 5.1 Å for KCl adsorbent.

The parameters used in the calculation were those listed in the appendix of the previous work,[1] together with the following values for CH_3Cl: $\alpha_{0(\parallel)} = 54.2 \times 10^{-25}$ ml,[5] $\chi_0 = -32.0 \times 10^{-6}$ cgs,[6] $\mu = 1.87$ D,[6] and $Q = 1.6 \times 10^{-26}$ esu.[7]

(4) H. Fröhlich, "Theory of Dielectrics," 2nd ed, Oxford Clarendon Press, London, 1958; J. D. Hoffman and H. G. Pfeiffer, *J. Chem. Phys.*, **22**, 132 (1954).
(5) J. O. Hirschfelder, C. F. Curtis, and R. B. Bird, "Molecular Theory of Gases and Liquids," Wiley, New York, N. Y., 1965.
(6) "Handbook of Chemistry and Physics," The Chemical Rubber Publishing Co., Cleveland, Ohio, 1965.
(7) D. L. Wanderhard and W. H. Flygare, *Mol. Phys.*, **18**, 77 (1970).

TABLE I: Theoretical and Experimental Results for CH_3Cl Adsorbed on NaCl

α, deg	r_{eq}, Å	$-\Phi_{min}$, kcal/mol	$\nu \times 10^{-12}$, sec^{-1}	ΔH_{calcd}, kcal/mol	ΔF_{calcd}*, kcal/mol	$-\Delta H_{exp}$, kcal/mol	ΔF_{expt}, kcal/mol
			$Q = 1.23 \times 10^{-26}$ esu				
0	3.1	4.61	1.7				
70	3.1	5.60	2.0	5.8	1.0	5.9	1.6(1.8)
180	4.5	1.1	0.52				
			$Q = 1.6 \times 10^{-26}$ esu				
0	3.2	4.2	1.6				
70	3.0	5.8	2.1	6.0	1.5	5.9	1.6(1.8)
180	4.5	1.0	0.5				

TABLE II: Theoretical and Experimental Results for CH_3Cl Adsorbed on K^+ Ion

α, deg	r_{eq}, Å	$-\Phi_{min}$, kcal/mol	$\nu \times 10^{-12}$, sec^{-1}	ΔH_{calcd}, kcal/mol	ΔF_{calcd}*, kcal/mol	ΔH_{expt}, kcal/mol	ΔF_{expt}*, kcal/mol
			$Q = 1.23 \times 10^{-26}$ esu				
0	3.3	4.41	1.7				
70	3.2	5.14	2.0	5.4	0.7	5.6	1.6
180	5.0	0.68	0.4				
			$Q = 1.6 \times 10^{-26}$ esu				
0	3.3	3.97	1.7				
70	3.2	5.26	2.0	5.5	1.2	5.6	1.6
180	5.1	0.6	0.3				

The theoretical value of Q is given in the literature with a large uncertainty as $(1.23 \pm 0.82) \times 10^{-26}$ esu. Using $Q = 1.23 \times 10^{-26}$ esu, ΔF^* was obtained as 1.02 kcal/mol for CH_3Cl adsorbed on NaCl, and 0.68 kcal/mol for KCl. When a value of $Q = 1.6 \times 10^{-26}$ esu was adopted (still in the range of the calculated magnitude) to obtain ΔH_{calcd} in agreement with the experimental isosteric heat of adsorption, ΔF_{calcd}* was 1.5 kcal/mol for NaCl and 1.2 kcal/mol for KCl. These figures are fairly close to the experimental ones, especially in case of NaCl.

In Tables I and II the main theoretical and experimental results are summarized.

As already stressed, two absorption regions were found for CH_3Cl adsorbed on NaCl crystals, while only one region was obtained for the KCl adsorbent. A similar result was found for SO_2 adsorbed on these two adsorbents, and was explained as due to adsorption on some other sites. These are probably Na^+ ions located at different positions such as the edges of the crystals or Na^+ ions located on a different crystal plane. The analog to this minimum was not found with the KCl adsorbent. This may be explained by the fact that the crystallites were larger than in the case of NaCl which decreased the proportion of the energetic sites.

Summary

The dielectric absorption of CH_3Cl adsorbed on NaCl and KCl crystals was measured at microwave frequencies by means of a sensitive heterodyne method. The results were explained by assuming that the molecule is adsorbed in different orientational positions separated by a potential barrier.

Calculation of adsorption potential as a function of angle of rotation shows that the two positions are equivalent.

The free energy of activation for orientation was calculated and found to be in good agreement with the experimental value obtained from the microwave measurements.

Nonadjacent Vibrational Transitions in Molecular Collisions. Interference between One- and Two-Quantum Excitation Processes[1a]

Hyung Kyu Shin

Department of Chemistry,[1b] University of Nevada, Reno, Nevada 89507 *(Received January 8, 1973)*

Publication costs assisted by the Air Force Office of Scientific Research

The problem of the interference between one- and two-quantum excitation processes in $0 \rightarrow n$ vibrational transitions taking place in molecular collision has been investigated. Specific consideration is given to $0 \rightarrow 1$ and $0 \rightarrow 2$ transitions in H_2–H_2 and I_2–I_2 collisions for which it is found that the interference becomes significant as collision velocities increase. The interference always leads to an increase in the transition probability over the result obtained for purely stepwise processes. For the $0 \rightarrow 2$ transition, both stepwise $0 \rightarrow 1 \rightarrow 2$ and direct $0 \rightarrow 2$ excitation processes have to be considered even at moderate velocities in these collision systems.

Introduction

In the studies of vibrational energy transfer for a forced harmonic oscillator it is known[2-4] that the $0 \rightarrow n$ transition probability can be obtained in the form of the Poisson distribution $P_{0n}^* = \epsilon^n \exp(-\epsilon)/n!$, where ϵ is the amount of vibrational energy transfer expressed in units of the vibrational quantum $\hbar\omega$. This expression represents the $0 \rightarrow n$ vibrational transition by stepwise process, *i.e.*, $0 \rightarrow 1 \rightarrow 2 \cdots \rightarrow n$. However, as the collision velocity increases, direct multiquantum excitation processes can become important so that the transition probability might deviate seriously from the result obtained by the Poisson expression. In the forced oscillator model, it is assumed that the oscillator is perturbed by the energy $-F(t)q$, where $F(t)$ is the time dependent perturbing force and q is the vibrational coordinate. However, this term is the leading contribution of the overall perturbation, and the second- and higher-order terms in q can become important as the collision velocity increases. The terms containing q^n are responsible for the direct $0 \rightarrow n$ transitions.

In this paper we shall derive an expression for the vibrational transition probability P_{0n} which includes the effect of stepwise one-quantum and direct two-quantum excitation processes. The deviation of P_{0n} from the Poisson expression P_{0n}^* is then due to the interference of one- and two-quantum excitation processes. For $0 \rightarrow n$, the present formulation therefore rigorously considers the stepwise $0 \rightarrow 1 \rightarrow 2 \cdots \rightarrow n$ process and the nonadjacent $0 \rightarrow 2 \rightarrow 4 \cdots \rightarrow n$ process. We shall assume the collinear collision of a diatomic molecule (BC) with a particle A (an atom or a molecule). The collision model is a simplified one, but we shall not attempt to test its accuracy; studies on such a test can be found elsewhere.[5] Application of the formulation is made to H_2–H_2 and I_2–I_2 by calculating P_{01} and P_{02}.

Vibrational Transition Probability

To formulate the transition probability P_{0n} including the nearest and next-nearest excitation processes, we start with the wave equation for the collision of BC with A under the time-dependent perturbation $H'(t)$

$$i\hbar \frac{\partial}{\partial t}|\psi(t)\rangle = [H + H'(t)]|\psi(t)\rangle \tag{1}$$

where $|\psi(t)\rangle$ represents the oscillator's dynamic state at a time t and H is the Hamiltonian of the free oscillator, $p^2/2M + M\omega^2q^2/2$, M and ω being the reduced mass and vibrational frequency ($2\pi\nu$) of the oscillator; q and p denote the coordinate and momentum of the oscillator. Note that the perturbation is also a function of the q; *i.e.*, $H'(t) \equiv H'(t,q)$. In the course of time, we postulate that the linear superposition of oscillator states is preserved, so that the correspondence between $|\psi(t)\rangle$ and the initial wave function $|\psi(t_0)\rangle$ is linear. By introducing the evolution operator[6,7] $U(t,t_0)$, we then express the wave function at a time t as

$$|\psi(t)\rangle = e^{-iHt/\hbar}U(t,t_0)e^{iHt/\hbar}|\psi(t_0)\rangle \tag{2}$$

in which the operator satisfies the equation

$$i\hbar \frac{\partial}{\partial t}U(t,t_0) = e^{iHt/\hbar}H'(t)e^{-iHt/\hbar}U(t,t_0) \equiv \bar{H}'(t)U(t,t_0) \tag{3}$$

This equation and the initial condition $U(t_0,t_0) = 1$ express the fundamental law of evolution of the quantum system. The operator can also be expressed by the integral equation

$$U(t,t_0) = 1 - \frac{i}{\hbar}\int_{t_0}^{t} \bar{H}(t')U(t',t_0)\mathrm{d}t' \tag{4}$$

It is important to observe some properties of this operator. If $\bar{H}'(t)$ is hermitian, $U(t,t_0)$ is a unitary operator. Since the perturbation Hamiltonian depends upon the time, we have

$$|\psi(t + \mathrm{d}t)\rangle = \left[1 - \frac{i}{\hbar}\bar{H}'(t)\mathrm{d}t\right]|\psi(t)\rangle \tag{5}$$

For $\bar{H}'(t)$ is hermitian, the evolution operator of this equation is then

$$U(t + \mathrm{d}t, t) \equiv 1 - \frac{i}{\hbar}\bar{H}'(t)\mathrm{d}t \tag{6}$$

(1) (a) This work was supported by the U. S. Air Force Office of Scientific Research, Grant AFOSR-72-2231. (b) Theoretical Chemistry Group Contribution No. 1042
(2) (a) M. S. Bartlett and J. E. Moyal, *Proc. Cambridge Phil. Soc.*, **45**, 545 (1949); (b) E. Kerner, *Can. J. Phys.*, **36**, 371 (1958).
(3) C. E. Treanor, *J. Chem. Phys.*, **43**, 532 (1965).
(4) H. Shin, *Chem. Phys. Lett.*, **3**, 125 (1969).
(5) H. Shin, *J. Chem. Phys.*, **49**, 3964 (1968).
(6) A. Messiah, "Quantum Mechanics," North-Holland Publishing Co., Amsterdam, 1968, Chapter 8.
(7) D. W. Robinson, *Nucl. Phys.*, **25**, 459 (1961).

and it is an infinitesimal unitary operator. As shown in eq 2, the operator $U(t,t_0)$ transforms $|\psi(t_0)\rangle$ into $|\psi(t)\rangle$ and is then a product of infinitesimal unitary operators.

We shall now derive the transition probability P_{0n} for the system perturbed by the Hamiltonian involving linear and quadratic terms in the vibrational coordinate

$$H'(t,q) = H(t,q) + H(t,q^2) \tag{7}$$

To facilitate the solution of the problem, we introduce the operators $\mathbf{a}^*$ and $\mathbf{a}$, which are hermitian conjugates of each other satisfying the commutation relation $[\mathbf{a},\mathbf{a}^*] = 1$. The oscillator's position variable q and the momentum p are linear combinations of these operators

$$q = \left(\frac{\hbar}{2M\omega}\right)^{1/2}(\mathbf{a}^* + \mathbf{a}) \tag{8-1}$$

$$p = i\left(\frac{M\hbar\omega}{2}\right)^{1/2}(\mathbf{a}^* - \mathbf{a}) \tag{8-2}$$

so that the perturbation Hamiltonian can now be explicity expressed in terms of these operators.

For the harmonic oscillator perturbed by the linear term alone, *i.e.*, $H(t,q) = -F(t)q$, where the $F(t)$ is the time-dependent perturbing force, the solution of eq 1 is well known.[8] For such a case, eq 3 takes the simple form

$$i\hbar\frac{\partial}{\partial t}V(t,t_0) = \bar{H}(t,q)V(t,t_0) \tag{9}$$

where

$$\bar{H}(t,q) = e^{iHt/\hbar}H(t,q)e^{-iHt/\hbar} = \left(\frac{\hbar}{2M\omega}\right)^{1/2}F(t)(\mathbf{a}e^{-i\omega t} + \mathbf{a}^*e^{i\omega t})$$

and its solution is

$$V(t,t_0) = \exp\left[-\frac{i}{\hbar}\int_{t_0}^{t}\bar{H}'(t',q)\mathrm{d}t'\right] = \exp\frac{i}{(2M\hbar\omega)^{1/2}}\left[\int_{t_0}^{t}F(t')e^{-i\omega t'}\mathrm{d}t'\mathbf{a} + \int_{t_0}^{t}F(t')e^{i\omega t'}\mathrm{d}t'\mathbf{a}^*\right] \tag{10-1}$$

This expression can also be expressed as[9,10]

$$V(t,t_0) = \exp[ic(t,t_0)\mathbf{a}^*]\exp[ic^*(t,t_0)\mathbf{a}]\times\exp[-\tfrac{1}{2}c(t,t_0)c^*(t,t_0)] \tag{10-2}$$

with

$$c(t,t_0) = \frac{1}{(2M\hbar\omega)^{1/2}}\int_{t_0}^{t}F(t')e^{i\omega t'}\mathrm{d}t'$$

We thus write the solution of eq 3 in the form

$$U(t,t_0) = V(t,t_0)W(t,t_0) \tag{11}$$

When this equation is substituted into eq 3, we obtain

$$i\hbar\frac{\partial W(t,t_0)}{\partial t} = V^*(t,t_0)\bar{H}(t,q^2)V(t,t_0)W(t,t_0) \tag{12}$$

where $\bar{H}(t,q^2) \equiv e^{iHt/\hbar}H(t,q^2)e^{-iHt/\hbar}$.

The solution of this equation to first order in $\bar{H}(t,q^2)$ is

$$W(t,t_0) = 1 - \frac{i}{\hbar}\int_{t_0}^{t}V^*(t',t_0)\bar{H}(t',q^2)V(t,t_0)\mathrm{d}t' \tag{13}$$

so that in the limit $t \to \infty$, and $t_0 \to -\infty$, since $V^*(t',t_0) = V(t_0,t')$ and $V(t',t_0) = V^*(t_0,t')$, the transformation operator is[7]

$$U(\infty,-\infty) = \left[1 - \frac{i}{\hbar}\int_{-\infty}^{\infty}V(\infty,t)\bar{H}(t,q^2)V^*(\infty,t)\mathrm{d}t\right]V(\infty,-\infty) \tag{14}$$

We now write the two-quantum excitation Hamiltonian $H(t,q^2)$ in the form $BF(t)q^2$, where B is a constant to be determined

$$H(t,q^2) = BF(t)\left(\frac{\hbar}{2M\omega}\right)(\mathbf{a}e^{-i\omega t} + \mathbf{a}^*e^{i\omega t}) \tag{15}$$

so that

$$\hat{H}(t,q^2) \equiv V(\infty,t)\bar{H}(t,q^2)V^*(\infty,t) = \frac{\hbar B}{2M\omega}F(t)\exp[iC(\infty,t)\mathbf{a}^*]\exp[iC^*(\infty,t)\mathbf{a}]\times(\mathbf{a}e^{-i\omega t} + \mathbf{a}^*e^{i\omega t})^2\exp[-ic^*(\infty,t)\mathbf{a}]\exp[-ic(\infty,t)\mathbf{a}^*] \tag{16}$$

From the commutation relations of the hermitian operators, we can immediately show

$$\exp[ic^*(\infty,t)\mathbf{a}]\mathbf{a}^* = [\mathbf{a}^* + ic^*(\infty,t)]\exp[ic^*(\infty,t)\mathbf{a}]$$

$$\exp[ic(\infty,t)\mathbf{a}^*]\mathbf{a} = [\mathbf{a} - ic(\infty,t)]\exp[ic(\infty,t)\mathbf{a}^*]$$

Therefore, eq 16 takes the form

$$\hat{H}(t,q^2) = \frac{\hbar B}{2M\omega}F(t)\{[\mathbf{a} - ic(\infty,t)]^2e^{-2i\omega t} + [\mathbf{a}^* + ic^*(\infty,t)][\mathbf{a} - ic(\infty,t)] + [\mathbf{a} - ic(\infty,t)][\mathbf{a}^* + ic^*(\infty,t)] + [\mathbf{a}^* + ic^*(\infty,t)]e^{2i\omega t}\} \tag{17-1}$$

In the present model, the oscillator is assumed to be initially in the ground state $|0\rangle$, so after rearranging eq 17-1 we can delete the terms containing the operators $\mathbf{a}^*\mathbf{a}$, $\mathbf{a}$, and $\mathbf{a}^2$ to obtain

$$\hat{H}(t,q^2) = \frac{\hbar B}{2M\omega}F(t)\{\mathbf{a}^*e^{-2i\omega t} - 2ic(\infty,t)(1 - e^{2i\omega t})\mathbf{a}^* + [1 + 2c^*(\infty,t)c(\infty,t) - c^2(\infty,t)e^{-2i\omega t} - c^{*2}(\infty,t)e^{2i\omega t}]\} \tag{17-2}$$

Then, the complete expression for $U(\infty,-\infty)$ is

$$U(\infty,-\infty) = \left[1 - \frac{iB}{2M\omega}\left\{\int_{-\infty}^{\infty}F(t)e^{2i\omega t}\mathrm{d}t\mathbf{a}^{*2} - 2i\int_{-\infty}^{\infty}F(t)c(\infty,t)(1 - e^{2i\omega t})\mathrm{d}t\mathbf{a}^* + \int_{-\infty}^{\infty}F(t)[1 + 2c^*(\infty,t)c(\infty,t) - c^2(\infty,t)e^{-2i\omega t} - c^{*2}(t)e^{2i\omega t}]\mathrm{d}t\right\}\right]V(\infty,-\infty) \equiv (1 + \alpha\mathbf{a}^{*2} + \beta\mathbf{a}^* + \gamma)V(\infty,-\infty) \tag{18}$$

where

$$V(\infty,-\infty) = \exp[ic(\infty)\mathbf{a}^*]\exp[ic^*(\infty)\mathbf{a}]\exp[-\tfrac{1}{2}c(\infty)c^*(\infty)]$$

$$c(\infty) = \frac{1}{(2M\hbar\omega)^{1/2}}\int_{-\infty}^{\infty}F(t)e^{i\omega t}\mathrm{d}t$$

The probability of $0 \to n$ vibrational excitation can now be expressed as

$$P_{0n} = |\langle n|U(\infty,-\infty)|0\rangle|^2 \tag{19}$$

Then, it is apparent that $U(\infty,-\infty)|0\rangle$ is the wave function for the perturbed oscillator and can be obtained in the form of a linear combination of the unperturbed oscillator wave functions. Since $\mathbf{a}^*|k\rangle = (k+1)^{1/2}|k+1\rangle$ and

(8) D. ter Haar, "Selected Problems in Quantum Mechanics," Academic Press, New York, N. Y., 1964, pp 152–154.
(9) See ref 6, p 442.
(10) See ref 8, pp 145–146.

$$\exp[ic(\infty)\mathbf{a}^*]\ \exp[ic^*(\infty)\mathbf{a}]|0> = \sum_{m=0}^{\infty}\frac{[ic(\infty)]^m}{(m!)^{1/2}}|m>$$

the perturbed wave function, from eq 18, is

$$(1 + \alpha\mathbf{a}^{*2} + \beta\mathbf{a}^* + \gamma)V(\infty,-\infty)|0> =$$
$$(1 + \gamma)\sum_{m=0}^{\infty}\frac{[ic(\infty)]^m}{(m!)^{1/2}}|m> + \beta\sum_{m=0}^{\infty}\left(\frac{m+1}{m!}\right)^{1/2} \times$$
$$[ic(\infty)]^m|m+1> + \alpha\sum_{m=0}^{\infty}\left[\frac{(m+1)(m+2)}{m!}\right]^{1/2} \times$$
$$[ic(\infty)]^m|m+2> \quad (20)$$

On the basis of the orthogonality relation $\langle n|s\rangle = \delta_{ns}$, we then obtain the final expression of the vibrational transition probability as

$$P_{0n} = \left\{1 + \left[\gamma' - \frac{\beta n}{\epsilon^{1/2}} - \frac{n(n-1)\alpha'}{\epsilon}\right]^2\right\}\frac{\epsilon^n \exp(-\epsilon)}{n!} \quad (21)$$

where $\epsilon = c^2(\infty)$, $\alpha = i\alpha'$, and $\gamma = i\gamma$. For the oscillator perturbed by the linear term $-F(t)q$ alone, the result is simply the Poisson distribution $P_{0n}^* = \epsilon^n \exp(-\epsilon)/n!$ so that eq 21 can be also expressed in the form

$$P_{0n} = f_n P_{0n}^* \quad (22)$$

where f_n denotes the interference term in eq 21.

We shall express the interaction potential for the collinear collision of BC with A in the form $U(z) = A\exp(-z/a)$, where z is the distance between the nearest atom of BC, say C, and A. This distance is $z = x - \rho(d + q)$, where x is the distance between the center of mass of BC and A, $\rho = m_B/(m_B + m_C)$, and d is the equilibrium distance of the B–C bond. Then, we can approximate $U(z)$ as

$$U(x,q) = A'\exp(-x/a)\left[1 + \frac{\rho}{a}q + \tfrac{1}{2}\left(\frac{\rho}{a}\right)^2 q^2 + \ldots\right]$$
$$\equiv U(x) + H(t,q) + H(t,q^2) + \ldots \quad (23)$$

where $A' = A\exp(\rho d/a)$. Since $F(t) = -(A'\rho/a)\exp(-x/a)$ with $x = x(t)$, we have $H(t,q)$, the linear term in q, is $-F(t)q$ and $H(t,q^2)$ is $-(\rho/2a)F(t)q^2$; thus the constant B introduced above is $-(\rho/2a)$. For the potential $U(x) = A'\cdot\exp(-x/a)$ with $A' = E$, the relative collision energy, $\frac{1}{2}\cdot\mu v^2$, the classical equation of motion can be readily solved to give[11]

$$\exp(-x/a) = \mathrm{sech}^2(vt/2a) \quad (24)$$

so that the perturbing force is

$$F(t) = (E\rho/a)\ \mathrm{sech}^2(vt/2a) \quad (25)$$

In eq 21, the terms β and γ' contain complicated integrals. However, these integrals can be integrated by parts. By taking the leading terms of the integrated result, we find

$$\beta = -\frac{B\epsilon^{1/2}}{M\omega}\left[\int_{-\infty}^{\infty}F(t)dt - \int_{-\infty}^{\infty}F(t)e^{2i\omega t}dt\right] \equiv$$
$$-\frac{B\epsilon^{1/2}}{M\omega}(I_0 - I_2) \quad (26)$$

$$\gamma' = -\frac{B}{2M\omega}\left[\int_{-\infty}^{\infty}F(t)dt + 2\epsilon\int_{-\infty}^{\infty}F(t)dt\right.$$
$$\left. - 2\epsilon\int_{-\infty}^{\infty}F(t)e^{2i\omega t}dt\right] \quad (27)$$
$$\equiv -\frac{B}{2M\omega}[(1 + 2\epsilon)I_0 - 2\epsilon I_2]$$

where

$$I_0 = \int_{-\infty}^{\infty}F(t)dt$$
$$I_2 = \int_{-\infty}^{\infty}F(t)e^{2i\omega t}dt$$

Note that

$$\epsilon = \frac{1}{(2M\hbar\omega)^{1/2}}\int_{-\infty}^{\infty}F(t)e^{i\omega t}dt \equiv \frac{1}{(2M\hbar\omega)^{1/2}}I_1$$

The integral I_0 can be readily integrated to obtain $2\rho\mu v$. The evaluation of two other integrals requires contour integration procedures, but the method is simple and well known.[12] The results are

$$I_1 = \frac{E\rho}{a}\left[4\pi\omega\left(\frac{a}{v}\right)^2\right]\mathrm{csch}\left(\frac{\pi\omega a}{v}\right) \quad (28)$$

$$I_2 = \frac{E\rho}{a}\left[8\pi\omega\left(\frac{a}{v}\right)^2\right]\mathrm{csch}\left(\frac{2\pi\omega a}{v}\right) \quad (29)$$

In general the inclusion of q^n in $H'(t,q)$ will lead to the appearance of the integrals $I_0, I_1, \ldots, I_n$ in the final expression. With the explicit forms of I_1 and I_2, we now find

$$\alpha' = \frac{\hbar}{4\pi\omega a^2\mu}\zeta$$

$$\beta = \epsilon^{1/2}\left(\frac{\mu\rho^2 v}{aM\omega} - \frac{\hbar}{2\pi\omega a^2\mu}\zeta\right)$$

$$\gamma' = \frac{\rho^2\mu v}{2aM\omega}(1 + 2\epsilon) - \frac{\hbar}{2\pi\omega a^2\mu}\zeta\epsilon$$

where

$$\zeta = \frac{1}{M\hbar\omega}\left\{\frac{E\rho}{a}\left[4\pi\omega\left(\frac{a}{v}\right)^2\right]\right\}^2\mathrm{csch}\left(\frac{2\pi\omega a}{v}\right)$$
$$\epsilon = \frac{1}{2M\hbar\omega}\left\{\frac{E\rho}{a}\left[4\pi\omega\left(\frac{a}{v}\right)^2\right]\right\}^2\mathrm{csch}\left(\frac{\pi\omega a}{v}\right)$$

For $2\pi\omega a/v \gg 1$, the quantity ζ is essentially identical with ϵ. Then, the explicit forms of the $0 \to 1$ and $0 \to 2$ probabilities are

$$P_{01} = \left\{1 + \left[\frac{\mu\rho^2 v}{2M\omega a}(1 - 2\epsilon) - \frac{\hbar}{4\pi\omega\mu a^2}(1 - \epsilon)\zeta\right]^2\right\} \times$$
$$\epsilon\exp(-\epsilon) = f_1 P_{01}^* \quad (30)$$

and

$$P_{02} = \left\{1 + \left[\frac{3\mu\rho^2 v}{2M\omega a}(1 - \tfrac{2}{3}\epsilon) - \frac{\hbar}{2\pi\omega\mu a^2}(1 - \epsilon)^2\frac{\zeta}{\epsilon}\right]^2\right\} \times$$
$$\frac{\epsilon^2\exp(-\epsilon)}{2} = f_2 P_{02}^* \quad (31)$$

The quantity ϵ appearing in the above expressions is the amount of energy absorbed by the classical oscillator which is driven by the perturbing force $F(t)$.[11] It is important to note that this expression of ϵ has been used in P_{0n}^* by Heidrich, Wilson, and Rapp[13] in their semiclassical and classical treatments of the collinear collision of an atom (A) and harmonic oscillator (BC). By replacing the relative energy $E(= \frac{1}{2}\mu' v^2)$ by $\frac{1}{2}\mu' v^2$, where $\mu' = m_A m_B/(m_A + m_B)$, they showed that the calculated values of P_{0n}^* are in good agreement with Secrest and Johnson's

(11) D. Rapp, *J. Chem. Phys.*, **32**, 735 (1960).
(12) For example, see C. R. Wylie, Jr., "Advanced Engineering Mathematics," McGraw-Hill Book Co., New York, N. Y., 1951, Chapter 12. Reference 11 shows the evaluation of I_1.
(13) F. E. Heidrich, K. R. Wilson, and D. Rapp, *J. Chem. Phys.*, **54**, 3885 (1971).

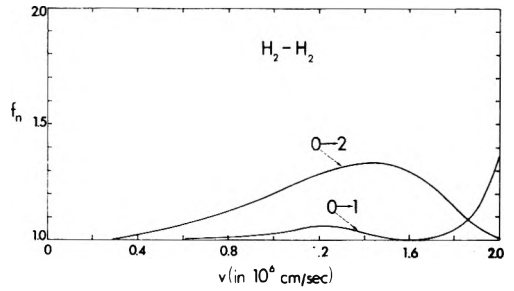

Figure 1. Plot of the interference term f_n for H_2–H_2 as a function of the collision velocity; the 0 → 1 and 0 → 2 transitions are considered.

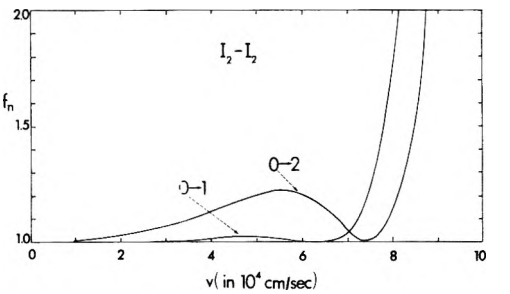

Figure 2. Plot of the interference term f_n for I_2–I_2 as a function of the collision velocity; the 0 → 1 and 0 → 2 transitions are considered.

exact quantum mechanical results.[14] However, in both studies the problem of the interference between one- and two-quantum processes was not considered.

Application and Discussion

We now use eq 30 and 31 to calculate the interference terms f_1 and f_2 for H_2–H_2 and I_2–I_2 collisions. The vibrational frequencies[15] are 7.836×10^{14} and 4.019×10^{13} sec^{-1} for H_2 and I_2, respectively. We assume a by 0.2 Å for both collision systems. In Figure 1, we plot the terms for H_2–H_2 as a function of the collision velocity. The result for I_2–I_2 is shown in Figure 2.

For the 0 → 2 vibrational transition in H_2–H_2, the interference between one- and two-quantum excitation processes is significant, thus indicating that the direct 0 → 2 nonadjacent transition makes an important contribution to the overall excitation process. The term f_2 takes a maximum value of 1.33 at 1.4×10^6 cm/sec. At 7×10^5 cm/sec, the constructive interference increases the transition probability by 10% over the Poisson distribution P_{02}* Extended calculation shows that f_2 rises rapidly with the velocity for $v > 2 \times 10^6$ cm/sec. The interference is not important for 0 → 1 up to about 2×10^6 cm/sec. The term f_1 is very close to unity at low collision velocities; it increases to 1.05 at 1.2×10^6 cm/sec and then decreases to a minimum value at 1.6×10^6 cm/sec. At still higher velocities, the interference term increases somewhat rapidly; *e.g.*, at 2×10^6 cm/sec, f_1 is 1.35. As shown in the above derivation of P_{0n}, the two-quantum process contributes to the 0 → 1 transitions, because $H(t,q^2)$ leads to the appearance of the terms containing $\mathbf{a}^*$.

For H_2, the average velocities at 1000, 2000, 3000, and 5000°K are 3.2×10^5, 4.6×10^5, 5.6×10^5, and 7.3×10^5 cm/sec, respectively. Therefore, the contribution of the nonadjacent transition becomes important in the excitation of the oscillator from $v = 0$ to 2 at higher collision velocities, which are substantially above the average velocities. The transition probabilities are small at the average collision velocities, but they can be large at the high velocities in the "tail" of the Boltzmann distribution curve; at such velocities the one- and two-quantum processes interfere strongly. For example, at 1.5×10^6 cm/sec, $\epsilon = 0.276$ and the probability P_{02}* is 0.0289 and $f_2 = 1.323$. At 1.7×10^6 cm/sec, $\epsilon = 0.6$, $f_2 = 1.233$, and P_{02}* = 0.0988. Therefore, the quadratic term makes an important contribution to P_{02} where the vibrational transition is quite efficient.

Figure 2 shows the plots of f_1 and f_2 for I_2–I_2 for the collision velocities up to 9×10^4 cm/sec. We should note that at 1000, 2000, 3000, and 4000°K, the average velocities of I_2 are 2.9×10^4, 4.1×10^4, 5.0×10^4, and 5.7×10^4 cm/sec, respectively. The term f_2 takes the maximum value of 1.22 at 5.5×10^4 cm/sec and decreases to a minimum values of f_2 do not lead to large transition probabilities of vibrational energy absorbed by the oscillator is about $\hbar\omega$. At velocities higher than 8×10^4 cm/sec, f_2 increases very rapidly and takes large values ($\gg 1$). Such large values of f_2 do not lead to large transition probabilities because at the velocities where f_2 is large, ϵ is also very large ($\gg 1$) so that P_{02}* is very small. For example, at $v = 9 \times 10^4$ cm/sec, $\epsilon = 4.65$, $f_2 = 4.419$, and P_{02}* = 0.1176. As shown in the figure, f_1 rises very rapidly with increasing velocity above 7.5×10^4 cm/sec. However, up to 7×10^6 cm/sec, the term f_1 is very close to unity; *i.e.*, the interference is negligible. At high velocities, both f_1 and f_2 increase very rapidly with the velocity due to the increased contribution of the quadratic term $BF(t)q^2$ over the linear term. However, at such high velocities, the amount of vibrational energy absorbed by the oscillator is so large that many other nonadjacent transitions might become efficient. Then, it should be necessary to include the cubic and higher-order terms in q. This will lead to an expression for the interference different from the result given in eq 21. Equation 21 presents an accurate situation of the interference between one- and two-quantum processes up to $\epsilon \simeq 2$.

For 0 → 1, P_{01}* deviates only slightly from P_{01} up to $v \simeq 1.7 \times 10^6$ cm/sec in H_2–H_2 and 7×10^4 cm/sec in I_2–I_2. At such velocities, however, P_{02}* can be significantly different from P_{02} in both collision systems; f_2 slowly increases with v from unity to a maximum value. For example, in H_2–H_2 at 1.7×10^6 cm/sec, the contribution of the direct 0 → 2 transition is to increase the result of the stepwise 0 → 1 → 2 excitation by a factor of 1.233. As shown in the figures, as v continues to increase, f_2 now decreases to a minimum value of $\simeq 1.0$ and then rapidly increases. This decrease in the interference occurs at velocities between 1.6×10^6 and 2.1×10^6 cm/sec in H_2–H_2 and between 6×10^4 and 8×10^4 cm/sec in I_2–I_2. At these velocities, the transition probability takes large values; *e.g.*, for H_2–H_2, $P_{02} = 0.246$ at 2×10^6 cm/sec and for I_2–I_2 it is 0.309 at 8×10^4 cm/sec. Therefore, the interference between one- and two-quantum processes decreases at velocities for which the particular state under consideration is efficiently excited. On the other hand, in both 0 → 1 and 0 → 2 excitations, the interference becomes very strong at higher velocities ($>2.2 \times 10^6$ cm/sec in H_2–H_2 and $>8 \times 10^4$ cm/sec in I_2–I_2) for which the state under consideration is being excited less efficiently in favor of

(14) D. Secrest and B. R. Johnson, *J. Chem. Phys.*, **45**, 4556 (1966).
(15) G. Herzberg, "Spectra of Diatomic Molecules," D. Van Nostrand Co., Princeton, N. J., 1950, Table 39.

higher states. The situation that $f_1 > f_2$ at higher velocities is then due to the increased efficiency of $0 \rightarrow 2$ excitations over $0 \rightarrow 1$. These results on the variation of f_n with the collision velocity is similar to those reported by Robinson for the multiple Coulomb excitation of vibrational nuclei.[7]

Conclusion

A general expression for the $0 \rightarrow n$ vibrational transition probability is obtained for the perturbation energy which includes linear and quadratic terms in the oscillator coordinate. The linear term is responsible for stepwise excitation process, whereas the quadratic term leads to the contribution of the direct two-quantum excitation process to the overall transition. The leading term of the final expression P_{0n} simply takes the form of the Poisson distribution, but the interference between the two processes leads to the appearance of an important factor in the expression. This factor always exceeds unity so the inclusion of the direct two-quantum process leads to the constructive interference.

For H_2–H_2 and I_2–I_2, the interference is important at substantially high velocities. Particularly, in the $0 \rightarrow 2$ probability the nonadjacent transition makes an important contribution to the overall process even at moderate collision velocities. This demonstrates that the conventional approach to calculate vibrational transition probabilities in terms of the linear forcing potential alone is inadequate at such collision velocities.

Ion Exchange in Molten Salts. VI. The Occluded Sodium Nitrate in Zeolite A as an Anion Exchanger. The Cl^-–NO_3 Exchange in Molten $Na(NO_3,Cl)$ Mixtures

M. Liquornik, B. Ale, and J. A. A. Ketelaar*

Laboratory for Electrochemistry of the University of Amsterdam, Amsterdam, The Netherlands *(Received November 16, 1972)*

Publication costs assisted by the Laboratory for Electrochemistry

Anion exchange of chloride and nitrate ions has been observed between a $Na(NO_3,Cl)$ melt and a sodium zeolite A with occluded $NaNO_3$: $Na_{22}(AlSiO_4)_{12}(NO_3)_{10}$ at 375 and 450°. The replacement exchange can be described by an ideal exchange isotherm with a maximum exchange capacity of 1.81 and 1.67 Cl^- ion per zeolite unit at 375 and 450°, respectively. The standard free enthalpy of exchange was found to be $\Delta G_{0.5} = -7.7$ kcal/mol at 375°.

Introduction

In a previous paper[1] one of the authors showed that the synthetic zeolite Linde A (subsequently called NaA), in contact with molten $NaNO_3$, loses its water and occludes ten Na^+–NO_3^- ion pairs.[2] It appears that there is no way of differentiating, by chemical means, between the occluded and the structural sodium cations and, therefore, the formula $Na_{22}\cdot(AlO_2)_{12}\cdot(SiO_2)_{12}\cdot(NO_3)_{10}$ for the unit cell of the so-called occluded zeolite was proposed. The question arises whether the NO_3^- ions are also exchangeable for another anion or, in other words, whether the occluded zeolite can be considered a bifunctional ion exchanger. This would be the first instance that *anion* exchange has been observed in a molten salt media.

Experimental Section

(a) Materials. NaA (20 g) was stirred with 250 ml of water, poured into a cylinder, and allowed to stand for 2–3 hr. The precipitate was practically free of gel and fines, and was collected, washed with distilled water, and dried at 110°. The product was kept open to the air to ensure equilibrium with the atmosphere and therefore constant weight was achieved. The water content was determined by the weight loss on heating to 900°. Reagent grade chemicals were used without further purification beyond drying at 105° for at least 24 hr.

(b) Methods. Air-dried NaA (1.2 g), 30.0 g of sodium nitrate, and varying amounts of sodium chloride were weighed into a 50-ml round-bottom centrifuge tube, introduced in the oven at 375° and kept there for 24 hr. After equilibration, the content of the tubes was transferred to a porcelain dish and allowed to cool. The mixture was dispersed in distilled water and the zeolite washed until it was free of chlorides, and then dissolved in dilute nitric acid. The equilibrium concentration of the chloride ion in the zeolite, C_{Cl}, was determined by precipitating it with excess silver nitrate, and potentiometrically back-titrating the excess silver with sodium chloride. The equilibrium concentration of chloride in the melt, C_{Cl}, was calculated from the difference between the initial amount of chloride and $\bar{C}_{Cl}$. In cases where it was found advisable to determine the concentration in the melt directly, this was done by the same method.

Sodium and silica were determined by spectrophotometric methods. Concentrations are expressed as molali-

(1) M. Liquornik and Y. Marcus, *J. Phys. Chem.*, **72** 2885 (1968).
(2) Attempts have also been made to extend this work to the zeolite Linde X, but they were unsuccessful due to the difficulties in isolating a fully occluded Na-X.

TABLE I: Experimental Results of the Distribution of Chloride between NaA and a Molten (NO_3,Cl)Na Solution at 375°

C_{Cl}	$\bar{C}_{Cl}$	D_{Cl}	$\bar{\eta}_{Cl}$[a]
0.0056 ± 0.004	0.17 ± 0.03	32 ± 2	0.29 ± 0.04
0.0144 ± 0.0006	0.32 ± 0.03	22 ± 2	0.54 ± 0.02
0.032 ± 0.001	0.57 ± 0.03	18 ± 2	0.97 ± 0.05
0.0550 ± 0.0002	0.63 ± 0.03	11 ± 1	1.07 ± 0.05
0.077 ± 0.001	0.71 ± 0.02	9.1 ± 0.4	1.21 ± 0.04
0.1473 ± 0.003	0.81 ± 0.02	5.5 ± 0.1	1.38 ± 0.03
0.220 ± 0.002	0.88 ± 0.02	4.03 ± 0.05	1.50 ± 0.03
0.468 ± 0.002	0.99 ± 0.05	2.1 ± 0.1	1.69 ± 0.1
0.7162 ± 0.0003	1.020 ± 0.002	1.425 ± 0.004	1.740 ± 0.004
0.965 ± 0.001	1.02 ± 0.02	1.05 ± 0.03	1.74 ± 0.04
1.1636 ± 0.0003	1.06 ± 0.01	0.91 ± 0.01	1.81 ± 0.02
	Reversibility Check		
0.106 ± 0.003	0.734 ± 0.02	6.9 ± 0.1	1.251 ± 0.002
0.105 ± 0.001	0.80 ± 0.04	7.6 ± 0.4	1.36 ± 0.06

[a] Number of moles of Cl^-/unit cell of NaA.

TABLE II: Experimental Results of the Distribution of Chloride between NaA and a Molten (NO_3,Cl)Na Solution at 450°

C_{Cl}	$\bar{C}_{Cl}$	D	$\bar{\eta}_{Cl}$
0.073 ± 0.001	0.86 ± 0.03	11.8 ± 0.5	1.47 ± 0.05
0.22	0.94	4.3	1.60
1.18 ± 0.02	0.9554 ± 0.0001	0.81 ± 0.1	1.6287 ± 0.0003
1.3493 ± 0.0000	0.9768 ± 0.0004	0.72 ± 0.01	1.6652 ± 0.0006
4.14 ± 0.5	0.98 ± 0.01	0.24 ± 0.03	1.67 ± 0.02

ties, *viz.*, mol/kg of solvent (*e.g.*, $NaNO_3$) or mol/kg of NaA anhydrous. The experiments were performed at 375 and 450°. The temperature of the oven was controlled by an Eurotherm temperature controller and the variations in temperature over a 24-hr period were not more than ±1.5°.

Results

Eight exchange experiments made with the same initial C_{Cl}, but at different times, gave the following average results: $\bar{C}_{Cl}$ = 1.01 ± 0.007, C_{Cl} = 0.97 ± 0.01, and D = 1.04 ± 0.01, were D, the distribution coefficient, equals $\bar{C}_{Cl}/C_{Cl}$. At lower chloride concentration a somewhat higher error is expected.

No significant change in the distribution coefficient as a function of time was found over a period of 24–216 hr. The variations in the distribution were random and less than 1% (D = 1.05 ± 0.01).

Samples of zeolite from the above experiments were subsequently used to check the reversibility of the exchange reactions. They were equilibrated with pure sodium nitrate at 375° and both phases were analyzed for their chloride content. The results are given in Table I.

The concentrations of the chloride ion in the molten sodium nitrate solution at 375° varied from 0.005 to 1.16 *m*; the limiting factor being analytical for the lower values and the solubility of sodium chloride at the higher values. The solubility was determined experimentally and found to be about 1.5 *m*. At 450°, the highest concentration, C_{Cl} = 4.14 *m*, was reached by using a melt saturated with solid sodium chloride. The equilibrium concentration of the solution was determined in a decanted and clear sample of the melt.

The results for the distribution of chloride from NaCl in $NaNO_3$ obtained at 375 and 450° are summarized in Table I and II, respectively. Each result is the average of two experiments and the variation given corresponds to the difference between duplicates. The tables also contain the values of the distribution coefficient $D = C_{Cl}/C_{Cl}$ and of the number $\bar{n}$ of occluded chloride ions per unit cell of zeolite A.

Table III gives the corresponding results for the distribution from an eutectic mixture of sodium–potassium nitrate at 375°.

Five samples of the exchanged zeolite were analyzed for sodium and silica. The Na/Si ratio proved to be within 2% of the theoretical value of 22/12 for the occluded zeolite with the formula mentioned above. We are dealing, therefore, with a selective anion exchange reaction with the occluded salt and not one of sodium chloride being additionally absorbed; the latter would have led to an increase of this ratio.

Discussion

Lumsden[3] has shown that the (NO_3,Cl) Na system can be considered in first approximation as an ideal solution. The very small positive deviations from ideality can be neglected and, therefore, the effects observed, *viz.*, the strong dependence of the distribution coefficient on the concentration, must be ascribed to the solid phase only. For $NaNO_3$ as a solvent the very high value of the distribution coefficient D at low concentrations points to a high activity coefficient for the chloride ion in the zeolite with respect to the occluded nitrate ion, or in other words to a strongly negative free enthalpy for the exchange of nitrate by chloride in the zeolite.

On the other hand, at high concentrations a maximum value for the number $\bar{n}$ of occluded chloride ions is observed, corresponding to a steep decrease of the distribution coefficient, even less than 1.

TABLE III: Experimental Results of the Distribution of Chloride between NaA and a Molten (NO_3,Cl)(KNa) Solution at 375°

C_{Cl}	$\bar{C}_{Cl}$	D	$\bar{n}_{Cl}$
0.0927 ± 0.0001	0.132 ± 0.001	1.42 ± 0.01	0.225 ± 0.002
0.0950 ± 0.0001	0.159 ± 0.005	1.68 ± 0.05	0.271 ± 0.008
0.2338 ± 0.0001	0.409 ± 0.001	1.752 ± 0.005	0.698 ± 0.002
0.2367 ± 0.0004	0.4340 ± 0.0001	1.833 ± 0.002	0.7398 ± 0.0002
0.473 ± 0.001	0.8457 ± 0.001	1.788 ± 0.003	0.4417 ± 0.0003
0.49 ± 0.02	0.891 ± 0.006	1.8 ± 0.1	1.52 ± 0.01
0.9517 ± 0.004	1.459 ± 0.003	1.533 ± 0.004	2.487 ± 0.006
0.9977 ± 0.005	1.57 ± 0.01	1.58 ± 0.01	2.68 ± 0.02

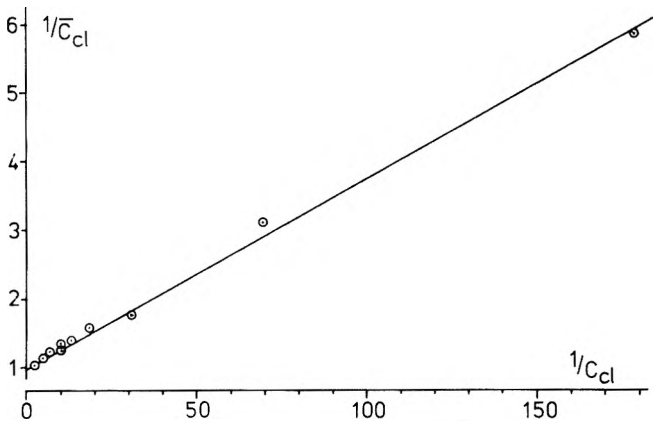

Figure 1. Reciprocal molalities $1/C_{Cl}$ *vs.* $1/\bar{C}_{Cl}$ of the chloride in the molten liquid and in the zeolite A phase, respectively: temperature 375°, line calculated for $\bar{C}_0 = 1.06$ and $K = 395$.

Curiously enough the (Na,K)(NO_3) eutectic, instead of $NaNO_3$ as a solvent for the chloride ions, gives a completely different picture with a distribution coefficient independent of the concentration. Here it seems as if the zeolite behaves as a rather neutral "sponge," without preference for either ion and without a clear restricted exchange capacity. However, in this case of a Na,K mixed solvent, exchange of sodium for potassium in the original zeolite framework will have taken place to some degree,[4] thus altering the anion exchange properties.

It has been observed that potassium-zeolite A does not occlude KNO_3 at all.[4,5] Because of this complication we have not gone into further detail about the combined anion-cation exchange in a mixed cation-anion solvent.

The hyperbolic shape of the distribution curve for the chloride concentration C_{Cl} in the zeolite *vs.* the concentration in the solution C suggest a dependence as given by an ion exchange equilibrium. Indeed if $1/\bar{C}$ is plotted as a function of $1/C$ a straight line is obtained over a large range (Figure 1).

This empical distribution function with two constants a and b

$$1/\bar{C} = a + b/C \qquad (1)$$

can be derived from the expression for the ideal ion exchange equilibrium[6]

$$K = \bar{x}(1 - x)/(1 - \bar{x})x \qquad (2)$$

K is the selectivity coefficient, x and $\bar{x}$ are the mole fractions of one component (Cl^-) in the solvent and in the solid phase, respectively, and $1 - x$ and $1 - \bar{x}$ the same for the other component (NO_3^-).

The molality C_{Cl} is expressed by

$$x/(1 - x) = C_{Cl}/11.76$$

as 1 kg of sodium nitrate contains 1000/85.01 = 11.76 mol.

Now $\bar{x}$ can be interpretated as the fraction occupied by Cl^- from the total number (per unit zeolite) of sites available for exchange by Cl^-. Thus $\bar{x} = \bar{n}/\bar{n}_0 = \bar{C}_{Cl}/\bar{C}_0$, with $\bar{C}_{Cl}$ as before the molality of chloride in the zeolite and $\bar{C}_0$ the value corresponding to maximum of exchange.[6]

Equation 2 can be thus transformed into

$$\bar{C}_0/\bar{C}_{Cl} = 1 + 11.76/KC_{Cl}$$

or

$$1/\bar{C}_{Cl} = 1/\bar{C}_0 + 11.76/K\bar{C}_0C_{Cl} \qquad (3)$$

Equation 3 is analogous to the empirical expression 1.

From Figure 1 we deduce as best values from the intercept $\bar{C}_0 = 1.06 \pm 0.02$ or $\bar{n}_0 = 1.81 \pm 0.035$ and from the slope $K = 395 \pm 7$, all at 375°. From the few data at 450° (Table II) it follows that $\bar{C}_0 = 0.98$ or $\bar{n}_0 = 1.67$, slightly lower than at 375°. A reliable value for K can not be obtained though it appears to be higher at 450° than at 375°.

From these results the conclusion is drawn that only slightly less than two nitrate ions out of the ten present in the occluded zeolite can be exchanged for chloride ions. It appears that this limit cannot be surpassed with $NaNO_3$ as a solvent. However, in the cation mixed solvent all ten nitrate ions appear to be exchangeable.

The selectivity coefficient K can also be expressed as the standard free enthalpy of exchange

$$-RT \ln K = \Delta G_{0.5}$$

At 375°, $\Delta G_{0.5} = -7.7$ kcal/mol. This standard free enthalpy is for the reaction

$$(Cl^-)_{liq} + (NO_3^-)_{occ} = (Cl^-)_{occ} + (NO_3^-)_{liq}$$

representing the substitution of an occluded nitrate ion by a chloride ion. The two standard states are for the occluded zeolite at 50% of maximum exchange and for the liquid at a composition with $x_{Cl} = x_{NO3} = 0.5$, respectively.

Acknowledgment. The investigations presented in this article have been carried out under the auspices of the Netherlands Foundation for Chemical Research (S.O.N.) and with the financial aid and a grant to one of the authors (M. L.) of the Netherlands Organisation for the Advancement of Pure Research (Z.W.O.).

(3) J. Lumsden, "Thermodynamics of Molten Salt Mixtures," London and New York, N. Y., 1966, p 124.
(4) M. Liquornik and Y. Marcus, *Isr. J. Chem.*, **6**, 115 (1968).
(5) M. Liquornik and Y. Marcus, *J. Phys. Chem.*, **75**, 2523 (1971).
(6) R. Kunin, "Ion Exchange Resins," 2nd ed, New York, N. Y., 1958, pp 17–26.

Electrochemistry of Chemisorbed Molecules. I. Reactants Connected to Electrodes through Olefinic Substituents

Ross F. Lane and Arthur T. Hubbard*

Department of Chemistry, University of Hawaii, Honolulu, Hawaii 96822 *(Received September 7, 1972)*

Publication costs assisted by the National Science Foundation and the Petroleum Research Fund

The tendency of olefins to chemisorb irreversibly on platinum electrodes is exploited to attach a variety of reactive entities to the electrode surface. Chelates connected to the electrode surface through an olefinic side chain allow metals to be selectively chemisorbed at the electrode surface. The stability of the chemisorbed metal complex is shown to vary with electrode potential, due to the influence of the electrical double layer, in such a way that the chelating ability of the chemisorbed chelate can effectively be "switched" on or off. Studies of the electrode reactions of chemisorbed complexes of Fe and Pt and of organic depolarizers such as substituted polyhydric phenols indicate that only in certain instances are the adsorbed reactants able to achieve a reactive orientation of the sort acquired readily by dissolved species. Evidence is presented that the π system of each adsorbed olefin studied undergoes ten-electron oxidation to form the corresponding carboxylic acid and/or CO_2. Equations which describe the electrochemistry of chemisorbed molecules are derived and tested.

Introduction

Alkenes and alkynes react with platinum surfaces to form irreversibly chemisorbed species[1,2] which are not removed from the surface by rinsing or by electrolysis apart from strongly oxidizing conditions.[2] Thus, when a substituent of interest is incorporated into an olefinic substance and the resulting compound allowed to react with the electrode surface, the substituent becomes connected to the surface (Figure 1). By this means, ionic species have been tethered within the double layer region in order to probe the mechanisms of electrode reactions involving platinum complexes, as described in the second article of this series.[3] Alternately, the electrochemical reactant itself can be connected to the electrode surface, allowing its reactivity to be observed as a function of charge, orientation, and structure, as described here. For example, allylamine may be used to induce the adsorption of metal ions or of organic electrode reactants such as allylhydroquinone (Figure 1).

The rather copious literature dealing with olefin adsorption on platinum group metals, summarized in ref 1, contains two commonly accepted formulations, both of which seem to be operative to at least some extent in most situations; the *associative* model stresses loss of double bond character with formation of two Pt–C bonds

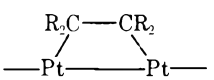

the *dissociative* model emphasizes retention of double bond character with cleavage of C–H bonds and formation of Pt–C and Pt–H bonds

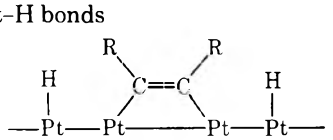

Careful measurements of surface coverage for the various surfactants used in this study indicate that at maximum coverage two Pt surface atoms are consumed per double bond upon adsorption from aqueous solution, corresponding to the associative model. Both models lead to essentially the same predictions concerning the location of the carbon chain within the double layer.

Experiments in which the adsorbed layer of alkene formed at a platinum single-crystal surface in ultrahigh vacuum was characterized by low-energy electron diffraction and work function determination indicate that highly ordered layers are formed, suggesting that a chemical reaction between the π system and individual surface metal atoms occurs in which the metal acts as the acceptor of electron density.[4] The structures of olefins adsorbed from solution are not known, although experiments leading toward that objective are in progress. It seems likely, however, that adsorption from solution at high coverage produces an ordered layer in which each adsorbed C interacts primarily with one Pt, in register with the original metal surface, in the familiar (1 × 1) pattern.

The interaction of metal ions in solution with electrostatic and chelating ligands at the surface of ion exchange resins has been studied with regard to possible use in separations.[5] Correlation of partition coefficients with double layer properties has been neglected for lack of a reliable method by which to assay the double layer at solid/liquid interfaces.[6] The analogy between ion exchange resins and the ligand-coated electrodes used in this work is obvious. A less obvious fact is that coated metal surfaces allow the double layer influence on the ion exchange process to be directly characterized through experiments in which surface coordination is switched on or off by variation of the electrode potential.

Current–potential data for the deposition of monolayer quantities of metal on substrates of a dissimilar metal have been acquired using thin layer electrodes by Schmidt

(1) E. Gileadi, Ed., "Electrosorption," Plenum Press, New York, N. Y., 1967.
(2) A. L. Y. Lau and A. T. Hubbard, *J. Electroanal. Chem.*, **33**, 77 (1971); **24**, 237 (1970).
(3) R. F. Lane and A. T. Hubbard, *J. Phys. Chem.*, **77**, 1411 (1973).
(4) G. A. Somorjai and F. J. Szalkowski, *J. Chem. Phys.*, **54**, 389 (1971).
(5) H. F. Walton, *Anal. Chem.*, **44**, 256 R (1972).
(6) M. Sborov, W. Moats, and A. T. Hubbard, University of Hawaii, unpublished experiments.

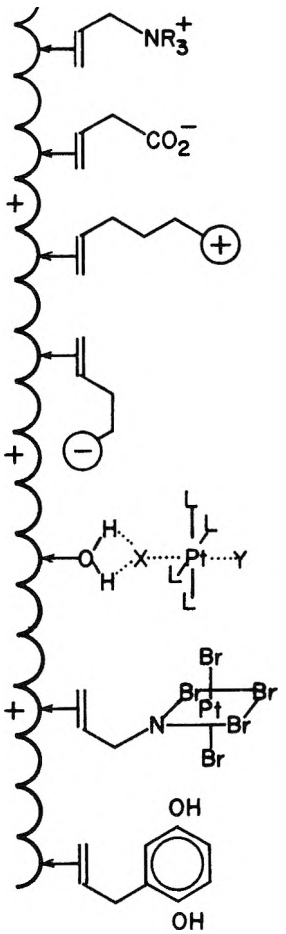

Figure 1. Adsorption of substituted olefins at platinum electrodes. The cases illustrated are, from top to bottom, allyltrialkylammonium ion; vinylacetic acid anion; alkenyl cation and anion oriented in the field of a positively charged electrode; halide bridged reactant complex, $Pt(II)L_4$; $PtBr_5$ (allylamine)$^-$; allylhydroquinone.

and Gygax.[7] Equations pertaining to the reversible deposition of metals were derived by them.[8] Equations which express the rates of irreversible electrode reactions of chemisorbed layers have not been presented, nor the influence of the electrical double layer on such reactions described, prior to the present work.

Experimental Equations

Suppose that the electrode surface contains a chemisorbed substance which reacts according to eq 1, and obeys the Nernst equation, eq 2. If a linear isotherm is

$$\text{Ox (ads)} + ne^- = \text{R} \tag{1}$$

$$E = E^0 + (RT/nF) \ln ({}_1a_{ox}/a_R) \tag{2}$$

used to represent the variation of the activity of chemisorbed reactant with coverage (eq 3), then the thin layer

$${}_1a_j = {}_1\gamma_j\,{}_1\Gamma_j \tag{3}$$

equations are surprisingly similar in form to those for unadsorbed reactants.[9] The results are

$$i = \frac{n^2F^2(-r)A^2\Gamma_{ox}^0 \exp\left[\frac{nF}{RT}(E - E^0)\right]}{RTV\,{}_1\gamma_{ox}\left\{1 + \frac{A}{{}_1\gamma_{ox}V}\exp\left[\frac{nF}{RT}(E - E^0)\right]\right\}^2} \tag{4}$$

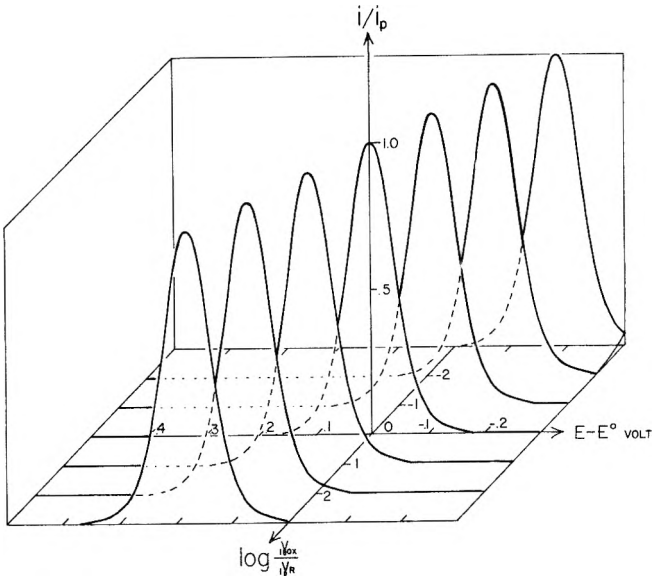

Figure 2. Theoretical thin layer current–potential curves for reversible reactions of chemisorbed molecules. Graphs of eq 4 for various values of ${}_1\gamma_{ox}$ and ${}_1\gamma_R$. The following values were employed in making the plots: A = 1.0 cm^2; $\Gamma_{ox}^0 = 10^{-9}$ mol cm^{-2}; $r = -2 \times 10^{-3}$ V sec^{-1}; n = 1; T = 298°K.

$$i_p = \frac{n^2F^2(-r)A\Gamma_{ox}^0}{4RT} \tag{5}$$

$$E_p = E^0 + \frac{RT}{nF}\ln\frac{{}_1\gamma_{ox}V}{A} \tag{6}$$

Graphs of eq 4 for constant values of ${}_1\gamma_{ox}$ appear in Figure 2. If ${}_1a_{ox}$ is replaced by a_{ox} (*i.e.*, if Ox is not chemisorbed), then eq 4–6 reduce to those for reversible reactions of soluble reactants. The peak potential should become less positive with increasing ${}_1\gamma_{ox}$ and is thus an indication of adsorption strength. The peak current is a function only of the initial coverage.

If the electrochemical products and reactants, all of which are chemisorbed, react according to eq 7, and obey

$$\text{Ox (ads)} + ne^- = \text{R (ads)} \tag{7}$$

the Nernst equation, the experimental equations describing the current–potential curve are the same as those for one reactant chemisorbed (eq 4-6), except that A/V must be replaced by ${}_1\gamma_R$. By combining eq 4-6, the current–potential expression is obtained in a particularly convenient form for comparison with experimental curves

$$i = 4i_p\frac{\exp\left[\frac{nF}{RT}(E - E_p)\right]}{\left\{1 + \exp\left[\frac{nF}{RT}(E - E_p)\right]\right\}^2} \tag{8}$$

In the event that the electrode reaction proceeds irreversibly, eq 9, eq 4-6 are not applicable. Instead, eq 10

$$\text{Ox (ads)} + ne^- \rightarrow \text{products} \tag{9}$$

$$i = -nFA(d\Gamma_{ox}/dt) \tag{10}$$

must be combined with the Tafel equation, written in the form appropriate to the reaction of interest, such as eq 11.

(7) For a discussion with references to other work, see E. Schmidt and H. R. Gygax, *J. Electroanal. Chem.*, **12**, 300 (1966).
(8) A. T. Hubbard and F. C. Anson in "Electroanalytical Chemistry," Vol. 4, A. J. Bard, Ed., Marcel Dekker, New York, N. Y., 1970.
(9) A. T. Hubbard, *J. Electroanal. Chem.*, **22**, 165 (1969).

$$i = nFA^{*}k^{0}{}_{1}\gamma_{ox}\,\Gamma_{ox}\,\exp\left[\frac{-^{*}\alpha F}{RT}(E - E^{0})\right] \quad (11)$$

For simplicity in describing totally irreversible reactions the current due to the back reaction has been noted to be negligible as the forward reaction proceeds.[8] For the present purposes ${}_{1}a_{ox}$ has been represented by a linear isotherm (eq 3).

Equation 11 is readily integrated to obtain the experimental equation for the cathodic current–potential curve observed at a thin layer electrode. The peak current and

$${}_{c}i = nFA^{*}k^{0}{}_{1}\gamma_{ox}\Gamma_{ox}{}^{0}\,\exp\left\{\frac{-^{*}\alpha F}{RT}(E - E^{0}) - \frac{RT^{*}k^{0}{}_{1}\gamma_{ox}}{^{*}\alpha F(-r)}\exp\left[\frac{-^{*}\alpha F}{RT}(E - E^{0})\right]\right\} \quad (12)$$

potential are given by eq 13 and 14. Analogous equations

$${}_{c}i_{p} = \frac{^{*}\alpha nF^{2}A(-r)\,\Gamma_{ox}{}^{0}}{RTe} \quad (13)$$

$${}_{c}E_{p} = E^{0} + \frac{RT}{^{*}\alpha F}\ln\frac{RT_{1}\gamma_{ox}{}^{*}k^{0}}{^{*}\alpha F(-r)} \quad (14)$$

are obtained for anodic current–potential curves of chemisorbed reactants by replacing $^{*}\alpha$ by $(1 - {}^{*}\alpha)$ and the subscript ox by the subscript R. Graphs of eq 12 for several values of $^{*}\alpha$ and $^{*}k^{0}$ appear in Figure 3.

Adherence of the experimental curves to the theory has been tested by comparing the experimental curves with a graph of the current–potential equation for values of $^{*}\alpha$ (or $(1 - {}^{*}\alpha)$) and $^{*}k^{0}{}_{1}\gamma$ calculated from the peak current and potential by means of eq 13 and 14. For convenience in comparing experiment with theory, these current–potential equations were rewritten in terms of the peak potential and peak current, as follows

$${}_{c}i = (e)_{c}i_{p}\,\exp\left\{\frac{-e_{c}i_{p}}{nFA(-r)\Gamma_{ox}{}^{0}}(E - {}_{c}E_{p}) - \exp\left[\frac{-e_{c}i_{p}}{nFA(-r)\Gamma_{ox}{}^{0}}(E - {}_{c}E_{p})\right]\right\} \quad (15)$$

$${}_{a}i = (e)_{a}i_{p}\,\exp\left\{\frac{e(-_{a}i_{p})}{nFAr\Gamma_{R}{}^{0}}(E - {}_{a}E_{p}) - \exp\left[\frac{e(-_{c}i_{p})}{nFAr\Gamma_{R}{}^{0}}(E - {}_{a}E_{p})\right]\right\} \quad (16)$$

That is, in verifying the applicability of the experimental equations, experimental values of the parameters $^{*}\alpha$ and $^{*}k^{0}$ have been inserted into the equations (through the intermediacy of ${}_{c}i_{p}$ and ${}_{c}E_{p}$, or ${}_{a}i_{p}$ and ${}_{a}E_{p}$), because of course the values of these parameters could not be calculated from first principles in the present state of chemical knowledge.

$^{*}\alpha$ and $^{*}k^{0}$, the *apparent* values of the rate parameters, are expected to depend markedly upon double layer composition, structure, and potential distribution. As described in part II[3] and ref 9, $^{*}\alpha$ and $^{*}k^{0}$ are related to the true (*i.e.*, double-layer-independent) values α and k^{0} by

$$^{*}\alpha = \alpha + \frac{C}{{}_{R}C_{d}}(Z_{R} - \alpha) \quad (17)$$

$$^{*}k^{0} = k^{0}\exp\left[(\alpha - Z_{R})\frac{F}{RT}{}_{R}\phi_{2}\right] \quad (18)$$

$${}_{R}\phi_{2} = \frac{C}{{}_{R}C_{d}}(E - E_{Z}) \quad (19)$$

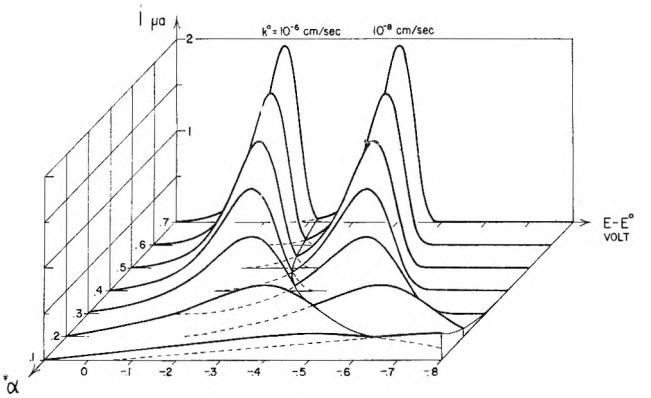

Figure 3. Theoretical thin layer current–potential curves for totally irreversible reactions of chemisorbed molecules. Graphs of eq 12 for various values of $^{*}\alpha$ and $^{*}k^{0}$. The following values were employed in making the plots: ${}_{1}\gamma_{ox} = 10^{3}$ cm^{-1}; A, $\Gamma_{ox}{}^{0}$, r, n, and T as in Figure 2.

For anodic reactions

$$(1 - {}^{*}\alpha) = (1 - \alpha) - \frac{C}{{}_{R}C_{d}}[Z_{R} + (1 - \alpha)] \quad (20)$$

$$^{*}k^{0} = k^{0}\exp\left\{-[(1 - \alpha) + Z_{R}]\frac{F}{RT}{}_{R}\phi_{2}\right\} \quad (21)$$

Thus, the magnitude of double layer influence is in direct correspondence with the ratio $C/{}_{R}C_{d}$ of double layer capacitance to diffuse layer component of the double layer capacitance. Since chemisorbed reactants tend to be located comparatively close to the surface, ${}_{R}C_{c}$ will tend to be large and ${}_{R}C_{d}$ small (corresponding to a thin compact layer and a thick diffuse layer from the viewpoint of the reactant). Accordingly, $C/{}_{R}C_{d}$ (and therefore ${}_{R}\phi_{2}$) will tend to be large, so that a large double layer influence is expected. For uncharged chemisorbed reactants ($Z_{R} = 0$) the effect of increasing the potential at the reaction plane, ${}_{R}\phi_{2}$, in the direction of potential scan (positive for anodic reactions, negative for cathodic) is always to retard the reaction. In absolute magnitude ${}_{R}\phi_{2}$ tends to be positive at platinum electrodes (E_{Z} = *ca.* −0.05 V *vs.* SCE), and thus it tends to decrease the value of $^{*}k^{0}$ for oxidation and increase $^{*}k^{0}$ for reduction reactions of neutral reactants. The diffuse layer always acts to decrease $^{*}\alpha$ for uncharged reactants (leading to proportionately decreased peak currents). These predictions are borne out by the results presented below.

Results and Discussion

1. Chemisorbed Chelates. A thin layer electrode was rinsed with 10^{-4} *F* Fe(III) in a 1 *F* $NaClO_4|HClO_4$ electrolyte at pH 3, while the electrode potential was maintained at 0.0 V *vs.* NaCE (calomel electrode prepared with 1 *F* NaCl), after which the current–potential curve appearing in Figure 4 was obtained. The electrode was then rinsed with a 10^{-3} *F* solution of 3-allylsalicylic acid (forming a chemisorbed layer), with water, and finally with the Fe(III) solution; the current–potential curve shows that the quantity of iron in the cell has been increased by an amount corresponding to one Fe per molecule of adsorbed salicylate. In contrast, when the electrode potential was held at 0.6 V *vs.* NaCE during rinsing of the coated electrode with the Fe(III) solution, an interfacial excess of Fe complexes did not accumulate. From this result it is evident that the electrode, when positively charged, attracts the salicylate anion into the compact

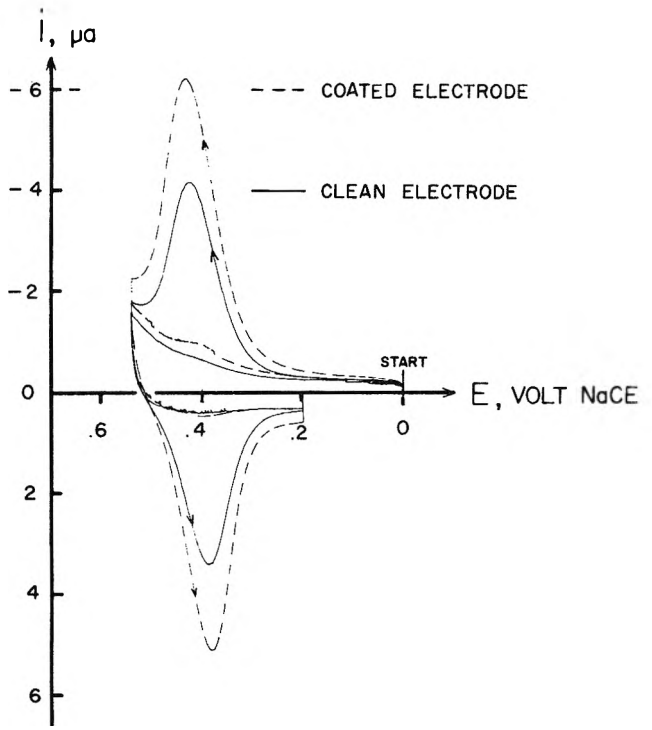

Figure 4. Thin layer current–potential curves for Fe(II) and Fe(III) at clean and 3-allylsalicylic acid coated platinum electrodes: (——) clean electrodes, (-----) electrodes containing chemisorbed 3-allylsalicylic acid. The electrode was cleaned and surfactant-treated as described in the Experimental Section. Reactant solutions initially contained 0.15 m*F* Fe(III) and 1 *F* $NaClO_4$, pH 3.0; thin layer volume, V = 3.88 μl; platinum electrode area, A = 1.15 cm^2; rate of potential sweep, r = 2.00 mV sec^{-1}; solution temperature, T = 23 ± 1°.

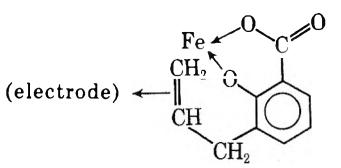

layer (while repelling Fe^{2+} and Fe^{3+}) and in so doing decreases the tendency for Fe complexes to coordinate with the adsorbed allylsalicylate, the anionic part of which will be abbreviated Sal^{2-}. Data for Fe^{z+} adsorption appear in Table I. The formation constant, ${}_zK_f$, can be written in a

$$Fe^{z+} + Sal^{2-} \overset{{}_zK_f}{\rightleftharpoons} Fe^{z+} - Sal^{2-} \quad (22)$$

$$(\text{compact layer}) + Sal^{2-} \rightleftharpoons (\text{compact layer}) \cdots Sal^{2-} \quad (23)$$

simple form when activity is expressed in terms of interfacial excess by means of eq 3 and activity coefficients are included within the constant at fixed ionic strength

$${}_zK_f' \equiv \frac{{}_2a(Fe^{z+} - Sal^{2-})}{{}_2a(Fe^{z+})a(Sal^{2-})} = \frac{{}_2\gamma(Fe^{z+} - Sal^{2-}){}_2\Gamma(Fe^{z+} - Sal^{2-})}{{}_2\gamma(Fe^{z+}){}_2[Fe^{z+}]{}_2\gamma(Sal^{2-}){}_2\Gamma(Sal^{2-})} \quad (24)$$

$${}_zK_f' \equiv \frac{{}_2\Gamma(Fe^{z+} - Sal^{2-})}{{}_2[Fe^{z+}]{}_2\Gamma(Sal^{2-})} = \frac{{}_2\Gamma(Fe^{z+} - Sal^{2-})}{{}_2[Fe^{z+}]\{\Gamma^0(Sal^{2-}) - {}_1\Gamma(Sal^{2-}) - \Gamma(Fe^{z+} - Sal^{2-})\}} \quad (25)$$

where $\Gamma^0(Sal^{2-}) \equiv$ total interfacial excess of allylsalicylate, including all forms. ${}_zK_f$ is assumed to have been corrected for incomplete dissociation to the salicylate dianion.

In part II[3] it is shown that the fraction of adsorbed *substituent* present as the "free" ion in the compact layer at a given instant, ${}_1\Gamma_s/({}_1\Gamma_s + {}_2\Gamma_s)$, can be estimated by means of a Boltzmann distribution. The result for the present case is

$$\frac{{}_1\Gamma(Sal^{2-})}{\Gamma^0(Sal^{2-}) - {}_2\Gamma(Fe^{z+} - Sal^{2-})} = \frac{1 - \exp[-\lambda(1 - x_1/x_2)]}{\exp[-\lambda(1 - L/x_2)] - \exp[-\lambda(1 - x_1/x_2)]} \equiv f(E) \quad (26)$$

where $\lambda \equiv Z_sF(E - E_z)/RT$; x_1, $x_2 \equiv$ distances of closest approach of the substituent (Sal^{2-}) and metal ion (Fe^{z+}), respectively, and ${}_1\Gamma(Sal^{2-})$, ${}_2\Gamma(Sal^{2-}) \equiv$ interfacial excesses in the compact and diffuse regions of the double layer, respectively; $L \equiv$ length of chemisorbed allylsalicylate dianion when fully extended. From the definition of ${}_zK_f'$ we find that

$${}_1\Gamma(Sal^{2-}) = \Gamma^0(Sal^{2-}) - {}_2\Gamma(Fe^{z+} - Sal^{2-}) \times \left\{1 + \frac{1}{{}_zK_f'{}_2[Fe^{z+}]}\right\} \quad (27)$$

Combining eq 26 and 27 gives an expression for the fractional coverage by metal complex in terms of bulk metal ion concentration and electrode potential

$$\frac{{}_2\Gamma(Fe^{z+} - Sal^{2-})}{\Gamma^0(Sal^{2-})} = \frac{1 - f(E)}{1 - f(E) + \frac{1}{{}_zK_f'{}_2[Fe^{z+}]}} \quad (28)$$

where $f(E)$ is defined in eq 26 and ${}_2[Fe^{z+}]$ is the concentration of Fe^{z+} in the vicinity of x_2 given by

$${}_2[Fe^{z+}] = [Fe^{z+}]\exp\left[\frac{-ZF}{RT}\phi_2\right] \approx [Fe^{z+}] \times \exp\left[\frac{-ZF}{RT}\frac{C}{C_d}(E - E_z)\right] \quad (29)$$

Equations 28 and 29 can be combined to give

$$[1 - f(E)]\exp\left[\frac{-ZF}{RT}\frac{C}{C_d}E\right] = \exp\left[\frac{-ZFCE_z}{RTC_d}\right]\frac{\rho}{{}_zK_f'[Fe^{z+}]\quad 1 - \rho} \quad (30)$$

where $\rho \equiv {}_2\Gamma(Fe^{z+} - Sal^{2-})/\Gamma^0(Sal^{2-})$ from which it can be seen that a graph of $[1 - f(E)]\exp[-ZFCE/(RTC_d)]$ *vs.* $\rho/(1 - \rho)$ should be linear with slope equal to $\exp[-ZFCE_z/RTC_d]/\{{}_zK_f'[Fe^{z+}]\}$. Graphs of eq 30 and the data of Table I are shown in Figure 5.

It may be worth pointing out that when the electrode is held at a zero charge potential, E_z, eq 28 predicts that efficient retention of metal ions will occur (*i.e.*, the chemisorbed chelate is "on") whenever $[Fe^{z+}] \geq 1/{}_zK_f'$ ($\approx 10^{-7}$ *M* at pH 3) and that the ions will be quantitatively released (the "off" state) when E exceeds E_z by as little as 0.2 V.

2. Chemisorbed Alkenyl Biphenols. The electrochemical reactivity of the following organic molecules when chemisorbed at platinum electrodes has been studied: 2-allylhydroquinone, I; 4-allylcatechol, II; 4-allyl-2-methoxyphenol (eugenol), III; 4-allyl-2,6-dimethoxyphenol, IV; 6-allyl-2-methoxyphenol, V. These compounds chemisorb rapidly from dilute aqueous solution, presumably by

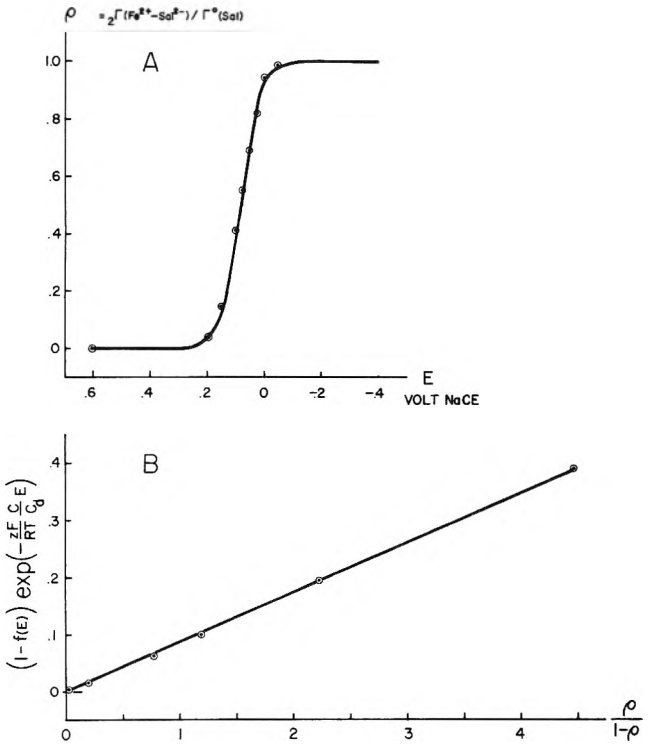

Figure 5. Potential dependence of Fe(II) adsorption induced by chemisorbed 3-allylsalicylic acid: (A) solid curve, graph of eq 28; circles, experimental points; (B) solid curve, graph of eq 30; circles, experimental points. The following values were employed in making the plots: $E_z = -0.010$ V *vs.* NaCE; $X_1 = 2.15$ Å; $X_2 = 3.1$ Å; $L = 7.3$ Å; $C/C_d = 0.050$; (see ref 3) $[Fe^{2+}] = 1.5 \times 10^{-4}$ *M*; $Z_s = -2$; $Z = +2$; $T = 298$°K. The experimental conditions are the same as in Table I.

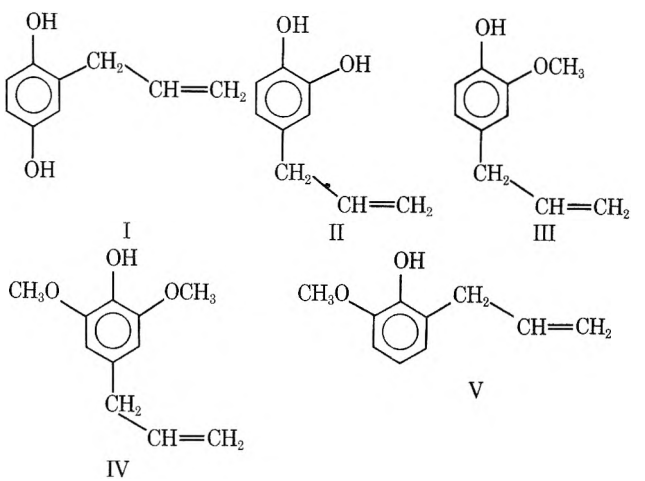

attachment at the allylic double bond. Compounds analogous to I–V, having saturated side chains, are not irreversibly chemisorbed to an appreciable extent under the same conditions. Coverages close to saturation are observed and the adsorbed material cannot be rinsed from the surface, as shown by direct electrochemical oxidation and by iodine-adsorption measurements. The initial reason for studying these materials was the expectation that the electrochemically reversible oxidation-reduction behavior observed for them in the "dissolved" state might persist in the chemisorbed state, thus providing an opportunity to test various theories of chemisorbed

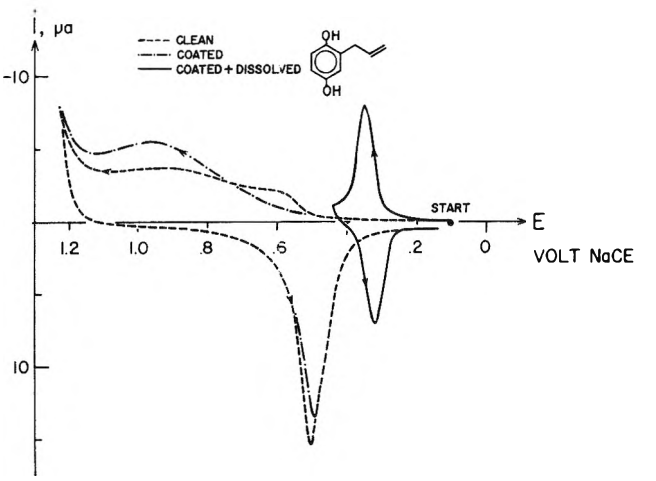

Figure 6. Thin layer current–potential curves for 2-allylhydroquinone at platinum electrodes: (-----) clean electrodes; (-·-·-) electrodes containing chemisorbed allylhydroquinone; (——) 2 m*F* allylhydroquinone at surfactant-coated electrode. The supporting electrolyte was 1 *F* $HClO_4$. Other experimental conditions as in Figure 4.

reactants, including eq 4–6. However, the expected reactivity is not observed. From the current–potential curves shown in Figure 6 it can be seen that 2-allylhydroquinone reacts reversibly from solution but is unreactive when chemisorbed, apart from destructive oxidation at very positive potentials involving oxidative desorption of the allyl side chain. All of the compounds, I–V, show the same behavior when chemisorbed. Blocking of the electrode by the adsorbed layer would be expected to prevent the reaction of dissolved as well as chemisorbed reactant and therefore cannot, alone, explain the unreactivity (see part II[3]). Examination of molecular models suggests a possible explanation; a consequence of the interaction of both carbons of the allylic double bond with the Pt surface is that the allylic carbon adjacent to the aromatic ring is rather close to the surface (2.8 Å for the "associative" scheme[1] and less for the "dissociative" scheme; the sum of Pt and C covalent radii is 2.14 Å); accordingly the two H atoms connected to that C are extremely close to the surface (2.3 Å in the most favorable conformer, and decreasing from there to a minimum of 1.9 Å; the covalent radii sum to 1.66 Å). The most stable conformer places the aromatic ring normal to the surface and on the opposite side of the allylic chain. The distance of the quinone from the surface, 4.5–7.8 Å, would prevent reactivity in this position even if it did not provide an unfavorable orientation of the oxygen lone pairs (hydroquinones) or π systems (quinones) for electron transfer with the surface. In fact, for unit ionic strength this places the quinones outside of the double layer, altogether.

In order to test the above explanation, compounds having longer unsaturated side chains (VI), for which a great-

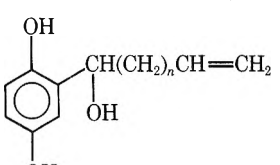

$n = 1$-4

VI

er variety of orientations is possible, have been studied with the expected result. Thus, the three compounds for

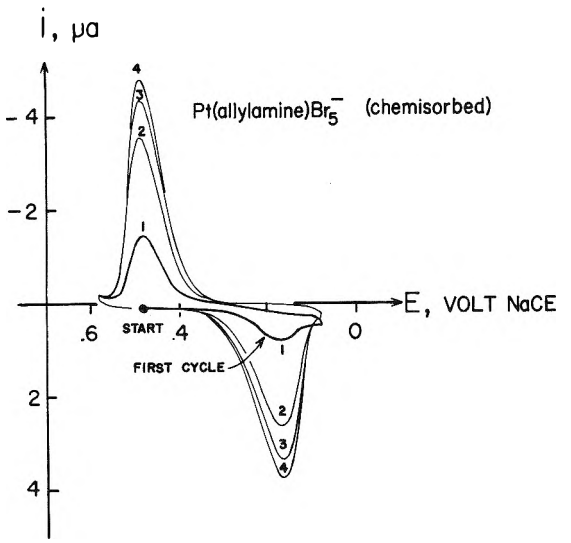

Figure 7. Cyclic thin layer current-potential curves for chemisorbed bromoallylaminoplatinum(II) and (IV) complexes. The thin layer electrode was cleaned and allowed to react with an aqueous solution of allylamine as described in the Experimental Section. Following rinsing with pure water to remove all dissolved, nonchemisorbed surfactant from the solution layer, the electrode was rinsed and filled with a freshly prepared 5 m*F* aqueous solution of K_2PtBr_6 and allowed to stand in contact with the Pt(IV) for 5 hr. This exposure was followed by thorough rinsing with water and then pure supporting electrolyte prior to recording the current-potential curve. The supporting electrolyte contained 10 m*F* $HClO_4$, 1 *F* $NaClO_4$, and 1 *F* NaBr. Other experimental conditions were identical with those of Figure 4.

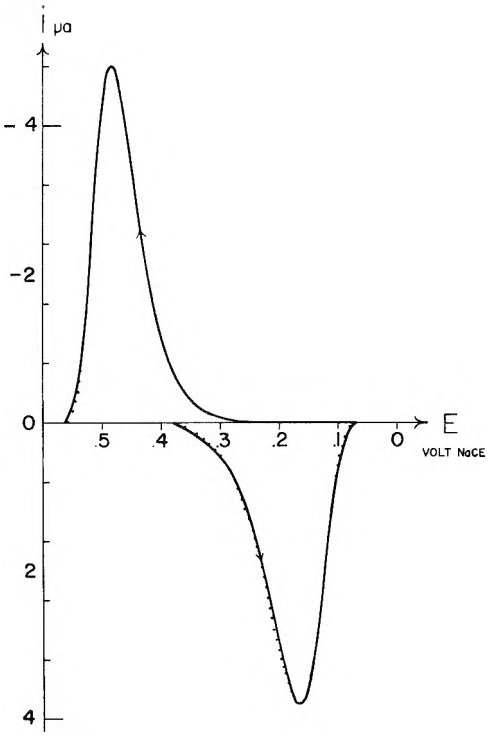

Figure 8. Theoretical thin layer current-potential curves for chemisorbed Pt^{II}(allylamine)Br_3^- and Pt^{IV}(allylamine)Br_5^-. Graphs of eq 15 and 16 for values of ${}_cI_p$, ${}_aI_p$, ${}_cE_p$, ${}_aE_p$, $\Gamma_{ox}{}^0$, and $\Gamma_R{}^0$ taken from Table II: solid curve, theoretical; dotted curve, experimental after correction for background current (where not visible, it has been obscured by the theoretical curve). The experimental conditions were the same as Figure 7.

which n = 2–4 reacted reversibly when chemisorbed. The chemisorbed compound for which n = 1 was reactive, but less so than those possessing longer side chains.

3. Chemisorbed Platinum Allylamine Complexes. When a platinum electrode is rinsed with a dilute aqueous solution of allylamine and then soaked in a solution of K_2PtBr_6, it acquires a layer of chemisorbed platinum complex which remains when the electrode is rinsed with electrolyte (1 *F* NaBr–1 *F* $NaClO_4$–10 m*F* $HClO_4$). Current-potential curves obtained for the electrode, thus coated, appear in Figure 7. The platinum-complex layer as formed initially is unreactive in the usual potential range of the $PtBr_6^{2-}$|$PtBr_4^{2-}$ couple; however, when exposed briefly (in the thin layer cavity) to a solution containing traces of added or electrogenerated Pt(II), the adsorbed layer becomes reactive. When rinsed with pure solvent the Pt(IV) adsorbed complex reverts within minutes to an unreactive state in the absence of Pt(II), whereas, of course, the Pt(II) adsorbed complex remains reactive.

The unreactive complex formed when $PtBr_6^{2-}$ reacts with adsorbed allylamine is probably the adsorbed *cis*-tetrabromo-*N,N'*-bis(allylamino)platinum(IV), $PtBr_4(C_3H_7N)_2$, VII. Chemisorbed complex VII is electro-

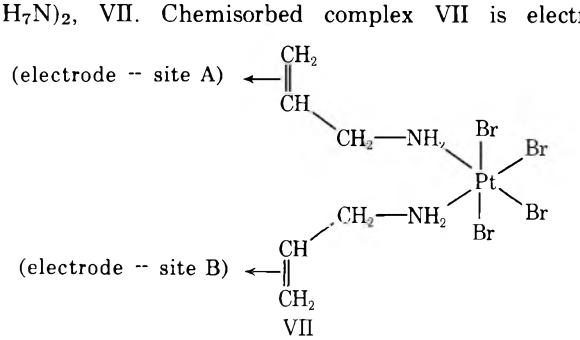

VII

inactive for the same reason as the chemisorbed allylhydroquinones, I–V; in the conformer involving minimal repulsion between the allylic carbon adjacent to the nitrogen, the substituent (the platinum complex) is located opposite the allyl chain from the electrode surface, at considerable distance from the surface and with highly restricted orientation. When exposed to traces of Pt(II), the electroinactive complex, VII, probably undergoes catalyzed release from one of the chemisorbed ligands to give a reactive complex VIII a process analogous to the familiar "trans-effect" in homogeneous substitution reactions of Pt(IV).[10] Examination of molecular models indicates that each of the Br ligands cis to the chemisorbed ligand in VIII is able to achieve an orientation in relation to the electrode surface appropriate to halide-bridged electron transfer (part II).[3]

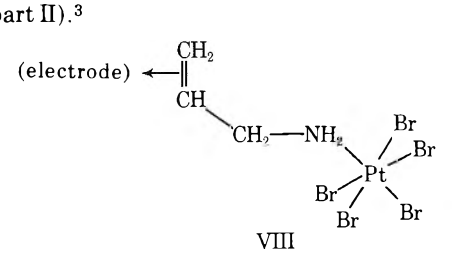

VIII

The reduction of $PtBr_5(C_3H_7N)_{ads}^-$, VIII, and the subsequent re-oxidation, eq 31, obeys eq 15 and 16. Figure 8 shows graphs of eq 15 and 16 along with the experimental current-potential curve. The agreement is excellent, from which it follows that it was permissible to employ a linear isotherm, eq 3, and constant values of α_{jk} and $k_{jk}{}^0$ (cor-

(10) F. Basolo and R. G. Pearson, *Advan. Inorg. Chem. Radiochem.*, **3**, 1 (1961).

TABLE I: Induced Adsorption of Fe(II) at a 3-Allylsalicylic Acid Coated Platinum Electrode[a,b]

E_i, V_{NaCE}	$Q - Q$(blank) for coated surfaces, μC	$Q - Q$(blank) for clean surfaces, μC	Q(adsorbed), μC	${}_2\Gamma(Fe^{2+} - Sal^{2-})$, mol/cm^2 × 10^{10}[c]
−0.050	185.6 ± 0.9		130.5 ± 1.3	11.76 ± 0.12
0.000	181.6 ± 0.5	55.1 ± 0.4	126.5 ± 0.9	11.40 ± 0.08
0.025	163.2 ± 0.8		108.1 ± 1.2	9.74 ± 0.11
0.050	146.9 ± 0.2		91.8 ± 0.6	8.27 ± 0.05
0.075	128.5 ± 0.5		73.4 ± 0.9	6.61 ± 0.08
0.100	110.2 ± 0.2		55.1 ± 0.6	4.96 ± 0.05
0.150	75.5 ± 0.9		20.4 ± 1.3	1.84 ± 0.12
0.200	59.2 ± 1.0		4.1 ± 1.4	0.37 ± 0.08

[a] Prior to each trial the coated electrode was potentiostated at an initial potential, E_i, rinsed with reactant solution for a minimum of 180 sec, then filled. The potential was then stepped to +0.600 V where the current was integrated. Values of Q(blank) were obtained by repeating the appropriate procedures in the iron-free supporting electrolyte. Each entry represents the average of several trials with the reproducibility shown. Volume, area, and temperature were as in Figure 4. [b] The reactant solution was 0.15 mF Fe(III) in 1 F $NaClO_4$ at pH 3. $\Gamma^0(Sal^{2-}) = 1.19 \times 10^{-9}$ mol/cm^2, as determined from iodide adsorption experiments. This coverage was obtained when the clean electrode was exposed to a saturated aqueous solution of 3-allylsalicylic acid for 1 hr. [c] Values of ${}_2\Gamma(Fe^{2+} - Sal^{2-})$ were calculated from the equation $Q = FVC^0(Fe^{2+}) + FA_2\Gamma(Fe^{2+} - Sal^{2-})$.

rected for double layer influence) over the range of the current-potential curve.

$$PtBr_5(C_3H_7N)_{ads}^- + 2e^- \xrightleftharpoons{1\ F\ Br^-} PtBr_3(C_3H_7N)_{ads}^- + 2Br^- \quad (31)$$

Chemisorbed complexes formed from $PtCl_4^{2-}$ or *trans*-$Pt(NH_3)_2Cl_2$ and allylamine-coated platinum electrodes yield current-potential curves which resemble those for unadsorbed complexes of comparable ionic charge and obey eq 15 and 16. The electrode reactions which occur are

$$PtCl_3(C_3H_7N)_{ads}^- + 2Cl^- \xrightarrow{1\ F\ NaCl} PtCl_5(C_3H_7N)_{ads}^- + 2e^- \quad (32)$$

$$trans\text{-}PtCl(NH_3)_2(C_3H_7N)_{ads}^+ + 2Cl^- \xrightarrow{1\ F\ NaCl} trans\text{-}PtCl_3(NH_3)_2(C_3H_7N)_{ads}^+ + 2e^- \quad (33)$$

At lower Cl^- concentrations (*ca.* 10^{-3} F), oxidation results in addition of one H_2O and one Cl^- rather than two Cl ligands, just as was observed for similar complexes reacting from solution.[11] None of the adsorbed complexes appearing in eq 32 and 33 tended to form unreactive species, probably because chloroamminoplatinum(IV) complexes are substantially less labile than Pt(IV) complexes containing several Br ligands,[12] and accordingly from the electroinactive bis(allylamine) complexes at the surface less rapidly.

Current-potential data for chemisorbed Pt complexes are given in Table II, from which it can be seen that the peak current (normalized for coverage) varies with reactant charge, Z_R, as expected from eq 17 and 20, in combination with eq 13. That is

$$ {}_ci_p(Z_{R^+}),\ {}_ai_p(Z_{R^-}) > {}_ci_p(Z_R{=}0),\ {}_ai_p(Z_R{=}0) > {}_ci_p(Z_{R^-}),\ {}_ai_p(Z_{R^+}) \quad (34)$$

This observation often provides a very useful clue as to the identity of electroactive species taking part in unfamiliar systems. It applies without exception to the variety of reactions studied to date, provided that variation in Z_R is not coupled with dramatic variation in ${}_2x_R$. The physical basis for eq 34 is the fact that for any irreversible reaction the electrode potential at which oxidation predominates is more positive than for reduction and accordingly the surface concentration of anionic reactants will be enhanced by electrostatic attraction to a greater extent during the anodic process than the cathodic. Thus, the anodic over-voltage is more efficient in promoting the oxidation of anions than of cations, and conversely. The distribution of potential between anodic and cathodic processes is reflected in the apparent charge transfer coefficient, to which the peak current is proportional.

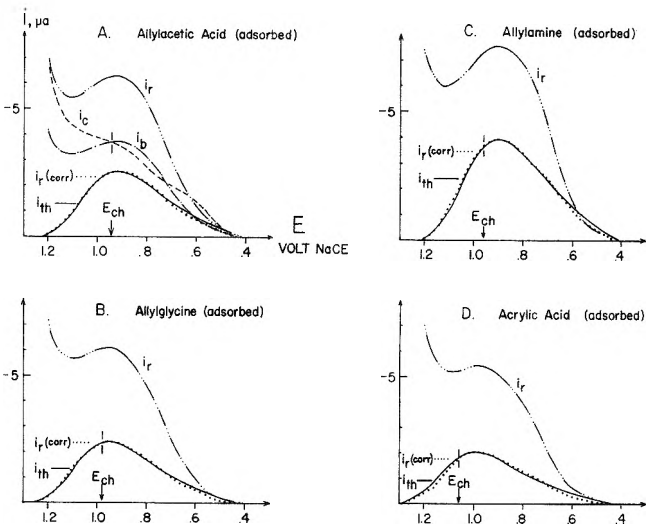

Figure 9. Thin layer current-potential curves for oxidation of chemisorbed, substituted olefins on platinum electrodes. Graphs of eq 16 for values of ${}_aE_p$, ${}_ai_p$, and Γ_R^0 taken from Table III: (·····) faradaic current for reactant-coated electrodes, i_r; (-----) background current for clean electrodes, i_c; (-·-·) background current for coated electrodes, i_b; (——) theoretical current for reactant-coated electrodes, i_{th}, from eq 16; (·····) true faradaic current for reactant-coated electrodes, i_r(corr), corrected for background current as outlined in text. The chemisorbed molecules are (A) allylacetic acid, (B) allylglycine, (C) allylamine, and (D) acrylic acid. The electrode was cleaned and surfactant treated prior to each trial as described in the Experimental Section. Supporting electrolyte was 1 F $HClO_4$. Other experimental conditions were identical with those of Figure 4.

4. Chemisorbed Substituted Alkenes. Oxidation of the Pt-C linkage was observed for each of the chemisorbed, substituted olefins studied here and in part II;[3] these are acrylic acid, $CH_2{=}CHCO_2H$; allylacetic acid, $CH_2{=}CH(CH_2)_2CO_2H$; allylamine, $CH_2{=}CHCH_2NH_2$;

(11) J. R. Cushing and A. T. Hubbard, *J. Electroanal. Chem.*, **23**, 183 (1969).
(12) A. T. Hubbard and F. C. Anson, *Anal. Chem.*, **38**, 1887 (1966).

TABLE II: Data from Thin Layer Current–Potential Curves for Chemisorbed Allylamine Complexes of Platinum(II) and (IV)[a]

Pt reactant	Pt product	$_aE_p$, V_{NaCE}	$_cE_p$, V_{NaCE}	$_aE_p - _cE_p$, V	a^iP, μA	c^iP, μA	$a^iP/\Gamma_R{}^{0\alpha}$	$c^iP/\Gamma_{ox}{}^{0\alpha}$	$^*\alpha$ from eq 13	$(1 - ^*\alpha)$ from eq 13	$_1\gamma_{ox}{}^*k^{z,e}$ sec^{-1}, from eq 14	$_1\gamma_R{}^*k^{z,e}$ sec^{-1}, from eq 14
$Pt^{IV}Br_5(C_3H_7N)_{ads}{}^{-b}$	$Pt^{II}Br_3(C_3H_7N)_{ads}{}^-$	0.49	0.17	0.32	4.80	3.50	5.93	4.43	0.66	0.88	6.51×10^{-4}	3.49×10^{-9}
$Pt^{IV}Cl_5(C_3H_7N)_{ads}{}^{-c}$	$Pt^{IV}Cl_5(C_3H_7N)_{ads}{}^-$	0.64	0.42	0.22	4.65	2.77	6.28	3.90	0.59	0.94	2.96×10^{-6}	1.0×10^{-11}
1 *F* Cl^-												
$Pt^{IV}Cl_3(C_3H_7N)_{ads}{}^{-c}$	$Pt^{IV}Cl_4(H_2O)(C_3H_7N)_{ads}$	0.64	0.52	0.12	4.67	3.61	6.31	5.01	0.75	0.95	1.48×10^{-8}	1.1×10^{-11}
2 *m F* Cl^-												
$Pt^{II}Cl(NH_3)_2(C_3H_7N)_{ads}{}^{+c}$	$Pt^{IV}Cl_3(NH_3)_2(C_3H_7N)_{ads}{}^+$	0.53	0.40	0.13	2.37	3.78	4.08	6.41	0.96	0.61	2.39×10^{-8}	1.62×10^{-7}
1 *F* Cl^-												

[a] The electrode was cleaned and allylamine pretreated as described in the Experimental Section. Preparation of the chemisorbed complexes was effected by exposing the electrode, thus coated, to an excess of a freshly prepared aqueous solution containing the appropriate platinum complex (see text) at 5 m*F* concentration. The exposure times employed to induce surface coordination to the extent shown were as follows: $Pt^{II}Cl(NH_3)_2(C_3H_7N)_{ads}{}^+$, 2 hr; $Pt^{II}Cl_3(C_3H_7N)_{ads}{}^-$, 1 hr; $Pt^{IV}Br_5(C_3H_7N)_{ads}{}^-$ and $Pt^{IV}Br_4(C_3H_7N)_2$ (unreactive), 5 hr. *V*, *A*, $|\Gamma|$, and *T* as in Figure 4. [b] The supporting electrolyte contained 10 m*F* $HClO_4$, 1 *F* $NaClO_4$, and 1 *F* NaBr. [c] The supporting electrolyte contained 1 *F* $HClO_4$ and the chloride concentration indicated. [d] Values of $\Gamma_J{}^0$ were determined by electronic integration of the current–potential curves; although less accurate than the potential step approach, this allowed $\Gamma_J{}^0$ and the rate parameters to be determined simultaneously in the same experiment. [e] Values of the formal standard potential E^0 are not available from which to calculate values of $\gamma_j{}^*k^0$. The rate constants $\gamma_j{}^*k^z$ are thus referred to the zero of the experimental potential scale, $E = 0$ V *vs* NCE.

4-allylcatechol, II; 4-allyl-2,6-dimethoxyphenol, IV; allylglycine, $CH_2{=}CHCH_2CH(NH_2)CO_2H$; 2-allylhydroquinone, I; 4-allyl-2-methoxyphenol, III; 6-allyl-2-methoxyphenol, V; allyltriethylammonium cation; fumaric acid; and vinylsulfonic acid, $CH_2{=}CHSO_3H$. Current–potential data are given in Table III. Since the reactive entity in each case is the Pt–C linkage derived from the electrode and the double bond, current–potential behavior for the various compounds is expected and observed to be very similar. Current–potential curves for a few of the compounds studied appear in Figure 9. In the figure, i_r denotes the current observed for the reactant-coated electrode, and i_c denotes the current observed for the clean electrode (exactly identical in each case). i_b, defined by eq 35, represents the background current (due to electrode

$$i_b = i_r\left[\frac{n_c}{n_r + n_c}\right] \tag{35}$$

surface oxidation) at a coated electrode. n_c and n_r are effective *n* values of surface metal atoms at clean and coated surfaces, respectively; they can be determined from iodide adsorption data, obtained as described in part II,[3] by means of

$$n_c \equiv (Q_c/FA)\Gamma_c = Q_c/FA\Gamma_I(c) \tag{36}$$

$$n_r \equiv (Q_r - Q_c)/FA\Gamma_r = \frac{Q_r - Q_c}{FA[\Gamma_I(c) - \Gamma_I(r)]} \tag{37}$$

where *Q* is the charge required for oxidation of the surface and c and r denote clean and coated surfaces, respectively. Equation 35 is based upon the assumption that each site becomes oxidized immediately upon oxidative removal of its adsorbed hydrocarbon. i_r(corr), defined by eq 38,

$$i_r(\text{corr}) = \begin{cases} i_r - i_b & \text{for } E \leq E_{ch} \\ i_r - i_c & \text{for } E > E_{ch} \end{cases} \tag{38}$$

represents the "true" current due to oxidation of adsorbed hydrocarbons. Values of i_{th}, calculated from the observed peak current, peak potential, and interfacial excesses by means of eq 16, are plotted in Figure 9 for comparison with i_r(corr). Substitution of i_c for i_b when $E > E_{ch}$ (eq 38) is necessary to allow for the fact that "massive" evolution of oxygen rather than surface oxidation becomes the predominant background reaction. The excellent agreement between the measured [i_r(corr)] and semiempirically calculated [i_{th}] values for all systems studied supports the correctness of the model.

The values of n_r for all of the compounds studied center around $n_r = 10$. Since the present experiments involved less than 10^{-9} mol of reactant per trial, it was not possible to perform subsequent, nonelectrochemical experiments upon the reaction products; however, the electrochemical results are consistent with oxidation of the adsorbed olefins according to

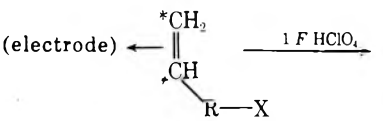

$$\text{(electrode)-Ox} + {}^*CO_2 + X{-}R{-}{}^*CO_2H + 10e^- \tag{39}$$

Implicit in eq 36–39 is the assumption that adsorbed I^- occupies two sites, in keeping with the observation that Γ_I approaches an upper limit of approximately 10^{-9} mol/cm^2 compared with approximately 2×10^{-9} mol/cm^2 of surface metal atoms, and that the adsorbed deposit behaves as a neutral species.[2] Although the mechanism of I^- ad-

TABLE III: Thin Layer Current–Potential Data for Chemisorbed Substituted Olefins on Platinum Electrodes

Chemisorbed reactant[a]	Γ_R^0, mol cm^{-2} × 10^9	$_aE_p$, V_{NaCE}	$-_ai_p$, μA	$(1 - {}^*\alpha)$ from eq 13	$_1\gamma_R{}^*k^Z$,[b] sec^{-1}, from eq 14
Acrylic acid	0.43	0.99	2.02	0.15	3.87×10^{-5}
Allylacetic acid	0.49	0.92	2.54	0.16	3.68×10^{-5}
Allylamine	0.76	0.90	3.89	0.16	4.43×10^{-5}
4-Allylcatechol	0.72	0.81	4.88	0.21	1.99×10^{-5}
4-Allyl-2,6-dimethoxyphenol	0.59	0.91	3.43	0.18	2.18×10^{-5}
Allylglycine	0.46	0.95	2.38	0.16	3.09×10^{-5}
2-Allylhydroquinone	0.68	0.93	4.26	0.20	1.21×10^{-5}
4-Allyl-2-methoxyphenol	0.55	1.01	3.17	0.18	1.13×10^{-5}
6-Allyl-2-methoxyphenol	0.51	0.99	2.66	0.16	2.28×10^{-5}
3-Allylsalicylic acid	0.63	0.93	3.74	0.19	1.69×10^{-5}
Allyltriethylammonium cation	0.62	0.90	3.69	0.19	2.07×10^{-5}
Fumaric acid	0.50	0.94	2.63	0.17	3.03×10^{-5}
Vinylsulphonic acid	0.40	1.00	1.81	0.14	4.32×10^{-5}

[a] Supporting electrolyte was 1 *F* $HClO_4$. Other experimental conditions were identical to those of Figure 4. [b] Values of the formal standard potential E^0 are not available from which to calculate va ues of $_1\gamma_R{}^*k^0$. The rate constants $_1\gamma_R{}^*k^Z$ are thus referred to the zero of the experimental potential scale, $E = 0$ V *vs.* NaCE.

sorption on Pt has not been investigated, the data presently available[13] are consistent with the suggestion that simultaneous adsorption of I^- and H^+ takes place, leading to a mixed deposit of I and H.

$$I^- + \underset{\text{(electrode)}}{\text{—Pt—Pt—}} + H_2O \longrightarrow \underset{\text{(electrode)}}{\overset{I\quad H}{\text{—Pt—Pt—}}} + OH^- \qquad (40)$$

Experimental Section

The theory and practice of electrochemistry with thin layer electrodes have been reviewed recently.[8] Experimental aspects of electrode rate measurements with thin layer cells are described in detail in recent papers dealing with the electrochemistry of platinum complexes.[2,11,14] The thin layer electrode design employed in this work, a platinum rod inserted into a close-fitting precision Pyrex capillary, was described in ref 14.

Electrode surface pretreatment was of critical importance in these studies and was made particularly difficult by the fact that chemisorbable materials were being placed in contact with the surface. Highly reproducible surfaces free of spurious peaks and giving exemplary anodic and cathodic background behavior were attained as follows: the platinum metal electrode was removed from the precision capillary and heated for 10 min in an oxidizing methane–oxygen flame, with occasional quenching in concentrated perchloric acid, allowed to cool for a few seconds, and then inserted into the capillary. A cyclic current–potential curve, recorded at 2 mV sec^{-1} in deaerated 1 *F* $HClO_4$ (0.4 to 1.3 V, then back to −0.3 V, and finally to 0.4 V (NaCE), served both to remove the last traces of adsorbed organic materials and to confirm the purity of the surface. The surface was undoubtedly polycrystalline; experiments with single-crystal surfaces are in progress.[15]

Prior to each experiment the thin layer electrode was pretreated by alternate potentiostatic oxidation (1.2 V NaCE) and reduction (0.0 V NaCE), followed by equilibration at 0.4 V NaCE for a minimum of 120 sec. This procedure appears to leave the electrode surface in a reproducible state with a minimum of adsorbed hydrogen and oxygen.[11]

In order to obtain reproducible surface coverage in various trials with the same surfactants, the electrode, thus cleaned, was exposed for exactly 180 sec to an excess of a freshly prepared solution containing the surfactant at 10 m*F* concentration in pure water. The electrode was thoroughly rinsed in water and then in supporting electrolyte (60 sec), and the current–potential curve was recorded immediately thereafter.

Most of the substituted olefins employed in this study were obtained from K & K Laboratories, Plainview, N.Y., and were used as received. 2-Allylhydroquinone and 4-allylcatechol were purchased from Burdick and Jackson Laboratories, Muskegon, Mich.

3-Allylsalicylic acid was prepared by selective oxidation of 3-allylsalicylaldehyde with silver oxide following the procedure described by Campaigne and LeSuer for 3-thenoic acid.[16] The Ag_2O oxidant was prepared from 2.1 g (0.012 mol) of $AgNO_3$ and 1.0 g (0.025 mol) of NaOH dissolved in 10 ml of water. To the chilled (0°) brown suspension was added dropwise with stirring, over a period of 1 hr, 1.0 g (0.006 mol) of 3-allylsalicylaldehyde. The mixture was stirred an additional 30 min, filtered, and the unsaturated acid precipitated by the addition of concentrated HCl to the filtrate. The acid was purified by dissolution of the crude product in a minimum amount of a dilute aqueous $NaHCO_3$ solution, filtering the insoluble impurities, and reprecipitating with HCl. After three such purifications the resulting white crystalline product was collected, washed with several portions of cold water, and dried *in vacuo*.

All solutions were prepared from reagent grade chemicals and triply distilled water, the second distillation having been made from a solution of 1 m*F* $KMnO_4$ in 1 m*F* NaOH. Experiments were performed at 24 ± 1°. Solutions were deaerated with prepurified nitrogen prior to and during use.

A conventional multipurpose electrochemical circuit based upon operational amplifiers and relays having mercury-wetted contacts was employed. Potentials were measured relative to a calomel electrode prepared with 1 *F* NaCl, denoted by NaCE, and are thus reported.

(13) A. T. Hubbard, R. A. Osteryoung, and F. C. Anson, *Anal. Chem.*, **38**, 692 (1966).
(14) C.-N. Lai and A. T. Hubbard, *Inorg. Chem.*, **11**, 2081 (1972).
(15) A. T. Hubbard, University of Hawaii, unpublished experiments.
(16) E. Campaigne and W. M. LeSuer, *Org. Syn.*, **33**, 94 (1953).

Acknowledgments. Acknowledgment is made to the donors of the Petroleum Research Fund, administered by the American Chemical Society, and to the National Science Foundation for support of this research.

Appendix. Notation

A = electrode area, cm^2
a_j = surface activity of species j, mol cm^{-3}
${}_1a_j$ = surface activity of species j adsorbed in the compact layer
${}_2a_j$ = surface activity of species j in the diffuse layer
α = charge transfer coefficient
$*$ = indication of an apparent value
C = differential double layer capacitance, F cm^{-2}
${}_jC_c$, ${}_jC_d$ = differential capacitance assignable to the "compact layer" or "diffuse layer" relative to species j, respectively, F cm^{-2}
E = electrode potential, V
E_{ch} = potential at which method of blank correction is changed in olefin oxidations (see text)
${}_aE_p$, ${}_cE_p$ = peak potential of positive- or negative-going current–potential curve, respectively
E^0 = formal standard potential
E_Z = a potential at which the electrode is uncharged
e = 2.718
F = Faraday constant, C equiv^{-1}
Γ_j^0, Γ_j = initial or instantaneous interfacial excess of species j, respectively, mol cm^{-2}
${}_1\Gamma_j$, ${}_2\Gamma_j$ = compact or diffuse layer interfacial excess of species j, respectively
${}_k\gamma_j$ = proportionality constant defined by ${}_ka_j = {}_k\gamma_j\,{}_k\Gamma_j$, cm^{-1}
${}_ai$, ${}_ci$ = current for positive- or negative-going current–potential curve, respectively, A
i_b = background current at a surfactant-coated surface
i_c = background current at a clean surface
i_r = current observed at a reactant-coated surface
i_{th} = current predicted from the experimental equation, after insertion of measured values of peak current and potential
${}_ai_p$, ${}_ci_p$ = peak current of positive- or negative-going current–potential curve, respectively
${}_jK_f$ = standard formation constant for valence state j, M^{-1}
${}_jK_f'$ = formal formation constant for valence state j, M^{-1}
k^0 = standard electrochemical rate constant, cm sec^{-1}
L = length of surfactant molecule when fully extended, cm
n = number of electrons transferred per molecule or per site
n_c = number of electrons transferred in the background reaction per *mol* of surface sites
n_r = number of electrons transferred per *mole* of adsorbed surfactant
${}_j\phi_2$ = potential at the plane of closest approach for species j, V
Q_c, Q_r = charge required to oxidize the clean or reactant-coated surface, respectively, C
R = gas constant, J mol^{-1} °K^{-1}
r = rate of potential scan, V sec^{-1}
T = temperature, °K
t = time, sec
V = volume of the thin layer electrode cavity, cm^3
${}_jx_1$, ${}_jx_2$ = position of inner and outer planes of closest approach of species j, respectively, cm
Z_j = ionic valence of species j

Electrochemistry of Chemisorbed Molecules. II. The Influence of Charged Chemisorbed Molecules on the Electrode Reactions of Platinum Complexes

Ross F. Lane and Arthur T. Hubbard*

Department of Chemistry University of Hawaii, Honolulu, Hawaii 96822 *(Received September 7, 1972)*

Publication costs assisted by the National Science Foundation and the Petroleum Research Fund

The influence of chemisorbed olefins having ionic substituents on the electrode rates of Pt(II) and Pt(IV) complexes at Pt electrodes has been studied. Chemisorption alters the potential at the reaction plane, $_R\phi_2$, with the result that ionic complexes tend to react more rapidly at surfaces coated with ionic olefins of opposite charge than at clean surfaces. A comparison of cationic coatings, such as allylammonium ion with anionic ones (such as allylacetic acid anion) adsorbed at potentials positive of the zero-charge condition, demonstrates that the extent to which $_R\phi_2$ is altered depends upon the *position* of the charged substituent in relation to the remainder of the double layer and not merely upon the magnitude of its interfacial excess. The detailed electrostatic effects can be predicted in terms of a Boltzmann distribution, taking into account the chain length, structure, functional group charge, electrodic charge, and position of the reactant during electron transfer. The precise extent to which the reactions are sterically hindered by the chemisorbed surfactant has been determined from the variation of electrode rate with surfactant coverage. The results indicate that *two* adjacent electrode sites are required to form the rate-limiting intermediate in halide-bridged reduction of Pt(IV) complexes.

Introduction

Alkenes and alkynes form chemisorbed deposits on platinum electrodes.[1,2] The adsorbed materials are unreactive over a wide range of potentials, and are not removed from the surface by typical solvents or electrolytes.[2,3] A limitless variety of surface-active substances are thus available with which to probe (or alter) the influence of the compact region of the electrical double layer on the rate of reaction. Adsorbed hydrocarbons having no ionic charge diminish the excess of anions in the compact layer (with the result that the potential $_R\phi_2$ at the reactant plane is rendered more *positive* than it would otherwise be) and hinder access of the reactant to the electrode surface.

Comparison of the reactivity of charged and neutral platinum complexes indicates that anionic reactants tend to react more rapidly at neutral-surfactant-coated surfaces than at clean surfaces because in this instance electrostatic effects typically predominate over steric effects, while neutral reactants suffer a small deceleration, and positively charged complexes exhibit greatly decreased reactivity due to the combined effects of blocking and electrostatic repulsion.[2,4,5]

Introduction of charged, chemisorbed species onto the electrode surface provides a means of varying the field in the interfacial region "independently" of the electrode potential. For instance, attachment of allylglycine, $CH_2{=}CHCH_2CH(NH_2)COOH$, to the electrode surface through the C=C double bond is expected to shift $_R\phi_2$ toward more positive values when acidic electrolytes are employed (wherein RNH_3^+ is the predominant species), whereas in basic solutions a negative shift is expected owing to the predominance of $RCOO^-$. The extent to which $_R\phi_2$ is altered will depend upon the *position* of the charged group in relation to the remainder of the double layer, and will reflect the influence of various factors, including chain length, functional group character, and electrodic charge on sorbate orientation.

Substituted hydrocarbons also allow the possibility of connecting reactive functional groups directly to the electrode surface, as described in part I.[3]

Changes in interfacial potential accompanying introduction of chemisorbed species can, in principle, be measured for solid electrodes by direct assay of the electrical double layer composition. An effective experimental approach is being developed.[6] In the meantime, electrode rate measurements by means of thin layer electrodes can be treated semiquantitatively with regard to electrostatic forces and the reactive electrode area in order to obtain information useful for deducing electrode reaction mechanisms.

Pt(IV) complexes, such as $Pt(tren)Cl_2^{2+}$, $Pt(NH_3)_5Cl^{3+}$, $PtCl_2((NH_3)(NO_2))_2$, and *trans*-$Pt(NO_2)_4Cl_2^{2-}$ are sub-

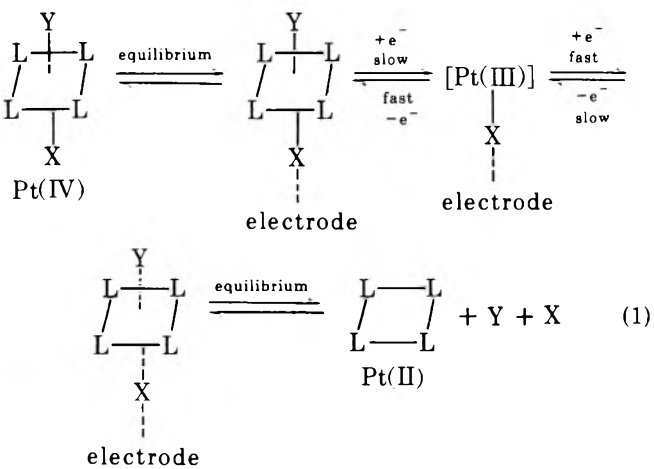

(1)

stitution inert to a high degree, are reduced electrochemi-

(1) E. Gileadi, Ed., "Electrosorption," Plenum Press, New York, N. Y., 1967.
(2) A. L. Y. Lau and A. T. Hubbard, *J. Electroanal. Chem.*, **33**, 77 (1971).
(3) R. F. Lane and A. T. Hubbard, *J. Phys. Chem.*, **77**, 1401 (1973).

TABLE I: Thin Layer Current–Potential Data for Complexes of Pt(II) and Pt(IV)[a,b]

Platinum complexes					
Pt(IV)	Pt(II)	Surfactant species	$_cE_p(s)$, V_{NaCE}	$_cE_p$, V_{NaCE}	$_cE_p(s) - {}_cE_p$, V
$Pt(NH_3)_5Cl^{3+}$	$Pt(NH_3)_4^{2+}$ [c]	Allylamine	0.155	0.280	−0.125
		Allylglycine	0.220	0.280	−0.060
		Allyltriethyl-ammonium	0.170	0.280	−0.110
		Allylacetic acid	0.215	0.280	−0.065
		Acrylic acid	0.220	0.280	−0.060
		Fumaric acid	0.230	0.280	−0.050
		Vinylsulphonic acid	0.230	0.280	−0.050
$PtCl_2\langle(NH_3)(NO_2)\rangle_2$	$Pt\langle(NH_3)(NO_2)\rangle_2$	Allylamine	0.395	0.425	−0.030
		Allylglycine	0.405	0.425	−0.020
		Allyltriethyl-ammonium	0.410	0.425	−0.015
		Allylacetic acid	0.410	0.425	−0.015
		Acrylic acid	0.405	0.425	−0.020
		Fumaric acid	0.400	0.425	−0.025
		Vinylsulphonic acid	0.415	0.425	−0.010
$Pt(NO_2)_4Cl_2^{2-}$	$Pt(NO_2)_4^{2-}$ [d]	Allylamine	0.360	0.235	0.125
		Allylglycine	0.295	0.235	0.060
		Allyltriethyl-ammonium	0.335	0.235	0.100
		Allylacetic acid	0.270	0.235	0.035
		Acrylic acid	0.255	0.235	0.020
		Fumaric acid	0.280	0.235	0.045
		Vinylsulphonic acid	0.255	0.235	0.020

[a] The experimental conditions employed were the same as Figure 1. [b] Supporting electrolyte, 1 *F* $HClO_4$ + 10 m*F* NaCl. [c] of $Pt(NO_2)_4^{2-}$ in 10 m*F* NaCl yields $Pt(NO_2)_4(H_2O)Cl^+$.

$_{c}i_{p}(s)$, μA	$_{c}i_{p}$, μA	$_{a}E_{p}(s)$, V_{NaCE}	$_{a}E_{p}$, V_{NaCE}	$_{a}E_{p}(s) - {}_{a}E_{p}$, V	$-{}_{a}i_{p}(s)$, μA	$-{}_{a}i_{p}$, μA
15.5	17.5	0.585	0.480	0.105	14.0	17.0
17.0	17.5	0.540	0.480	0.060	14.7	17.0
16.1	17.5	0.565	0.480	0.085	14.5	17.0
17.0	17.5	0.530	0.480	0.050	15.1	17.0
16.7	17.5	0.520	0.480	0.040	15.5	17.0
16.5	17.5	0.515	0.480	0.035	15.4	17.0
17.1	17.5	0.525	0.480	0.045	15.6	17.0
13.4	13.7	0.665	0.660	0.005	12.9	14.0
13.5	13.7	0.670	0.660	0.010	13.2	14.0
13.6	13.7	0.675	0.660	0.015	13.0	14.0
13.3	13.7	0.672	0.660	0.012	13.2	14.0
13.2	13.7	0.665	0.660	0.005	13.4	14.0
13.5	13.7	0.680	0.660	0.020	13.0	14.0
13.3	13.7	0.660	0.660	0.000	13.4	14.0
7.0	7.0	0.765	0.860	−0.095	10.0	11.3
6.6	7.0	0.825	0.860	−0.035	10.6	11.3
6.8	7.0	0.780	0.860	−0.080	10.2	11.3
7.0	7.0	0.830	0.860	−0.030	10.5	11.3
6.9	7.0	0.840	0.860	−0.020	10.8	11.3
6.7	7.0	0.835	0.860	−0.020	10.3	11.3
6.9	7.0	0.850	0.860	−0.010	10.5	11.3

Electrooxidation of $Pt(NH_3)_4^{2+}$ in 10 m*F* NaCl yields $Pt(NH_3)_4Cl_2^{2+}$. [d] Electrooxidation

cally at a convenient rate, and provide reactant charges varying from +3 to −2.[2-5,7] Their reduction, which takes place over a range of potentials well removed from that for decomposition of the electrode, electrolyte, or adsorbed material, appears to proceed through a halide-ligand-bridged electron transfer intermediate (eq 1) and thus is sensitive to coverage of the electrode by chemisorbed species (*i.e.*, sensitive to the structure and composition of the "compact" region of the double layer).

This work has been carried out using thin layer electrodes, by means of which it has been possible to maintain a high level of surface cleanliness, and to observe surface effects with extraordinary clarity. Thin layer electrodes exhibit very simple physical behavior and as a result follow comparatively simple experimental equations, allowing unambiguous interpretation of experimental results, a preliminary analytical and kinetic description typically being obtained from a single experimental curve. The theory and practice of electrochemistry with thin layer cells have been reviewed recently[8] and experimental equations have been derived for various reaction types.[9]

Results and Discussion

Data illustrating the influence of charged chemisorbed molecules on the electrode rates of platinum complexes appear in Table I. The predominance of coulombic factors over steric effects in these reactions is immediately evident from the data. When the reactant is charged oppositely from the surfactant, the electrolysis rate exceeds the normal value at a clean electrode (Figure 1C). Conversely, when charges of the same sign interact, the electrode rate is abnormally low (Figure 1A). When both members are uncharged, only the steric effect is observed, which leads to slight deceleration (Figure 1B).

Most of the charged chemisorbed molecules used in this work were derived from amines and carboxylic acids, with the result that the surfactant charge depends upon the pH (*cf.* allylglycine). Therefore, it is implicit in the data of Table I and in the equations derived below that the potential ${}_{R}\phi_2$ at the reaction plane can be made to vary predictably with pH. As a consequence, the electrode rate can be made to vary by adjusting the pH while holding the voltage applied to the electrode constant.

Very simple equations which adequately predict the changes in ${}_{j}\phi_2$ caused by chemisorption and the resulting variation in electrode reaction rate can be obtained by assuming that the double layer behaves as a pair of ideal capacitors in series,[10] at least over the narrow range of potentials encompassed by a single current-potential "peak" (*ca.* 100 mV). The excess ionic charge of the diffuse, compact, and total double layer regions can then be related to the change in potential difference across the diffuse double layer, due to chemisorption, by means of the definition of capacitance

$$\Delta q_{dl} = \Delta q_c = \Delta q_d = \sum_k Z_k F[{}_{1}\Gamma_k(s) - {}_{1}\Gamma_k] = {}_{j}C_d\Delta({}_{j}\phi_2) \quad (2)$$

(Please refer to the Appendix at the end of this article for definitions of the symbols employed.) Thus, the change in ${}_{j}\phi_2$ is simply proportional to the change in the excess of ionic charge in the compact layer and inversely proportional to the diffuse layer capacitance. Although overly simple, this assumption is adequate for the present purpose, which is the comparison of electrode rates at very similar potentials in the presence and absence of chemisorbed molecules. ${}_{j}\phi_2$ and ${}_{j}C_d$ depend upon the distance of closest approach, ${}_{j}x_2$, of the ionic species in question, j.

$$\Delta({}_{j}\phi_2) = \frac{\sum_k Z_k F[{}_{1}\Gamma_k(s) - {}_{1}\Gamma_k]}{{}_{j}C_d} \quad (3)$$

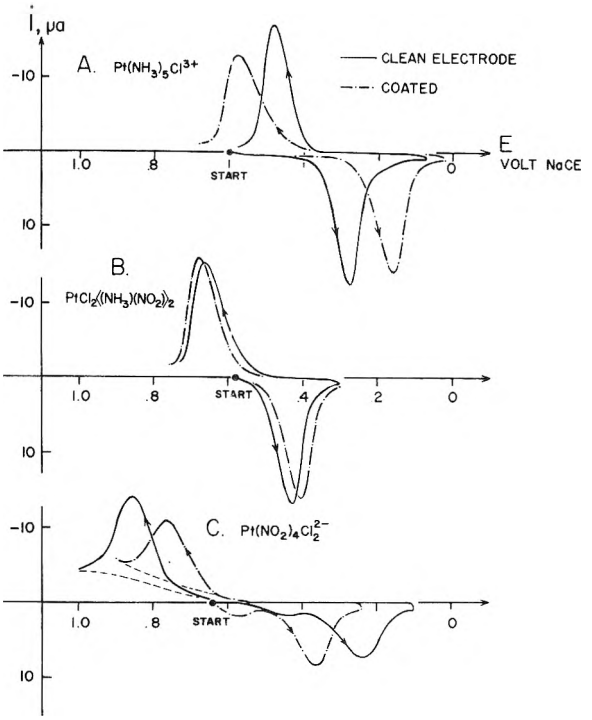

Figure 1. Thin layer current–potential curves for complexes of Pt(II) and Pt(IV) at clean and surfactant-coated platinum electrodes: (——) clean electrodes, (- · - · -) electrodes containing chemisorbed allylamine. The reactant complexes were (A) $Pt^{IV}(NH_3)_5Cl^{3+}$ and $Pt^{II}(NH_3)_4^{2+}$, (B) $Pt^{IV}Cl_2(NH_3)(NO_2))_2$ and $Pt^{II}(NH_3)(NO_2))_2$, (C) $Pt^{IV}(NO_2)_4Cl_2^{2-}$ and $Pt^{II}(NO_2)_4^{2-}$. The electrode was cleaned and surfactant treated as described in the Experimental Section. Reactant solutions initially contained 1 m*F* Pt(IV), 1 *F* $HClO_4$, and 10 m*F* NaCl. Thin layer volume, V = 3.88 μl; platinum electrode area, A = 1.15 cm²; rate of potential sweep, r = 2.00 mV sec⁻¹; solution temperature, T = 23 ± 1°.

Electrochemical reduction of the Pt(IV) complexes studied to date follows eq 4 whenever the reaction is carried out under totally irreversible conditions.[4,5] The apparent charge transfer coefficient, $*\alpha_{43}$, depends upon the distribution of potential between the diffuse and compact regions of the double layer,[9] treated as ideal capacitors in series

$$i = nF^*A^*k_{43}{}^0C_4^* \exp\left[\frac{-*\alpha_{43}F}{RT}(E - E_{43}{}^0)\right] \quad (4)$$

$$*\alpha_{43} = \alpha_{43} + \frac{C}{{}_{R}C_d}(Z_4 - \alpha_{43}) \quad (5)$$

The apparent standard electrochemical rate constant, $*k_{43}{}^0$, is a function of the potential ${}_{R}\phi_2$ as well as the dis-

(4) J. R. Cushing and A. T. Hubbard, *J. Electroanal. Chem.*, **23**, 183 (1969).
(5) A. L. Y. Lau and A. T. Hubbard, *J. Electroanal. Chem.*, **24**, 237 (1970).
(6) M. Sborov, W. Moats, and A. T. Hubbard, University of Hawaii, unpublished experiments.
(7) C.-N. Lai and A. T. Hubbard, *Inorg. Chem.*, **11**, 2081 (1972).
(8) A. T. Hubbard and F. C. Anson in "Electroanalytical Chemistry," Vol. 4, A. J. Bard, Ed., Marcel Dekker, New York, N. Y., 1970.
(9) A. T. Hubbard, *J. Electroanal. Chem.*, **22**, 165 (1969).
(10) P. Delahay, "The Electrochemical Double Layer and Electrode Kinetics," Interscience, New York, N. Y., 1965.

TABLE II: Coverage Data for Charged Surfactants on Platinum Electrodes[a]

Surfactant	Γ_s, mol cm^{-2} × 10^9	θ_s	$(1 - \theta_s)$
Allylamine	0.76 ± 0.02	0.62	0.38
Allylglycine	0.46 ± 0.01	0.38	0.62
Allyltriethylammonium cation	0.62 ± 0.02[c]	0.51	0.49
Allylacetic acid	0.49 ± 0.01	0.40	0.60
Fumaric acid	0.50 ± 0.02	0.41	0.59
Acrylic acid	0.43 ± 0.01	0.36	0.64
Vinylsulphonic acid	0.40 ± 0.02	0.33	0.67
Chloride	0.23 ± 0.03[b]		

[a] These coverages resulted from rinsing the electrode (at open circuit) with a 10 m*F* aqueous solution of the surfactant for a period of 3 min, followed by rinsing with pure water. Measurement of interfacial excess, Γ_s, and fractional coverage, θ_s, was based upon determination of adsorbed iodide, as described in the Experimental Section. In calculating Γ_s from Γ_I it was assumed that adsorption of each double bond requires two sites. [b] Electrode potential was 0.25–0.40 V *vs.* NaCE during adsorption of chloride. [c] This coverage was obtained by exposing the clean electrode to a 10 m*F* aqueous solution of allyltriethylammonium bromide for 30 min.

tribution of potential

$$*k_{43}^0 = k_{43}^0 \exp\left[(\alpha_{43} - Z_4)\frac{F}{RT}\,{}_R\phi_2\right] \quad (6)$$

Equations 5 and 6 were obtained, after substituting eq 7 for ${}_R\phi_2$ into the appropriate form of the Tafel equation, by collecting the potential-independent terms into $*\alpha_{43}$ and the potential-dependent terms into $*k_{43}^0$.

$${}_R\phi_2 = \frac{C}{{}_RC_d}(E - E_z) \quad (7)$$

The rate of oxidation of Pt(II) complexes in chloride solutions is proportional to the chloride interfacial excess in the compact region of the double layer and, at sufficiently high halide concentrations, to the bulk concentration of chloride ion.[4] The rate of halide-bridged electrooxidation of Pt(II) complexes is given by eq 8 when Y = H_2O (*cf.* eq 1) and by eq 9 when Y = Cl^-

$$i = nF^*A\gamma_1\Gamma_{Cl^-}*k_{23}{}^0C_2^* \exp\left[\frac{(1 - *\alpha_{23})F}{RT}(E - E_{23}{}^0)\right] \quad (8)$$

$$i = nF^*A\gamma_1\Gamma_{Cl^-}Ka_{Cl^-}*k_{23}{}^0C_2^* \exp\left[\frac{(1 - *\alpha_{23})F}{RT}(E - E_{23}{}^0)\right] \quad (9)$$

where $K = [Pt^{II}L_4Y]/[Pt^{II}L_4][Y]$. Equations similar to 5 and 6 may be obtained, relating apparent kinetic parameters to the true quantities corrected for the influence of the double layer, for oxidation of Pt(II) complexes

$$(1 - *\alpha_{23}) = (1 - \alpha) - [Z_2 + (1 - \alpha)]\frac{C}{{}_RC_d} \quad (10)$$

$$*k_{23}{}^0 = k_{23}{}^0 \exp[-(1 - \alpha) - Z_2]\frac{F}{RT}\,{}_R\phi_2 \quad (11)$$

Assignment of a numerical value to the ratio $C/{}_RC_d$ is necessary for evaluation of eq 5 and 10. For mercury electrodes in 1 *F* NaF at $(E - E_z) = 0.5$ V, Grahame[11] calculated the value $C/C_d = 0.067$ (consistent with $C = 40$ μF cm^{-2} and $C_d = 600$ μF cm^{-2} for Pt in 1 *F* $HClO_4$[12]), which will be employed here. The value $C/C_d = 0.050$ will be used for surfactant-coated electrodes.[2]

If the transition state entails interaction between the reactant molecule (or electron transfer bridge) and *m* contiguous adsorption sites at the interface, the apparent electrode area, $*A$, is expected to be related to the true area, *A*, and the fractional coverage, θ_s, by means of

$$*A = A(1 - \theta_s)^m \equiv A[1 - {}_1\Gamma_s/{}_1\Gamma_s(\max)]^m \quad (12)$$

For halide ligand bridged reduction of Pt(IV), $m = 2$, consistent with the suggestion that reduction of Pt(IV) requires two adjacent vacant sites.[2] Similarly, $m = 1$ for oxidation of Pt(II) complexes by the chloride-assisted path, corresponding to the suggestion that one vacant site *adjacent to the adsorbed bridge* is required for transition state formation. These results are consistent with scale molecular models of the proposed transition state. The measurement of *m* and its significance will be discussed in detail below. Coverage data for all surfactants used in this work are summarized in Table II.

Comparison of electrode rates in the presence and absence of the chemisorbed layer is conveniently accomplished by forming the ratio $*k_{43}{}^0(s)/*k_{43}{}^0$ using eq 6, written for $*k_{43}{}^0(s)$ and $*k_{43}{}^0$

$$*k_{43}{}^0(s)/*k_{43}{}^0 = k_{43}{}^0(s)/k_{43}{}^0 \exp\left\{\frac{F}{RT}[\alpha_{43}(s) - Z_4]_R\phi_2(s) - \frac{F}{RT}[\alpha_{43} - Z_4]_R\phi_2\right\} \quad (13)$$

Equation 13 can be simplified by assuming that $\alpha_{43}(s) = \alpha_{43}$ and that $k_{43}{}^0(s) = k_{43}{}^0$, on the premise that the influence of surfactant on electrode rate is fully accounted for by the terms containing ${}_R\phi_2$ and $*A$. The result, eq 14, will be employed for estimation of the surfactant-induced change in ${}_R\phi_2$ potential from the observed value of the ratio $*k_{43}{}^0(s)/*k_{43}{}^0$.

$$*k_{43}{}^0(s)/*k_{43}{}^0 = \exp\left[\frac{F}{RT}(\alpha_{43} - Z_4)\Delta({}_R\phi_2)\right] \quad (14)$$

Similar equations may be written for the oxidation of Pt(II)

$$*k_{23}{}^0(s)/*k_{23}{}^0 = \exp\left\{\frac{F}{RT}[Z_2 - (1 - \alpha_{23}(s))]_R\phi_2(s) - \frac{F}{RT}[Z_2 - (1 - \alpha_{23})]_R\phi_2\right\} \quad (15)$$

which will be written in the form of

$$*k_{23}{}^0(s)/*k_{23}{}^0 = \exp\left\{\frac{F}{RT}[Z_2 - (1 - \alpha_{23})]\Delta({}_R\phi_2)\right\} \quad (16)$$

where $\Delta({}_R\phi_2) = {}_R\phi_2(s) - {}_R\phi_2$. Combining eq 3 and 14 betrays the exponential dependence of $*k_{43}{}^0$ upon surfactant coverage

$$*k_{43}{}^0(s)/*k_{43}{}^0 = \exp\left\{\frac{F}{RT}[\alpha_{43} - Z_4] \times \sum_j Z_jF({}_1\Gamma_j(s) - {}_1\Gamma_j)/{}_RC_d\right\} \quad (17)$$

Forming the ratio of currents $i(s)/i$ by means of eq 4 yields eq 18, from which it can be seen that the influence

$$i(s)/i = [1 - {}_1\Gamma_s/{}_1\Gamma_s(\max)]^m \exp\left\{\frac{F}{RT}[\alpha_{43} - Z_4] \times \sum_j Z_jF({}_1\Gamma_j(s) - {}_1\Gamma_j)/{}_RC_d\right\} \quad (18)$$

of surfactant is exponential in coverage, whereas steric ef-

(11) D. C. Grahame, *J. Amer. Chem. Soc.*, **76**, 4819 (1954).
(12) M. Breiter, *Electrochim. Acta*, **8**, 925 (1963).

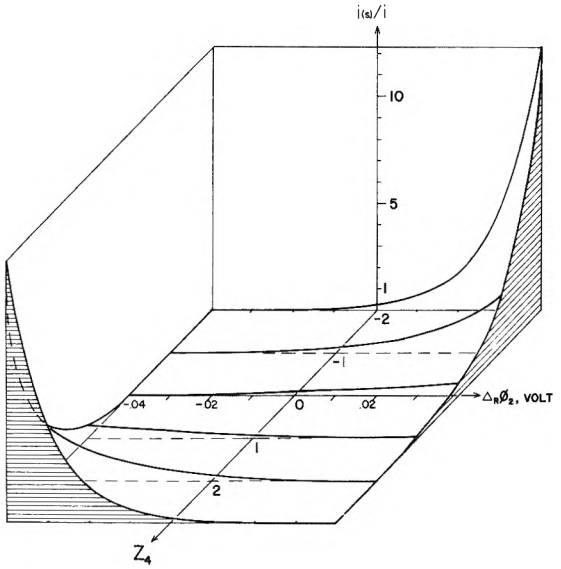

Figure 2. Ratio of electrode rates at surfactant-coated and clean electrodes, $i(s)/i$. Graph of eq 18 for various values of Z_4 and $(_R\phi_2(s) - {}_R\phi_2)$. The following values were assumed in making the plots: ${}_1\theta_s = \frac{1}{2}$; number of sites required in the transition state, $m = 2$; $\alpha = \frac{1}{2}$; ${}_RC_d = 600\ \mu F/cm^2$; $T = 298°K$.

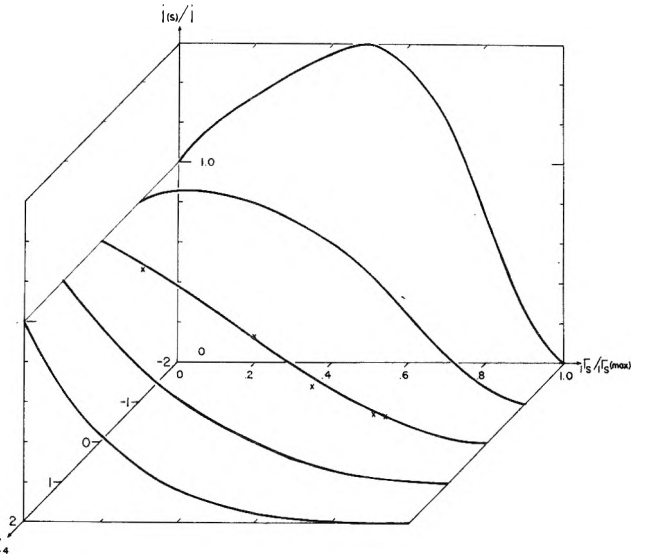

Figure 3. Ratio of electrode rates at surfactant-coated and clean electrodes, $i(s)/i$. Graphs of eq 18 for various values of Z_4 and ${}_1\theta_s$. The following values were assumed in making the plots: $Z_s = 0$; ${}_1\Gamma_{Cl^-} = 2.3 \times 10^{-10}$ mol cm^{-2}; ${}_1\theta_s$, m, ${}_RC_d$, and T as in Figure 2: (——) theoretical curves; $\alpha(s) = 0.65$; (×) experimental points for electroreduction of $Pt^{IV}Cl_2((NH_3)(NO_2))_2$ at allylacetic acid coated platinum electrodes; $\alpha(s) = 0.65$.

fects are second order ($m = 2$) in coverage. A graph of eq 18 appears in Figure 2. Values of $\Delta({}_j\phi_2)$ calculated on the basis of eq 3 represent calculated changes in the ${}_j\phi_2$ potential attending incorporation of ionic charge into the compact region of the double layer. It should be noted that the quantity ${}_1\Gamma_s$ appearing in eq 18 is not necessarily equal to the total interfacial excess of charged surfactant Γ_s. Values of ${}_1\Gamma_s$ are calculated from measured values of Γ_s by means of equations presented below. In the event that Z_s is opposite in sign from Z_4, eq 18 predicts that the electrostatic effect (exponential term) should accelerate the reaction, and that the rate should increase with increasing coverage until a maximum is reached, after which the exponential term changes only slowly while the steric term, $(1 - \theta_s)^m$, decreases rapidly to zero as ${}_1\Gamma_s$ nears ${}_1\Gamma_s(max)$ so that the rate approaches zero. A graph of eq 18 as a function of ${}_1\Gamma_s$ and Z_4 appears in Figure 3.

Rate constant ratios, $*k^0(s)/*k^0$, indicative of the effect of various charged surfactants on the electrode kinetics of typical cationic, neutral, and anionic platinum complexes are summarized in Tables III and IV. Calculation of individual kinetic parameters from thin layer electrode data is described in the Experimental Section.

The data of Tables III and IV suggest that the degree to which cationic chemisorbed molecules influence the electrode rate depends on the length of the carbon chain connecting the amine substituent to the electrode. For instance, allylaminonium ion $CH_2{=}CHCH_2NH_3^+$, the shortest of the alkenylamino cations, displays the most prominent influence, whereas allylglycine in acid solution, $CH_2{=}CHCH_2CH(NH_3^+)COOH$, exerts an influence on ${}_R\phi_2$ similar to that of a neutral molecule.

In contrast, the chain length of carboxylate anions has little or no influence on the electrode rate. Fumarate, *trans*-$HOOCCH{=}CHCOO^-$, vinylsulphonate, $CH_2{=}CHSO_3^-$, acrylate, $CH_2{=}CHCOO^-$, vinylacetic acid anion, $CH_2{=}CHCH_2COO^-$, and allylacetic acid anion, $CH_2{=}CH(CH_2)_2COO^-$ influence ${}_R\phi_2$ to a similar degree in spite of differences in chain length. Since the platinum surface retains a net positive charge at the potentials of interest here, it is evident that cationic substituents seek to travel as far from the positively charged electrode surface as chain length will permit (with the result that their electrostatic influence may be neutralized by association with a counter anion), whereas anionic substituents are attracted to the surface and do not take advantage of their chain length to acquire a counter cation.

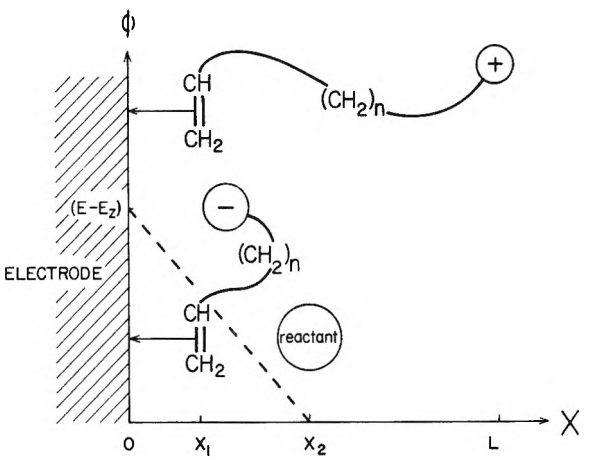

Figure 4. Schematic representation of potential and charge distribution at platinum electrodes containing chemisorbed alkenyl amines and carboxylic acids.

A simple estimate of the influence of chain length on the extent to which the charged chemisorbed molecule alters ${}_j\phi_2$ can be obtained by treating the charged substituent as a point charge tethered within a linear potential gradient in the vicinity of the electrode surface (Figure 4). The differential element of charged substituent interfacial excess, $d\Gamma$, at a distance, x, from the surface will be estimated using the Boltzmann distribution equation

$$d\Gamma = N\Gamma_s \exp(-w/RT)\, dx \qquad (19)$$

where N is a normalization constant to be evaluated below. The coulombic potential energy of the charged

TABLE III: Rate Parameters Derived from Thin Layer Current–Potential Curves[a,b]

Platinum complexes		Surfactant species	$\frac{*k_{43}^0(s)}{*k_{43}^0}$	$\frac{i_{43}(s)}{i_{43}}$	${}_R\phi_2(s) - {}_R\phi_2$ from eq 14, V	$\frac{*k_{23}^0(s)}{*k_{23}^0}$	$\frac{*A_1\Gamma_{Cl^-}(s)}{A_1\Gamma_{Cl^-}}$[c]	$\frac{{}_1\Gamma_{Cl^-}(s)}{{}_1\Gamma_{Cl^-}}$	$\frac{i_{23}(s)}{i_{23}}$	${}_R\phi_2(s) - {}_R\phi_2$ from eq 16, V
Pt(IV)	Pt(II)									
$Pt(NH_3)_5Cl^{3+}$	$Pt(NH_3)_4^{2+}$ [d]	Allylamine	0.066	0.010	0.030	6.03	0.144	0.38	0.87	0.017
		Allylglycine	0.31	0.12	0.012	1.51	0.384	0.62	0.58	0.004
		Allyltriethyl-ammonium	0.076	0.018	0.027	3.77	0.240	0.49	0.91	0.012
		Allylacetic acid	0.28	0.10	0.014	1.85	0.360	0.60	0.67	0.005
		Acrylic acid	0.25	0.10	0.015	1.86	0.410	0.64	0.76	0.006
		Fumaric acid	0.37	0.13	0.011	1.72	0.348	0.59	0.60	0.005
		Vinylsulphonic acid	0.39	0.17	0.010	2.23	0.436	0.66	0.97	0.007
$PtCl_2(NH_3)(NO_2))_2$	$Pt(NH_3)(NO_2))_2$ [d]	Allylamine	2.59	0.37	0.037	1.94	0.144	0.38	0.28	0.026
		Allylglycine	1.35	0.52	0.012	1.20	0.384	0.62	0.46	0.008
		Allyltriethyl-ammonium	2.64	0.64	0.037	1.66	0.240	0.49	0.40	0.019
		Allylacetic acid	1.45	0.52	0.015	1.34	0.360	0.60	0.48	0.011
		Acrylic acid	1.23	0.50	0.008	1.29	0.410	0.64	0.53	0.009
		Fumaric acid	1.52	0.53	0.017	1.29	0.348	0.59	0.45	0.010
		Vinylsulphonic acid	1.29	0.56	0.010	1.08	0.436	0.66	0.47	0.004
$Pt(NO_2)_4Cl_2^{2-}$	$Pt(NO_2)_4^{2-}$ [d]	Allylamine	33.89	4.88	0.036	0.15	0.144	0.38	0.022	0.032
		Allylglycine	4.32	1.66	0.015	0.51	0.384	0.62	0.20	0.011
		Allyltriethyl-ammonium	12.76	3.06	0.025	0.15	0.240	0.49	0.037	0.031
		Allylacetic acid	4.33	1.56	0.015	0.42	0.360	0.60	0.15	0.014
		Acrylic acid	2.96	1.21	0.011	0.72	0.410	0.64	0.30	0.007
		Fumaric acid	4.18	1.45	0.015	0.35	0.348	0.59	0.12	0.017
		Vinylsulphonic acid	2.79	1.22	0.011	0.50	0.436	0.66	0.22	0.010

[a] The experimental conditions employed were the same as Figure 1. [b] Supporting electrolyte, 1 *F* $HClO_4$ + 10 m*F* NaCl. [c] Approximate values of ${}_1\Gamma_{Cl^-}(s)/{}_1\Gamma_{Cl^-}$ were calculated from the data of Table II. [d] Oxidation of the surfactant occurred to a slight extent during the oxidation of these Pt(II) complexes, resulting in partial removal of the surfactant. Thus, the values determined for the anodic reactions are less exact than those for the cathodic reactions.

TABLE IV: Rate Parameters Derived from Thin Layer Current-Potential Curves for Complexes of Platinum(IV)[a]

Platinum complexes	Surfactant species	$_cE_p(s)$, V_{NaCE}	$_cE_p$, V_{NaCE}	$_cE_p(s) - _cE_p$, V	$_ci_p(s)$, μA	$_ci_p$, μA	$^*k_{43}^0(s)/^*k_{43}^0$	$i_{43}(s)/i_{43}$	$_R\phi_2(s) - _R\phi_2$ from eq 14, V
$Pt(tren)Cl_2^{2+}$	Allylamine	0.030	0.120	−0.090	13.6	15.0	0.50	0.072	0.015
	Allylglycine	0.055	0.120	−0.065	14.5	15.0	0.41	0.16	−0.017
	Allylacetic acid	0.205	0.120	0.085	14.6	15.0	23.56	8.48	−0.058
	Acrylic acid	0.195	0.120	0.075	14.8	15.0	17.29	7.08	−0.053
	Fumaric acic	0.200	0.120	0.080	14.5	15.0	20.46	7.12	−0.056
	Vinylsulphonic acid	0.180	0.120	• 0.060	14.8	15.0	10.88	4.74	−0.047
$PtCl_2(NH_3)(NO_2))_2$	Allylamine	0.395	0.420	−0.025	13.4	14.1	2.10	0.30	0.027
	Allylglycine	0.415	0.420	−0.005	13.6	14.1	1.52	0.58	0.015
	Allylacetic acid	0.350	0.420	−0.070	13.1	14.1	0.23	0.083	−0.054
	Acrylic acid	0.370	0.420	−0.050	13.2	14.1	0.35	0.14	−0.041
	Fumaric acid	0.350	0.420	−0.070	13.1	14.1	0.24	0.084	−0.053
	Vinylsulphonic acid	0.355	0.420	−0.065	13.3	14.1	0.25	0.11	−0.052
$Pt(NO_2)_4(H_2O)Cl^-$	Allylamine	0.360	0.395	−0.035	7.7	7.9	3.58	0.52	0.022
	Allylglycine	0.390	0.395	−0.005	7.7	7.9	2.05	0.79	0.013
	Allylacetic acic	0.305	0.395	−0.090	5.8	7.9	0.17	0.061	−0.033
	Acrylic acid	0.300	0.395	−0.095	6.0	7.9	0.17	0.070	−0.031
	Fumaric acid	0.295	0.395	−0.100	5.8	7.9	0.16	0.056	−0.032
	Vinylsulphoric acid	0.310	0.395	−0.085	6.0	7.9	0.18	0.078	−0.030

[a] The supporting electrolyte contained 1 *F* $NaClO_4$ + 10 m*F* NaCl, pH 7.0. Other experimental conditions were the same as in Figure 1.

substituent in the double layer field will be calculated for a linear potential gradient (eq 20). Normalization of eq 19

$$w = q_s\phi = Z_sF\phi \approx \begin{cases} Z_sF(E - E_z)(1 - x/{}_Ex_2), & {}_sx_1 \le x \le {}_Ex_2 \\ 0 & x > {}_Ex_2 \end{cases} \quad (20)$$

according to $\int_{x1}^{L} d\Gamma = \Gamma_s$, followed by integration over the compact layer region, ${}_sx_1 \le x \le {}_Ex_2$, gives

$$ {}_1q_s/q_s = {}_1\Gamma_s/\Gamma_s = \frac{1 - \exp[-\lambda(1 - {}_sx_1/{}_Ex_2)]}{\exp[-\lambda(1 - L/{}_Ex_2)] - \exp[-\lambda(1 - {}_sx_1/{}_Ex_2)]} \quad (21)$$

where $\lambda \equiv Z_sF(E - E_z)/RT$. Evaluation of eq 21 requires a knowledge of the positions, ${}_sx_1$ and ${}_Ex_2$, of the inner plane of closest approach of the surfactant and the outer plane of closest approach of the anion of the supporting electrolyte, respectively. Consideration of olefinic chemisorption in terms of "associative" bonding through the π system[1] yields a value for ${}_sx_1$ of 2.15 Å, corresponding to the sum of the covalent radii of a platinum surface atom and a paraffinic carbon. Formulation of surfactant chemisorption in terms of the alternative "dissociative" bonding scheme decreases the value of ${}_sx_1$ by about 0.1 Å (the difference between the covalent radii of single and double-bonded carbon atoms), and values of L would be altered proportionately. The question of chemisorption as a two-site or four-site process is therefore not of particular importance to the present analysis. ${}_Ex_2$ is represented as the average distance of closest approach of the supporting electrolyte anion (if an intervening chemisorbed H_2O is assumed to be present, ${}_Ex_2$ = 3.08 Å). A graph of eq 21 appears in Figure 5. Thus, if the surfactant chain length is greater than ${}_Ex_2$, the values of ${}_1\Gamma_s$ required for application of eq 18 must be computed by means of eq 21, which corrects the total interfacial excess, Γ_s, for neutralization by

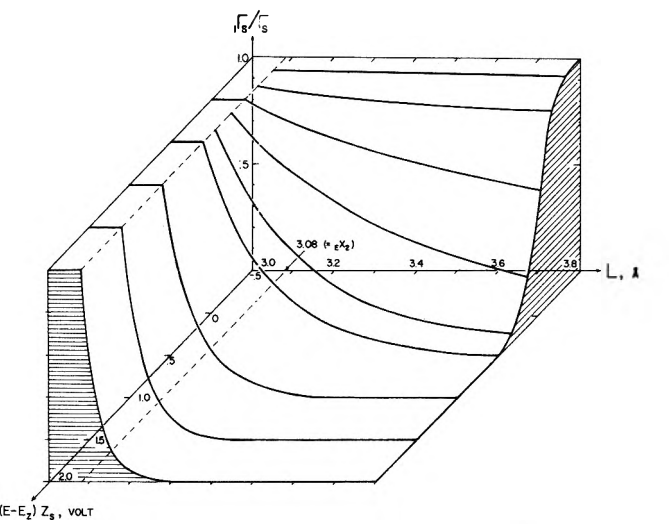

Figure 5. Fraction of charged substituent located a distance x from the electrode surface ${}_sx_1$ = 2.15 Å; ${}_Ex_2$ = 3.08 Å.

ions of the electrolyte. It can be seen from Figure 5 that L is expected to influence sharply the extent to which cationic surfactants alter ${}_i\phi_2$ at a positively charged electrode. In particular, an unipositive surfactant is expected to exert a negligible electrostatic influence on the electrode rate when the maximum distance from the double bond to the charged substituent, $L - {}_sx_1$, exceeds 1.6 Å. In contrast, the theory predicts virtually complete inclusion of anionic surfactants within the compact layer at a positively charged electrode, even for chain lengths as large as 9 Å.

Values of ${}_1q_s$ calculated from Γ_s by means of eq 21 appear in Table V. The fact that ${}_1q_s/q_s$ is very small for allylglycine in its cationic form serves to account for the similarity of its influence on electrode rates to that of neutral surfactants (Table III). Conversely, the anionic

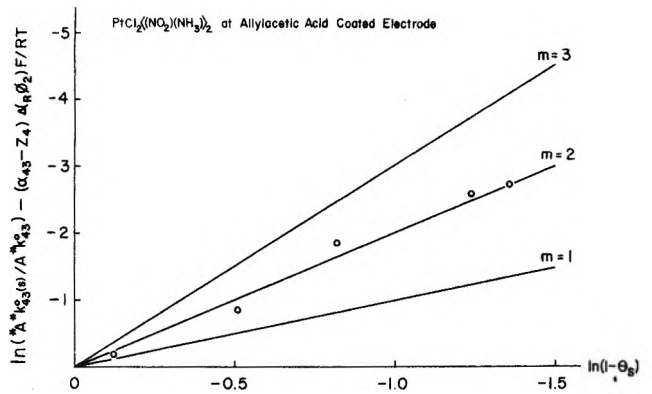

Figure 6. Variation in Pt(IV) electroreduction rate with surface coverage by allylacetic acid: solid curves are graphs of eq 23 for various values of m; circles are experimental points corresponding to reduction of $PtCl_2((NO_2)(NH_3))_2$. The experimental conditions were as in Figure 1. Surface coverages were determined as described in the Experimental Section.

TABLE V: Contribution of Charged Surfactants to Alteration of the $_E\phi_2$ Potential at Platinum Electrodes

Surfactant	pH	$_1q(s)$,[a] $\mu C\ cm^{-2}$	$\frac{_1\Gamma_{Cl^-}(s)}{_1\Gamma_{Cl^-}}$	$\Delta(_E\phi_2)$,[b] V
Allylamine	0	8.60	0.38	+0.038
	7.0			+0.021
Allylglycine	0	0.02	0.62	+0.014
	7.0			+0.013
Allyltriethyl-ammonium	0	6.90	0.49	+0.030
	7.0	6.90		+0.030
Allylacetic acid	0		0.60	+0.015
	7.0	−47.3		−0.059
Fumaric acid	0		0.59	+0.015
	7.0	−48.1		−0.060
Acrylic acid	0		0.64	+0.013
	7.0	−42.3		−0.057
Vinylsulphonic acid	0		0.67	+0.012
	7.0	−40.0		−0.054

[a] $_1q(s) = Z_sF_1\Gamma_s$; $_1\Gamma_s$ from eq 21. [b] Values of $\Delta(_E\phi_2)$ were calculated by means of eq 3 using data from Table II.

surfactants have values of $_1q_s/q_s$ close to unity; in fact, the anionic charge introduced into the compact layer by anionic olefins is more than equivalent to the charge carried by specifically adsorbed chloride displaced by the olefin, leading to a net negative shift in $_f\phi_2$, in agreement with the observed trend in electrode rate (Table IV).

Values of the quantity $(1 - \theta)^m$ can be extracted from measured values of $*k_{43}^0(s)*A/*k_{43}^0A$ (see eq 23, below) by multiplying both sides of eq 17 by $*A/A$ and rearranging to give

$$(1-\theta)^m = (*k_{43}^0(s)*A/*k_{43}^0A) \times \exp\left\{\frac{-F}{RT}(\alpha_{43} - Z_4)\Delta(_R\phi_2)\right\} \quad (22)$$

The uncertainty in the electrostatic correction (the exponential term on the right-hand side of eq 22) may be minimized experimentally by utilizing uncharged reactants and surfactants (*i.e.*, $Z_4 = Z_s = 0$). Approximate values of $\Delta(_R\phi_2)$ for substitution into eq 22 have been obtained from measured values of Γ_s (Table VI) by means of eq 3

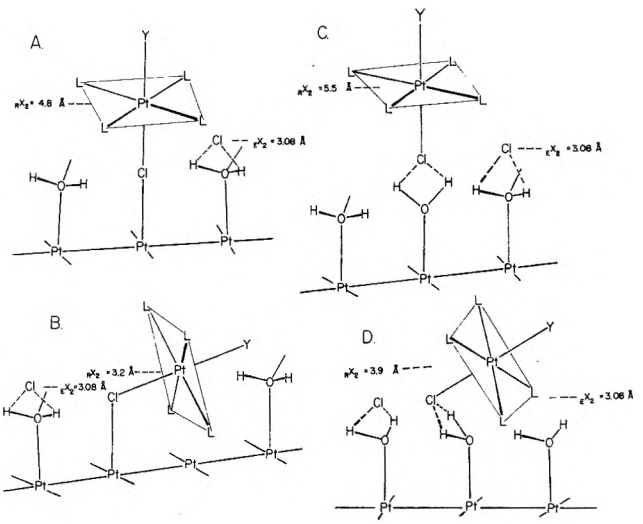

Figure 7. Molecular models illustrating possible nuclear configurations of the Pt(II)–Pt(IV) halide-bridged transition state.

and 22 on the assumption that $\Delta(_R\phi_2) = \Delta(_E\phi_2)$; a more detailed calculation of $\Delta(_R\phi_2)$ is described below. Taking the logarithm of both sides of eq 22 indicates that a plot of the logarithm of the measured quantity on the right-hand side *vs.* the logarithm of $(1 - \Theta)$ should be linear with zero intercept and slope equal to m (eq 23). A graph of eq 23 for reduction of $Pt^{IV}Cl_2((NO_2)(NH_3))_2$ at various

$$\ln\left(*k_{23}^0(s)*A/*k_{43}^0A\right) - \frac{F}{RT}(\alpha_{43} - Z_4)\Delta(_R\phi_2) = m \ln(1-\theta) \quad (23)$$

surfactant coverages appears in Figure 6. Data from which the graphs were prepared are presented in Table VI. The fact that m values close to 2 are obtained is suggestive of a transition state structure in which the interface-bridge-reactant axis is "bent," that is, one site is required by the bridge and another by the apex of the reactant octahedron closest to the surface.

Quantitative consideration of electrode rate variation with surfactant coverage, chain length, and ionic type betrays the location of the reactant in the interfacial region. In particular, the rate depends upon $_R\phi_2$, which depends in turn upon the distance of closest approach of the reactant to the electrode surface, $_Rx_2$. Use of the Gouy–Chapman–Stern model of the diffuse region of the double layer leads to the following equation relating $_R\phi_2$, $_E\phi_2$, $_Rx_2$, and $_Ex_2$ in the presence of a large excess of Z_E–Z_E valent supporting electrolyte[10]

$$_Rx_2 - {}_Ex_2 = -\frac{1}{\delta}\ln\left\{\frac{\tanh\left[\frac{Z_EF}{4RT}\,{}_R\phi_2\right]}{\tanh\left[\frac{Z_EF}{4RT}\,{}_E\phi_2\right]}\right\} \approx \frac{-1}{\delta}\ln(_R\phi_2/{}_E\phi_2) = \frac{-1}{\delta}\ln[_R\phi_2(s)/{}_E\phi_2(s)] \quad (24)$$

where $\delta \equiv [8\pi Z_E^2F^2C_E/\kappa\epsilon RT]^{1/2}$ and $_Rx_2 \geq {}_Ex_2$. The approximate form of eq 24 applies within ±1% whenever $|Z_E|_R\phi_2$ and $|Z_E|_E\phi_2$ are less than 20 mV, and can be used to relate the difference, $_R\phi_2(s) - {}_R\phi_2$ ($\equiv \Delta(_R\phi_2)$, evaluated by rate measurements, and the quantity, $_E\phi_2(s)$

TABLE VI: Rate Data for Electroreduction of $Pt^{IV}Cl_2((NH_3)(NO_2))_2$ at Allylacetic Acid Coated Platinum Electrodes[a]

${}_1\theta_s$	${}_cE_p(s)$, V_{NaCE}	${}_cE_p$, V_{NaCE}	${}_cE_p(s) - {}_cE_p$, V	${}_ci_p(s)$, μA	${}_ci_p$, μA	${}^*\alpha_{43}(s)$	${}^*k_{43}{}^0(s){}^*A / {}^*k_{43}{}^0A$
0.00	0.423	0.423	0.000	13.7	13.7	0.64	1.000
0.11	0.452	0.423	0.029	12.7	13.7	0.59	0.859
0.40	0.410	0.423	−0.013	13.3	13.7	0.62	0.522
0.55	0.390	0.423	−0.033	13.0	13.7	0.61	0.255
0.71	0.370	0.423	−0.053	12.8	13.7	0.60	0.137
0.74	0.367	0.423	−0.056	12.8	13.7	0.60	0.128

[a] The experimental conditions employed were the same as Figure 1.

TABLE VII: Estimation of Reactant Location During Halide-Bridged Electroreduction of Pt(IV) Complexes[a]

Platinum complexes	Surfactant species	$\frac{\Delta({}_R\phi_2)}{\Delta({}_E\phi_2)}$	${}_RX_2 - {}_EX_2$ from eq 25, Å
$Pt(NH_3)_5Cl^{3+}$	Allylamine	0.79	+0.66
	Allyltriethylammonium	0.91	+0.25
	Allylglycine	0.95	+0.13
	Allylacetic acid	0.98	+0.06
	Acrylic acid	1.20	−0.50
	Fumaric acid	0.77	+0.75
	Vinylsulphonic acid	0.87	+0.40
$PtCl_2((NH_3)(NO_2))_2$	Allylamine	0.99	+0.03
	Allyltriethylammonium	1.25	−0.63
	Allylglycine	0.87	+0.40
	Allylacetic acid	1.04	−0.10
	Acrylic acid	0.75	+0.79
	Fumaric acid	1.15	−0.38
	Vinylsulphonic acid	0.83	+0.53
$Pt(NO_2)_4Cl_2^{2-}$	Allylamine	0.96	+0.11
	Allyltriethylammonium	0.85	+0.46
	Allylglycine	1.12	−0.32
	Allylacetic acid	1.06	−0.17
	Acrylic acid	0.88	+0.35
	Fumaric acid	1.02	−0.04
	Vinylsulphonic acid	0.87	+0.38

[a] The experimental conditions employed were the same as Figure 1.

$- {}_E\phi_2$ ($\equiv \Delta({}_E\phi_2)$), determined from interfacial excess data, to the unknown quantity, ${}_RX_2 - {}_EX_2$. In particular, solving the approximate form of eq 24 for ${}_R\phi_2$ and ${}_R\phi_2(s)$, forming the difference and rearranging, yields

$$ {}_RX_2 - {}_EX_2 = -\frac{1}{\delta} \ln[\Delta({}_R\phi_2)/\Delta({}_E\phi_2)] \qquad (25) $$

Implicit in the use of eq 25 is the assumption that the steric influence of surfactant can be represented by $(1 - \theta)^m$ with m assigned the same value for a given surfactant as was obtained from plots of eq 23 for an uncharged complex otherwise resembling the reactant (Table VI). Values of ${}_RX_2 - {}_EX_2$ for various reactant-surfactant combinations appear in Table VII. ${}_RX_2$ and ${}_EX_2$ are qualitatively equal; that is, the average distance of closest approach of the Pt nucleus of the reactant complex to the electrode surface is comparable to that of the supporting electrolyte anion, ClO_4^-.

Figure 7 shows molecular models for four possible nuclear configurations of the halide-bridged transition state. For clarity the models are shown for the (100) plane of the face-centered cubic Pt electrode, although polycrystalline electrodes were used in this study. Figure 7A and 7B represent direct bonding between the halide bridge and an electrode surface atom, while Figure 7C and 7D reflect electrode-solvent-halide bonding at closest approach to the surface. Linear alignment of the three centers along an axis normal to the electrode surface, Figure 7A and 7C, appears unlikely as an *average* interfacial orientation because it implies a one-site transition state whereas measurements of m indicate that approximately two contiguous sites are involved in the rate-limiting process (Table VI), and because it implies values of ${}_RX_2$ which are much too large (Table VII). Linear configurations could, however, occur as vibrational excited states of the bent configuration. The bent structures, Figure 7B and 7D, by contrast, successfully account for the experimental results presented here and also correlate nicely with previous work,[7] in which it was shown that the $a_{1g}(\sigma^*)$ $[5d_2]$ orbital of the platinum complex and the $3d_z2$ orbital of the chloride bridge are likely candidates for participation in the electron-transfer step. Owing to the lack of appreciable difference in the expected values of ${}_RX_2$ for the two bent structures, it is not possible to decide between them on this basis. Double layer experiments and semiempirical molecular orbital calculations directed toward the ques-

tion of electron transfer through solvent molecules in the compact layer are in progress.[13,14]

Experimental Section

Electrode surface pretreatment, reagents, and experimental conditions were as in part I.[3]

Platinum compounds used in this work were taken from samples described in ref 7, except as indicated below.

[Pt(tren)Cl$_2$] · 2Cl. To an aqueous solution of $H_2PtCl_6 \cdot 6H_2O$ was added slightly less than the stoichiometric amount of 2,2′,2″-triaminotriethylamine-3-hydrochloride, "tren" (Strem Chemicals Inc., Danvers, Mass.), dissolved in a minimum of water. The orange addition compound, $C_6H_{12}N_4 \cdot H_4Pt_2Cl_{12} \cdot 10H_2O$, which separated immediately, was filtered and air dried. This compound (1.7 g, 1.8×10^{-3} mol) was added to a solution containing 1.7 g (7.0×10^{-3} mol) of tren · 3HCl in 35 ml of water and the reaction mixture was allowed to stand at 75° for 16 hr (higher temperatures resulted in decomposition to a black product). The resulting solution was filtered while hot; the yellow crystalline product was collected, recrystallized from hot water, and dried under vacuum. Concentration of the mother liquor under reduced pressure yielded additional product. The combined yield was 69% based upon Pt(IV). *Anal.* Calcd for [Pt(tren)Cl$_2$] · 2Cl: C, 14.90; H, 3.75; N, 11.59; Cl, 29.35; Pt, 40.38. Found: C, 14.63; H, 3.72; N, 11.23; Cl, 29.26; Pt, 40.17.

The interfacial excess of electroactive chemisorbed molecules may be determined directly by means of potential-step coulometry.[2,3] Adsorbed chloride and the chemisorbed alkenes studies in this work were determined in this way. The results are summarized in Table II.

The free surface area remaining after treatment with a chemisorbed species was estimated using the following approach.[2] The electrode was rinsed with a solution of the organic surfactant and then with a solution of KI; the potential of the thin layer electrode was then adjusted so that the adsorbed halogen was converted to dissolved IO_3^-; finally, the IO_3^- was determined by thin layer coulometric reduction to I_2.[15] Iodide reacts with the surface only at points left vacant by the organic surfactant. It is assumed that the electrode reactions of Pt(IV)|Pt(II) couples proceed at these vacant points. Determination of the vacant sites in this manner rather than by comparison of the organic coverage with an elusive "saturation value" has the advantages that it avoids the necessity of forming a very small difference (vacancies) between two larger numbers (coverage and saturation coverage), and that it does not depend upon estimation of such tenuous quantities as the "number of sites per molecule" of the organic surfactant. The free area was thus calculated by means of

$$*A \equiv A\left[1 - \frac{{}_1\Gamma_s}{{}_1\Gamma_s(\max)}\right]^m = A\left[\frac{{}_1\Gamma_I(s)}{{}_1\Gamma_I}\right]^m \quad (26)$$

where ${}_1\Gamma_I(s)$ refers to the interfacial excess of I at an organic-surfactant-pretreated electrode surface. The results appear in Table II.

Apparent values of the charge transfer coefficient, $*\alpha_{43}$, and of the standard electrochemical rate constant, $*k_{43}^0$, were obtained from thin layer current potential curves by means of[9]

$$*\alpha_{43} = \frac{2.718RT_c i_p}{nF^2V(-r)C_4^0} \quad (27)$$

$$*k_{43}^0 = \frac{2.718RT_c i_p}{nF*AC_4^0}\exp\left[\frac{2.718{}_ci_p({}_cE_p - E_{43}^0)}{nFV(-r)C_4^0}\right] \quad (28)$$

$(1 - *\alpha_{23})$ and $*k_{23}^0$ are given by

$$(1 - *\alpha_{23}) = \frac{2.718(-{}_ai_p)RT}{nF^2VrC_2^0} \quad (29)$$

$$*k_{23}^0(Y = H_2O)\gamma_1\Gamma_{Cl^-} = \frac{2.718(-{}_ai_p)}{nF*AC_2^0}\exp\left\{\frac{2.718(-{}_ai_p)[{}_aE_p - E_{23}^0(Y = H_2O)]}{nFVrC_2^0}\right\} \quad (30)$$

$$*k_{23}^0(Y = Cl^-)\gamma_1\Gamma_{Cl^-}Ka_{Cl^-} = \frac{2.718(-{}_ai_p)}{nF*AC_2^0}\exp\left[\frac{2.718(-{}_ai_p)({}_aE_p - E_{23}^0)}{nFVrC_2^0}\right] \quad (31)$$

Standard potentials, E_{43}^0 and E_{23}^0, for the Pt(IV)|Pt(III) and Pt(II)|Pt(III) couples are not available. However, this is not a serious problem in the present instance, since the standard potential is not required for calculation of the ratios $*k_{43}^0(s)/*k_{43}^0$ and $*k_{23}^0(s)/*k_{23}^0$.

Acknowledgments. Acknowledgment is made to the donors of The Petroleum Research Fund, administered by the American Chemical Society, and to the National Science Foundation for support of this research. We are thankful to Dr. Henry Freiser, University of Arizona, for his suggestions relative to this work.

Appendix. Notation

A	= electrode area, cm^2
α_{43}	= charge transfer coefficient of a Pt(IV)|Pt(III) couple (etc.)
*	= indication of an empirical value
C	= differential double layer capacitance per unit area, F cm^{-2}
${}_jC_c$, ${}_jC_d$	= differential capacitance assignable to the "compact layer" or "diffuse layer" relative to species j per unit area, respectively
C_j	= concentration of species j, mol cm^{-3}
E	= electrode potential, V; as a subscript, E refers to (supporting) electrolyte
${}_aE_p$, ${}_cE_p$	= peak potential of positive or negative-going current–potential curve, respectively
E^0	= formal standard potential
E_z	= zero-charge potential
e	= 2.718
ϵ	= permittivity constant, 8.849×10^{-14} F cm^{-1}
F	= Faraday constant, C equiv^{-1}
${}_1\Gamma_j$, Γ_j	= compact layer or total interfacial excess of ionic substituent j, respectively, mol cm^{-2}
γ	= parameter, cm^{-1}, reflecting approximate proportionality between ${}_1\Gamma_{Cl^-}$ and surface activity of Cl^- ion
i	= current, A
${}_ai_p$, ${}_ci_p$	= peak current of positive or negative-going current–potential curves, respectively
k_{43}^0	= standard electrochemical rate constant of a Pt(IV)|Pt(III) couple (etc.), cm sec^{-1}
κ	= dielectric constant of solvent
L	= length of surfactant molecule when fully extended, cm

(13) R. F. Lane and A. T. Hubbard, University of Hawaii, unpublished experiments.
(14) M. A. Leban and A. T. Hubbard, University of Hawaii.
(15) A. T. Hubbard, R. A. Osteryoung, and F. C. Anson, *Anal. Chem.*, **38**, 692 (1966).

m = number of contiguous sites occupied by reactant in transition state
n = number of electrons transferred per molecule
ϕ = potential at a point in the double layer, V
${}_j\phi_2$ = potential at the plane of closest approach for species j, V
$\Delta({}_j\phi_2)$ = change in ϕ_2 for species j caused by introduction of surfactant at constant potential
q_c, q_d = excess ionic charge per unit area assignable to the "compact layer" or "diffuse layer," respectively, C cm^{-2}
q_{dl} = excess ionic charge in the double layer
R = gas constant, J mol^{-1} °K^{-1}; as a subscript, R refers to "reactant"
r = potential sweep rate, V sec^{-1}
(s) = indicates surfactant or surfactant-coated electrode
T = temperature, °K
tren = tris(2-aminoethyl)amine
V = volume of the thin layer electrode cavity, cm^3
w = coulombic energy of ion in double layer field, J mol^{-1}
x = position relative to electrode (metal) surface, cm
x_1, x_2 = location of plane of closest approach of specifically adsorbed or unadsorbed molecules, respectively, cm
Z_j = ionic valence of ion j

Association of Alkali Metal Cations with Triphenylphosphine Oxide in Tetrahydrofuran Solvent[1]

H. B. Flora, II, and W. R. Gilkerson*

Department of Chemistry, University of South Carolina, Columbia, South Carolina 29208 *(Received November 22, 1972)*

The electrical conductivities of solutions of the lithium, sodium, potassium, and rubidium salts of 2,4-dinitrophenol in tetrahydrofuran solvent at 25° have been measured with and without added triphenylphosphine oxide. Values of the ion pair dissociation constants of the salts have been derived from variation of the conductivities with salt concentration. These ion pair dissociation constants increase with increasing cation size as one would expect for contact ion pairs. Values of cation–ligand association constants, K_L, have been derived from the increases in the conductivities in the presence of added triphenylphosphine oxide. The values of K_L are for lithium, 3500 M^{-1}, for sodium, 250 M^{-1}, for potassium, 87 M^{-1}, and for rubidium, 53 M^{-1}. This is just the order of association expected from the ion radii. It is found that an ion–dipole model, modified according to Kirkwood and Westheimer to take into account the influence of surrounding polarizable solvent, is able to account very well for the results reported here.

We have been engaged in a continued effort in this laboratory to sort out the factors of importance in determining the extent (and energetics) of specific ion–molecule interaction in solution.[2-5] Briefly, we have found[3] that ligand basicity and dipole moment affect the extent of formation of the 1:1 complex between a tertiary ammonium cation and a series of Lewis bases, eq 1, in low dielectric solvents. A crude ion–dipole model has been proposed[2,3] to account for our results.

$$M^+ + L \rightleftharpoons M^+,L \qquad K_L = [M^+,L]/[M^+][L] \quad (1)$$

We now report results of an investigation of the effect of cation size on the extent of a process represented by eq 1. Our experimental approach is based on the measurement of the increased conductivity observed when added Lewis base molecules capture cations from a salt highly associated into ion pairs. The alkali metal salts of 2,4-dinitrophenol and tetrahydrofuran, THF, as solvent were chosen because of their suitability for our purposes; the salts are sufficiently soluble in this solvent and the ions are highly associated into ion pairs in the 10^{-4} M concentration range for our experimental appraoch to succeed.

Experimental Section

Tetrahydrofuran (Matheson Coleman and Bell) was stored overnight over sodium ribbon, refluxed with barium oxide for 3 hr, and then distilled on a 40 × 2 cm column filled with glass helices. A middle fraction (bp 65.6–66°) was stored over alumina (Alcoa grade F-20) which had been heated to approximately 800° for 1 hr. Just prior to use the THF was passed through a 35 × 2 cm column, the lower 32 cm of which was packed with fired alumina and the top 3 cm with molecular sieve (Linde type 4-A). The specific conductivities of batches of the solvent ob-

(1) This work has been supported in part by Grant No. GP-13139 from the National Science Foundation. Presented in part at the Third International Conference on Non-Aqueous Solvents, Michigan State University, East Lansing, Mich., July 7, 1972.
(2) E. R. Ralph, III, and W. R. Gilkerson, *J. Amer. Chem. Soc.*, **86**, 4783 (1964).
(3) W. R. Gilkerson and J. B. Ezell, *J. Amer. Chem. Soc.*, **89**, 808 (1967).
(4) J. B. Ezell and W. R. Gilkerson, *J. Phys. Chem.*, **72**, 144 (1968).
(5) H. B. Flora, II, and W. R. Gilkerson, *J. Amer. Chem. Soc.*, **92**, 3273 (1970).

tained in this way were in the neighborhood of 2×10^{-10} ohm^{-1} cm^{-1}.

The alkali metal 2,4-dinitrophenolates were prepared by adding a concentrated solution of the corresponding alkali metal carbonate to an aqueous paste of 2,4-dinitrophenol, HDNP (Matheson Coleman and Bell). The resulting salts were washed with ethanol and extracted twice with boiling benzene. The salts were recrystallized from ethanol three times and dried *in vacuo* at 80°. The melting points (dec) are LiDNP, 312.5–314.5°; NaDNP, 312–313° (lit.[6] 311–312°); KDNP, 319–320°; and RbDNP, 316.5–318.5°.

Triphenylphosphine oxide (K & K Laboratories) was recrystallized from ethanol and dried *in vacuo* before each use.

Solids were weighed in a nitrogen-filled drybox. All solutions were made up by weight. Concentrations of solutes were calculated assuming the densities of the solutions to be the same as that of pure solvent. The conductivities of the salt solutions in the presence of added triphenylphosphine oxide, Ph_3PO, were determined by adding weighed increments of a concentrated stock solution of the phosphine oxide dissolved in salt solution to a known weight of salt solution of the same concentration in the conductance cell.

Conductance measurements were carried out using cells, a bridge, and a thermostat already described.[2]

The physical properties of the THF at 25° are taken to be:[7] density, 0.880 g ml^{-1}; viscosity, 0.460 cP; and dielectric constant, 7.39.

Results and Discussion

The alkali metal salts of 2,4-dinitrophenol are highly associated to form ion pairs in the concentration range 0.1–1 mM in THF

$$M^+,X^- \rightleftharpoons M^+ + X^- \quad K_0 = [M^+][X^-]y_\pm^2/[M^+,X] \tag{2}$$

where $[M^+,X^-]$ represents the molar concentration of ion pairs, M^+,X^- and $y\pm$ is the mean molar ionic activity coefficient, taken to be given by a form of the Debye–Huckel limiting law.[8] The Shedlovsky conductance function, which is applicable when association is large,[8,9] is given in eq 3 where S is the Shedlovsky function. Typically, in our systems the values of molar conductivity,[10] Λ, range from 0.1 to 1 ohm^{-1} cm^2 mol^{-1}. Since limiting molar conductivities, Λ_0, are of the order of 100 conductance units (see below), and values of S and $y\pm^2$ are very close to unity, the conductance eq 3 reduces to

$$1/\Lambda S = 1/\Lambda_0 + \Lambda S C y_\pm^2/\Lambda_0^2 K_0 \tag{3}$$

$$\Lambda^2 C \simeq \Lambda_0^2 K_0 \tag{4}$$

We find that the product $\Lambda^2 C$ increases linearly with salt concentration in pure THF, the relative effect being the greatest for LiDNP and becoming negligible for RbDNP. Such behavior is indicative that one of the two possible ion triples is favored[11,12]

$$M^+ + MX \rightleftharpoons M_2X^+,K_3^+ \tag{5a}$$

$$X^- + MX \rightleftharpoons MX_2^-,K_3^- \tag{5b}$$

Wooster plots,[12] $\Lambda^2 C$ *vs.* C (neglecting ion atmosphere effects), were made in the case of each salt. The intercepts as $C \rightarrow 0$ for these plots were taken to be the values of $\Lambda_0^2 K_0$. We estimate the uncertainty in the values of $\Lambda_0^2 K$ to be ±10%.

TABLE I: Ion Pair Dissociation of Alkali Metal Salts in THF at 25°

	Anion		
Cation	DNP^- $10^{10}K_0$[a]	BPh_4^- 10^5K_0[b]	Fluorenyl$^-$ 10^7K_0[c]
Li^+	2.3	7.96	39
Na^+	9.3	8.52	6.2
K^+	150	3.22	
Rb^+	350		
Cs^+		0.187	0.14

[a] Units of K_0 are all M. [b] Reference 7. [c] Reference 14.

We are unable to make reliable measurements in dilute enough solutions to obtain values of Λ_0 for these salts. Estimates of Λ_0 for each of the salts are made using the following information and assumptions: (1) the values of ionic molar conductivities of Li^+, Na^+, K^+, Rb^+, and Bu_4N^+ due to Smid and Szwarc,[7] (2) the assumption that the ratio of the limiting molar conductivity of tetra-*n*-butylammonium picrate to that for tetra-*n*-butylammonium tetraphenylborate in THF is equal to the same ratio in 1,2-dichloroethane (the Walden product, $\Lambda_0\eta_0$, for tetra-*n*-butylammonium tetraphenylborate has been found to be almost the same in THF[7] as in 1,2-dichloroethane[13]), and finally (3) the assumption that the ionic mobility of the 2,4-dinitrophenolate anion is approximately the same as that of the picrate (2,4,6-trinitrophenolate) anion. We estimate in this way that for LiDNP, Λ_0 is 89.9, for NaDNP, Λ_0 is 101.5, for KDNP, Λ_0 is 103.1, and for RbDNP, Λ_0 is 105.6, all in units ohm^{-1} cm^2 mol^{-1}.

Values of the ion pair dissociation constants for the salts calculated from the intercepts, $\Lambda_0^2 K_0$, and the above values of Λ_0 are given in Table I, along with those of some other alkali metal salts in THF for comparison.

Note that the dissociation constants of the dinitrophenolates increase as the cation radius increases from lithium to rubidium. The variation of the dissociation constants of the tetraphenylborates with cation size are intermediate between those of the dinitrophenolates and those for the fluorenyl salts. The increases in K_0 with increasing cation size observed for the dinitrophenolates indicates that the electrostatic potential energy of interaction between cation and anion in contact in the ion pair is the controlling factor for these salts

$$U_{el} = -z^2e^2/\epsilon a \tag{6}$$

where ϵ is the dielectric constant and a is the distance of the closest approach at contact. Since $a = r_+ + r_-$, where r_+ *is the cation radius and* r_- is an effective anion radius, then a increases as r_+ increases so that the U_{el} decreases

(6) H. P. Crocker and R. H. Hall, *J. Chem. Soc.*, 4439 (1955).
(7) D. N. Bhattacharyya, C. L. Lee, J. Smid, and M. Szwarc, *J. Phys. Chem.*, **69**, 608 (1965).
(8) C. De Rossi, B. Sesta, M. Ballistini, and S. Petrucci, *J. Amer. Chem. Soc.*, **94**, 2961 (1972).
(9) R. Shedlovsky, *J. Franklin Inst.*, **225**, 739 (1938).
(10) The conductance data will appear following these pages in the microfilm edition of this volume of the journal. Single copies may be obtained from the Business Operations Office, Books and Journals Division, American Chemical Society, 1155 Sixteenth St., N.W., Washington, D. C. 20036. Remit check or money order for $3.00 for photocopy or $2.00 for microfiche, referring to code number JPC-73-1421.
(11) R. M. Fuoss and C. A. Kraus, *J. Amer. Chem. Soc.*, **55**, 2387 (1933).
(12) C. B. Wooster, *J. Amer. Chem. Soc.*, **59**, 377 (1937).
(13) J. J. Zwolenik and R. M. Fuoss, *J. Phys. Chem.*, **68**, 903 (1964).

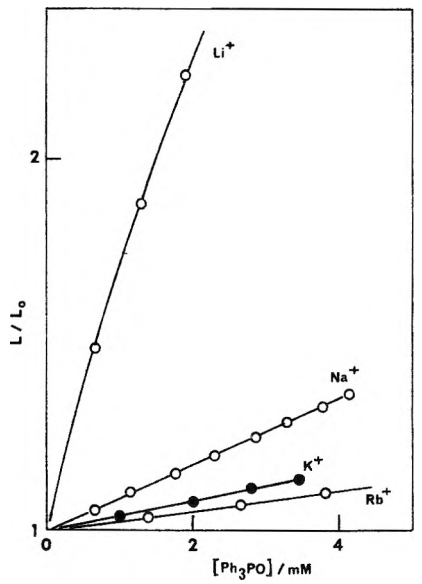

Figure 1. The ratio of the specific conductivity L in the presence of phosphine oxide to that L_0 in the absence of phosphine oxide. Salt concentrations were LiDNP, 0.374 m*M*; NaDNP, 0.404 m*M*; KDNP. 0.233 m*M*; and RbDNP, 0.201 m*M*.

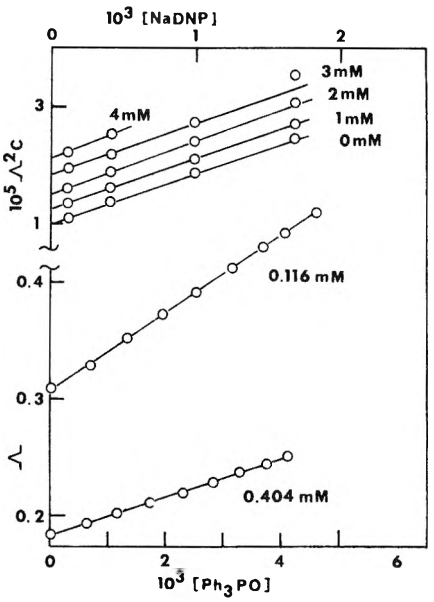

Figure 2. Conductances of NaDNP in THF with added Ph_3PO treated to minimize the effects due to presence of triple ions. The lower portion shows typical plots of titrations of NaDNP solutions of the two concentrations indicated with salt solutions containing Ph_3PO. Values of Λ at round values of [Ph_3PO] were read from these and similar plots at other salt concentrations. These values of Λ were used to calculate sets of values of Λ^2C for each of the several round values of ligand concentration. Plots of these values of Λ^2C at the indicated ligand concentrations appear in the upper portion plotted *vs.* salt concentrations. The extrapolation of the values of Λ^2C to infinite salt dilution eliminates effects of ion triples on the ion pair dissociation constants.

in magnitude resulting in a decreased extent of ion association. Smid and coworkers[14,15] have explained the results in the cases of the tetraphenylborates and particularly the fluorenyl salts in terms of specific solvent interaction resulting in preferential formation of "solvent-separated" ion pairs by the smaller cations. These latter type ion pairs tend to be less associated than if the ions were in contact.

Addition of triphenylphosphine oxide to alkali metal dinitrophenolate solutions in THF has a marked effect on the conductivities of these solutions. The relative increases in conductivity are shown in Figure 1 for lithium, sodium, potassium, and rubidium dinitrophenolates. We have previously shown[16] that conductivity increases occuring upon the addition of triphenylphosphine oxide to tributylammonium picrate solutions in THF were due to the association of the cation with a molecule of Ph_3PO to form a 1:1 cation–ligand complex, eq 1. We advance cation–ligand complex formation as the principal explanation for the conductivity increases shown in Figure 1.

There is some dependence of the relative conductivities in the presence of added Ph_3PO on the salt concentration; the relative increase for a given concentration of added Ph_3PO was greater the smaller salt concentration. Such effects have been noted previously.[4] In the systems here, the effect of finite salt concentration was moderate for LiDNP, pronounced for NaDNP, moderate again for KDNP, and very slight for RbDNP. To minimize these effects, values of Λ^2C for each salt concentration at round values of the concentration of phosphine oxide were determined. A graph was made of Λ (Λ^2 in the case of LiDNP) *vs.* [Ph_3PO] for a given salt concentration; see, for example, the lower portion of Figure 2. The particular function of Λ chosen was that which gave the most linear plot. Smooth curves were drawn through the experimental points. Values of Λ (or Λ^2) were then read off at round values of [Ph_3PO]. Then, for each value of [Ph_3PO], the set of values of Λ and C so obtained was used to make a plot[12] Λ^2C *vs.* C; see the upper portion of Figure 2 for an example. The intercepts of these plots as $C \rightarrow 0$ were taken to be values of Λ_0^2K, where K is the apparent ion pair dissociation constant in the absence of ion triples of the salt at the given concentration of Ph_3PO. We have already shown[4] that the limiting molar conductivity of a tertiary ammonium salt in which the cation is complexed with triphenylphosphine oxide is only 10% less than the value of Λ_0 for the uncomplexed salt. Similarly, we assume here that the value of Λ_0 for $ML^+ + X^-$ is the same as for $M^+ + X^-$. Then the ratio $\Lambda_0^2K/\Lambda_0^2K_0$ becomes K/K_0, which we have shown to be

$$K/K_0 = 1 + K_L[L] \qquad (7)$$

when the ligand L forms a 1:1 complex with the cation. These ratios for Li^+, Na^+, K^+, and Rb^+ appear in Figure 3, plotted *vs.* concentration of triphenylphosphine oxide. The initial slopes of these (as [L] $\rightarrow$ 0) are taken to be values of K_L. These values of K_L at 25° are for Li^+, 3500 M^{-1}; for Na^+, 250 M^{-1}; for K^+, 87 M^{-1}; and for Rb^+, 53 M^{-1}.

Kebarle and Dzidić[17] have reported experimental values of $\Delta H°$ and $\Delta S°$ for the addition of one and of higher numbers of waters of hydration to the alkali metal ions in the gas phase. They found the order of increasingly negative enthalpy change (and free energy change) to be $Cs^+ < Rb^+ < K^+ < Na^+ < Li^+$. This is the same order we find for the free energy of association of Ph_3PO with the alkali metal ions in THF. Frensdorff[18] has determined the first association constants of the alkali metal ions with

(14) T. E. Hogen-Esch and J. Smid, *J. Amer. Chem., Soc.*, **88**, 318 (1966).
(15) J. Smid, *Angew. Chem., Int. Ed. Engl.*, **11**, 112 (1972).
(16) J. B. Ezell and W. R. Gilkerson, *J. Amer. Chem. Soc.*, **88**, 3486 (1966).
(17) J. Dzidic' and P. Kebarle, *J. Phys. Chem.*, **74**, 1466 (1970).
(18) H. K. Frensdorff, *J. Amer. Chem. Soc.*, **93**, 600 (1971).

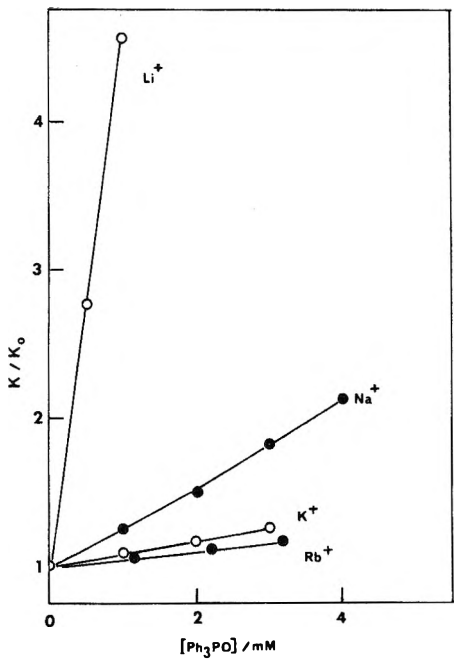

Figure 3. The ratio of the ion pair dissociation constants of the alkali metal dinitrophenolates in tetrahydrofuran at 25° in the presence of phosphine oxide, K, to that in the absence of phosphine oxide, K_0. Values of K/K_0 for LiDNP at higher concentrations than the two shown fall on the same straight line, but are not shown so that the scale would show those for RbDNP and KDNP separately.

certain "crown" cyclic polyethers in water solution and finds that with the A isomer of dicyclohexyl-18-crown-6 polyether, the stability of the complex increases from Li^+ to Na^+ to K^+ and then decreases for Cs^+. Izatt, *et al.*,[19] found that enthalpies of complexation in water for the same isomer A polyether with the alkali metal ions became less negative from K^+ to Rb^+ to Cs^+. Similar results have been found for the selectivity of a "crown" cyclic polyether toward alkali metal ion pairs in THF solvents,[20] where the maximum in binding stability occurs with Na^+ rather than K^+.

The variations in cation-ligand interaction energies in the case of the alkali metal ions (and pairs) with the crown ethers as ligands are attributed[18-20] to the rigid structure of the ligand and the position of the cation in the complex and the variation of specific cation-solvent interaction with cation size. The cation-ligand system we examine here has less severe steric requirements associated with the ligand and more closely resembles a solution version of the ion-molecule associations studied by Kebarle[17] in the gas phase

$$M^+(g) + L(g) \rightleftharpoons ML^+(g) \qquad (8)$$

Kebarle reported[17] that calculations of the energy changes for reaction 8 based on an ion-dipole model gave results which were quite a bit larger in magnitude than their experimental results. The interaction energies, $\Delta E°$, for the ions with the first molecule of water were calculated using the expression

$$\Delta E° = \text{EDIP} + \text{EPOL} + \text{EDIS} + \text{REP} \qquad (9)$$

where EDIP stands for the energy due to ion-permanent dipole attraction, EPOL for the ion-induced dipole attraction, EDIS for the energies due to London dispersion forces, and REP for short-range repulsion between ion and ligand. The repulsion term was taken to be of the form A/r^{12}, with the constant A being estimated from A values for the noble gases. The other energy terms were set down in terms of the distance between ion and dipole r and the known values of the dipole moment for water, the polarizability of the ions and of water, and the ionization potentials of each. Values of $\Delta E°$ were minimized with respect to the distance parameter r. The values of r_{min} which they obtained by this procedure are all somewhat small, being approximately the ion crystal radius plus 0.7 to 0.8 Å.

Goldman and Bates have recently reported[21] calculations of enthalpies and free energies of hydration of a number of ions using a model similar to that of Kebarle[17] for the interaction of the ion with water molecules in the first hydration layer. The energy of interaction of the hydrated ions with surrounding water outside the first hydration layer was calculated using the Born equation for the interaction of an ion with a dielectric fluid. Goldman and Bates were successful in calculating values for the thermodynamic quantities which agreed fairly well with values derived from experiment. They used a different procedure than Kebarle to evaluate the repulsion constant and the distance parameters. Goldman and Bates took the distance between ionic charge and solvating dipole (treated as separated charges) to be the ionic crystal radius, r_+, plus an effective radius for the water molecule, r_w. Goldman and Bates fitted these parameters for the water molecule to the data of Kebarle[17] in the gas phase. They determined values of the repulsion constant by setting

$$(\partial \Delta E°/\partial r)_{r=r_c+r_w} = 0 \qquad (10)$$

Others[22,23] have carried out similar calculations based on an ion-dipole model. In all of these there are a number of more or less arbitrary choices that must be made regarding values of certain parameters.

We feel that our results are particularly useful in and pertinent to the study of some features of specific ion-solvent interaction in solution. We propose an ion-dipole model, similar in some respects to those discussed above, to apply to the ion-ligand association complexes we have studied here. A comparison is first made of calculations based on our proposed model with the particularly uncomplicated experimental gas-phase data of Kebarle and coworkers.[17] Then we apply the model to our results in order to examine (a) the effect of ion radius on the energetics and (b) the possible influences of surrounding solvent on the interaction between the ion and a molecule in the first solvation layer.

Our model of an alkali metal ion in THF solvent is one in which the ion is surrounded by a number (perhaps four or six) of tightly bound molecules of THF,[24] each oriented so that the negative end of its dipole is toward the center of the cation. One of these specifically solvating THF molecules is displaced by the incoming Ph_3PO molecule in the formation of the cation-ligand complex. A crude representation of the process is given in eq 11. We assume

(19) R. M. Izatt, D. P. Nelson, J. H. Rytting, B. L. Haymore, and J. J. Christensen, *J. Amer. Chem. Soc.*, **93**, 1619 (1971).
(20) K. H. Wong, G. Konizer, and J. Smid., *J. Amer. Chem. Soc.*, **92**, 666 (1970).
(21) S. Goldman and R. G. Bates, *J. Amer. Chem. Soc.*, **94**, 1476 (1972).
(22) J. S. Muirhead-Gould and K. J. Laidler, *Trans. Faraday Soc.*, **63**, 944 (1967).
(23) A. D. Buckingham, *Discuss. Faraday Soc.*, **24**, 151 (1957).
(24) See, for instance, A. L. Van Geet, *J. Amer. Chem. Soc.*, **94**, 5583 (1972).

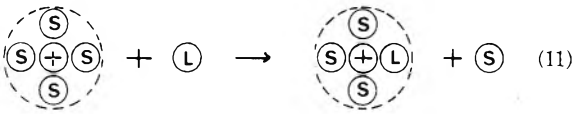

(11)

the environment surrounding the solvated cation in the initial state is the same as that around the cation–ligand complex in the final state. The solutions are dilute enough so that the uncomplexed ligand and solvent may be presumed to be ideal. We take the distance r_s between the center of cation charge and the point dipole of solvent THF to be the sum of the crystal radius of the cation plus the van der Waals radius of oxygen, 1.40 Å. We chose Waddington's set[25] of ionic radii from among the three sets considered[21] to be applicable. Waddington seems to have made a careful assessment of the errors and assumptions involved in the methods of arriving at a consistent set of ionic radii. In using the van der Waals radius of the oxygen atom, we are assuming the point dipole in the THF molecule to be located at the center of the oxygen atom. The distance, r_{L}, between the center of cation charge and the point dipole of the ligand, Ph_3PO, is taken to be the cation radius, r_+, plus the van der Waals radius of oxygen, r_O, plus one-half the length of the phosphoryl P–O bond distance, r_{PO} = 1.44 Å, the value found in several phosphate esters.[26]

We calculated values of $\Delta H°$ for the association of one water molecule with the series of alkali metal cations using the model outlined above with the water dipole moment located at the distance r_s from the center of nuclear charge. Only one term was neglected on the RHS of eq 9; the value of EDIS was assumed to be negligible. Kebarle had found EDIS to constitute only 5% of the total energy in the case of Na^+, and Bates and Goldman found EDIS to make only a small contribution to the total energy of interaction. The explicit expression for the energy change corresponding to reaction 8 is given by

$$\Delta E° = -Nze\mu_s/r_s^2 - Nz^2e^2\alpha_s/2r_s^4 + A/r^{12} \quad (12)$$

Condition eq 10 was applied to eq 12 to obtain the values of A. The constants μ_s and α_s for water were taken to be 1.85 D and 1.50 × 10^{-24} cm^3, respectively.[21] Values of $\Delta E°$ so calculated were converted into values of $\Delta H°$ at 25° by subtracting the quantity RT at that temperature. These values of ΔH_{calcd} are plotted in Figure 4 *vs.* experimental values of $\Delta H_0°_1$ reported by Kebarle and coworkers.[17] We regard the agreement between calculation and experiment to be excellent.[27]

Having assured ourselves that our relatively simple approach to evaluation of the energies of interaction between ions and molecules in the gas phase is capable of giving reasonable results, let us now return to the more complex reaction in solution modeled by eq 11. Kirkwood and Westheimer[28] have already shown that a surrounding dielectric may result in the reduction in the potential energy of interaction between a set of charges in a sphere. This would affect Δ(EDIP). Additional terms should be added to account for the difference in the energy of interaction of free ligand (or displaced specifically solvating solvent) with solvent and the energy of interaction of ligand (or specifically solvating solvent) not only with the ion in the cation–ligand (or solvent) complex but with other solvent molecules in the vicinity of the cation complex. Both Kebarle[17] and Goldman and Bates[21] have accounted for interaction of a solvating molecule with the other solvating molecules within the solvation sphere. The

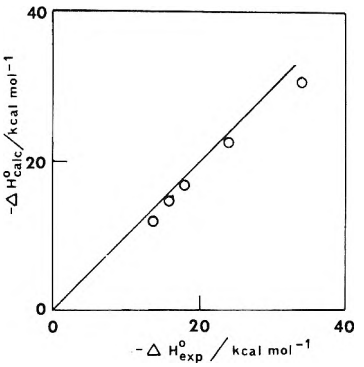

Figure 4. Calculated values of $\Delta H_{calcd}°$ of the enthalpies of monohydration of the alkali metal ions in the gas phase according to eq 12 *vs.* experimental values $\Delta H_{expt}°$ from ref 16.

possible interactions of the complexed ligand (and complexed solvent) with surrounding uncomplexed solvent was not included in the calculations of Goldman and Bates for the ions in solution. The problem is an extremely difficult one.[29] For this reason, we shall assume that positive and negative contributions to the net energy difference from these sources are approximately of the same magnitude and cancel one another.

An approach to ion-induced dipole interaction, EPOL in eq 9, illustrates some other complexities in the overall problem. Water molecules are very compact compared to either THF or Ph_3PO. Use of equations of the form $-Z^2e^2\alpha/R^4$ where one considers the polarizability α to be effectively localized at a point R distant from the ion is probably a good approximation in the case of a water molecule of solvation. The total value of α for Ph_3PO is made up of relatively large contributions from the more distant (from the ion) three phenyl groups, and a smaller contribution from the neighboring phosphoryl group. Since these energies fall off as the inverse fourth power of the distance a better approach to the problem might be to break the total up into contributions from each bond in the ligand (or solvent) molecule. It is further recognized[30] that the contribution from a given bond is not isotropic and is better represented as resolved into components perpendicular and parallel to the bond. Given these complexities and that the oxygen atom is closest to the cation in the case of both THF and Ph_3PO, we assume the contribution to the net energy difference due to ion-induced dipole interaction is small enough to be neglected in comparison with that due to ion–dipole interaction and cation–oxygen repulsion.

We neglect contributions to the net energy for reaction 11 from van der Waals dispersion forces, EDIS in eq 9. Both Kebarle and Goldman and Bates found that the values of EDIS were only a few per cent of the total energies of interaction in the case of the alkali metal ions and water.

We take the contribution due to short-range repulsion of the cation and the oxygen atom in either THF or

(25) T. C. Waddington, *Trans. Faraday Soc.*, **62**, 1482 (1966).
(26) D. M. Nimrod, D. R. Fitzwater, and J. G. Verkade, *J. Amer. Chem. Soc.*, **90**, 2780 (1968).
(27) These calculations were carried out after the values of the distance parameters had been selected. These parameters were not adjusted to yield a best fit.
(28) J. G. Kirkwood and F. H. Westheimer, *J. Chem. Phys.*, **6**, 506 (1938).
(29) See, for instance, a very recent paper where a determined effort is made to take these interactions into account, J. O'M. Bockris and P. P. S. Saluja, *J. Phys. Chem.*, **76**, 2298 (1972).
(30) K. G. Denbigh, *Trans. Faraday Soc.*, **36**, 936 (1940).

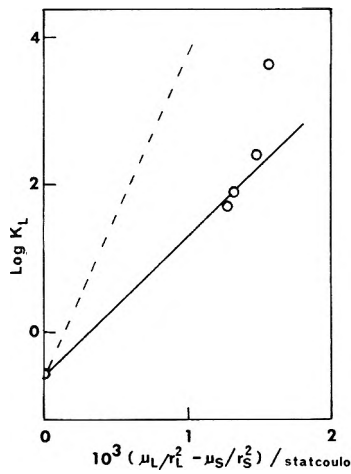

Figure 5. Ligand association constants of the alkali metal ions with triphenylphosphine oxide in tetrahydrofuran at 25° plotted according to eq 15, based on an ion-dipole model uncorrected for the effect of surrounding polarizable solvent. Slope of dashed line calculated using eq 13 in eq 15.

Ph_3PO to be given by an inverse twelth power function of r, and with the constant determined by application of eq 10.

The total energy of interaction of the cation ligand less that with the displaced solvent molecule is given by

$$\Delta E_t = -(5/6)Nze(\mu_L/r_L^2 - \mu_s/r_s^2) \quad (13)$$

The dipole moment of Ph_3PO was taken as 4.31 D[31] and that for THF was 1.73 D.[31] Recall that up to this point we have neglected the effect of surrounding dielectric[28] on the RHS of eq 13. The factor 5/6 in eq 13 arises from combining the repulsion term, Δ(REP), with the ion-dipole term, Δ(EDIP). We shall first apply eq 13 to our results and we find that it overestimates the change in energy of interaction. We shall then see if the effect of surrounding polarizable solvent can account for the magnitude of the deviation from eq 13.

The equilibrium constant K for the displacement reaction

$$M,^+S + L \rightleftharpoons M,^+L + S \quad (14)$$

is $K = K_L[S]$, where [S] is the molar concentration of solvent in solvent. We assume that the only contribution to $\Delta S°$ for eq 14 is a statistical factor[32] n, equal to the number of equivalent solvent molecules bound to the cation which are available for displacement by the incoming ligand. We shall assume a reasonable value[24] of $n = 4$ for this parameter. Then $\Delta S° = R \ln 4$. We further equate $\Delta H°$ for eq 14 with ΔE_t, given by eq 13. Then

$$\log K_L = \log (4/[S]) - \Delta E_t/2.303RT \quad (15)$$

We have plotted log K_L *vs.* $(\mu_L/r_L^2 - \mu_S/r_S^2)$ in Figure 5. Note that when the ion-dipole term in eq 15 becomes zero, then log K_L = log (4/[S]). Using this point as a hold point in Figure 5, we drew the solid straight line to pass near the points for Na^+, K^+, and Rb^+. It is possible that log K_L for Li^+ lies above the line because of short-range interactions of a covalent nature. The slope of the solid line in Figure 5 is less than that given by eq 15 by a factor of 2.3. This is the direction of deviation one would predict from Kirkwood and Westheimer's work. But the deviation could be the result of contributions meglected in deriving eq 13. There is no way of predicting the effects of those approximations we have made explicitly. We can estimate the result of the effect of surrounding polarizable dielectric on the ion-dipole energy term Δ(EDIP) using a simple model, a sphere with the cation at its center and the ligand (or solvent) dipole oriented as

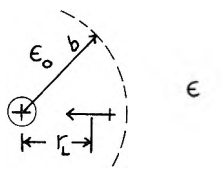

Kirkwood and Westheimer[28] give for the potential

$$U = (1/2)\sum_{k,l=1}^{v} e_k e_l/\epsilon_0 r_{kl} + (1/2)\sum_{n=0}^{\infty}(\epsilon_0 - \epsilon)(n+1)G_n/\epsilon_0 b^{2n+1}[(n+1)\epsilon + n\epsilon_0] \quad (16)$$

where ϵ_0 is the dielectric constant within the sphere of radius b and ϵ is the dielectric constant of the fluid outside the sphere. We take $e_1 = +e$ at $r_1 = 0$, $e_2 = -e$ at $r_2 = r_L - \mu_L/2e$, and $e_3 = +e$ at $r_3 = r_L + \mu_L/2e$. The function G_n, given[28] as a sum over pairs of charges, in our case has only one term different from zero

$$G_n = 2e_2e_3r_2^n r_3^n P_n(\cos \vartheta_{23}) = -2e^2 r_2^n r_3^n \quad (17)$$

The first sum on the RHS of eq 16 has only two terms (e_1e_2 and e_1e_3), that due to the product e_2e_3/r_{23} being subtracted out as being the self energy of the dipole (a choice of zero of potential energy). When r_2 and r_3 in terms of r_L and μ_L are inserted into eq 16, a recurring factor is $r_L^2(1 - \mu_L^2/4e^2r_L^2)$. The ratio $\mu_L^2/4e^2r_L^2$ is only 0.02 for the smallest value of r_L here and is even less for solvent instead of ligand; we drop this term since it is small compared to unity. Then the potential energy difference becomes

$$U_L - U_S = -(ze/\epsilon_0)(\mu_L/r_L^2 - \mu_s/r_s^2) + [2(\epsilon - \epsilon_0)e^2/(2\epsilon + \epsilon_0)b^3](r_L^2 - r_S^2) + \ldots \quad (18)$$

Now since there is no intervening matter between the cation and either the ligand or the solvent molecule it displaces, we take ϵ_0 to be unity, the value in free space. The higher terms in eq 18 are in higher powers of r/b. Retaining only the first two terms in eq 18 then

$$\log K_L = \log (4/[S]) - \Delta E_t/2.303RT - B(r_L^2 - r_S^2) \quad (19)$$

where the coefficient $B = 14(\epsilon - 1)Ne^2/2.303RT(2\epsilon + 1)6b^3$. A factor of 7/6 in B is due to repulsion, from the application of eq 10. Note that in this development the only additional variable introduced is the radius of the sphere b. Taking b as an adjustable parameter we did a least-squares fit of eq 19 in the form

$$(\log K_L + \log ([S]/4) + \Delta E_t/2.303RT) = D + B(r_L^2 - r_S^2) \quad (20)$$

where experimental values of K_L and [S] were used and the values of ΔE_t were those calculated from eq 13. Deviations were minimized with respect to the parameter D and B. D should be zero according to eq 19. The value of D found was imperceptibly different from zero on the

(31) A. L. McClellan, "Tables of Experimental Dipole Moments," W. H. Freeman, San Francisco, Calif., 1963.
(32) For sufficiently dilute solutions of ligand, see D. R. Cogley, J. N. Butler, and E. Grunwald, *J. Phys. Chem.*, 75, 1477 (1971).

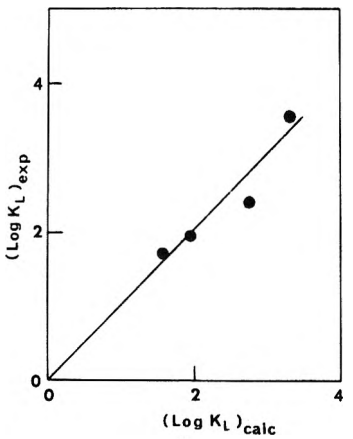

Figure 6. Experimental values, $(\log K_L)_{expt}$ for alkali metal ions with triphenylphosphine oxide in tetrahydrofuran at 25° *vs.* values, $(\log K_L)_{calcd}$, calculated using eq 20 based on an ion-dipole model corrected for surrounding polarizable solvent.

scale of our plot. The value of B found corresponded to a value of the radius of the sphere $b = 6.9 \times 10^{-8}$ cm. The plot of $(\log K_L)_{expt}$ *vs.* values of $(\log K_L)_{calcd}$ calculated from eq 19 using the B value ($= 0.695 \times 10^{16}$ cm^{-2}) found above appears in Figure 6.

The radius of the sphere containing cation and ligand (or solvent molecule) required to fit our data to eq 20 (or 19) is very reasonable. The diameter of a molecule of THF may be estimated from models to be ~5.5 Å. This would lead to an estimate of b of 6.5 to 7 Å. For Ph_3PO, the effective b value would be expected to be somewhat larger.

We conclude that ion-dipole interaction, modified to include the effects of surrounding polarizable solvent, can account for the values of cation-ligand association constants of the alkali metal cations with triphenylphosphine oxide in tetrahydrofuran solvent. Of course, we cannot say that we have proven that these are the only factors that affect the process. As we have pointed out above, we have neglected several factors in our equation which are known to be involved: ion-induced dipole interaction, dipole-dipole repulsion in the complex, and van der Waals dispersion interaction. We have advanced what we consider to be good reasons for neglecting the contributions due to these factors. In order to assess the relative importance of these terms we have neglected, it would be advantageous to have cation-ligand association data for several other dipole ligands with the alkali metal ions. We hope to accumulate such information in the future.

We further conclude that the effect of surrounding polarizable solvent on the energy of interaction between ions and solvent molecules in the first solvation layer[28] should be taken into account in efforts to calculate energies of solvation.[21,29]

Conformational Transitions of Hydrophobic Polyacids in Denaturant Solutions. The Effect of Urea

P. Dubin[1] and U. P. Strauss*

School of Chemistry, Rutgers University, The State University of New Jersey, New Brunswick, New Jersey 08903
(Received November 27, 1972)

Publication costs assisted by the United States Public Health Service

The effect of urea on the charge-induced transition from hypercoiled to extended conformation of alkyl vinyl ether-maleic acid copolymers has been investigated in 0.04 M sodium chloride solutions in the presence and absence of 5 M urea. Potentiometric titrations indicate that the free energy of stabilization of the uncharged compact state relative to the hypothetical uncharged extended state is reduced upon addition of urea from 310 to 120 cal/mol of residue for the polyacid with butyl side chains, and from 1070 to 830 cal/mol of residue for the hexyl copolymer. Intrinsic viscosity results obtained with the ethyl and butyl copolymers at various degrees of dissociation show that urea expands the molecular dimensions of the copolymers in both hypercoiled and extended conformations. Urea appears to destabilize the hypercoiled state by enhancing the solvent affinities of the hydrophobic side chains as well as the polar backbone of the polyacids.

Introduction

Considerable interest has arisen concerning the mode of action of denaturants on biological marcromolecules, inasmuch as such processes are thought to elucidate the forces stabilizing the native state. The denaturant activity of such widely varied substances as alcohols, detergents, and urea and guanidine compounds is currently rationalized in terms of the several types of interactions which maintain secondary and tertiary structure in biopolymers. Studies

(1) Present address: Dynapol Corporation, Palo Alto, Calif. 94304.

with small molecule model compounds, chemically similar to protein moieties, have been of great value in identifying plausible sites of interaction and estimating corresponding thermodynamic contributions to the denaturation process.[2] It is nonetheless quite difficult to specify exactly the mechanism of action of a denaturant, such as urea, which is primarily effective at very high concentrations. For example, considerable evidence exists from model compound studies to the effect that urea (1) interacts strongly with peptide backbone groups, thus weakening interpeptide hydrogen bonds;[3,4] and (2) enhances the solubility of nonpolar groups, thus reducing hydrophobic interactions, either by altering the bulk properties of the solvent or through more localized effects,[3,5,6] It is difficult to assess the relative significance of such effects in studies with natural biopolymers.[7,8]

An alternative approach to this problem may be available through the use of synthetic macromolecular model compounds. In our laboratory, for example, we have studied hydrolyzed copolymers of maleic anhydride and alkyl vinyl ethers which undergo conformational transitions resembling those occurring in the denaturation of biopolymers. When their alkyl side chains contain four or more methylene groups, these copolymers exist at low pH in highly compact conformations with intrinsic viscosities similar to those of globular proteins.[9,10] These "hypercoiled" states, stabilized by cooperative hydrophobic interactions among side chains, undergo reversible conformational transitions to expanded polyelectrolyte configurations upon progressive neutralization of the carboxylic acid groups.[9,10]

We present here an exploratory study of the effects of concentrated urea on such copolymers and their conformational transitions. Our aims are to investigate whether there are, indeed, effects similar to those observed with proteins, and if so, whether and to what extent any such effects can be ascribed to action on specific chemical groupings, such as the hydrophobic groups belonging to the side chains and/or the more hydrophilic backbone. Attempts at such a differentiation appear promising with our synthetic copolymers, because the length of their hydrophobic side chains may be varied, a procedure not generally feasible with natural biopolymers. Specifically, we shall consider the effect of 5 *M* urea on the difference in free energy between the uncharged compact and (hypothetical) expanded states of the butyl and hexyl vinyl ether copolymers in dilute sodium chloride solution. This free energy difference is obtained from potentiometric titration data for these polyacids, in conjunction with those of the nonhypercoiling homolog, the ethyl vinyl ether copolymer.[10] These data are supplemented by results obtained under the same conditions giving the effect of 5 *M* urea on the dependence of the intrinsic viscosity on the degree of dissociation for the ethyl and butyl vinyl ether copolymers.

Experimental Section

Materials. The preparation and characterization of the copolymers of maleic anhydride and ethyl vinyl ether (A-VI), butyl vinyl ether (B-II), and hexyl vinyl ether (C) have been described previously.[10] Mann Ultrapure urea was recrystallized from hot ethanol. Fischer Certified 0.200 *N* sodium hydroxide and hydrochloric acid solutions were used as titrants. All water was deionized and doubly distilled.

Preparation of Polymer Solutions. All studies were performed in 0.04 *M* NaCl, either with or without 5 *M* urea. In order to avoid degradation, polymer stock solutions were prepared in the dark at 4° by stirring a weighed amount of the dry anhydride form of the polymer with an amount of NaOH solution equivalent to the total carboxylic acid content of the polymer, neutralizing with HCl, and, finally, adding sufficient water and NaCl to make the solution 0.02 *N* in carboxylic acid and 0.08 *M* in NaCl. Prior to titration or viscometry, an aliquot of the refrigerated stock solution was mixed with an equal volume of either water or freshly prepared 10 *M* urea. Polymer concentrations were determined from titration equivalence points.

Potentiometric Titrations. Titrations of polymer solutions and appropriate solvent blanks were performed as previously described[10] under nitrogen and at 30°, using a Radiometer pHM26 pH meter equipped with Radiometer G202c glass and K4016 calomel electrodes. Titrant, 0.200 *N* NaOH, was added with a 2.0-ml Gilmont micrometer buret. The value of the degree of dissociation α (defined as unity at the equivalence point of the first acid group), corresponding to a desired pH, was determined from the volumes of added titrant at that pH and at the first equivalence point, corrected for the volume of 0.200 *N* HCl required to bring a blank to the desired pH from the pH of the equivalence point.[10] It was assumed that the activity coefficient of hydrogen ion is the same in polymer and blank solutions.

Viscometry. Viscosities were measured in a Cannon-Ubbelhode dilution viscometer at 30° by successively adding appropriate volumes of solvent adjusted to the pH of the initial polymer solution. The use of solvent as diluant, as opposed to external dialysis solution, affects the slope of the reduced viscosity–concentration plots, but not the values of the intrinsic viscosity obtained by extrapolation of those plots.[11] Because of acid-catalyzed hydrolysis, solutions containing urea at low pH exhibit a slow pH drift (*ca.* +0.1 pH unit/hr) resulting in a gradual increase in the measured viscosity of the polymer solution. When the pH drift was small, either because the pH was not very low and/or the measurements were made rapidly, the pH of the final, most dilute solution was used to obtain the value of α corresponding to the extrapolated value of the intrinsic viscosity. In order to obtain reliable measurements at the lowest pH values, and to verify the other data, the following procedure was employed to maintain constant pH throughout the measurement. A sample of polymer solution identical with that introduced into the viscometer was placed in the (thermostated) titration vessel and diluted with solvent simultaneously along with the viscometer sample. Constant pH was maintained in the duplicate sample by intermittent addition of 0.200 *N* HCl, and identical volumes of HCl were added to the dilution bulb of the viscometer. With this procedure, the pH of the

(2) C. Tanford, *Advan. Protein Chem.*, **24**, 1 (1970).
(3) Y. Nozaki and C. Tanford, *J. Biol. Chem.*, **238**, 4074 (1963).
(4) D. R. Robinson and W. P. Jencks, *J. Amer. Chem. Soc.*, **87**, 2462 (1965).
(5) D. B. Wetlaufer, S. K. Malik, L. Stoller, and R. L. Coffin, *J. Amer. Chem. Soc.*, **86**, 508 (1964).
(6) W. Bruning and A. Holtzer, *J. Amer. Chem. Soc.*, **83**, 4865 (1961).
(7) J. R. Warren and J. A. Gordon, *J. Biol. Chem.*, **245**, 4097 (1970).
(8) T. T. Herskovits, H. Jaillet, and B. Gadegbeku, *J. Biol. Chem.*, **245**, 4544 (1970).
(9) P. Dubin and U. P. Strauss, *J. Phys. Chem.*, **71**, 2757 (1967).
(10) P. Dubin and U. P. Strauss, *J. Phys. Chem.*, **74**, 2842 (1970).
(11) U. P. Strauss, *J. Polymer. Sci.*, **33**, 291 (1958).

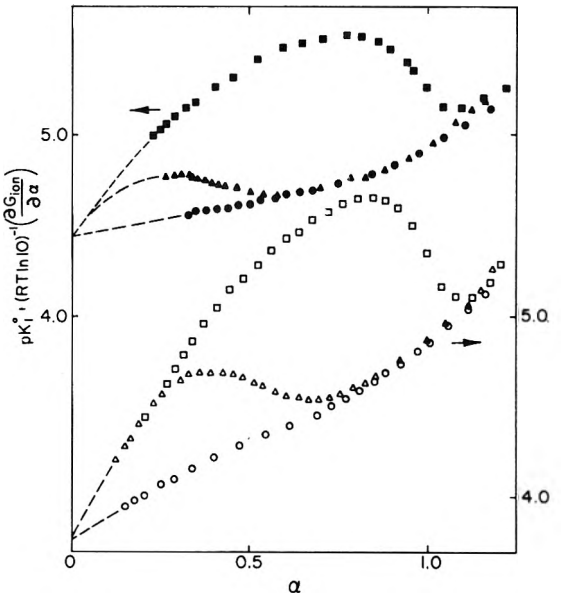

Figure 1. Potentiometric titration data at 30°, plotted according to eq 2: (○) ethyl, (△) butyl, and (□) hexyl copolymers in 0.04 *M* NaCl (ordinate on right); (●) ethyl, (▲) butyl, and (■) hexyl copolymers in 5 *M* urea + 0.04 *M* NaCl (ordinate on left).

final solution in the viscometer usually differed from the initial value by less than 0.02 pH units. The total amount of HCl added was always too small to have a measurable effect on polymer concentration or ionic strength. For urea solutions above pH 5, viscosity measurements could be made in the usual way, as no pH drift was observed.

Results

Potentiometric Titrations. The pH of a poly(monoprotic acid) is given by the well-known equation[12,13]

$$\mathrm{pH} + \log\left(\frac{1-\alpha}{\alpha}\right) = \mathrm{p}K^0 + (RT \ln 10)^{-1}(\partial G_{\mathrm{ion}}/\partial\alpha) \quad (1)$$

where $\partial G_{\mathrm{ion}}$ is the change in the excess free energy of the polyacid accompanying an incremental change in the degree of dissociation, and K^0 is the intrinsic ionization constant, obtained by extrapolating the left-hand side of eq 1 to $\alpha = 0$, at which point the second term of the right-hand side of eq 1 vanishes. The analogous equation for a poly(diprotic acid) is[10]

$$\mathrm{pH} + \log y = \mathrm{p}K_1^0 + (RT \ln 10)^{-1}(\partial G_{\mathrm{ion}}/\partial\alpha) \quad (2)$$

where

$$y = \left(\frac{1-\alpha}{2\alpha}\right) + \left[\left(\frac{1-\alpha}{2\alpha}\right)^2 + \frac{K_2^0}{K_1^0}\left(\frac{2-\alpha}{\alpha}\right)\right]^{1/2}$$

and where α is defined as unity at the equivalence point of the first acid group, and K_1^0 and K_2^0 are the first and second intrinsic ionization constants of a diprotic acid residue.

Titration data for the ethyl, butyl, and hexyl copolymers, in 0.04 *M* NaCl with and without 5 *M* urea, are presented in Figure 1 in the form of $\mathrm{p}K_1^0 + (RT \ln 10)^{-1} \cdot (\partial G_{\mathrm{ion}}/\partial\alpha)$, obtained from eq 2, against α. By means of a procedure described previously,[10] $\mathrm{p}K_1^0$ and $\mathrm{p}K_2^0$ are found to be 3.8 and 6.6, respectively, for all three copolymers in the absence of urea. The corresponding values in the presence of urea are found to be 4.4 and 7.2. A similar decrease in acid strength in the presence of urea has been noted for a number of simple dicarboxylic acids.[14] The procedure for extrapolating the curve for the butyl copolymer in the presence of urea is based on the assumption that the values of $\mathrm{p}K_1^0$ and $\mathrm{p}K_2^0$, respectively, are identical for all three copolymers, and that the titration curves for the butyl and hexyl copolymers coincide at low values of α. These assumptions are supported by previous titration data in pure water,[10] as well as by our present findings in the absence of urea.

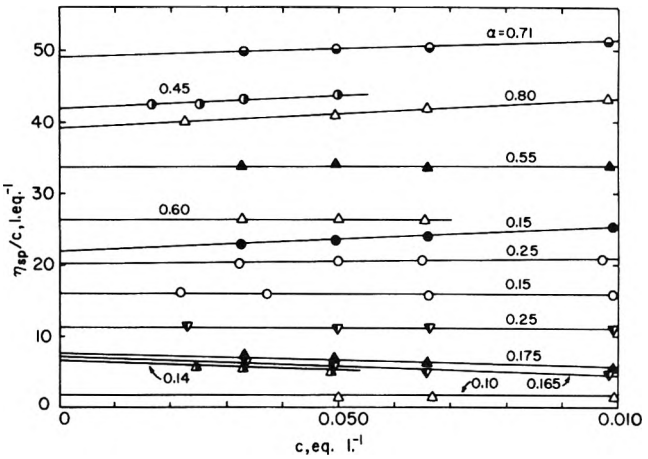

Figure 2. The dependence of the reduced viscosity on polymer concentration at varying degrees of dissociation: (○) ethyl copolymer in 0.04 *M* NaCl; (△) butyl copolymer in 0.04 *M* NaCl; (◑, ⊖, ●) ethyl copolymer in 0.04 *M* NaCl + 5 *M* urea (procedures 1, 2, and 3, respectively, see text); (▲, ▼, ▲) butyl copolymer in 0.04 *M* NaCl + 5 *M* urea (procedures 1, 2, and 3, respectively).

The regions of negative slope in the titration curves of the butyl and hexyl copolymers in both solvents correspond to transitions from hypercoiled to expanded conformations.[10] The standard state free energy change per mole of residue for the (hypothetical) conformational transition at zero charge, ΔG_t^0, is proportional to the area between the curve of the copolymer undergoing the transition and that of the ethyl copolymer in the same solvent. The details of and justification for this method of determining ΔG_t^0 have been given previously.[10] The value of ΔG_t^0 for the butyl copolymer, expressed in cal per mole residue, is 310 ± 10 in the absence of urea, and 120 ± 20 in the presence of urea. The corresponding values for the hexyl copolymer are 1070 ± 30 and 830 ± 30. These error limits encompass the range of reasonable extrapolations of the data to $\alpha = 0$. The areas between the curves are found to be rather insensitive to the extrapolated value of $\mathrm{p}K_1^0$. It is noteworthy that these ΔG_t^0 values are considerably more precise than those obtained by a similar procedure for the helix–coil transition of ionizable polypeptides, in which case the titration curve for the random coil conformation is not experimentally accessible.[15]

Viscosity. Several representative extrapolations to infinite dilution of viscosity data for the ethyl and butyl copolymers in the two solvents are shown in Figure 2. In order to facilitate comparisons between the two copoly-

(12) A. Katchalsky and J. Gillis, *Recl. Trav. Chim. Pays-Bas*, **68**, 879 (1949).
(13) A. Arnold and J. Th. G. Overbeek, *Recl. Trav. Chim. Pays-Bas*, **69**, 192 (1950).
(14) M. Levy and J. P. Magoulas, *J. Amer. Chem. Soc.*, **84**, 1345 (1962).
(15) See, for example, T. V. Barskaya and O. B. Ptitsyn, *Biopolymers*, **10**, 2181 (1971).

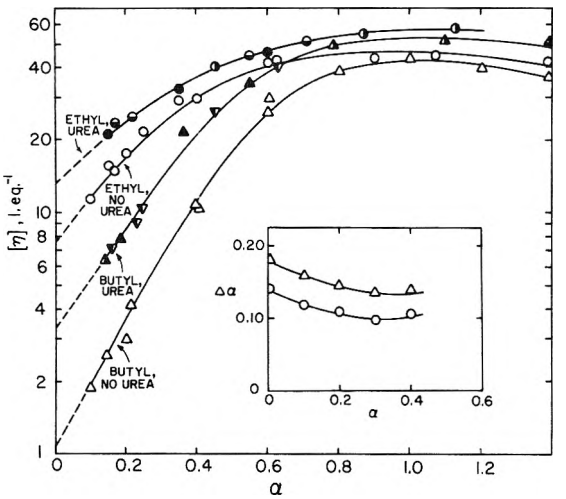

Figure 3. Intrinsic viscosity as a function of α for ethyl and butyl copolymers in 0.04 *M* NaCl, with and without 5 *M* urea. Symbols identified in Figure 2. Inset shows $\Delta\alpha$ *vs.* α for ethyl (○) and butyl (△) copolymers (see text).

mers of different monomer weights, concentration units are equivalents liter^{-1}, each monomer residue contributing 2 equiv of carboxylic acid.

The slopes of the reduced viscosity plots for both polymers in 0.04 *M* NaCl are negligibly small at low charge, and increase with α, presumably as a result of enhanced intermolecular interactions. Since the diluting solvent was not in dialysis equilibrium with the polymer solution, the observed slopes may be lower than those corresponding to the true Huggins' constants, if one component is preferentially absorbed by the polymer.[11] Such interactions may explain the negative slope of the butyl copolymer in urea at low α.

Semilogarithmic plots of intrinsic viscosity against α are presented in Figure 3. This type of plot was chosen in order to facilitate the empirical extrapolation to $\alpha = 0$. It is of interest that comparable data for polyacrylic and polymethacrylic acids[16] are also found to conform to linear semilogarithmic plots in the region of low α.

Discussion

Inspection of the appropriate areas of Figure 1 reveals immediately that the free energies of stabilization of the uncharged butyl and hexyl hypercoils are considerably reduced in the presence of 5 *M* urea. In the case of the butyl copolymer, ΔG_t^0 is reduced by 190 ± 25 cal/mol (about 60%), while the corresponding decrease in ΔG_t^0 of the hexyl copolymer is 240 ± 35 cal/mol (about 22%).

The effect of denaturants on the conformational stability of the native state of proteins has frequently been analyzed in terms of the behavior of small molecule model compounds.[2] In such treatments, it is customary to assume that hydrophobic peptide side chains are withheld from the solvent in the native state and exposed upon denaturation. The presumably additive contribution of one such group to the overall denaturant effect on the free energy of the conformation change then corresponds to its free energy of transfer from pure solvent to denaturant solution, which may be estimated from appropriate model compound partition or solubility measurements.

Let us examine the consequences of applying an analogous procedure for the case of the butyl and hexyl copolymers of this study. The values of ΔG_t^0 result from several contributions, which include the hydrophobic interactions among alkyl side groups, other interactions of the various groups with one another and with the solvent components, and conformational changes of the polymer chain. If we assume additivity of the interactions involving the two extra methylene groups of the hexyl copolymer, one-half the difference in the ΔG_t^0 values of the butyl and hexyl copolymers, both obtained in the same solvent, should represent $\Delta G_{CH_2}^0$, the free energy of transfer of a methylene group from the hypercoiled form to the extended form, in the chosen solvent. We find $\Delta G_{CH_2}^0$ to be 380 ± 15 cal/mol in the absence of urea, and 355 ± 15 cal/mol in the presence of urea. If we assume further, as is frequently done in the analogous treatment of denaturant effects on proteins, that in the compact conformation the environment of the methylene groups of the hydrophobic side chains is independent of the solvent, we obtain from the difference in the $\Delta G_{CH_2}^0$ values a value of −25 ± 20 cal/mol for the transfer of methylene groups from 0.04 *M* NaCl to the same solvent containing 5 *M* urea. For comparison, the data of Wetlaufer, *et al.*,[5] for the solubility of various hydrocarbons in water and in concentrated urea may be interpolated to give a value of −60 ± 10 cal/mol for the same process, and those of Nozaki and Tanford,[3] for solubilities of leucine and glycine in water and aqueous urea, lead to a value of −50 ± 10 cal/mcl. Our result is of the right magnitude. However, this may be somewhat fortuitous in view of the assumptions implicit in the course of the calculations. For instance, the effect of urea on the intrinsic viscosity of the butyl copolymer at low values of α, to be discussed below, throws some doubt on the assumption of nonaccessibility to solvent of the hydrophobic side chains in the hypercoiled conformation. The implicit assumption that the hydrophobic side chains are completely exposed to the solvent in the random coil conformation may also be questioned. These considerations suggest that the agreement may in part be due to a cancellation of neglected effects, and that therefore in comparisons of this type applied to biological or other synthetic macromolecules caution should be exercised in evaluating the significance of apparent agreement of this sort.

Further information about the effects of urea on the conformations of these copolymers may be obtained from the intrinsic viscosity results shown in Figure 3. The intrinsic viscosity is a measure of the molecular dimensions, which, in turn, depend on the interactions of the macromolecules with the solvent. Whereas the potentiometric titration method as applied here yields only the effect of urea on the difference in free energies of the hypercoiled and hypothetical extended states at zero charge, the intrinsic viscosity should allow an estimate of the effect of urea on the copolymers in their actual states at both zero and finite charge. The data show that urea raises the intrinsic viscosity of both ethyl and butyl copolymers over the whole range of α investigated. Since the butyl copolymer is in its hypercoiled form at low values of α and in its random coil form at high values of α, and the ethyl copolymer is in its extended form under all conditions, we see that urea significantly enhances the solvation of both compact and extended forms. However, a meaningful quantitative interpretation of the effects of urea on the two forms from a numerical comparison of the intrinsic

(16) I. Noda, T. Tsuge, and M. Nagasawa, *J. Phys. Chem.*, **74**, 710 (1970).

viscosity changes appears impossible, primarily because of the lack of adequate theoretical expressions relating the viscosity of the hypercoiled conformation to the free energy of interaction with the solvent.

Nevertheless, a somewhat more limited quantitative interpretation of the results may be obtained by means of an alternative procedure for which no explicit mathematical relationship involving the intrinsic viscosity is needed. In this procedure the intrinsic viscosity is employed essentially as an indicator for comparing the effect of urea on the macromolecular dimensions with that brought about by a change in the degree of dissociation without urea. At any value of α, the change from 0 to 5 M urea leads to a certain increase in the intrinsic viscosity, as shown by the vertical displacement between the "no urea" and "urea" curves of Figure 3. At not too high values of α (see below) an identical intrinsic viscosity increase may be brought about by the addition of an appropriate amount of sodium hydroxide (in the absence of urea). The resulting increase in the degree of dissociation, denoted by $\Delta\alpha$, is given by the horizontal distance between the appropriate urea curve (at α) and no urea curve (at $\alpha + \Delta\alpha$) of Figure 3, and is plotted as a function of α for the two copolymers in the inset of that figure.

The increase in $[\eta]$ accompanying an increase in α is due to an enhancement of the solvent affinity of the carboxylate groups attached to the polymer backbone. If urea, like NaOH, affected the solvent affinity of the backbone region alone, $\Delta\alpha$ would be independent of alkyl side chain length. In fact, $\Delta\alpha$ is observed to be greater for the butyl than for the ethyl copolymer. from $\alpha = 0$ to $\alpha = 0.4$, beyond which the method is not applicable because of the maxima in the $[\eta]$ *vs.* α curves.[17] The difference in $\Delta\alpha$ for the two copolymers represents clear-cut evidence that urea enhances the solvent affinity of the hydrophobic side chains. On the other hand, the relatively large value of $\Delta\alpha$ for the ethyl copolymer indicates that urea also enhances the solvent affinity of groups close to or part of the polymer backbone. The slight decrease of $\Delta\alpha$ with increasing α may reflect a relative change in the solvent affinities of carboxylic acid groups and carboxylate groups, in favor of the former, brought about by the addition of urea. Such a preference is indicated by the observation that the dissociation of carboxylic acids in aqueous solution is generally diminished by the addition of urea.[14]

Concentrated urea thus reduces the stability of the hypercoiled relative to the random coil conformation by a combination of effects which involve enhancements of the solvent affinities of both kinds of conformations. Intramolecular interactions of the hydrophobic side chains as well as of the groups located in the immediate domain of the polymer backbone are affected. In view of the complex interdependence of these interactions with one another and with the macromolecular dimensions, a quantitative resolution of the effects of urea into additive contributions of the various chemical groups appears to be unwarranted with the data thus far available.

Acknowledgment. The support of this research by grants from the United States Public Health Service (Grant No. GM 12307) and from S. C. Johnson and Son, Inc., is gratefully acknowledged. We also wish to thank Sylvia Taylor for expert technical assistance.

(17) Such maxima, which are observed for these poly(diprotic acids) with sodium but not with tetramethylammonium ion as the counterion, may be attributed to the specific binding of sodium ion to the polyacids above $\alpha = 1$.[16,19]
(18) A. W. Schultz and U. P. Strauss, *J. Phys. Chem.*, **76**, 1767 (1972).
(19) A. J. Begala and U. P. Strauss, *J. Phys. Chem.*, **76**, 354 (1972).

Proton Magnetic Resonance Investigations of Alkylammonium Carboxylate Micelles in Nonaqueous Solvents. II.[1] Effects of Carboxylate Structure in Benzene and in Carbon Tetrachloride

E. J. Fendler, J. H. Fendler,* R. T. Medary, and O. A. El Seoud

Department of Chemistry, Texas A & M University, College Station, Texas 77843 *(Received October 5, 1972)*

Publication costs assisted by The Robert A. Welch Foundation

Proton magnetic resonance spectroscopic investigations of octylammonium propionate (OAP), butyrate (OAB), hexanoate (OAH), nonanoate (OAN), dodecanoate (OAD), and tetradecanoate (OAT) surfactants in benzene and in carbon tetrachloride indicated the formation of small micellar aggregates. From the observed chemical shifts of 2–3 protons as functions of surfactant concentration, the critical micelle concentrations (cmc), aggregation numbers (n), and the equilibrium constants for micelle formation (K) have been obtained. In benzene, the cmc values increase with increasing hydrocarbon chain length of the surfactant carboxyl group (cmc values at 30° are OAP = $(1.5\text{–}1.7)10^{-2}$; OAB = $(3.5\text{–}3.9)10^{-2}$; OAH = $(4.1\text{–}4.5)10^{-2}$; OAN = $(6\text{–}8)10^{-2}$; OAD = $(9.3\text{–}10.0)10^{-2}$; and OAT = $(10\text{–}11)10^{-2}$ M) and are unaffected by β-halogen substitution in the carboxyl group (cmc values for dodecylammonium propionate, 3-bromopropionate, and 3-iodopropionate are $(3\text{–}7)10^{-3}$, $(2\text{–}3)10^{-3}$, and $(2\text{–}3)10^{-3}$ M, respectively). In carbon tetrachloride, the cmc values for OAP, OAB, OAH, OAN, and OAT are in the range of $(2\text{–}4.5)10^{-2}$ M and thus are relatively independent of the hydrophobic hydrocarbon chain length. Values of n and K for these surfactants in benzene and in carbon tetrachloride are in the ranges of 3–7 and 10^3–10^8 M^{1-n}, respectively.

Introduction

The observed dramatic rate enhancements of several reactions by micellar surfactants in nonpolar solvents[2-4] led us to initiate a systematic investigation of the physical-chemical properties of alkylammonium carboxylate micelles in nonpolar solvents.[1] Using proton magnetic resonance spectroscopic techniques we have examined the micellar properties of alkylammonium propionate surfactants in benzene and in carbon tetrachloride.[1] The obtained data indicated the formation of small micelles, with aggregation numbers in the range of 3–7, in which the polar headgroups are located in the interior while the hydrophobic hydrocarbon chains are in contact with the nonpolar solvent. Critical micelle concentrations in benzene were found to decrease in the order butyl (BAP) > hexyl (HAP) > octyl (OAP) > decyl (DeAP) > dodecyl (DAP) ammonium propionate.[1] In carbon tetrachloride, on the other hand, the cmc values for these surfactants remained essentially constant as a function of chain length.[1] Micellar properties of alkylammonium carboxylates have been examined as functions of the structural changes introduced in the alkylammonium and carboxylate groups.

Experimental Section

Reagent grade benzene was distilled from sodium onto Linde type 5A molecular sieve, and reagent grade carbon tetrachloride was dried and stored over Linde type 5A molecular sieve.

The surfactants were prepared and purified using established methods.[1,5] Repeated fractional distillation or recrystallization from hexane yielded colorless liquids or white crystals, respectively. Some of these surfactants are very hygroscopic and appropriate care was taken to exclude atmospheric moisture in making up stock solutions. Dodecylammonium 3-iodopropionate (DAIP) was found to be light sensitive and liberated iodine unless it was kept in the dark. Light was excluded from all solutions of the halogenated dodecylammonium propionates during and subsequent to dilution to the appropriate volume by using aluminum foil and storing in the dark. The purity of the surfactants was established by the observation of sharp melting or boiling points and by their infrared and proton magnetic resonance spectra. The following uncorrected melting and boiling points were obtained: octylammonium butyrate (OAB) 84.5° (0.42 Torr); octylammonium propionate (OAP) 79° (0.40 Torr); octylammonium hexanoate (OAH) 95° (0.35 Torr); octylammonium nonanoate (OAN) 39.5–42.5°; octylammonium dodecanoate (OAD) 52–53°; octylammonium tetradecanoate (OAT) 46.9–49.0°; dodecylammonium 3-bromopropionate (DABrP) 190–192° (dec); dodecylammonium 3-iodopropionate (DAIP) 67–68.5°.

The 100-MHz nuclear magnetic resonance spectra were obtained on a modified Varian Associates HA-100 spectrometer with a Hewlett-Packard Model 200 ABR audio oscillator and frequency counter. Each spectrum was recorded at least three times after equilibration to the ambient probe temperature of 30°. All spectra were determined on freshly prepared solutions in benzene or carbon tetrachloride and were measured relative to neat TMS

(1) J. H. Fendler, E. J. Fendler, R. T. Medary, and O. A. El Seoud, *J. Chem. Soc., Faraday Trans. 1*, **69**, 280 (1973), is considered to be part I.
(2) E. J. Fendler, J. H. Fendler, R. T. Medary, and V. A. Woods, *Chem. Commun.*, 1497 (1971).
(3) J. H. Fendler, *J. Chem. Soc., Chem. Commun.*, 269 (1972).
(4) J. H. Fendler, E. J. Fendler, R. T. Medary, and V. A. Woods, *J. Amer. Chem. Soc.*, **94**, 7288 (1972).
(5) A. Kitahara, *Bull. Chem. Soc. Jap.*, **28**, 234 (1955); A. Kitahara, *ibid.*, **30**, 586 (1957).

contained in a Wilmad 520-2 internal coaxial capillary tube. A upfield difference of 47.5 Hz at 100 MHz in the chemical shift was observed between the "external" neat TMS in the coaxial tube and internal 10 vol % TMS for a solution of $CHCl_3$ in CCl_4 (10% v/v). Individual measurements are accurate to ±0.01 at 100 MHz. Coupling constants were measured from the spectra obtained at 500-Hz sweep widths and are accurate to ±0.2 Hz. Bulk susceptibility corrections were not applied; however, they are predictably small and would not affect the obtained results significantly.

Results and Discussion

Proton Nmr Spectra. The proton nmr spectra of the octylammonium carboxylates in benzene and in carbon tetrachloride consist of single weight-averaged resonances for the protons of the monomeric and micellar (or aggregated) species at all concentrations approaching and above the cmc indicating that the association is rapid on the nmr timescale (10^{-4} sec). The spectra of 0.10 *M* surfactant in benzene and in carbon tetrachloride consist of triplets for the terminal methyl protons of the ammonium and carboxylate ions, broad singlets or unresolved multiplets for the intermediate methylene protons of both ions, apparent triplets for the $CH_2CO_2^-$ (with the exception of those for DAP which are well-resolved quartets) and $CH_2N^+H_3$ protons, and a relatively sharp singlet for the ammonium protons (Table I). The coupling constants given in Table I are unremarkable but demonstrate that, within experimental error, the values are relatively insensitive to changes in the nonpolar solvent for these aggregated systems.

Chemical Shifts as a Function of Surfactant Concentration. As a function of increasing stoichiometric surfactant concentration the surfactant proton resonances generally shift to lower magnetic field strength in benzene whereas they shift upfield in carbon tetrachloride. This behavior suggests that the protons of the monomeric surfactants are appreciably shielded by interaction with the high electron density π system of the solvent benzene and deshielded by carbon tetrachloride.

Figure 1 illustrates plots of the chemical shift of the methylene protons of the ammonium ion and of the carboxylate ion as a function of octylammonium hexanoate concentration in benzene. It is apparent that the chemical shifts of the protons of and immediately adjacent to the hydrophilic head groups are most sensitive to changes in surfactant concentration. For each proton there is a pronounced break, within experimental error, at the same concentration. Changes in the slopes of the lines of these plots indicate the aggregation of individual surfactant molecules and the discontinuities correspond to the critical micelle concentration. ^{19}F nmr investigations of carboxylate surfactants *in water* have indicated that the chemical shifts are independent of surfactant concentration below the cmc,[6-10] however, concentration dependence has been observed for short alkyl chain surfactants,[11,12] and for phenothiazine derivatives[13] in water as well as for dodecylammonium salts in CCl_4.[14] In nonpolar solvents the chemical shifts of organic molecules are well known to be slightly concentration dependent and those which undergo association equilibria and/or which can interact with the solvent *via* a variety of forces often exhibit a relatively more pronounced concentration dependence similar to that observed below the cmc for alkylammonium carboxylates (Figure 1). An additional difference between the chemical shift behavior in water and in nonpolar solvents is that reasonably well-pronounced breaks are obtained in the latter while theory predicts unresolvable curves for surfactants with small aggregation numbers in water.[9] Values for the critical micelle concentration of OAP, OAB, OAH, OAN, OAD, OAT, DAP, DABrP, and DAIP determined from plots similar to those given in Figure 1 are collected in Table II. The value obtained for DAP in benzene agrees reasonably well with that (2×10^{-3} *m*) determined by solubilization of water at 26°.[15] Critical micelle concentrations for octylammonium carboxylates increase with an increasing number of carbon atoms in the carboxylate group in benzene, but remain essentially constant in carbon tetrachloride. Equation 1 (where *a* is

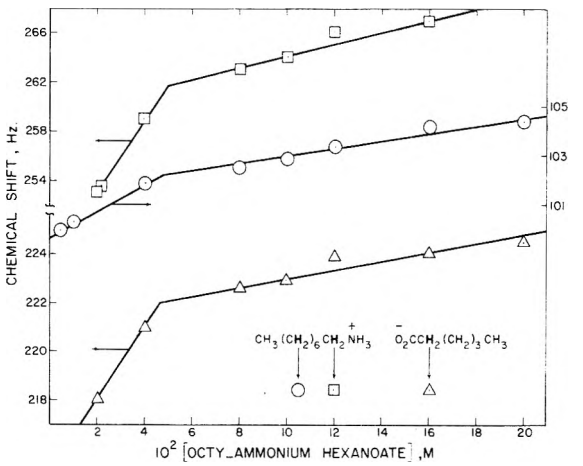

Figure 1. Observed chemical shifts at 100 MHz and 30° of the methylene protons of OAH as a function of its concentration in benzene.

$$\log \text{cmc} = a - bx \qquad (1)$$

related to the electrostatic free energy per molecule, *b* to the van der Waals energy of interaction per CH_2 group per molecule, and *x* is the number of carbon atoms in the chain) describes satisfactorily the relationship between the critical micelle concentrations and surfactant chain length in aqueous solutions for many systems.[16] Equation 1 was found to be applicable to reversed micelles in benzene; critical micelle concentrations of alkylammonium propionates decrease with increasing number of carbon atoms in the alkyl chain.[1] The present work demonstrates an opposite trend; increasing the number of carbon atoms in octylammonium carboxylate micelles results in an increase of the cmc in benzene. Figure 2 compares the effects of changes in the *n*-alkyl chain length of the ammonium and the carboxyl groups for alkylammonium carboxylate surfactants. It is also apparent that longer hydrophobic alkyl chains on the ammonium ion promote micelle formation, or aggregation, whereas the converse is

(6) H. Inoue and T. Nakagawa, *J. Phys. Chem.*, **70**, 1108 (1966).
(7) N. Muller and R. H. Birkhahn, *J. Phys. Chem.*, **71**, 957 (1967).
(8) N. Muller and R. H. Birkhahn, *J. Phys. Chem.*, **72**, 583 (1968).
(9) N. Muller and T. W. Johnson, *J. Phys. Chem.*, **73**, 2042 (1969).
(10) N. Muller and F. E. Platko, *J. Phys. Chem.*, **75**, 547 (1971).
(11) R. Haque, *J. Phys. Chem.*, **72**, 3056 (1968).
(12) R. E. Bailey and G. H. Cady, *J. Phys. Chem.*, **73**, 1612 (1969).
(13) A. T. Florence and R. T. Partiff, *J. Phys. Chem.*, **75**, 3554 (1971).
(14) J. F. Yan and M. B. Palmer, *J. Colloid Interface Sci.*, **30**, 177 (1969).
(15) A. Kitahara in "Cationic Surfactants," E. Jungermann, Ed., Marcel Dekker, New York, N. Y., 1970, p 303.
(16) I. J. Lin and P. Somasundaran, *J. Colloid Interface Sci.*, **37**, 731 (1971), and references cited therein.

TABLE I: ^{1}H Nmr Parameters for Octylammonium Carboxylates in Benzene and in Carbon Tetrachloride[a]

	Chemical shift, ppm										
	OAP		OAB		OAH		OAN		OAD	OAT	
	C_6H_6	CCl_4	C_6H_6	CCl_4	C_6H_6	CCl_4	C_6H_6	CCl_4	C_6D_6	C_6H_6	CCl_4
$\delta(CH_3(CH_2)_7N^+)$	0.658	1.361	0.685	1.334	0.700	1.359	0.707	1.341[b]	0.712	0.721	1.336[b]
$\delta(CH_3(CH_2)_xCO_2^-)$	1.020	1.467	0.820	1.370				*b*			*b*
$\delta(CH_3(CH_2)_6CH_2N^+)$	0.968	1.742	0.997	1.745	1.029	1.746	1.036	1.731	1.039	1.048	1.706
$\delta(CH_3(CH_2)_xCH_2CO_2^-)$			1.575	1.955	c	c	c	1.731	1.106	1.115	1.706
$\delta(CH_3(CH_2)_xCH_2CO_2^-)$	2.189	2.557	2.217	2.519	2.229	2.552	2.309	2.487	2.321	2.320	2.485
$\delta(CH_3(CH_2)_6CH_2N^+)$	2.520	3.242	2.583	3.200	2.640	3.209	2.572	3.172	2.558	2.580	3.172
$\delta(NH_3^+)$	8.538	9.093	8.565	9.160	8.846	9.301	8.042	8.587	8.161	7.955	8.620
$J(CH_3CH_2\ldots N^+)$		5.0			6.5	5.5	5.5	6.0	5.0	6.0	6.5
$J(CH_3CH_2\ldots CO_2^-)$	7.7	7.9	7.5	7.0							
$J(CH_2CH_2CO_2^-)$	7.6	7.0	7.0	7.0	7.5	7.5	7.8	7.0	7.6	8.0	7.5
$J(CH_2CH_2N^+)$	7.8	8.0	7.8	8.1	8.0	8.0	7.5	8.0	7.9	8.0	8.0

[a] At 100 MHz and 30°; [surfactant] = 0.10 *M*. [b] Only one triplet is apparent; assigned as that of $CH_3(CH_2)_7N^+H_3$. [c] Shoulder on broad $(CH_2)_x$ resonance; no value assigned.

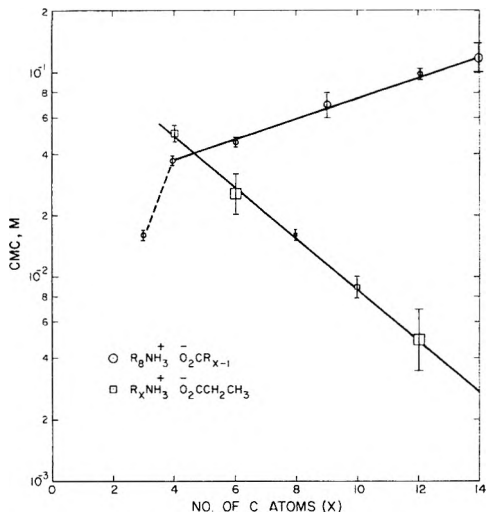

Figure 2. Logarithms of the critical micelle concentrations (cmc), *M*, as a function of hydrocarbon chain length (*x*), eq 1, for octylammonium carboxylates (⊙) and alkylammonium propionates (⊡) in benzene.

true for the carboxylate ion in benzene. The dependence of the cmc on the alkyl chain length of both the ammonium and carboxylate groups in benzene is considerably smaller (b = −0.12 and +0.05, respectively) than that generally found for micelles in aqueous solutions.[16] Halogen substitution in the carboxylate ion of dodecylammonium propionates results in a small decrease in the cmc (Table II), *i.e.*, promotes aggregation slightly, possibly as a consequence of the increased acidity of the carboxylate anion. The similarity of the cmc values of DAP, DABrP, and DAIP, however, suggests that steric factors are relatively unimportant. On the other hand, critical micelle concentrations in carbon tetrachloride are independent of the hydrocarbon chain length of the ammonium and carboxyl groups at least for the present surfactants. Investigations of micellar parameters in a variety of nonpolar solvents will allow meaningful discussions of the role of solvents in stabilizing reversed micelles.[17]

An alternative treatment of the data is to plot the observed chemical shift, δ, against the reciprocal stoichiometric surfactant concentration, $1/C_D$, as has been done previously for aqueous micellar systems.[6-12,18] Assuming that the concentration of monomers remains essentially constant above the cmc, the observed chemical shift, δ, can be expressed in terms of the chemical shifts of the monomeric, δ_m, and micellar, δ_M, species

$$\delta = \delta_M + \frac{\text{cmc}}{C_D}(\delta_m - \delta_M) \qquad (2)$$

Treatment of the present data according to eq 2 gave reasonable plots of δ *vs.* $1/C_D$, but just as in the case of alkylammonium propionate micelles in nonpolar solvents[1] more accurate cmc values can be obtained from plots of δ *vs.* C_D analogous to those in Figure 1. However, using eq 2, the micellar chemical shift, δ_M, can be obtained from the intercept of plots of δ *vs.* $1/C_D$. The chemical shifts of the monomeric surfactant, on the other hand, can be obtained from extrapolation of the observed chemical shift below the cmc in plots of δ *vs.* C_D to zero surfactant concentration (*e.g.*, Figure 1). The values of δ_m and δ_M for octylammonium carboxylates are given in Table III. Since the monomer (δ_m) and micelle (δ_M) contributions to the observed chemical shift (δ) vary in magnitude as well as in sign (*e.g.*, the $(CH_2)_xCH_2CO_2^-$ protons of OAB and OAH), these values are more meaningful than the observed chemical shifts. In general, both the monomeric and micellar species shift to higher magnetic field or show no appreciable trend as a function of increasing chain length in both benzene and carbon tetrachloride with the exception of the $CH_2CO_2^-$ protons of OAB and OAH in benzene. For both the terminal methyl and methylene protons of the carboxylate ion, the difference in the chemical shifts between carbon tetrachloride and benzene ($\Delta\delta(CCl_4-C_6H_6)$) is appreciably greater for the monomeric than for the aggregated, or micellar, species ($\Delta\delta(CCl_4-C_6H_6)$ for the monomeric and micellar carboxyl methyl protons of OAP is 0.62 and 0.38 ppm, respectively, and that for the methylene protons adjacent to the carboxyl group of OAH is 0.43 and 0.28 ppm, respectively). Since the interaction of the solvent with the hydrophilic groups of the surfactant would predictably decrease upon aggregation, these results are compatible with an aggregate structure in which the polar hydrophilic head groups are oriented spherically or ellipsoidally around an interior "cavi-

(17) J. H. Fendler, E. J. Fendler, R. T. Medary, and O. A. El Seoud, unpublished results.
(18) J. C. Eriksson, *Acta Chem. Scand.*, **17**, 1478 (1963).

TABLE II: Micellar Parameters in Benzene and in Carbon Tetrachloride[a]

Surfactant	C_6H_6 Cmc, M[b]	C_6H_6 n	C_6H_6 K, M^{1-n}	CCl_4 Cmc, M[b]	CCl_4 n	CCl_4 K, M^{1-n}
OAP	$(1.5-1.7)\ 10^{-2}$	5 ± 1	10^8	$(2.6-3.1)10^{-2}$	3 ± 1	10^8
OAB	$(3.5-3.9)\ 10^{-2}$	3 ± 1	10^3	$(2.5-3.2)10^{-2}$	4 ± 1	10^5
OAH	$(4.1-4.5)\ 10^{-2}$	3 ± 1	10^3	$(4.2-4.5)10^{-2}$	5 ± 1	10^6
OAN	$(6-8)\ 10^{-2}$	3 ± 1	10^3	$(2.9-4.0)10^{-2}$	5 ± 1	10^7
OAD[c]	$(9.3-10)\ 10^{-2}$	7 ± 1	10^8			
OAT	$(10-11)\ 10^{-2}$	3 ± 1	10^3	$(2.8-4.0)10^{-2}$	3 ± 1	10^3
DAP	$(3-7)\ 10^{-3}$			$(2.1-2.5)10^{-2}$		
DABrP	$(2-3)\ 10^{-3}$					
DAIP	$(2-3)\ 10^{-3}$					

[a] Mean values and estimated errors in following 2–3 protons. [b] Obtained from plots of δ *vs.* C_D. [c] In C_6D_6.

TABLE III: Chemical Shifts of the Monomeric (δ_m) and Micellar (δ_M) Protons of Octylammonium Carboxylates in Benzene and in Carbon Tetrachloride

Surfactant	C_6H_6 δ_m, ppm	C_6H_6 δ_M, ppm	CCl_4 δ_m, ppm	CCl_4 δ_M, ppm
OAP				
$CH_3(CH_2)_xCO_2^-$	0.880	1.079	1.500	1.456
$CH_2CO_2^-$			2.620	2.470
NH_3^+			6.842	9.740
OAB				
$CH_3(CH_2)_7N^+$	0.717	0.832		
$CH_3(CH_2)_xCO_2^-$			1.397	1.366
$CH_2CO_2^-$	2.091	2.270		
NH_3^+			5.010	9.720
OAH				
$CH_3(CH_2)_6CH_2N^+$	0.995	1.063		
CH_2CO_2	2.151	2.259	2.582	2.541
$CH_3(CH_2)_6CH_2N^+$	2.476	2.697		
NH_3^+			6.140	9.740
OAN				
$CH_3(CH_2)_6CH_2N^+$	0.989	1.056		
$CH_2CO_2^-$			2.596	2.476
$CH_3(CH_2)_6CH_2N^+$	2.451	2.682		
NH_3^+			5.090	9.120
OAD[a]				
$CH_3(CH_2)_7N^+$	0.999	1.054		
$CH_2CO_2^-$	2.293	2.339		
NH_3^+	6.720	8.980		
OAT				
$CH_3(CH_2)_7N^+$	0.669	0.770		
$CH_3(CH_2)_6CH_2N^+$	1.001	1.076		
$CH_3(CH_2)_xCH_2CO_2^-$	1.062	1.149		
$CH_2CO_2^-$			2.568	2.436
NH_3^+			5.200	9.310

[a] In C_6D_6.

ty" with the hydrophobic chains extending into the bulk nonpolar solvent. An additional implication of these results is that the solvent does not appreciably penetrate the interior of these aggregates.

Knowledge of δ_M and δ_m values affords the calculation of the concentration of monomeric surfactant, [S], at a given C_D value

$$[S] = \frac{C_D(\delta_M - \delta)}{\delta_M - \delta_m} \quad (3)$$

Figure 3 illustrates a typical monomer–micelle concentration profile, calculated from the chemical shifts of the terminal methyl protons of the butyrate ion and the ammonium ($^+NH_3$) protons of OAB in carbon tetrachloride. Similar profiles have been obtained for all the other observable protons in all systems.[19] Evidently, the concentration of monomers and micelles as a function of stoichiometric surfactant concentration change as expected from an idealized equilibrium between monomers, S, and micelles, S_n,

$$nS \overset{K}{\rightleftharpoons} S_n \quad (4)$$

$$K = [S_n]/[S]^n \quad (5)$$

where K is the equilibrium constant for the formation of the micelle and n is the aggregation number. Taking the logarithm and rearrangement of eq 5 leads to

$$\log (nK) = \log (n[S_n]) - n \log [S] \quad (6)$$

Assuming that the concentration of monomers remains essentially constant above the cmc, substitution of the relationship between monomeric, micellar, and stoichiometric surfactant concentrations

$$[S_n] = \frac{C_D - [S]}{n} \quad (7)$$

into eq 5 gives

$$\log (C_D - [S]) = \log nK + n \log [S] \quad (8)$$

(19) Extrapolation of the micelle line to zero micelle concentration is slightly closer to the "true" cmc obtained from plots of δ *vs.* C_D (Table II) than that taken from the intersection of the monomer and micelle lines. In fact a referee preferred these cmc values and criticized our method of obtaining the cmc values from plots of δ *vs.* C_D (Figure 1) and the use of eq 2, primarily on grounds that the "key assumption" in the derivation of eq 2 is that below the cmc $\delta = \delta_m$. There are several cases where cmc values have been determined by the use of eq 2 even when δ_m was not constant.[11-14] We believe that the more important assumption used in the derivation of eq 2 is that above the cmc the monomer concentration remains constant, and hence [S] = cmc. Although the available information on micelle formation in nonaqueous solvents is meager, this latter assumption, just as in the case of aqueous micellar solutions, is unlikely to be rigorously correct. In the strickest sense of the word, neither nmr spectroscopy nor, as a matter of fact, any other available technique provide a means for determining true cmc values.[20] We are content, however, at the present stage of our investigation of micelles in nonaqueous solvents to use internally consistent operational cmc values and believe that those obtained from plots of δ *vs.* C_D are more useful for our purpose, since extrapolation of the micelle line to zero concentration (as in Figure 3, for example) involves greater uncertainties owing to the method of obtaining δ_m and δ_M from intercepts. Agreement among our cmc values, those determined independently,[15] and those obtained by plotting chemical shifts of the different protons either as δ *vs.* C_D or according to eq 2 (see Figure 1 in ref 1, for example), as well as those expected from the kinetic behavior of micelle catalyzed reactions in these systems,[2-4] lends credence to this approach.

(20) P. Mukerjee and K. J. Mysels, *Nat. Stand. Ref. Data Ser., Nat. Bur. Stand.*, **No. 36** (1971).

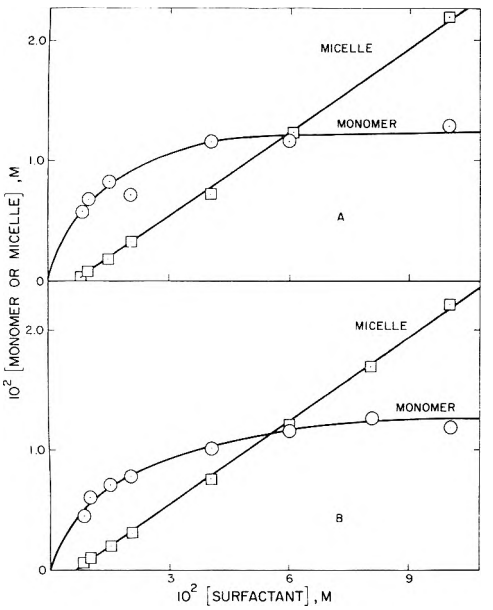

Figure 3. Concentration of monomers (⊙) and micelles (⊡) as a function of [OAB], *M*, in CCl_4 calculated from eq 2-4: A, from the terminal methyl carboxyl protons and B, from the ammonium protons.

which affords the calculation of the aggregation number, *n*, and the equilibrium constant for micelle formation, *K*. Reasonable plots were obtained on treating our data according to eq 8. Figure 4 illustrates plots of the data according to eq 8 for OAP in carbon tetrachloride. Table II gives the aggregation number, *n*, and the monomer–micelle equilibrium constant, *K*. These values are the mean of those obtained from the different proton shifts and their accuracy depends on the errors in δ_m and δ_M. Thus values for *n* and *K* are considered to be accurate within ± 1 and $\pm 10^2$, respectively. Octylammonium carboxylate and alkylammonium propionate[1] micelles in benzene and in carbon tetrachloride are rather small. In fact, that the term micelle is used here to describe these aggregates is justified only by following the established terminology.[5] From the nmr data, monomer and micelle concentrations

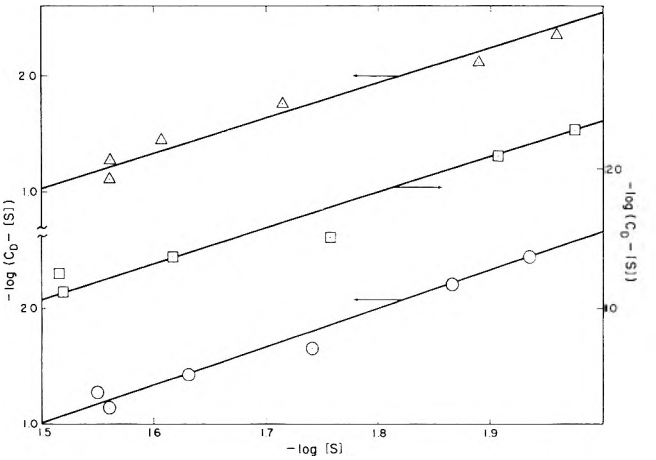

Figure 4. Plots of log (C_D − [S]) *vs.* log [S] (eq 8) for OAP in CCl_4; △, $CH_3CH_2CO_2^-$; ⊡, $CH_3CH_2CO_2^-$; and ⊙, N^+H_3 protons.

can be calculated at given stoichiometric surfactant concentrations (eq 2 and 3). Figure 3 illustrates such a dependence for octylammonium butyrate in carbon tetrachloride. It appears, therefore, that the general behavior of alkylammonium aggregates in nonpolar benzene and carbon tetrachloride is similar to that observed for micelle-forming surfactants in aqueous solutions. Although at present there are no clear-cut theoretical justifications for using the idealized approach in deriving eq 2-8, they allow the calculation of parameters describing surfactant aggregates in nonpolar solvents. These parameters, in turn, provide an understanding of the different factors which influence the stabilities of reversed micelles in apolar solvents. Such information is necessary for the meaningful analysis of the remarkable catalysis manifested by these surfactant systems.

Acknowledgments. Support for this work from The Robert A. Welch Foundation is gratefully acknowledged. E. J. F. is a Research Career Development Awardee of the National Institutes of Health, U. S. Public Health Service.

Measurement of Diffusion Coefficients of Octane Isomers by the Chromatographic Broadening Method

Eli Grushka* and Virgil R. Maynard

Department of Chemistry, State University of New York at Buffalo, Buffalo, New York 14214 *(Received December 19, 1972)*

The diffusion coefficients of seven octane isomers in helium were measured by the chromatographic broadening technique with excellent precision and an estimated accuracy of 1%. This was accomplished by computer manipulation of the data. It is found that as branching increases, the diffusion coefficients also increase. This can be explained by Giddings' shielding treatment. A direct correlation is found between the diffusion coefficients of the isomers and their critical volumes and related parameters. Data analysis indicates that the critical volume of 2,2,4-trimethylpentane quoted in the literature might be too high. An attempt is made to modify the Fuller, Schettler, and Giddings estimating equation to take into account molecular branching.

Mass transport phenomena play a major role in many and diverse fields of both basic and practical science. For example, diffusion is important in chemical reactions and in designing absorbers, distillation columns, etc. Two excellent reviews by Mason and Marrero[1,2] recently appeared which contained both a theoretical treatment of diffusion and a discussion of experimental diffusion measurements. There are many equations which attempt to predict the mutual diffusion coefficient, D_{AB}, of components in binary gaseous mixtures. A compilation of estimating equations can be found in a paper by Fuller and Giddings[3] and in the text by Reid and Sherwood.[4]

In general, it can be said that some theoretical treatments are based on the hard-sphere model and elastic collisions, while others use the Chapman-Enskog theory with reasonable intermolecular potentials.[2] Similarly, the bulk of the experimental work is carried out with small molecules where spherical force fields can be applied. For a detailed analysis of the experimental data up to 1970, see the review by Marrero and Mason.[2]

In polyatomic molecules, the internal degrees of freedom are important and the elastic collision treatment is no longer valid. One must use quantum mechanics to describe the inelastic collisions in the diffusion process. The resulting collision integral expression is rather complicated and various approximations must be made for it to be manageable.[2] Relatively little experimental work has been done with polyatomic molecules. Again, for references up to about 1970, see Marrero and Mason's review.[2] Since 1970, most of the work involving relatively large species was carried out by Watts and his associates.[5-9] Haung, *et al.*,[10] have also looked into this problem. Watts in his work has noticed that when the mutual diffusion coefficients of homologous alkanes or alcohols in air are plotted *vs.* the reduced masses of the two components, a straight line is obtained.[7-9] Humphreys and Mills,[11] using an extremely crude model, have indicated that Watts' observation is expected over a narrow range of intermediate reduced masses. Wakeham and Slater have supported experimentally[12] Humphreys and Mills' contention.

Very little attention has been centered on the effect of the molecular geometry on diffusion properties and only sketchy information can be found in the literature. More specifically, the diffusion behavior of structural isomers has not been studied systematically. Fuller, Ensley, and Giddings[13] briefly investigated the effect of the position of various halogen atoms in some hydrocarbons. In general, they noted that smaller diffusion coefficients are obtained when the halogen atom is in the 1 position as compared to the 2 or 3 position. Examination of Ubbelohde's work in two papers[14,15] shows some discrepancies in his data. For example, in one paper[14] 2,2,4-trimethylpentane had a lower diffusion coefficient than octane in argon. In the second paper[15] not only is there disagreement in the absolute values of the coefficients, but also, in argon, isooctane has now a larger D_{AB} value than octane. The recent work of Lugg[16] shows that branched isomers very frequently have larger diffusion coefficients than the normal compounds. Huang[10] shows that in H_2, *sec*-butyl alcohol has a lower diffusion coefficient than normal butyl alcohol. Elliott and Watts[9] find that with pentane iso > normal while the inverse is true with butane. Their data also indicate that D_{AB} of 2,2-dimethylpropane is less than that of 2-methylbutane,[9] although theoretical arguments predict the opposite trend. Clearly then, a systematic investigation of the dependence of diffusion on the structure of isomers is desirable.

Two factors increase the desirability of such a study. (A) Some of the diffusion coefficient estimating equations,

(1) E. A. Mason and T. R. Marrero, "Advances in Atomic and Molecular Physics," D. R. Bates and I. Easterman, Ed., Academic Press, New York, N. Y., 1970, p 155.
(2) T. R. Marrero and E. A. Mason, *J. Phys. Chem. Ref. Data*, **1**, 3 (1972).
(3) E. N. Fuller and J. C. Gidcings, *J. Gas Chromatogr.*, **3**, 222 (1965).
(4) R. C. Reid and T. K. Sherwood, "The Properties of Gases and Liquids," McGraw-Hill, New York, N. Y., 1966.
(5) H. Watts, *Can J. Chem.*, **49**, 67 (1971).
(6) M. Cowie and H. Watts, *Can. J. Chem.*, **49**, 74 (1971).
(7) R. W. Elliott and H. Watts, *Nature (London). Phys. Sci.*, **234**, 98 (1971).
(8) R. F. Bar and H. Watts, *J. Chem. Eng. Data*, **17**, 45 (1972).
(9) R. W. Elliott and H. Watts *Can. J. Chem.*, **50**, 31 (1972).
(10) T. C. Haung, F. J. F. Yang, C. J. Huang, and C. H. Kuo, *J. Chromatogr.*, **70**, 13 (1972).
(11) A. E. Humphreys and A. Mills, *Nature (London), Phys. Sci.*, **238**, 46 (1972).
(12) W. A. Wakeham and D. H. Slater, *Nature (London), Phys. Sci.*, **239**, 109 (1972).
(13) E. N. Fuller, K. Ensley, and J. C. Giddings, *J. Phys. Chem.*, **73**, 3679 (1969).
(14) G. A. McD. Cummings and A. R. Ubbelohde, *J. Chem. Soc.*, 3751 (1953).
(15) J. K. Clarke and A. R. Ubbelohde, *J. Chem. Soc.*, 2050 (1957).
(16) G. A. Lugg, *Anal. Chem.*, **40**, 1022 (1968).

e.g., the Fuller, Schettler, and Giddings equation[17] as well as Gilliland's[18] do not take into account molecular shapes and it is desirable to be able to modify these equations for shape effects. (B) Collision cross sections of relatively large molecules and their isomers can be obtained from the diffusion data. In this paper, we report the diffusion coefficients of seven octane isomers and examine the relations between D_{AB} and the molecular structure.

The experimental diffusion coefficients were determined using the gas chromatographic broadening method, which is usually attributed to Giddings.[19] A general review of the method as well as a bibliography of papers employing this technique up to 1970 is given in ref 2. Since 1970, several other papers have appeared reporting the use of this method.[10,20-22] Mason, in reviewing the method, stated that the reliability of the data is average. His criticism dealt mainly with instrumentation problems and, more importantly, with the errors associated with manual measurements of retention times and peak widths. Our system, which will be described shortly, together with computer data handling produces values with a precision of less than 1% relative error and with an estimated accuracy within 1%.

In this method of measurement, a narrow plug of the solute (the organic isomer) is injected into a flowing stream, in a long and empty tube, of the solvent (in our case, helium). From the resulting peak width, the diffusion coefficient, D_{AB}, is obtained. The chromatographic method can be mathematically described from two approaches. In the first, the following mass balance relation is used.

$$\frac{\partial c}{\partial t} - D_{AB}\left[\frac{\partial^2 c}{\partial x^2} + \frac{1}{r}\frac{\partial}{\partial r}\left(r\frac{\partial c}{\partial r}\right)\right] + 2\bar{U}\left[1-\left(\frac{r}{r_0}\right)^2\right]\frac{\partial c}{\partial x} = 0 \quad (1)$$

$\bar{U}$ is the cross sectional averaged velocity of the flowing carrier, r_0 is the radius of the tubing, r is the radial coordinate, x is the axial coordinate, t is time, and c is the concentration of the organic vapor solute. Using the boundary conditions that no mass transport occurs through the column wall and that the radial concentration gradient of the solute at the center of the tube is zero, together with some initial conditions such as a δ function injection profile and zero concentration of the solute at $t = 0$, a solution of eq 1 is given by

$$C(t,L) = A\left[\frac{D_{eff}t}{L^2}\right]^{-1/2} \exp\left[\frac{-(1-\bar{U}t/L)^2L^2}{4D_{eff}t}\right] \quad (2)$$

L is the tubing length, A is a constant related to the amount injected, and D_{eff} is a dispersion coefficient given by[2]

$$D_{eff} = D_{AB} + (r_0^2\bar{U}^2/48D_{AB}) \quad (3)$$

Equation 2 is a modified Gaussian and when the quantity $D_{eff}/\bar{U}L$ is small, the equation tends to a pure Gaussian profile.[23] The variance (converted to length units) of the concentration profile is given by

$$\sigma^2 = \frac{2D_{AB}L}{\bar{U}} + \frac{r_0^2\bar{U}L}{24D_{AB}} \quad (4)$$

Since the chromatographic plate height, H, is defined as

$$H = \sigma^2/L \quad (5)$$

it is seen that the chromatographic system can allow the measurement of D_{AB}

$$D_{AB} = (\bar{U}/4)\left[H \pm \sqrt{H^2 - r_0^2/3}\right] \quad (6)$$

since H and $\bar{U}$ are easily obtained experimentally. Alternatively, one can start with the Golay equation for the plate height in capillary columns.[24] In the case of empty tubing, with no adsorption on the tubing wall, the Golay equation is reduced to

$$H = \frac{2D_{AB}}{\bar{U}} + \frac{r_0^2\bar{U}L}{24D_{AB}} \quad (7)$$

Upon rearrangement eq 7 yields eq 6. The meaning and importance of the two terms on the right-hand side of eq 7 were already discussed by us.[22] Whether the positive or negative root of eq 6 is the physically significant one depends upon the solvent velocity. At low velocities, the positive root is used, while at high velocities the negative root is the important quantity. The switch over from one root to another occurs at the velocity that minimizes eq 7 (or eq 4, for that matter).

Experimental Section

Apparatus. Our system resembled the one described by Fuller, Ensley, and Giddings.[13] Several modifications, however, were made in order to increase the precision of measurement. The oven used was a Hotpack drying oven which was converted to chromatographic use. A high-speed fan and several baffles were installed to eliminate temperature gradients. The heating system in the oven was described by us previously.[25] Temperatures at any point in the oven could be held to ±0.02°. Temperature gradients in the volume occupied by the column were held to within 0.1–0.2°. All the diffusion measurements were done at 100 ± 0.1°. The column was 316 stainless steel tubing, 1526.1 ± 0.6 cm in length having an inner radius of 0.270 ± 0.002 cm. The radius was measured at both ends with the aid of a micrometer. The volume of the column was 348.7 ± 0.5 cc. The column was placed in the oven in a coil form, 19 in. in diameter. The temperature along the coiled column was monitored with four copper–constantan thermocouples placed at positions roughly equivalent to 12, 3, 6, and 9 o'clock. The thermocouple outputs were monitored with a Leeds and Northrup Model 8686 millivolt potentiometer. The column was connected by a capillary tube (0.03 in. i.d.) on one side to a Carle microvalve with sample loop volume of 50 μl, and on the other side to a Beckman GC-4 flame ionization detector. The volume of these connecting tubes was a few microliters.

The signal from the detector was amplified by a Keithley Model 417K chromatograph electrometer. The electrometer output was digitized with an Infotronic CRS-30 voltage-to-frequency (V/F) converter which drove a BRPE 11 Teletype paper tape punch. The signal was also displayed on an Esterline-Angus Model S-601-S Speedservo chart recorder. The punched tape was converted to cards which were analyzed by a CDC-6400 computer.

(17) E. N. Fuller, P. D. Schettler, and J. C. Giddings, *Ind. Eng. Chem.*, **58**, 19 (1966).
(18) E. R. Gilliland, *Ing. Eng. Chem.*, **26**, 681 (1934).
(19) J. C. Giddings and S. L. Seager, *J. Chem. Phys.*, **33**, 1579 (1960).
(20) Z. Balenovic, M. N. Myers, and J. C. Giddings, *J. Chem. Phys.*, **52**, 915 (1970).
(21) J. C. Liner and S. Weissman, *J. Chem. Phys.*, **56**, 2288 (1972).
(22) E. Grushka and V. Maynard, *J. Chem. Educ.*, **49**, 565 (1972).
(23) O. Levenspiel and W. K. Smith, *Chem. Eng. Sci.*, **6**, 227 (1957).
(24) M. J. E. Golay, "Gas Chromatography," D. H. Desty, Ed., Academic Press, New York, N. Y., 1958.
(25) V. Maynard and E. Grushka, *Anal. Chem.*, **44**, 1427 (1972).

Reagents. The following solutes were purchased from Chemical Samples Co. (Columbus, Ohio): (a) *n*-octane (99.8% pure), (b) 3-methylheptane (99% pure), (c) 2,2,4-trimethylpentane (99.9% pure), (d) 2,3-dimethylhexane (99% pure), (e) 2,4-dimethylhexane (99% pure), and (f) 3-ethyl-2-methylpentane (99% pure). Methane (99.97% purity) was bought from Matheson. The carrier gas (or solvent) was commercially available helium which was passed over molecular sieves and preheated before entering the column.

Procedure. Upon actuation of the sample valve, which introduces the solute vapor to the flowing helium, an electric timer was started. Several seconds before the emergence of the peaks, the digitizer and the perforator were turned on. After digitizing for a predetermined amount of time (depending upon the peak width), the V/F converter was turned off and the whole cycle was reinitiated. On the average, ten runs were made per data point.

The baseline of the digitizer was set so that the electrometer gave a constant background count. The output of the electrometer was monitored by a Keithley Model 160 DVM. We took between 30 and 100 digital points before and after each peak. This allows the computer to establish a baseline and correct (algorithmically) for any noise spikes or baseline drifts. Within the peak, we took between 150 and 400 digital points. The reasons for obtaining such large numbers of points will be discussed later.

To check the self consistency of the data, we also made some runs on a 3051-cm long (0.270 cm radius) tubing.

Results and Discussion

A large number of digital data points per peak was taken to minimize error due to insufficient data information. The errors resulting from insufficient information were thoroughly analyzed by Cram.[26] Also the limitation of our voltage-to-frequency converter, which acts as a low pass filter,[27] should be recognized. Although the time base accuracy is very good (0.01%), the overall accuracy of the system has a maximum error of 0.1%.

As mentioned, Mason and Marrero[1,2] indicate that the reliability of the chromatographic data is average. However, with special instrumentation design, the precision can be improved. In a study on extracolumn contributions to peak spreading, Maynard and Grushka[25] have demonstrated that if the connecting tubings are short and narrow their contributions to the peak variance are negligible. In addition, the initial volume occupied by the solute is very small compared to that of the diffusion column, the gas flow is laminar, and band broadening due to column coiling (the so called "race track" effect) and to secondary flows are minimal.[13] Adsorption of the solute on the tubing wall can contribute to the peak dispersion. However, in our case, the ratio of the wall surface area to column volume was small and the temperature was high. The octanes' peaks were symmetrical and their retention times were equal to that of methane, thus indicating absence of measurable adsorption effects.

Additional precision in the data is obtained by eliminating hand measurements of H, the plate height. As indicated the present study uses digitized data and a computer for the calculation of H. The measurement of the plate height is done by three different methods: (a) from the width of the peak at half its height, (b) from the second central moment, and (c) from the variance (second central moment) of a Gaussian which is least-squares fitted to the experimental points. In case a the computer must frequently interpolate between two points in order to get the width at half the height. Consequently, this measurement is the least precise among the three methods. On the other hand, the least-squares fitting of a Gaussian gives the best precision since it tends to smooth the small amount of noise which originates in either the chromatographic or digitizing process. The agreement between the calculation of D_{AB} by method b and c was usually within 1%. In the following only the least-squared Gaussian data will be discussed.

TABLE I: Diffusion Least-Squared Data of Methane in He at 100 ± 0.1°

	He velocity	
	1.5 cm/sec	3.0 cm/sec
Column A. L = 1526.1 cm; Radius = 0.270 cm		
D_{AB}, cm²/sec	1.014	1.029
Standard deviation	0.007	0.003
Relative error, %	0.69	0.29
Column B. L = 3051.1 cm; Radius = 0.270		
D_{AB}, cm²/sec	1.000	1.006
Standard deviation	0.003	0.007
Relative error, %	0.3	0.70

To check the accuracy of our system, we determined the diffusion coefficient of methane in helium at 100° under four different conditions which are summarized in Table I. These values are to be compared with the value of 1.005 cm²/sec given by Fuller, Schettler, and Giddings.[17] The D_{AB} values are larger at higher velocities, a phenomenon which might be attributed to flow eddies at the column inlet where the flow in the capillary tubing expands. These eddies extend for approximately eight inside diameters along the wider tube, the exact length depending on the actual geometry and flow rate.[28] The contribution of these eddies to the plate height were discussed by us before.[25] The increase in D is less significant with the longer column since the effect of the flow disturbance in the column inlet is diminished. The phenomenon of increasing D_{AB} values with increasing velocities was observed by other workers.[10] No statistical analysis of the data presented in Table I was attempted due to (a) the apparent systematic error in the diffusion coefficient as a function of the velocity of the solvent, and (b) the lack of the precision in the value given by Fuller, *et al.* If, however, we compare our least-squared results at 1.5 cm/sec to the one reported by Fuller, *et al.* (1.005 cm²/sec), we see that the agreement is well within our experimental error and it is less than 1%.

The diffusion coefficients of seven octane isomers in helium as obtained on the 1526.1-cm column are shown in Table II. The values are corrected to 760 mm pressure. The pressure drop across the column was negligible and the correction involved taking into account the ambient pressure. We assumed here that the product D_{AB} times the pressure is constant over a small pressure range. The precision of the least-squared data is excellent, with octane having the largest error of 1.03%. For the rest of the isomers, the precision is 0.3% or less. Although we feel that the least-squared data is the most accurate, the D_{AB}

(26) S. N. Chesler and S. P. Cram, *Anal. Chem.*, **43**, 1922 (1971).
(27) S. N. Chesler and S. P. Cram, *Anal. Chem.*, **44**, 2240 (1972).
(28) W. Kaufman, "Fluid Mechanics," McGraw-Hill, New York, N. Y., 1963, p 111.

TABLE II: Diffusion Coefficients (cm^2/sec) of Octane Isomers in He at 100 ± 0.1° Corrected to 1 Atm

Compound[b]	LS[a]	M[a]	$W_{1/2}$[a]
n-Octane (125.8°)	0.3161 ± 0.0033	0.3106 ± 0.0078	0.3194 ± 0.0038
3-Methylheptane (122.2°)	0.3334 ± 0.0009	0.3312 ± 0.0018	0.3369 ± 0.0018
2,4-Dimethylhexane (109.4°)	0.3340 ± 0.0008	0.3314 ± 0.0019	0.3387 ± 0.0014
3-Ethylhexane (118.5°)	0.3363 ± 0.0007	0.3331 ± 0.0019	0.3416 ± 0.0027
3-Ethyl-2-methylpentane (115.7°)	0.3398 ± 0.0004	0.3373 ± 0.0030	0.3442 ± 0.0046
2,3-Dimethylhexane (115.6°)	0.3420 ± 0.0006	0.3400 ± 0.0018	0.3468 ± 0.0025
2,2,4-Trimethylpentane (99.2°)	0.3455 ± 0.0011	0.3408 ± 0.0009	0.3521 ± 0.0027

[a] *M*, LS, and $W_{1/2}$ indicate, respectively, determination of D_{AB} by the second moment, least-squares fitting of a Gaussian, anc width at half the peak height. [b] The numbers next to each compound indicate the boiling temperatures.

values as obtained from the other two methods of calculation are also included in Table II for comparison. The data were treated statistically, using the *t* test to check for accuracy at the 95% confidence level. In most cases, only one or two experimental values per data point (out of at least ten runs) were rejected. The lone exception is 3-ethyl-2-methylpentane where four values were eliminated.

The data in Table II clearly indicate that the diffusion coefficients have a higher value with branched isomers. In fact, as the octane molecules became more branched the diffusion coefficients increase; that is, branched molecules have smaller collision cross sections. Although collision integrals for polyatomic molecules can be written[1,2,29] their solution can be obtained in special cases only. Hence, our discussion here will be mainly qualitative. Measurements of D_{AB} of systems such as described here over a large range of temperature can be utilized to obtain the force constants of the interaction between unlike molecules as pointed out by Hirschfelder, Curtis, and Bird.[29] Such a study is now underway.

The decrease in the collision cross section can be discussed using the shielding method developed by Fuller, Ensley, and Giddings.[13] According to their treatment outer groups in the branched hydrocarbon can shield groups at the interior of the molecule from collision. The shielding probability S_i is given as[13]

$$S_i = 1 - \pi \underset{j \neq 1}{} (i - s_{ij}) \qquad (8)$$

where s_{ij} is given by

$$s_{ij} = \left(\frac{\sigma_{He} + \sigma_j}{4d_{ij}}\right)^2 \qquad (9)$$

σ_{He} is the collision diameter of helium, σ_j is the collision diameter of the *j*th shielding group, and d_{ij} is the distance between the shielding group *j* and the interior group *i*. The parameter s_{ij} is the probability that group *j* intercepts the collision path.[13] As branching increases the number of shielding groups increases thus decreasing the overall collision cross section of the molecule. This is verified by the data shown in Table II. Although the molecular conformation of octane in the gas phase is most likely "crumpled," it's collision cross section is larger than that of 3-methylheptane. There is a large increase in the diffusion coefficient as the solute is changed from octane to 3-methylheptane. Further branching does not produce as great a change in D_{AB}. However, as the overall molecular shape becomes more spherical, the collision cross section decreases. There are several interesting points concerning the data in Table II. With the exception of 2,4-dimethylhexane, the diffusion coefficient increases as the boiling points of the isomers decrease. This perhaps is not surprising since some of the estimating equations, *e.g.*, Arnold's,[30] can be expressed in terms of the boiling points of the diffusing species.[3]

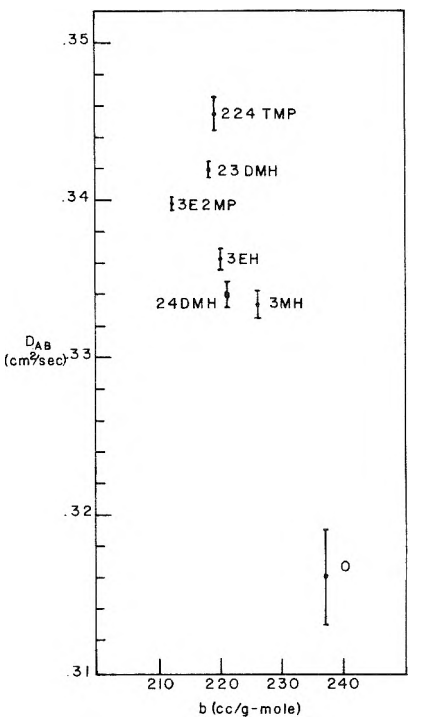

Figure 1. D_{AB} *vs. b:* O = octane; 3MH = 3-methylheptane; 24DMH = 2,4-dimethylhexane; 3EH = 3-ethylhexane; 3E2MP = 3-ethyl-2-methylpentane; 23DMH = 2,3-dimethylhexane; 224TMP = 2,2,4-trimethylpentane.

Since many of the estimating equations rely on critical volumes of the diffusing species we decided to study the dependence of the diffusion coefficients on various volume quantities. Perhaps, the simplest parameter is the van der Waals *b* term which is related to the molecular volume. In Figure 1, the diffusion coefficient, from the least-squared scheme, is plotted *vs. b*. The parameter *b* was obtained from the critical temperature, pressure, and volume and the van der Waals compressibility factor. It is seen that as the *b* value decreases, the diffusion coefficients increase. It is possible that the D_{AB} value of 2,3-dimethylhexane is slightly higher than it should be. However, since the accuracy is most likely within 1%, this compound falls within the acceptable range. The situation is different with the isooctane. As expected, its diffusion coefficient is higher than the rest of the isomers. However, its *b* value is not the smallest. As will be shown shortly the same phenomenon is observed when critical volumes are plotted. We re-

(29) J. O. Hirschfelder, C. F. Curtiss, and R. B. Bird, "Molecular Theory of Gases and Liquids," Wiley, New York, N. Y., 1964.
(30) J. H. Arnold, *Ind. Eng. Chem.*, **22**, 1091 (1930).

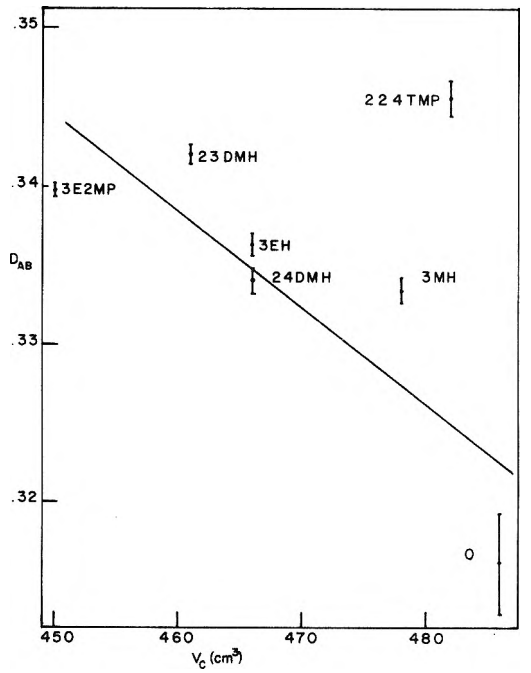

Figure 2. D_{AB} *vs.* the critical volumes of the octane isomers. Abbreviations have same meanings as in Figure 1.

peated the measurements with the 2,2,4-trimethylpentane and the value which we obtained was 0.3448 ± 0.0018 cm²/sec. The two D_{AB} values are within experimental errors and an F test shows that the two variances are in agreement within the 95% confidence level.

The same effect is shown in Figure 2 where D_{AB} is plotted *vs.* the critical volumes of the seven isomers. The V_C values were obtained from Reid and Sherwood,[4] who in turn used estimated values.[31] The review by Kobe and Lynn[32] indicates that uncertainties exist in the literature as to the value of V_C of 2,2,4-trimethylpentane. From the general trend in Figures 1 and 2, it is possible that the critical volume of isooctane is overestimated, and perhaps a V_C of about 450 cc is correct. Without the 2,2,4-trimethylpentane value, the diffusion coefficients increase as the critical volumes decrease, as expected. It should be pointed out that some of the critical volumes are estimated and small errors will shift the points around. The average values of the diffusion coefficients were least-squares fitted to a straight line. We did not use a weighted least-squares method due to the uncertainties in the V_C values. The slope of the line was −0.613 and the correlation coefficient was −0.846 which indicates 95% confidence level of a linear relationship between D_{AB} and V_C. Plots such as these can be used to estimate critical volumes from diffusion data.

Since, as indicated before, some of the estimating equations are based on V_C values, we decided to plot the log D_{AB} *vs.* the log of $V_{CA}^{0.4} + V_{CB}^{0.4}$ (Figure 3). V_{CA} is the critical volume of the isomer while V_{CB} is that of helium. The similarity to Figure 2 is expected. The solid line was obtained by using the mean log diffusion coefficient values (unweighed) in a linear regression analysis. The slope of the line was −3.11 and the correlation coefficient was −0.834 which indicates 95% confidence level of a linear relationship between log D_{AB} and log $(V_{CA}^{0.4} + V_{CB}^{0.4})$. An estimating equation by Othmer and Chen[33] predicts a slope of −2.46. Considering the approximation in the V_{CA} values, the agreement in the slopes is good.

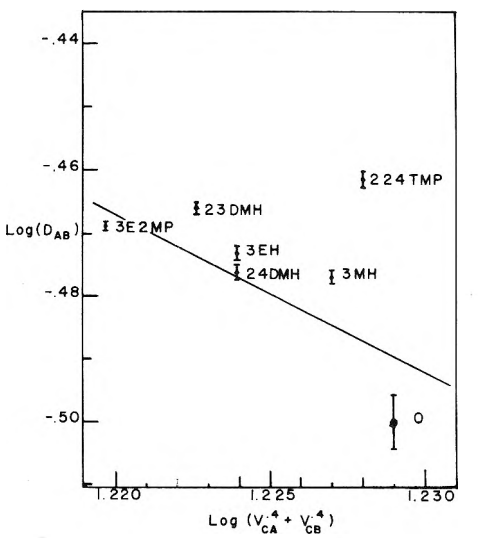

Figure 3. Log D_{AB} *vs.* log $(V_{CA}^{0.4} + V_{AB}^{0.4})$. Abbreviations have same meanings as in Figure 1.

One of the better estimating equations, according to Reid and Sherwood,[4] is that of Fuller, Schettler, and Giddings[17]

$$D_{AB} = \frac{1.00 \times 10^{-3} T^{1.75} (1/M_A + 1/M_B)^{1/2}}{p[(\Sigma_A V_i)^{1/3} + (\Sigma_B V_i)^{1/3}]^2} \quad (10)$$

T is the absolute temperature, M_A and M_B are the molecular weights of the two components, p is the pressure in atmospheres, and the V_i's are "atomic diffusion volumes to be summed over the atoms, groups, and structural features of each diffusing species."[17] Some atomic diffusion volumes are given in ref 13. At present, however, this equation cannot differentiate between isomers since the molecular weights and the summed atomic diffusion volumes are the same for all the isomers. It is desirable, then, to modify the above equation to take into account branching effects. Thus, for 3-methylheptane, we can write

$$\left[\left(\frac{A}{D_{AB}}\right)^{1/2} - V_{He}^{1/3}\right]^3 - \Sigma V_{C_7H_{15}} = V_{CH_3} \quad (11)$$

where A is a constant which, according to eq 10, depends on T, p, M_A, and M_B. Using the atomic diffusion volumes for He, C, and H given in ref 13, the *group* diffusion volume of $-CH_3$ is found to be 26.2 cm³. In the case of 2,4-dimethylhexane each methyl group has a group diffusion volume of 24.2 cm³. For 2,3-dimethylhexane the value for each methyl group is 20.5 cm³. With 2,2,4-trimethylpentane each methyl group contributed 18.7 cm³. Several remarks must be made here. (a) It is not certain that each of the methyl groups, in isomers where there are more than one, contributes equally to diffusion volumes. (b) As the number of methyl groups in the molecule increases the contribution of CH_3 decreases. (c) The contribution of each CH_3- group seems to be position dependent; *e.g.*, the 2,4- and 2,3-dimethylhexane. The latter two points seem consistent with the shielding processes suggested by Fuller, *et al.*[13] Further work is now being carried out to check (a) if the above values are qualitative and (b) if the position of the side chains are indeed important.

(31) See ref 16 on p 585 of our ref 4.
(32) K. A. Kobe and R. E. Lynn, *Chem. Rev.*, **52**, 117 (1953).
(33) D. F. Othmer and H. T. Chen, *Ind. Eng. Chem., Proc. Des. Devel.*, **1**, 249 (1962).

To summarize, branching causes a noticeable increase in the diffusion coefficients of the molecule in helium. This is due to a decrease in collision diameters and molecular volumes, since there seems to be a correlation between the D_{AB} values and critical volumes. It was demonstrated that as branching increases, so does the diffusion coefficient. Although straight chain molecules exist in the gas phase in a crumpled position, due to net attractive interaction between molecular segments, branched molecules have still lower collision cross sections. More work is needed in order to ascertain the exact effect of molecular structure on diffusion coefficients.

Vaporization Kinetics of Sodium Chloride. I. The Solid

Curtis T. Ewing* and Kurt H. Stern

Electrochemistry Branch, Naval Research Laboratory, Washington, D. C. 20375 *(Received August 29, 1972)*

Publication costs assisted by the Naval Research Laboratory

The vaporization rate of sodium chloride has been measured from 530° to the melting point. From 530 to 660° the vaporization rate is given by $\log J$ (mg cm^{-2} min^{-1}) = $11{,}297/T$ (°K) + 12.910. The vaporization coefficient is 0.7, independent of temperature and dislocation density (for densities between 10^5 and 10^7 cm^{-2}). Vaporization rates of (111) and (110) faces are equal to those of (100) since they facet to (100) during evaporation. Activation enthalpies and entropies are nearly equal to the corresponding thermodynamic quantities. Above 660° the vaporization coefficient decreases progressively with increasing temperature. These results are interpreted in terms of a two-step mechanism: (1) crystal → surface state, (2) surface state → vapor. Below 660° the surface concentration has its equilibrium value, above 660° the rate of vaporization is limited by step 1 and the surface concentration of the adsorbed species is reduced below its equilibrium value.

Introduction

Although the maximum rate at which solids and liquids may vaporize into a vacuum was derived a long time ago,[1-3] there has recently arisen renewed interest in the vaporization kinetics of crystalline solids.[4-8] The focus of most of these studies has been the mechanism whereby an atom or molecule in the crystal lattice reaches the vapor phase. Of particular importance in this vaporization path are the various intermediate surface states between the lattice and the vapor. Depending on the material, any of the intermediate steps may be rate determining; according to Searcy[8] the activated complex may even be the vapor molecule itself.

The surface of a solid is structurally complex. Various lattice defects, kinks and ledges, as well as a mobile adsorbed film constitute the "surface." By contrast, all the positions in a liquid surface are equivalent. It seems then, that a comparison of the vaporization kinetics of the same substance for both the solid and liquid states can provide a great deal of insight into the contribution of the surface features of the solid to the vaporization mechanism. For such a study it is necessary to choose a substance which vaporizes at a measurable rate in both the solid and liquid state. Moreover, since the maximum possible vaporization rate is a function of the equilibrium vapor pressure, this value must be well established over a wide range of temperature, and the vapor composition must be known. In addition, if a molecular theory is to be developed, the molecular properties necessary to construct partition functions should be known.

Sodium chloride fulfills all these requirements. Its vaporization kinetics has already been studied up to 650° by Lester and Somorjai[7] who were particularly interested in the effect of dislocations and dopants on the vaporization rate. In this work we report measurements to the melting point (800°). Particular care was taken to eliminate artifacts caused by, *e.g.*, a heat transport limited rate. Measurements of the major crystal faces were carried out and the effect of dislocation density, varying by a factor of 10^2, was studied.

Thermodynamic Data for Sodium Chloride

Since the theory of the kinetics of vaporization requires a knowledge of the parameters for vaporization under equilibrium conditions, a choice of the most reliable thermodynamic quantities is of considerable importance. Therefore the equilibrium partial pressures were calculat-

(1) H. Hertz, *Ann. Phys.*, **17**, 177 (1882).
(2) M. Knudsen, *Ann. Phys.*, **47**, 697 (1915).
(3) I. Langmuir, *J. Amer. Chem. Soc.*, **35**, 931 (1913).
(4) O. Knacke, R. Schmolke, and I. N. Stranski, *Z. Kristallogr.*, **109**, 184 (1957).
(5) G. M. Rothberg, M. Eisenstadt, and P. Kusch, *J. Chem. Phys.*, **30**, 517 (1959).
(6) J. P. Hirth and G. M. Pound, *J. Chem. Phys.*, **26**, 1216 (1957).
(7) J. E. Lester and G. A. Somorjai, *J. Chem. Phys.*, **49**, 2940 (1968).
(8) A. W. Searcy in "Chemical and Mechanical Behavior of Inorganic Materials," A. W. Searcy, D. V. Ragone, and U. Colombo, Ed., Wiley-Interscience, New York, N. Y., 1970, Chapter 6.

ed from data given for the solid and for the gaseous monomer and dimer in the JANAF tables.[9] These tables cover a wide temperature range and are based on a careful evaluation of data in the literature. Trimers and tetramers constitute only a very small fraction of the vapor molecules[10] and have therefore been neglected in all calculations.

In order to compare vacuum vaporization rates with those expected under equilibrium conditions the monomer/dimer ratio must be known. The degree of dimerization under free evaporization has been measured by Lester and Somorjai[7] and by Eisenstadt, Rao, and Rothberg.[11] Both of these studies report somewhat less dimerization than the equilibrium values in JANAF. However, their values are close to the equilibrium values of Miller and Kusch.[12] One must conclude, therefore, that although the monomer/dimer ratio is not known as accurately as one would like, the available evidence indicates the ratio to be independent of pressure. We have, therefore, made this assumption in our calculations.

Over the temperature range of this study the molar enthalpies of vaporization of monomer and dimer are essentially constant: ΔH_m° = 52.2 kcal, ΔH_D° = 56.9 kcal. The enthalpy for the formation of 1 mol of vapor of equilibrium composition from the requisite amount of solid is given by $\Delta H_V^\circ = N_m \Delta H_m^\circ + N_D \Delta H_D^\circ$ = 53.3 kcal, constant over the temperature range. The same result is obtained from the total pressure and the Clausius-Clapeyron equation. Since the monomer/dimer ratio is temperature dependent, ΔH_V° represents the vaporization of different weights of solid to give 1 mol of the equilibrium vapor at each temperature.

Experimental Method

Free evaporation rate data were obtained isothermally by heating small samples of sodium chloride cemented into graphite crucibles and determining the weight loss with time. The instrument used was an automatic recording Mettler thermoanalyzer which has been described in detail elsewhere.[13] All runs were performed under apparent vacuums of 10^{-5} Torr or lower.

Within the Mettler system the crucible was positioned on the top of a two-hole ceramic tube containing the thermocouple so that the hot junction was in direct contact with the base of the crucible. Equilibrium temperature readings from this couple were observed external of the Mettler system with a precision potentiometer. The thermocouples of platinum—platinum-10% rhodium were indirectly calibrated by the direct calibration at the National Bureau of Standards of couples from the same rolls of wire.

In order to define the isothermality of the furnace space in which the crucible is positioned, preliminary tests were made by installing fine-wire differential thermocouples on the walls of a 5/16-in. diameter metal crucible. For the high-temperature Mettler furnace (designated range 25–1600°) in the temperature range from 500 to 1000°, gradients of about 4°/cm were observed when the crucible was positioned on tubes of standard length. It was necessary for this study to lengthen the standard tube and the quartz mantle by 1 in. in order to reduce the thermal gradient to an acceptable value of less than 1°/cm.

The isothermality of the selected furnace zone was further confirmed by observing melting point breaks for large samples of sodium carbonate and sodium chloride. With the crucible positioned on a tube which is 1 in. longer than standard the observed melting points were within 1° of the accepted values.[14]

The Mettler balance is provided with 1- and 0.1-g standard weights for internal calibration of both ranges. To supplement this, all traces were frequently calibrated by adding and removing standard weights from a large crucible serving as a balance pan. The weight differences observed on the traces were generally within 0.03 mg of the standard weight for the 0.1-g range and within 0.3 mg for the 1.0-g range, and no correction factors were required. The chart speed was also periodically checked and no calibration or adjustment was required.

The majority of the crystals used were grown at the Naval Research Laboratory by the Czochralski technique. Those with low dislocation densities were grown with additional precautions by the same technique. Kinetic information was also obtained for optical grade single crystals procured from the Harshaw Chemical Co. and for polycrystalline samples obtained by shaping solidified melts of an ultrapure grade of powder from Alfa Inorganics. All boules or lots of sodium chloride were analyzed spectroscopically for cation impurities (Table I). The samples were generally of equal purity, with the major impurities being silicon and aluminum. No analysis was made for anion impurities, but the work of Lester and Somorjai[7] indicates that these are primarily ions containing bromine and oxygen which do not affect the vaporization rate.

The crystals to be vaporized were formed by cleaving with a razor blade or by cutting with diamond string saws, and faces were generally oriented to within ±0.5° of the desired crystallographic plane. Preliminary vaporization rates observed for (100) faces were found to be independent of surface preparation. Surfaces which were ground, cleaved, scraped, or cut gave identical rates. The test surface dimensions were measured with micrometers before and sometimes after the experiments. It has been suggested by several investigators[15,16] that diffusion pump oil and other contaminants such as water may affect the rate of vaporization. It is believed that the probability of significant coverage of the salt surface by contaminants is low. Even at the low temperature of 570° multiple layers of sodium chloride are stripped off in the time that one monolayer of adsorbed impurity would be expected to form.

Several possible procedures for mounting single crystals were considered. The technique of cementing with gold paste into graphite was selected because this crucible material has a high thermal conductivity and a high surface emissivity for the receipt of radiant energy from the furnace. A crucible as machined usually contained a few milligrams of volatiles and was prefired at 900° to constant weight. For each weight-loss determination, a crystal was cemented with its test surface flush with the top of the crucible and the assembly preheated for several hours to

(9) D. R. Stull and H. Prophet, *Nat. Stand. Ref. Data Ser., Nat. Bur. Stand.*, **No. 37** (1971).
(10) D. H. Feather and A. W. Searcy, *High Temp. Sci.*, **3**, 155 (1971).
(11) M. Eisenstadt, V. S. Rao, and G. M. Rothberg, *J. Chem. Phys.*, **30**, 604 (1959).
(12) R. C. Miller and P. Kusch, *J. Chem. Phys.*, **25**, 860 (1956).
(13) H. G. Wiedemann, *Chem. Ing. Tech.*, **36**, 1105 (1964).
(14) "Selected Values of Chemical Thermodynamic Properties," *Nat. Bur. Stand. (U. S.), Circ.*, **No. 500** (1952).
(15) G. A. Somorjai and J. E. Lester, "Progress in Solid State Chemistry," Vol. IV, Pergamon Press, Oxford, 1967.
(16) W. L. Winterbottom and J. P. Hirth, "Condensation and Evaporation of Solids," Gordon and Breach, New York, N. Y., 1964.

TABLE I: Comparison of Cation Impurities for Sodium Chloride from Different Sources[a]

Cation	Single crystal, first boule grown at NRL	Single crystal, second boule grown at NRL	Single crystal, low dislocation boule grown at NRL	Single crystal, from Harshaw	Solidified melt, Alfa ultrapure
Mg	1–10	<1	Nd[b]	<1	<1
Mn	<1	Nd	Nd	Nd	Nd
Pb	Nd	<1	Nd	<1	Nd
Si	10–100	10–100	10–50	10–100	10–100
Fe	1–10	<1	<1	1–10	<1
Al	100–1000	10–100	1–10	10–100	<1
Ca	1–10	1–10	10–50	1–10	1–10
Cu	1–10	<1	10–50	<1	<1
Ag	<1	<1	1–5	Nd	Nd
Li	<1	Nd	<1	1–10	<1
K	1–10	Nd	<1	<1	<1
Cs	<1	Nd	Nd	<1	<1
Rb	<1	Nd	Nd	<1	<1
Cr, Sr, Ba	Nd	Nd	Nd	Nd	Nd

[a] All values in ppm. [b] Not detected.

constant weight at 400°. This procedure removes any volatile impurities, such as water.

Since vaporization rates are so often said to be influenced by trace contaminants, a number of preliminary and comparative vaporization tests were made at temperatures below 600° using crystals tightly wrapped with gold, platinum–10% rhodium, and palladium foils. It was shown quite conclusively in this manner that rates observed with crystals cemented into graphite were not influenced by the graphite, by the gold, or by any other material in the cementing paste.

Dislocation densities of sodium chloride were determined with the method used in the study of Lester and Somorjai,[7] by counting etch pits formed chemically on (100) faces. The same etching solution of mercuric chloride in ethyl alcohol was used and a proportionality factor of unity was arbitrarily assumed between the etch-pit count and the dislocation density.

Results

A. Collisional Effects and the Rate of Vaporization. It was found experimentally, as would be expected from the work of Knacke, *et al.*,[4] that the steady-state, isothermal rate of vaporization from a single crystal decreased slowly but systematically as the vaporizing surface receded from the top of the crucible. This decrease in rate, which results from the random reflection of molecules off the walls back onto the vaporizing surface, is a function of l/a, and can be accurately calculated at any value of l/a from molecular-flow theory and Clausing factors.[17] The true steady-state rate of vaporization for any isothermal experiment was obtained either by extrapolating observed rates to zero time or by recording the initial rate. Since the decrease in rate with time was slow for most of the temperature range, the initial rate was quite satisfactory.

It was also recognized that a small fraction of the vapor molecules may be reflected back onto the vaporizing surface from the walls of the quartz tube surrounding the sample. The studies of Coleman and Egerton[18] indicate that this effect should not have reduced the observed rate by more than 1%, and no correction was applied. As an additional precaution, comparative rate determinations were made at temperatures above 750° with crystals cemented into the reverse side of the graphite crucible so that they faced downward, toward the vacuum system. Rates were independent of the crystal directions and this argues against any significant rate reduction from the presence of vapor clouds or from other factors associated with instrument parameters and also argues that the crucibles were uniform in temperature from top to bottom.

For the rather extensive study of the effect of dislocation density, orientation, roughness, and other factors on the kinetics of the vaporization of sodium chloride, most of the rate information was obtained with square vaporizing surfaces (0.63 cm on a side) at temperatures below 665°. For these measurements apparent Knudsen numbers (based on equilibrium flux quantities) were well above unity and molecular-flow conditions should have been predominant in the vapor flux. However, for the other phase of the experimental study at higher temperatures from 665° to the melting point, observed flux rates were as high as 50 mg cm^{-2} min^{-1}; and Knudsen numbers for the same nominal sample size were below unity. Along with the higher rates in this range, significant curvature was observed in the Arrhenius plot (Figure 1) with vaporization coefficients defined by eq 4 dropping from about 0.7, the nearly constant value at lower temperatures, to a value of about 0.2 near the melting point. The possibility that intermolecular collisions contributed to this reduction in rate could not be overlooked.

Under the conditions of our experiments, the flux from the surface of a salt crystal (except for possible condensation of any molecules reflected back onto the vaporizing surface) is analogous to the mass flow of a gas through an orifice into an evacuated space. It has been shown conclusively in studies by Searcy and Schulz[19] and by Carlson, *et al.*,[20] that mass flows in the intermediate and the near hydrodynamic regions are always equal to or larger than those which would be predicted from the Hertz-Knudsen equation. It is, therefore, unlikely for our experimental range that gas-phase collisons can restrict the mass flow from a salt crystal.

(17) S. Dushman, "Scientific Foundations of Vacuum Technique," Wiley, New York, N. Y., p 90.
(18) F. F. Coleman and A. Egerton, *Phil. Trans. A*, **234**, 177 (1934).
(19) A. W. Searcy and D. A. Schulz, *J. Chem. Phys.*, **38**, 772 (1963).
(20) K. D. Carlson, P. W. Gilles, and R. J. Thorn, *J. Chem. Phys.*, **38**, 2725 (1963).

The conclusion reached above was further confirmed by experimental tests. Vaporization rates for square crystals 3.5 and 7.7 cm on edge were measured (and compared) at temperatures above 740°. If intermolecular collisions were important, the effective vaporization rate per unit area should vary with the linear dimensions of the vaporizing surface,[21] whereas the observed rate was found to be independent of the crystal dimension. Perhaps the most striking experimental evidence is provided by our preliminary study (to be reported in a subsequent paper) of the vaporization kinetics of liquid sodium chloride. In these experiments, rates up to 500 mg/cm² min (a magnitude greater than the maximum reported for the single crystal) were observed. If the rate of vaporization from the solid were significantly limited by vapor cloud formation and intermolecular collisions, it would not be possible to obtain the higher rates observed for the liquid.

B. Surface Topography and the Rate of Vaporization. The effect of surface structure on rate was studied generally only below 665°. The macroscopic roughness of vaporizing surfaces was observed at room temperature by thermally quenching samples undergoing free evaporation. The degree of roughness was characterized by comparison of surfaces at a magnitude of 300×.

Roughness at this magnification was found to be a function both of the crystallographic plane, and the precision of orientation. Only one of the three possible orientations, the (100) face, had a smooth vaporizing surface; and even this face was smooth only when it was within about 1° of the true crystallographic plane. Surface roughness with an estimated absolute area at least double the geometric value was readily introduced by cutting faces a few degrees from the true orientation.

At temperatures below about 665°, evaporation topographies found to be associated either with deviations from the (100) face or with nonuniform evaporation from the face, were similar to those described by Budke[22] and Rosenblatt.[23] The macroroughness (visible at 300×) usually consisted of square-cornered pits and ledges with interconnecting multistepped terraces. Electron micrographs of flat evaporating surfaces revealed no ledges higher than 50 Å. This absence of microscopic fine structure also agrees with Budke's[22] findings.

The ability to introduce roughness in the (100) face permitted a determination of the effect of absolute area. Vaporization rates were determined experimentally in the temperature range from 530 to 665° for a number of samples with both smooth and rough vaporizing surfaces, and the rate was found to be completely independent of the apparent degree of roughness. In addition, massive roughness was generated by drilling 50 0.4-mm holes into the surface of single crystals to a depth of 2 mm. Rates observed for this type of surface at 563 and at 755° were the same as those observed for nominal (100) faces. The fluxes reported in this article, therefore, are based on geometric areas and represent absolute quantities.

Structure associated with both the (110) and (111) surfaces appeared to be independent of the precision of orientation. The degree and size of the roughness parameters did vary with temperature and other factors, but there was always a characteristic shape and form for each orientation. The (110) surface had distinctive rod-like structures (Figure 2) made up of long narrow ridges and multistep terraces. For each (110) surface the (100) planes are oriented either 45 or 90° from this surface. The characteristic ridges were always parallel to the planes at 45° and perpendicular to those at 90°. It will be shown later that this has significance from the standpoint of faceting. The (111) vaporizing surface was similar to that described by Lester and Somorjai[7] with a major portion covered by small projecting crystallites.

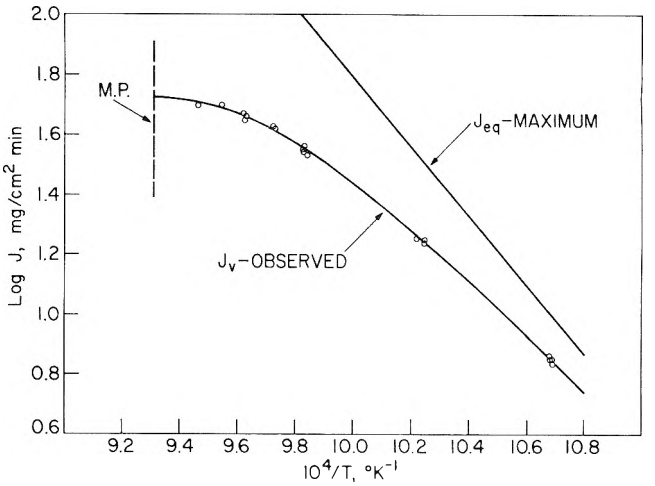

Figure 1. Arrhenius plot of experimental vaporization fluxes for sodium chloride crystals at temperatures from 660 to 785° and comparison with maximum equilibrium fluxes.

Evaporating (110) and (111) surfaces, when thermally quenched from temperatures above 700°, were smoother than the macrostructures observed at lower temperatures. This is consistent with sintering theory and the proposition that surfaces at temperatures just below the melting point are covered by a liquid-like film.[24] The thermal quenching was performed in the Mettler system, and the shallow structure observed may have been introduced by evaporation at lower temperatures during the quench.

C. Heat Transfer Processes and the Rate of Vaporization. Vaporization is an endothermic process and, in experimental studies involving rapid evaporation rates, control is often not exerted by the vaporizing step but by the heat-transfer process from the source of the heat to the vaporizing surface.[25-27] To eliminate this possibility, a series of additional measurements, some preliminary to the final results reported in this paper, were performed to show that the radiant heat-transfer rate to the crucible was sufficient to offset the heat loss due to vaporization and that the rate of heat transfer within the crucible, interface, and crystal was sufficient to eliminate errors from self-cooling effects.

The influence of radiant heat transfer to the crucible was investigated at 560 and 755° by increasing the external radiation surface of the graphite crucible from 14 to 40 cm² and comparing observed vaporization rates. The rate was found to be independent of the surface area of the crucible at both temperatures.

To study the influence of self-cooling on observed vaporization rates, single crystals of sodium chloride were

(21) G. Burrows, *J. Appl. Chem.*, 7, 375 (1957).
(22) J. Budke, *J. Amer. Ceram. Soc.*, **51**, 238 (1968).
(23) G. M. Rosenblatt in "Heterogeneous Kinetics at Elevated Temperatures," G. R. Belton and W. L. Worrell, Ed., Plenum Press, New York, N. Y., 1970, p 209.
(24) H. G. Jellinek, *J. Colloid Interface Sci.*, **25**, 192 (1967).
(25) A. W. D. Hill, *Chem. Eng. Sci.*, **23**, 297 (1968).
(26) G. V. Narsimhan, *Chem. Eng. Sci.*, **16**, 7 (1961).
(27) K. H. Stern and E. L. Weise, *Nat. Stand. Ref. Data Ser., Nat. Bur. Stand.*, **No. 30**, (1969).

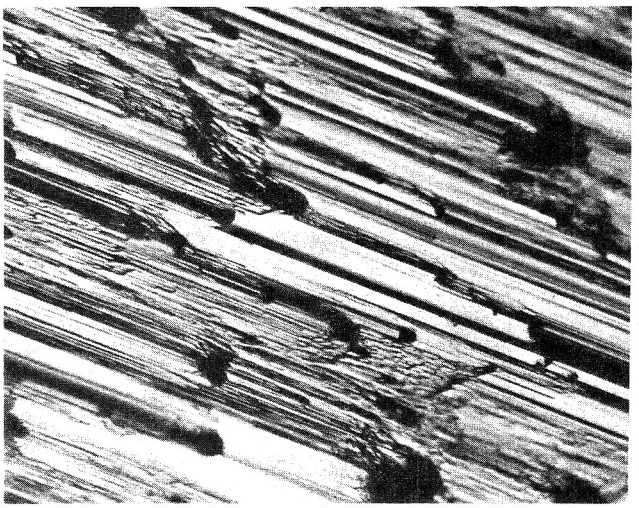

Figure 2. Typical structure of a (110) surface vaporizing into a vacuum at 560°.

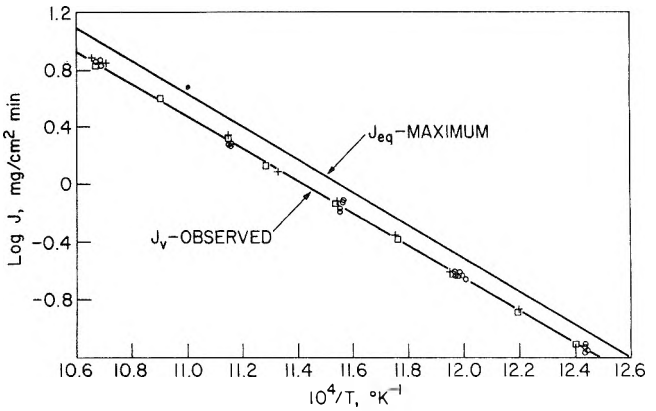

Figure 3. Arrhenius plot at low temperatures of experimental vaporization fluxes from (100) surfaces of sodium chloride crystals with different dislocation densities and comparison with maximum equilibrium fluxes: O, crystals with normal dislocation densities (2–5 × 10^6); □, crystals with low dislocation densities (2 × 10^5); +, crystals with high dislocation densities (>1 × 10^7).

cemented into graphite crucibles and holes were drilled through the graphite into the crystals themselves, so that the measurement thermocouple extended into the crystal to a point within 0.2 or 0.3 cm of the vaporizing surface. Rates observed in this manner at temperatures just below the melting point were compared to those obtained in the normal manner, and no difference was ever observed. Significant self-cooling was therefore absent.

D. Dislocation Density and Rate of Vaporization. The (100) face, since it is the only one for sodium chloride which exhibits a relatively smooth, facet-free vaporizing surface, was used for the study of the effect of dislocation density. As the initial step in this study and in a study of the effect of crystal orientation, rate information for the (100) face was obtained for a large number of crystals in the temperature range from 530 to 665°. These crystals had normal dislocation densities (2–5 × 10^6 etch-pit counts) and were obtained from two of the boules grown at this Laboratory and from Harshaw optical crystals. The size of the vaporizing surface was nominally about 0.40 cm^2, but sample thickness varied from 0.2 to ~0.7 cm. The test faces on most of the crystals were cut and oriented by X-ray, but a few of the (100) surfaces were formed by cleaving.

Samples with high dislocation densities (>1 × 10^7 etch-pit counts) were prepared by plastically deforming Harshaw crystals, and samples with low dislocation densities (~2 × 10^5 etch-pit count) were cleaved with sharp blades from the special crystals grown at this laboratory. Samples with the different dislocation densities were of comparable purity (see Table I). Vaporization rates were determined from 530 to 665° for several crystals of each type.

In Figure 3 vaporization rates for crystals of low, normal, and high dislocation densities are plotted on an Arrhenius-type plot. It is apparent that all the data are fitted by the same straight line, *i.e.*, the vaporization rate is independent of dislocation density. On the same figure, a curve representing maximum rates at equilibrium is presented for comparison. The coefficient of vaporization appears to vary uniformly from about 0.76 at 530° to 0.70 at 660°. However, the coefficient is independent of temperature within the precision of all the measurements involved in obtaining it. For a more precise comparison Arrhenius activation energies and preexponential factors were calculated by least-squares treatment of the data for samples with low, normal, and high dislocation densities with the Arrhenius equation in the form

$$\ln J\ (\text{mg cm}^{-2}\ \text{min}^{-1}) = \ln A - \Delta E_a/RT \quad (1)$$

Values are shown in Table II. Within experimental error the values are independent of dislocation densities which differ by two orders of magnitude. These results are in marked contrast to those of Lester and Somorjai[7] who reported a vaporization coefficient of unity for crystals with dislocation densities near 10^7 cm^{-2} and a coefficient of 0.5 for dislocation densities of 2 × 10^6 cm^{-2}. Since a healing of dislocation densities in LiF had been reported to result from thermal cycling,[28] we repeated the etch-pit counts on several samples after the thermal cycling involved in the rate measurements. Although the reproducibility of the counting procedure is no better than a factor of 2, no change in dislocation density was observed which could be attributed to thermal cycling. At present we have no explanation for the difference in the results.

E. Vaporization Rates from (110) and (111) Faces of Crystals with Normal Dislocation Densities. Steady-state vaporization rates were determined from 530 to 665° for several crystals accurately oriented with (110) and (111) faces. The results are compared in an Arrhenius plot (Figure 4) with smoothed results for the (100) face. It is clearly shown in Figure 4 and in Table II that free evaporation rates are the same for all three crystallographic planes.

F. Vaporization Rates from (100) Faces at Higher Temperatures. Experimental results for a large number of different crystals in the temperature range from 665 to 785° are presented graphically in Figure 1 where the logarithm of the observed flux is plotted *vs.* the reciprocal temperature. Crystals were generally cleaved or cut (with orientation to (100) faces) from the boules grown at this laboratory or from Harshaw optical crystals. All were of similar purity and similar dislocation density.

The majority of the experiments were performed with single crystals cemented into graphic crucibles. However, as was pointed out in the section on experimental methods, several parameters were systematically varied to test

(28) D. L. Howlett, J. E. Lester, and G. A. Somorjai, *J. Phys. Chem.*, **75**, 4049 (1971).

TABLE II: Coefficients in Arrhenius Equation[a] for the Rate of Vaporization of Sodium Chloride Single Crystals Showing the Effect of Dislocation Density and Crystallographic Orientation

Crystal type	Arrhenius activation energy, ΔE_a, kcal mol^{-1}	Log of preexponential factor, ln A
(100) face normal dislocation densities ($2-5 \times 10^6$)	51.69 ± 0.44[b]	29.73 ± 0.26[c]
(100) face low dislocation densities ($2-3 \times 10^5$)	52.91 ± 0.65	30.38 ± 0.38
(100) face high dislocation densities ($>1 \times 10^7$)	51.30 ± 0.74	29.53 ± 0.43
(110) face normal dislocation densities	50.93 ± 1.79	29.33 ± 1.05
(111) face normal dislocation densities	53.53 ± 1.38	30.79 ± 0.80

[a] Equation: $\ln J$ (mg cm^{-2} min^{-1}) = $\ln A - \Delta E_a/RT$. [b] Variance.

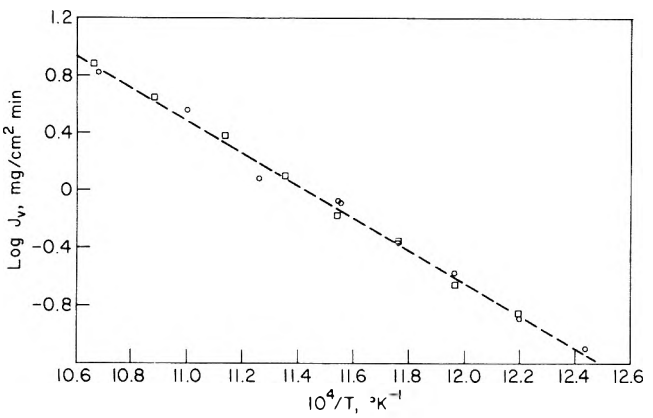

Figure 4. Arrhenius plot at low temperatures of experimental vaporizat on fluxes from (110) and (111) crystallographic surfaces of sodium chloride crystals and comparison with curve for (100) surface: O, (110) surface; □, (111) surface.

the validity of the results. The area of the vaporizing surface was varied from 0.12 to 0.66 cm^2 and the external area of the graphite crucible was varied from 14 to 40 cm^2. Crystals were also vaporized in an upside-down position. Holes were drilled in some crystals and the temperature measuring thermocouple inserted into the crystal itself. Roughness was varied by drilling small holes into the test surface. One experimental point at a temperature of 765.7° represents vaporization from a cylindrical sample, shaped from a solidified melt of the Alfa Inorganics powder, and cemented with gold paste into a finned palladium crucible. These parameter changes were necessary at the high vaporization rates to test for any effect from intermolecular collisions, from slow heat-transfer rates, or from crystal self-cooling. All observed rates were satisfactorily represented by a single curve, and no significant deviation was associated with any of the parameter changes.

In the temperature region below 665°, the free evaporation rate is less than the maximum rate calculated from the Hertz-Knudsen equation (see eq 5); but the vaporization coefficient, the activational energy, and other kinetic quantities are essentially independent of temperature. This is not true at higher temperatures. Above 665°, the steady-state rate of vaporization (see Figure 1) falls away progressively from the maximum equilibrium rate in a manner similar to that observed by Davy and Somorjai[29] for ice crystals.

The flux rates in the temperature range from the melting point down to 665° are represented by the following least-squares equation

$$\log J \text{ (mg cm}^{-2} \text{ min}^{-1}) = -262.0687 + 77.3610(10^4/T) - 7.4922(10^4/T)^2 + 0.2391(10^4/T)^3 \quad (2)$$

and the apparent coefficient of vaporization by

$$\log \alpha = -275.3246 + 78.5083(10^4/T) - 7.4922(10^4/T)^2 + 0.2391(10^4/T)^3 \quad (3)$$

where

$$\alpha = J/J_{eq} \quad (4)$$

J is expressed in mg cm^{-2} min^{-1} and J_{eq} is given by the Hertz-Knudsen equation

$$J_{eq} = \Sigma[N_i P_{eq}(2\pi RT/M_i)^{-1/2}] \quad (5)$$

where the summation extends over all species in the vapor phase.

Discussion

The most notable feature of the log J *vs.* $1/T$ plot is the essentially constant slope from 530 to ~660° and the progressively decreasing slope from that temperature to the melting point (Figure 1). Such a change in slope is generally related to a change in mechanism, but we defer a discussion of this and consider first the results below 660°.

We note first that the vaporization rates of (100), (110), and (111) faces are essentially the same. Vaporization from (110) (Figure 2) and (111) faces results in faceting to (100) faces, so that the steady-state vaporization proceeds from (100) surfaces in all three cases. This possibility was suggested by Stranski[30] many years ago. For the (110) face there is only a single direction (perpendicular to those (100) planes that are 90° from the (110) face) which permits faceting to long continuous ledges as a result of molecules breaking away from ledges. The long rods and ledges (Figure 2) observed on quenched (110) faces have

(29) J. G. Davy and G. A. Somorjai, *J. Chem. Phys.*, **55**, 3624 (1971).
(30) I. N. Stranski, *Z. Phys. Chem. B*, **11**, 342 (1931).

TABLE III: Activational and Thermodynamic Enthalpies for the Vaporization of Sodium Chloride from 530 to 665°

	Monomer	Dimer	Equilibrium composition
ΔH^*, kcal mol^{-1}	51.1	56.2	52.4
ΔH_{vap}°, kcal mol^{-1}	52.2	56.9	53.3
ΔS^*, cal mol^{-1} deg^{-1}	27.8	30.3	29.4
ΔS°, cal mol^{-1} deg^{-1}	33.0	35.8	33.8

been shown experimentally to be preferentially aligned in this direction. For the (111) face, faceting to (100) faces during vaporization should produce pyramids, and projecting crystallites are observed on these surfaces.

The formation of (100) surfaces from (110) and (111) planes results in an increase of real surface area. Nevertheless, as seen from Figure 4, and also from the experiment in which holes were drilled into a crystal to increase the real surface area by ~20%, the vaporization rate depends only on the geometric (projected) surface area. As pointed out by Lester and Somorjai[7] based on the geometric analysis of Melville,[31] when $\alpha = 1$, the initially larger flux from a rough surface is reduced to the smooth surface value because molecules vaporizing from one part of the surface can recondense on another. Melville[31] further showed that unless α is very small and the angle at the base of the cracks also very small, this conclusion is nearly correct for values of α well below unity.

The generally accepted mechanism for the evaporation of crystals[4,6-8] consists of a two-step process: (1) molecules move from positions in the lattice, usually considered to be at some repeatable step, *e.g.*, a "half-crystal position,"[4] to some point on the surface; (2) molecules move from the surface into the vapor (desorption). Which of these steps is rate determining will depend on (a) the energies for each of the steps and (b) the concentration of molecules available for reaction.

Activational enthalpies can be obtained from[32]

$$\frac{\mathrm{d} \ln \alpha}{\mathrm{d}(1/T)} = \frac{-(\Delta H^* - \Delta H_v^\circ)}{R} - \frac{T}{2} \qquad (6)$$

and activational entropies from[32]

$$J = e^{\Delta S^*/R} e^{-\Delta H^*/RT} \qquad (7)$$

Our results show that $\mathrm{d} \ln \alpha/\mathrm{d}(1/T) = 0$.

The activational parameters for the formation of 1 mol of the equilibrium vapor as well as for the individual monomer and dimer species can also be obtained through use of Langmuir pressures and the assumption that the monomer/dimer ratio is independent of pressure. Then

$$J_i = [N_i\sqrt{i}/\Sigma(N_i\sqrt{i})]J \qquad (8)$$

$$P_i^* = J_i(2\pi RT/M_i)^{1/2} \qquad (9)$$

$$\Delta H_i^* = (\mathrm{d} \ln P_i^*/\mathrm{d}T)RT^2 \qquad (10)$$

$$\Delta H^* = N_m \Delta H_m^* + N_D \Delta H_D^* = [\mathrm{d} \ln (P_m^* + P_D^*)/\mathrm{d}T]RT^2 \qquad (11)$$

The results are shown in Table III. The close agreement between the activational and equilibrium values is consistent with a model in which the activated complex is essentially a gas molecule and the surface concentration is approximately equal to the equilibrium concentration. Searcy[8] has described the case when $\alpha < 1$ and $\Delta H^* \simeq \Delta H^\circ$ as one limited by the number of suitable desorption sites or by the probability that atoms which form the product will collide in the adsorption layer. Lester and Somorjai[7] have argued that the large adsorption energy calculated by Hove[33] for KCl ion pairs on a KCl surface suggests that such ion pairs on removal from the lattice only travel a few lattice spacings before being desorbed. If this is so then the equilibrium surface concentration is not uniformly distributed, but piled up near ledges. In that case the desorption rate might well be limited by the number of suitable sites. The fraction of the surface covered by adsorbed molecules can be calculated from a theory developed by Gregory.[34] For NaCl at 900°K the concentration of activated molecules is 8.2×10^{-19} mol cm^{-2}, whereas the normal surface concentration is 4.8×10^{-10} mol cm^{-2}. Hence the fraction of surface covered is only 1.7×10^{-9}, and intermolecular collisions on the surface will depend on the degree to which the adsorbed molecules are concentrated near the ledges. Thus of the two possibilities mentioned by Searcy the less-than-unity value of α is more plausibly accounted for by a paucity of desorption sites. However, we do not yet know precisely what the characteristics of a desorption site are. Any detailed model should, in any case, be consistent with a surface in which the actual surface is higher in chloride ion than expected from the overall stoichiometry.[35]

The distance between ledges is determined by the dislocation density. Thus it is reasonable to argue[7] that as the latter decreases the rate will eventually decrease. There are, however, no theoretical predictions as to the relation between dislocation density and the value of α to be expected. Thus there is at present no *a priori* method for deciding whether our results or those of Lester and Somorjai[7] are more likely to be correct. Both sets of results give the same ΔH^*, but our results give $\alpha = 0.7$, independent of dislocation density between 2×10^5 and $>10^7$ cm^{-2}, whereas they obtain $\alpha = 1$ for 10^7 cm^{-2} and $\alpha \simeq 0.5$ for a density of 2×10^6 cm^{-2}. These differences are probably outside the experimental errors of both studies. For example, the *maximum* scatter of all our data is ±10%, but most of them fall within ±5%. If we regard both sets of results as *experimentally correct*, it follows that the NaCl used in the two studies must have been different in some way which is not yet well understood. (However, we obtained the same results with crystals from several different sources.) It is already well established[7,29] that small concentrations of divalent cationic impurities markedly affect the rate. Conceivably, there are other effects which determine the detailed features of the surface stoichiometry.

In any case, both sets of results disagree with those of Rothberg, Eisenstadt, and Kusch[5] who reported $\alpha = 0.2$, and activation enthalpies considerably in excess of thermodynamic values.

The high-temperature vaporization (above 660°) is characterized by a continuously decreasing slope of the log J *vs.* $1/T$ plot (Figure 1). Since this behavior at high vaporization rates can be produced so readily by several artifacts as well as by changes in the vaporization mecha-

(31) H. W. Melville, *Trans. Faraday Soc.*, **32**, 1017 (1936).
(32) J. H. Stern and N. W. Gregory, *J. Phys. Chem.*, **61**, 1226 (1957).
(33) J. E. Hove, *Phys. Rev.*, **99**, 480 (1955).
(34) N. W. Gregory, *J. Phys. Chem.*, **67**, 618 (1963).
(35) G. C. Benson, P. I. Freeman, and E. Dempsey, *Advan. Chem. Ser.*, **No. 33** (1961).

nism, the former possibility was carefully examined. The probabilities of rate control by heat-transfer processes and of temperature error (due to self-cooling of crystal surfaces) were reduced to low values by a series of experiments (previously described) in which the surface area of the graphite and the position of the thermocouple were varied. Any probability of rate control by cloud formation above the vaporizing surface (*i.e.*, molecules are not removed rapidly enough to prevent the scattering of molecules back onto the surface due to gas-phase collisons) was also effectively eliminated by performing another series of experiments in which rates were compared for crystals with different dimensions and with different positions. Since all known instrumental artifacts were eliminated, we conclude that the changing slope above 660° is related to the mechanism of vaporization.

To see if this mechanism in any way involved dimerization in the vapor state, we carried out preliminary vaporization measurements on CsI, a salt whose vapor is entirely monomeric.[5] Although the vaporization rate of CsI is much lower than that of NaCl, a similar curvature of the log J *vs.* $1/T$ plot was observed as the melting point was approached. This provides further evidence that the curvature is not caused by a vapor cloud and also eliminates dimerization as a factor.

At the higher temperatures, α decreases abruptly toward (an extrapolated values of) 0.15 at the melting point. In terms of the two-step mechanism (crystal $\rightarrow$ (1) adsorbed surface state $\rightarrow$ (2) vapor), the rate constant of reaction 2 increases more rapidly than that of reaction 1 so that the surface concentration of adsorbed species drops increasingly below its equilibrium value and the net vaporization rate becomes progressively limited by the rate at which absorbed species can be supplied from crystal positions. If this interpretation is correct a discontinuity might be expected at the melting point with much higher rates above this temperature.

Acknowledgments. We are greatly indebted to Dr. Philipp H. Klein for growing single crystal sodium chloride for us; special low dislocation density crystals were supplied by Dr. J. W. Davisson. Crystals were oriented crystallographically by Dr. F. L. Carter and Mr. W. C. Sadler, and analyzed spectroscopically by Mr. S. H. Cress.

Helpful discussions with Drs. E. R. Plante and R. C. Paule of the National Bureau of Standards are also acknowledged.

Appendix I. Nomenclature

a	minimum linear dimension of vaporizing surface
A	empirical preexponential factor in Arrhenius equation
ΔE_a	activation energy in Arrhenius equation
ΔH	enthalpy change, kcal mol^{-1}
J	flux, mg cm^{-2} min^{-1}
$\bar{J}$	Flux, mol cm^{-2} sec^{-1}
l	mean free path
M	molecular weight
N	mole fraction in vapor
P	vapor pressure
R	gas constant
T	absolute temperature, °K
ΔS	entropy change
α	vaporization coefficient

Subscripts

D	quantity for dimeric species
eq	quantity at equilibrium
i	any molecular species
m	quantity for monomeric species
V	vaporization quantity

Superscripts

*	activation quantity or Langmuir pressure
°	standard state, 1 atm for gas

Semiempirical Unrestricted Hartree–Fock Treatment for Trapped Electrons in Water, Ammonia, and Hydrogen Fluoride

Shingo Ishimaru, Hiroshi Kato,[1] Tokio Yamabe, and Kenichi Fukui*

Department of Hydrocarbon Chemistry, Kyoto University, Kyoto, Japan and Department of General Education, Nagoya University, Nagoya, Japan *(Received January 3, 1973)*

The electronic states of solvated electrons in water, ammonia, and hydrogen fluoride and the related properties of solvent molecules are investigated. The cavity formed by four or six solvent molecules is then considered and, in each case, two models showing the orientation of a solvent molecule are introduced. In calculation, the semiempirical unrestricted Hartree–Fock treatment based on the INDO approximation is used and three methods for the selection of the basis set are examined. Consequently, with two of the methods which use not only valence AO's of solvent molecules but also hydrogen-like AO's located at the cavity center, the solvation energies and the excitation energies in water and ammonia and the photoelectric threshold in ammonia can be appropriately estimated and, noticeably, the absolute value of the proton spin density of water deduced from the esr data and the negative proton spin density of ammonia found in the nmr experiment are also obtained. From the aspect of spin density, the cavity will probably be in favor of the configuration in which only one of the hydrogen atoms of a solvent molecule points toward the cavity center. Calculated dipole moments of solvent molecules describe the polarization mechanism of the molecules by a trapped electron, being consistent with the polaron theory. Finally, the electron distributions of the hydrated electron and water molecules and the potential formed by water molecules are drawn and the results inherent in the system of assembled molecules are found, justifying the conventional cavity model.

I. Introduction

The solvated electron in a polar medium has been extensively investigated by many workers and there is a great deal of information concerning the physical and chemical properties of solutions with the excess electron.[2a] Particularly, recent developments of various experimental techniques make it possible to observe the delicate interactions between the trapped electron and solvent molecules.[2b-4]

On the other hand, several theories which throw light on these facts have been proposed.[5-8] In the cavity model, which was first proposed by Ogg,[5] an excess electron is assumed to be confined within a spherical cavity in solution. This model was developed by Jortner[6] with use of the polaron theory[9] as the continuum model and, after that, the structural model[7] by Natori and Watanabe and the semicontinuum model[8] by Fueki, *et al.*, followed. Nowadays, it is supposed that, in polar solvents, most of the excess electrons would be present in cavities. The continuum model uses only long-range polarization potentials of the medium and does not explicitly consider the structure of the solvated electron; the wave function for an excess electron is approximated by the hydrogen-like atomic orbital (AO). The structural model treats only electrostatic short-range attractive interactions between an excess electron and four water molecules pointing one of the OH bonds of each molecule tetrahedrally toward the cavity center; the wave function is taken as the linear combination of four 1s-like AO's of the inside hydrogen atoms. This model is further investigated by Weissmann and Cohan using the unrestricted CNDO/2 method[10] and they asserted that the model is unfavorable compared with the normal ice model. The recent INDO calculation by Howat and Webster,[11] however, seems to support the above tetrahedral model. The semicontinuum model includes both the long-range polarization potential and short-range attractive interactions; the wave function is similar to that of the continuum model.

As pointed out in our previous paper,[12] in spite of the great success brought about by the above treatments, there still remain several interesting problems to be elucidated. According to the proton magnetic resonance study of sodium–ammonia solution,[2b] in particular, the spin density on the proton of the ammonia molecule is small and negative. This is almost undoubtedly caused by the spin polarization of the electrons of solvent molecules by an excess localized electron. Moreover, Bennett, *et al.*,[3] reported the esr spectrum of the trapped electron in a deposit of ice and alkali metals at 77°K, in which seven equally spaced (5.6 ± 0.5 G) hyperfine lines were resolved. They concluded that the electron is trapped in a cavity formed by six water molecules orienting one of the OH bonds toward the center. Ohno, *et al.*,[4] assert that the observed multiplet is not the septet but the quintet with the

(1) Department of General Education, Nagoya, University.
(2) (a) R. F. Gould, *Advan. Chem. Ser.*, **No. 50** (1965); (b) T. R. Hughes, Jr., *J. Chem. Phys.*, **38**, 202 (1963).
(3) J. E. Bennett, B. Mile, and A. Thomas, *J. Chem. Soc. A*, 1502 (1969). The deduced proton spin density of water molecules is 0.011 ± 0.001 in the absolute value.
(4) K. Ohno, I. Takemura, and J. Sohma, *J. Chem. Phys.*, **56**, 1202 (1972). The deduced proton spin density of water molecules is 0.009 ± 0.001 in the absolute value.
(5) R. A. Ogg, *Phys. Rev.*, **69**, 668 (1946).
(6) (a) J. Jortner, *J. Chem. Phys.*, **27**, 823 (1957); (b) *ibid.*, **30**, 839 (1959).
(7) M. Natori and T. Watanabe, *J. Phys. Soc. Jap.*, **21**, 1573 (1966); M. Natori, *ibid.*, **24**, 913 (1968).
(8) (a) K. Fueki, Da-Fei Feng, and L. Kevan, *J. Phys. Chem.*, **74**, 1976 (1972); (b) Da-Fei Feng, K. Fueki, and L. Kevan, *J. Chem. Phys.*, **57**, 1253 (1972).
(9) L. Landau, *Phys. Z. Sowjetunion*, **3**, 664 (1953).
(10) M. Weissmann and N. V. Cohan, *Chem. Phys. Lett.*, **7**, 445 (1970).
(11) G. Howat and B. C. Webster, *J. Phys. Chem.*, **76**, 3714 (1972).
(12) S. Ishimaru, H. Kato, T. Yamabe, and K. Fukui, to be submitted for publication.

hyperfine splitting of 4.7 ± 0.5 G and that the electron is trapped in a cavity surrounded tetrahedrally by four neighboring water molecules pointing one of the OH bonds toward the center. It should be noted that these observed values of hyperfine splitting show that the absolute value of the proton spin density will be *ca.* 0.01. The above values detected by nmr and esr are quite important data concerning the electron trapping center. Nevertheless, there has been no theoretical investigation which interprets the proton spin density including its sign.[13-15] In particular, the theoretical treatments using the electrostatic potential[6-8] are essentially unable to describe the spin polarization mechanism, because no interaction between an excess electron and the electrons which belong to the solvent molecules is explicitly included.

Therefore, in the present paper, we will investigate the electronic states of solvated electrons in water, ammonia, and hydrogen fluoride and the related properties of the solvent molecules by the use of the UHF treatment based on the INDO approximation. Furthermore, the electron distributions of the hydrated electron and water molecules and the potential formed by water molecules are visualized in several diagrams and discussed. Parameters applied in the calculation are also examined in detail.

II. Models

To describe the microscopic structure of the hydrated electron, two ice-like models have been introduced. The one is the quasitetrahedral model by Natori and Watanabe[7] which is formed by four water molecules with one OH bond tetrahedrally oriented around the cavity center and the other is the natural cavity model by Nilsson[16] which is formed by twelve water molecules in the first coordination shell. In the latter model, six water molecules in the first coordination shell are nearer to the cavity center than the other six molecules and hence the electron in this cavity will be considered to interact mainly with these inner solvent molecules. According to other investigations[8,17] also, the number, four or six, of solvent molecules in the first coordination shell is found to be favorable. In the present calculation, referring to the above models and the experimental suggestions,[3,4] we will examine the cavity formed by four or six water molecules coordinating with T_d or O_h symmetry in regard to oxygen atoms. Furthermore, two models are introduced and compared in each case for a more detailed description of the molecular rearrangement and an examination of the experimental result: namely, model I, where only one of the hydrogen atoms of a water molecule points toward the cavity center, and model II, where both of the hydrogen atoms surround the cavity center. The distance from the cavity center to the oxygen atom is taken to be 2.92 Å according to the X-ray diffraction experiments in water.[18,19] For example, the configuration of model I in T_d symmetry is shown in Figure 1. In both ammonia and hydrogen fluoride solutions, since no decisive physical data concerning the coordination of solvent molecules has hitherto been obtained, similar models to those for water are examined. Model II for ammonia indicates the configuration that all of the hydrogen atoms of an ammonia molecule surround the cavity. Models I and II in the case of hydrogen fluoride are identical. The distances between the atoms N and F and each cavity center are determined to be 3.01 and 2.92 Å so that the distance between the cavity center and the inside hydrogen atom in model I may be 2.0 Å in the analogy of the case of water.

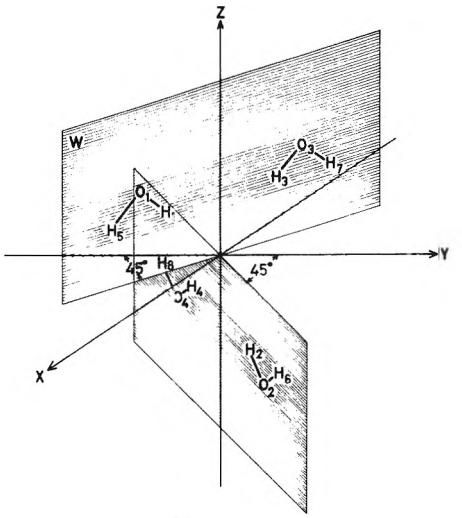

Figure 1. Configuration of water molecules with T_d symmetry (model I). The configuration where the outside hydrogen atoms are rotated by the angle of 180° is slightly more unstable in the neutral state compared with this configuration.

III. Method of Calculation and Choice of Parameters

The present calculation is carried out by the use of the unrestricted open shell treatment[20] based on the INDO approximation[21] which has been found to be useful for estimating the spin density or the hydrogen bond energy.[22] Moreover, the following three methods for the selection of the basis set are examined.

Method 1. Only valence AO's of solvent molecules are used.

Method 2. Not only valence AO's of solvent molecules but, as the basis functions of an excess electron, the additional two groups of hydrogen-like AO's located at the cavity center are also used in order to join the one-electron model with the molecular model and to investigate the extent of the localization of an excess electron; 1s AO for the ground state and 2p and 2s AO's for the excited state.

Method 3. The additional two groups are simultaneously adopted, because, with method 2, the wave functions of the ground and excited states are only approximately orthogonal to each other.

Parameters for the additional basis functions in method 2 are tested chiefly concerning the ionization potential $I_p = -\epsilon_{HO^\alpha}$ (ϵ_{HO^α} represents the energy of the highest occupied orbital with α spin) and the spin density of the inside proton, ρ_H, in the case of hydrated electron (T_d symmetry; model I); because of the expected localization of the trapped electron, assuming that the energy of an excess electron in its free state is small, $-\epsilon_{HO^\alpha}$, may correspond

(13) D. E. O'Reilly, *J. Chem. Phys.*, **41**, 3736 (1964).
(14) K. Fueki, *J. Chem. Phys.*, **45**, 183 (1966).
(15) C. M. L. Kerr and F. Williams, *J. Phys. Chem.*, **76**, 3838 (1972).
(16) G. Nilsson, *J. Chem. Phys.*, **56**, 3427 (1972).
(17) D. A. Copeland, N. R. Kestner, and J. Jortner, *J. Chem. Phys.*, **53**, 1189 (1970).
(18) J. Morgan and B. E. Warren, *J. Chem. Phys.*, **6**, 666 (1938).
(19) G. W. Brady and W. J. Romanov, *J. Chem. Phys.*, **32**, 306 (1960).
(20) J. A. Pople and R. K. Nesbet, *J. Chem. Soc.*, 571 (1954).
(21) J. A. Pople, D. L. Beveridge, and P. A. Dobosh, *J. Chem. Phys.*, **47**, 2026 (1967).
(22) P. A. Kollman and L. C. Allen, *Chem. Rev.*, **72**, 283 (1972); L. Pederson, *Chem. Phys. Lett.*, **4**, 280 (1969).

TABLE I: Summarized Experimental Data

Solvent	Solvation energy, eV	Photoelectric threshold, eV	Excitation energy, eV	Spin density	Oscillator strength
Water	1.7[a]		1.72[d]	0.01[f]	0.65[d]
Ammonia	1.7 ± 0.7[b]	1.6[c]	0.80[e]	Negative[g]	0.77[e]

[a] J. H. Baxendale, *Radiat. Res. Suppl.*, **4**, 139 (1964). J. Jortner and R. M. Noyes, *J. Phys. Chem.*, **70**, 770 (1966). [b] Reference 6b. [c] G. W. Teal, *Phys. Rev.*, **71**, 138 (1948). [d] W. C. Gottschall and E. J. Hart, *J. Phys. Chem.*, **71**, 2102 (1967). [e] R. K. Quinn and J. J. Lagowski, *J. Phys. Chem.*, **73**, 2326 (1969). [f] In the absolute value. See ref 3 and 4. [g] From ref 2b.

TABLE II: Dependency of the Energy of the Highest Occupied Orbital and the Proton Spin Density on the Parameters in Method 2 for Water[a]

ζ, a_0^{-1}	$(I + A)_{1s}/2$, eV	β^0, eV	ϵ_{HO}^{α}, eV	ρ_H
0.2	0.0	−9.0	−4.25	−0.013
	−3.0	−4.5	−1.60	−0.007
0.3	0.0	−9.0	−3.45	−0.021
	−3.0	0.0	−1.27	−0.002
		−4.5	−0.98	−0.012
		−9.0	−0.77	−0.023
0.4	0.0	−9.0	−3.69	−0.024
	−3.0	−4.5	−1.33	−0.015

[a] T_d symmetry, model I.

TABLE III: Dependency of the Energy of the Highest Occupied Orbital, the Proton Spin Density, and the Excitation Energy on the Parameters in Method 3 for Water[a]

ζ, a_0^{-1}	$(I + A)_{2s(2p)}/2$, eV	ϵ_{HO}^{α}, eV	ρ_H, eV	$h\nu$, eV
0.2	−3.0	−1.75	−0.006	6.85
	−0.6	−1.77	−0.006	6.00
	1.3	−1.52	−0.005	1.58
0.3	−3.0	−1.27	−0.009	6.27
	1.3	−1.46	−0.005	2.05
	1.65	−1.52	−0.005	1.42
0.4	−3.0	−1.59	−0.011	6.60
	1.3	−1.80	−0.007	2.42
	2.0	−1.86	−0.006	2.00

[a] T_d symmetry; model I; $(I + A)_{1s}/2 = -3.0$, $\beta^0 = -4.5$ in eV.

approximately to the solvation energy as will be shown in the next section or to the photoelectric threshold and, from esr studies, $|\rho_H|$ is considered to be almost 0.01.[3,4] In Table I, the experimental data are summarized. The results are listed in Table II, where ζ is the orbital exponent, $(I + A)_{1s}/2$ the Mulliken-type electronegativity, and β^0 the bonding parameter for the additional 1s AO. The selection of orbital exponent refers to the result of Jortner.[23] The value, −3.0, of $(I + A)_{1s}/2$ is taken since it gives the small absolute value of the local core matrix element concerning the 1s state of the excess electron, U_{11}. Then it will be easily understood that (1) ϵ_{HO}^{α} depends mainly on the value of $(I + A)_{1s}/2$ and varies slightly with β^0 (this inclination will be interpreted using the approximate expression for ϵ_{HO}^{α} in the next section); for example, only 0.5 eV accompanies the change of β^0 from 0.0 to −9.0 (the value for hydrogen atom) at $\zeta = 0.3$ and (2) ρ_H depends considerably on β^0 and hardly varies with the change of electronegativity. For the three values of ζ, if one takes $(I + A)_{1s}/2$ and β^0 as −3.0 and −4.5, respectively, both ϵ_{HO}^{α} and ρ_H seem to be reasonable, so that the parametrization is adopted in method 2. For the 2s and 2p AO's, the same values as those for 1s AO are used for convenience.[24]

In method 3, parameters are the same as those in method 2 except the electronegativities of 2s and 2p AO's which are lowered by considering the electronic repulsion energy between 1s and 2s(2p) AO's.[25] The dependency of ϵ_{HO}^{α}, ρ_H, and $h\nu$ (the excitation energy from 1s to the lowest 2p) on the electronegativity of 2s(2p) is shown in Table III. As is expected, ϵ_{HO}^{α} and ρ_H are scarcely influenced by the electronegativity for the additional 2s(2p) AO's, but the excitation energy varies remarkably. In the present calculation, the values of $(I + A)_{2s(2p)}/2$ are taken as 1.3 ($\zeta = 0.2$), 1.65 ($\zeta = 0.3$), and 2.0 ($\zeta = 0.4$). It should be noticed that the electronegativity of 1s AO in the case of ammonia is varied downward by the amount of 1.0 eV, because, according to the INDO method, the electron density of hydrogen of the ammonia molecule is excessively estimated and hence the stabilization energy becomes small; the correction causes simultaneously the acceleration of the convergency of the calculation.

In conjecturing the parameters in methods 2 and 3, the approximate formulae are also utilized as will be discussed in the following section.

IV. Results and Discussion

At the outset, we calculated the electronic states of the assembled molecules forming the cavity (Table IV). Concerning the total energy of each system, the value differs only slightly from that of an isolated molecule (see Table IV, footnote *a*) times the number of molecules forming the cavity (hence, the main part of the medium rearrangement energy is small). Moreover, the energy of the lowest unoccupied orbital, ϵ_{LU}, charge density, and dipole moment scarcely vary compared with those of the isolated molecule. The effect of the second solvation shell seems to be most marked for the value of ϵ_{LU}.

In Table V, the results for model I obtained by method 1 are listed. The stabilization energy, ΔE, which corre-

(23) J. Jortner, *Radiat. Res. Suppl.*, **4**, 24 (1964).

(24) Core integrals for the 2s and 2p AO's are given by setting the number of electrons equal to zero. As for the orbital exponent, this approximation will be supported by the investigation of other authors; for examples, see ref 6 and 17.

(25) According to the CNDO method, the Fock operator for the additional 2s or 2p AO (denoted by "2") is given by

$$F_{22} = U_{22} + \left(P_{AA} - \frac{1}{2}P_{22}\right)\gamma_{AA} + \sum_{B \neq A}(P_{BB}\gamma_{AB} - V_{AB})$$

(see eq 3.35 of ref 30). In the summation of the above equation, when atom B corresponds to the additional 1s AO (denoted by "1"), P_{BB} will be near the value of unity. However, because the additional 2s or 2p AO's will be almost vacant, the term $P_{11}\gamma_{12}$ should be trivial. The error thus brought about is corrected by modifying U_{22} in the present paper.

TABLE IV: Electronic States of the Assembled Molecules Forming the Cavity

Solvent	Symmetry	Model	Total energy,[a] eV	ϵ_{LU}, eV	Charge densities[b] q_H	q_X	$q_{H'}$	Dipole moment,[c] D
Water	T_d[d]	I	−2069.62	7.92	0.838	6.330	0.831	1.22 (0.67)
			(−4135.79)	(7.21)	(0.832)	(6.337)	(0.824)	(1.24 (0.67))
		II	−2069.60	7.80	0.837	6.329		2.14 (1.22)
	O_h	I	−3104.42	7.48	0.842	6.329	0.828	1.29 (0.77)
		II	−3104.38	7.30	0.837	6.325		2.16 (1.24)
Ammonia	T_d	I	−1454.48	7.85	0.917	5.251	0.915	0.75 (0.58)
		II	−1454.48	7.78	0.916	5.250		2.01 (1.55)
	O_h	I	−2181.74	7.68	0.918	5.253	0.915	0.74 (0.59)
		II	−2181.75	7.49	0.916	5.250		2.01 (1.55)
Hydrogen fluoride	T_d[d]		−2950.67	7.05	0.733	7.266		1.93 (0.76)
			(−5902.94)	(4.81)	(0.708)	(7.246)		(1.96 (0.67))
	O_h		−4425.81	6.25	0.741	7.258		1.90 (0.76)

[a] The energies of the isolated molecules given by the INDO method are −517.41, −363.62, and −737.70 eV for water, ammonia, and hydrogen fluoride, respectively. [b] The subscripts H, X, and H′ indicate the inside hydrogen, the heteroatom (O, N, F), and the outside hydrogen of a molecule in the first coordination shell, respectively. [c] The values for models I and II are those toward the H–X bond pointing to the cavity center and the molecular axis, respectively; according to the INDO method, the dipole moments of the isolated molecule are 1.25 (H_2O), 0.76 (NH_3), and 1.97 (HF) toward the H–X bond and 2.14 (H_2O) and 1.90 (NH_3) toward the molecular axis. The values in parentheses are the contributions of the hybridization term. [d] The values in the parentheses are those for the configuration of double solvation shells. The distances between the oxygen and fluorine atoms in the first coordination shell and those in the second coordination shell are taken from the data of the hydrogen bonded system.

TABLE V: Results for Model I Obtained by Method 1

Solvent	Symmetry	ΔE, eV	$\epsilon_{HO}{}^{\alpha}$, eV	Spin densities[a] ρ_H	$\rho_{H'}$	Charge densities[a] q_H	q_X	$q_{H'}$
Water	T_d[b]	7.78	7.62	0.085	0.048	0.930	6.395	0.926
		(5.42)	(7.06)	(0.088)	(0.021)	(0.917)	(6.386)	(0.883)
	O_h	7.32	7.16	0.056	0.024	0.897	6.370	0.890
Ammonia	T_d	7.67	7.49	0.057	0.040	0.981	5.285	0.992
	O_h	6.87	7.36	0.036	0.023	0.954	5.280	0.967
Hydrogen fluoride	T_d[b]	7.03	7.00	0.140		0.878	7.372	
		(4.68)	(4.50)	(0.149)		(0.842)	(7.328)	
	O_h	6.20	6.15	0.085		0.826	7.340	

[a] See footnote *b* of Table IV. [b] See footnote *d* of Table IV.

sponds to the solvation energy with the opposite sign, will be given by the difference between the energy of the assembled molecules including an excess electron and that of an excess electron plus the same number of free solvent molecules. In the present treatment, the energy of an excess electron, which will be represented by the local core matrix element concerning the additional 1s AO, is taken to be near zero and is neglected. Moreover, the medium rearrangement energy is also neglected because of the smallness of its main part as mentioned above. Namely, the stabilization energy shown indicates the energy difference between the anion radical group[26] and the neutral group with the same structure. ΔE and $\epsilon_{HO}{}^{\alpha}$ are obviously too high to explain the experimental solvation energies in water and ammonia and the photoelectric threshold in ammonia, respectively. Furthermore, the positive values of ρ_H of ammonia and large absolute values of ρ_H of water are definitely in disagreement with the experimental data. The difference between charge densities, q_H and $q_{H'}$, is small, that is, an excess electron trends to delocalize over all of the solvent molecules according to this method. The values for the configuration of double solvation shells are noted in parentheses in Table V. Though ΔE and $\epsilon_{HO}{}^{\alpha}$ are improved slightly and ρ_H increases disclosing the tendency of the increasing localization of an excess electron into the cavity, the localization on the proton is unfavorable when referred to the experimental results. Therefore, in the framework of the minimal basis set, it seems difficult to describe the state of the solvated electron accurately and to obtain the appropriate physical quantities.

In Table VI, the results for model I obtained by method 2 are shown. ΔE, $\epsilon_{HO}{}^{\alpha}$, and $h\nu$ are roughly comparable with the experimental data except in a few cases of ammonia in which the present restriction of applying the same orbital exponent for 1s, 2s, and 2p AO's seems too strict. As for hydrogen fluoride, −4.58 eV of ΔE and 3.69 eV of $h\nu$ are theoretically estimated by Raff and Pohl using the dimer model[27] and are comparable with the present data. The corrected stabilization energies in parentheses (Table VI) are given by the difference between the energy of the anion radical group and the energy of the neutral group which is calculated using the same basis set as that for the open shell system. This corrected ΔE will be considered as the net stabilization energy from which the ambiguity brought about by the parametrization connected with the additional basis functions is excluded as far as possible and will be less erroneous than ΔE. The effectiveness of the corrected ΔE will be made clear in method 3. The excitation energies are all those for the 1s → 2p transition. In this method, the 2s excited state is often more stable than the 2p excited state.[28]

(26) The energy of the anion radical group is approximated by that calculated with use of the UHF method.
(27) See p 173 of ref 2a.

TABLE VI: Results for Model I Obtained by Method 2

Solvent	Symmetry	ζ, a_0^{-1}	ΔE,[a] eV	ϵ_{HO}[a], eV	$h\nu$, eV	f	Spin densities[b] ρ_H	Spin densities[b] $\rho_{H'}$	Charge densities[b] q_H	Charge densities[b] q_X	Charge densities[b] $q_{H'}$	Charge densities[b] q_{ls}
Water	T_d	0.2	−2.81	−1.60	5.04	3.09	−0.007	−0.002	0.732	6.442	0.821	1.018
		0.3	−2.99 (−0.92)	−0.98	3.09	0.84	−0.012	−0.002	0.747	6.405	0.843	1.020
		0.4	−3.46	−1.33	1.23	0.19	−0.014	−0.002	0.752	6.390	0.853	1.021
	O_h	0.3	−4.59 (−1.52)	−1.56	2.83	0.77	−0.011	−0.002	0.753	6.402	0.840	1.032
Ammonia	T_d	0.2	−1.94	−0.39	3.56	2.18	−0.006	−0.002	0.804	5.385	0.902	1.031
		0.3	−2.31 (+0.08)	+0.09	1.03	0.28	−0.009	−0.002	0.818	5.326	0.923	1.037
		0.4	−2.75	−0.36	−0.44	−0.07	−0.011	−0.002	0.824	5.301	0.933	1.037
	O_h	0.3	−3.56 (−0.06)	−0.04	0.04	0.01	−0.008	−0.002	0.823	5.326	0.922	1.052
Hydrogen fluoride	T_d	0.2	−3.27	−2.35	5.89	3.61	−0.006		0.643	7.355		1.005
		0.3	−3.66 (−2.01)	−2.07	4.60	1.25	−0.011		0.660	7.339		1.004
		0.4	−4.25	−2.54	3.87	0.59	−0.011		0.668	7.330		1.012
	O_h	0.3	−5.56 (−3.08)	−3.14	3.92	1.07						

[a] The values in parentheses are the corrected stabilization energies. [b] See footnote *b* of Table IV. Is indicates the additional Is AO.

TABLE VII: Results for Models I and II Obtained by Method 3

Solvent	Symmetry	Model	ζ, a_0^{-1}	ΔE,[a] eV	ϵ_{HO}[a], eV	$h\nu$, eV	Spin densities[b] ρ_H	Spin densities[b] $\rho_{H'}$	Charge densities[b] q_H	Charge densities[b] q_X	Charge densities[b] $q_{H'}$	Charge densities[b] q_{ls}	Dipole moment,[c] D
Water	T_d	I	0.2	−5.32	−1.58	1.58	−0.005	−0.001	0.734	6.424	0.816	0.961	1.71 (0.70)
			0.3	−9.22 (−1.48)	−1.52	1.42	−0.005	−0.0006	0.747	6.366	0.828	0.864	1.75 (0.74)
			0.4	−12.54	−1.86	2.00	−0.006	−0.0004	0.739	6.347	0.834	0.898	1.82 (0.77)
		II	0.3	−9.41 (−1.54)	−1.39	1.51	−0.002		0.777	6.368		0.819	2.47 (1.22)
	O_h	I	0.3	−13.75 (−2.29)	−2.33	2.87	−0.004	−0.0006	0.754	6.366	0.825	0.900	1.67 (0.74)
		II	0.3	−13.93 (−2.36)	−2.16	2.16	−0.001		0.788	6.366		0.858	2.42 (1.23)
Ammonia	T_d	I	0.2	−6.47	−1.69	1.62	−0.003	−0.0008	0.810	5.356	0.895	0.924	1.12 (0.49)
			0.3	−11.41 (−1.79)	−1.60	2.13	−0.003	−0.0004	0.817	5.283	0.908	0.856	1.16 (0.54)
			0.4	−14.85	−1.97	3.10	−0.004	−0.0003	0.804	5.260	0.915	0.907	1.28 (0.57)
		II	0.3	−11.26 (−1.50)	−1.22	1.64	−0.0001		0.878	5.286		0.759	2.26 (1.55)
	O_h	I	0.3	−16.39 (−1.66)	−2.05	2.93	−0.002	−0.0002	0.825	5.285	0.907	0.856	1.13 (0.54)
		II	0.3	−16.17 (−1.97)	−1.59	2.42	−0.0001		0.880	5.254		0.783	2.20 (1.54)
Hydrogen fluoride	T_d		0.2	−5.06	−2.49	2.38	−0.005		0.642	7.344		0.989	2.29 (0.71)
			0.3	−8.33 (−2.34)	−2.39	2.16	−0.007		0.654	7.311		0.954	2.26 (0.73)
			0.4	−11.49	−3.11	2.91	−0.007		0.652	7.293		0.959	2.30 (0.76)
	O_h		0.3	−12.42 (−3.51)	−3.60	3.91	−0.006		0.664	7.302		0.966	2.22 (0.74)

[a] See footnote *a* of Table VI. [b] See footnote *b* of Table IV. [c] See footnote *c* of Table IV.

Then, the excitation energy is calculated by the approximate first-order perturbation method using the UHF result (see Appendix). The values of oscillator strength, though they vary considerably with the orbital exponent, are reasonable somewhere between the cases of $\zeta = 0.3$ and 0.4 except in the case of ammonia. The most noticeable results given by method 2 are that the absolute value of ρ_H in the case of water almost coincides with that obtained by the hyperfine splitting of esr and that the negative proton spin density of an ammonia molecule is successfully explained. Every charge density in the additional 1s AO, q_{1s}, cited in the last column of Table VI is quite favorably near unity, which shows that an excess electron is almost completely localized in the cavity. On the other hand, by this localized electron, the electron of the inside hydrogen atom is slightly pushed out (consequently solvent molecules are more polarized) as seen from the values of charge densities. Thus, method 2 is effective in interpreting thermal and optical quantities. However, as mentioned in section III, the wave functions of the ground and excited states satisfy the orthogonality condition only approximately. Hence, we will now examine method 3.

Following the results of models I and II in Table VII, the value of ΔE is clearly too low, which may be caused by the overestimation of the interactions between an electron in the additional basis functions, especially 2s and 2p AO's, and the cores of atoms of solvent molecules. The corrected ΔE is satisfactorily improved as shown in parentheses in Table VII of the column for ΔE. The values of $\epsilon_{HO}{}^{\alpha}$ and $h\nu$ (for the 1s $\rightarrow$ 2p transition which is always the first transition by this method) are reasonable except $h\nu$ of ammonia which is directly influenced by the change of the electronegativity of the 1s AO. It should be noted here that the spin densities in model I are definitely negative and that in model II, however, the values become small in their absolute values and almost zero in the case of ammonia. The results in model II are due to the attenuation of the spin polarization effect of an excess localized electron, because the change of the spin delocalization effect is found out to be negligibly small. Therefore, from the standpoint of the spin density, model I is more realistic than model II. The values of charge densities are analogous to those of method 2 except q_{1s} which becomes smaller by the delocalization of an excess electron to 2s AO. The dipole moments of solvent molecules[29] increase generally by the amount of 0.3 $\sim$ 0.6 D compared with those in free states or vacant states of cavities as suggested by the polaron theory. The oscillator strength obtained is unfavorable, which circumstance seems to be caused by the unsuitable contribution of 2s AO in the highest occupied orbital.

In Table VIII, the wave functions for the excess electron given by the three methods are listed and compared. Though the contribution of the inside hydrogen atoms is dominant in the wave function of method 1, the electron in this state fairly delocalizes over all of the solvent molecules. In contrast with method 1, methods 2 and 3 give the wave functions well localized to the additional basis functions.

Next, we will reexamine the parametrization applied in methods 2 and 3. Considering that an excess electron in the ground state is almost completely localized in the additional 1s AO, the stabilization energy of solvated electron with α spin is given by the use of the INDO approximation and the notation of Pople, *et al.*,[30] as follows

$$E = E(e_M^-) - [E(M) + U_{11}] = \left(\sum_A \tilde{E}_A + \sum_{A<B} \tilde{E}_{AB}\right) - \left[\sum_A E_A + \sum_{A<B} E_{AB} + U_{11}\right] \cong \tilde{E}_1 + \sum_B \tilde{E}_{1B} - U_{11} \quad (1)$$

where $E(e_M^-)$ and $E(M)$ are the energies of the solvated electron and the solvent molecules and E_A and E_{AB} are the monoatomic and diatomic parts of the total energy ($\tilde{E}$ indicates the value for the open shell system); 1 in the subscript denotes the additional 1s AO. Moreover, since an excess electron is localized in the additional 1s AO in the ground state

$$\tilde{E}_1 \cong U_{11} \quad (2)$$

and then

$$\Delta E \cong \sum_B \tilde{E}_{1B} = -\sum_B Q_B \gamma_{1B} + \sum_\nu^B [2P_{1\nu}\beta_{1\nu} - (P_{1\nu}{}^{\alpha^2} + P_{1\nu}{}^{\beta^2})\gamma_{1B}] \quad (3)$$

Because $P_{1\nu}{}^{\alpha}$ and $P_{1\nu}{}^{\beta}$ (followingly $P_{1\nu}$ also) are small, ΔE is dominated by the net charges of the atoms in the first coordination shell through $\Sigma_B Q_B \gamma_{1B}$.

The energy of the highest occupied orbital is likewise obtained, namely

$$\epsilon_{HO}{}^{\alpha} \cong U_{11} - \sum_B Q_B \gamma_{1B} + \sum_\nu^B [2c_{\nu,HO}{}^{\alpha}\beta_{1\nu} - 2c_{\nu,HO}{}^{\alpha}P_{1\nu}{}^{\alpha}\gamma_{1B}] \quad (4)$$

where the approximation, $c_{1,HO}{}^{\alpha} \cong 1$, is used. Since $c_{\nu,HO}{}^{\alpha}$ is small, $\epsilon_{HO}{}^{\alpha}$ depends directly on U_{11}, being consistent with the inclination found in section III, and is mainly stabilized by the atoms in the first coordination shell like ΔE. Furthermore, for $U_{11} \cong 0$

$$\epsilon_{HO}{}^{\alpha} \cong \Delta E \quad (5)$$

as mentioned in section III.

In Table IX, the comparison between the values calculated by method 3 and those obtained by using eq 3 and 4 is shown. Concerning both ΔE and $\epsilon_{HO}{}^{\alpha}$, the values are well in agreement.

Finally it will be interesting to draw the electron distributions of solvated electrons and solvent molecules and the potential formed by solvent molecules. In Figures 2–5, the right-hand side is the X-Z plane and the left-hand side is the W plane in Figure 1. In Figure 2, the electron distribution of water molecules (T_d symmetry; model I) is shown. The neighboring water molecules form the barrier of the electron cloud, reflecting the bonding character between inside hydrogen atoms and consequently there appears a depression of the distribution in the center. Figure 3 is the electron distribution of the hydrated electron in the ground state given by method 2 at $\zeta = 0.3$. It is interesting to note that there still remains a sizable amount of excess charge in the region outside the first coordination shell and hence it will be necessary to consider the effect of the second solvation shell in order to describe the hy-

(28) T. Huang, I. Eisele, D. P. Lin, and L. Kevan, *J. Chem. Phys.*, 56, 4702 (1972).
(29) In each of the molecules, the sum of the net charges is not zero, but the absolute value of the excess negative charge is very small ($\leq$0.03), and so the dipole moment can be approximately estimated.
(30) J. A. Pople and D. L. Beveridge, "Approximate Molecular Orbital Theory," McGraw-Hill, New York, N. Y., 1970.

TABLE VIII: Wave Functions for the Excess Electron in Water[a]

Orbital group[b]	Method 1	Method 2		Method 3	
	Ground state	Ground state	Excited state	Ground state	Excited state
1s ($H_1H_2H_3H_4$)	−0.310 (++++)	0.006 (++++)	0.008(+−+−)	0.005(++++)	0.007 (+−+−)
2s ($O_1O_2O_3O_4$)	0.185 (++++)	0.088 (++++)	0.078 (+−+−)	0.046 (++++)	0.079 (+−+−)
2px ($O_1O_2O_3O_4$)	−0.044 (++−−)	−0.042 (++−−)	−0.017 (+−−+)	−0.034 (++−−)	−0.018 (+−−+)
2py ($O_1O_2O_3O_4$)	0.044 (+−−+)	0.042 (+−−+)	0.017 (++−−)	0.034 (+−−+)	0.018 (++−−)
2pz ($O_1O_2O_3O_4$)	−0.250 (++++)	−0.014 (++++)	−0.025 (+−+−)	−0.010 (++++)	−0.025 (+−+−)
$1s_{ad}$		−0.967		−0.886	0.0
$2s_{ad}$			0.0	0.433	0.0
$2px_{ad}$			0.0	0.0	0.0
$2py_{ad}$			0.0	0.0	0.0
$2pz_{ad}$			−0.985	0.0	−0.985

[a] The results of methods 2 and 3 are obtained by using the orbital exponent 0.3 for the additional basis functions. The listed values are the coefficients of AO groups and the signs in parentheses correspond to those of AO's. [b] ϕ ($A_1A_2A_3A_4$) represents the group of ϕ AO belonging to the atoms A_1, A_2, A_3, and A_4 (see Figure 1). ad denotes the additional AO.

TABLE IX: Comparison between the Values Calculated by Method 3 at ζ = 0.2 and Those Obtained by using Eq 3 and 4

Quantity	Method 3	Eq 3 and 4
ΔE, eV	−5.32	−4.0
ϵ_{HO}, eV	−1.58	−1.7

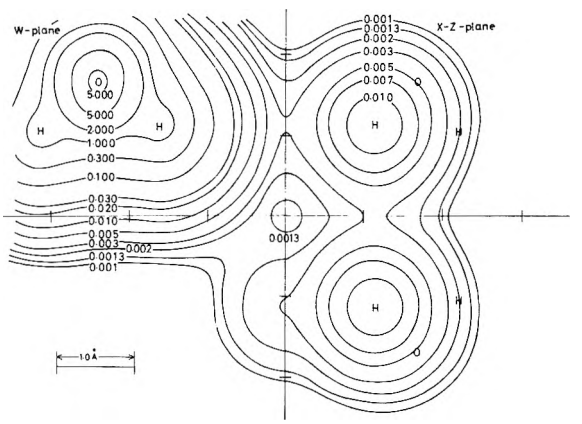

Figure 2. Electron distribution of water molecules (T_d symmetry, model I).

drated electron more accurately. When the distribution of an excess electron in the 1s AO is excluded from that given in Figure 3, the resulting distribution, which is shown in Figure 4, will be regarded as that of water molecules only. From the change of contours of 0.0013 and 0.003, one can easily understand that the electron cloud of water molecule is forced out slightly by the electronic repulsion with an excess electron, namely, that water molecules are somewhat polarized by an excess electron initially trapped by the potential depression due to the molecules. In Figure 5, the electron distribution of the hydrated electron in the 2pz excited state given by method 2 at ζ = 0.4 is drawn. The maximum value for an excess electron exists near or outside of the barrier, which suggests that, if an excess electron is excited, the probability that the electron flys out of the cavity will increase.

In Figure 6, the potential formed by the water molecules along the X axis is shown, taking the corrected ΔE as the approximate potential. The shape is rather flat for $X \leq 1.0$ Å, reflecting the gently sloping electron distribution in this region (see the right-hand side of Figure 2) and increases rapidly in the region of 1.0 Å $\leq X \leq$ 2.0 Å,

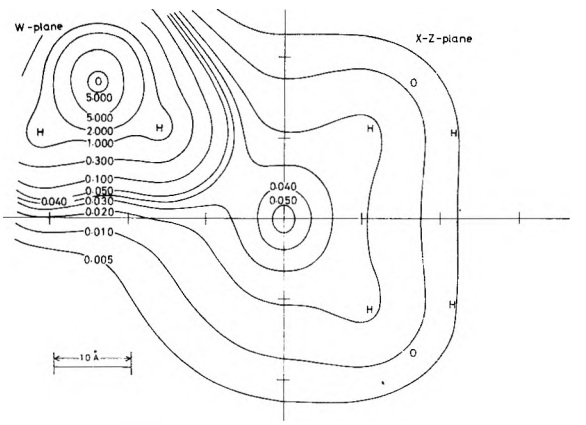

Figure 3. Electron distribution of the hydrated electron in the ground state given by method 2 at ζ = 0.3 (T_d symmetry, model I).

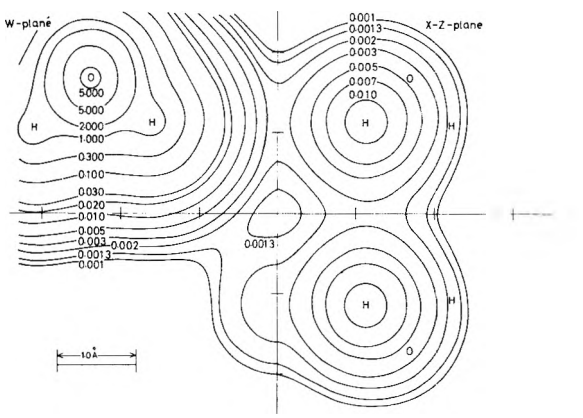

Figure 4. Electron distribution of water molecules in Figure 3.

where the electron cloud forms a barrier ($X \sim 1.2$ Å). The shape will change in the other cross section; for instance, if one calculates the potential along the direction combining the cavity center and the oxygen atom on the left-hand side plane of Figure 2, the potential will have a maximum like that given by Jortner, *et al.*,[31] in the calculation of the pseudopotential of the helium atom. The curve drawn with a fine line is the Jortner-type potential

(31) J. Jortner, N. R. Kestner, S. A. Rice, and M. H. Cohen, "New Developments in Quantum Chemistry, Istanbul Lectures," Part II, O. Sinanoğlu, Ed., Academic Press, New York, N. Y., 1965, p 129.

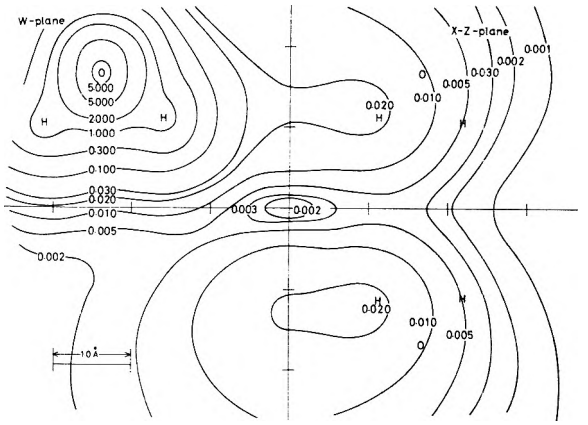

Figure 5. Electron distribution of the hydrated electron in the 2pz excited state given by method 2 at $\zeta = 0.4$ (T_d symmetry, model I).

(used in the continuum model) with the cavity radius of 1.0 Å and the depth of about 0.9 eV. At short range, the discrepancy between two potential is small but, at long range, becomes larger, which will lead to the difference of the description of the excited state such as the number of the bound excited states.

For the electron distribution and the potential in ammonia and hydrogen fluoride, the analogous results to those of water will be obtained.

V. Conclusion

Several properties observed for the solvated electron have been reasonably explained by the use of the cavity model and methods 2 and 3, and method 1 with the minimal basis set has contrarily been found to give only poor results, which implies that the trapped electron in polar solvents will be fully localized in the cavity. Particularly, the absolute value of the proton spin density of water and the negative proton spin density of ammonia obtained in model I, namely, in the model where only one of the hydrogen atoms of a solvent molecule points toward the cavity center, coincide with those observed in several experiments; furthermore, the sign of the former is negative and the absolute value of the latter is of the order $10^{-2} \sim 10^{-3}$ in the present calculation From the aspect of the spin density, therefore, the cavity will probably be in favor of the configuration of model I with T_d or O_h symmetry. Calculated charge densities and dipole moments of solvent molecules well describe the polarization mechanism of the molecules by a trapped electron, being consistent with the polaron theory.

The electron distribution shows that solvent molecules forming the cavity make an enclosure of electron cloud which is due to the bonding character between inside hydrogen atoms and the situation is also visualized by the approximate potential curve. The above result is inherent in the system of assembly of molecules and justifies the conventional cavity model.

As for the oscillator strength, the present result is not satisfactory, especially in method 3, and more improvement of the wave function will be necessary to obtain accurate values. Concerning the excited state of the solvated electron, the present treatment only suggests that the lowest excited state will be near the zero energy level. Further investigation is hoped for in order to clarify the nature of the excited state of the electron, particularly in

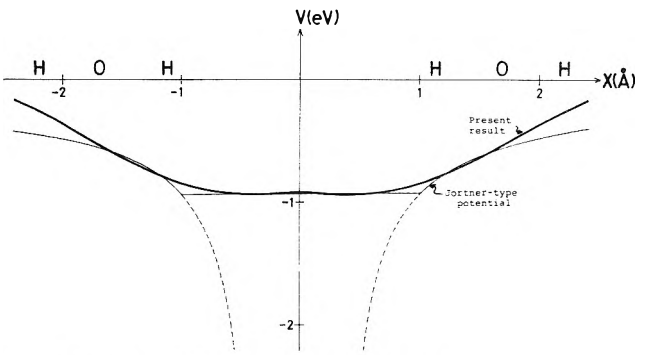

Figure 6. Potential along the X axis of Figure 1.

connection with the lifetime and autoionization into the continuum of the excited state.[32]

Acknowledgments. We thank one of the reviewers for supplying ref 11 and 15 and giving us significant comment concerning our manuscript. We wish to thank Mr. Hirao for his kind assistance in dealing with the INDO program and Mr. Minato for his help with this paper. It is a pleasure to express our gratitude to the Data Processing Center, Kyoto University. for its permission to use the FACOM 230-60 computer.

Appendix

In the unrestricted Hartree-Fock theory, Fock operators for the radical with $S_z = 1/2$ are given by

$$F^{\alpha} = H_N + \sum_k (J_k^{\alpha} + J_k^{\beta} - K_k^{\alpha}) + J_m^{\alpha} - K_m^{\alpha} \quad \text{(for the } \alpha\text{-spin part)} \quad \text{(A1)}$$

$$F^{\beta} = H_N + \sum_k (J_k^{\alpha} + J_k^{\beta} - K_k^{\alpha}) + J_m^{\alpha} \quad \text{(for the } \beta\text{-spin part)} \quad \text{(A2)}$$

where H_N is the Hamiltonian of an electron in the field of nuclei alone and J_i and K_i are well-known Coulomb and exchange operators. The subscripts, k, m, and n (used below), indicate the doubly and singly occupied and the vacant orbitals in the sense of the restricted Hartree-Fock theory, respectively. Now, using the SCF wave functions for the closed system without an excess unpaired electron, the approximate orbital energies for the open shell system, $\epsilon_k^{\alpha(\beta)}$, $\epsilon_m^{\alpha(\beta)}$, and $\epsilon_n^{\alpha(\beta)}$, are related to the eigenvalues for the closed shell system, ϵ_k, ϵ_m, and ϵ_n, as follows

$$\epsilon_k^{\alpha} = \langle k|F^{\alpha}|k\rangle = \epsilon_k + J_{mk} - K_{mk} \quad \text{(A3)}$$

$$\epsilon_k^{\beta} = \langle k|F^{\beta}|k\rangle = \epsilon_k + J_{mk} \quad \text{(A4)}$$

$$\epsilon_m^{\alpha} = \epsilon_m \quad \text{(A5)}$$

$$\epsilon_m^{\beta} = \epsilon_m + J_{mm} \quad \text{(A6)}$$

$$\epsilon_n^{\beta} = \epsilon_n + J_{mn} - K_{mn} \quad \text{(A7)}$$

$$\epsilon_n^{\beta} = \epsilon_n + J_{mn} \quad \text{(A8)}$$

Since the transition energy for $m \rightarrow n$ corresponds to $\epsilon_n - \epsilon_m$, the following expression will be obtained using the UHF result

$$h\nu \simeq \epsilon_n^{\beta} - \epsilon_m^{\alpha} - J_{mn}^{\alpha} \quad \text{(A9)}$$

(32) Some instructive investigations are recently presented; for example, see T. Kajiwara, K. Funabashi, and C. Naleway, *Phys. Rev., A*, **6**, 808 (1972).

Water on Silica and Silicate Surfaces. I. Partially Hydrophobic Silicas

K. Klier,* J. H. Shen, and A. C. Zettlemoyer

Center for Surface and Coatings Research, Lehigh University, Bethlehem, Pennsylvania 18015 *(Received January 22, 1973)*

Publication costs assisted by the National Science Foundation

The predominant active centers for water adsorption on partially hydrophobed HiSil silicas are the surface OH groups, despite the presence of sodium and other foreign elements in these materials. In initial stages of adsorption, water adsorbs "oxygen down" and forms a 1:1 complex in which the surface OH groups are donors and the water molecules acceptors of the hydrogen bond. At about one-half of the OH groups occupied, water starts to agglomerate into clusters. The reasons for an apparent hydrophobicity of the silicas are primarily weak bonding of water to the OH groups ("energetic hydrophobicity") and in some cases also a low concentration of these groups ("concentration hydrophobicity"). The existence of clusters is a necessary prerequisite for heterogeneous nucleation of ice on these surfaces.

1. Introduction

Silicas can possess a wide range of surface properties which are determined by the biography of preparation, calcination temperatures, and concentrations of various impurities. With regard to water adsorption, silicas are often referred to as hydrophilic or hydrophobic depending whether the adsorption heat for water is larger or smaller than the heat of liquefaction. In the present paper (part I), we report on the surface properties of partially hydrophobed HiSils. These materials are non-porous, amorphous, wet-precipitated silicas which recently found an unexpected application in promoting heterogeneous nucleation of ice.[1] To the extent that silicas and silicates are used as catalysts and catalyst supports in processes in which water is a product or a reactant, there is a wide interest in learning about the mechanism and dynamics of water adsorption and agglomeration on a variety of surfaces. In subsequent papers, therefore, we intend to report on the properties of water in zeolite cavities (part II), on porous silicas, and on a number of metal oxides. The questions of primary interest will be the identification of active centers for water adsorption, the determination of the structure of surface complexes involving water, specification of conditions under which water clusters are formed, and the detection of phase transformations in adsorbed layers.

2. Experimental Section

Sample Preparation and Characterization. The original material used in this work as a substrate is HiSil 233 (Pittsburgh Plate Glass Industries) the surface properties of which were modified by a heat treatment for 2 hr at 800 [HiSil (800)], at 700 [HiSil (700)], and at 650° in the presence of NaCl [Na-HiSil (650)]. The last substrate is identical with the sample denoted 1:2 NaCl/HiSil in ref 1, and is investigated here for the purpose of specifying the possible role of sodium ions in water adsorption, as compared to the role of surface OH groups. Prior to adsorption measurements, the samples were outgassed *in vacuo* at 170° for several hours. The above treatments produced surfaces having, under corresponding relative pressures, a lower adsorption capacity for water than for argon, as demonstrated by the comparison of the BET monolayer volumes in Table I, columns 1 and 2. The water isotherms, represented in Figure 1, show a pronounced decline of adsorption capacity for water with increased temperature of the heat treatment, although the total argon surface area is only slightly reduced (column 3, Table I). The primary cause for the diminished capacity toward water is the loss of surface hydroxyls as follows from the comparison of intensities of the first stretching overtones of the surface hydroxyls (silanols) on substrates from which molecular water was completely removed (Figure 2). The quantitative estimates of the silanol concentration have been made on the basis of simultaneous water adsorption and spectral intensity measurements and are described below. The results of these estimates are incorporated in Table I (column 4) in terms of the average area in $Å^2$ per OH group. The substrates were further characterized by total analyses for sodium and chlorine, and by Auger analysis for any detectable element. Since the penetration depth of Auger electrons is estimated to be a few atomic layers, Auger spectroscopic analysis pertains essentially to the surface composition. The results of analyses are given in columns 5 and 6 of Table I. It is noted that the commercial samples already contain some sodium, the amount of which is slightly increased by heat treatment in the presence of sodium chloride. All surfaces contain, apart from the major elements O and Si, also traces of aluminum. In addition, sodium and chlorine are present in small amounts in the surface of Na-HiSil (650).

Spectroscopic and Adsorption Measurements. The spectra were measured in a vacuum quartz reflectometric cell similar to one described in ref 2. The standard was dehydrated MgO (Merck) placed in a matching vacuum cell. The spectrophotometer used was Cary 14R equipped with a double-beam reflectance attachment operating in undispersed diffuse illumination mode and alternately analyzing light reflected from the sample and the standard by passage through monochromator and into the detector. The instrument was balanced using two identical standards in matching vacuum cells. The sample cell had a thermostatting jacket and a thermistor probe close to the reflecting surface, allowing thus temperature control of the sample to within 0.2°. The reflectance cell was con-

(1) D. R. Bassett, E. A. Boucher, and A. C. Zettlemoyer, *J. Colloid Interface Sci.*, **34**, 3 (1970).
(2) K. Klier, *Catal. Rev.*, 1 (2), 207 (1967).

TABLE I: Characterization of HiSil Silicas

Sample	Argon (−196°) v_m, cc/g (1)	Water (25°) v_m, cc/g (2)	BET argon surface area, m^2/g, σ = 16.6 Å² (3)	Å²/OH (4)	Elemental analyses (5) Na / (Na + Cl + Si) × 100	Elemental analyses (5) Cl / (Na + Cl − Si) × 100	Auger analyses (6) Major elements	Auger analyses (6) Other elements
HiSil (800)	13	7	87	34	1.68	0.39	O, Si	
HiSil (700)	21	18	96	11	1.68	0.39	O, Si	
Na-HiSil (650)	23	22	104	10	2.77	1.94	O, Si	Al, Na

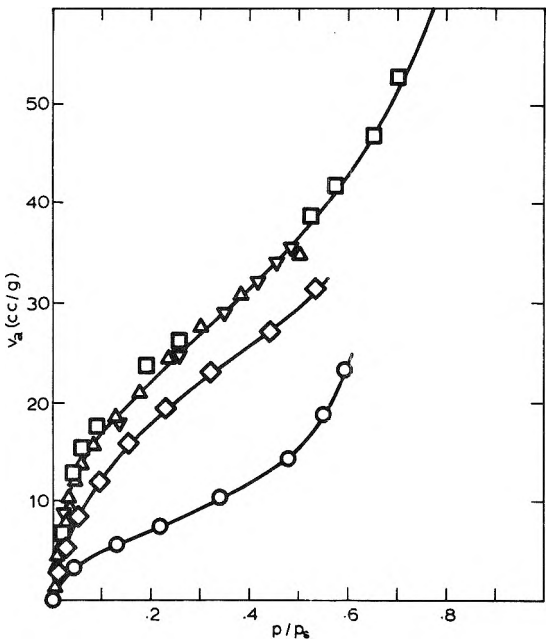

Figure 1. Water adsorption isotherms at 25° on Na-HiSil (650) [▽, △, two runs in volumetric apparatus with Apiezon oil manometer and the sample placed in reflectance cell for simultaneous spectra measurements; □, gravimetric measurement using vacuum quartz spring balance], on HiSil (700) (◇), and on HiSil (800) (○). v_a is the volume adsorbed in cc (STP) per gram and p/p_s, the relative pressure of water at equilibrium.

nected *via* a greased ground joint and stopcocks with a volumetric vacuum apparatus containing an Apiezon oil manometer and water vapor handling system so that water isotherms could be measured simultaneously with the spectra. The background pressure was 10^{-6} Torr, sufficient for removing all adsorbed water from the surfaces studied, and water isotherms could be measured in the pressure range 0–22 Torr. The spectral data were recorded by a digital readout system in intervals of 1 nm on the wavelength scale, processed by the CDC 6400 computer, and plotted in suitable coordinates. The spectra were evaluated by the Schuster-Kubelka-Munk (SKM) theory which gives the ratio of the absorption (K) to the scattering (S) coefficients[3] as

$$\frac{K}{S} = \frac{(1 - R_\infty)^2}{2R_\infty} = F(R_\infty)$$

where R_∞ is reflectance measured as the ratio of the total intensities of light reflected from the sample and from the standard. Both the sample and the standard are required to have a semiinfinite thickness. Experimental tests were made to show that this requirement was satisfied in the 5-mm thick cell in our system. Within the range of spectral bands studied, the scattering coefficients of the silicas are constants independent of the wavelength, as proven by the coincidence of the log $F(R_\infty)$ representation of the spectra of water condensed in these materials, and the log k_M representation of bulk water spectra on transmission, k_M being the specific molar absorption coefficients. However, the scattering coefficient does depend on the particle size, and therefore $F(R_\infty)$ represents the absorption spectrum but for a multiplicative constant $1/S$, and log $F(R_\infty)$ the logarithm of absorption coefficient but for an additive constant $-\log S$.

The spectral bands chosen for this study were the combination band $\nu_2 + \nu_3$ of molecular water at 5300 cm^{-1}, denoted as H_2O ($\nu + \delta$) band, the $\nu_1 + \nu_3$ band of molecular water (with some $2\nu_3$ and $2\nu_1$ admixtures) at 7150 cm^{-1}, denoted as H_2O (2ν) band, and the surface OH 2ν band at 7300 cm^{-1}, denoted SiOH (2ν). The assignments of the water bands are given in the Landolt-Börstein Tables[4] and the assignment of SiOH (2ν) is due to Anderson and Wickersheim.[5] The advantage of the present choice is in the easy distinction between the adsorbed molecular water and the surface OH groups, owing to the fact that the H_2O ($\nu + \delta$) band is intense, does not overlap with lattice bands of the silica and with the surface OH vibrational bands, and is present only when molecular water is present.

In condensed phases, including adsorbed layers, molecular vibrations undergo changes due to the interactions with neighbors and the surface, resulting in band center shifts up to several hundreds of reciprocal centimeters and in changes of the band shapes. The former effects permit determination of the structure of adsorbates, and are primarily reported here, while the latter effects contain information on the character of the rotational motion of the molecules and have been reported in another communication.[6]

3. Results and Discussion

Submonolayer and Monolayer Coverages. Active Centers and Structure of Adsorbates. The properties of adsorbed molecular water were determined by following the changes in the H_2O ($\nu + \delta$) absorption over the whole range of surface coverages by water (Figures 3–5).[7,8] The

(3) The discussion of validity of the SKM theory is given in G. Kortüm, "Reflectance Spectroscopy," Springer-Verlag, New York, N. Y., 1969, pp 103–127, 170–216, and also in K. Klier, *J. Opt. Soc. Amer.*, **62**, 882 (1972).
(4) Landolt-Börstein, "Zahlenwerte and Funktionen," 2. Teil, Molekein I, p 333.
(5) J. H. Anderson and K. A. Wickersheim, *Surface Sci.*, **2**, 252 (1964).
(6) K. Klier, *J. Chem. Phys.*, 58, 737 (1973).
(7) Intensities in the present work are given in terms of the SKM function $F(R_\infty) = K/S$ as stated in Experimental Section. Errors on ordinate axes amounting to a multiplicative factor of 5.5 occurred in the preliminary communication by A. C. Zettlemoyer and K. Klier, *Discuss. Faraday Soc.*, 52 993 (1971).
(8) Figures 4, 5, 7, 8, and 12 and Tables III and IV will appear following these pages in the microfilm edition of this volume of the journal. Single copies may be obtained from the Business Operations Office, Books and Journals Division, American Chemical Society, 1155 Sixteenth St., N.W., Washington, D. C. 20036. Remit check or money order for $3.00 for photocopy or $2.00 for microfiche, referring to code number JPC-73-1458.

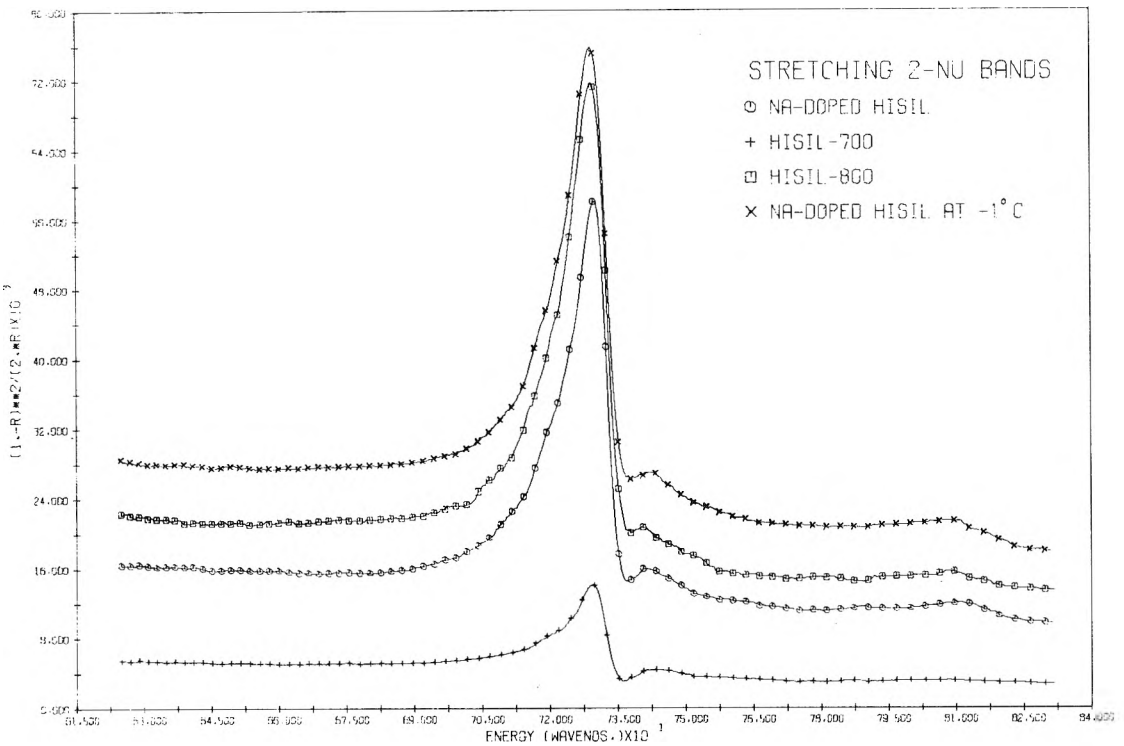

Figure 2. The 2ν stretching bands of surface hydroxyls on Na–HiSil (650) (×), HiSil (700) (Ⓞ), and HiSil (800) (+) at 25°. The spectrum of Na–HiSil (650) at −1° (□) is shown for comparison. All substrates are vacuum degassed and contain no molecular water: ordinates, the SKM function $F(R_\infty)$ 10^3; abscissae, wave numbers in thousands of reciprocal centimeters (*e.g.*, abscissa labeled 73.500 × 10^{-1} corresponds to 7350 cm^{-1}).

vacuum-degassed substrates contained no molecular water, as is evident from the initial absence of the H_2O (ν + δ) bands on all samples. On admissions of water vapor at pressures specified in isotherms in Figure 1 and in Tables II–IV (columns 2 and 3),[8] the H_2O (ν + δ) bands appear and their intensities increase with growing surface coverage. The frequencies of the H_2O (ν + δ) bands are between that of critical water and bulk liquid water, and they shift to the value for bulk liquid water when the substrate is exposed to saturated vapor pressure. These shifts are related to the mode of hydrogen bonding and will be discussed simultaneously with the shifts in the 2ν region.

The changes of the near-infrared spectra in the 2ν region with increased amount of adsorbed water clearly demonstrate that the surface hydroxyls are active centers for water adsorption on all substrates investigated here (Figures 6–8)[8] and that the differences between these substrates are only of a quantitative nature. The degassed, molecular water-free substrates contain SiOH groups whose 2ν frequency is initially at 7300 cm^{-1} (Figure 2; Figures 6–8, ref 8, curves marked by crosses). On exposure to water vapor, simultaneously with the appearance of the H_2O (ν + δ) bands, the intensities of the SiOH (2ν) bands at 7300 cm^{-1} decrease and new bands appear in the 2ν region at lower frequencies (Figures 6–8, ref 8, curves represented by continuous lines). In the initial stages of adsorption, bands develop at 7180–7130 cm^{-1}. These bands contain the 2ν stretching vibrations of molecular water as well as the 2ν stretching modes of silanols which are now shifted by at least 100 cm^{-1} to lower frequencies (Tables II–IV, ref 8, columns 6 and 7) from their original position on water-free surfaces. The magnitude of this shift is close to that observed for a *donor hydrogen bond* in water dimers isolated in solid nitrogen matrices of the order of 100 cm^{-1},[9] and therefore the silanols provide a donor hydrogen bond to the adsorbing water molecules. On the other hand, the molecular water bands H_2O (ν + δ) are only slightly shifted (~30 cm^{-1}, Tables II–IV ref 8, columns 4 and 5; graphical representation is in Figure 2 of part II) with respect to water in critical state (lower part of Table II) which is chosen as a reference state representing monomeric water not bonded by hydrogen bonds.[10] The mixed 2ν bands at 7180 cm^{-1} containing both H_2O (2ν) and SiOH (2ν) vibrations are also only ~30 cm^{-1} shifted with respect to the corresponding H_2O (ν + δ) as well as the H_2O (2ν) band, and a large shift of the SiOH (2ν) band therefore favor a surface water–silanol complex in which SiOH is a donor and water an acceptor of the hydrogen bond. Hence from the possibilities in Chart I, structure II is ruled out by infrared shifts. Structure III can futhermore be ruled out on the basis of quantitative relations between the amount of adsorbed water and the intensities of the H_2O (ν + δ) and the free (7310 cm^{-1}) SiOH (2ν) bands. This structure (III) would require that water is initially bound to two surface hydroxyls and, with proceeding adsorption, one water molecule becomes bound in average to one hydroxyl by nonlinear hydrogen bonds. Quantitative analysis of the spectra in Figures 9–11[8] shows that this is not so and that each water molecule is initially bound to one hydroxyl, corresponding to structure I. The intensities at 2ν-band maxima of the free silanols decrease linearly with increasing water coverage concurrently with a linear increase of intensities at band maxima of the H_2O (ν + δ) band, up to about one-half of the silanols being bound to water molecules. (The quantitative basis for this statement is less significant for the HiSil (800) sample, Figure 11, but the essential features of the intensity-water coverage relations are the same as for Na–HiSil (650),

(9) A. J. Tursi and E. R. Nixon, *J. Chem. Phys.*, **52**, 1521 (1970); M. Van Thiel, E. D. Becker, and G. C. Pimentel, *ibid.*, **27**, 486 (1957).

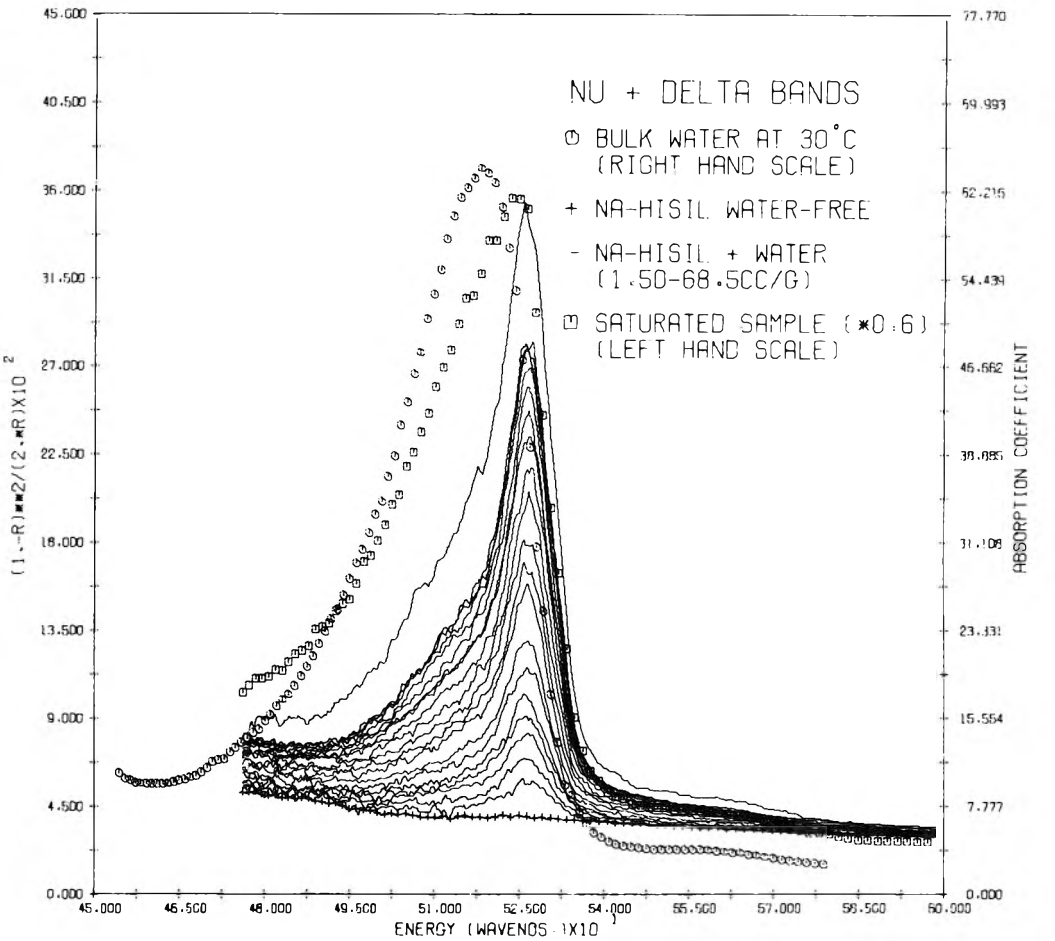

Figure 3. The H_2O ($\nu + \delta$) bands in the progress of water adsorption on Na-HiSil (650) at 25°. The adsorbed amounts, wave numbers, and intensities corresponding to the individual bands are listed in Table II. The H_2O ($\nu + \delta$) band of bulk liquid water at 30° is shown for comparison (⊙); ordinates, the SKM function $F(R_\infty)10^2$ for adsorbed water (left-hand scale), and the absorption coefficient for bulk liquid water (right-hand scale); abscissae, wave numbers in thousands of reciprocal centimeters (*e.g.*, abscissa labeled 52.500 × 10^{-1} corresponds to 5250 cm^{-1}).

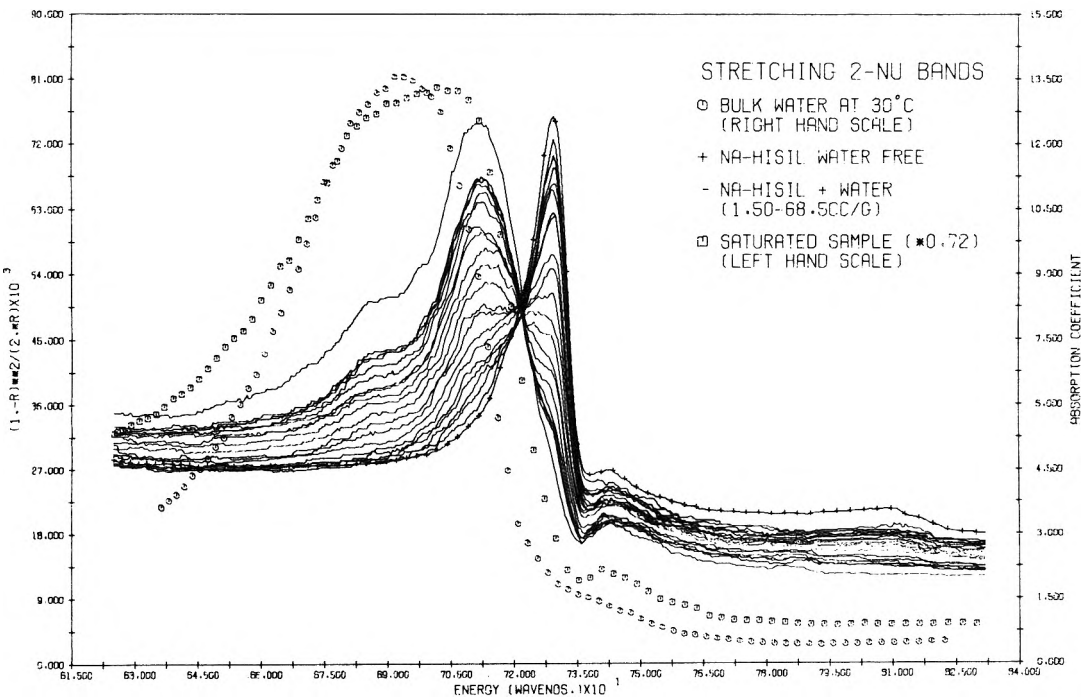

Figure 6. The spectra of silanols and water in the 2ν region in Na-HiSil (650). The adsorbed amounts, wave numbers, and intensities corresponding to the individual bands are listed in Table II. The H_2O (2ν) band of bulk liquid water is shown for comparison (⊙); ordinates, the SKM function $F(R_\infty)10^3$ for adsorbed water (left-hand scale), and the absorption coefficient for bulk liquid water (right-hand scale); abscissae, wave numbers in thousands of reciprocal centimeters (*e.g.*, abscissa labeled 73.500 × 10^{-1} corresponds to 7350 cm^{-1}).

TABLE II: Equilibrium Adsorbed Amounts of Water, Frequencies, and Intensities of Water ($\nu + \delta$) and (2ν) Bands and Silanol (2ν) bands on Na–HiSil (650) at 25°[a]

Substance	No. of admission (1)	v_a, cc/g (2)	p, Torr (3)	H_2O ($\nu + \delta$) bands $\tilde{\nu}$, cm^{-1} (4)	$\Delta\tilde{\nu}$, cm^{-1} (5)	Free SiOH (2ν), cm^{-1} (6)	Bound SiOH (2ν) and H_2O (2ν) bands $\tilde{\nu}_I$, cm^{-1} (7)	$\Delta\tilde{\nu}_I$, cm^{-1} (8)	$\tilde{\nu}_{II}$, cm^{-1} (9)	$\Delta\tilde{\nu}_{II}$, cm^{-1} (10)
Water adsorbed	1	0	0			7300				
on Na–HiSil	2	9.23	1.6	5272	−19	7300	7140	−20	6870	−290
(650), run 1[e]	3	19.15	0.51	5272	−19	7300	7135	−25	6830–6900	−330 to −260
	4	26.2	3.20	5272	−19	7300	7135	−25	6800–6900	−360 to −260
	5	31.1	2.81	5272	−19	7300	7135	−25	6800–6950	−360 to −210
	6	34.4	5.38	5270	−21	7300	7135	−25	6800–6950	−360 to −210
	7	36.45	7.3	5270	−21	7300	7135	−25	6800–6950	−360 to −210
	8	38.0	8.97	5270	−21	7300	7135	−25	6800–6950	−360 to −210
	9		8.71	5270	−21	7300	7135	−25	6820–6950	−340 to −210
	10	46.5	9.48	5270	−21		7130	−30	6840–6950	−320 to −210
	11	*b*	13.3	5233	−58		7110	−50	6840–6950	−320 to −210
Water adsorbed	1	0	0			7294				
on Na–HiSil	2	1.53	0.033	5258	−33	7294	7162		6917	−243
(650), run 2[e]	3	3.84	0.13	5258	−33	7294	7170		6858	−302
	4	5.24	0.40	5263	−28	7294	7170		6875	−285
	5	6.49	0.55	5263	−28	7294	7137	−23	6875	−285
	6	7.64	0.69	5258	−33	7289	7113	−47	6875	−285
	7	8.69	0.75	5263	−28	7294	7125	−35	6858	−302
	8	9.77	0.75	5263	−28	7299	7133	−27	6875	−285
	9	11.31	1.07	5263	−28	7294	7125	−35	6875	−285
	10	14.90	1.43	5263	−28	7289	7110	−50	6875	−285
	11	16.93	1.95	5258	−33	7289	7147	−13	6858	−302
	12	19.64	3.08	5258	−33	7289	7133	−27	6868	−292
	13	22.43	4.20	5266	−25	7289	7138	−22	6858	−302
	14	25.21	5.65	5271	−20	7294	7133	−27	6875	−285
	15	28.48	7.15	5266	−25	7289	7123	−37	6858	−302
	16	28.48	7.15	5266	−25	7289	7117	−43	6875	−285
	17	31.68	9.12	5263	−28	7289	7127	−33	6858	−302
	18	35.50	11.97	5269	−22	7260	7133	−27	6853	−307
	19	40.23	14.28	5263	−28	7294	7117	−43	6875	−285
	20	48.54	14.96	5271	−20	7294	7123	−37	6875	−285
	21	57.97	14.78	5260	−31	7294	7133	−27	6887	−273
	22	68.46	12.14	5258	−33	7294	7123	−37	6875	−285
	23	*c*	19.37	5241	−50		7057	−103	6858	−302
Critical state[d]				5291	0		7160	0		
Water at 30°[d]				5181	−110				6940	−220
Water at 10°[d]				5160	−139				6870	−290
Ice[d]				5051	−240				6700	−460

[a] $\tilde{\nu}$ are frequencies at absorption maxima, $\Delta\tilde{\nu}$ are their shifts with respect to the frequency of the corresponding band at critical state, v_a is the adsorbed volume in cc(STP)/g, and p is the equilibrium pressure. [b] 2.5 hr exposure at 22.8°. [c] 6 days exposure at 26°. [d] from Luck's data.[9] [e] Run 1 was conducted by recording the spectra on a paper chart, and the wave numbers are therefore estimated from graphical rather than from digital record as in run 2 and in all experiments listed in Tables III and IV.

Figure 9, and HiSil (700), Figure 10). The ratio of ordinate scale factors for the H_2O ($\nu + \delta$) and the SiOH (2ν) intensities in Figures 9–11[8] was chosen 5:1 because the ratio of intensities of the H_2O ($\nu + \delta$) and the H_2O (2ν) band is approximately 5:1.[10] Extrapolation of the linear portion of the dependence of the SiOH (2ν) intensities on the amount of adsorbed water to the abscissae axis gives us a measure of the total amount of water necessary to "titrate" all hydroxyls present. Taking one molecule of water per each hydroxyl, the amount of silanols can be calculated, and the effective area per silanol can be obtained from the total area determined by argon adsorption divided by the number of hydroxyls found in the described manner. The areas per silanol estimated in this way are given in Table I, column 4.

The regions of initial departure from a linear relationship between the intensities of the SiOH (2ν) and the H_2O ($\nu + \delta$) bands and water coverage in Figures 9–11 roughly coincide with water monolayer volumes estimated by the BET theory (column 2 in Table I). However, the water monolayer does not exhaust all surface OH groups available for adsorption, and the BET monolayer volumes correspond to 55% of occupied silanols on Na–HiSil (650), to 54% of occupied silanols on HiSil (700), and roughly to 50% of occupied silanols on HiSil (800). These ratios are independent of the concentrations of sodium, chlorine, and other impurities both in the bulk and on the surfaces, and therefore the OH groups appear to be the sole active centers for water adsorption. The formation of a single hydrogen bond in structure I explains why the adsorption heat at less than monolayer coverages attains values as low as 6 kcal/mol[1] and why the water molecules tend to form clusters, in which the energy per molecule is close to the heat of liquefaction, 10.6 kcal/mol, long before all adsorption centers are occupied.

(10) W. A. P. Luck, *Ber. Bunsenges. Phys. Chem.*, **69**, 626 (1965).

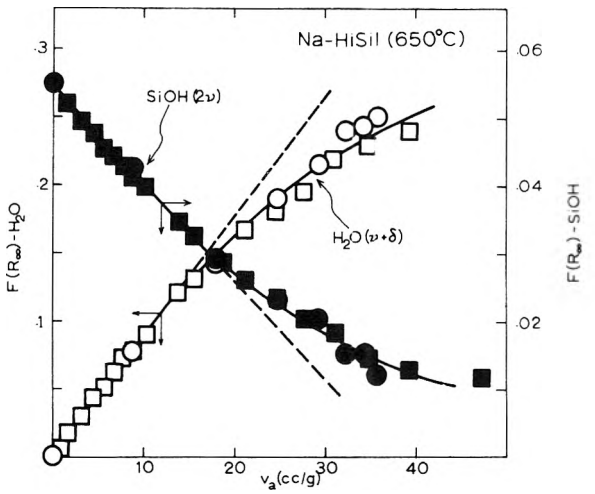

Figure 9. Relation between intensities at band maxima of the SiOH (2ν) band (right-hand scale, full symbols) of the H_2O ($\nu + \delta$) band (left-hand scale, open symbols) and the amount of water adsorbed (abscissa axis) at 25° on Na–HiSil (650). Two runs (circles and squares) correspond to two runs (▽ and △) in Figure 1.

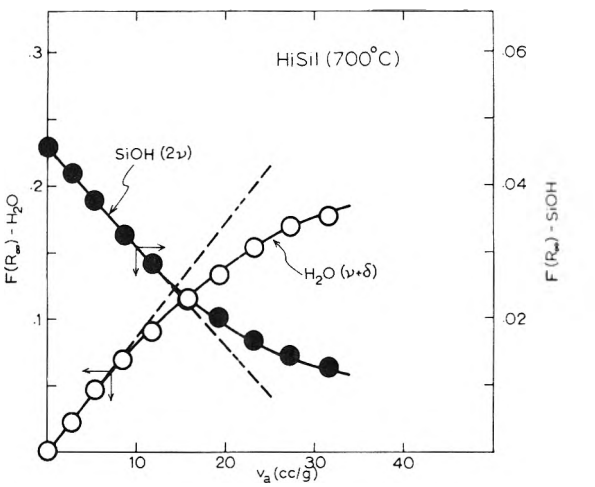

Figure 10. Relation between intensities at band maxima of the SiOH (2ν) band (right-hand scale, full symbols) of the H_2O ($\nu + \delta$) band (left-hand scale, open symbols) and the amount of water adsorbed (abscissa axis) at 25° on HiSil (700).

Chart I: Structures and Frequency Shifts in SiOH–H_2O Complexes

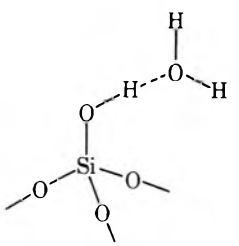

SiOH is donor, H_2O is acceptor
Expected: small shift of H_2O ($\nu + \delta$)
large shift of SiOH (2ν)

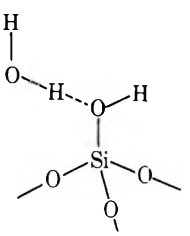

SiOH is acceptor, H_2O is donor
Expected: large shift of H_2O ($\nu + \delta$)
small shift of SiOH (2ν)

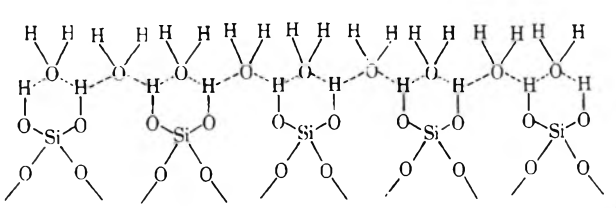

III

SiOH is donor, H_2O is acceptor
Expected: small shift of H_2O ($\nu + \delta$), large shift of SiOH (2ν)

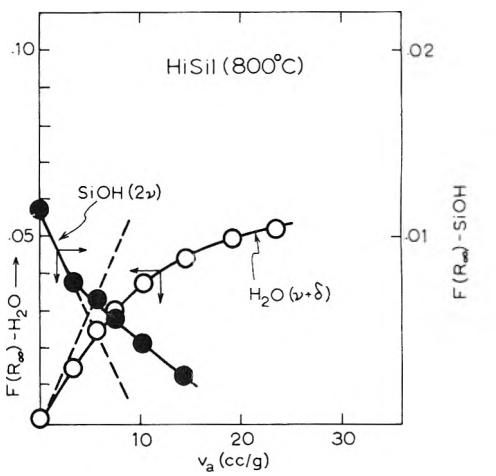

Figure 11. Relation between intensities at band maxima of the SiOH (2ν) band (right-hand scale, full symbols) of the H_2O ($\nu + \delta$) band (left-hand scale, open symbols) and the amount of water adsorbed (abscissa axis) at 25° on HiSil (800).

The behavior of submonolayer water, that is of the structure I, is little temperature dependent in a wide range of temperatures. For example, this water does not freeze as is evident from the fact that the frequencies of the H_2O ($\nu + \delta$) and H_2O (2ν)–SiOH (2ν) band maxima remain constant at 5260 cm^{-1} ($\nu + \delta$) and 7180 cm^{-1} (2ν) between 25 and −20°, and do not show any formation of ice characterized by corresponding bands at much lower frequencies, 5050 ($\nu + \delta$) and 6700 cm^{-1} (2ν). The quantitative relations between the intensities of the H_2O ($\nu + \delta$) and SiOH (2ν) bands at submonolayer coverages during an adsorption experiment carried out at subfreezing temperatures exhibit the same features as adsorption above the freezing temperatures.[11] This observed invariance of spectral and adsorption behavior across and well below the freezing point rules out the possibility of a "two-dimensional ice" formation in monolayers on the present substrates.

(11) Figure 12 (to appear in the microfiche edition, *cf.* ref 8) demonstrates the intensity coverage relations for adsorption equilibria of water on Na–HiSil (650) at −1°.

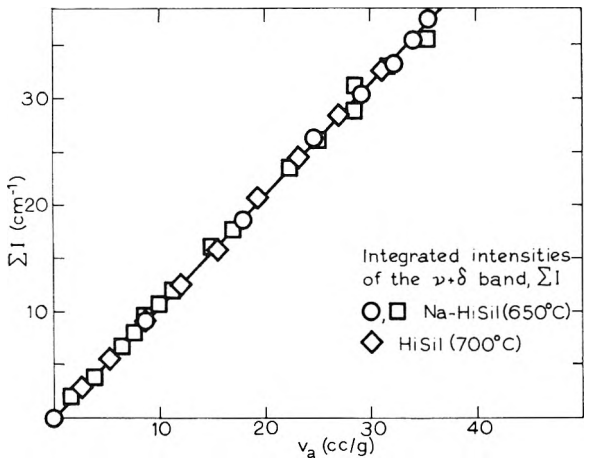

Figure 13. The integrated intensities of the H_2O ($\nu + \delta$) bands on Na-HiSil (650) (O, □ correspond to the runs ∇, Δ in Figure 1) and on HiSil (700) (◇) *vs.* water coverage in cc (STP)/g (abscissa axis).

Cluster Formation. The departures from linearity in the graphs representing the H_2O ($\nu + \delta$) band intensity *vs.* amount of adsorbed water (Figures 9–11) are accompanied by the growth of low-frequency shoulders (Figures 3–5, ref 8) at a frequency close to that of bulk liquid water H_2O ($\nu + \delta$) band, 5180 cm^{-1} (at 30°).[10] This feature repeats in the 2ν region as a distinct band emerging at 6800–6950 cm^{-1} (Figures 6–8, frequencies $\tilde{\nu}_{II}$ in column 9, Tables II–IV, *cf.* ref 8), also close to the bulk liquid H_2O (2ν) band frequency. The appearance of the low-frequency H_2O ($\nu + \delta$) and H_2O (2ν) bands marks the onset of clustering of adsorbed water, and is accompanied by an increase of adsorption heat.[1] The integrated intensities of the H_2O ($\nu + \delta$) band, which include both the cluster band and the band of monolayer water attached to the silanols, remain proportional to the amount of adsorbed water (Figure 13). The clusters are therefore formed on the account of further buildup of the monolayer, and the diminished growth of the structure I band is compensated for by the growth of the cluster band. The beginning of cluster formation is completely controlled by the amount of surface hydroxyls, as is seen from an approximate coincidence of the low-frequency shoulder formation on the molecular water bands, BET monolayer volumes for water, increasing heats of adsorption, and a constant fraction (about one-half) of occupied hydroxyls at water monolayer. It is noteworthy that the cluster frequencies are quite distinct and close to the bulk water frequencies in very early stages of cluster formation. The clusters undergo a phase transformation at subzero temperatures and their ($\nu + \delta$) as well as (2ν) frequencies shift toward the values for ice. However, this process requires an extensive amount of adsorbed water, equivalent to at least six-ten monolayers. With respect to freezing, therefore, not only monolayer water but also clusters too small in size or sparsely abundant, are insufficient for ice formation. These results indicated that heterogeneous ice nucleation on silicas is a three-dimensional phenomenon in which long-range order can only be attained in large-size prenucleation clusters.

Comparison with Other Work. No previous study on quantitative relations between the infrared spectra and the concentrations of water and surface OH groups has been reported in the literature. However, qualitative measurements permitting some comparison with the present results have been made. In particular, the presently observed frequencies of the OH groups of water in monomeric state and of water clusters agree well with those reported by Anderson and Wickersheim for silica gels.[5] The essential features of the mechanism of water adsorption proposed here and in Anderson and Wickersheim's work also agree. There may occur quantitative differences between the silica gels and the nonporous HiSil, such as in the equivalence of the number of OH groups to the number of water molecules in the initial stages of adsorption and in the surface coverages at which clusters start to grow. In the present work on HiSil silicas, the initial equivalent is one water molecule per one hydroxyl, as discussed earlier, while it is expected that in the more densely hydroxylated silica gels two hydroxyls may initially bind one water molecule. It is also anticipated that filling of pores by water in silica gels will take place simultaneously with adsorption and clustering on the outer surfaces. The HiSil silicas do not have pores and therefore do not exhibit this last property.

Some features of the spectra of water-free HiSils can also be compared with the literature. Figure 2 shows that the SiOH (2ν) bands tail to low frequencies although they cannot be resolved into any small number of individual components. This tailing may arise by various mechanisms such as by mutual perturbations of the vibrations of closely spaced OH groups, by rotational broadening, by perturbations by the underlying lattice, by hydrogen bonding of some hydroxyls to others, and by surface heterogeneity in general. Most of these mechanisms have been suggested in the literature, and it appears quite difficult to assess their individual contributions to the band broadening and tailing. It has been possible to resolve the silanol stretching fundamentals on Aerosil silicas into up to three components[12,13] but the assignment given to the individual components by the different groups of authors varied. Other authors[14] pointed out that the resolution may be artificial and observed on asymmetric band.

However, it is comparatively easy to distinguish between hydrogen-bonded silanols and silanols with free hydrogens as the difference in their frequency is at least 100 cm^{-1}. The tailing of the bands in Figure 2 could be caused by a small amount of mutually hydrogen bonded hydroxyls. This possibility is diminished by the finding that the tail shape does not depend upon the degree of dehydroxylation, except if dehydroxylation should leave patches of hydroxyls on the surface. The rotational broadening is unlikely because of the temperature independence of the band shape (Figure 2). A plausible interpretation of the tailing seems to be one in which the vibrations of single OH groups are perturbed by the vibrations of the underlying lattice, because in this case the dependence of the band shape upon the extent of dehydroxylation and on the temperature will be minimal. This interpretation is closest to one put forward by Van Cauwelaert, Jacobs, and Uytterhoven.[13]

Despite the uncertainty in identifying the broadening mechanism, the donor hydrogen bonding of the surface silanols to water molecules has been firmly established from the large shifts of the SiOH (2ν) band on water adsorption. Therefore, if there are different kinds of OH groups

(12) M. L. Hair and W. Hertl, *J. Phys. Chem.*, **73**, 2372 (1969).
(13) F. H. Van Cauwelaert, P. A. Jacobs, and J. B. Uytterhoeven, *J. Phys. Chem.*, **76**, 1434 (1972).
(14) J. A. Hockey, *J. Phys. Chem.*, **74**, 2570 (1970).

in the surface represented by the observed SiOH (2ν) band, those constituting the predominant species represented by the frequency maximum are the primary active centers for water adsorption.

Finally, it has been suggested in the literature that water may diffuse into the silica and form hydroxyl groups in the interior.[15] The average distance a molecule diffuses in 1000 min was estimated, by extrapolating the high-temperature diffusion coefficients for fused silicas,[16] to be 6 Å at room temperature. The presently investigated water–HiSil systems did not show any signs of water diffusion into the silica. The adsorption equilibria were rapidly established and all water could be removed by mild degassing without leaving either residual water or increased amounts of hydroxyls in the specimen. These results indicate that the extrapolation of the high-temperature diffusion data to room temperature does not lead to realistic estimates of the penetration rates of water through the surface layer and that diffusion and rehydroxylation does not influence the room temperature adsorption phenomena to any significant degree.

Acknowledgments. The authors are indebted to the National Science Foundation for support of this work through Grant No. GA-29526. The Auger analyses were carried out by Dr. G. W. Simmons and the gravimetric adsorption measurements on Na–HiSil (650) by Dr. W. C. Hamilton, which contributions are gratefully acknowledged.

(15) R. H. Doremus, *J. Phys. Chem.*, **75**, 3147 (1971).
(16) A. J. Moulson and J. P. Roberts, *Trans. Faraday Soc.*, **57**, 1208 (1961).

Infrared Spectra of the Isolated Hydroxyl Groups on Silica

B. A. Morrow* and I. A. Cody

Department of Chemistry, University of Ottawa, Ottawa KIN 6N5, Canada *(Received August 23, 1972)*

Infrared spectra in the OH stretching region of the isolated SiOH groups on the surface of silica have been obtained. The silica samples had been preheated to 750° and spectra were recorded with sample temperatures ranging from −145 to 400°. Extreme caution has been taken to ensure that virtually all atmospheric water was removed from the spectrometer and with perfect double-beam compensation, no splitting of the SiOH band was observed, nor were any distinct shoulders apparent. This finding is in contradiction to an earlier similar study and only when the double-beam compensation with respect to atmospheric water is not perfect has it been possible to reproduce spectra showing distinct shoulders. The infrared band profile of the SiOH groups observed in this work was virtually identical with those observed from SiOD groups and band fitting techniques have been used to show that both types of band can be fitted with a two-component curve. A general discussion of the validity of using band-fitting techniques for "resolving" closely overlapping bands in infrared spectra is included.

Van Cauwelaert, Jacobs, and Uytterhoeven[1] have recently reported that the 3750-cm^{-1} absorption band in the infrared spectrum of silica (due to isolated surface hydroxyl groups) has two distinct shoulders to high and low wave number of the main band. The shoulders were more pronounced at higher sample temperatures and their exact position relative to the main band depended on this temperature. Using a curve analyzer they "decomposed" the band contour into a three-component curve which reflects the positions of these shoulders. In an earlier investigation, Hair and Hertl[2] produced a spectrum which showed that with a sample temperature of 25° the same band consisted of three clearly resolved components, but this finding was later refuted by Hockey[3] who claimed that the "splitting" of this band was an artifact due to improper double-beam compensation in this region of strong infrared absorption by atmospheric water. Hockey's spectrum showed a relatively sharp band centered near 3750 cm^{-1} which was degraded into a tail on the low wave number side, and similar spectra at this temperature were reported by Van Cauwelaert, *et al.*,[1] and by Morrow and Devi.[4]

Van Cauwelaert, *et al.*,[1] claimed that the appearance of distinct shoulders could not be attributed to improper atmospheric compensation because the shoulders would not shift with changes in temperature. However, this would not necessarily be true if the shoulders were due to inverse absorption in an improperly compensated spectrometer if the peak position of the SiOH band changes with temperature. They state, however, that a perfectly straight baseline was obtained in the 3750-cm^{-1} spectral region when the silica sample was removed from the sample beam of the double-beam spectrometer. None the less, it is not

(1) F. H. Van Cauwelaert, P. A. Jacobs, and J. B. Uytterhoeven, *J. Phys. Chem.*, **76**, 1434 (1972).
(2) M. L. Hair and W. Hertl, *J. Phys. Chem.*, **73**, 2372 (1969).
(3) J. A. Hockey, *J. Phys. Chem.*, **74**, 2570 (1970).
(4) B. A. Morrow and A. Devi, *Can. J. Chem.*, **48**, 2454 (1970).

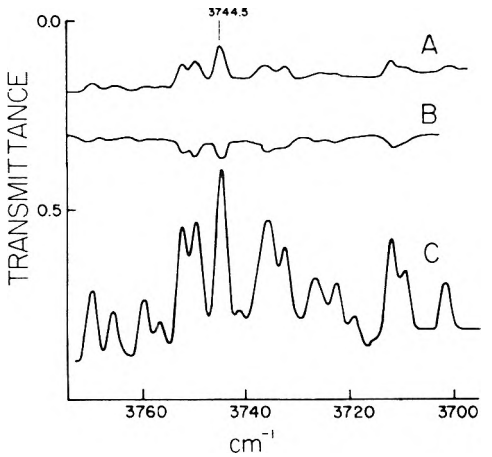

Figure 1. A. Single beam spectrum of residual atmospheric water with complete flushing. B. Double-beam spectrum of uncompensated cell. C. Single-beam spectrum with sample chamber exposed to the atmosphere. The transmittance scale applies to spectrum C; the other spectra are linearly displaced for purposes of presentation.

clear whether a compensating cell of equivalent pathlength was placed in the reference beam during their experimental runs, and no quantitative indication was given of the extent to which their spectrometer was purged with dry air.

In their band-fitting work, no mention is given of the accuracy of their band-fitting procedure, nor is an overall computed spectrum shown. The validity of assuming a constant shape ratio (0.65) for the Lorentzian–Gaussian band function for all temperatures is questionable, as is the basic assumption that because a single OH band in other oxides gave this ratio, that this ratio should apply to the reputedly more complex overlapping band system in the case of silica.

Finally their band parameters (particularly the half-width) of the low- and high-frequency components do not change appreciably with temperature. This is particularly surprising for a temperature change of 400°.

In the present paper we have reinvestigated the infrared spectrum of the isolated hydroxyl groups on silica and have found no evidence for the existence of distinct shoulders. Also included is a discussion of the validity of using band-fitting procedures for resolving closely overlapping band systems.

Experimental Section

The silica samples (Cab-O-Sil, H5) used in this work were utilized in the form of pressed disks 2.5 cm in diameter containing 5 mg of silica per cm^2 and were pressed in a stainless steel die at about 1000 lb/in.^{2} for a few seconds. The disks were heated for several hours at 750° in a quartz cell and they were then transferred to a variable temperature cell[5] where they were evacuated for 1 hr (this procedure is similar to that used by Van Cauwelaert, *et al.*[1]). About 10 Torr of helium was added to the evacuated cell to ensure good thermal conductivity.

The spectrometer used was a modified Perkin-Elmer Model 13G filter-grating double-beam ratio recording infrared spectrometer, and spectra in the OH stretching region were recorded with a spectral slit width of 2.2 cm^{-1} at a scan speed of 4.9 cm^{-1} min^{-1}, this value for the slit width being chosen because of an optimum signal-to-noise ratio for digitization purposes. Band shapes did not alter with a narrower slit width, and identical although "noisier" spectra were observed using a 1.4-cm^{-1} spectral slit width. The chopper is before the sample compartment in this spectrometer so that problems due to sample emission at elevated temperatures are eliminated. After dry air flushing, the total single-beam absorption due to residual water is shown in Figure 1A and a perfectly straight base line could be obtained in double-beam operation either with or without the sample cell in place, provided all sample areas were totally flushed with dry air. When we refer below to an "uncompensated cell," this means spectra recorded with the sample chamber (13-cm path length) totally open to the atmosphere and with the sample cell (path length 7 cm) in the sample beam only. The residual "uncompensated" spectrum is shown in Figure 1B and the total single-beam atmospheric spectrum under those conditions is shown in Figure 1C.

For computational purposes, the spectra were digitized at 0.2-cm^{-1} intervals between 3771.0 and 3684.2 cm^{-1} and band-fitting computations were carried out on an IBM 360/65 computer using the programs developed by Pitha and Jones[6] for fitting a Lorentzian–Gaussian product or an unrestrained Lorentzian–Gaussian sum function to spectral bands. Plots were recorded on a Milgo plotter.

For a discussion the various types of mathematical function used to fit infrared spectra, the reader is referred to several original articles on the subject.[7] The accuracy of our various computer calculations is expressed in terms of the following parameters: DIS (discrepancy) is the root mean squared of the residual differences between the calculated and experimental spectrum in transmittance; WFM is the wave number of the maximum discrepancy; MAX is the maximum discrepancy at WFM. Other parameters are the half-width, the shape ratio (the Lorentzian–Gaussian ratio), and the peak intensity in absorbance.

All spectra were calibrated against atmospheric water bands and the experimental data reported in this investigation are believed to be accurate to ±0.2 cm^{-1}.

Results

Experimental spectra of the SiOH band of silica at −145, 25, 200, and 400° are shown in Figures 2A and 3A. The total band area and the wave number of the maximum absorption in each case is given in Table I. These spectra are very different from those shown by Van Cauwelaert, *et al.*,[1] at the same temperatures (except for the spectrum at −145° which is unique to this work) in that the distinct shoulders on either side of the main absorption peak are absent.

Since the spectra observed by Van Cauwelaert, *et al.*,[1] had shoulders to high and low wave number of the main absorption band, a band analyzer was used to decompose this band into three components. They used a Voight type Lorentzian–Gaussian product function assuming a 65% Lorentzian shape ratio in this fitting, and although they do not say what their criterion of a good "fit" was, we will not dispute that a reasonable fit can be achieved. However, there is no *a priori* reason to assume that the same shape ratio should apply to all bands, nor is one justified in assuming that the same shape ratio should apply over a

(5) B. A. Morrow, *J. Sci. Instrum.*, **43**, 487 (1966).
(6) J. Pitha and R. N. Jones, NRC Bulletin No. 12 and 13, National Research Council of Canada, Ottawa, 1968.
(7) (a) R. N. Jones, *Appl. Opt.*, **8**, 597 (1969); (b) K. S. Seshadri and R. N. Jones, *Spectrochim. Acta*, **19**, 1013 (1963); (c) J. Pitha and R. N. Jones, *Can. J. Chem.*, **45**, 2347 (1967).

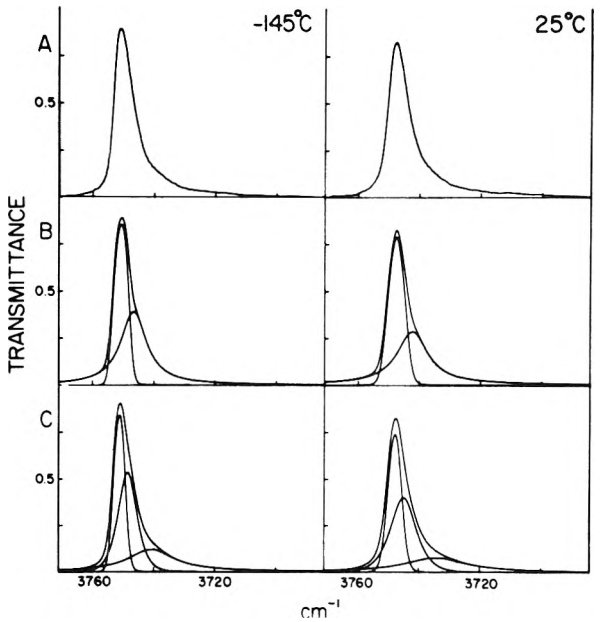

Figure 2. A. Experimental spectra of SiOH band at −145 and 25°. B. Computed spectra using a two-component sum function. C. Computed spectra using a three-component product function.

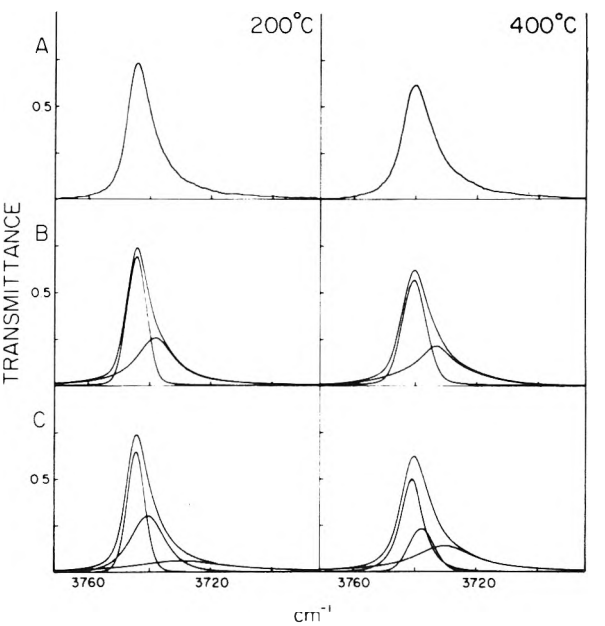

Figure 3. A. Experimental spectra of SiOH band at 200 and 400°. B. Computed spectra using a two-component sum function. C. Computed spectra using a three-component product function.

TABLE I: Experimental Data for the Spectra shown in Figures 2A and 3A

Temp, °C	Wave number, cm^{-1} (at max intensity)	Peak intensity in absorbance	Band area
−145	3751.4	0.97	6.56
25	3748.2	0.76	6.11
200	3744.7	0.57	6.05
400	3740.6	0.41	5.63

400° temperature range.[7] The parameters derived from a mathematical analysis of closely overlapping band systems depend very much on the type of function used and on the number of components assumed. Therefore, it is doubtful that their calculated band parameters are unique and certainly without stating some measure of the error of their fit, they are at best a rough guide.

As an illustration of the above point, we have carried out band-fitting analysis of our own spectra, using a Lorentzian-Gaussian sum function and a Lorentzian-Gaussian product function.[6] Since there is a tail to low wave number of the main band, we tried to fit the spectra to a two-component curve (one strong band at the peak position and one weak band in the region of the tail) and to a three-component curve (one strong band with two weak bands in the tail). Figures 2B and 3B show the plotted results for the two band sum function and Figures 2C and 3C show the results for a three-band product function. The data obtained from the use of these functions are collected in Table II. In all cases we consider that a good fit was obtained when the discrepancies were 0.01 or less, this particular value being satisfactory for a very intense narrow band where errors are likely to be large where the band rises most steeply (hence DIS is greater with the low-temperature spectra). The values of the parameters by which we judged the accuracy of a particular fit for the functions used in Figures 2 and 3, and for two other trial functions, are shown in Table III. DIS is smaller for the three-component curves and we could have improved our

TABLE II: Parameters for the Computed Spectra in Figures 2 and 3

Function and (N)[a]	Temp, °C	Wave number, cm^{-1}	Intensity absorbance	Half-width, cm^{-1}	Shape ratio[b]
S(2)	−145	3750.8	0.84	4.1	0.0
		3746.7	0.38	8.8	1.0
P(3)	−145	3751.2	0.80	3.2	0.54
		3748.5	0.33	6.1	0.70
		3740.8	0.05	17.7	0.99
S(2)	25	3748.0	0.68	4.7	0.11
		3742.7	0.14	11.4	0.88
P(3)	25	3748.2	0.58	4.1	0.55
		3745.4	0.22	8.7	0.70
		3735.1	0.03	23.9	0.99
S(2)	200	3744.5	0.51	5.9	0.29
		3738.5	0.13	13.8	1.0
P(3)	200	3744.7	0.45	5.5	0.64
		3741.0	0.15	12.1	0.69
		3730.8	0.02	33.9	0.99
S(2)	400	3740.7	0.36	7.8	0.38
		3733.6	0.10	15.7	0.52
P(3)	400	3741.2	0.30	7.2	0.79
		3738.1	0.11	9.3	0.41
		3730.7	0.06	22.6	0.99

[a] S denotes the Lorentzian-Gaussian sum function and P denotes the L-G product function. The number in parentheses is the number of components which were fitted. [b] The shape ratio is the fraction of Lorentzian character in a given band.

fit by increasing the number of components, but this is meaningless for curves where no distinct shoulders are apparent. We could also have obtained a satisfactory fit with a weak high wave number band, since any true Lorentzian or Gaussian band can be decomposed into as many components as desired.

We consider that the two-band fit in itself is not significant because the tail to lower wave number is probably just the manifestation of intramolecular perturbations which are bound to be present in a sample of this type

TABLE III: Computed Parameters which Reflect the Accuracy of Some Trial Functions

Function and (N)[a]	Temp, °C	DIS[b]	WFM[b]	MAX[b]
S(2)	−145	0.014	3747.0	0.039
P(2)	−145	0.014	3752.2	0.033
S(3)	−145	0.009	3745.2	0.021
P(3)	−145	0.004	3752.2	0.013
S(2)	25	0.010	3749.2	0.038
P(2)	25	0.010	3746.8	0.031
S(3)	25	0.008	3749.4	0.021
P(3)	25	0.005	3746.8	0.014
S(2)	200	0.007	3749.0	0.016
P(2)	200	0.006	3766.4	0.014
S(3)	200	0.006	3751.6	0.016
P(3)	200	0.003	3749.8	0.008
S(2)	400	0.005	3742.4	0.016
P(2)	400	0.005	3742.6	0.015
S(3)	400	0.007	3765.4	0.015
P(3)	400	0.003	3751.4	0.008

[a] See footnote a, Table II. [b] See Experimental Section for description of these terms.

where the minute silica particles are in intimate and random contact with their neighbors. This view has been discussed by Hambleton, *et al.*,[8] and has been expressed by Van Cauwelaert, *et al.*[1] Further, no significance is to be attached to the shape ratios listed in Table II. Our band fitting programs vary the shape ratio so as to obtain a best fit, and one may note that for the product function our shape ratios are near those used by Van Cauwelaert, *et al.*,[1] whereas for the sum function, the main band was always given a high Gaussian character, and the bands in the tail, a Lorentzian profile. The latter is not unexpected when an intense band is degraded to one side as in our case, since for equal height and area, a Gaussian function has a greater breadth near the peak.[7b] Nor is a Gaussian profile unexpected for very narrow intense absorption bands because the instrumental distortion factors essentially introduce a Gaussian perturbation on the true band shape.[7b] Therefore, as the half-band width approaches the spectral slit width (particularly true at low temperatures) then it is to be expected that the Gaussian contribution to an experimentally obtained profile will increase.

Our spectra for deuterated silica in the SiOD stretching region (2760 cm^{-1}) were the same as those reported by Van Cauwelaert, *et al.*[1] These were fitted by the latter to a two-band component curve. We also obtained spectra of mixed isotopic species by partially deuterating the sample and again, an excellent two or three band fit to the experimental data could be achieved.

Discussion

As a result of this investigation, the following observations have been made concerning the infrared spectrum of the isolated hydroxyl groups on highly dehydroxylated silica: (1) the spectral band profiles attributable to isolated surface OH or OD groups are similar, (2) no distinct shoulders appear in the SiOH band profile as the temperature is changes, (3) both the SiOH and the SiOD band are slightly asymmetric to the low wave number side of the main band, and (4) both the SiOH and the SiOD spectra can be fitted using band-fitting techniques to a two- or a three-component curve, as can the spectra of the mixed isotopic species. In conclusion, there is no spectroscopic

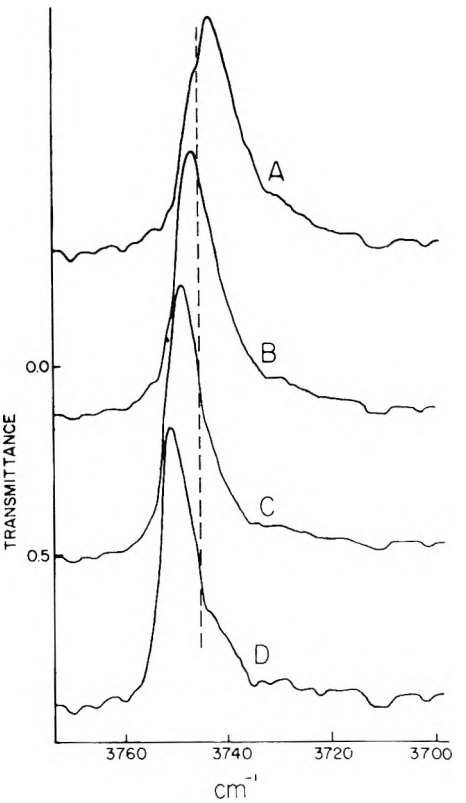

Figure 4. Experimental spectra of the SiOH band with an uncompensated cell: A, 400°; B, 200°; C, 25°; D, −145°. The scan speed used was 20 cm^{-1}/min and the peak positions are slightly shifted relative to the slower scans used for Figures 2 and 3. The dashed line corresponds to the position of the 3744.5-cm^{-1} band in Figure 1. The transmittance scale applies to spectrum D, the other spectra have been linearly displaced for convenience of presentation.

evidence to suggest that the infrared spectrum of the SiOH groups is in any way different from that of the SiOD groups.

Our failure to detect distinct shoulders in our spectra of the SiOH band on silica is in contradiction to the experimental results of Van Cauwelaert, *et al.*[1] In an attempt to try to duplicate their spectra, we considered the possibility that because gaseous atmospheric water so strongly absorbs in this spectral region, then by intentionally introducing a slight imbalance in the double-beam compensation we might be able to reproduce spectra resembling theirs. The spectra shown in Figure 4 were recorded under conditons in which complete atmospheric compensation was not achieved,(see Experimental Section). These spectra clearly show shoulders on both sides of the main band and it can be seen by comparing the spectra in Figures 4 and 1 that the position of the bands of maximum intensity in the atmospheric water spectrum (or in the uncompensated double-beam spectrum) coincide with the positions of the main shoulders in the spectra shown in Figure 4. A dashed line has been drawn in Figure 4 to indicate the position of the strongest band at 3744.5 cm^{-1}.

In the experimental spectra shown in Figures 2A, 3A, and 4, the peak position shifts to higher wave number, the peak intensity increases, and the band width decreases as the temperature is lowered. Since the positions of the atmospheric water bands do not change with temperature, the shoulders in the uncompensated spectra apparently

(8) F. H. Hambleton, J. A. Hockey, and J. A. G. Taylor, *Trans. Faraday Soc.*, **62**, 801 (1966).

shift with temperature. The spectra in Figure 4 closely resemble those shown by Van Cauwelaert, *et al.*,[1] in their Figure 1, except that the "dips" in our spectra due to improper compensation are quite large. Van Cauwelaert, *et al.*, have assured us in a private communication that, as stated in their paper, their own atmospheric compensation was perfect and that the irregular fluctuations to either side of the main band in their spectra are simply due to random electronic noise.

Van Cauwelaert, *et al.*,[1] also studied the effect on the band shape of adsorbing benzene and triethylamine on silica. With benzene, they reported that the overall band intensity decreased but that the peak position did not change, whereas the peak position changed on adsorbing triethylamine and the relative intensity of the three-components changed. We have also observed these effects, only we found that with an uncompensated spectrometer the relative intensity of the shoulders varied because again, as the peak shifts, the dips due to atmospheric water remained fixed, as they do with temperature changes. With a perfectly compensated spectrometer, no shoulders were observed, although the strong central band decreased in intensity at a faster rate than did the tail to lower wave number. This is not unreasonable since a physically adsorbed species would be expected to interact preferentially with the totally free hydroxyls, as opposed to those which might be perturbed due to intramolecular interactions and hence absorb at slightly lower wave number.

It is difficult to account for the differences in the spectra observed by Van Cauwelaert, *et al.*,[1] and ourselves on chemical grounds. The silica samples used in both investigations were prepared by similar methods and the overall band widths at half-peak height are comparable at each temperature. It is always possible that our samples were quite different owing to different pressures used for preparing disks[9] (Van Cauwelaert, *et al.*, did not state their conditions). The fact that the relative positions of shoulders observed by ourselves do not exactly coincide with theirs is possibly just a manifestation of the sensitivity of the SiOH peak positon to conditions of preparation.[8] Alternatively, this could be due to slight differences in sample temperatures, since the peak position shifts by about $0.20\ cm^{-1}/10°$ change in temperature.

As for the question of the peak shift and changes in band width with temperature, a discussion of this is not warranted here. Such questions are somewhat involved from the theoretical point of view[10] and even for well-ordered systems (gases and crystals) theory and experiment still do not exactly agree.[11] However, peak intensification and band narrowing with decreasing temperature is not unexpected.[12] We have only just started an investigation of the band shape problem for adsorbed species from a theoretical point of view and we will discuss this topic when the work is complete.

Finally, there are two points to be stressed concerning the general use of band-fitting techniques. One is a plea for caution in applying such methods for the "resolution" of overlapping band envelopes. It is most important to indicate one's criteria for a "satisfactory fit," since an infinite number of such fits can be obtained if the permissible discrepance (DIS) is large enough. This is particularly important when the bands are closely overlapping. Secondly, when the spectral slit width approaches the half-band width of any component, the instrumental distortion may determine the nature of the experimentally observed band profile.[7b,12,13] Unless the instrument function is known accurately, such analyses can be subject to error.

Acknowledgment. We are grateful to the National Research Council of Canada and to the Department of National Health and Welfare for financial support for this work. We also wish to thank Dr. R. N. Jones of the National Research Council for many helpful discussions concerning the utility of his band-fitting programs, and Mr. L. W. Thomson for help with the experimental work.

(9) F. H. Hambleton, J. A. Hockey, and J. A. G. Taylor, *Nature (London)*, **208**, 138 (1965).
(10) K. H. Illinger and D. E. Freeman, *J. Mol. Spectrosc.*, **9**, 191 (1962); D. P. Chock, J. Jortner, and S. A. Rice, *J. Chem. Phys.*, **49**, 610, (1968); J. Horiuti and T. Toya, "Solid State Surface Science," Vol. 1, Marcel Dekker, New York, N. Y., 1969, p 43.
(11) J. C. Breeze, C. C. Ferriso, C. B. Ludwig, and W. Malkmus, *J. Chem. Phys.*, **42**, 402 (1965); M. P. Lisitsa and Yu. P. Tsyashchenko, *Opt. Spectrosc.*, **10**, 79 (1961).
(12) D. A. Dows, "Physics and Chemistry of the Organic Solid State," Vol. 1, Interscience, New York, N. Y., 1963, pp 675 and 682.
(13) R. N. Jones, R. Venkataraghavan, and J. W. Hopkins, *Spectrochim. Acta, Part A*, **23**, 925, 941 (1967).

COMMUNICATIONS TO THE EDITOR

A-Type Hydroxyls on Silica Surfaces

Sir: Morrow and Cody have critically examined the hydroxyl band around 3750 cm^{-1} on silica.[1] In contradiction to our earlier work they could not resolve a shoulder on the high-frequency side of the 3750-cm^{-1} band. They consider the possibility that the presence of the shoulder can be due to water absorption in an improperly compensated spectrometer. Therefore we feel obliged to add detailed experimental conditions of our previous work and new data which can help to resolve the conflicting situation.

The drying system of the Beckman IR12 spectrometer is a continuous flow of air from which water and CO_2 are removed by activated alumina. The exit of dry air is through the spectrometer windows in the sample compartment. The stream of air is sufficient to minimize diffusion of wet air in the spectrometer. All the experiments were performed with a sample cell and a reference cell of 12.0-cm pathlength. The sample compartment of the spectrometer was 13 cm long. The force exerted on the silica platelets was 1.3×10^5 kgf.

The extent to which the spectrometer is purged with dry air is shown in Figure 1. Spectrum a shows the single-beam absorption due to residual water. Curve b shows the corresponding double-beam spectrum, the compensating cell being in the reference beam. In both cases, the sample compartment is open to the atmosphere. Curves c and d shown in Figure 1 were obtained with the sample chamber closed and purged to the same extent as the spectrometer. The residual water content is decreased only slightly if the sample compartment is closed and can be balanced out completely after careful tuning of the two beams.

The spectra in Figure 1 are scanned under the same conditions as those of the silica wafers in Figure. 2. The spectral slit was 2 cm^{-1} and the scan speed 3.2 cm^{-1} min^{-1}. The chopper after the sample compartment was stopped to avoid modulation of radiation due to sample emission. In Figure 2, high-temperature spectra of the band around 3750 cm^{-1} on a Degussa Aerosil sample are shown. The extent of purging is the same as shown in Figure 1c. The platelets are 2.5 cm in diameter and were pressed between two stainless steel dies at different pressures for 1 min. The total forces exerted on the silica disks are respectively (a) 5.13×10^5 kgf, (b) 1.30×10^5 kgf, and (c) 1.79×10^3 kgf. The force used in b is the same as the one used in our previous work.[2] The platelets were dehydroxylated at 800° in air for 8 hr. Spectra a and b show clearly a shoulder on the high-frequency side of the 3750-cm^{-1} band. Spectra c for the disks pressed at a much smaller force, do not show the high-frequency shoulder. From the data given by Morrow and Cody, we estimate that the pressure used for making pellets does not exceed 1790 kgf. It should be noted that silica wafers a and b are glassy and transparent for visible radiation, while wafer c is opaque and shows the original white color of the silica powder.

From these new data, it seems that the discrepancy between the two papers[1,2] is certainly not due to improper balance of the spectrometer as claimed by Morrow and Cody,[1] but rather to differences in the pressures exerted on the disks. The possible influence of pressure on the freely vibrating hydroxyls was first studied by McDonald[3] and further investigated by Hambleton, *et al.*[4,5] We can agree with Morrow and Cody that differences in the SiOH peak positions are merely a manifestation of the sensitivity of this peak to conditions of preparation.

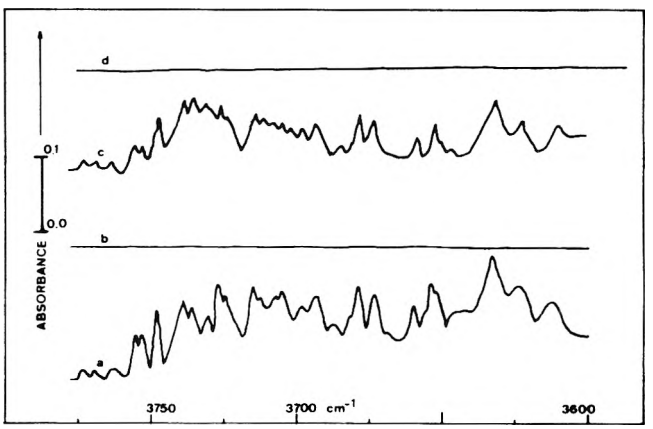

Figure 1. (a) Single-beam spectrum of residual water after a complete purging of the spectrometer; the sample and compensating cell are in the spectrometer and the sample chamber is open to the atmosphere. (b) Double-beam spectrum corresponding to a. (c) Single-beam spectrum of residual water after complete flushing of the sample area both cells being in the spectrometer. (d) Double-beam spectrum corresponding to b.

The decomposition of the 3750-cm^{-1} band was first proposed by Hair and Hertl[6] studying the reactions of chlorosilanes with the surfaces hydroxyls. These authors seem to use pressures of the order of 20.000 lb/in.[2] to get disks that exhibit adequate transmission.[7] It might be possible that their decomposition, although assigned to geminal and single hydroxyls, was also due to these high pressures. It seems, therefore, that we used silica wafers that have undergone sintering to some extent due to the combined effect of the relatively high pressure used in making the pellets and the outgassing at 800°. This is confirmed by water sorption measurements that we carried out on wafers b and c. In a thermobalance platelets of the type b adsorb only 1.59% by weight at 0°. Platelets c adsorb 1.94%. This is also consistent with the difference observed in pre-

(1) B. A. Morrow and I. A. Cody, *J. Phys. Chem.*, **77**, 1465 (1973).
(2) F. H. Wan Cauwelaert, P. A. Jacobs, and J. B. Uytterhoeven, *J. Phys. Chem.*, **76**, 1434 (1972).
(3) R. S. McDonald, *J. Phys. Chem.*, **62**, 1168 (1958).
(4) F. H. Hambleton, J. A. Hockey, and J. A. G. Taylor, *Nature (London)*, **208**, 138 (1965).
(5) F. H. Hambleton, J. A. Hockey, and J. A. G. Taylor, *Trans. Faraday Soc.*, **62**, 801 (1966).
(6) M. L. Hair and W. Hertl, *J. Phys. Chem.*, **73**, 2372 (1969).
(7) M. L. Hair, "Infrared Spectroscopy Surface Chemistry," Marcel Dekker, New York, N. Y., 1967, p 68.

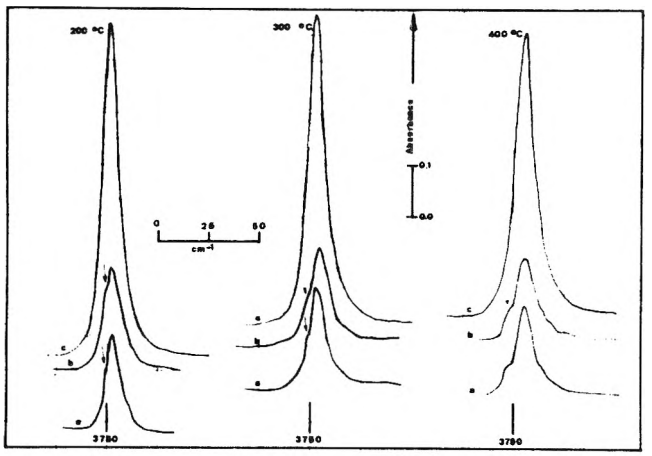

Figure 2. High-temperature spectra of the 3750-cm^{-1} band after outgassing at 800° for 8 hr. The pressure on the platelet is (a) 5.13 × 10^5 kgf, (b) 1.30 × 10^5 kgf, and (c) 1.79 × 10^3 kgf.

vious work between the spectroscopic and volumetric adsorption isotherm (ref 2, Figures 3 and 4). Indeed, the spectroscopic isotherm was carried out on type b samples, the volumetric isotherm on powder that has not been pressed previously.

The presence of two shoulders on the main band in the original work[2] led us to the use of a curve resolver to break down the spectra into three components, the number of the components and their shape being constant. Although some of our assumptions (constant band shape for all temperatures and all components) can be questionable, the procedure is very helpful for a deeper understanding of the spectral changes that have been observed, at least on a semiquantitative basis.

Acknowledgment: P. A. J. acknowledges financial support by N.F.W.O. Belgium.

Centrum voor Oppervlaktescheilunde en Colloidale Scheikunde
De Croylaan 42
B-3030 Heverlee, Belgium

F. H. Van Cauwelaert*
P. A. Jacobs
J. B. Uytterhoeven

Received February 27, 1973

Fluidity and Liquid Structure

Sir: Hildebrand[1] published a paper in 1971 on "Motions of Molecules in Liquids: Viscosity and Diffusivity" in which he altered an equation for the viscosity of unassociated liquids published by Batschinski[2] in 1913

$$\eta = c/(v - \omega) \quad (1)$$

c is a constant for each liquid, v is specific volume, ω is similar to the van der Waals b. Hildebrand reasoned that fluidity, $\phi = 1/\eta$, should be a linear function of the ratio of intermolecular volume to the volume, V_0, at which, as temperature decreases, molecules become too closely crowded to permit either free flow or self-diffusion; he wrote

$$\phi = B(V - V_0)/V_0 \quad (2)$$

B is a constant whose value depends upon capacity of the molecules to absorb momentum because of their mass, flexibility, or inertia of rotation. Plots of ϕ against V showed straight lines over long ranges of temperature. Extrapolation to $\phi = 0$ gives values of V_0, and slopes give B/V_0. Hildebrand and Lamoreaux[3] later gave values of B and V_0 for scores of liquids; they showed that the equation holds for propane for pressures up to 544 atm, that V_0 values are fixed fractions of critical volumes, and that plotted lines can remain straight nearly to critical temperatures.

Early in 1972 Eicher and Zwolinski[4] published a paper titled "Limitations of the Batschinski-Hildebrand Shear Viscosity Equation." On the basis of a "least-squares analysis" they asserted, "It can be seen that the simple form of eq 1 or eq 2 will not satisfactorily represent the experimental data for the four substances, *n*-hexane, *n*-decane, *n*-heptadecane, or 1-propanol over reasonable temperature ranges, within experimental uncertainties."

The question thus raised is far more important than merely one of fitting experimental data; equations of very different kinds can be tailored to fit the same data by introducing adjustable, nonoperational parameters. The basic question is whether a very simple equation, based upon the concept of molecular chaos implicit in the van der Waals equation, is adequate for dealing with transport processes in liquids, or whether it is necessary to imagine the presence of "solid-like" structures. Our objective in studying viscosity has been to compare the validity of different concepts of the liquid state.

Let us see whether the conclusion that Eicher and Zwolinski have drawn from their mean squares calculation is correct. In Figure 1 the data for *n*-hexane by Giller and Drickamer[5] are plotted as ϕ against V. We see that the four upper points, between −60 and 20°, surely "a reasonable range," fall on a straight line. The nine divergent points at the bottom, close to the freezing point −95.3°, lie between −90.3 and −98.5°. Eicher and Zwolenski must have given all points equal weight. In doing this they overlooked what Giller and Drickamer wrote about these points.

"There is a small but consistent increase in [free energy of activation] for each compound near the freezing point, which would represent the increased activation energy necessary because of a certain degree of order developing in the liquid." This sort of divergence in a region of high viscosity is usual with substances whose molecules are so unsymmetrical that they do not gain full freedom of motion till the liquid has expanded a little more after melting. Magill and Ubbelohde[6] showed that this effect can be increased by using species such as tridiphenylmethane. We found it with $(C_4F_9)_3N$ but never with monatomic molecular species.

The second liquid they offer as evidence against eq 2 is *n*-heptadecane, from measurements by Doolittle and Peterson.[7] The plot in Figure 2 shows a straight line from ~0.8 to 6 cP^{-1}, and points diverging near the lower end as in Figure 1.

(1) J. H. Hildebrand, *Science*, **174**, 490 (1971).
(2) A. J. Batschinski, *Z. Phys. Chem.*, **84**, 643 (1913).
(3) J. H. Hildebrand and R. H. Lamoreaux, *Proc. Nat. Acad. Sci. U. S.*, **69**, 3428 (1972).
(4) L. D. Eicher and B. J. Zwolinski, *Science*, **177**, 369 (1972).
(5) F. G. Giller and H. G. Drickamer, *Ind. Eng. Chem.*, **41**, 2067 (1949).
(6) J. H. Magill and A. H. Ubbelohde, *Trans. Faraday Soc.*, **54**, 1811 (1958).
(7) A. K. Doolittle and R. H. Peterson, *J. Amer. Chem. Soc.*, **73**, 2145 (1951).

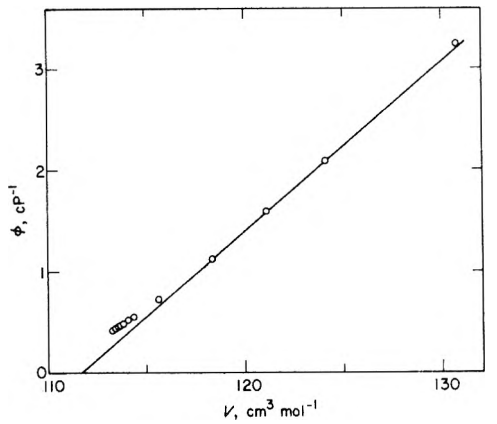

Figure 1. Fluidity against molal volume of *n*-hexane, showing divergence near melting point.

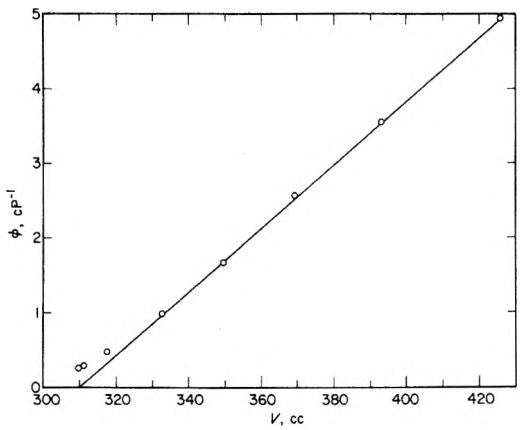

Figure 2. Fluidity against molal volume for *n*-heptadecane.

TABLE I: Constancy of $\phi/(V - 184.0)$ at 171° up to High Pressures for *n*-Decane

P, atm	ϕ, cP^{-1}	*V*, cm^3	$\phi/(V - V_0)$
13.6	4.725	232.2	0.0098
27.2	4.640	231.0	0.0099
54.4	4.505	229.9	0.0098
68.0	4.264	227.9	0.0097
204.0	3.450	220.4	0.0095
340.0	2.989	214.8	0.0097
408.0	2.801	212.3	0.0099

Their third liquid is *n*-decane, whose viscosity was measured by Lee and Ellington[8] over ranges of 250° and 408 atm. At 1 atm, the plot is quite like those for *n*-C_6H_{14} and *n*-$C_{17}H_{36}$. To test the applicability of eq 2 at different pressures, we give in Table I values of $\phi/(V - V_0)$ at 171° and seven pressures up to 408 atm: V_0 = 184 cm^3. The virtual constancy of the ratio shows that fluidity is uniquely determined by values of $V - V_0$, irrespective of whether changes in volume result from changes of temperature or of pressure.

Their fourth example is an alcohol, an associated liquid, and therefore not pertinent to the validity of eq 2.

It has been asserted that viscosity is not a function of liquid volume alone, that it decreases with increasing temperature at constant volume. We reply by referring to Figure 3 of ref 3 and the accompanying discussion, where variations of *V* for C_3H_8 and CO_2 are shown from V_0 to

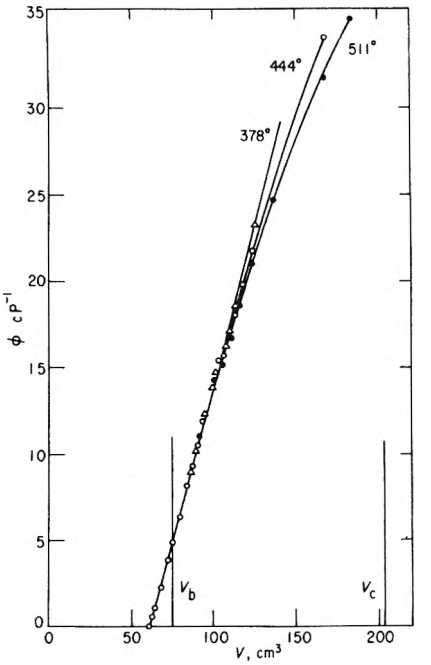

Figure 3. Values of ϕ against *V* for propane from V_0 to V_c.

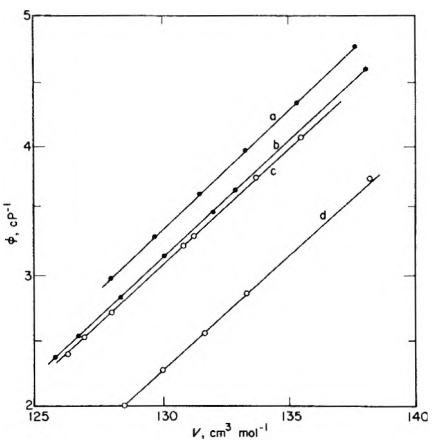

Figure 4. Linearity of $\phi/(V - V_0)$ for five isomeric hexanes.

1000 cm^3. We reproduce here in Figure 3 a plot of fluidity against molal volume of propane from V_0 to its critical volume, V_c, using data by Starling, Eakin, and Ellington[9] obtained at 378, 444, and 511°K, and at pressures up to 544 atm.

The points for ϕ from 0 to 5 cP^{-1} are at 1 atm, and below the boiling point, the usual range of viscosity data.

The points for ϕ from 5 to about 18 cP^{-1} were determined at various values of pressure and temperature within the range stated above. It can be seen that values of ϕ over this enormous range depend upon values of *V* only. As *V* increases further, however, the single line splits increasingly into three, with fluidity at any value of *V* largest at the *lowest* temperature; in other words, viscosity *increases* with temperature.

As we explained in ref 3, mean free paths at boiling points are very much shorter than molecular diameters. In the case of propane, $(V_b - V_0)/V_0$ is only 0.23. At its critical point, V_c = 203.2 and the fractional expansion is 2.32,

(8) A. L. Lee and R. T. Ellington, *J. Chem. Eng. Data*, **10**, 346 (1965).
(9) K. E. Starling, B. E. Eakin, and R. T. Ellington, *AIChE J.*, **6**, 438 (1960).

TABLE II: Evidence for Strict Linearity of the Line for 2-$CH_3C_5H_{11}$ in Figure 3

V, cm^3 mol^{-1}	ϕ, cP^{-1}	$\phi/(V - 113.0)$
126.27	2.447	0.1814
126.92	2.528	0.1816
128.03	2.723	0.1812
130.85	3.236	0.1813
131.27	3.308	0.1815
133.82	3.771	0.1811
135.48	4.070	0.1810

where molecules can acquire some momentum between collisions. We have explained that the parameter, B, of eq 2, depends upon the capacity of the species to resist externally imposed momentum by reason of mass, softness, or rotational inertia, or their own thermal momentum, which is, for molecules in free space, $(3mkT)^{1/2}$. This is approached as length of mean free paths increases.

We turn finally to data on five isomeric hexanes measured by Eicher and Zwolinski[10] themselves. Their figures for viscosity and density at different temperatures yield the values of ϕ and V plotted in Figure 4. All points fall on straight lines except one, which is off by only 0.3 cP^{-1}. The excellence of the fit we illustrate in Table II for 2-$CH_3C_5H_{11}$, whose line is the longest of all. The intercept gives V_0 = 113.0 cm^3. The ratios in the last column show that the line is even straighter than could be inferred from a good plot.

We summarize the foregoing evidence by asserting that (a) the data are accurate, (b) they all conform closely with eq 2, (c) the concept of molecular chaos that served as foundation for it is adequate, and that no highly structured model of the liquid state is required for dealing with transport processes.

Acknowledgment. Acknowledgment is made to the donors of The Petroleum Research Fund, administered by the American Chemical Society, for support of this research.

(10) L. D. Eicher and B. J. Zwolinski, *J. Phys. Chem.*, **76**, 3295 (1972).

Department of Chemistry
University of California
Berkeley, California 94720

J. H. Hildebrand*
R. H. Lamoreaux

Received December 6, 1972

Infrared Frequency Shifts Due to Hydrogen Bonding of Surface Amino Groups on Silica

Sir: There have been numerous H-bonding studies of hydroxylic compounds by means of infrared spectroscopy.[1] The occurrence of H bonding is observed as a perturbation of the free OH stretching vibration band to a lower frequency and an increase in the integrated intensity of the perturbed band. Often, more fundamental information can be obtained in the absence of interfering solvent effects by observing the H-bonding interactions between surface hydroxyl groups and various gaseous adsorbates which form H bonds with these hydroxyl groups. Surface silanol groups have been extensively studied for this purpose. Attempts have been to correlate the observed frequency shifts with polarizability,[2] quadrupole moment,[3] ionization potential,[4-6] and heat of adsorption.[5,7] To a much lesser extent, the H-bonding behavior of other surface M-OH groups has been studied.[8,9] Despite the number of studies, there is still controversy concerning the origin, and thus the quantitative treatment, of the hydroxyl band frequency shifts. Less attention has been paid to H-bonding interactions involving -NH groups[10] and apparently no studies have been carried out in the absence of solvents. With a view to determining if the H-bonding behavior of surface -NH groups shows any essential difference from the behavior of surface -OH groups, the frequency shifts of the free -NH group band were measured when various gaseous adsorbates interacted with these groups.

A silica surface can be covered with amino groups.[11,12] Peri[12] reacted CCl_4 with surface silanol groups above 350° and obtained a surface covered with Si-Cl groups. At these temperatures NH_3 reacts with the Si-Cl groups leaving Si-NH_2 groups on the surface, and NH_4Cl sublimes to cooler parts of the vacuum system. Such an aminated surface was prepared, using pressed silica (Cab-O-Sil, Cabot Co., Boston, Mass.) disks.

A compensated infrared cell for holding sample disks, equipped with a side arm, was connected to a vacuum rack. The silica disk, preheated to 800° in air, was placed in the side arm, around which a furnace was mounted. The silica was treated with CCl_4 vapor at 420° for 15 min, evacuated, and then treated with NH_3. Deposited NH_4Cl was observed on the cooler parts of the side arm after this procedure. By tipping the cell, the silica disk dropped from the side arm into the infrared cell. The spectra were recorded on a Perkin-Elmer Model 621 infrared spectrophotometer.

Bands due to the surface amino groups are observed at 3444(s), 3530(w), and 1555(s) cm^{-1}, which arise from the symmetrical stretching, asymmetrical stretching,[11] and bending frequencies, respectively. The band due to the free OH stretching frequency at 3747 cm^{-1}, present before reaction, is completely absent.

When various gases are admitted to the aminated sample at 30° the NH bands are perturbed, due to the hydrogen bonding interaction. Very dry adsorbate gases are necessary, since even traces of moisture result in rapid hydrolysis of the Si-N bond to produce Si-OH groups. Some typical spectra are given in Figure 1. The frequency shift due to the perturbation of the 3444-cm^{-1} symmetrical NH stretching band is readily measured. The 3530-cm^{-1} asymmetrical NH stretching band is low and broad, and for most of the adsorbates the perturbed band was also too broad to obtain an exact measure of the frequency shift. The perturbations of this asymmetrical NH band

(1) G. C. Pimentel and A. L. McClellan, "The Hydrogen Bond," W. H. Freeman, San Francisco, Calif., 1960.
(2) R. S. McDonald, *J. Amer. Chem. Soc.*, **79**, 850 (1957).
(3) G. J. C. Fromsdorff and G. L. Kington, *Trans. Faraday Soc.*, **55**, 1173 (1959).
(4) M. R. Basila, *J. Chem. Phys.*, **35**, 1151 (1961).
(5) W. Hertl and M. L. Hair, *J. Phys. Chem.*, **72**, 4676 (1968).
(6) F. H. VanCauwelaert, J. B. VanAssche, and J. B. Uytterhoeven, *J. Phys. Chem.*, **74**, 4329 (1970).
(7) G. A. Galkin, A. V. Kiselev, and V. I. Lygin, *Russ. J. Phys. Chem.*, **41**, 20 (1967).
(8) M. L. Hair and W. Hertl, *J. Phys. Chem.*, **74**, 91 (1970).
(9) J. A. Cusumano and M. J. D. Low, *J. Phys. Chem.*, **74**, 1950 (1970).
(10) S. Mukherjee, S. R. Palit, and S. K. De, *J. Phys. Chem.*, **75**, 2404 (1971).
(11) M. Folman, *Trans. Faraday Soc.*, **57**, 2000 (1961).
(12) J. B. Peri, *J. Phys. Chem.*, **70**, 2937 (1966).

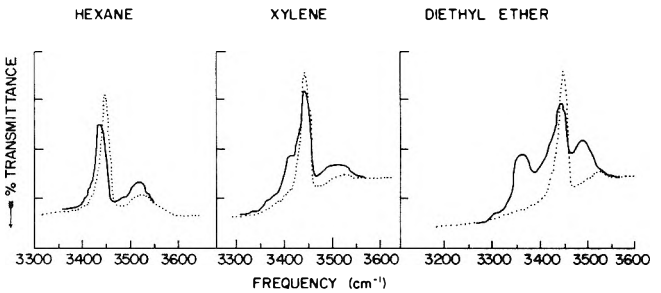

Figure 1. Spectra of amino groups on silica *in vacuo* (dotted line) and in the presence of gas (solid line): 80 Torr of hexane, 6 Torr of *p*-xylene, 100 Torr of diethyl ether.

appeared to parallel those of the symmetrical NH band, with approximately, but not the same, frequency shifts. On the aminated samples obtained by Peri, who used a silica aerogel, and by Folman, who used porous Vycor glass, the unperturbed asymmetrical NH band was much better defined than on the silica used here.

The NH bending frequency at 1555 cm^{-1} was also perturbed in the presence of the adsorbates, and was observed as a decrease in the intensity of the band. The decrease in peak extinction due to the hydrogen bonding was approximately that observed with the symmetrical stretching frequency band. No bands were observed which could be identified as being due to a perturbed NH band. The only bands observed were the CH bending frequencies below 1500 cm^{-1} due to the adsorbed molecules. Below about 1400 cm^{-1} no observations are possible due to the strong Si–O stretching bands which obscure the spectrum.

For a given pressure of ambient gas, a smaller fraction of the NH groups is perturbed than are the Si–OH groups, indicating a weaker interaction. As with silanol groups, the integrated intensity of the perturbed band is much greater than the integrated intensity of the free band. This is generally ascribed to an enhancement of the dipole moment.

The observed frequency shifts of the symmetrical NH stretching band are given in Table I, together with the corresponding frequency shifts observed with silanol groups. The relationship between the two shifts is roughly linear, although there is scatter in the points. The amine

TABLE I: Observed Frequency Shifts (in cm^{-1}) of Surface NH (3444 cm^{-1}) and OH (3747 cm^{-1}) Stretching Bands for Various Adsorbates

Adsorbate	$\Delta\nu_{NH}$[a]	$\Delta\nu_{OH}$
Carbon tetrachloride	7	45
n-Pentane	8	45
n-Hexane	11	30
Carbon disulfide	14	60
Trichloroethylene	18	60
Dichloroethylene	19	95
Bromobenzene	24	95
Trimethylchlorosilane	24	135
Nitrobenzene	25	112
Methyl iodide	28	125
Benzene	30	120
p-Xylene	35	155
Acetaldehyde	46	280
Methyl ethyl ketone	67 ± 3	360
Diethyl ether	89 ± 3	460
Triethylamine	198 ± 5	975

[a] The estimated experimental accuracy of the NH frequency shifts is ±2 cm^{-1}, unless otherwise indicated.

band shifts are about one-fifth as great as the hydroxyl band shifts. A least-mean-squares analysis of the data, with the standard deviations, gives a line with an intercept of 1.46 ± 1.50 and a slope of 0.197 ± 0.005.

The roughly linear relationship suggests that the H-bonding interactions which occur on these NH groups arise from the same types of interactions which give rise to the shifts observed with OH groups. However, more extensive data of this type would be valuable in order to test the various correlations which have been proposed to explain frequency shifts.

(13) Present address, Research and Development Laboratories, Corning Glass Works, Corning, N. Y. 14830.

Departamento de Química
Facultad de Ciencias
Universidad de los Andes
Mérida, Venezuela

William Hertl[13]

Received January 2, 1973

Journal of Chemical and Engineering Data

APRIL 1973, Vol. 18, No. 2

TABLE OF CONTENTS

From the borders of organic chemistry . . . To the borders of theoretical physics:

Inorganic Chemistry brings you a broad range of authoritative information presenting both experimental and theoretical studies in all phases of inorganic chemistry.

Each month, this rapidly growing journal brings you the data you need on synthesis and properties of new compounds, quantitative studies regarding structure, and thermodynamics of inorganic reactions.

When you've seen the 50 or more papers offered in each issue, you'll also want to look through the Notes and Correspondence sections for their concise exchange of scientific views and ideas.

To order INORGANIC CHEMISTRY today, just complete and return the form below.

. . *another ACS service*

Inorganic Chemistry

Inorganic Chemistry
American Chemical Society
1155 Sixteenth Street, N.W.
Washington, D.C. 20036

Yes, I would like to receive INORGANIC CHEMISTRY at the one-year rate checked below:

	U.S.	*Canada*	*Latin America*	*Other Nations*
ACS Member Personal-Use One-Year Rate	☐ $18.00	☐ $22.00	☐ $22.00	☐ $23.00
Nonmember	☐ $54.00	☐ $58.00	☐ $58.00	☐ $59.00

Bill me ☐ Bill company ☐ Payment enclosed ☐

Name _____

Street _____ Home ☐ Business ☐

City _____ State _____ Zip _____

P-73

INVALUABLE INFORMATIVE IN DEMAND

these internationally respected, basic research journals of The American Chemical Society

The Journal of Physical Chemistry

*ACS Members:	Nonmembers:
U.S. $20.00	U.S. $60.00
Canada, PUAS $25.00	Canada, PUAS $65.00
Other Nations $26.00	Other Nations $66.00

The Journal of Chemical and Engineering Data

*ACS Members:	Nonmembers:
U.S. $15.00	U.S. $45.00
Canada, PUAS $18.00	Canada, PUAS $48.00
Other Nations $18.50	Other Nations $48.50

Biochemistry

*ACS Members:	Nonmembers:
U.S. $20.00	U.S. $60.00
Canada, PUAS $25.00	Canada, PUAS $65.00
Other Nations $26.00	Other Nations $66.00

Inorganic Chemistry

*ACS Members:	Nonmembers:
U.S. $18.00	U.S. $54.00
Canada, PUAS $22.00	Canada, PUAS $58.00
Other Nations $23.00	Other Nations $59.00

The Journal of the American Chemical Society

*ACS Members:	Nonmembers:
U.S. $22.00	U.S. $66.00
Canada, PUAS $27.00	Canada, PUAS $71.00
Other Nations $28.00	Other Nations $72.00

The Journal of Agricultural and Food Chemistry

*ACS Members:	Nonmembers:
U.S. $10.00	U.S. $30.00
Canada, PUAS $13.50	Canada, PUAS $33.50
Other Nations $14.00	Other Nations $34.00

Macromolecules

*ACS Members:	Nonmembers:
U.S. $12.00	U.S. $36.00
Canada, PUAS $15.50	Canada, PUAS $39.50
Other Nations $16.00	Other Nations $40.00

The Journal of Organic Chemistry

*ACS Members:	Nonmembers:
U.S. $20.00	U.S. $60.00
Canada, PUAS $25.00	Canada, PUAS $65.00
Other Nations $26.00	Other Nations $66.00

The Journal of Medicinal Chemistry

*ACS Members:	Nonmembers:
U.S. $15.00	U.S. $45.00
Canada, PUAS $19.00	Canada, PUAS $49.00
Other Nations $20.00	Other Nations $50.00

Analytical Chemistry

*ACS Members:	Nonmembers:
U.S. $5.00	U.S. $7.00
Canada, PUAS $9.00	Canada $11.00
Other Nations $10.00	PUAS $19.00
	Other Nations $20.00

American Chemical Society
1155 Sixteenth Street, N.W. Washington, D.C. 20036

name _____ position _____

address _____

city _____ state/country _____ zip _____

your company _____ nature of company's business _____

*NOTE: Subscriptions at ACS member rates are for personal use only

☐ I am an ACS member ☐ I am not an ACS member ☐ Bill me for $_____

☐ Payment enclosed (*payable to American Chemical Society*) in the amount of $_____. Payment must be made in U.S. currency, by international money order, UNESCO coupons, or U.S. bank draft, or order through your book dealer

Please enter a one year subscription for the following journals:

- ☐ The Journal of the American Chemical Society
- ☐ The Journal of Organic Chemistry
- ☐ The Journal of Physical Chemistry
- ☐ Biochemistry
- ☐ The Journal of Agricultural and Food Chemistry
- ☐ The Journal of Medicinal Chemistry
- ☐ The Journal of Chemical and Engineering Data
- ☐ Inorganic Chemistry
- ☐ Macromolecules
- ☐ Analytical Chemistry

444x

24 a.m. 2516